

Summary Report

CONCEPTUAL DESIGN OF A SPACECRAFT FOR THE HIGH ENERGY ASTRONOMY OBSERVATORY (HEAO) MISSION C

Edited by J. M. Duffie

November 1970



FACILITY FORM 602	N71-15318	(ACCESSION NUMBER)		(THRU)
	542	(PAGES)	63	(CODE)
	CR-102982	(NASA CR OR TMX OR AD NUMBER)	31	(CATEGORY)

 **TELEDYNE**
BROWN ENGINEERING

Research Park • Huntsville, Alabama 35807

Reproduced by
**NATIONAL TECHNICAL
INFORMATION SERVICE**
Springfield, Va. 22151


REF ID: A66000		PUB. DATE NOV. 1970		ACCESSION NO.	
CONTRACT NO. (S) NAS8-26003		REPORT TYPE CE-MSEP-1257			
		PERIOD <i>Season and Report</i>			
SOURCE TELEDYNE BROWN ENG.		AUTHOR (S) J M DUFFIE		TEMPORARY NO 71-00071	
TITLE: CONCEPTUAL DESIGN OF A SPACECRAFT FOR THE HIGH ENERGY ASTRONOMY OBSERVATORY HEAD MISSION C			SECURITY CLASS U <input checked="" type="checkbox"/> CRD <input type="checkbox"/> C <input type="checkbox"/> SRD <input type="checkbox"/> S <input type="checkbox"/>		DRF BLANKET <input type="checkbox"/>
AD	CR 102982	TMX		ATTACHED <input type="checkbox"/>	
PB	LOAN	YES <input type="checkbox"/>	DATE	REQUESTED <input type="checkbox"/> 12.14	
NO. COPIES 2	NO <input checked="" type="checkbox"/>	12.14		DATE	
PLEASE COMPLETE REVERSE SIDE OF THIS FORM <i>Marshall</i>					
				RETURNED <input checked="" type="checkbox"/> 1.25 DATE	


This document has been dup-checked against a minimum of three of the following Facility records:

REPORT NO. AUTHOR SOURCE
CONTRACT NO. TITLE OTHER _____
INITIALS OF DUP-CHECK CLERK _____

SUMMARY REPORT
SE-MSFC-1257

Δ

CONCEPTUAL DESIGN OF A SPACECRAFT FOR THE
HIGH ENERGY ASTRONOMY OBSERVATORY (HEAO) MISSION C 

 Edited By

J. M. Duffie

November 1970

Prepared For

MISSION AND PAYLOAD PLANNING OFFICE
PROGRAM DEVELOPMENT
GEORGE C. MARSHALL SPACE FLIGHT CENTER
HUNTSVILLE, ALABAMA

Contract No. NAS8-26003

Prepared By

RESEARCH AND ENGINEERING DEPARTMENT
SCIENCE AND ENGINEERING DIVISION
TELEDYNE BROWN ENGINEERING
HUNTSVILLE, ALABAMA


ABSTRACT

A conceptual design has been made for the High Energy Astronomy Observatory (HEAO) Mission C spacecraft and its major systems, including structural, attitude sensing, attitude control, thermal control, electrical power, communications, and data handling. The spacecraft and system requirements are based upon a candidate list of experiments consisting primarily of two grazing incidence X-ray telescopes and their associated detectors. Both the mirrors and detectors are mounted to an optical bench which is contained within the spacecraft and which must be controlled thermally within narrow limits.

The mission duration is one to two years in a 300-nautical mile, circular, 35-degree inclination, Earth orbit. Attitude control is provided by control moment gyros (CMGs). Momentum saturation of the CMGs is prevented by the use of magnetic torquers which react with the geomagnetic field to produce desaturating torques on the spacecraft. Thermal control of the optical bench is achieved by insulating the bench from the spacecraft and choosing a thermal filter of proper design which both prevents unwanted solar heat from entering the telescope and also controls the heat emitted from the telescope to space.

Spacecraft ground contact will be limited to data dumps, clock updates, and relatively infrequent ground control commands. Both STADAN and MSFN ground stations will be used.

Approved:


Harry C. Crews, Jr.
Manager
Advanced Systems

Approved:



J. E. White, Jr.
Deputy Director
Science and Engineering Division

TABLE OF CONTENTS

	Page
1. INTRODUCTION	1-1
Mission Description	1-1
Spacecraft Coordinate Axes System	1-2
Study Guidelines.	1-2
Acknowledgements	1-6
2. EXPERIMENTS	2-1
Alignment and Pointing Requirements	2-6
Observational Requirements.	2-6
Observation Program	2-7
Number of Sources	2-9
Typical Day's Observations	2-12
Experiment Control and Data Management System	2-14
Radiation Tolerance	2-20
Magnetic Field Tolerance	2-21
Thermal Control Requirements.	2-24
3. SPACECRAFT DESCRIPTION	3-1
Configuration.	3-1
Spacecraft Systems.	3-1
Communications and Data Handling	3 6
Missions B and D System Interfaces and Flight Differences	3-11

TABLE OF CONTENTS - Continued

	Page
4. SPACECRAFT STRUCTURE	4-1
Vibration Mounts	4-5
Thermal Deflection.	4-7
Structural Design	4-15
Bending and Shear Stiffness Distributions	4-19
Base Ring Design	4-19
Skin Panel Design	4-30
Total Structure Weight	4-42
Meteoroid Penetrations	4-44
Conclusions	4-45
5. ATTITUDE SENSING SYSTEM	5-1
Summary of System Operation	5-4
Star Tracker Field of View and Sensitivity	5-14
HEAO-C Star Tracker.	5-44
Star Mapper Attitude Sensing System.	5-46
Television Aspect System	5-49
Comparison of Alternative Systems	5-60
6. ATTITUDE CONTROL SYSTEM.	6-1
Disturbance Torques	6-4
Survey of Attitude Control Systems	6-6

TABLE OF CONTENTS - Continued

	Page
Momentum Storage Devices	6-9
System Capacity Requirements	6-11
Reaction Wheel Sizing	6-16
Control Moment Gyro Sizing	6-18
Comparison of Wheels and CMG Configurations	6-25
Availability of Suitable Hardware	6-27
Desaturation of Momentum Storage Devices	6-29
Magnetic Torquer Sizing	6-29
Availability of Suitable Hardware	6-37
Computer Simulation.	6-38
Summary of System Operation	6-41
CMG Control Loop Components	6-44
Reference Gyros	6-44
Signal Processor	6-47
Control Moment Gyros	6-52
Spacecraft Dynamics Simulation	6-65
Basic Equations	6-65
Simulation Results	6-70
Acquisition Mode	6-90
Slewing Mode.	6-94
The Slew Maneuver	6-95
Slewing Errors	6-100
Additional Considerations	6-108
Gas Thrustor System	6-110
System Design.	6-110
Use in Slewing Mode.	6-121

TABLE OF CONTENTS - Continued

	Page
HEAO- B and -D Missions	6-123
Attitude Control Requirements	6-123
Orbits and Mass Characteristics.	6-123
Suitability of Mission A System for B and D Missions.	6-124
7. THERMAL CONTROL ANALYSIS	7-1
Thermal Design Requirements	7-3
Optical Bench	7-3
Spacecraft Structure.	7-7
Experiments and Subsystems	7-7
Analytical Approach	7-12
Determination of Environmental Heat Rates	7-12
Evaluation of Spacecraft Temperature Response.	7-16
Discussion of Results	7-25
Spacecraft Oriented Broadside to Sun	7-25
Spacecraft Axis Inclined 15 Degrees Toward the Sun	7-38
Spacecraft Axis Inclined 30 Degrees Toward the Sun	7-42
Thermal Control of HEAO- B and HEAO-D Spacecraft.	7-49
HEAO- B Mission	7-50
HEAO- D Mission	7-58
Conclusions	7-60
8. ELECTRICAL POWER SYSTEM	8-1

TABLE OF CONTENTS - Continued

	Page
Design Requirements	8-1
Electrical Power Load Requirement	8-1
Other Design Requirements	8-9
Design Approach	8-10
Solar Cell Module Approach	8-10
Radioisotope Thermoelectric Generator Approach	8-12
Specific Solar Cell Module System Design	8-14
System Performance Factor	8-16
Solar Cell Module Sizing	8-19
Charger-Battery-Regulator Module Sizing	8-31
Reliability Considerations	8-34
Thermal Considerations	8-36
Component Descriptions	8-36
Specific Radioisotope Thermoelectric Generator System Design	8-37
Conclusions	8-38
9. COMMUNICATIONS AND DATA HANDLING SYSTEM.	9-1
Design Requirements	9-1
Design Approach	9-2
Timing Subsystem	9-2
Data Handling Subsystem	9-3
Command Handling Subsystem	9-4
Beacon and Status Transmission Subsystem	9-4
Design Analysis	9-4
Ground Station Contact	9-4
Oscillator Update	9-6

TABLE OF CONTENTS - Continued

	Page
Data Accumulation	9-6
Command Capability	9-6
Specific System Design	9-9
Timing Subsystem	9-9
Data Handling Subsystem	9-11
Command Handling Subsystem	9-11
Beacon and Status Transmission Subsystems.	9-12
Component Descriptions	9-12
Magnetic Tape Recorders	9-12
Signal Conditioner	9-15
Antennas.	9-15
Transmitters	9-16
Command Receiver	9-16
Command Decoder	9-16
Conclusions	9-17
10. CONCLUSIONS	10-1
Study Conclusions	10-2
System Capability Margins	10-4
System Flight Commonality	10-5
APPENDIX A. COMPUTER SIMULATION RESULTS OF MOMENTUM DUMPING.	A-1
Momentum Dumping Control Law	A-1
Simulation Results	A-5
Disturbance Torques	A-86
Gravity Torque	A-86
Aerodynamic Torque.	A-87
Magnetic Torque	A-91
Solar Radiation Torque	A-91
Internal Disturbance Torques.	A-93
Conclusions.	A-94
Other CMG Configurations Considered	A-96

TABLE OF CONTENTS - Concluded

	Page
Three Single-Degree-of-Freedom Gyros . . .	A-96
Three Two-Degree-of-Freedom Gyros. . . .	A-99
Four Single-Gimbal-Gyros.	A-101

LIST OF ILLUSTRATIONS

Figure	Title	Page
1-1	HEAO-C Spacecraft Coordinate Axes System	1-3
2-1	HEAO-C Experiments	2-4
2-2	HEAO-C Experiment Operating Modes and Controls	2-5
2-3	HEAO-C Observing Geometry	2-8
2-4	Hypothetical X-Ray Source Locations for One Day's Observations	2-15
2-5	Electron Flux Contours for $E > 1$ MeV at an Altitude of 324 Nautical Miles (600 Kilometers)	2-22
2-6	Proton Flux Contours for $E > 5$ MeV at an Altitude of 324 Nautical Miles (600 Kilometers)	2-23
3-1	HEAO-C System Locations	3-2
3-2	HEAO-C System Component Locations	3-7
4-1	Optical Bench and Connecting Structure Configuration	4-3
4-2	Vibration Mount for Isolation of the Optical Bench from the Spacecraft	4-6
4-3	Environmental Heat Flux Distribution Around HEAO Spacecraft for Worst Case Circumferential Temperature Gradient	4-9
4-4	Predicted Temperature Distribution on the Spacecraft Skin as a Function of Equivalent Wall Thickness	4-10
4-5	ΔT_{MAX} as a Function of Equivalent Spacecraft Wall Thickness	4-12

LIST OF ILLUSTRATIONS - Continued

Figure	Title	Page
4-6	Spacecraft-Optical Bench Thermal Deflections .	4-14
4-7	Spacecraft Structure	4-17
4-8	Spacecraft and Optical Bench Distributed Weight	4-19
4-9	EI as a Function of Spacecraft Station for All Axes	4-26
4-10	AG as a Function of Spacecraft Station for All Axes	4-27
4-11	EI as a Function of Bench Station about y and z Axes	4-28
4-12	AG as a Function of Bench Station about y and z Axes	4-29
4-13	Base Ring Structure	4-31
4-14	Base Ring Loads in Pounds	4-32
4-15	Base Ring Shear, Moment, and Axial Compression Diagrams	4-33
4-16	Maximum Compressive Stress in Spacecraft Skin and Longerons	4-34
4-17	Spacecraft Shear and Moment Diagrams	4-36
4-18	Compressive Buckling Coefficient for Long Stringer Stiffened Panels as a Function of b/t .	4-37
4-19	Reduction in Compressive Buckling Coefficient Resulting from Shear as a Function of the Ratio of Top and Bottom Panel Stresses	4-38

LIST OF ILLUSTRATIONS - Continued

Figure	Title	Page
5-1	Orientation of HEAO-C Spacecraft in the Pointing Mode	5-2
5-2	Roll Map Matching	5-6
5-3	Star Population as a Function of Limiting Magnitude, m_v	5-18
5-4	Required Field of View as a Function of Limiting Magnitude, m_v	5-19
5-5	Mercator Projection of Critical Pointing Directions	5-23
5-6	Polar Projection of Critical Pointing Directions	5-24
5-7	Spectral Response of Photodetectors	5-27
5-8	Television Aspect System	5-51
5-9	Estimate of Star-Field Translation	5-54
5-10	Estimate of Rotation	5-55
6-1	HEAO-C Spacecraft Principal Axes System and Location of Center of Mass	6-3
6-2	Angular Momentum Required for Slewing the Spacecraft on z Axis for Different Levels of Applied Torque	6-13
6-3	x-Axis Reaction Wheel Weight as a Function of Rotor Radius for Various Peak Power Levels .	6-19
6-4	Reaction Wheel Weight as a Function of Rotor Radius for Either the y or z Axis	6-20
6-5	Three Pairs of Single Degree of Freedom Gyros (Scissored Pairs)	6-23

LIST OF ILLUSTRATIONS - Continued

Figure	Title	Page
6-6	Total Momentum Stored in the Momentum Storage Device for Case II	6-40
6-7	Attitude Control System	6-42
6-8	Reference Gyro Components (One Axis Only)	6-45
6-9	Circuit to Generate Approximate Rate	6-50
6-10	Signal Processor	6-51
6-11	Dynamics of CMG Scissored Pair Configuration	6-54
6-12	Simplified CMG Dynamics	6-59
6-13	Transfer Function of Simplified CMG	6-61
6-14	Behaviour of Saturation Function	6-62
6-15	CMG Arranged for Simulation	6-66
6-16	Representation of One Axis of a Three-Axis Simulation	6-71
6-17	Effect of Integration Step Size on Control System Response	6-76
6-18	Control System Response to a 0.03 ft-lbf Torque Step for Different Noise Filter Constants and Damping Ratios	6-78
6-19	Reference Star Capture from Slew Rate	6-88
6-20	Slewing Maneuver	6-96
6-21	Slewing Mechanism (y Axis)	6-98
6-22	Ten-Degree Slew	6-101
6-23	Gas Thrustor Unit (one of Two)	6-114

LIST OF ILLUSTRATIONS - Continued

Figure	Title	Page
6-24	Gas Thrustor System Mechanization (for Two-Unit System)	6-115
7-1	Proposed HEAO-C Thermal Control Scheme . . .	7-2
7-2	Illustration of Thermally Induced Bending of the Optical Bench	7-5
7-3	Spacecraft Orbit/Orientations Considered in Thermal Analysis	7-13
7-4	Nodal Representation Used in Thermal Model to Determine Spacecraft Orbital Heating Rates . .	7-17
7-5	Illustration of Nodal Representation of the Optical Bench and Multilayer Insulation	7-19
7-6	Equivalent Resistance Network between Two Nodes	7-20
7-7	Structural Model Assumed in Derivation of Thermal Properties of HEAO-C Solar Panels . .	7-23
7-8	Direct Incident Heat Flux on Thermal Control Filter During Orbit and Resulting Filter Temperature Response for Case I Orientation . .	7-26
7-9	Direct Incident Heat Flux on Thermal Control Filter During Orbit and Resulting Temperature Response for Case II Orientation	6-27
7-10	Predicted Temperature Envelope of Optical Bench Structure with Spacecraft Oriented Broadside to Sun (Cases I and II)	7-29
7-11	Predicted Temperature Envelope of Telescope Mirrors with Spacecraft Oriented Broadside to Sun (Cases I and II)	7-30

LIST OF ILLUSTRATIONS - Continued

Figure	Title	Page
7-21	Transient Effects on Telescope Mirror Temperatures of 30-Degree Off-Axis Shift Toward the Sun for One Orbit (Case IV)	7-47
7-22	HEAO-B Experiment Envelope	7-51
7-23	Estimated Weights of Closed-Cycle Space- Borne Refrigeration Systems	7-55
7-24	Experiment Locations on the HEAO-D Spacecraft	7-59
8-1	Solar Cell Module System Concept	8-11
8-2	Radioisotope Thermoelectric Generator System Concept	8-13
8-3	Electrical Power System Block Diagram	8-15
8-4	Power Losses Diagram.	8-17
8-5	System Performance Factor as a Function of Orbital Nighttime Duration	8-20
8-6	Flush Mounted Solar Cell Module Configuration .	8-22
8-7	Folded-Out Solar Cell Module Configuration . .	8-23
8-8	Solar Cell Module Power Availability for the Flush Mounted Configuration	8-24
8-9	Solar Cell Module Power Availability for the Folded-Out Configuration	8-27
8-10	Solar Cell Module Average Power Availability for the Folded-Out Configuration	8-11
8-11	Solar Cell Module Average Power Availability for the Folded-Out Configuration	8-28
8-12	Solar Cell Module Power Margin for the Flush- Configuration	8-29

LIST OF ILLUSTRATIONS - Continued

Figure	Title	Page
7-12	Predicted Solar Panel and Spacecraft Backside Temperature Histories During Orbit for Case I Orientation	7-33
7-13	Predicted Solar Panel and Spacecraft Backside Temperature Histories During Orbit for Case II Orientation	7-34
7-14	Orbital History of Maximum Lateral Temperature Difference Across HEAO-C Spacecraft	7-37
7-15	Direct Incident Heat Flux on and Temperature of the Thermal Control Filter During Orbit with Spacecraft End Inclined 15 Degrees Toward Sun (Case III)	7-39
7-16	Predicted Longitudinal Distribution of Optical Bench Structure Temperature After 69 Hours in Orbit with Spacecraft Axis Inclined 15 Degrees Toward the Sun (Case III)	7-40
7-17	Predicted Longitudinal Distribution of Telescope Mirror Temperatures after 69 Hours in Orbit with Spacecraft Axis Inclined 15 Degrees Toward the Sun (Case III)	7-41
7-18	Predicted Solar Panel Temperature History During Orbit with the Spacecraft Axis Inclined 15 Degrees Toward the Sun (Case III).	7-43
7-19	Direct Incident Heat Flux on Thermal Control Filter and Resulting Temperature Response During Orbit with Spacecraft Viewing End Inclined 30 Degrees Toward Sun (Case IV)	7-45
7-20	Transient Effects on Optical Bench Structure Temperature Resulting from 30-Degree Off-Axis Shift for One Orbit (Case IV)	7-46

LIST OF ILLUSTRATIONS - Continued

Figure	Title	Page
8-13	Solar Cell Module Power Margin for the Folded-Out Configuration	8-30
8-14	Battery Cyclic Life as a Function of Depth of Discharge	8-32
8-15	Depth of Discharge as a Function of Orbital Nighttime Duration	8-33
8-16	Solar Panel Sectioning	8-35
9-1	Ground Station Contact Time Profile	9-5
9-2	Data Accumulation Profile	9-7
9-3	Communications and Data Handling System	9-10
A-1	Case I Simulation - Secular Torque in y Axis	A-7
A-2	Case II Simulation - Secular Torque in z Axis	A-9
A-3	Case III Simulation - Secular Torque in x Axis	A-10
A-4	Simulation Results for Case I	A-14
through A-27		A-37
A-28	Simulation Results for Case II	A-38
through A-51		A-61
A-52	Simulation Results for Case III	A-62
through A-75		A-85
A-76	Location of Center of Pressure for Angle of Attack of 90 Degrees	A-90

LIST OF ILLUSTRATIONS - Concluded

Figure	Title	Page
A-77	Three Single-Degree-of-Freedom (Single Gimballed) Gyros	A-97
A-78	Three Two-Degree-of-Freedom (Double Gimballed) Gyros	A-100
A-79	Arrangement of Four Single-Degree-of- Freedom Gyros	A-102
A-80	The Path of Motion of the Angular Momentum Vectors for Four CMGs.	A-103

LIST OF TABLES

Table	Title	Page
2-1	HEAO-C Experiment Weights and Power Requirements	2-2
2-2	Optical Bench Experiments	2-10
2-3	X-Ray Source Intensity Distribution	2-11
2-4	HEAO-C Time Budget for One-Year Operation (Preliminary)	2-13
2-5	Sources Observed	2-16
2-6	Sequence and Duration of Typical Day's Observations	2-17
2-7	Summary of Time Allocations	2-19
3-1	HEAO-C Systems Components List	3-9
3-2	HEAO-C Spacecraft Weight Summary	3-12
3-3	HEAO-C Spacecraft Power Summary	3-13
3-4	Comparison of Spacecraft Capabilities for HEAO Missions A, B, C, and D	3-17
4-1	Distributed Weight for Optical Bench and Spacecraft	4-20
4-2	Lump Weights for Optical Bench	4-21
4-3	Lump Weights for Spacecraft	4-22
4-4	Computation of Allowable Stresses and Actual Safety Factors for Spacecraft Skin Panels Between Stringers	4-40
4-5	Computation of Allowable Stresses and Actual Safety Factor for Buckling of Skin Panels Across Stringers	4-41

LIST OF TABLES - Continued

Table	Title	Page
4-6	Spacecraft Structural Weight Statement	4-43
4-7	HEAO-C Spacecraft Meteoroid Vulnerability	4-44
5-1	Summary of Attitude Control Requirements for the HEAO-C Spacecraft	5-1
5-2	Reference Gyro Characteristics	5-9
5-3	Star Tracker Photodetectors	5-12
5-4	Attitude Sensing System Using Star Trackers	5-15
5-5	Typical Sun Sensor Characteristics	5-15
5-6	Representative Attitude Control Computer	5-16
5-7	Angular Radii, θ , of Required Fields of View (from Ref. 5-2)	5-20
5-8	Centers of Critical Fields of View (from Ref. 5-2).	5-21
5-9	Classification of Critical Pointing Directions (from Ref. 5-2)	5-22
5-10	Star Tracker Photodetector Response	5-25
5-11	Fixed Star Trackers	5-32
5-12	Average Number of Stars Seen	5-34
5-13	Gimballed Star Trackers	5-40
5-14	Projected HEAO-C Star Tracker Characteristics	5-45
5-15	CDC Star Mapper Characteristics	5-48
5-16	Star Mapper System Weight and Power Breakdown	5-48

LIST OF TABLES - Continued

Table	Title	Page
5-17	Star Field Analysis Algorithm	5-56
5-18	Attitude Sensing with Television Aspect System	5-59
5-19	Comparison of Attitude Sensing Systems.	5-61
5-20	Comparison of HEAO-A and HEAO-C Attitude Sensing Equipment	5-63
5-21	Comparison of HEAO-C and HEAO-D Attitude Sensing Equipment	5-65
6-1	Maximum Expected Disturbance Torques and Momentums Accumulated per Orbit.	6-6
6-2	Torque and Momentum Capability Requirement for Momentum Storage Devices	6-15
6-3	Comparison of Reaction Wheels and CMG Configurations for Three Axis Control	6-26
6-4	Properties of Ferro-Magnetic Materials	6-32
6-5	Minimum Weight of Electromagnet for Three Core Materials	6-36
6-6	Comparison of Core Materials	6-36
6-7	Reference Gyro Characteristics	6-48
6-8	CMG Dynamics	6-55
6-9	Key to Figure 6-16	6-72
6-10	Significance of Cross-Coupling Terms	6-74
6-11	CMG Control System Response to Step Torques in All Axes	6-77
6-12	Control System Response to an x-Axis Disturbance Torque of 0.003 ft-lbf with a 3-Degree Misalignment of the CMG	6-80

LIST OF TABLES - Continued

Table	Title	Page
6-13	Large Rotation, Showing Momentum Interchange .	6-83
6-14	Reference Star Capture From Slew Rate	6-89
6-15	y-Axis Slewing Error Budget	6-107
6-16	Slewing Data Requirements	6-109
6-17	Gas System Weight Breakdown (Two Units)	6-113
6-18	Gas System Weight Breakdown (Single Unit)	6-120
6-19	Disturbance Torques Acting on the HEAO Spacecraft for Missions A, B, C, and D	6-125
7-1	Heat Dissipation Requirements for HEAO-C Experiments and Subsystems	7-9
7-2	Illustration of Thermally Induced Bending of the Optical Bench	7-5
7-3	Thermal Control System Weight	7-25
7-4	Predicted Experiment and Subsystem Operating Temperature Extremes	7-32
8-1	Experiments Power Requirements	8-3
8-2	Attitude Sensing System Power Requirements	8-5
8-3	Attitude Control System Power Requirements	8-5
8-4	Communications and Data Handling System Power Requirements	8-7
8-5	Thermal Control System Power Requirements	8-7
8-6	Total HEAO-C Power Requirements	8-8
8-7	Power System Weight	8-37

LIST OF TABLES - Concluded

Table	Title	Page
9-1	Communications and Data Handling System Weight	9-13
A-1	Maximum Disturbance Torque and Momentum Accumulation in One Orbit	A-95

1. INTRODUCTION

The HEAO-C mission is the third of a four mission sequence of high energy astronomy observatory launches. Each spacecraft will carry equipment to take electromagnetic radiation measurements that cannot be obtained from the Earth's surface. The missions are unmanned, and have Earth orbit lifetimes from one to two years. The launch schedule is:

- HEAO-A - 1974
- HEAO-B - 1975
- HEAO-C - 1976
- HEAO-D - 1977.

Mission A will be primarily a survey mission, Mission B will be divided between survey and pointing, Mission C will be pointing exclusively, and Mission D will be a random pointing mission.

A feasibility study of a spacecraft for the HEAO-C mission has been performed by Teledyne Brown Engineering. The resulting conceptual designs of the spacecraft systems are presented in this report. In addition, selected analyses were performed for the HEAO-B and HEAO-C missions. These results will be found under the appropriate system headings.

MISSION DESCRIPTION

The objective of the HEAO-C mission is operation of pointed X-ray experiments in Earth orbit for a period of one to two years. It is anticipated that the HEAO-A and -B missions will have resulted in the discovery of a large number of celestial X-ray sources and the determination of their locations to within 1 minute of arc. During the HEAO-C mission, preselected sources will be viewed by more sophisticated instruments for varying periods of time of the order of one-orbit duration.

The HEAO-C orbit has not been chosen; however a 300-nautical-mile altitude circular orbit inclined at an angle of 35 degrees to the equator was considered typical and was used in the analyses discussed in this report. The orbit period is 96 minutes. The duration of the time that the spacecraft is in the Earth's shadow varies from 21 to 36 minutes, depending upon the angle between the orbit plane and the solar vector.

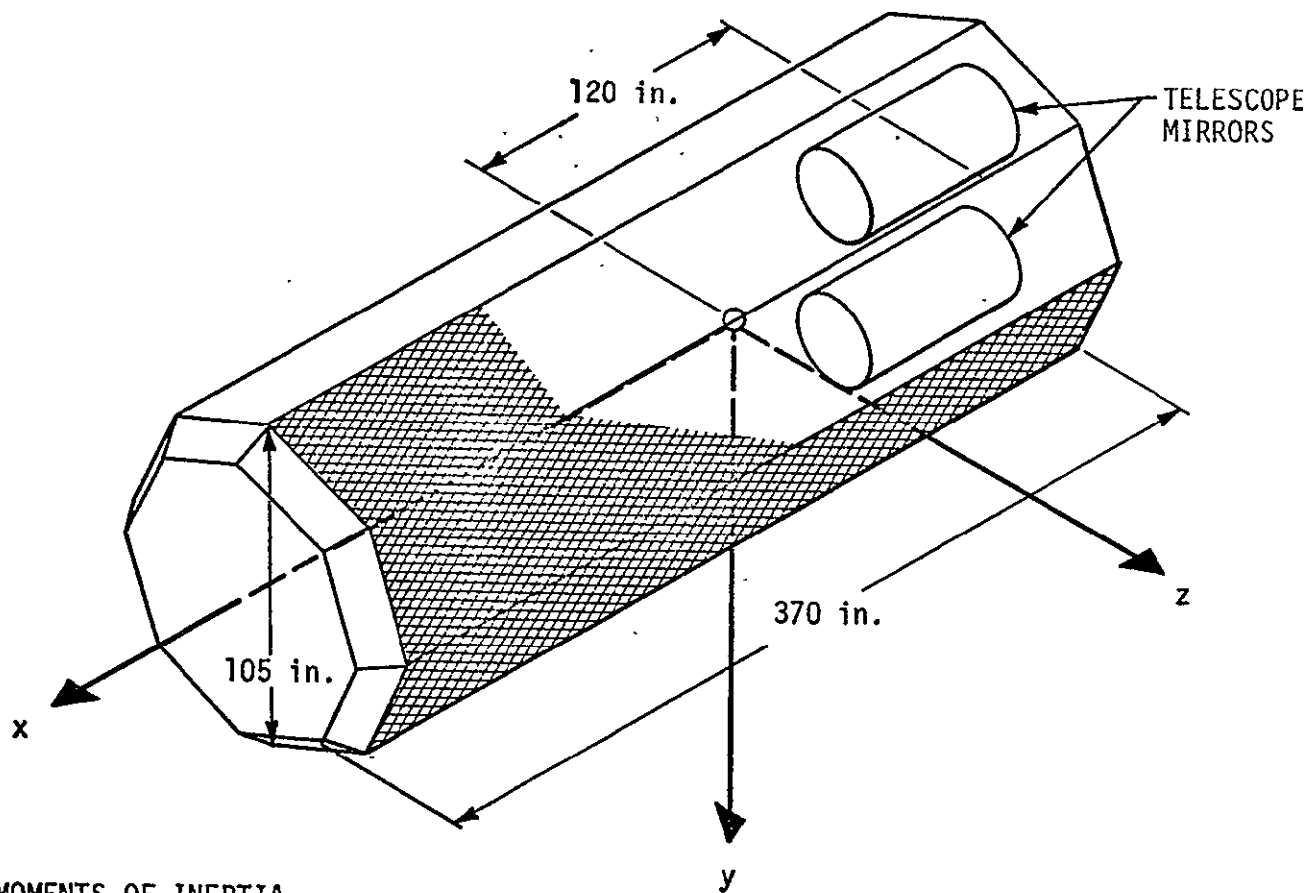
SPACECRAFT COORDINATE AXES SYSTEM

The HEAO-C spacecraft coordinate axis system is shown in Figure 1-1. The spacecraft is a 370-inch-long octagonal prism. Solar panels are mounted on three of the eight spacecraft sides. Two grazing incidence X-ray telescope mirrors are located at the viewing end of the spacecraft and the focused X-ray detectors are located near the opposite end.

The origin of the spacecraft coordinate system is the spacecraft center of gravity. The z axis is perpendicular to the middle solar panel. The x axis is normal to the z axis and parallel to the spacecraft longitudinal axis; the positive direction is the launch direction of the launch vehicle, or up as the payload is in position on the launch pad. The y axis completes the three-axes right-hand coordinate system. In the nominal spacecraft attitude, the z axis is pointed to within 15 degrees of the solar vector.

STUDY GUIDELINES

Study guidelines, requirements, and goals were provided by personnel of the Mission and Payload Planning Office and the Preliminary Design Office of Program Development, Marshall Space Flight Center, Huntsville, Alabama.



MOMENTS OF INERTIA

$$I_x = 4,600 \text{ slug-ft}^2$$

$$I_y = 46,800 \text{ slug-ft}^2$$

$$I_z = 47,300 \text{ slug-ft}^2$$

FIGURE 1-1. HEAO-C SPACECRAFT COORDINATE AXES SYSTEM

- The HEAO-C mission shall be unmanned..
- Target launch date - 1976
- Orbit - Circular, 300-nautical-mile altitude, 35-degree inclination to the equator
- Launch vehicle - Titan III D kick stage
- Launch site - Eastern Test Range
- Maximum payload dynamic envelope - 107.27 inches in diameter
- Maximum spacecraft diameter - 105 inches
- Spacecraft design goals
 - ▲ Low cost
 - ▲ High reliability
 - ▲ Maximum use of proven components
- The spacecraft systems and subsystems shall have a minimum lifetime of one year with two years desired.
- The HEAO-C mission will make maximum use of the Space Tracking and Data Acquisition Network (STADAN). Consideration shall also be given to the use of the Manned Space Flight Network (MSFN).
- Pointing at sources will be accomplished by roll maneuvers around the nominally Sun-oriented z axis.
- For normal operation, the z axis will be oriented to ± 15 degrees of the solar vector. The spacecraft shall be capable of continuous operation in this orientation.
- The spacecraft shall have the capability of operating for one orbit each 24 hours at a z-axis orientation to the solar vector of as much as ± 30 degrees.
- The maximum experiment data rate will be compressed to 25 kbits/sec.
- The experiments associated with the X-ray telescopes will require 200-five-bit command words per orbit.

- Spacecraft operational requirements
 - ▲ The oriented line of sight of the spacecraft to the selected target shall be within 1 arc minute of the desired direction.
 - ▲ The oriented line of sight of the spacecraft shall be confined within an error circle of less than 1 arc second in diameter during 1 second of time.
 - ▲ Spacecraft angular error about the optical (X-ray telescopes) axis shall be controlled to ± 5 arc minutes.
 - ▲ The spacecraft should have the capability to point at selected targets for at least two-thirds of an orbit.
 - ▲ The spacecraft will have the capability to perform a 100 degree rotation maneuver about the Sun line (spacecraft z axis) in one-third of an orbit (32 minutes).
 - ▲ The spacecraft will have the capability to rotate 360 degrees about the optical line of sight (X-ray telescope axis) during the minimum dark portion of an orbit (21 minutes).
- Other spacecraft requirements
 - ▲ The spacecraft shall provide clock signals which must be accurate to at least 0.1 millisecond per day for pulsar observations. Absolute timing accuracy must be within 0.1 millisecond.
 - ▲ The spacecraft and spacecraft experiment interfaces will be designed so that single-point failures will have a minimum effect on mission success.
 - ▲ Meteoroid protection will be provided for all spacecraft components.

Searches were made to determine the availability of suitable proven components for use in the spacecraft system conceptual

designs. In some cases, suitable components were identified and designated as part of a baseline system. In cases for which suitable proven components were not available, the required characteristics were identified and components weights and power requirements were estimated. The identification of specific components was not meant to constitute a recommendation, but simply an indication that qualified components are available.

ACKNOWLEDGEMENTS

A relatively large number of persons participated in this study, primarily serving as technology specialists. The principal contributors to material contained in this report were:

- J. M. Duffie Project Engineer
- G. J. Fishman Experiments
- O. E. Cathey, Jr. Structure
- F. Godwin Attitude Sensing
 CMG Simulation
- K. D. Bishnoi Attitude Control
- J. L. Thurman Thermal Analysis
- V. O. Heflin Thermal Analysis
- J. D. Wilson Power
 Communications and Data Handling
- W. A. Dendy Layout and System Locations

2. EXPERIMENTS

The HEAO-C experimental package consists of a group of highly specialized experiment components which operate both independently and with one another to perform detailed investigations of discrete X-ray sources. All of the experiments considered in this study, with the exception of the scintillation counter, were based on a proposal for HEAO submitted by American Science and Engineering, Inc. (AS&E), Massachusetts Institute of Technology (MIT), Columbia University, and Goddard Space Flight Center.(Ref. 2-1). The Principal Investigator is Dr. R. Giacconi of AS&E.

Two large X-ray mirrors provide X-ray images of sources that are then analyzed by the optical bench experiments which may be interchanged in the focal plane of the mirrors. An optical bench rigidly connects the mirrors with the focal plane experiments. In addition to the experiments that are associated with the X-ray mirrors, there are three additional "front-end" experiments which view along the telescope axis. A flare detector is used to observe transient events that occur within a large segment of the sky. The experiment components, along with their weights, power requirements and envelope dimensions, are listed in Table 2-1. Their locations on the HEAO-C spacecraft are shown in Figure 2-1. The interrelation of the experiment components and their various modes of operation are shown in Figure 2-2. From this figure, it can be seen that there are a large number of experimental combinations and possible modes of operation. This versatility gives the HEAO-C spacecraft the capability to perform a wide range of observations on any of the anticipated X-ray sources.

TABLE 2-1. HEAO-C EXPERIMENT WEIGHTS AND POWER REQUIREMENTS

Experiment Components	Field of View	Abbreviation	Weight (lb)	Power (W)	
				Inside Bench	Outside Bench
OPTICAL BENCH		OB	1,515		
HIGH RESOLUTION TELESCOPE					
HR Mirror Assembly	60'	HR	2,025		
HR Image Detector	17'	I1	20	13.5	
Electronics Module		I1E	24		19.0
HR Polarization Crystal		PC	5		
HR Crystal Spectrometer	17'	CS	397	21.0*	
HR Experiment Transport Mechanisms		T1	70	**	
Transmission Grating	17'	TG	60	**	
Filter Wheel		FW	40	**	
LARGE AREA TELESCOPE					
LA Mirror Assembly	60'	LA	2,400		
LA Image Detector	26'	I2	100	1.0	
Electronics Module		I2E	50	13.5	
Multiple Polarimeter	5'	MP	20	1.0	
Electronics Module		MPE	60	8.6	
Solid State Detector	5'	SS	90	2.0	
Electronics Module		SSE	25		6.2*
LA Experiment Transport Mechanisms		T2	115	**	
Mosaic Crystal	5'	MC	300		**
Electronics Module		MCE	10		0.5

TABLE 2-1. - Continued

Experiment Components	Field of View	Abbreviation	Weight (lb)	Power (W)	
				Inside Bench	Outside Bench
FLARE DETECTORS					
Coarse Detector (4)	90° x 30° 8°	FD1	60	***	4.0
Fine Detector (1)		FD2	27		
Electronics Modules (5)		FDE	150		32.0
SCINTILLATION COUNTER	2°	SC	316		11.0
MONITOR PROPORTIONAL COUNTER	1°	MPC	98	1.0	
Electronics Module		PCE	44		8.0
FLAT CRYSTAL SPECTROMETER	1°	FC	110		
Electronics Modules (2)		FCE	52		15.0
ASPECT DETECTOR	7.5°	AD	100	8.0	
Electronics Modules		ADE	21		6.0
COMPUTER		C	72		145.0
CABLING			160		
On Bench - 30					
On Spacecraft - 130					
TOTAL			<u>8,536</u>	<u>28.5</u>	<u>262.6</u>

*Not to be included in maximum power configuration

**Uses 6 watts during operation; duty cycle is negligible

***Uses 1 watt during operation; duty cycle is negligible

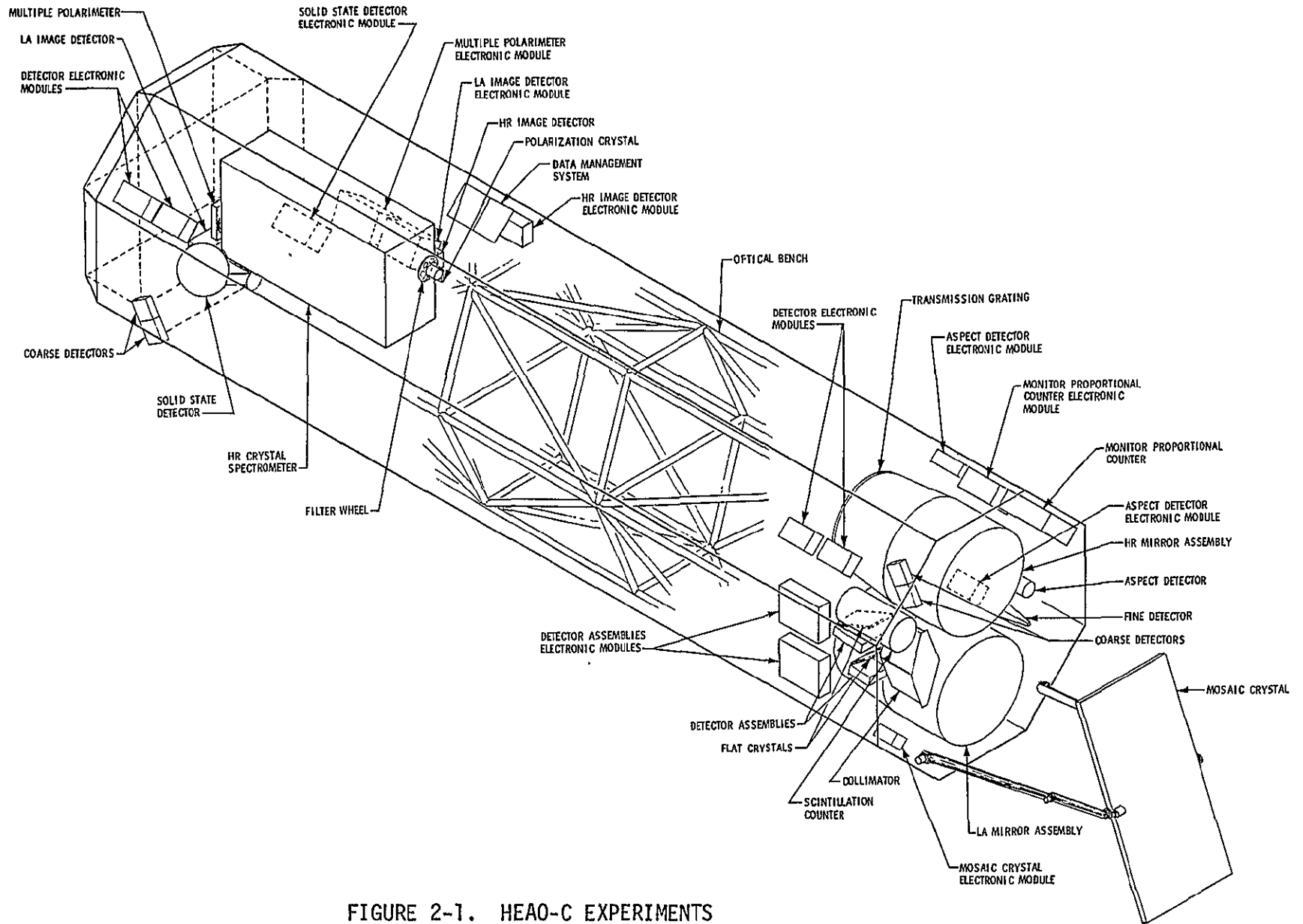
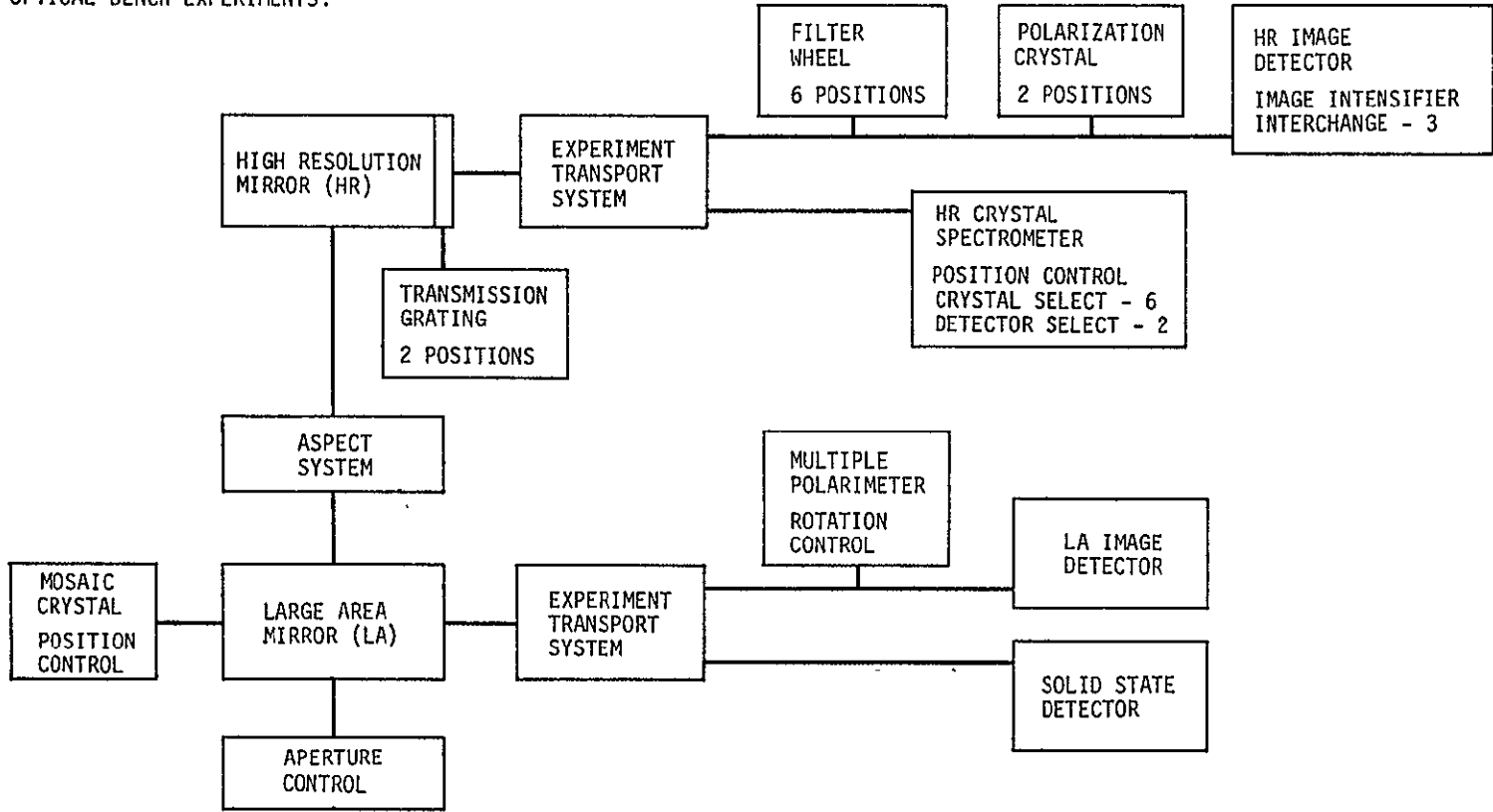
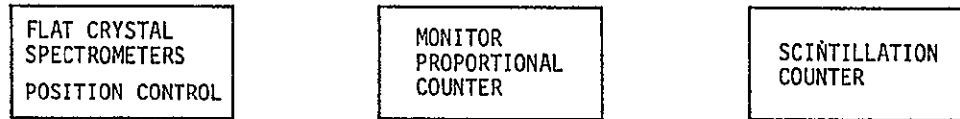


FIGURE 2-1. HEAO-C EXPERIMENTS

OPTICAL BENCH EXPERIMENTS:



"FRONT-END" EXPERIMENTS:



FLARE DETECTORS:

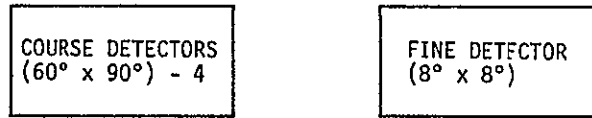


FIGURE 2-2. HEAO-C EXPERIMENT OPERATING MODES AND CONTROLS

ALIGNMENT AND POINTING REQUIREMENTS

All experiments are required to be aligned to a common axis with an accuracy of approximately one-tenth of their field of view. The alignment must be maintained throughout the orbital lifetime despite deformations of the spacecraft structure. The optical bench structure is designed to maintain the required alignment and all experiments except the scintillation counter and the mosaic crystal will be rigidly coupled to it.

The pointing requirement for the optical bench axis is that it be oriented within a half-cone angle of one (1) arc minute of the required source direction. The drift rate within this angle is required to be less than one (1) arc second per second of time about any axis. The angular error about the optical bench axis is required to be less than 5 arc minutes in either direction. There is no requirement for the spacecraft to perform slow scan maneuvers while operating the experiments.

OBSERVATIONAL REQUIREMENTS

The general observational plan for HEAO-C will be to perform a predetermined sequence of experiments on known X-ray sources with the requirement that the spacecraft z axis (normal to the middle solar panel) be maintained within 15 degrees of the solar vector and the x-axis (optical bench axis) of the spacecraft will be within one (1) arc minute of the desired X-ray source vector. Aspect information for experimental data reduction will be provided by the aspect system which is a part of the experimental package. Aspect data will be analyzed on the ground to determine the telescope pointing direction to within one arc second.

Two important deviations from the general observational plan are required by the mosaic crystal spectrometer experiment and the imaging polarimetry experiment. For observations by the mosaic crystal, the

X-ray source will be in the general observing band (± 15 degrees from the normal to the solar vector) but will be from 50 to 140 degrees from the spacecraft x axis, depending on the angle setting of the mosaic crystal. Imaging polarimetry experiments will be performed by rotating the spacecraft about the x axis for observations during a 20- to 36-minute period while the spacecraft is in darkness.

Transient events observed by the flare detectors may necessitate further excursions of the spacecraft x axis of up to 15 degrees on either side of the general observing band. In these cases, the decreased solar power available to the spacecraft may alter the normal experiment sequencing in order to conserve power. Figure 2-3 shows the geometry of the HEAO-C observations.

OBSERVATION PROGRAM

Because of the extremely large number of possible experimental modes (over 1000) and the unknown number and nature of the X-ray sources to be observed, a detailed observational program for the HEAO-C spacecraft would be impossible to formulate at this time. In actual operation, the HEAO-C observational program will be determined by the Principal Investigators and the Guest Observers. Most likely, the observational program will be modified during the orbital lifetime of the spacecraft according to the quality of the data received, the discovery of new phenomena of known X-ray sources, and the discovery of new X-ray sources. However, for the present feasibility study of the HEAO-C spacecraft, it is necessary to make estimates of

- The number of sources that will be observed by the HEAO-C spacecraft
- The types of experiments and duration of the experiments that will be performed on each source
- A representative sequence of observations performed by the HEAO-C spacecraft.

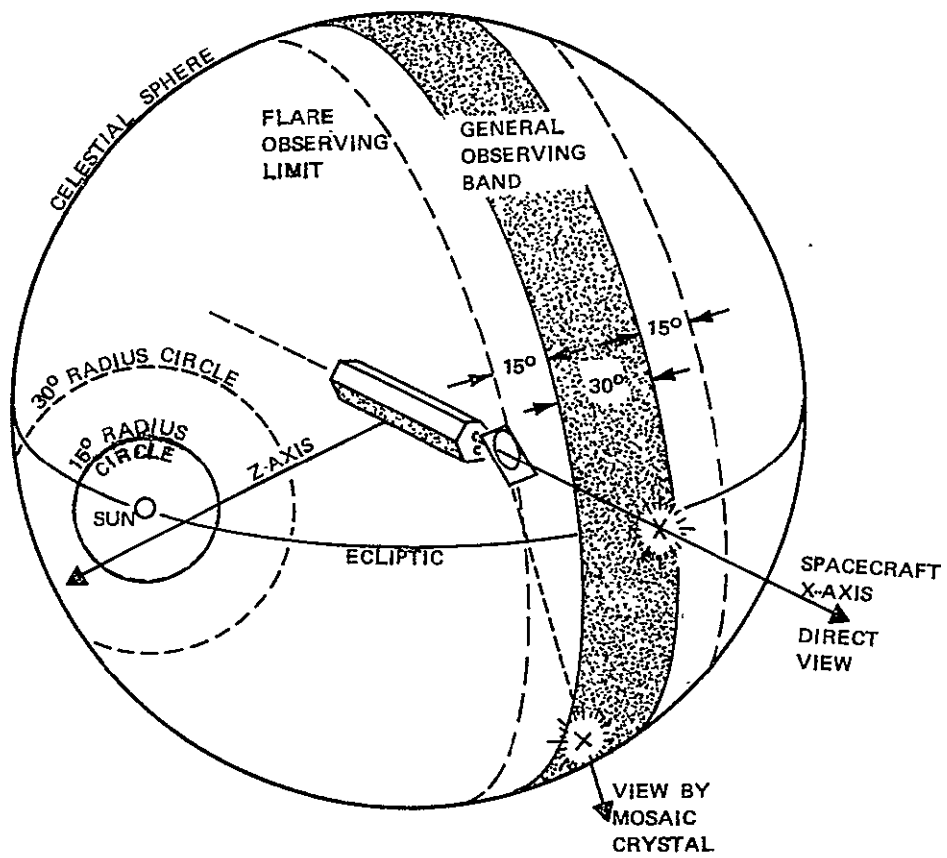


FIGURE 2-3. HEAO-C OBSERVING GEOMETRY

These estimates will be used for planning purposes in the areas of attitude control, power requirements and the mission profile in the current study.

It is assumed that the observational program will be determined by the optical bench experiments. Other experiments, which are constrained to view along the optical bench axis but do not use the X-ray mirrors, will usually operate simultaneously with the optical bench experiments but will not affect the observational program. Table 2-2 lists the various optical bench experiments and the telescope mirrors and instruments that they employ.

Number of Sources

At present, there are 53 confirmed X-ray sources with widely differing properties and intensities. Most of these objects are near the Galactic plane and thus are assumed to be in our galaxy. In the next few years, more sensitive X-ray surveys of the celestial sphere will identify the locations of thousands of new X-ray sources. In Table 2-3 the expected intensity distribution of X-ray sources is estimated. X-ray magnitudes from I to IX were assigned to the hypothetical sources based on the photon flux from 2 keV to 10 keV. The number of sources expected at each magnitude level or brighter was derived assuming that this number is inversely proportional to the first power of the X-ray flux. This assumption follows from the two-dimensional nature of the source distribution within the Galaxy. Modifications to this distribution may be expected because of extragalactic sources, interstellar absorption and variations in intrinsic X-ray source luminosity; however, the modifications from the above effects on the actual source distribution are unknown at this time. For the present, the source distribution given in Table 2-3 will be used. This distribution closely matches the known X-ray source distribution for X-ray magnitudes I to IV, as given in Column 4 of Table 2-3.

TABLE 2-2. OPTICAL BENCH EXPERIMENTS

<u>Experiment</u>	<u>Mirror and Instruments*</u>
Image Observations	
High Resolution Image Detector	HR-I1-FW
High Efficiency Image Detector	LA-I2
High Speed Spectroscopy	
Transmission Grating	HR-I1-TG
Solid State Detector	LA-SS
Mosaic Crystal Spectroscopy	LA-I2-MC
Low Speed Spectroscopy	HR-CS
Polarimetry	
Imaging Polarimetry	HR-I1-PC
Multiple Polarimetry	LA-MP
Flare Observations	Combination of Above

* See Table 2-1 for abbreviations.

TABLE 2-3. X-RAY SOURCE INTENSITY DISTRIBUTION

X-Ray Mag.	F* Photons (cm ² -sec)	No. = 10 F ^{-1.0} (Cumulative)	Known at Present	Estimated Known By 1975	HEAO-C Experiments						
					IMAGE OBSERVATIONS	HIGH SPEED SPECTROSCOPY	MOSAIC CRYSTAL SPECTROSCOPY	LOW SPEED SPECTROSCOPY	MULTIPLE POLARIMETRY	IMAGING POLARIMETRY	
I	10	1	1	1							
II	3	3	2	2							
III	1	10	10	10							
IV	0.3	30	34	34							
V	0.1	100	53	100							
VI	0.03	300	-	300							
VII	0.01	1,000	-	1,000							
VIII	0.003	3,000	-	3,000							
IX	0.001	10,000	-	4,000	4,000	4,000	800	400	200	40	

Number of Sources to be Observed

Note: *2 to 10 KeV

Also shown in Table 2-3 are the types of experiments that may be performed by the HEAO-C spacecraft on the various magnitude sources. For example, all 4,000 sources that are assumed to have been identified by the time of HEAO-C mission will undergo image observations and high speed spectroscopy; however, only 40 sources will be so intense as to permit observations by the imaging polarimetry experiment.

Using the number of sources to be observed by each type of experiment as given in Table 2-3, a preliminary time budget for one year of operation of the HEAO-C spacecraft may be made. The observation time per source per experiment is assumed to range from 30 to 100 minutes, as given in Column 2 of Table 2-4. It is assumed that a total of 8,800 spacecraft maneuvers will be made during the first year, with an average maneuvering angle of 5 degrees and an average maneuvering time of 5 minutes, including the final nulling of the attitude control system. In addition to performing observations and maneuvering, the spacecraft will be occulted by the Earth for an estimated 17 percent of the time. It is assumed that the observational program will be based in part upon the spacecraft orbital parameters so that the occultation time will be minimized.

Typical Day's Observations

Using the time budget for observations outlined above, it is now possible to derive a sequence of observations that would be typical of those performed during one day of operation of the HEAO-C spacecraft. Naturally, the actual observational sequence will vary greatly from day to day, depending upon the sources observed; but it is useful to define a nominal day for planning purposes in the areas of power consumption and attitude control.

On the average, ten or eleven sources will be observed each day throughout the year. The sources to be observed and the experiment

TABLE 2-4. HEAO-C TIME BUDGET FOR ONE-YEAR OPERATION (PRELIMINARY)

<u>Experiment</u>	<u>Observation Time per Source (min)</u>	<u>Number of Sources</u>	<u>Percent of Sources</u>	<u>Total Observation Time (hr)</u>	
				<u>H.R. Telescope</u>	<u>L.A. Telescope</u>
Image Observations	30 H.R., 35 L.R.	4,000	100	2,000	2,300
High Speed Spectroscopy	30	4,000	100	2,000	2,300
Mosaic Crystal Spectroscopy	(6 × 15) = 90	800	20	0	1,200
Low Speed Spectroscopy	100	400	10	660	0
Multiple Polarimetry	30	200	5	0	100
Imaging Polarimetry	60	40	1	40	0
Flare Observations	1,000	12	-	<u>200</u>	<u>200</u>
TOTALS				<u>4,900</u>	<u>6,100</u>

<u>Maneuvers</u>	<u>Number</u>	<u>Summary</u>		
Direct Source Observations	4,000	Viewing Time	70%	6,100 hr
Mosaic Crystal Observations	<u>4,800</u>	Maneuvering Time	8%	730 hr
Total Number of Maneuvers Required	<u>8,800</u>	Transport Experiment	5%	400 hr
		Occultation	<u>17%</u>	<u>1,530</u> hr
		TOTALS	<u>100%</u>	<u>8,760</u> hr/yr

sequences will be predetermined and stored on board the spacecraft. For this particular day's observations, it is assumed that the spacecraft is to view ten sources in an area of the celestial sphere that is within the general observing band and is at galactic midlatitudes. In this region, the number of X-ray sources per unit area of the sky is about one-half of the average so that the spacecraft maneuvers between sources are about twice that of the average. These sources are contained in an area 12 by 18 degrees, which is equivalent to 1/191 of the celestial sphere. The source positions within this area were located by a random process and are shown in Figure 2-4. Table 2-5 lists the magnitudes and identifications of the 10 hypothetical sources. These characteristics were also assigned in a random manner but are typical of those expected in such a sample. The experiments to be performed for each source depend upon the intensity and nature of the source, according to Table 2-3. Table 2-6 lists the sequence and duration of the various experiments and maneuvers that are performed during the day and Table 2-7 summarizes the time allocations for each of the ten sources.

EXPERIMENT CONTROL AND DATA MANAGEMENT SYSTEM

Reference 2-1 contains, as part of the experiment package, a data management and experiment control system designed to reduce the overall telemetry and command requirements of the spacecraft. The functions of the data management system are as follows:

- To provide onboard processing of selected observational data to reduce the amount of telemetry output data in order to remain within the constraints of the maximum telemetry data rate
- To provide optimum telemetry output data formats corresponding to observational modes involving different combinations of active experiments

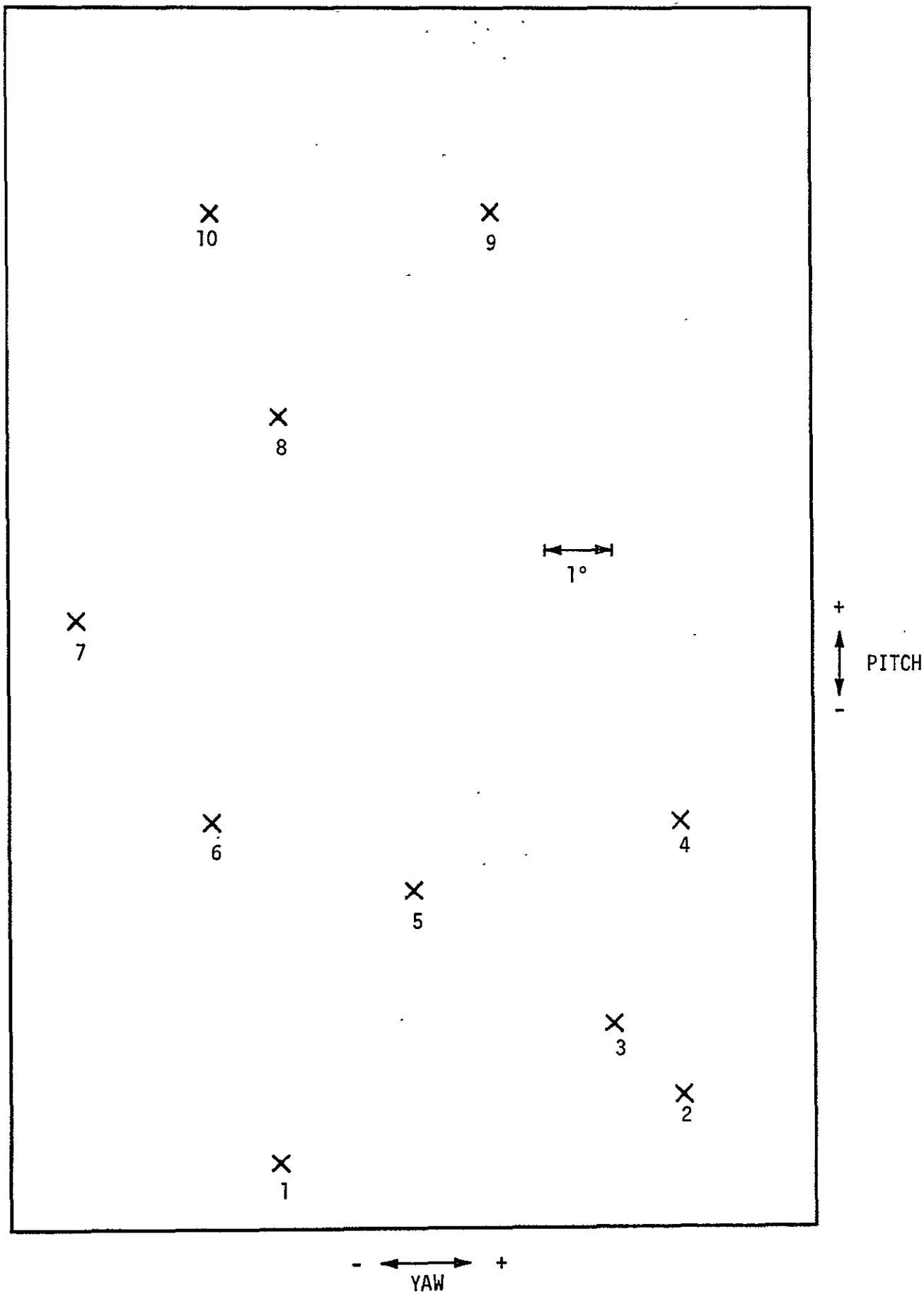


FIGURE 2-4. HYPOTHETICAL X-RAY SOURCE LOCATIONS FOR ONE DAY'S OBSERVATIONS

TABLE 2-5. SOURCES OBSERVED

<u>Source No.</u>	<u>X-Ray Magnitude</u>	<u>Identification</u>	<u>Experiments (Opt. Bench)</u>
1	VIII	Unidentified	HR-I1-FW, TG; LA-I2, SS
2	IX	Unidentified	HR-I1-FW, TG; LA-I2, SS
3	VIII	Unidentified	HR-I1-FW, TG; LA-I2, SS
4	V	Unidentified	HR-I1-FW, TG; LA-I2, SS, MC-LA-I2, LA-MP-I2, HR-CS
5	VII	Spiral Galaxy	HR-I1-FW, TG; LA-I2, SS, MC-LA-I2, HR-CS
6	VIII	Unidentified	HR-I1-FW, TG; LA-I2, SS
7	VIII	Near Pulsar	HR-I1-FW, TG; LA-I2, SS
8	VIII	Unidentified	HR-I1-FW, TG; LA-I2, SS
9	VII	Unidentified	HR-I1-FW, TG; LA-I2, SS
10	VIII	Unidentified	HR-I1-FW, TG; LA-I2, SS

TABLE 2-6. SEQUENCE AND DURATION OF TYPICAL DAY'S OBSERVATIONS

<u>Event</u>	<u>Duration (min)</u>
Maneuver to Source No. 1 (Pitch +5°, Yaw +5°)*	5
Experiment Sequence** HR-I1-FW; LA-SS	30
Transport Experiments HR-I1-TG; LA-I2	5 30
Maneuver to Source No. 2 (Pitch +1°, Yaw +6°)	5
Experiment Sequence HR-I1-TG; LA-I2.	30
Transport Experiments HR-I1-FW; LA-SS	5 30
Maneuver to Source No. 3 (Pitch +1°, Yaw -1°)	5
Experiment Sequence: Similar to Source No. 1	65
Maneuver to Source No. 4 (Pitch +3°, Yaw +1°)	5
Experiment Sequence: HR-I1-TG; LA-SS	30
Transport Experiments HR-CS; LA-MP-I2	5 100
Transport Experiments HR-I1-FW; LA-SS	5 30
Deploy Mosaic Crystal, Transport Experiments	10
Mosaic Crystal Observations MC and S/C Maneuvers (6)	60 30
Remove MC, Transport Experiments, Maneuver to Source No. 5 (Pitch -1°, Yaw -4°)	10
Experiment Sequence: Similar to Source No. 4, Substitute LA-I2 for LA-MP-I2	270
Remove MC, Transport Experiments, Maneuver to Source No. 6 (Pitch +1°, Yaw -3°)	10
Experiment Sequence: Similar to Source No. 2	65

TABLE 2-6. - Concluded

<u>Event</u>	<u>Duration (min)</u>
Maneuver to Source No. 7 (Pitch +3°, Yaw -2°)	5
Experiment Sequence HR-11-FW; LA-12	60
Transport Experiments HR-11-TG; LA-SS	5 30
Maneuver to Source No. 8 (Pitch +3°, Yaw +3°)	5
Experiment Sequence: Similar to Source No. 1	65
Maneuver to Source No. 9 (Pitch +3°, Yaw +3°)	5
Experiment Sequence: Similar to Source No. 1	65
Maneuver to Source No. 10 (Pitch 0°, Yaw -4°)	5
Experiment Sequence: Similar to Source No. 1	65

* Pitch = Rotation about Spacecraft X-axis
 Yaw = Rotation about Spacecraft Y-axis

** See Table 1 for experiment abbreviations.

TABLE 2-7. SUMMARY OF TIME ALLOCATIONS

<u>Source</u>	<u>Maneuvering and Transporting Experiments (min)</u>	<u>Observing Time (min)</u>
1	10	60
2	10	60
3	10	60
4	55	220
5	60	220
6	15	60
7	10	90
8	10	60
9	10	60
10	<u>10</u>	<u>60</u>
TOTAL	<u>200</u>	<u>950</u>

1,150 min Total

Earth Occultation (17%) 230

1,380 = 23.0 hr

- To provide control of instrumentation requiring real-time calculation of and implementation of X-ray source positional data
- To provide onboard storage and execution of complex and/or lengthy command sequences, thus relieving the command system of the requirement to process these sequences by ground command
- To provide monitoring of selected data from the experiments, providing improved quick-look capability with respect to the operational condition of the various experiments.

The data management system will supply to the spacecraft telemetry system a constant experiment data stream in a variable format of 25 kbits/sec. The command system for the spacecraft experiments should be capable of providing 300 command words per orbit (average). The spacecraft clock should be accurate to at least 0.1 msec/day, as required for pulsar observations. The absolute timing accuracy should be 0.1 millisecond or greater.

RADIATION TOLERANCE

The preliminary nature of the experiments does not allow a detailed analysis of the susceptibility of the experiments to external radiation. However, several general statements may be made regarding radiation limits.

The detectors with large surfaces exposed to the outside of the spacecraft such as the coarse flare detectors and the monitor proportional counter will be more susceptible to being saturated than the less exposed detectors such as those in the focal regions of the X-ray mirrors. Saturation of these detectors could permanently damage them so that provision must be made to turn them off before their saturation limit is reached. A rough estimate of the saturation flux is 10^4 energetic photons or particles/cm²-sec incident on the detectors.

At low orbital altitudes and inclinations, saturation fluxes would occur only in regions of the South Atlantic Anomaly. Figures 2-5 and 2-6 show the flux contours at 324 n.mi. (600 km) in particles/cm²-sec for electrons with energies greater than 1 MeV and protons with energies greater than 5 MeV (Ref. 2-2). The regions of fluxes greater than 10⁴ would most likely saturate the exposed detectors; however, the effect on the focal plane detectors would depend upon the radiation transport, mainly by electron bremsstrahlung, from the surface of the spacecraft to the focal region. The average time that the HEAO-C spacecraft will spend within the 10⁴ flux contour is estimated to be 5 to 10 percent, assuming a 300 n.mi. altitude, 35-degree inclination orbit.

Another potential radiation problem is the effect of prolonged radiation exposure of the mosaic crystal spectrometer. High energy protons could damage the lattice structure of the crystals and thereby reduce their reflection efficiency. The major contribution of damaging radiation will come from high energy protons (greater than 1 MeV) in the region of the South Atlantic Anomaly. If further study provides evidence of a serious degradation of the mosaic crystal by radiation, provision may be made for storage in a shield when the experiment is not in operation.

Because of the sensitivity of the detectors to radiation, no radioactive materials should be placed aboard the HEAO-C spacecraft.

MAGNETIC FIELD TOLERANCE

Experiments aboard HEAO-C that contain photomultiplier tubes or image tubes will be affected by strong magnetic fields. It is assumed that such components will contain magnetic shields capable of reducing the ambient field by at least a factor of 100. These experiments include the scintillation counter, the aspect detector, and the high resolution

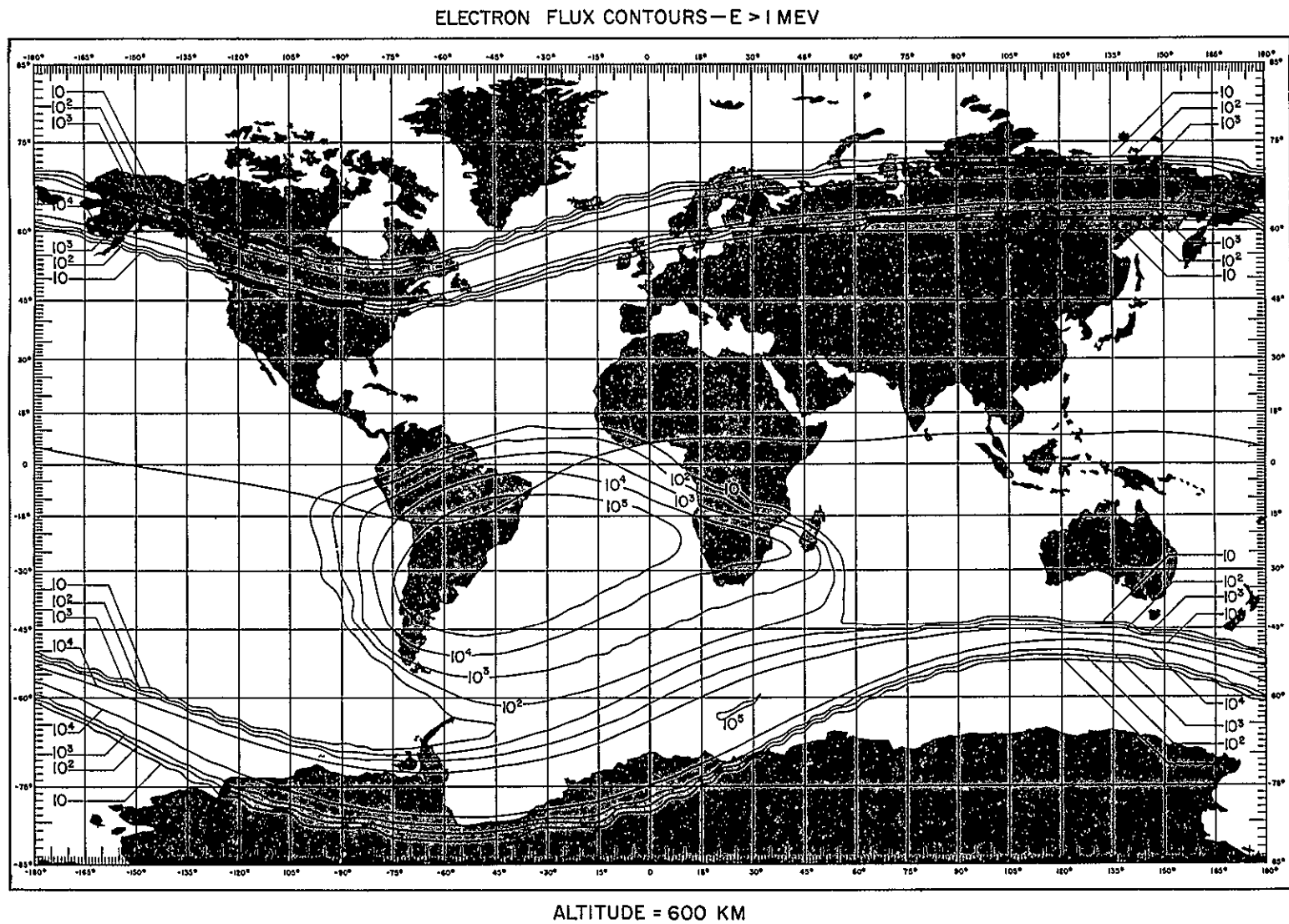


FIGURE 2-5. ELECTRON FLUX CONTOURS FOR $E > 1$ MeV AT AN ALTITUDE OF 324 NAUTICAL MILES (600 KILOMETERS)

PROTON FLUX CONTOURS—E > 5 MEV

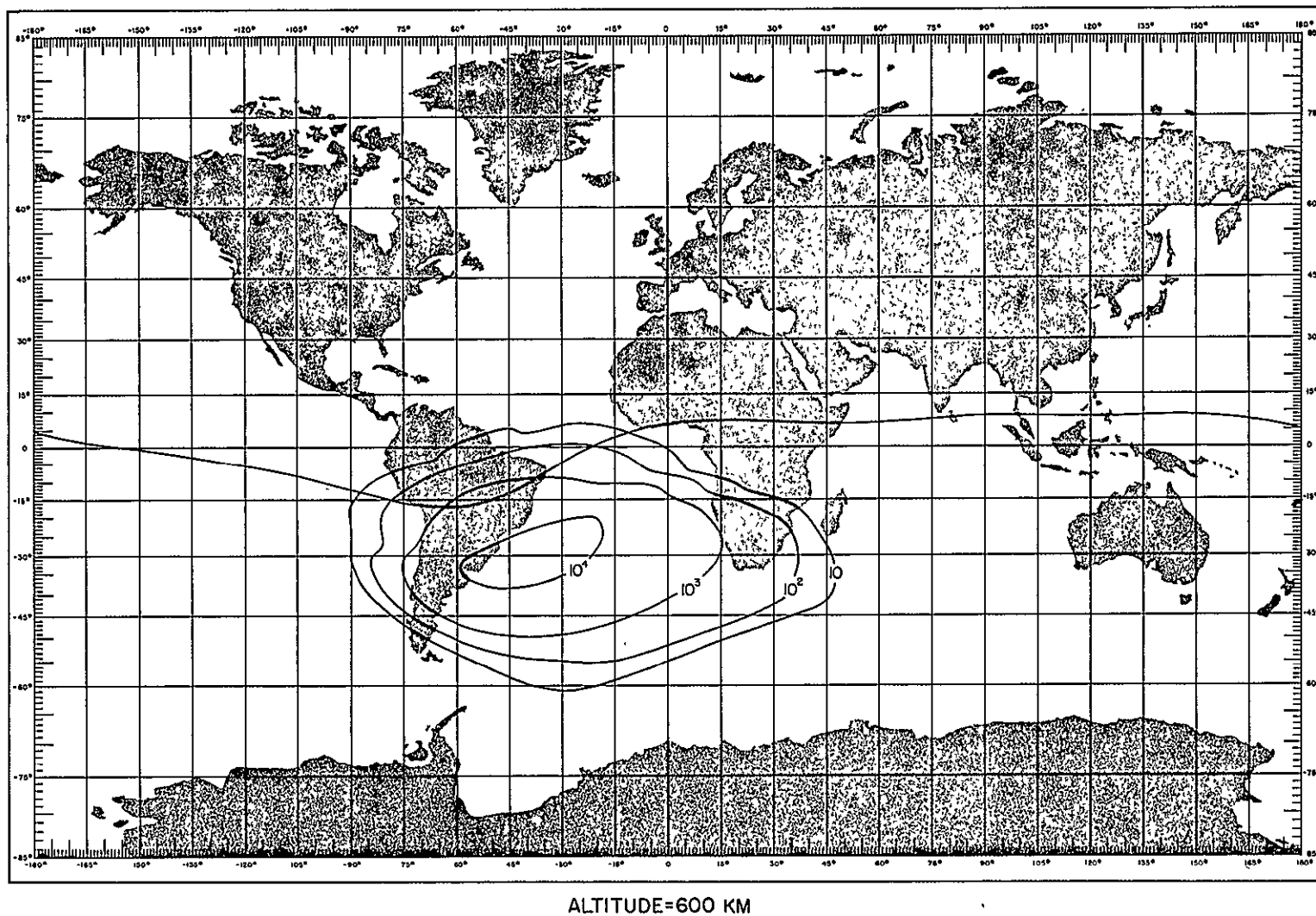


FIGURE 2-6. PROTON FLUX CONTOURS FOR E > 5 MeV AT AN ALTITUDE OF 324 NAUTICAL MILES (600 KILOMETERS)

image detector. Magnetic fields generated by spacecraft components such as the magnetic torquers are not expected to produce fields greater than 10 gauss at any of the above experiments.

THERMAL CONTROL REQUIREMENTS

The thermal requirements for components within the optical bench are derived from the alignment and focusing requirements of the two telescopes. The overall thermal requirement for the optical bench system is that it should be maintained at a temperature of $70^{\circ} \pm 10^{\circ}\text{F}$. The derivation of these requirements is presented in Section 7. The temperature limits for the exterior of all other experiment components are undefined at this time. It is assumed that they will all operate properly in the temperature range of 14° to 86°F (-10° to $+30^{\circ}\text{C}$).

REFERENCES - Section 2

- 2-1. Anon., "Large Orbiting X-Ray Telescope for the HEAO", prepared by American Science and Engineering, Cambridge, Mass., et al, 2410-I, May 27, 1970
- 2-2. Stassinopoulos, E. G., "World Maps of Constant B, L, and Flux Contours", NASA SP-3054, prepared by Goddard Space Flight Center, Greenbelt, Maryland, 1970

3. SPACECRAFT DESCRIPTION

CONFIGURATION

The configuration of the HEAO-C spacecraft is an octagonal prism of two sections, a 360-inch straight section and a 10-inch tapered section. The maximum spacecraft cross section dimension is 105 inches. This configuration is quite similar to that of the HEAO-A spacecraft. The 10-inch tapered section was needed to accommodate some components that could not be located in the 360-inch section occupied by the optical bench. Some adjustment in side dimensions was necessary to prevent the solar panel corners from extending past the maximum allowable diameter of 105 inches.

The majority of the spacecraft interior is occupied by the optical bench. The optical bench is a rigid 360-inch long structure. Two grazing incidence X-ray telescope mirrors are mounted near the viewing end of the spacecraft and X-ray detectors and other associated instruments are mounted near the opposite end of the optical bench. All spacecraft system components are mounted external to the optical bench. The locations of the major system components are shown in the isometric drawing of Figure 3-1. The experiment locations were shown in Figure 2-1 of Section 2. The optical bench is shown in Figure 4-1 of Section 4.

SPACECRAFT SYSTEMS

The HEAO-C spacecraft has one passive system, the structure, and the following active systems:

- Attitude Sensing
- Attitude Control
- Thermal Control
- Electrical Power
- Communications and Data Handling.

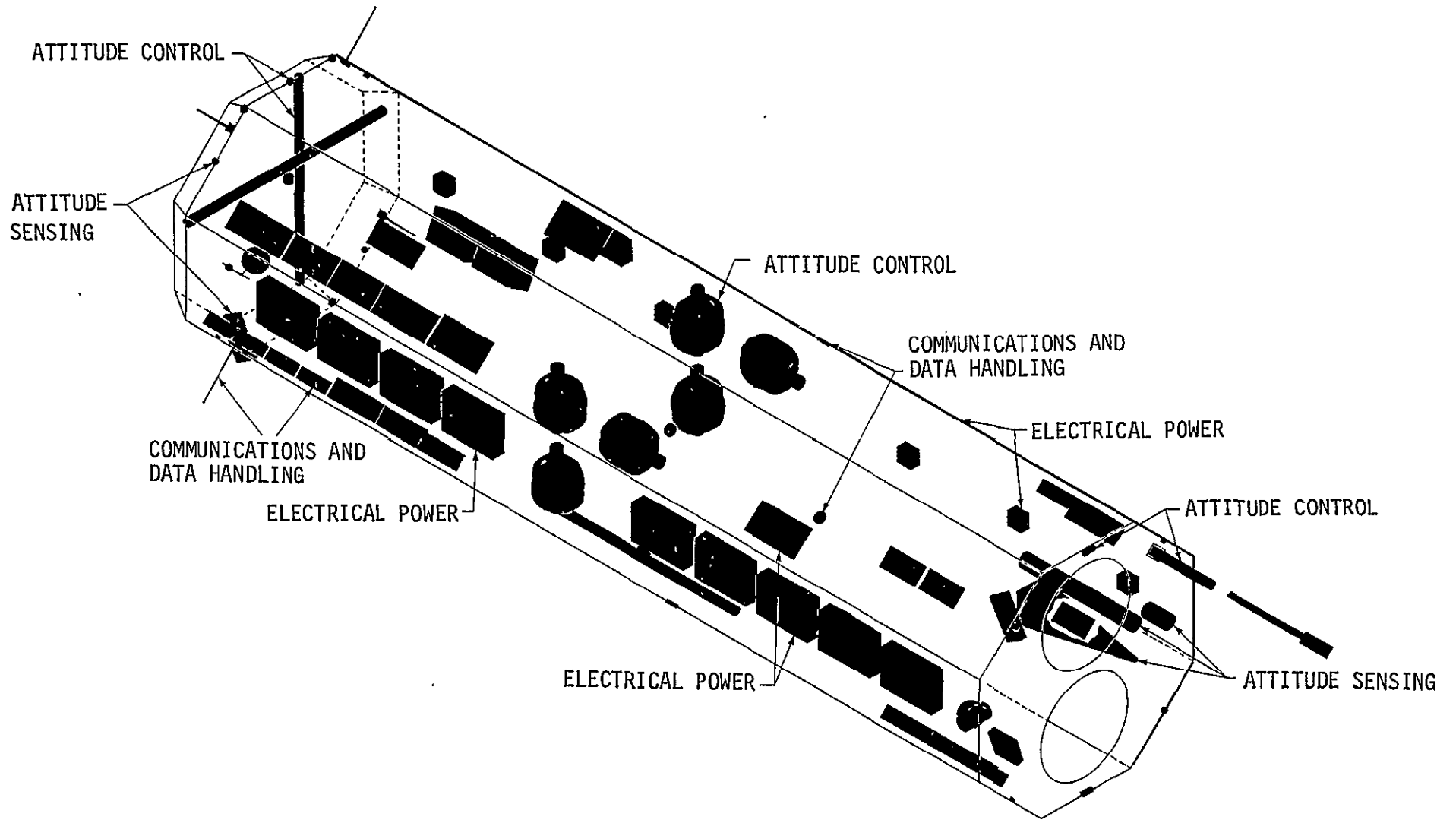


FIGURE 3-1. HEAO-C SYSTEM LOCATIONS

The experiments, although not a spacecraft system, must be treated as an active system since they have interfaces with the spacecraft power and communications and data handling systems.

Functions and Interfaces

Attitude Sensing - The function of the attitude sensing system is to determine the orientation, or attitude, of the spacecraft at all times, to provide this information to the communication and data-handling system for recording, and to the attitude control system to be used in maintaining the desired spacecraft attitude. The spacecraft attitude is determined by processing signals from visual and inertial sensors. The attitude is then compared with a reference position to determine the error magnitude and direction.

The attitude sensing system interfaces with the attitude control system, the electrical power system, and with the communications and data handling system. The interface between the attitude sensing and attitude control systems is the spacecraft control computer, where the analog voltage signals from the sensors are processed to determine the spacecraft attitude. This attitude is then compared with the desired attitude and, if necessary, the appropriate commands are routed to the attitude control system for an attitude adjustment. The commodities transferred across the interface are information and commands and the most appropriate method of transmission is believed to be analog voltage.

The interface with the power system for this and all other active systems is for the supply of electrical power. Power is transferred in the form of 28 Vdc. No other form of power is required by the attitude sensing system.

The interface with the communications and data handling system is for the transfer of system status information. This data is transferred in the form of an analog voltage signal which is conditioned and converted to a digital signal. The data is recorded for transmission to a ground station; a portion of this data will also be transmitted in real time by the beacon transmitter.

Attitude Control - The function of the attitude control system is to maintain the spacecraft attitude (orientation) to within the prescribed limits of the reference attitude. Attitude control torques will be provided by a system of control moment gyros (CMGs). CMG desaturation will be provided by magnetic torquers that react with the geomagnetic field to produce torques on the spacecraft. One magnetic torquer will be mounted parallel to each spacecraft axis.

The attitude control system interfaces with the attitude sensing system, the electric power system, and the communications and data handling system. As with the attitude sensing system, the interfaces with the power and communications and data handling systems are for the transfer of electric power and system status information, respectively. Alternating current is required for the control moment gyro rotor motors. The 28 Vdc power received from the spacecraft power system is converted into the appropriate form by power conditioning equipment that is a part of the CMG subsystem.

Thermal Control System - The function of the thermal control system is to maintain all experiments and spacecraft components within prescribed temperature limits. The most critical subsystem is the optical bench, which must be controlled to a temperature of $70 \pm 10^\circ\text{F}$. Almost all of the spacecraft system components are located on the side of the spacecraft opposite the solar panels. The reasons for

this are because there is more room there and because the back side of the spacecraft is much cooler than the solar panel side.

The optical bench is covered on all sides and on one end by a 1.5-inch thick layer of superinsulation. The only heat path for dissipation of heat given off by the experiments inside the bench is through the thermal filter over the viewing end of the spacecraft. The function of the thermal filter is to prevent the transmission of too much solar and planetary thermal radiation into the optical bench and to permit the radiation of the heat given off by the optical bench experiments. When the heat dissipated by experiments within the optical bench is low, strip heaters are activated to maintain the bench temperature within the prescribed limits.

The thermal control system interfaces with the electrical power system and with the communications and data handling system. Power is supplied in the form of 28 Vdc for use by the strip heaters and by temperature sensors. System status information is transferred to the communications and data handling system in digital form by way of the experiment data management subsystem.

Electrical Power - The function of the electrical power system is to supply all experiments and systems with regulated electrical power at 28 Vdc. The baseline power system consists of solar panels and rechargable batteries. The power system interfaces with the attitude sensing system, the attitude control system, the thermal control system, the communications and data handling system, and with the experiments. All power is transferred across the system interface in the form of regulated 28 Vdc power. Power system status information is transmitted to the communications and data handling system in the form of analog voltage signals.

COMMUNICATIONS AND DATA HANDLING

The function of the communications and data handling system is to record and telemeter all experiment and spacecraft data to ground receiving stations and to receive, acknowledge, and execute commands from ground stations. An S-band system will be used for data transmission to selected Satellite Tracking and Data Acquisition Network (STADAN) and Manned Space Flight Network (MSFN) stations.

The communications and data handling system interfaces with the experiments, the attitude sensing system, the attitude control system, the electrical power system, and the thermal control system. Experiment data, experiment status information, and commands are transferred across the experiment-communications and data handling system interface. System status data and commands are transferred across the spacecraft systems interfaces. Information is transferred to the communications and data handling system in the form of analog and digital signals. The analog signals are converted to digital signals and combined with the digital stream which is then multiplexed and recorded on tape for later transmission to ground stations. A portion of the systems status data is also transmitted in real time by the beacon transmitter.

Component Locations

The locations of experiments on the HEAO-C spacecraft were shown previously in Figure 2-1. The system component locations are shown in Figure 3-2. The components are identified in Table 3-1.

During the majority of the current study it was believed that fixed star trackers would be capable of providing the required star reference data and this thinking is evidenced in the layout drawing of Figure 3-2, which includes two of these instruments. It was later

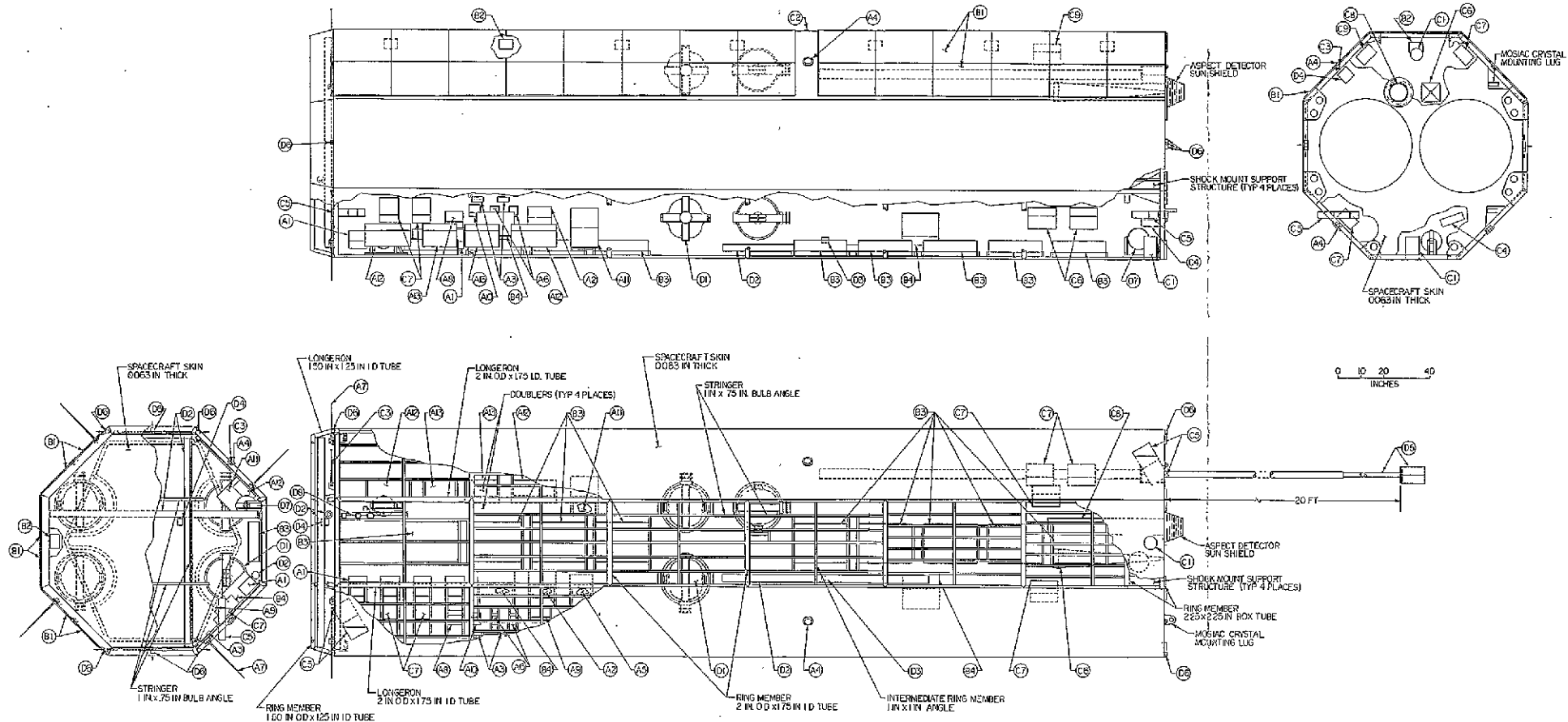


FIGURE 3-2. HEAO-C SYSTEM COMPONENT LOCATIONS

TABLE 3-1. HEAO-C SYSTEMS COMPONENTS LIST

<u>Identification Number</u>		<u>Number Required</u>	<u>Unit Weight (lb)</u>	<u>Unit Size (in.)</u>	<u>Unit Power Required (W)</u>	<u>Operating Time</u>	<u>Unit Heat Dissipated (W)</u>	<u>Operational Temperature Allowed (°F)</u>
<u>Communications and Data Handling System</u>								
A1	Tape Recorders	4	15	5x8x7	25 Maximum (Play) 5 Minimum (Record)	12 min/orbit Continuous	25 5	0 to 130
A2	Switching Network	2	10	2x8x12	0	Continuous	N/A	Max. 160
A3	Beacon Transmitters	2	1	5x2x7	4 Maximum	Continuous	2	Max. 160
A4	S-Band Antennas	4	1	4 Dia.	N/A		N/A	Unlimited
A5	Power Combiner	1	10	1x1x2	N/A	Continuous	N/A	Unlimited
A6	Command Receiver	2	1	4x5x1	0.4 Maximum 0.2 Minimum	Continuous	0.4/0.2	Max. 160
A7	VHF Antenna	4	1	22 Long	N/A	Continuous	N/A	Unlimited
A8	Command Decoder	1	6	8x6x3	4 Maximum	Continuous	4	Max. 160
A9	Multiplexer	1	8	6x6x10	5 Maximum	Continuous	5	Max. 160
A10	Signal Conditioner	1	3	3x2x4	8 Maximum	Continuous	8	Max. 160
A11	Computer	1	72	13x11x9	145 Maximum	Continuous	145	0 to 120
A12	S-Band Decoder/Transmitter	2	36	20x10x4	30	Continuous	30	Max. 160
A13	S-Band Power Amplifiers	2	18	15x8x4	130 Maximum 15 Minimum	12 min/orbit Continuous	110 for 12 min. 15 remainder of orbit.	Max. 160
<u>Electrical Power System</u>								
B1	Solar Cell Modules	84	3.5	20x25x1/2	N/A	Continuous	N/A	Max. 212
B2	Solar Combiners	7	15	6x6x4	N/A ¹	Continuous	15	Max. 160
B3	Charger Battery Reg. Modules	9	110	17x23x5	N/A ¹	Continuous	70	-20 Minimum
B4	Load Distributors	2	30	16x14x8	N/A ¹	Continuous	30	Max. 160

TABLE 3-1 - Concluded

<u>Identification Number</u>		<u>Number Required</u>	<u>Unit Weight (lb)</u>	<u>Unit Size (in.)</u>	<u>Unit Power Required (W)</u>	<u>Operating Time</u>	<u>Unit Heat Dissipated (W)</u>	<u>Operational Temperature Allowed (°F)</u>
<u>Attitude Sensing System</u>								
C1	Star Tracker ²	2	40	5 Dia. x 10	25	Continuous	25	0 to 140
C2	Fine Sun Sensor	1	2	1x1x1/2	1	Continuous	N/A	-10 to 140
C3	Coarse Sun Sensors	8	1	1 Dia. x 5/8	.125	Continuous	N/A	-10 to 140
C4	Three Reference Gyros, Gyro and Sun Sensor Electronic Module	1	7	10x10x5	35	Continuous	35	0 to 140
C5	Coarse Flare Detectors	4	15	8x8x3	1	Continuous	1	Unknown
C6	Fine Flare Detector	1	27	8x8x48	1	<1%	1	Unknown
C7	Flare Detector Electronic Modules	5	30	12x5x8	6.4	4 Continuous 1 - <1%	6.4 6.4	Max. 160
C8	Aspect Detector	1	100	7 Dia x 50	8	Continuous	8	Unknown
C9	Aspect Detector Electronic Module	1	21	12x5x8	6	Continuous	6	Max. 160
<u>Attitude Control System</u>								
D1	Control Moment Gyros	6	45	25x20x18	15 (average)	Continuous	15	-40 to 120
D2	Magnetic Control Torquers	3	31	2 Dia. x 90	7 (average)	2/3 of orbit	7	-30 to 120
D3	Single Axis Magnetometer	1	1		1	Continuous	1	-30 to 120
D4	Double Axis Magnetometer	1	1		1	Continuous	1	+30 to 120
D5	Three Axis Magnetometer and Boom	1	17	5x5x10 20 ft. Boom	3	Continuous	3	-30 to 120
D6	N ₂ Cold Gas Nozzles	12	.33	1x1x1	N/A	N/A	N/A	
D7	N ₂ Tanks	2	7.5	9 in. Dia.	N/A	N/A	N/A	
D8	Values and Lines		29		0	Pulsed	0	

- NOTES: 1. Heat is dissipated due to inefficiency in the units. Power dissipated is allowed for in the power conversion performance factor.
 2. Fixed star trackers are shown in the layout of Figure 3-2. However, the use of gimballed trackers has been assumed for the HEAD-C mission and appropriate weight and power requirement allowances have been made.

decided that fixed star trackers might not be adequate and that gimballed star trackers might be required. The analysis required to determine whether or not the fixed instrument could fulfill the mission requirements is beyond the scope of the present study. Since the adequacy of the fixed trackers is questionable at this time, the use of gimballed trackers has been assumed and appropriate allowances in system weight and power requirements were made. However, the larger volume required by the gimballed trackers was not available at the fixed tracker locations on the layouts. Accommodation of the gimballed trackers will require some modification of the layout shown in Figure 3-2.

Weight and Power Summaries

The spacecraft weight summary by systems is given in Table 3-2. System weight breakdowns are given in the system description sections of the report. The payload separation mechanism includes the pyrotechnics, wiring, and control circuits necessary to separate the payload from the booster at orbit injection. The payload truss connects the base of the spacecraft (viewing end) to the booster; it distributes the payload weight to the booster attach points.

The spacecraft power requirement summary by systems is given in Table 3-3. System power requirement breakdowns are given in the system description sections of the report.

MISSIONS B AND D SYSTEM INTERFACES AND FLIGHT DIFFERENCES

The HEAO-B and HEAO-D spacecrafts will be very similar to the HEAO-A and HEAO-C spacecrafts. The HEAO-B and HEAO-D spacecrafts are expected to have the following systems:

TABLE 3-2. HEAO-C SPACECRAFT WEIGHT SUMMARY

Experiments		8,536
Experiments	6,789	
Computer	72	
Optical Bench Structure	1,515	
Cabling	160	
Attitude Sensing System		110
Attitude Control System		440
Power System		1,849
Components	1,449	
Cabling	400	
Communications and Data Handling System		327
Components	247	
Cabling	80	
Spacecraft Structure		2,360
Structural Members	2,170	
Spacecraft-Bench Connection Equipment	100	
Mosaic Crystal Deployment Structure	90	
Thermal Control System		445
Bench Heaters	10	
Bench Insulation	203	
Spacecraft Insulation and Coatings	232	
Booster Payload Separation Mechanism		100
Payload Truss		<u>100</u>
	TOTAL PAYLOAD WEIGHT	<u><u>14,267</u></u>

TABLE 3-3. HEAO-C SPACECRAFT POWER SUMMARY

<u>System</u>	<u>Power (W)</u>	
	<u>Average</u>	<u>Peak</u>
Experiments	284*	284
Attitude Sensing System	85	87
Attitude Control System	115	265
Communications and Data Handling System	147	366
Thermal Control System	<u>10</u>	<u>35</u>
Totals	641	1,037

*Combination of experiments in operation that requires maximum power.

- Attitude Sensing
- Attitude Control
- Thermal Control
- Electrical Power
- Communications and Data Handling

Attitude Sensing

The attitude sensing system on the HEAO-B spacecraft interfaces with the attitude control system, the electrical power system, and the communications and data handling system, as it does on the HEAO-C spacecraft. The commodities transmitted across these interfaces will be the same as in the HEAO-C spacecraft. The system components will probably be essentially the same as those used on the HEAO-A mission, since the B mission spacecraft will also be spun about its Z axis.

Since the HEAO-D experiments have no attitude control requirements, the spacecraft attitude control requirements and hence the attitude sensing requirements have not been defined for this mission. The D spacecraft may have a single axis attitude control system for solar panel orientation or it may have no attitude control at all. In the latter event, it may or may not have an attitude sensing system. If there is an attitude sensing system on the HEAO-D spacecraft, it will probably interface with the attitude control system, the electrical power system, and the communications and data handling system. The same commodities will be transferred as in the HEAO-C spacecraft.

Attitude Control

The HEAO-B attitude control system is expected to be very similar to the HEAO-A attitude control system. It will interface with the attitude sensing system, the electrical power system, and the communications and data handling system. The commodities transferred across these interfaces will be the same as for the HEAO-C

spacecraft. If an attitude control system is required for the HEAO-D spacecraft, it is expected to interface with the same systems as the HEAO-C spacecraft with the same commodities being transferred.

Thermal Control

The thermal control requirements are not well defined for the HEAO-B and HEAO-D missions. Passive thermal control systems are currently anticipated for these flights, but the trade offs in the use of an active refrigeration system have not been completely explored. If the thermal control systems are completely passive, the only interface may be with the communications and data handling system for the transfer of system status data. If the thermal control systems include any active components, an electrical power interface will be required.

Electrical Power

The electrical power systems on both the HEAO-B and HEAO-D spacecrafts are expected to interface with the communications and data handling systems and with the experiments. The power system on the HEAO-B spacecraft will also interface with the attitude sensing and the attitude control systems. The power will be transferred in the form of 28 Vdc power.

Communications and Data Handling

The communications and data handling systems on both the HEAO-B and HEAO-D spacecrafts will interface with the experiments and with all active systems. Data on experiment results plus experiment status information will be transferred from the experiments in the form of digital signals. Commands will be transferred to all experiments and active systems.

SPACECRAFT CAPABILITIES FOR MISSIONS A, B, C AND D

A comparison of spacecraft capabilities for the HEAO A, B, C, and D missions is presented in Table 3-4. Total spacecraft weights are expected to be slightly lower for the C and D missions. This is because the launches occur in years in which the 11-year solar activity cycle causes the 2σ atmospheric density to be greater at a given altitude. The result is that the C and D missions will have to be conducted at greater altitudes than the A and B missions and payloads will probably be reduced.

Many of the HEAO-D spacecraft capabilities have not been established. Attitude hold capability appears to be adequate for the A and B missions in the scanning mode and for the C mission.

TABLE 3-4. COMPARISON OF SPECECRAFT CAPABILITIES
FOR HEAO MISSIONS A, B, C, AND D

System	<u>HEAO Missions</u>			
	<u>A</u>	<u>B</u>	<u>C</u>	<u>D</u>
Experiments				
Weight (lb)	12,500	12,800	8,500	11,800 (Est)
Power Required (W)	265	275	284	250 (Est)
Attitude Control				
Attitude Hold	Not Established	Not Established	±30 Arc Seconds	Not Established
Scan Axis	±0.2 Degree	±0.2 Degree	Not Applicable	Not Established
Maneuver Capability	Not Established	Not Established	y and z axes: 100 Deg in 30 Min x axis: 360 deg in 21 Min	Not Established
Electrical Power				
Total Requirement (W)	660	745	705	600 (Est)
Total Available Initially	845	845	762	Not Established
Margin (Initially)	185	100	57	Not Established
Evaluation	Adequate for two years	Adequate for two years	Barely adequate for two years. Max. temp. problem on middle solar panel	Not Established
Total Weight (lb)	18,700	19,300	14,300	15,000 (Est)

3-17/3-18

4. SPACECRAFT STRUCTURE

The optical bench, which supports the telescope mirrors, experiment detectors that utilize the X-ray optics, certain additional peripheral experiments, and selected attitude sensors and detectors, is supported within and by the spacecraft structure. The spacecraft structure envelops the optical bench and the majority of its volume is filled by the bench. The spacecraft systems components are located in the spaces between the optical bench and the spacecraft structure.

The function of the optical bench is to provide a rigid, undeformed connection between the telescope mirrors on the viewing end of the spacecraft and the detectors located 20 and 26 feet from the mirrors. Alignment of the various detectors with the mirrors is critical and the bench temperature must be controlled to ± 10 °F to insure proper focus. In order to achieve the required thermal control, the bench must be thermally isolated from the spacecraft to the greatest practical extent. To achieve this the optical bench is covered on all sides and over one end with 1.5 inches of superinsulation; the viewing end is covered only by a thin sheet of aluminized mylar. As a further measure for thermal isolation, the bench is connected to the spacecraft structure only at the ends.

The optical bench and its connecting structure are shown in Figure 4-1. The original bench design was provided by American Science and Engineering (AS&E); it was modified by Teledyne Brown Engineering designers somewhat in order to fit in the HEAO-C spacecraft configuration. The bench is constructed of 3-inch OD by 2.875-inch ID tubular Invar steel. This material was chosen for its extremely low coefficient of thermal expansion, 8×10^{-7} inch/inch-degree F.

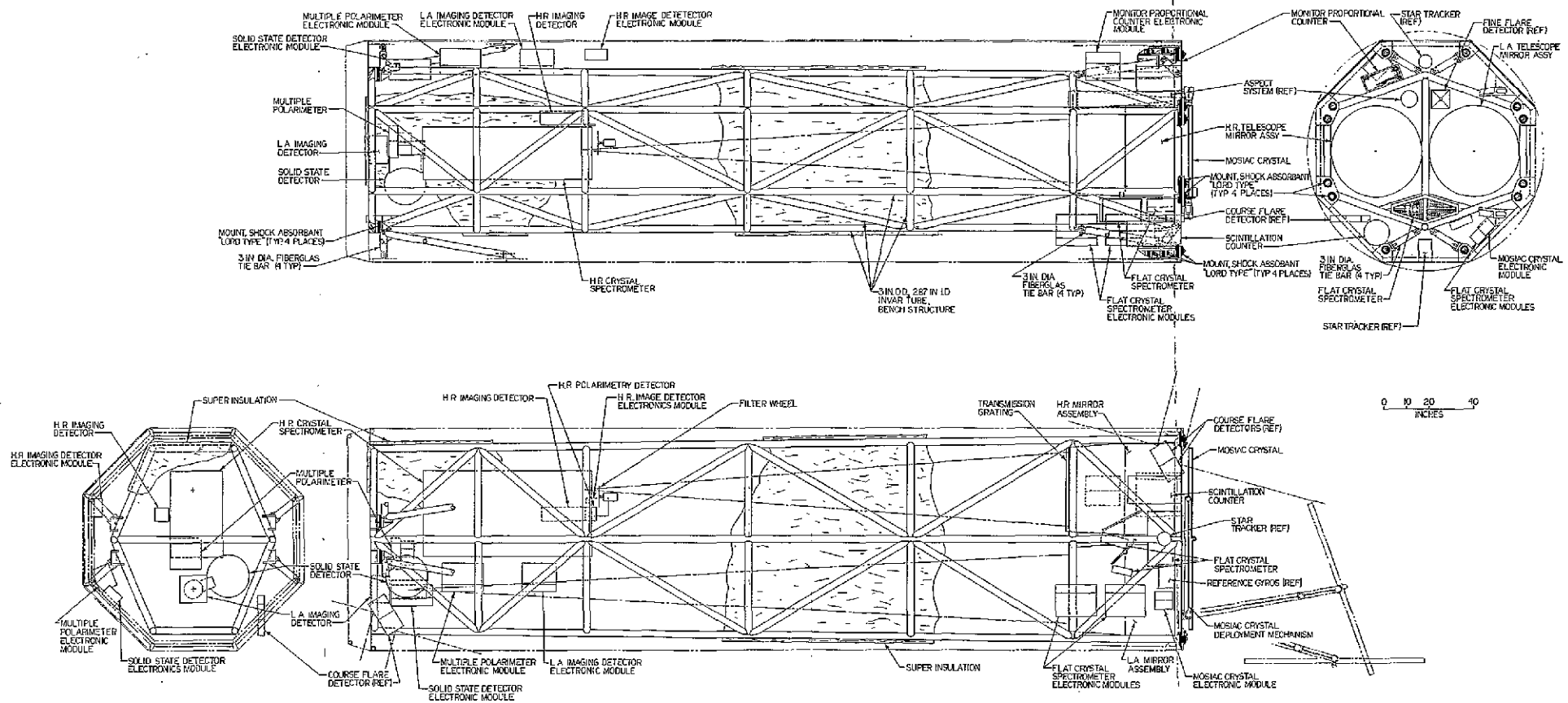


FIGURE 4-1. OPTICAL BENCH AND CONNECTING STRUCTURE CONFIGURATION

VIBRATION MOUNTS

Precise alignment of the X-ray detectors with the focusing X-ray mirrors is necessary for proper operation of the primary experiments on the HEAO-C spacecraft. Various detectors and associated instruments will be moved into and out of the focal planes as the different experiments are conducted. These detectors must be protected from the acoustical environment produced by the launch vehicle during the launch operation; however, the requirement for precision alignment prevents the use of vibration damping mounts between the experiments and the optical bench. For this reason, vibration mounts must be used on the connections between the optical bench and the spacecraft.

The structural design includes the use of 20 vibration mounts near the base, (launch position) or viewing end, of the optical bench and 4 vibration mounts near the upper end of the bench. The mount design concept is shown in Figure 4-2 and consists of a BTR silicone rubber bushing that is compressed between two flat plates at the bench attach point. The type mount shown is manufactured by the Lord Manufacturing Company (Ref. 4-1). The size used in this application is six inches in diameter and has a load capacity of 3000 pounds.

The bench support members to which the vibration mounts are attached are to be made of fiberglass for minimum thermal conduction between the bench and spacecraft. These tie bars and the vibration mounts are shown in Figure 4-1.

A limited amount of information was obtained on the properties of vibration mounts manufactured by the Lord Company from the results of thermal vacuum tests conducted by the Marshall Space Flight Center Materials Laboratory (Ref. 4-2). As a result of these tests the Lord mounts were found acceptable for use on the Apollo Telescope Mount (ATM) mission. It was demonstrated that the higher weight molecular

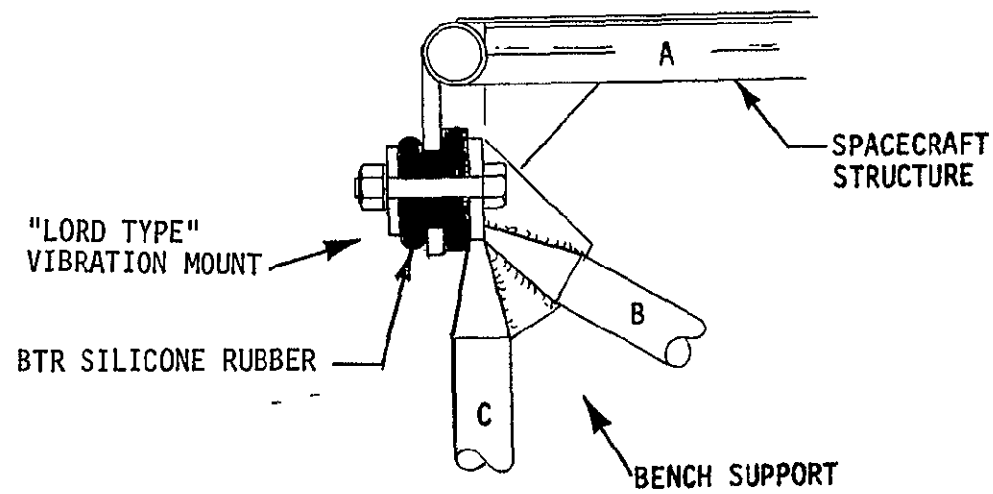
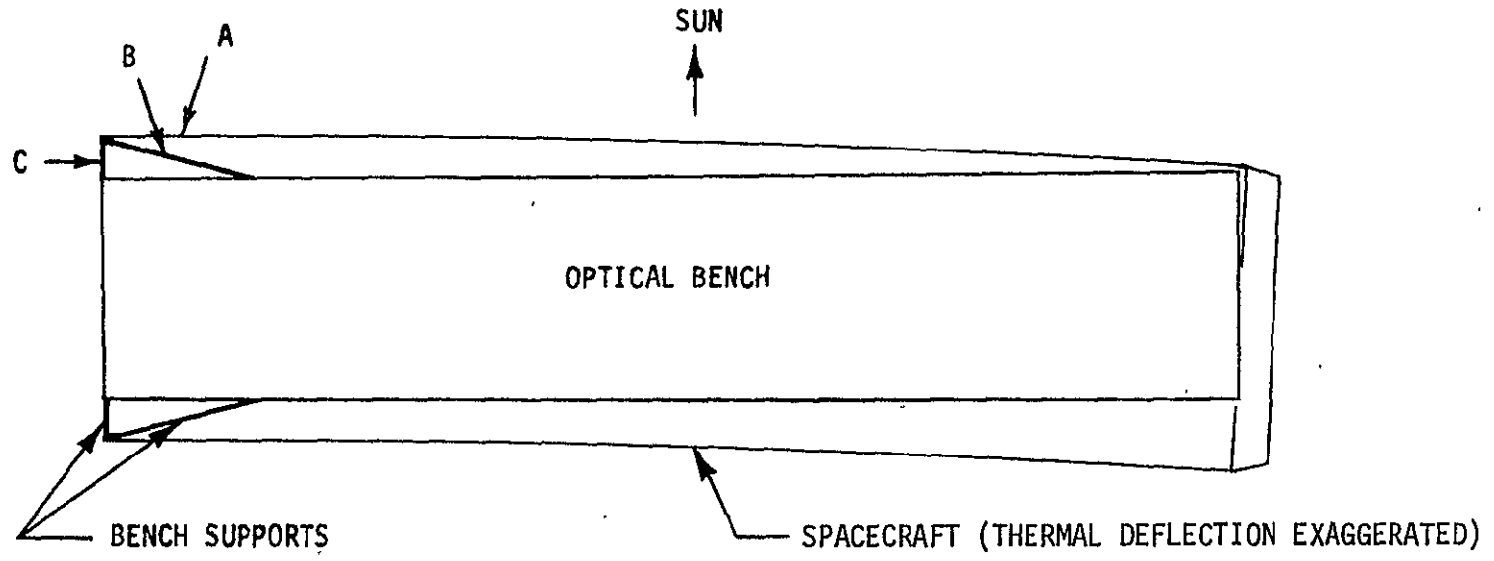


FIGURE 4-2. VIBRATION MOUNT FOR ISOLATION OF THE OPTICAL BENCH FROM THE SPACECRAFT

weight fragments did not condense and adsorb on surfaces in the ATM thermal environment. In one MSFC outgassing test, a sample of BTR silicone rubber lost 0.7 percent of its weight, and the outgassing rate decreased to zero in less than 16 hours. It was also found that outgassing did not cause the BTR silicone to lose any of its mechanical properties. Additional tests will be required to insure that outgassing will not have harmful effects on the HEAO-C experiments.

To insure accurate pointing of the X-ray telescopes the star trackers, which provide the spacecraft attitude reference, are located on the optical bench structure, rather than on the spacecraft structure. Therefore, some relative movement between the optical bench and spacecraft will not affect pointing accuracy.

THERMAL DEFLECTION

Unequal solar heating of the HEAO-C spacecraft sides toward and away from the Sun will result in induced thermal stresses in the spacecraft which will cause a deflection, or "hot dogging", of the spacecraft structure. If the optical bench remains rigidly connected at both ends to the spacecraft structure after orbit insertion, the bench will restrict the spacecraft deflection and accept a large bending moment in the process. This bench deflection cannot be tolerated by the X-ray telescope experiments. Bench deflection can be avoided by disconnecting the bench from the spacecraft at its upper end, i. e., the end opposite to the viewing end after orbit insertion.

A preliminary heat transfer analysis was performed near the beginning of the study to predict spacecraft skin temperatures for use in the spacecraft thermal deformation calculations. The thermal model consisted of a thin, cylindrical, aluminum shell having an outside diameter of 100 inches and unit length. The shell thickness, \bar{t} , was varied from 0.125 to 1 inch to permit evaluation of the effect of variation in

equivalent wall thickness on circumferential temperature distribution. One-dimensional, steady-state heat conduction in the circumferential θ direction was assumed. The inside wall of the shell was assumed to be adiabatic, i. e., radiation heat exchange between various segments of the inside wall was neglected.

The environmental heat flux distribution on the outer skin was extracted from previous orbital heat flux calculations for the HEAO-A spacecraft (Ref. 4-3). Examination of the previous HEAO-A calculations revealed that the most severe temperature gradient around the circumference occurs when the spacecraft first emerges from the Earth's shadow with the Earth-Sun line lying on the orbit plane. Accordingly, the instantaneous heat flux distribution (Figure 4-3) representing this position was imposed on the spacecraft skin in the present analysis, and the resulting steady-state temperature distribution of the cylindrical shell was calculated.

The solar absorptivity, α_s , and infrared emissivity, ϵ , of the half of the shell facing the Sun (representing the solar panels) were assumed to be 0.7 and 0.8, respectively; values of α_s and ϵ of the opposite side of the shell were assumed to be 0.35 and 0.85, respectively. The temperature calculations were accomplished using the Chrysler CINDA digital computer program. The thermal network consisted of 16 nodes spaced at equiangular positions around the circumference.

The predicted temperature distributions around the shell for various values of equivalent wall thickness, \bar{t} , are presented in Figure 4-4. As illustrated in Figure 4-4, the maximum temperature difference, ΔT_{\max} , between two stations spaced 180 degrees apart on the shell occurs between the subsolar point ($\theta = 0^\circ$) and the station 180 degrees away ($\theta = 180^\circ$). Predicted values of ΔT_{\max} for equivalent wall thicknesses of 0.125, 0.5 and 1.0 inch are 366°F, 283°F and 222°F, respectively. These values of ΔT_{\max} are conservatively high, since heat transfer from the system components adjacent to the wall opposite

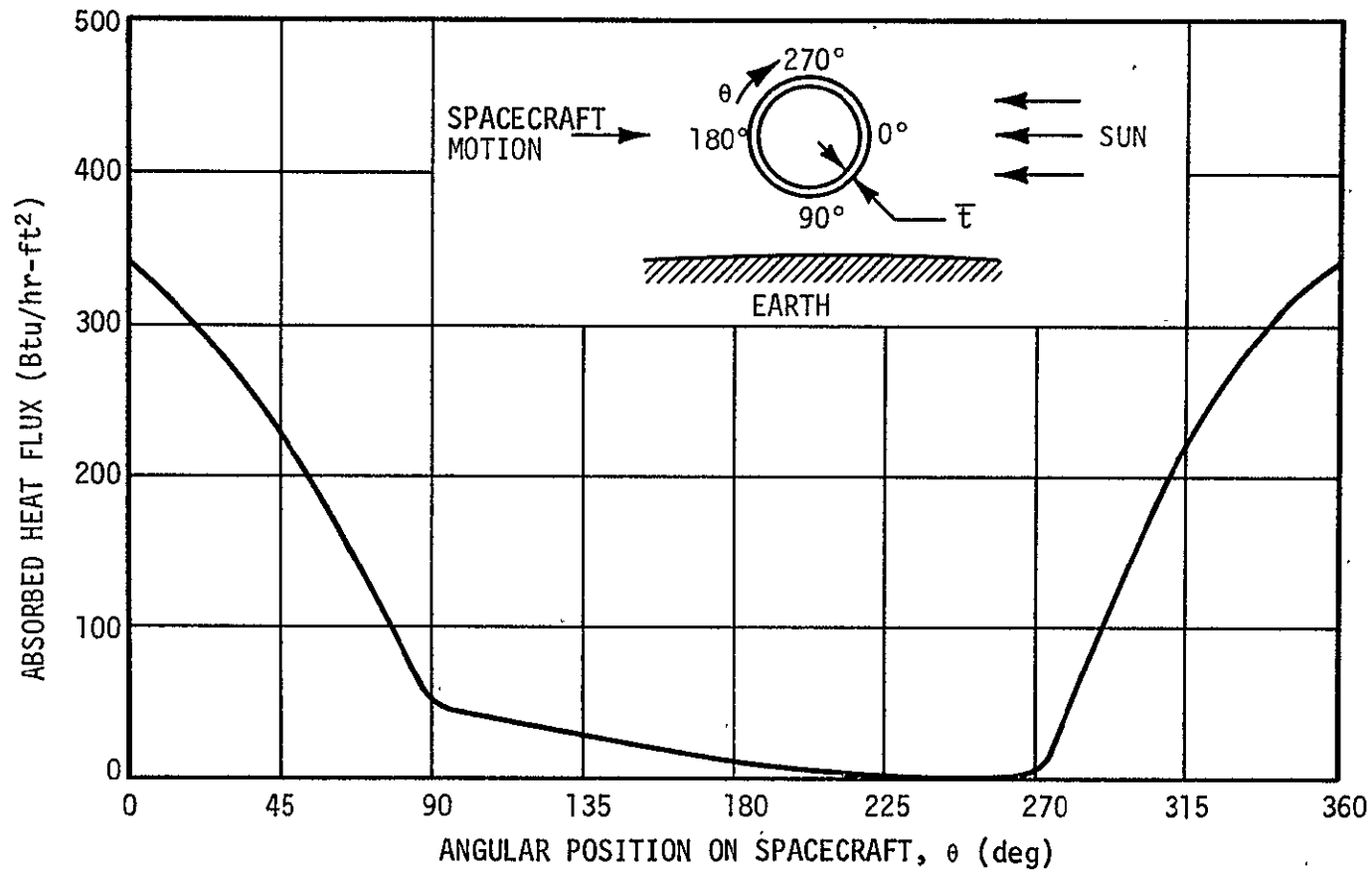


FIGURE 4-3. ENVIRONMENTAL HEAT FLUX DISTRIBUTION AROUND HEAO SPACECRAFT FOR WORST CASE CIRCUMFERENTIAL TEMPERATURE GRADIENT

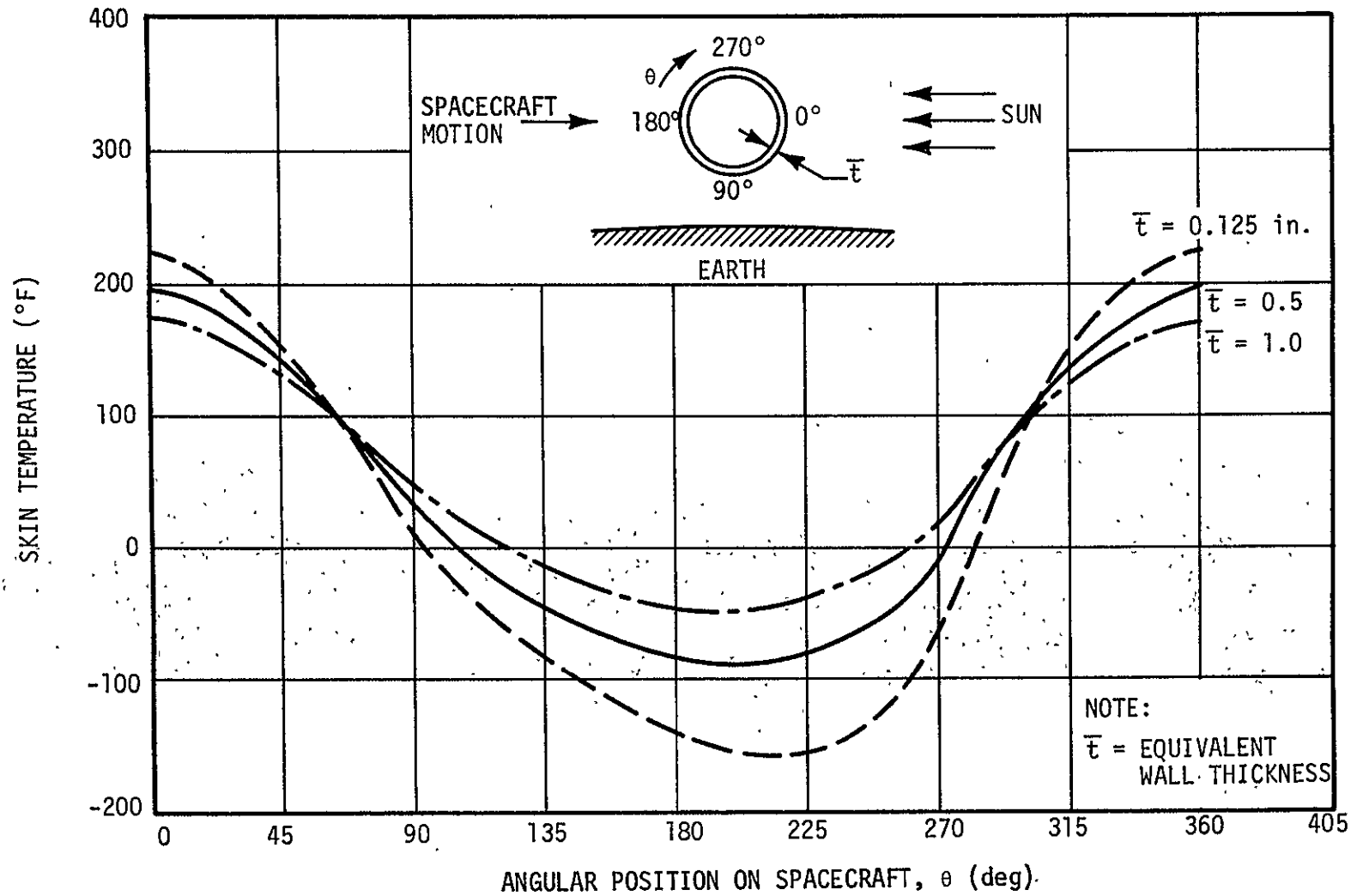


FIGURE 4-4. PREDICTED TEMPERATURE DISTRIBUTION ON THE SPACECRAFT SKIN AS A FUNCTION OF EQUIVALENT WALL THICKNESS

the solar panels will raise its temperature and reduce ΔT_{\max} . In addition the solar absorptivity and emissivity values for the backside of the spacecraft were reduced later in the study from the values used in this analysis. The result of this change is a warmer backside and therefore a lower ΔT_{\max} than is indicated in the present analysis.

Figure 4-5 is a plot of ΔT_{\max} as a function of equivalent wall thickness. Figures 4-4 and 4-5 demonstrate that an eight-fold increase in \bar{t} produced a reduction in ΔT_{\max} of only 39 percent, even for a material with good heat conduction characteristics, such as aluminum. Thus ΔT_{\max} is relatively insensitive to variation in wall thickness. The equivalent wall thickness of the HEAO-C spacecraft structure is approximately 0.125 inches. Therefore, the maximum expected temperature differential between the hot and cold sides of the spacecraft, based upon this conservative analysis is 366°F.

The thermal deflection δ of a 100-inch diameter shell spacecraft was calculated using the following equation, which was derived from the theory presented in the Handbook of Engineering Mechanics, Section 43 (Ref. 4-4).

$$\delta = \alpha \frac{2\Delta T R^2 t}{3I} X^2$$

where

- δ - the thermal deflection at point X, inches
- X - distance from the fixed end of a cantilever beam with a thin wall, circular section, 360 inches
- α - the coefficient of thermal expansion of the spacecraft material, 6061 T6 Aluminum, 13.1×10^{-6} in/(in - °F)
- I - average spacecraft moment of inertia (41.5×10^3 in⁴)
- ΔT_{\max} - the difference in temperature between opposite sides of the spacecraft, 366°F

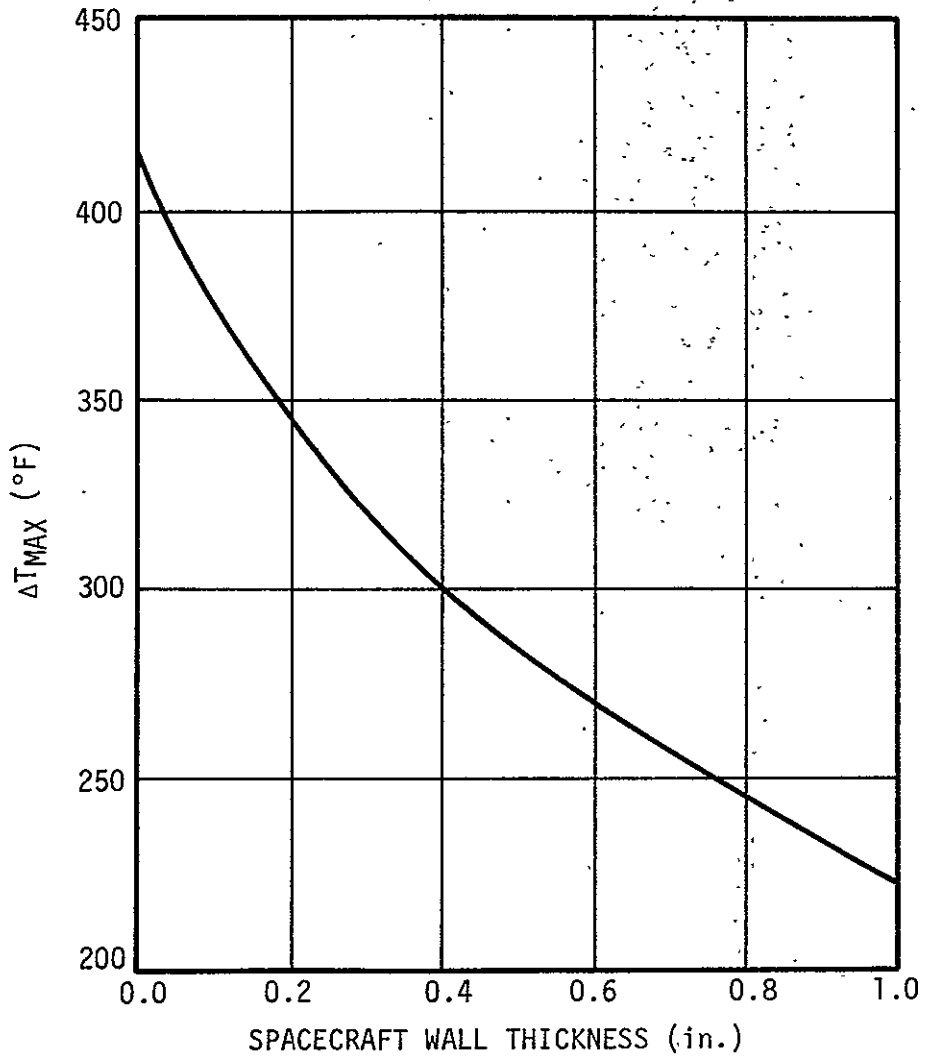


FIGURE 4-5. ΔT_{MAX} AS A FUNCTION OF EQUIVALENT SPACECRAFT WALL THICKNESS

- t - average spacecraft wall thickness (0.117 inches including longeron)
- R - the spacecraft radius, 50 inches.

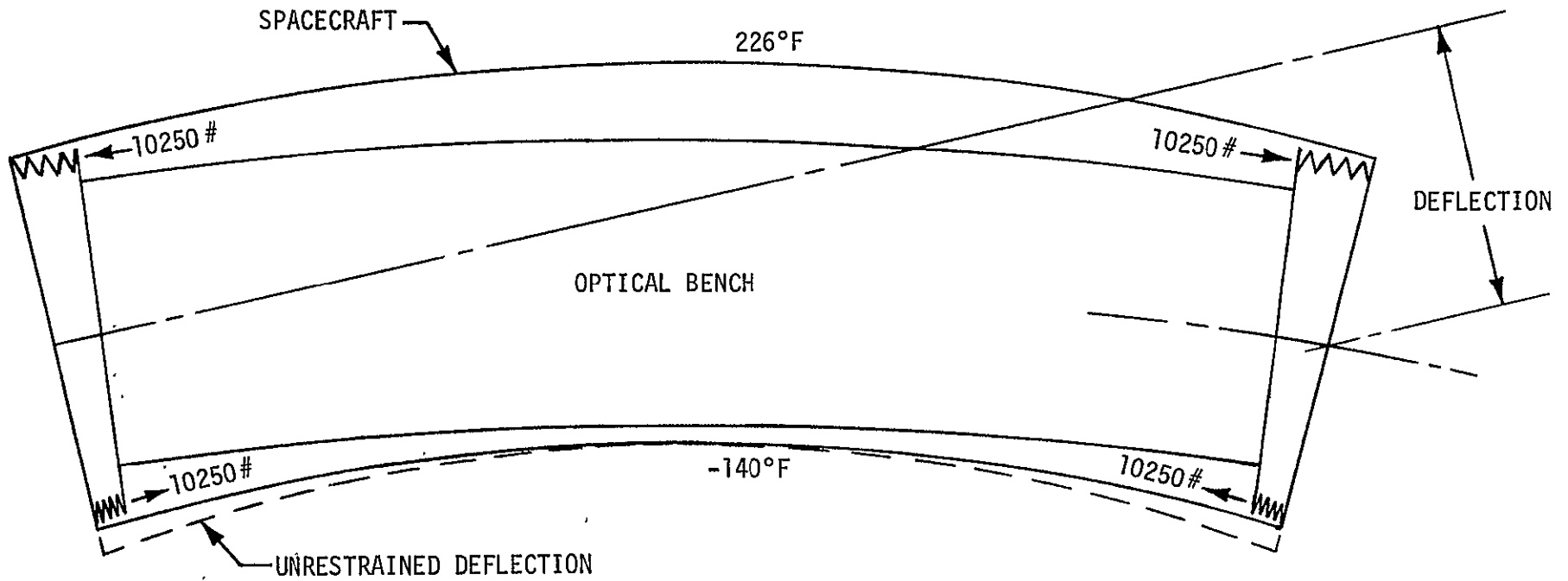
The calculated thermal deflection for the spacecraft structure is 2.92 inches.

Loads equivalent to 10,250 pound reactions on the bench will be induced if the optical bench remains rigidly connected at both ends to the spacecraft; this will cause a bench deflection of 2.23 inches. Bench deflection can be avoided by decoupling the bench from the spacecraft at the nonviewing end after orbit insertion. This will allow the spacecraft to be deflected without affecting the optical bench. The bench is illustrated schematically in the coupled configuration in Figure 4-6; coupled and decoupled deflections are also given. The bench is illustrated in the decoupled configuration in Figure 4-2. Decoupling will be achieved by the use of electro-mechanical separation mechanisms located on the connecting fiberglass struts.

The optical bench design provided by AS&E was modified somewhat to permit a clearance of 3.0 inches between it and the spacecraft structure at the non-viewing end and proportionally lesser clearances at all points along the longitudinal axis. The system components were attached to the spacecraft structure at locations where they would not violate the clearance envelope.

STRUCTURAL DESIGN

The structural configuration of the HEAO-C spacecraft is shown in Figure 4-7. View B of this figure shows the spacecraft cross section dimensions, which are constant except for the last 10 inches of length. As can be seen in View B, the spacecraft cross section differs slightly from a regular octagon. The deviation is necessary in order to mount the ATM type solar panels on three spacecraft sides without violating a 105-inch spacecraft diameter envelope. The dimensions shown in



	DEFLECTIONS	
	BOTH ENDS ATTACHED	ONE END FREE
SPACECRAFT	2.71 in.	2.92 in.
OPTICAL BENCH	2.23 in.	0.0 in.

FIGURE 4-6. SPACECRAFT-OPTICAL BENCH THERMAL DEFLECTIONS

View B of Figure 4-7 are member center to member center dimensions. The width of each of the three solar panels is approximately 40 inches, which is determined by the two rows of ATM type solar modules which make up each panel. The center to center length of the member beneath the middle solar panel (39 in.) is shorter than the panel width, however the top dimension of this member is equal to the panel width. The length of the members beneath the two side panels (40 in.) is equal to the panel widths; however, the panel ends are not directly over the member ends.

The dimensions of the remaining five sides were dictated by the 105 inch envelope. The spacecraft cross section could be made a regular octagon by permitting the corners of the solar panels to violate the 105 inch envelope by approximately 0.5 inch at the corners.

Spacecraft member sizes and skin thicknesses are shown in Figure 4-7. Aluminum alloy 6061-T6 was selected as the spacecraft material in preference to other aluminum alloys because of its availability in sheet form, good welding properties, and high thermal conductivity. The mechanical properties of 6061-T6 aluminum are:

- Modulus of elasticity $E = 10 \times 10^6 \text{ lb/in}^2$
- Modulus of rigidity $G = 3.75 \times 10^6 \text{ lb/in}^2$
- Density $p = 0.098 \text{ lb/in}^3$
- Yield strength $F_{ty} = F_{cy} = 35,000 \text{ lb/in}^2$.

Loading for the spacecraft structure was taken from the weight locations shown on the layout drawings (Section 3). It is presented here as the combination of a distributed weight, as shown in Figure 4-8 and summarized in Table 4-1, and a series of point loads corresponding to the lump weights shown in Tables 4-2 and 4-3.

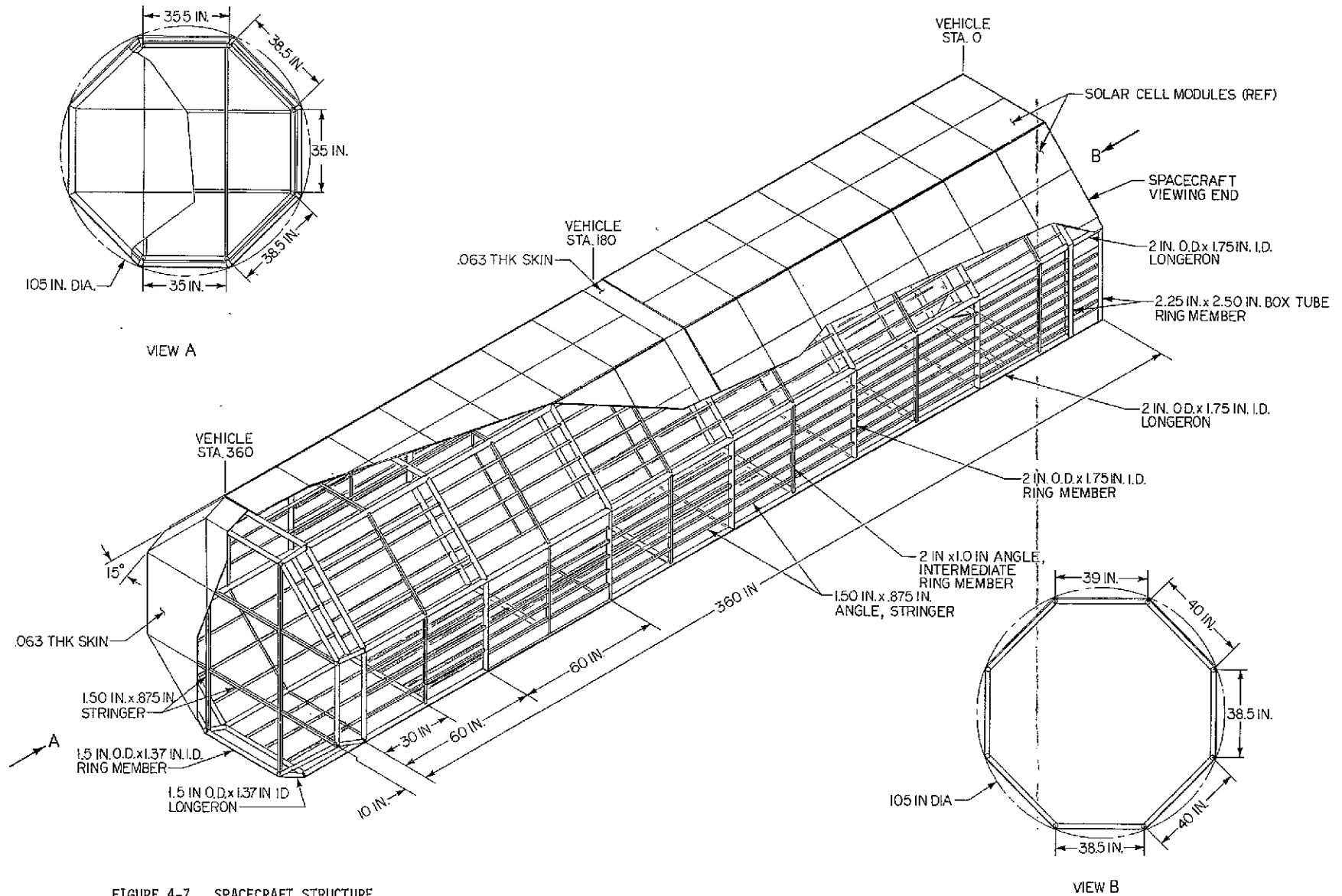


FIGURE 4-7. SPACECRAFT STRUCTURE

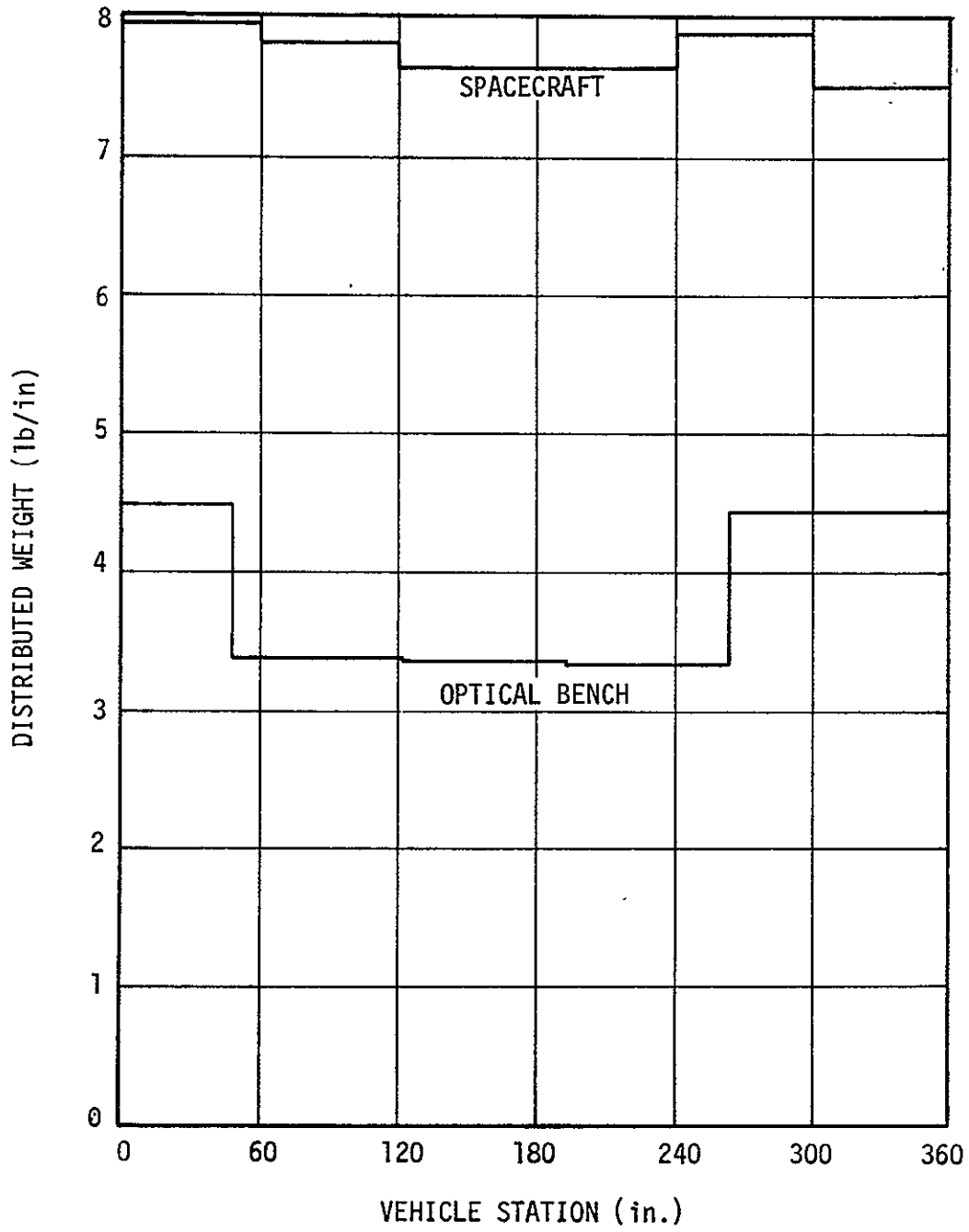


FIGURE 4-8. SPACECRAFT AND OPTICAL BENCH DISTRIBUTED WEIGHT

TABLE 4-1. DISTRIBUTED WEIGHT FOR OPTICAL BENCH AND SPACECRAFT

<u>Optical Bench</u>		<u>Total Weight</u> <u>(lb)</u>
<u>Item</u>		
Structure		1,117
Longerons	367	
Diagonals	450	
Brackets and Contingency	300	
Insulation		203
Cabling		30
Heaters		<u>10</u>
TOTAL OPTICAL BENCH DISTRIBUTED WEIGHT		<u>1,360</u>
 <u>Spacecraft</u> 		
Structure		1,625
Skin	711	
Stringers	306	
Longerons	208	
Brackets and Contingency	400	
Insulation and Coatings		232
Solar Panels		294
Cabling		610
Communications and Attitude		
Sensing Miscellaneous Hardware		<u>43</u>
TOTAL SPACECRAFT DISTRIBUTED WEIGHT		<u>2,804</u>
Spacecraft/Bench Connections		<u>100</u>

TABLE 4-2. LUMP WEIGHTS FOR OPTICAL BENCH

<u>Item</u>	<u>Station (in.)</u>	<u>Weight (lb)</u>
Structure	0	61
Star Tracker (2)	6	80
Monitor Proportional Counter	9	98
Flat Crystal Spectrometer	16	110
L.A. Mirror Assembly	24	2400
H.R. Mirror Assembly	24	2025
Aspect Detector	25	100
Fine Flare Detector	25	27
Structure	48	57
Transmission Grating	50	60
Structure	120	55
Structure	192	55
Filter Wheel Assembly	254	40
H.R. Polarization Crystal	262	5
Structure	264	55
H.R. Experiment Transport Mechanism	264	40
H.R. Image Detector	275	20
H.R. Crystal Spectrometer	300	397
Structure	312	55
Solid-State Detector	344	90
Multiple Polarimeter	346	20
L.A. and H.R. Experiment Transport Mechanism	348	145
L.A Image Detector	355	100
Structure	360	<u>60</u>
 TOTAL OPTICAL BENCH LUMP WEIGHTS		 <u><u>6,155</u></u>

TABLE 4-3. LUMP WEIGHTS FOR SPACECRAFT

<u>Item</u>	<u>Station (in.)</u>	<u>Weight (lb)</u>
Mosaic Crystal	-5	300
Mosaic Crystal Deployment Structure	-2	90
Structure	0	44
Coarse Sun Sensor (4)	0	4
Reference Gyro (3), Gyro and Sun Sensor Electronics Module	3	7
Coarse Flare Detector (2)	6	30
Mosaic Crystal Electronics Module	7	10
Structure	8	83
Gas Design Module	11	25
Scintillation Counter	11	316
Structure	15	44
Solar Combiner	24	15
Flat Crystal Spectrometer Electronic Module	24	26
Structure	30	15
Monitor Proportional Counter Electronic Module	34	44
Flare Detector Electronic Module	36	30
CBR Module	37	110
Flat Crystal Spectrometer Electronic Module	46	26
Aspect Detector Electronic Module	51	21
Flare Detector Electronic Module	52	30
Flare Detector Electronic Module	54	30
Structure	60	26
CBR Module	65	110
Solar Combiner	74	15
Three Axis Magnetometer and 20-Foot Boom	76	17
Structure	90	15
CBR Module	93	110
Load Distributor	104	30
CBR Module	120	110
Structure	120	26

TABLE 4-3. - Continued

<u>Item</u>	<u>Station (in.)</u>	<u>Weight (lb)</u>
Solar Combiner	124	15
Electromagnet and Single Axis Magnetometer	146	32
CBR Module	148	110
Structure	150	15
Fine Sun Sensor	154	2
S-Band Antenna (4)	154	4
CMG (2)	175	90
Structure	180	26
Solar Combiner	184	15
CMG (4)	207	180
Structure	210	15
Solar Combiner	234	15
CBR Module	235	110
Structure	240	26
Computer	251	72
H.R. Image Detector Electronic Module	259	24
CBR Module	262	110
Switching Network (2)	269	20
Multiplexer	270	8
Structure	270	15
S-Band Decoder/Transmitter	273	36
Command Receiver	282	1
Solar Combiner	284	15
L.A. Image Detector Electronic Module	285	50
Beacon Transmitter	286	1
Load Distributor	289	30
CBR Module	290	110
Command Receiver	290	1
S-Band Power Amplifier	294	18
Beacon Transmitter	297	1
Signal Conditioner	298	3

TABLE 4-3. - Continued

<u>Item</u>	<u>Station (in.)</u>	<u>Weight (lb)</u>
Structure	300	26
Command Decoder	307	6
Tape Recorder	307	15
S-Band Power Amplifier	314	18
CBR Module	318	110
Multiple Polarimeter Electronic Module	319	60
Flare Detector Electronic Module	321	30
Tape Recorder	321	15
Structure	330	15
Solar Combiner	334	15
Flare Detector Electronic Module	335	30
Tape Recorder	335	15
S-Band Decoder/Transmitter	336	36
Gas Despin Module	340	25
Solid State Detector Electronic Module	341	25
Tape Recorder	349	15
Coarse Flare Detector (2)	353	30
Coarse Sun Sensor (4)	360	4
VHF Antenna (4)	360	4
Structure	360	26
Electromagnet	363	31
Electromagnet and 2 Axis Magnetometer	366	32
Structure	370	<u>128</u>
TOTAL OF SPACECRAFT LUMP WEIGHTS		<u><u>3,640</u></u>

A safety factor of 1.5 used in the design was applied to the following loading condition:

- 6 g's axial acceleration
- 1.5 g's lateral acceleration.

BENDING AND SHEAR STIFFNESS DISTRIBUTIONS

The product of modulus of elasticity and moment of inertia (EI) is a measure of the bending stiffness of a structure. The product of structure member cross sectional area and modulus of rigidity (AG) is a measure of the shear stiffness of a structure. EI and AG curves for the resulting spacecraft configuration and the optical bench are shown in Figures 4-9, 4-10, 4-11, and 4-12. This data can be used in building a dynamic model of the system. The loads induced at the top and the bottom of the spacecraft due to the accelerated bench weight are distributed according to the relative axial and lateral stiffnesses of the spacecraft and the bench. The resultant vertical reaction at the top of the spacecraft is 9700 pounds and the lateral reaction is 4500 pounds. The top spacecraft/bench connecting structure transfer this vertical reaction to the spacecraft structure at Station 300. The connecting structure transfers the 4500-pound lateral reaction from the bench to the spacecraft at Station 360.

BASE RING DESIGN

During launch, the optical bench impacts large eccentric loads to the base of the spacecraft. Special rings are required in this area to transfer the optical bench base reactions to the spacecraft. This special structure will consist of two rings spaced 15 inches apart and connected by the spacecraft/optical bench mounting structure brackets. Details of this portion of the spacecraft structure are shown in Figure 4-13.

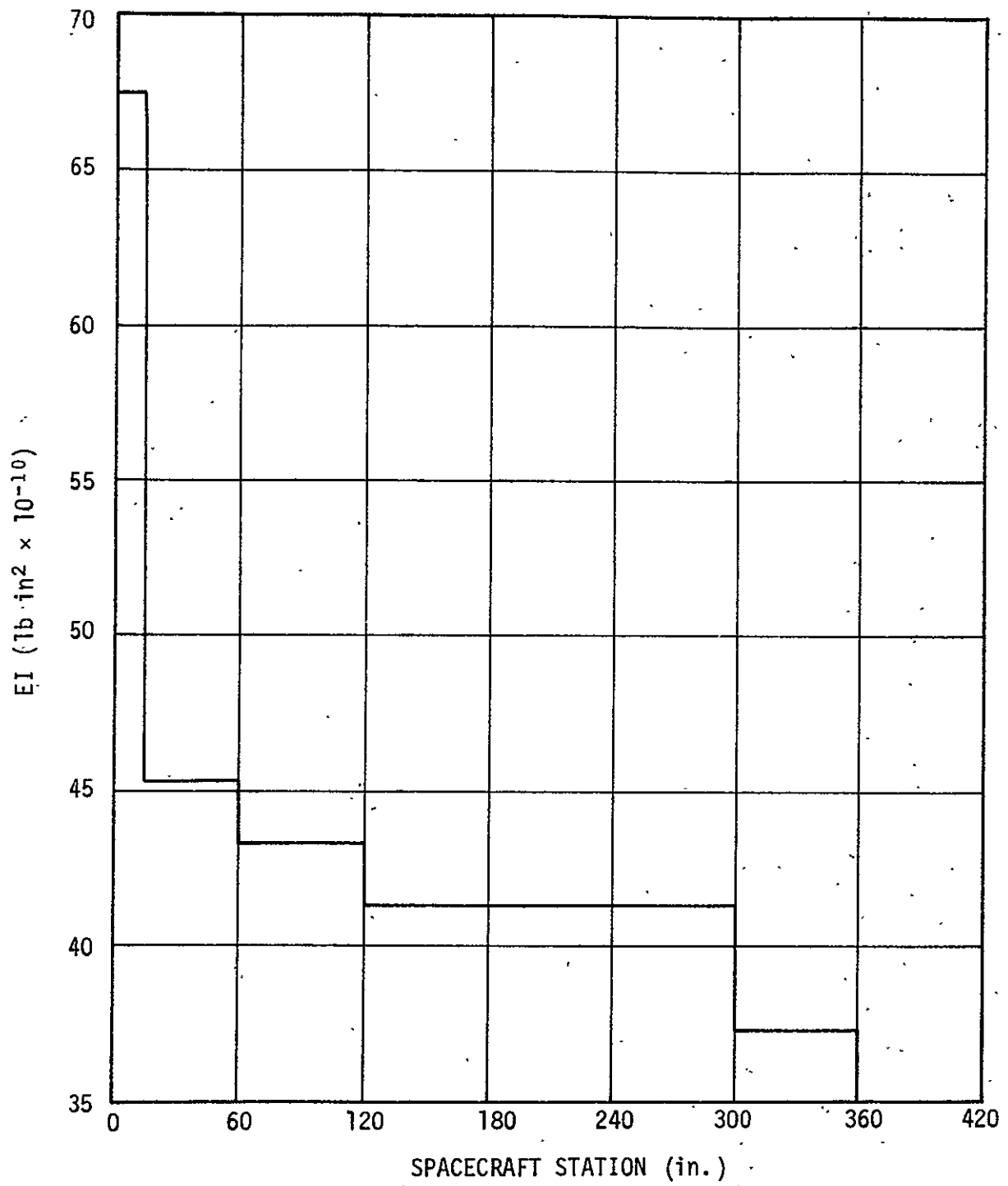


FIGURE 4-9. EI AS A FUNCTION OF SPACECRAFT STATION FOR ALL AXES

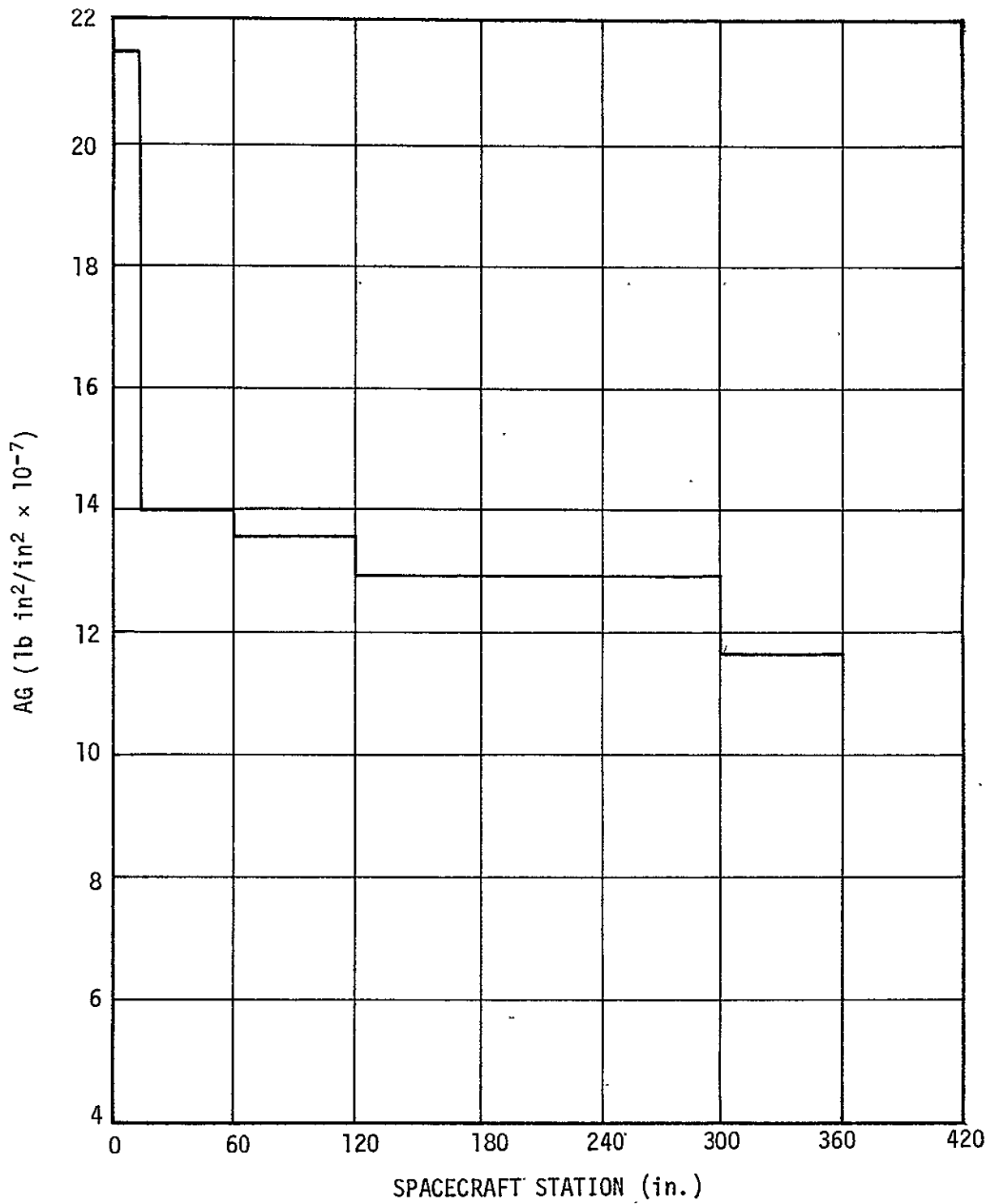


FIGURE 4-10. AG AS A FUNCTION OF SPACECRAFT STATION FOR ALL AXES

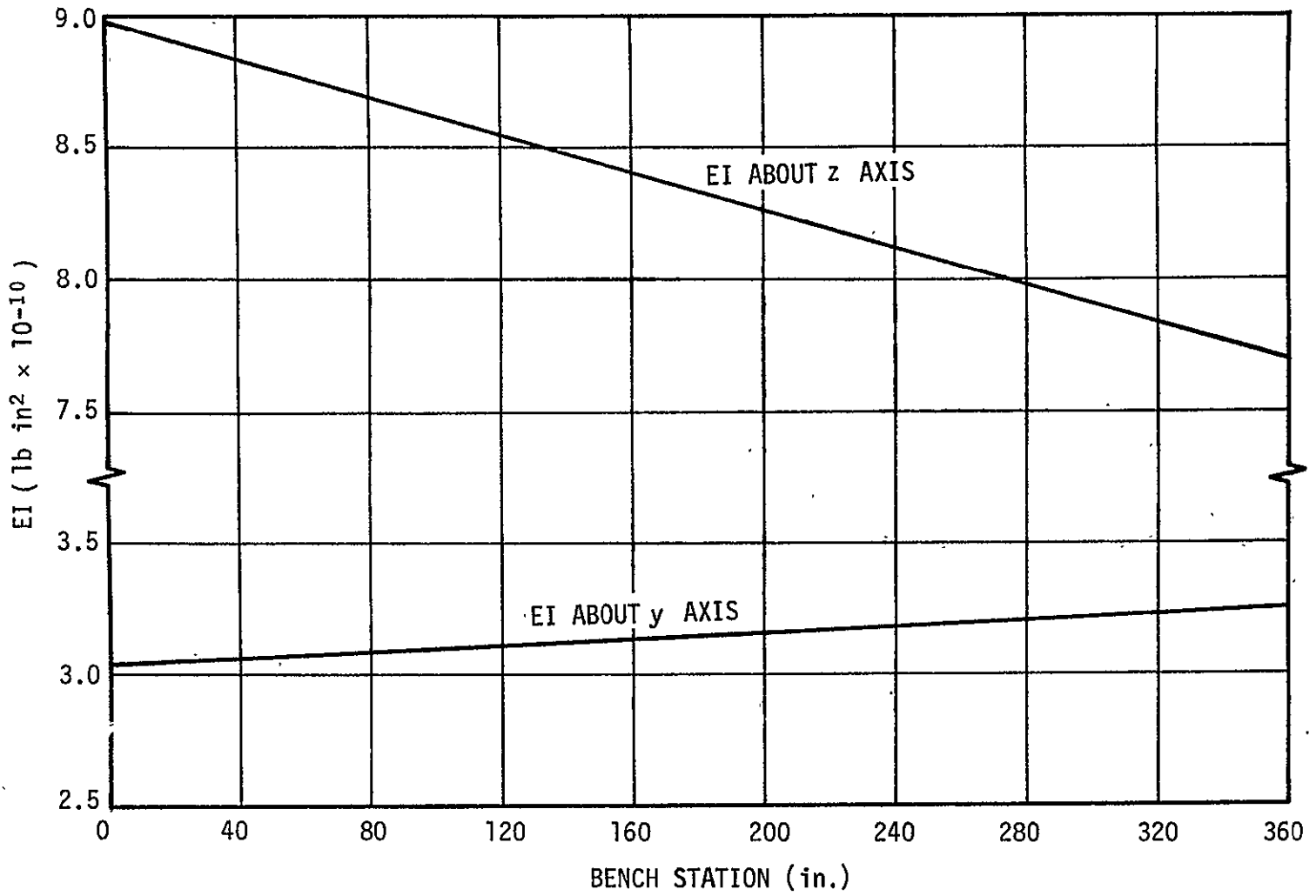


FIGURE 4-11. EI AS A FUNCTION OF BENCH STATION ABOUT y AND z AXES

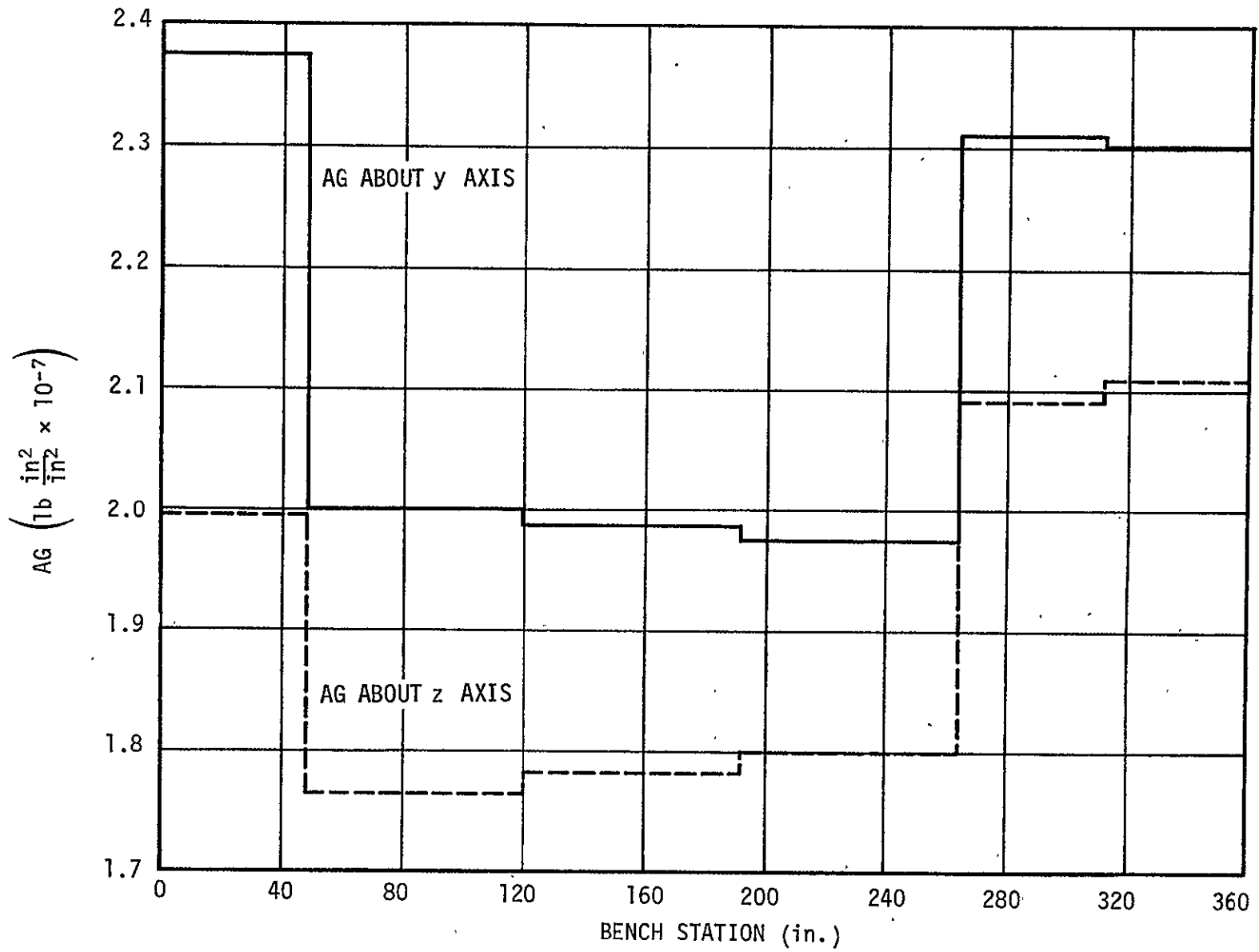


FIGURE 4-12. AG AS A FUNCTION OF BENCH STATION ABOUT y AND z AXES

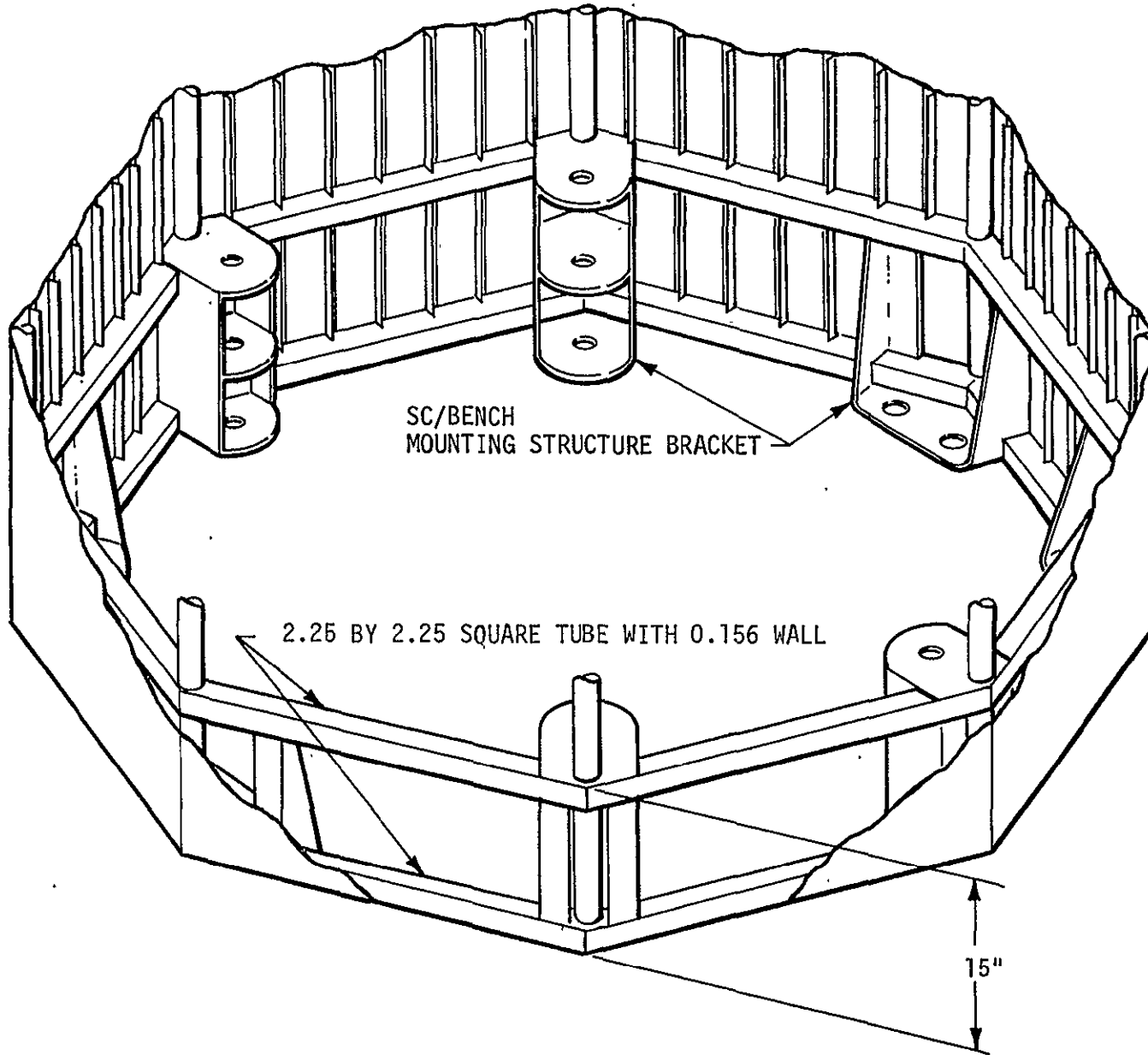


FIGURE 4-13. BASE RING STRUCTURE

The loads on this structure resulting from the bench reactions, which are eccentric approximately 6 inches to the rings, are shown in Figure 4-14 for each corner of the structure. Shear, moment and axial compression diagrams for the top ring are shown in Figure 4-15 as a function of angular position about the base, identified as the angle ϕ . The total weight of this portion of the spacecraft structure including the spacecraft/bench support brackets and the skin doublers that are used between vehicle stations 0 and 15 is 171 pounds. This weight does not include the longerons, skin or stringers.

SKIN PANEL DESIGN

The controlling design parameter for the spacecraft structure is the critical compressive buckling stress for the skin. The solar panels attached to the spacecraft skin were considered brittle in this analysis, such that if skin wrinkling behind the solar panels were allowed the solar panels would be damaged.

Figure 4-16 presents the maximum compressive stress for both the spacecraft skin and longerons versus vehicle station. If the skin is not allowed to buckle, the maximum skin stress and maximum longeron stress are normally the same since they are both the same distance from the neutral axis in this configuration. The deviations from the skin stress curve in the longeron stress curve result from the concentrated optical bench reactions. The curve for the maximum skin stress applies to that portion of the skin at the center of the worst case panel. Skin stresses would exceed these values for outer portions of the panel between Stations 0.0 and 15.0 where the skin serves as the base ring web, except that skin doublers were added to relieve the additional stress. The conservative assumption was made that all of the top optical bench reaction would be lagged into the skin between Stations 240.0 and 300.0.

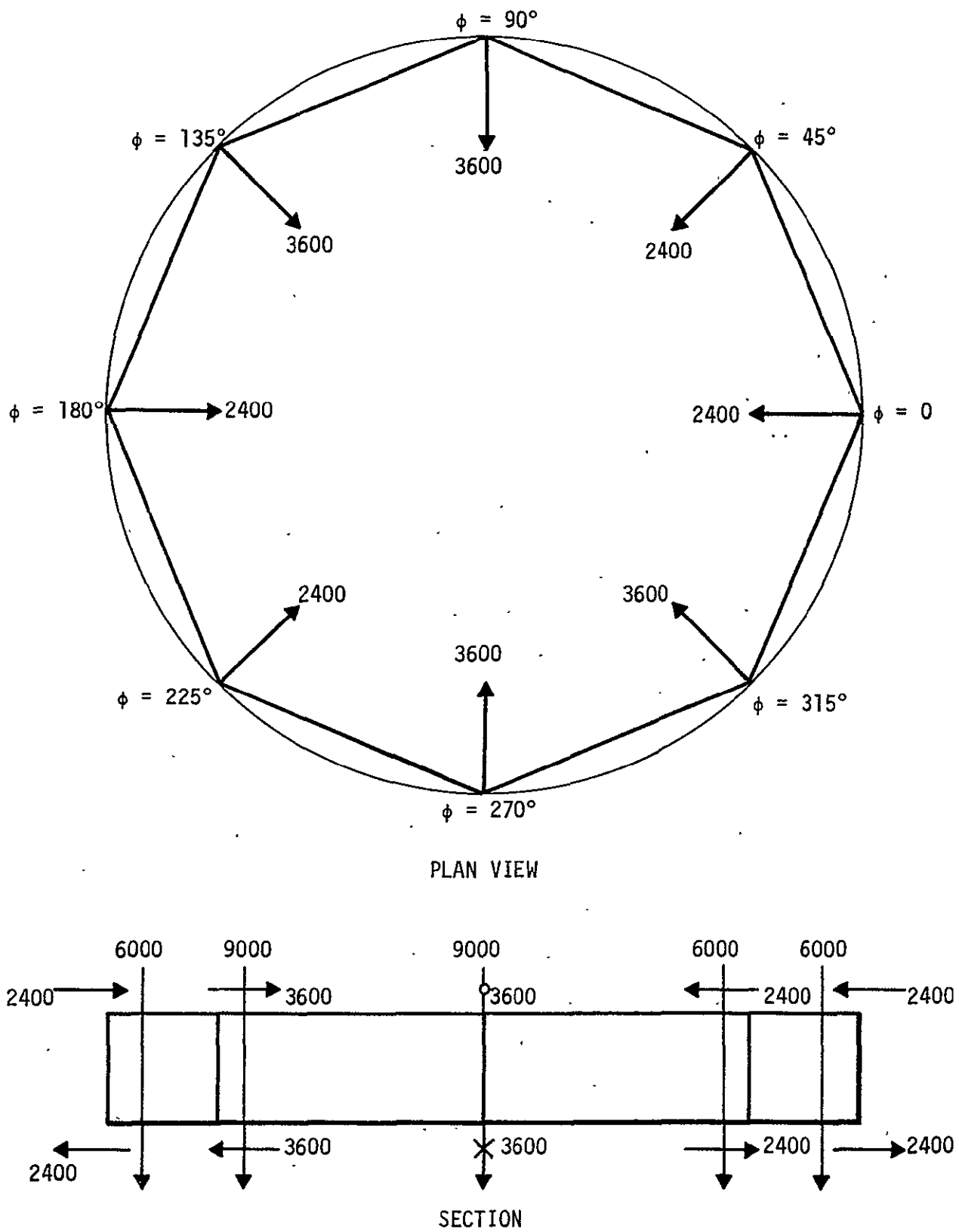


FIGURE 4-14. BASE RING LOADS IN POUNDS

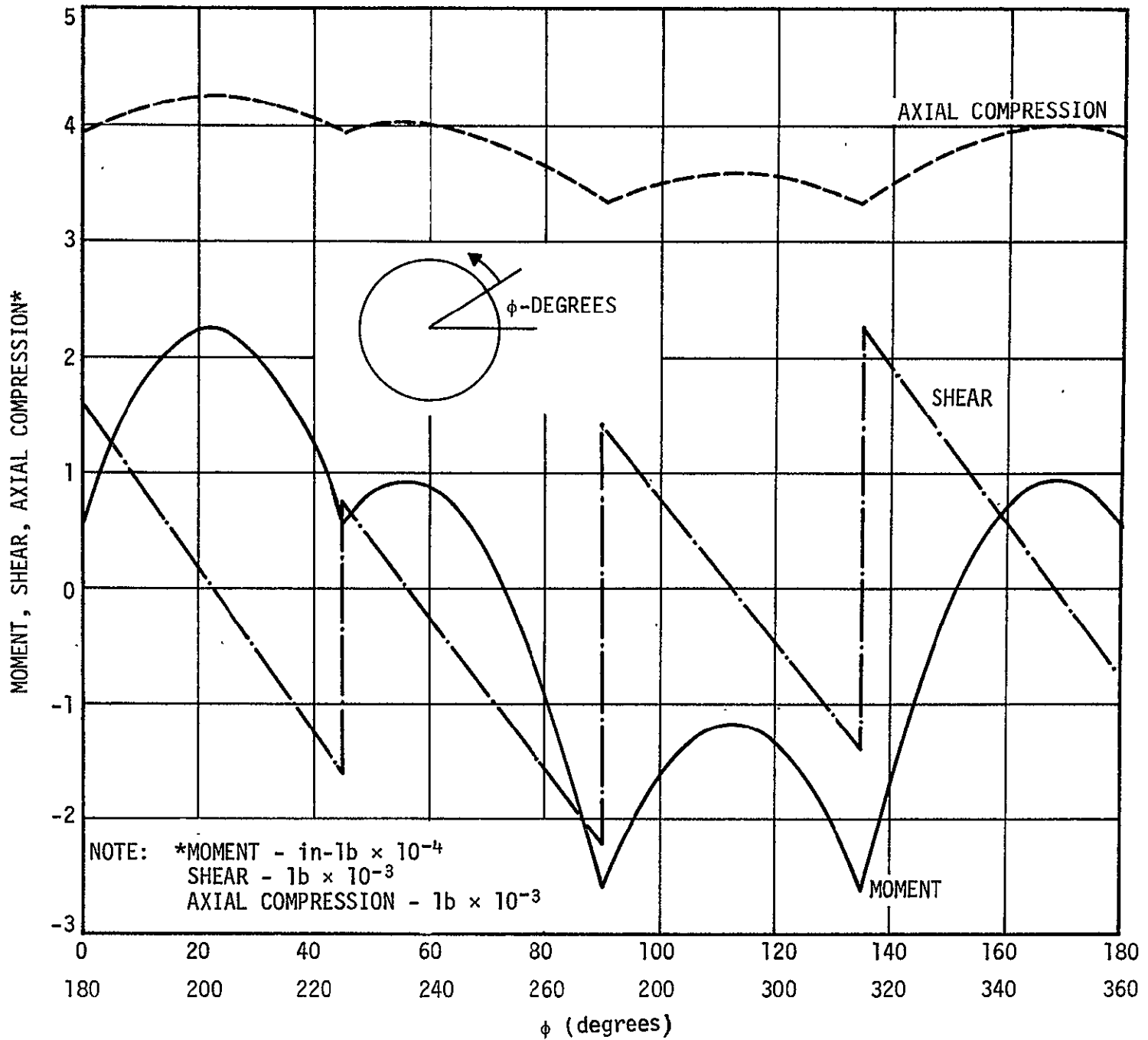


FIGURE 4-15. BASE RING SHEAR, MOMENT, AND AXIAL COMPRESSION DIAGRAMS

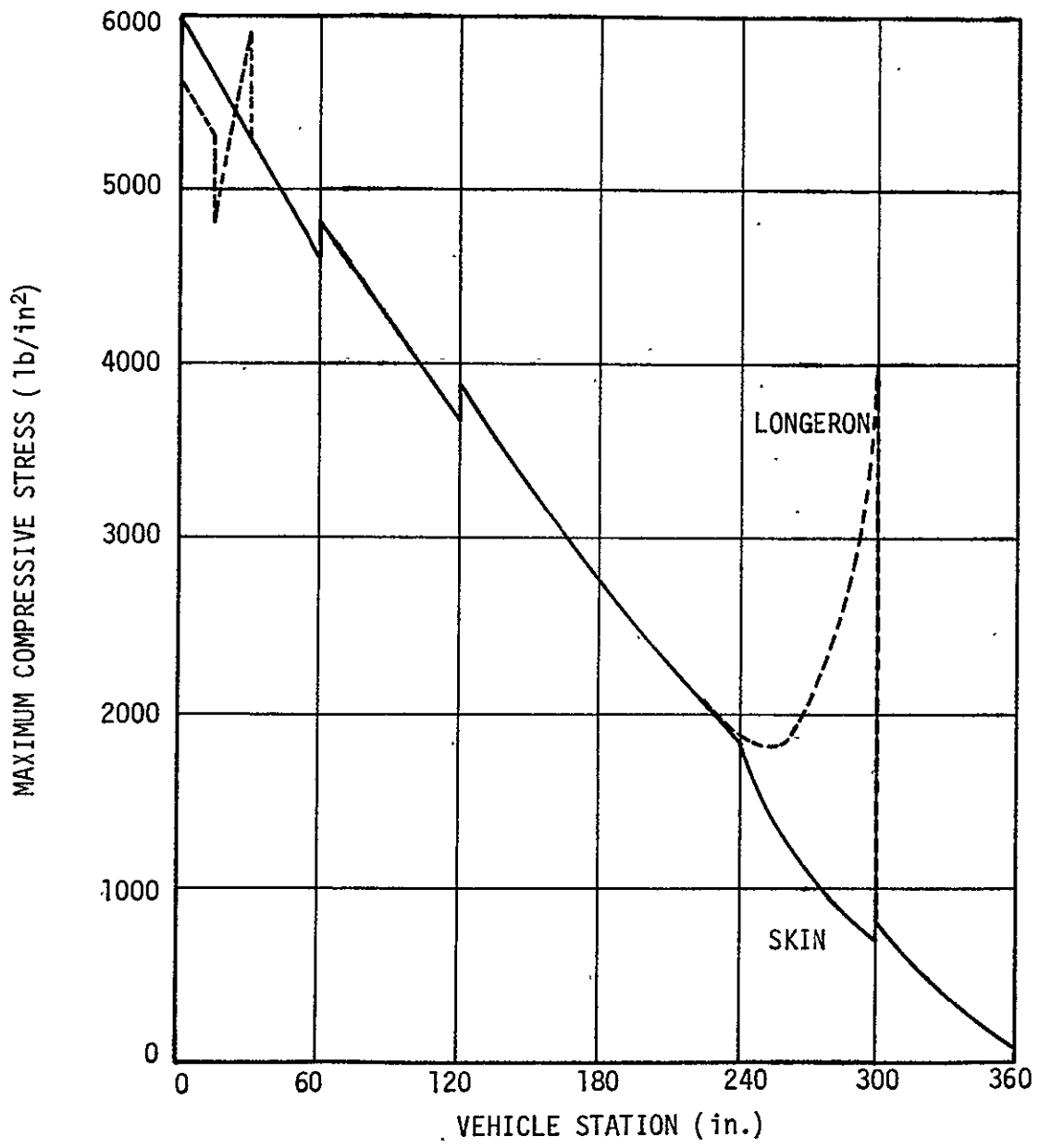


FIGURE 4-16. MAXIMUM COMPRESSIVE STRESS IN SPACECRAFT SKIN AND LONGERONS

The data presented in Figure 4-16 was derived using an IBM 1130 computer program written especially for this problem. This program solves for the top vertical bench reaction by setting the vertical deflections of the spacecraft and optical bench equal. This solution requires that the deflection of the vibration mounts be equal at the top and bottom supports. The number and size of the vibration mounts at each location, however, can be easily adjusted to ensure that these deflections are the same. After finding the bench reactions, the program calculates spacecraft stresses and deflections. Shear and moment diagrams for the spacecraft are shown in Figure 4-17.

The critical buckling stress (F_c) for these panels is expressed by the equation:

$$F_c = \frac{K_c \pi^2 E}{12 (1 - \mu^2)} \left(\frac{t}{b} \right)^2$$

where

- t - panel skin thickness, in.
- b - stringer spacing, in.
- μ - Poisson's ratio (0.3)
- K_c - buckling coefficient for the panel configuration
- E - modulus of elasticity.

The buckling coefficients (K_c) for the various skin panels of the spacecraft are developed in Figures 4-18 and 4-19. Figure 4-18 presents

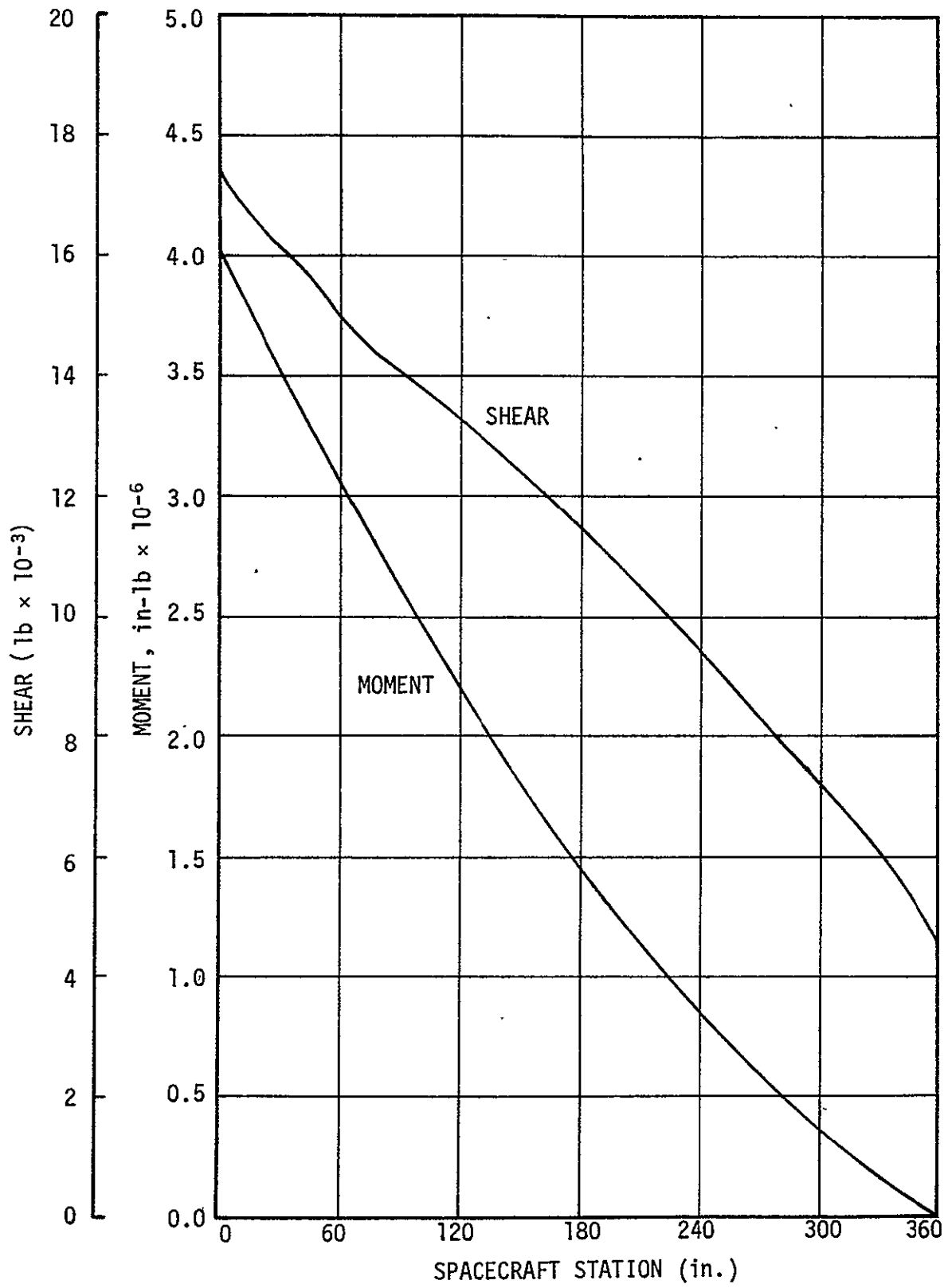


FIGURE 4-17. SPACECRAFT SHEAR AND MOMENT DIAGRAM

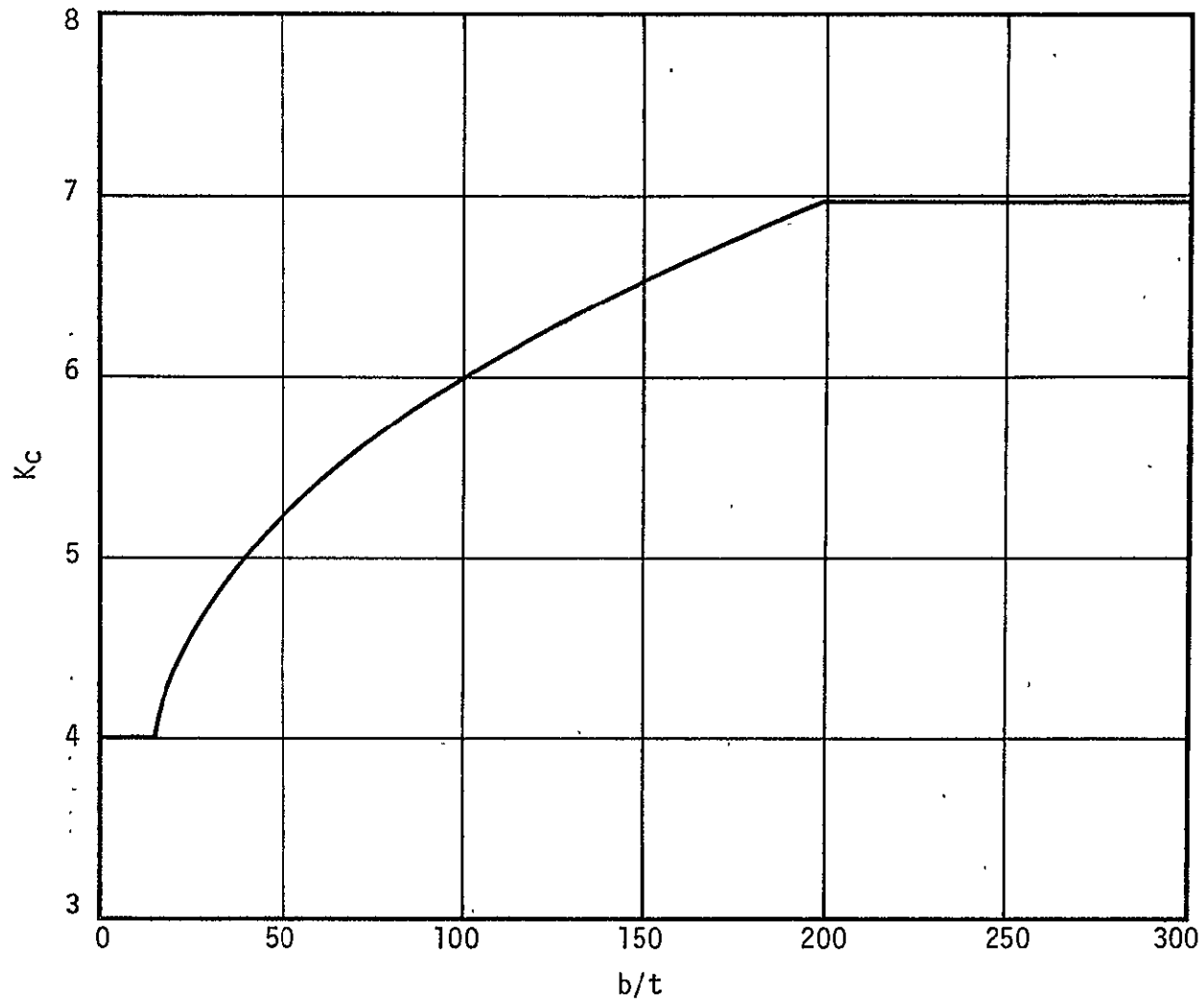


FIGURE 4-18. COMPRESSIVE BUCKLING COEFFICIENT FOR LONG STRINGER STIFFENED PANELS AS A FUNCTION OF b/t

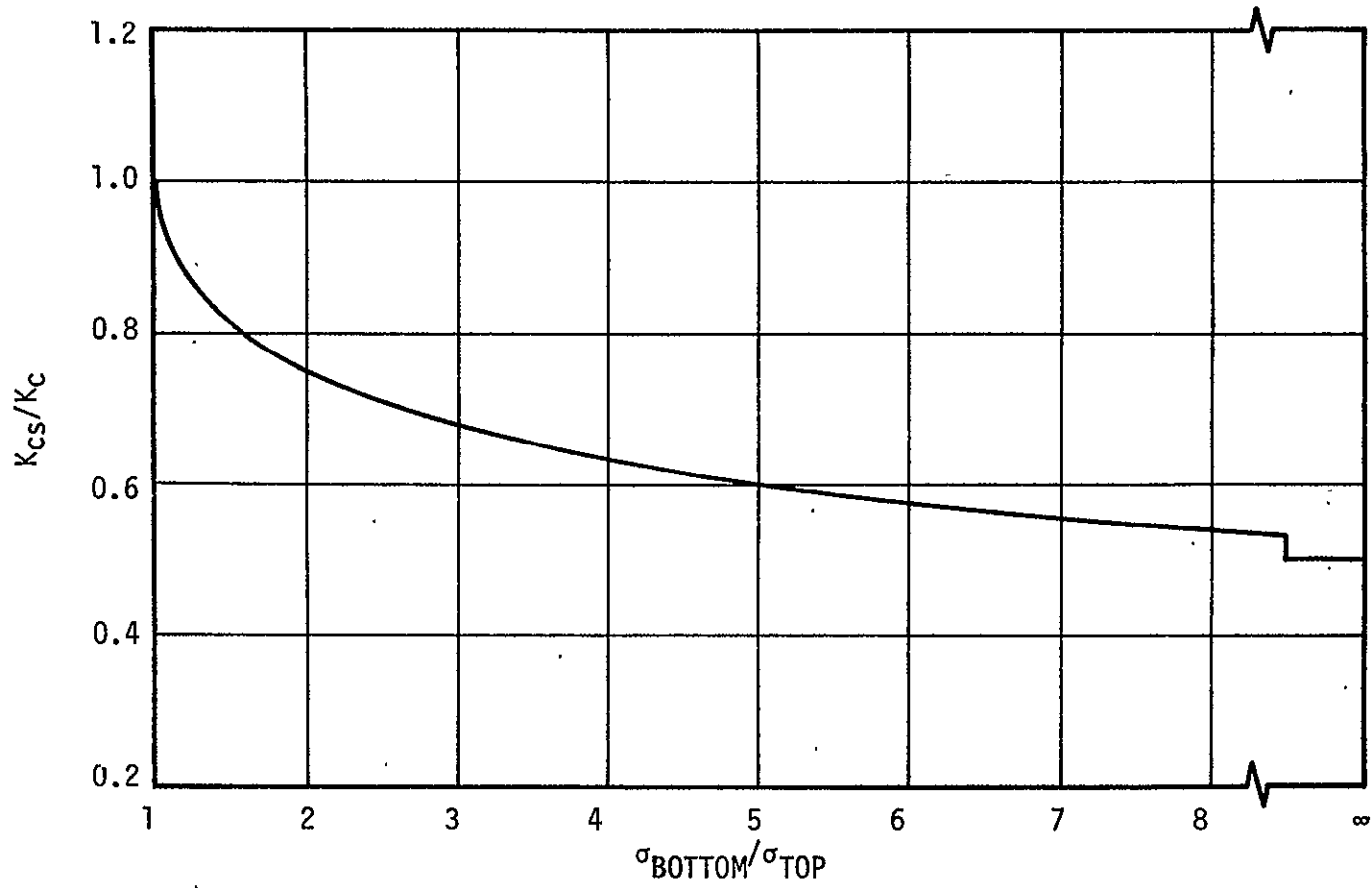


FIGURE 4-19. REDUCTION IN COMPRESSIVE BUCKLING COEFFICIENT RESULTING FROM SHEAR AS A FUNCTION OF THE RATIO OF TOP AND BOTTOM PANEL STRESSES

K_c for panels under compression as a function of b/t . The panels of this configuration, however, are also under shear. Figure 4-19 presents an operator for the development of a new coefficient, K_{CS} , which takes shear into account through the ratio of panel bottom to top stresses, i. e., $\sigma_{\text{bottom}}/\sigma_{\text{top}}$. The data for Figures 4-18 and 4-19 was taken from Reference 4-5. Table 4-4 presents the computation of the allowable stresses and actual factors of safety for each of the six skin panels on the spacecraft. The skin thickness for all panels is 0.063 inch.

Stringer design is based on the same type of calculation used to determine the stringer spacing. Table 4-4 has demonstrated that skin buckling will not occur between stringers. Table 4-5 demonstrates that stringer area is large enough to prevent general buckling of a panel across one or more stringers. The effective skin thickness, calculated for the axial direction, is based on the stringer spacing shown in Table 4-4 and a 1.5 by 0.875 inch Army-Navy series bulb angle with an area of 0.211 in². The K_c value is based on a 40 by 30 inch unstiffened panel. Each 60 inch panel contains two such 30 inch panels, with the stress ratio shown in Table 4-5 being the worst of the two.

The equation defining the minimum moment of inertia of a panel stringer (I_{min}) required to prevent panel buckling is taken from Reference 4-5 as follows:

$$I_{\text{min}} = 2.29 \frac{b}{t} \left(\frac{q a^2}{33E} \right)^{\frac{4}{3}}$$

where

- q - panel shear, lb/in
- a - panel length, in.

TABLE 4-4. COMPUTATION OF ALLOWABLE STRESSES AND ACTUAL SAFETY FACTORS FOR SPACECRAFT SKIN PANELS BETWEEN STRINGERS

Vehicle Station (Internal)	Number Of Stringers Per Panel	Stringer Spacing (in.)	σ Bottom Top (Figure 4-16)	K_{cs} (Figures 4-18 and 4-19)	Allowable Stress (lb/in ²) $\frac{K_{cs} \pi^2 E}{12(1-\mu^2)} \left(\frac{t}{b}\right)^2$	Maximum* Stress (lb/in ²) (Figure 4-16)	Actual Factor Of Safety
300 - 360	3	10.0	10.10	3.40	1220	810	2.26
240 - 300	5	6.7	2.68	4.25	3410	1850	2.76
180 - 240	5	6.7	1.51	4.95	3970	2800	2.13
120 - 180	5	6.7	1.39	5.05	4050	3890	1.56
60 - 120	6	5.7	1.31	4.97	5510	4830	1.71
0 - 60	7	5.0	1.30	4.87	7010	5990	1.76

*Includes a 1.5 safety factor applied to the loading condition.

TABLE 4-5. COMPUTATION OF ALLOWABLE STRESSES AND ACTUAL SAFETY FACTOR FOR BUCKLING OF SKIN PANELS ACROSS STRINGERS

<u>Vehicle Station (Internal)</u>	<u>Effective Skin Thickness (in.)</u>	$\frac{\sigma \text{ Bottom}}{\sigma \text{ Top}}$	<u>K_c</u>	<u>Allowable Stress (lb/in²)</u>	<u>Maximum* Stress (lb/in²)</u>	<u>Actual Factor Of Safety</u>
300 - 360	0.084	5.00	5.40	3810	810	7.0
240 - 300	0.096	1.70	7.06	6500	1850	5.3
180 - 240	0.096	1.25	7.80	7190	2800	3.8
120 - 180	0.096	1.18	8.00	7370	3890	2.8
60 - 120	0.100	1.16	8.05	8050	4830	2.5
0 - 60	0.105	1.15	8.10	8900	5990	2.2

*Includes a 1.5 safety factor applied to the loading condition.

For the worst case solution of the equation, applicable to the bottom panel, where b is minimum and the vertical shear is maximum at 372 lb/in,

$$I_{\min} = 0.0182 \text{ in}^4.$$

Since each panel has one intermediate ring, the value of a, panel length, is 30 inches. The 1.5 by 0.875 inch Army-Navy series bulb angle stringers have a moment of inertia of 0.059 in^4 .

Intermediate rings for the panels are designed as stringers to stiffen the panel against transverse shear. The same minimum moment of inertia criteria is used except that an effective thickness of 0.113 inches calculated for the transverse direction is substituted for the value 0.065 used for t previously to account for the presence of the stringers running at right angles to the intermediate ring. The required I_{\min} for the intermediate rings is 0.176 in^4 . A 2 by 1 inch Army-Navy series bulb angle with a moment of inertia of 0.190 is suggested for this member.

Longeron member sizes were selected to increase the spacecraft moment of inertia sufficiently to prevent skin buckling. Various combinations of skin, stringer and longeron sizes were investigated in this design until the minimum weight combination was found which would satisfy the buckling criteria. Actual safety factor for the longeron with respect to stress is approximately 6.

TOTAL STRUCTURE WEIGHT

A weight statement for the spacecraft structure is presented in Table 4-6. This statement includes a 100 pound allowance for the spacecraft-optical bench connecting structure, which consists of the following items:

TABLE 4-6. SPACECRAFT STRUCTURAL WEIGHT STATEMENT

<u>Item</u>	<u>Weight (lb)</u>
Skin	711
Stringers	306
Longerons (8)	208
Main Rings (6)	156
Intermediate Rings (6)	90
Base Ring Structure	171
Top End Cover Structure	128
Mounting Brackets	200
Spacecraft/Bench Connection	100
Mosaic Crystal Deployment Structure	90
Contingency	<u>200</u>
TOTAL SPACECRAFT STRUCTURE WEIGHT	<u><u>2,360</u></u>

- Eight 3-inch diameter fiberglass tubes
- Twenty-four 6-inch diameter "Lord Type" vibration mounts
- Electromechanical decoupling mechanisms for 4 fiberglass tubes

The total spacecraft structural weight is 2360 pounds.

METEOROID PENETRATIONS

An assessment of the vulnerability of the HEAO-C spacecraft to meteoroid penetration was made based upon the spacecraft orbit, exposed surface area, and orbit lifetime. Equations and information given in Reference 4-6 were used to calculate the probabilities of no penetrations during a one and during a two year mission with a 0.063 inch skin thickness, as specified in the spacecraft structural design. The results are presented in Table 4-7.

TABLE 4-7. HEAO-C SPACECRAFT METEOROID VULNERABILITY

MISSION DURATION	PROBABILITY OF NO PENETRATION	EXPECTED NUMBER OF PENETRATIONS
1 year	0.074	2.6
2 years	0.0055	5.2

These results indicate that it is extremely likely that the spacecraft will be penetrated by a meteoroid. Protection could be provided by increasing the skin thickness; however, it may be possible to provide equal protection at lighter weight by using a double wall skin or by providing separate component protection. The most suitable technique was not determined in the present study. Individual components for the most part will have some form of covers which will provide a measure

of protection. The locations of individual components and their cover materials and thicknesses must be considered in evaluating the alternatives.

CONCLUSIONS

The following conclusions were drawn on the spacecraft structural design.

- Total spacecraft structural weight is estimated to be 2360 pounds.
- The use of decoupling attachments on the end of the optical bench opposite the viewing end will permit thermal deflection of the spacecraft without inducing stress into the optical bench.
- A skin thickness of 0.063 is sufficient to prevent skin buckling during launch, but will not prevent meteoroid penetration.
- "Lord type" vibration mounts will protect the bench mounted experiments from the acoustical launch environment and their mechanical properties will not degrade during the mission. Mount outgassing will be small, but its effect on the experiments must be determined.

REFERENCES - SECTION 4

- 4-1. Lord Manufacturing Company, Center Bonded Mountings, Technical Bulletin No. 712, 1967
- 4-2. Marshall Space Flight Center, Materials Laboratory, ATM Materials Control for Contamination Due to Outgassing, Revision B, SOMO2442, January 2, 1968
- 4-3. Duffie, J. M. and R. C. Watson, Jr. (Editors), "Feasibility Study of a High Energy Astronomy Observatory (HEAO) Spacecraft", Teledyne Brown Engineering, SMSD-PD-1087, January 1970
- 4-4. Flügge, W., Handbook of Engineering Mechanics, McGraw-Hill, 1962
- 4-5. Bruhn, E. F., "Analysis and Design of Flight Vehicle Structures", Tri-State Offset Company, Cincinnati, Ohio, 1965
- 4-6. "Meteoroid Environment Model - 1969", NASA SP-8013, March 1969

5. ATTITUDE SENSING SYSTEM

The operating mode of the HEAO-C spacecraft is a pointing or hold mode. In this mode the two telescope lines of sight (spacecraft x-axis) are aligned with a stellar X-ray source and the two transverse spacecraft axes are oriented so that the normal to the middle solar panel surface (z-axis) is aligned within a few degrees of the solar vector as indicated in Figure 5-1. In this orientation the spacecraft can be rotated about the spacecraft z-axis to align the X-ray telescopes with any X-ray source located within the limited band on the celestial sphere illustrated in Figure 5-1.

The function of the attitude sensing system is to supply the attitude data needed by the attitude control system in each of its operating modes. Attitude sensing accuracies must be at least as good as the control accuracies of Table 5-1.

TABLE 5-1. SUMMARY OF ATTITUDE CONTROL REQUIREMENTS FOR THE HEAO-C SPACECRAFT

<u>Axis</u>	<u>Position (arc min)</u>	<u>Rate (arc sec/sec)</u>
x	5	5
y	1	1
z	1	1

The first problem is the source of attitude data. The Earth, Moon, Sun, and stars are possible long-term attitude references. The Moon is an inconvenient reference because of its motion and its large changes in luminosity, apparent shape, and size. The Earth has been

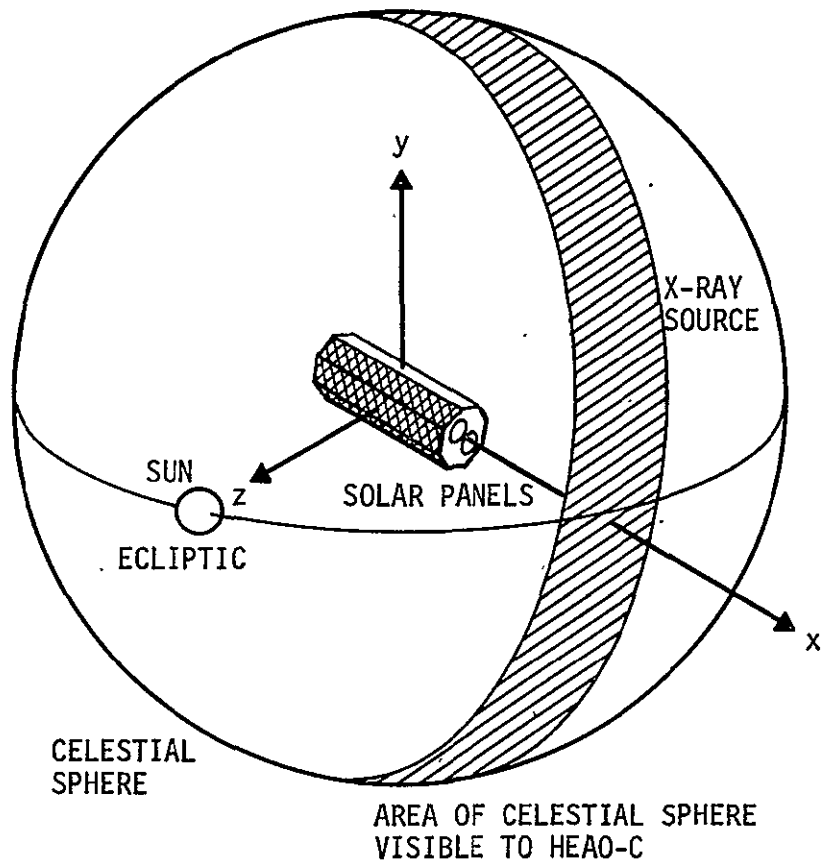


FIGURE 5-1. ORIENTATION OF HEAO-C SPACECRAFT IN THE POINTING MODE

used for many satellites stabilized with respect to the local vertical, but for a spacecraft such as the HEAO-C, which for most of its mission is stabilized with respect to inertial space, Earth sensing would require continuously rotating trackers. In addition, conventional Earth trackers are accuracy-limited by the imperfect definition of the Earth horizon. Unconventional Earth trackers, identifying specific terrestrial landmarks, can be visualized but seem unsuitable for an unmanned mission where maximum use of state-of-the-art equipment is desired. Therefore, Earth trackers were not considered further.

Sun sensors with an accuracy in the range from degrees to minutes of arc are readily available. More precise Sun sensors, accurate to seconds of arc, have been devised, but they require gimbaling to maintain accuracy when the spacecraft is turned away from the Sun. An additional sensor of a different type is needed to provide a three-axis reference system. Because of these limitations, the Sun has been eliminated as a primary source of attitude data for precise pointing. It remains useful for both preliminary orientation and backup use in the event of system failures.

The stars, then, were selected as the primary source of accurate attitude data. They are sufficiently distant to eliminate significant parallax and sufficiently numerous to permit location of a reference in any part of the sky, provided a sensitive instrument is used. Stellar attitude sensing devices fall into three categories:

- Star trackers, tracking single known stars
- Star field trackers, sensitive to motion of a star field
- Star mappers, capable of identifying and tracking star patterns.

A star tracker must be aligned near the desired star before it can operate. A star field tracker must first be oriented exactly in the desired direction. A star mapper includes star atlas data so that prior information on attitude is not needed.

A number of star trackers have been developed and flown. Star field trackers have been developed but not used. One manufacturer has developed a star mapping instrument, part of which has been tested in orbit. Because it is closest to the present state of the art, the star tracker has been chosen for the baseline HEAO-C system. However, systems using star field sensing and star mapping will also be described.

SUMMARY OF SYSTEM OPERATION

The baseline attitude sensing and control system operates in four modes. The modes and their attitude data requirements are listed below.

Despin Mode

Upon separation from the final stage of the launch vehicle, the payload may have some residual motion about one or more axes. In the despin mode, angular rates are measured by rate sensors and eliminated by the attitude control system. Rates must be measured from the maximum anticipated initial rate (of the order of 1 to 3 deg/sec), down to the deadband rate for each axis. Conventional rate gyros can conveniently meet attitude sensing requirements for this mode.

Acquisition Mode

To acquire the desired reference star, the spacecraft z-axis is first aligned with the solar vector. The Sun provides an easily identified reference to begin the process of locating the desired star.

The procedure used is a standard one known as roll map matching, in which the spacecraft is rolled about the solar vector. A star tracker boresighted with the X-ray telescope will generate an output characteristic of the stars scanned during a revolution about the solar vector (Figure 5-2). Star tracker and star mapper work of the past few years has resulted in a number of star maps compiled in computer form. Such a map could easily be used to generate a simulated star tracker output trace for rotation about the solar vector, when tracker sensitivity and time of year are known. This permits immediate establishment of a roll reference by roll map matching, i. e., by manually matching telemetered and simulated tracker outputs. Once roll reference information is command transmitted to the spacecraft, orientation to a desired target can be accomplished under rate gyroscope control.

Errors at the end of this stage are caused by sensor and tracker alignment errors, gyroscope drift, and offsets, drifts, and calibration errors in the electronics. These effects are analyzed in Section 6 of this report. It is shown there that using existing gyros, slewing can always be performed to about 0.1 degree or better, i. e., accurately enough for the tracker to identify and lock onto the reference star. Provided a succession of correctly identified reference stars is unbroken, the spacecraft may be slewed from target to target as many times as desired, using only onboard stored data. Ground control of spacecraft attitude is required only in the event of a malfunction, which results in failure to find the next star.

In the acquisition mode the system requires data on solar vector angle and rate, and on rate about the z-axis. Suitable solar sensors are available and the rate data can be provided by gyros. The spacecraft must be held on the solar vector accurately enough for star identification; requirements here depend on the characteristics of the star sensor.

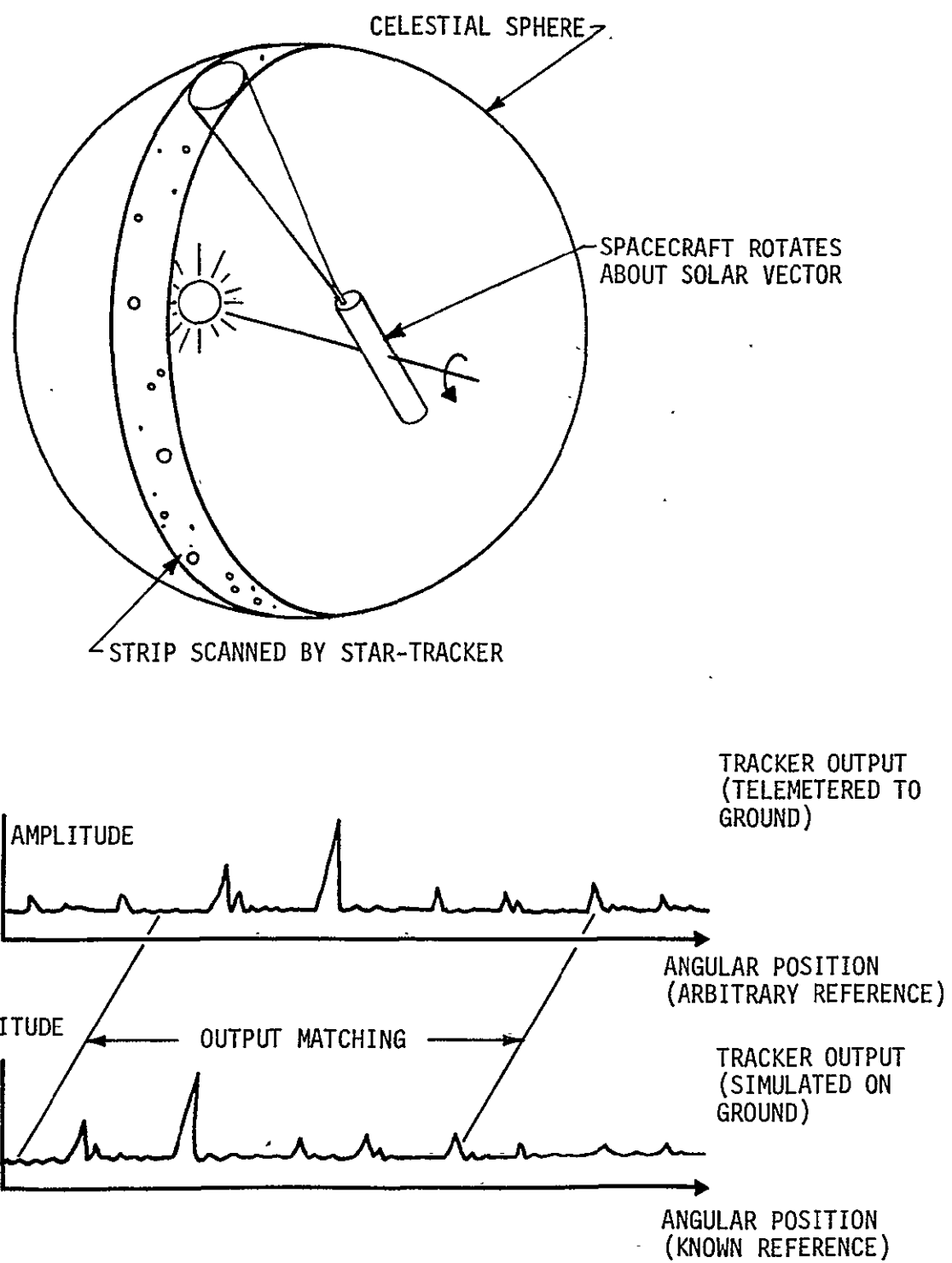


FIGURE 5-2. ROLL MAP MATCHING

Slewing Mode

In the slewing mode, the spacecraft rotates about its z-axis to align its x-axis with the star, and subsequently rotates to new positions in inertial space as X-ray observations proceed. Slewing must be accurate enough for correct identification of the new reference star each time. The attitude sensing system must sense angular rate accurately enough for star acquisition.

Pointing Mode

In the pointing mode, the spacecraft x-axis is maintained in some direction in inertial space for observation of an X-ray source. Stars provide a reference for pointing, but the actual pointing direction generally does not coincide with a visible star. Therefore, the system must measure the angle of stars from the x-axis. The size of the angles depends on tracker design, but whatever their size, they must be measured accurately enough to meet the requirements of Table 5-1, even after taking into account spacecraft motion due to control system dynamics.

Occultation

When the guide star is occulted by the Earth, the X-ray target is occulted also. High-resolution scientific observations are therefore suspended; however, attitude stability must be maintained to provide continued output from the solar panels and to permit reliable, prompt reacquisition of the guide star and X-ray source at the end of occultation. One solution is to provide a second star tracker aimed perhaps 180 degrees away from the first one; another solution is to provide a gas-bearing reference gyro. The choice of these alternatives may eventually be made on the basis of opinions as to the in-space reliability of these two components. Both trackers and gyros can theoretically operate for a two-year mission, but meaningful statistical

data on in-space performance of these components is very sparse. They appear to compare in reliability, and, at this stage, a tentative choice of a gyro is made because it is more conveniently accommodated than an additional star tracker.

Reference Gyros

It can be seen that gyros play a role in all four modes. It seems convenient to make gyros the source of all direct attitude data and to use the star sensors indirectly to update them as necessary. If this is done, occultation and reacquisition do not interrupt system operation.

One gyro which appears to be suitable is produced by the Kearfott Systems Division of Singer-General Precision, Inc. (Wayne, New Jersey). Table 5-2 gives the gyro characteristics, as furnished by the manufacturer. The manufacturer states that the drift figure of 0.001 deg/hr is expected to apply to continuous operation during a period such as occultation (0.6 hr). The resulting error at the end of occultation, considering gyro drift alone, is only 0.0006 degree, or 2.2 arc seconds. Because of the very small magnitude of the expected drift, a detailed error budget for the occultation period has not been compiled. It is shown in Section 6 that an accuracy of 0.1 deg/axis is sufficient for unambiguous reidentification of the guide star. Therefore, the gyro drift could increase by two orders of magnitude before becoming significant. Because the requirement appears to be well within the state of the art, no attempt has been made to survey gyro manufacturers and to identify the best instrument. The Kearfott gyro is presented simply as an indication that the requirement can be met. Like most such instruments, it has a single degree of freedom and thus three gyros are required to provide a complete axis system.

The gyro will be used in a rate mode, with integration performed electronically, enabling it to accommodate the large rotations involved in slewing. The gyro can also be used during the acquisition phase of

TABLE 5-2. REFERENCE GYRO CHARACTERISTICS

<u>Item</u>	<u>Data</u>
Manufacturer	Kearfott Division of Singer- General Precision, Inc. Wayne, New Jersey
Designation	Gas bearing gyro C70 2590 003
Weight, lb	1.0
Length, in.	3.2
Diameter, in.	2.1
Short-term random drift ($1 - \sigma$), deg/hr	0.001
Long-term run-to-run drift ($1 - \sigma$), deg/hr	0.01
Heatup power	80 W at 115 volts
Heatup duration (typical), min	4
Spinup power	15 W at 26 volts, 3 ϕ 800 Hz
Spinup duration, sec	25
Heater power while running	0 or 25 W (on/off)
Spin power while running	7.5 W at 26 volts, 3 ϕ 800 Hz
Torquer capacity, deg/sec	3.06

the mission, when it is necessary to monitor angular rates while these rates are reduced below some threshold. The gyro can accept torquer command rates up to 3.06 deg/sec, exceeding the anticipated initial rate of 3.0 deg/sec. This is an advantage in that it is unnecessary to provide additional gyros for the acquisition phase.

Roll Axis Reference

Discussion thus far has been limited to trackers that are capable of establishing the direction of the x-axis. The star tracker boresighted with the x-axis is locked onto a star having specified y and z coordinates within the tracker's field of view, and changes in y and z are read out as attitude errors. Since the star generally is not at the center of the field of view, the system requires stability about the optical axis (x-axis) also. In fact, Table 5-1 shows that this axis is to be stabilized to 5 arc minutes, or 0.083 degree. Roll about the x-axis appears as an x-axis position error to an x-axis star tracker that is locked on a reference star that is not in the center of the tracker field of view. The worst case of apparent error occurs when the guide star is at the edge of a six-degree field of view, three degrees away from the optical axis. In this case the apparent pointing error is

$$0.083 \times \sin 3^\circ = 0.004 \text{ deg} = 14 \text{ arc sec} .$$

A roll reference is required to measure roll about the x-axis.

The Earth is unsuitable as a roll reference in view of the inertially fixed nature of the pointing requirement. The Sun and stars remain as possible roll references. Any roll sensing system must include provisions for operating during occultation of its reference, which can be done by using more than one reference, or, alternatively, by including a gyro as for the Y and Z axes.

It seems that spacecraft development and testing would be facilitated if the number of different components employed were kept to a minimum. Accordingly, it is suggested that the x-axis attitude sensing system consist of a second star tracker, located on the y or z axes, and an additional gyro. This gyro can be identical to those used for the y and z axes. However, the operation of the tracker can be somewhat simplified. If initial x, y, and z directions are specified and the spacecraft performs a specified rotation about the y axis and then the z axis, the new directions of all three axes are determined. The x-axis tracker need not identify any of the new stars now found within its field of view; it need only lock onto one star and detect its motion in one direction. Attitude can be sensed to the same accuracy obtained for the y and z axes, even though no attempt need be made to control the spacecraft to this precision about the x-axis. If this attitude sensing data is used, the y and z star tracker outputs can be processed to remove any apparent error contributed by x-axis roll.

Advantages of Gimballed Star Tracker

In the past, star trackers have been designed to align a spacecraft toward a specified star throughout the mission. The conventional star tracker is built around a photodetector equipped to scan a small field. Table 5-3 (Ref. 5-1) lists available types of detectors and their characteristics. The tracker scans its field of view to locate the star image, then tracks it and generates error signals proportional to the distance of the image from the tracker optical axis. The control system uses these signals to rotate the spacecraft until the star lies on the axis. Because the instrument operates in a nulling mode, there is no requirement for especially precise measurement of angles. A typical tracker weighing 10 pounds and fitting inside a 5-inch-diameter by 11-inch-long cylinder can align a spacecraft within a few arc seconds of a star.

TABLE 5-3. STAR TRACKER PHOTODETECTORS

Quality	Photomultiplier	Image Dissector	Vidicon	Solid-State Element
Form	Photoemissive surface in vacuum	Photoemissive surface in vacuum	Photoconductive surface in vacuum	Photoconductive or photovoltaic chip
Color sensitivity	Near UV to near IR with blue dominant	Near UV to near IR with blue dominant	Approximately photopic	Red to near IR
Frequency response limitations (as used)	None in most applications	None in most applications	10 Hz	Silicon: none CdSe: 100 Hz
Associated modulation or scan	Mechanical modulation	Electronic modulation or scan past aperture plate	Electronic scan of stored image	Mechanical modulation
Advantage	Low internal noise Simple	Lowest internal noise Easily offset scan and track	Background tolerance Easily offset scan	Background tolerance Compact

Such trackers typically have fields of view of a few degrees or less. Thus if a tracker is fixed-mounted, it has only electronic means of deflection (offset), and its accuracy in measuring the angle of a star from the optical axis is limited by nonlinearities in the electronic optics (generally more severe than imperfections in the lens system). These nonlinearities typically take the form of pincushion distortion plus a fixed offset or bias. If no attempt at correction is made, they limit accuracy to about one part in 300 or 500 of the width of the field of view. If careful measurement and calibration is done on the ground, compensation can be built into the electronics and the error reduced; however, aging and temperature changes will introduce a varying offset or bias as the mission progresses. This can be corrected only by the use of some other star detector providing perfect directional information. The consensus of the tracker manufacturers is that accuracy for fixed trackers operating in the offset mode is limited to roughly one part in 1,000 at best. Thus if an accuracy of 30 arc seconds is required, the tracker field of view cannot be wider than 30,000 arc seconds or about 9 degrees, even if all possible corrections are made.

On the other hand, if the tracker is gimbal-mounted, it may have quite a small field of view and yet be rotated accurately through much larger angles. In this case directional accuracy is maintained by the gimbal pickoffs which generally take the form of optical encoders. Existing encoders can provide 30 arc seconds accuracy through angles as large as desired. The tracker can be pointed directly at a star and so its nonlinearities do not affect accuracy. It has not been determined whether suitable reference stars will be available to permit the use of fixed star trackers on the HEAO-C mission. For this reason, the use of gimballed trackers will be assumed for this mission and appropriate allowances made in the weight and power budgets.

Component Summary

The attitude sensing system includes two star trackers, three reference gyros, fine and coarse Sun sensors, and associated electronics (see Table 5-4). Table 5-5 gives the characteristics of suitable Sun sensors; such sensors are readily available. Analog electronic functions require a specially built unit. Digital (logic) functions are assigned to a general-purpose digital computer which forms part of the attitude control system. Representative computer characteristics are given in Table 5-6, which is derived from American Science and Engineering, Inc., data.

Local wiring is the wiring in the immediate vicinity of the components. Long wiring runs extending through the spacecraft structure are not included here.

STAR TRACKER FIELD OF VIEW AND SENSITIVITY

Determination of Critical Requirements

The tracker must have a large enough field of view (or large enough gimbal freedom) and a high enough sensitivity to be able to see at least one guide star in any portion of the sky. A starting point for analysis of this requirement is provided by Reference 5-2, which describes a study using computer-readable data on all stars brighter than +4.7 magnitude. These data made it possible to carry out a computer search process to identify the most sparsely populated regions of the sky. The required field of view to detect at least one, two, or three stars was determined. With a given limiting magnitude, the program would, for example, determine the largest circle that could be projected on the celestial sphere that would contain no stars brighter than this magnitude. Then any tracker with a larger field of view would always detect at least one star above this magnitude. A similar procedure was used to determine fields of view to detect at least two or at least three stars.

TABLE 5-4. ATTITUDE SENSING SYSTEM USING STAR TRACKERS

<u>Item</u>	<u>Weight (lb)</u>	<u>Average Power (W)</u>	<u>Power When Operating (W)</u>
Star trackers, gimballed (2)	80	50	50
Reference gyros (3)	3	30	30
Coarse Sun sensors and mounting (3)	8	-	1
Fine Sun sensor	2	-	1
Gyro and Sun sensor electronics*	4	5	5
Mounting hardware and local wiring	<u>14</u>	<u>-</u>	<u>-</u>
TOTAL	<u>110</u>	<u>85</u>	<u>87</u>

*For analog electronics functions

TABLE 5-5. TYPICAL SUN SENSOR CHARACTERISTICS

<u>Item</u>	<u>Data</u>
Coarse Sun sensors	
Weight (each), with mounting, lb	1
(total array), lb	8
Field of view (each), deg	±80
Null accuracy, deg	±5
Fine Sun sensor	
Weight, with mounting, lb	2
Field of view, deg	±15
Null accuracy	1 arc-sec

TABLE 5-6. REPRESENTATIVE ATTITUDE CONTROL COMPUTER

<u>Item</u>	<u>Data</u>
Weight with 8K memory, lb	72
Power, W	145
Command instruction time, μ sec	3
Multiply/divide cycle, μ sec	60
Word length, bits	32
Typical models	Honeywell HDC-501 (Atlas/Agona) IBM TC-1 (ATM)

Figure 5-3 (Ref. 5-2) shows the total number of stars brighter than a given magnitude; Figure 5-4 shows the total angle of the required tracker field of view to be able to see n or more stars of given magnitude. It can be calculated that a tracker with the required field will observe an average of 10 to 12 stars for the range of magnitudes shown. This provides some basis for extrapolation of the graph to fainter stars.

It must be considered that these data are based on star visual magnitude. The magnitude of a given star is a function of the spectral response of the detector; visual magnitudes are based on a response curve resembling that of the human eye. The tracker field and star population data given here would be different with a different detector. These data can be generated only by compiling a modified star map with new star magnitudes and repeating the computer search process. Such a task was not attempted in the present study.

Table 5-7 gives the exact coordinates of the points in Figures 5-3 and 5-4; Tables 5-8 and 5-9, together with Figures 5-5 and 5-6, identify the actual pointing directions found to determine the required tracker field for each magnitude. It is noteworthy that some critical directions are found to be well removed from the galactic poles.

Detector Response Sensitivity

An indication of the importance of star color (star spectral curve) and detector response is found in Reference 5-1, from which Table 5-10 is taken. Reference 5-1 discusses the origin of these data: a series of direct narrow-band photometric measurements on 985 stars, carried out by the Lunar and Planetary Laboratory of the University of Arizona.

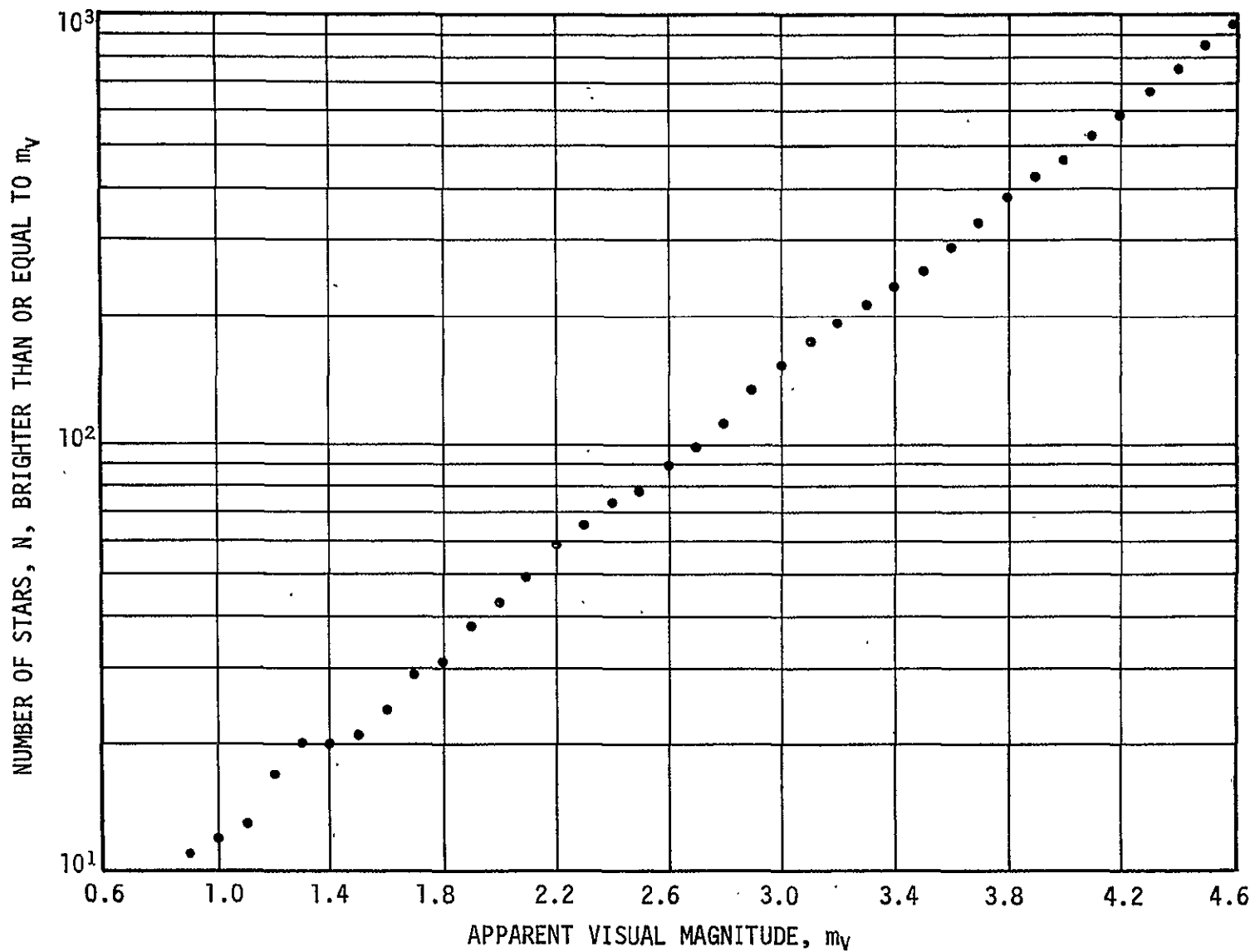


FIGURE 5-3. STAR POPULATION AS A FUNCTION OF LIMITING MAGNITUDE, m_v (from Reference 5-2)

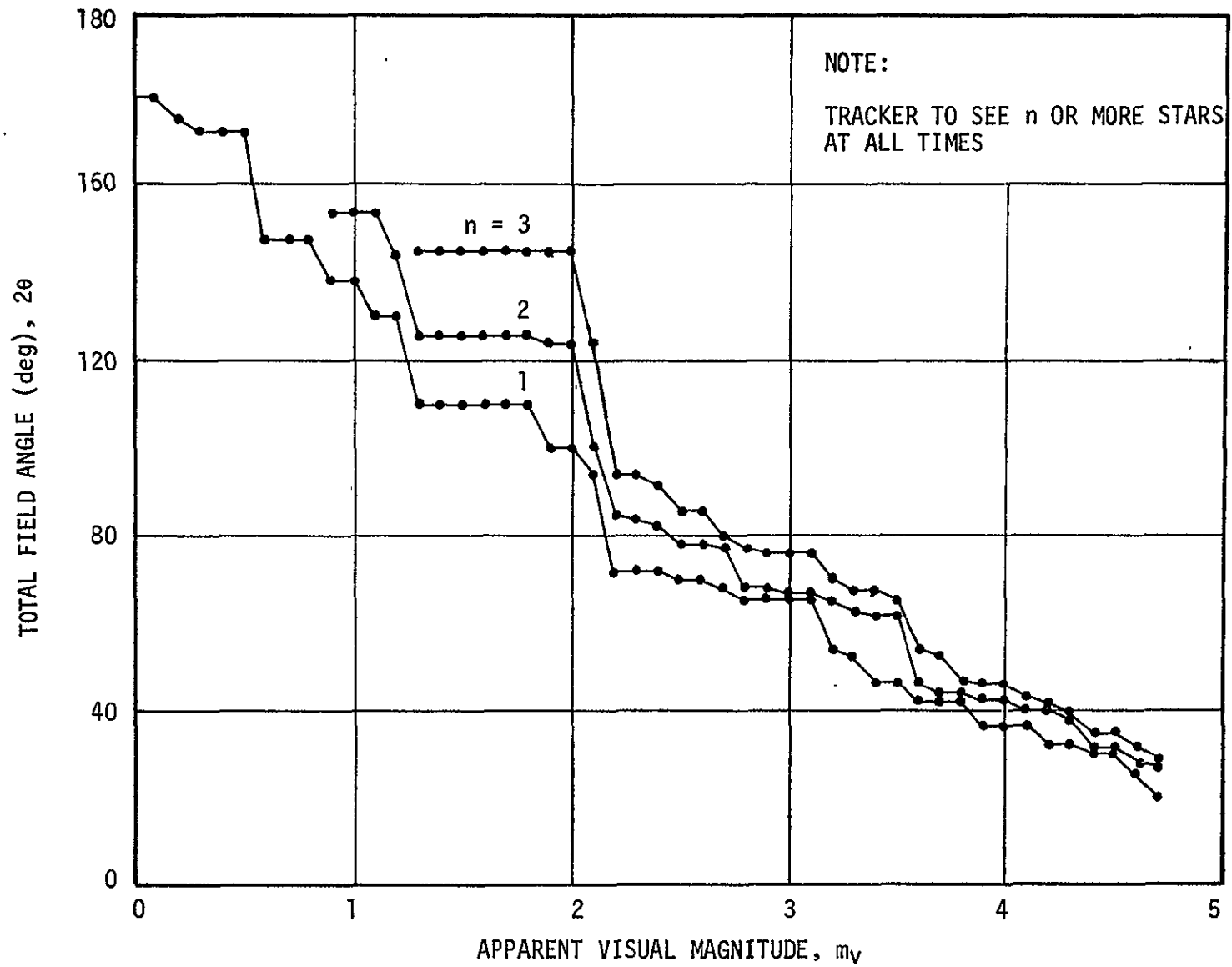


FIGURE 5-4. REQUIRED FIELD OF VIEW AS A FUNCTION OF LIMITING MAGNITUDE, m_V
(from Reference 5-2)

TABLE 5-7. ANGULAR RADII, θ , OF REQUIRED FIELDS OF VIEW (from Ref. 5-2)

m_v	N	$\theta^\circ, n=1$	$\theta^\circ, n=2$	$\theta^\circ, n=3$	m_v	N	$\theta^\circ, n=1$	$\theta^\circ, n=2$	$\theta^\circ, n=3$
0.1	4	89.784	>90	>90	2.5	79	34.780	39.140	43.052
0.2	6	87.647	>90	>90	2.6	89	34.780	39.140	43.052
0.3	7	86.177	>90	>90	2.7	99	34.217	38.627	40.292
0.4	7	86.177	>90	>90	2.8	112	32.710	34.217	38.627
0.5	8	86.177	>90	>90	2.9	134	32.710	34.217	38.411
0.6	9	73.698	>90	>90	3.0	153	32.710	33.577	38.411
0.7	9	73.698	>90	>90	3.1	175	32.710	33.577	38.411
0.8	9	73.698	>90	>90	3.2	193	26.951	32.710	34.817
0.9	11	69.239	77.329	>90	3.3	213	26.035	31.555	33.666
1.0	12	69.239	77.329	>90	3.4	236	23.457	31.292	33.666
1.1	13	65.114	77.329	>90	3.5	255	23.457	31.292	32.466
1.2	17	65.114	72.543	>90	3.6	291	21.148	23.309	27.315
1.3	20	55.358	63.228	72.543	3.7	330	21.148	22.162	26.434
1.4	20	55.358	63.228	72.543	3.8	378	21.148	22.096	23.309
1.5	21	55.358	63.228	72.543	3.9	427	18.280	21.006	22.972
1.6	24	55.358	63.228	72.542	4.0	465	18.280	21.006	22.972
1.7	29	55.358	63.228	72.543	4.1	526	17.660	19.767	21.362
1.8	31	55.358	63.228	72.543	4.2	587	16.140	19.767	20.471
1.9	38	50.484	62.426	72.543	4.3	675	16.140	18.653	19.493
2.0	43	50.484	62.426	72.543	4.4	754	15.053	15.624	17.264
2.1	49	46.805	50.484	62.426	4.5	852	15.053	15.624	17.001
2.2	59	36.044	42.571	46.805	4.6	962	12.492	14.027	15.522
2.3	65	36.044	42.048	46.805	4.7	1064	10.269	13.521	14.423
2.4	74	36.044	41.530	45.806					

θ - half cone angle of circular field of view.

TABLE 5-8. CENTERS OF CRITICAL FIELDS OF VIEW (from Ref. 5-2)

m _v	n=1		n=2		n=3		m _v	n=1		n=2		n=3	
	α°	δ°	α°	δ°	α°	δ°		α°	δ°	α°	δ°	α°	δ°
0.1	12.622	4.900	-	-	-	-	3.0 to 3.1	46.585	-28.719	45.190	-29.616	39.054	-16.257
0.2	359.833	-7.485	-	-	-	-	3.2	37.703	-32.114	46.585	-28.719	22.116	-22.617
0.3 to 0.5	349.796	-16.581	-	-	-	-	3.3	52.422	-38.954	18.160	-12.695	12.533	-9.286
0.6 to 0.8	358.491	13.187	-	-	-	-	3.4	35.200	-18.310	18.260	-12.338	12.533	-9.286
0.9 to 1.0	7.650	10.497	192.702	15.787	-	-	3.5	35.200	-18.310	18.260	-12.338	16.309	-11.247
1.1	2.892	5.388	192.702	15.787	-	-	3.6	79.448	67.109	105.887	66.486	154.276	-15.062
1.2	2.892	5.388	3.752	-23.718	-	-	3.7	79.448	67.109	163.753	-6.483	151.056	-14.298
1.3 to 1.8	10.124	19.489	5.273	3.958	3.752	-23.718	3.8	79.448	67.109	88.465	67.449	105.887	66.486
1.9 to 2.0	1.405	17.803	2.233	2.483	3.752	-23.718	3.9 to 4.0	72.655	71.074	79.638	68.006	86.071	81.115
2.1	30.043	-10.821	1.405	17.803	2.233	2.483	4.1	91.170	71.925	192.762	32.589	91.214	66.283
2.2	333.385	4.792	315.377	2.846	30.043	-10.821	4.2	100.110	73.575	192.762	32.589	193.390	31.544
2.3	333.385	4.792	340.955	12.151	30.043	-10.821	4.3	100.110	773.575	107.232	78.765	83.926	65.833
2.4	333.385	4.792	339.426	11.502	325.943	-1.576	4.4	111.484	74.837	104.507	74.158	102.909	76.009
2.5 to 2.6	47.110	-26.674	38.835	-15.137	31.062	-5.516	4.5	111.484	74.837	104.507	74.158	8.844	-25.627
2.7	46.693	-24.500	39.514	-16.349	38.073	-18.466	4.6	106.037	70.946	79.922	74.312	14.463	-28.490
2.8	46.585	-28.719	46.693	-24.500	39.514	-16.349	4.7	72.240	-84.360	15.140	-31.013	14.166	-29.577
2.9	46.585	-28.719	46.693	-24.500	39.054	-16.257							

TABLE 5-9. CLASSIFICATION OF CRITICAL POINTING DIRECTIONS (from Ref. 5-2)

Group I		Group II		Group III	
n=1	None	n=1	$m_V = 0.1 - 3.5; 4.7$	n=1	$m_V = 3.6 - 4.6$
n=2	$m_V = 0.9 - 1.1; 3.7;$ $4.1 - 4.2$	n=2	$m_V = 1.2 - 3.5; 4.7$	n=2	$m_V = 3.6; 3.8 - 4.0;$ $4.3 - 4.6$
n=3	$m_V = 3.6 - 3.7; 4.2$	n=3	$m_V = 1.3 - 3.5;$ $4.5 - 4.7$	n=3	$m_V = 3.8 - 4.1;$ $4.3 - 4.4$

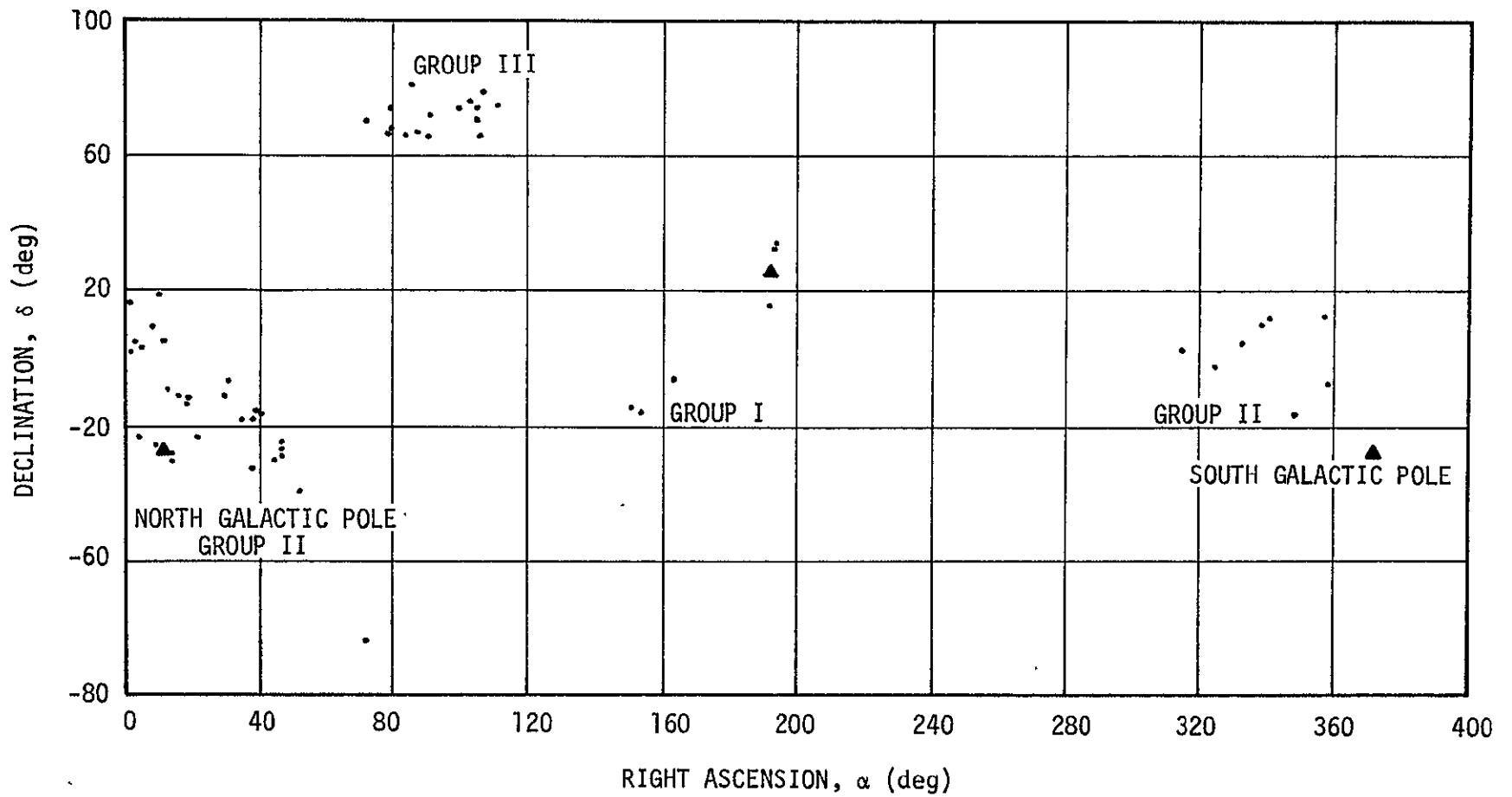
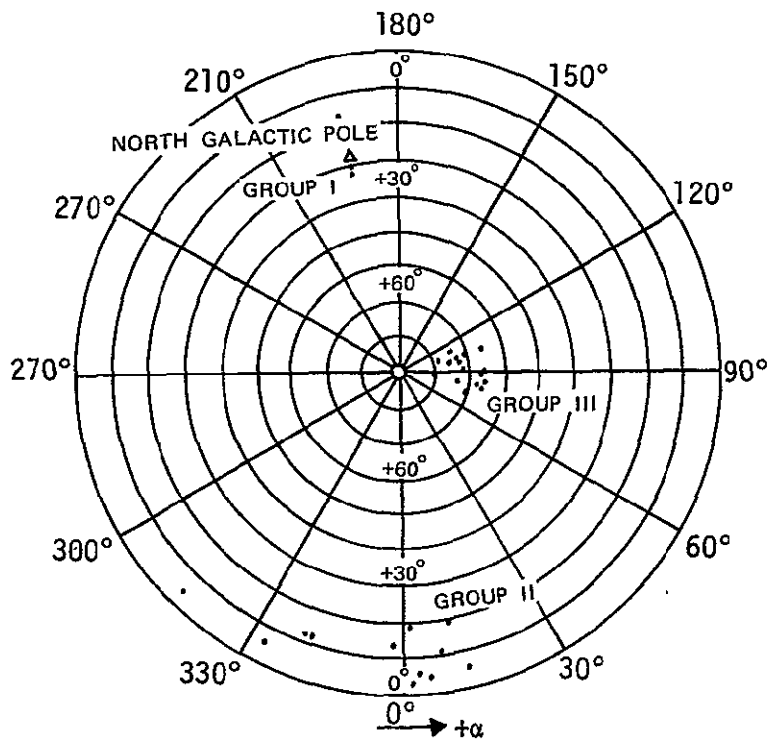
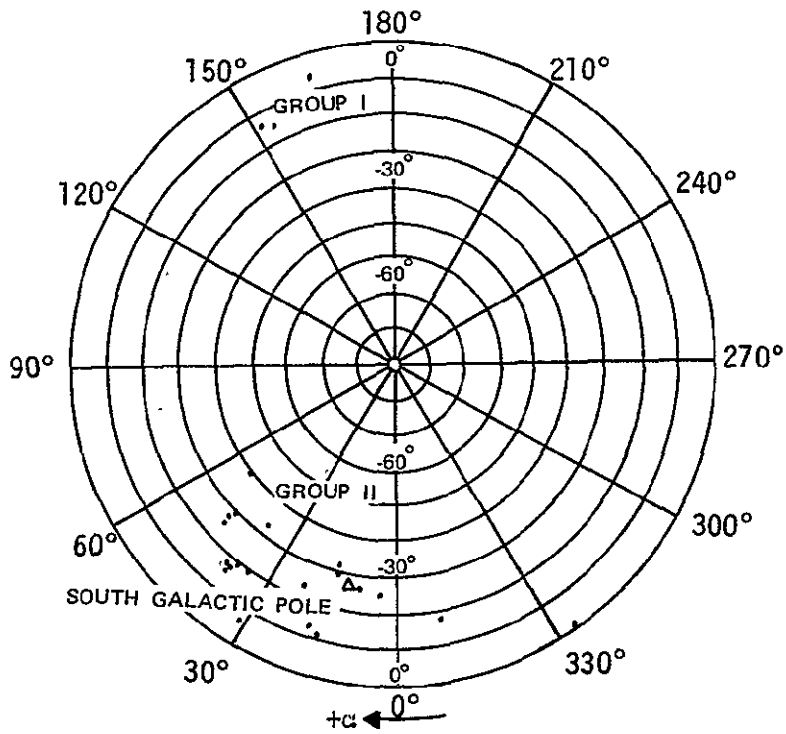


FIGURE 5-5. MERCATOR PROJECTION OF CRITICAL POINTING DIRECTIONS (from Reference 5-2)



(a) NORTH CELESTIAL POLAR PROJECTION



(b) SOUTH CELESTIAL POLAR PROJECTION

FIGURE 5-6. POLAR PROJECTION OF CRITICAL POINTING DIRECTIONS
(from Reference 5-2)

TABLE 5-10. STAR TRACKER PHOTODETECTOR RESPONSE

Nav No	B.S No	Const	S H A	Dec	MK Spect	V	Detector Type									
							Amperes/cm ² of Telescope Aperture									
							S-1	S-4	S-11	S-17	S-20	Balkali	Silicon			
18	2491	α CMa	259° 03'	-16° 40'	A1 V	-1.45	0.994E-14	0.181E-12	0.224E-12	0.400E-12	0.315E-12	0.281E-12	0.185E-11			
17	2326	α Car	264 11	-52 41	F0 Ib-II	-0.75	0.542E-14	0.832E-13	0.102E-12	0.186E-12	0.150E-12	0.127E-12	0.107E-11			
38	5459D	α Cen	140 37	-60 42	G2 V	-0.28	0.349E-14	0.349E-13	0.444E-13	0.813E-13	0.709E-13	0.526E-13	0.758E-12			
37	5340	α Boo	146 26	19 20	K2 IIIp	-0.05	0.395E-14	0.198E-13	0.268E-13	0.493E-13	0.483E-13	0.289E-13	0.869E-12			
49	7001	α Lyr	81 02	38 45	A0 V	0.03	0.254E-14	0.459E-13	0.569E-13	0.101E-12	0.803E-13	0.713E-13	0.483E-12			
12	1708	α Aur	281 24	45 58	G8 III	0.08	0.278E-14	0.254E-13	0.318E-13	0.581E-13	0.514E-13	0.368E-13	0.606E-12			
11	1713	β Ori	281 44	8 14	B8 Ia	0.13	0.313E-14	0.514E-13	0.625E-13	0.114E-12	0.861E-13	0.800E-13	0.452E-12			
20	2943	α CMi	245 34	5 18	F5 IV-V	0.37	0.199E-14	0.254E-13	0.319E-13	0.579E-13	0.477E-13	0.388E-13	0.402E-12			
5	472	α Eri	335 52	-57 24	B5 IV	0.47	0.231E-14	0.418E-13	0.505E-13	0.927E-13	0.691E-13	0.648E-13	0.335E-12			
35	5267	β Cen	149 36	-60 13	B1 II	0.62	0.266E-14	0.467E-13	0.560E-13	0.104E-12	0.745E-13	0.728E-13	0.298E-12			
16	2061V	α Ori	271 37	7 24	M2 Iab	0.42	0.573E-14	0.924E-14	0.130E-13	0.242E-13	0.308E-13	0.132E-13	0.116E-11			
51	7557	α Aql	62 41	8 47	A7 IV-V	0.76	0.132E-14	0.203E-13	0.254E-13	0.457E-13	0.369E-13	0.314E-13	0.265E-12			
30	4730D	α Cru	173 47	-62 56	B1 IV	0.76	0.243E-14	0.417E-13	0.500E-13	0.929E-13	0.667E-13	0.651E-13	0.276E-12			
10	1457V	α Tau	291 28	16 27	K5 III	0.86	0.226E-14	0.675E-14	0.942E-14	0.174E-13	0.191E-13	0.970E-14	0.480E-12			
42	6134V	α Sco	113 07	-26 22	M2 I	0.91	0.331E-14	0.607E-14	0.845E-14	0.158E-13	0.193E-13	0.870E-14	0.675E-12			
33	5056V	α Vir	159 06	-11 00	B1 V	0.97	0.185E-14	0.320E-13	0.391E-13	0.722E-13	0.513E-13	0.499E-13	0.207E-12			
21	2990	β Gem	244 08	28 06	K0 III	1.14	0.108E-14	0.762E-14	0.101E-13	0.185E-13	0.171E-13	0.112E-13	0.239E-12			
56	8728	α Psa	16 01	-29 47	A3 V	1.16	0.869E-15	0.150E-13	0.185E-13	0.336E-13	0.267E-13	0.231E-13	0.170E-12			
53	7924	α Cyg	49 55	45 10	A2 Ia	1.25	0.909E-15	0.145E-13	0.177E-13	0.317E-13	0.254E-13	0.226E-13	0.163E-12			
26	3982	α Leo	208 19	12 07	B7 V	1.35	0.880E-15	0.159E-13	0.195E-13	0.352E-13	0.269E-13	0.248E-13	0.140E-12			
19	2618	ε CMa	255 39	-28 56	B2 II	1.50	0.111E-14	0.197E-13	0.237E-13	0.440E-13	0.317E-13	0.307E-13	0.130E-12			
31	4763V	γ Cru	172 38	-56 56	M3 II	1.63	0.207E-14	0.338E-14	0.466E-14	0.864E-14	0.107E-13	0.489E-14	0.417E-12			
45	6527	λ Sco	97 07	-37 05	B1 V	1.63	0.955E-15	0.173E-13	0.208E-13	0.386E-13	0.278E-13	0.270E-13	0.112E-12			
13	1790	γ Ori	279 08	6 19	B2 III	1.64	0.974E-15	0.170E-13	0.207E-13	0.382E-13	0.274E-13	0.266E-13	0.114E-12			
14	1791	β Tau	278 55	28 35	B7 III	1.65	0.726E-15	0.130E-13	0.159E-13	0.289E-13	0.218E-13	0.203E-13	0.108E-12			
24	3685	β Car	221 47	-69 35	A1 IV	1.68	0.566E-15	0.100E-13	0.123E-13	0.223E-13	0.176E-13	0.155E-13	0.108E-12			
15	1903V	ε Ori	276 20	1 13	B0 Ia	1.69	0.959E-15	0.159E-13	0.194E-13	0.361E-13	0.256E-13	0.248E-13	0.106E-12			
55	8425	α Gru	28 26	-47 07	B5 V	1.74	0.688E-15	0.123E-13	0.148E-13	0.273E-13	0.205E-13	0.190E-13	0.101E-12			
32	4905	ε UMa	166 49	56 07	A0 p	1.77	0.519E-15	0.946E-14	0.116E-13	0.207E-13	0.164E-13	0.147E-13	0.981E-13			
27	4301	α UMa	194 32	61 55	K0 III	1.79	0.601E-15	0.392E-14	0.523E-14	0.961E-14	0.900E-14	0.578E-14	0.133E-12			
9	1017	α Per	309 29	49 45	F5 Ib	1.79	0.513E-15	0.600E-14	0.762E-14	0.137E-13	0.116E-13	0.915E-14	0.110E-12			
22	3307V	ε Car	234 32	59 25	K0 p	1.86	0.429E-15	0.359E-14	0.468E-14	0.872E-14	0.764E-14	0.530E-14	0.947E-13			
48	6879	ε Sgr	84 28	-34 24	A0 V	1.86	0.506E-15	0.921E-14	0.112E-13	0.204E-13	0.158E-13	0.142E-13	0.910E-13			
34	5191	γ UMa	153 25	49 28	B3 V	1.86	0.672E-15	0.120E-13	0.147E-13	0.269E-13	0.197E-13	0.178E-13	0.903E-13			
43	6217	α TrA	108 39	-68 58	K4 III	1.92	0.612E-15	0.277E-14	0.373E-14	0.692E-14	0.711E-14	0.402E-14	0.135E-12			
52	7790	α Pav	54 12	-56 50	B3 IV	1.94	0.651E-15	0.118E-13	0.143E-13	0.263E-13	0.193E-13	0.184E-13	0.860E-13			
25	3748	α Hya	218 29	-8 31	K4 III	1.97	0.618E-15	0.258E-14	0.357E-14	0.661E-14	0.682E-14	0.373E-14	0.135E-12			
6	617	α Ari	328 39	23 19	K2 III	2.00	0.520E-15	0.304E-14	0.409E-14	0.751E-14	0.720E-14	0.446E-14	0.115E-12			
4	188	β Cet	349 30	-18 09	K1 III	2.02	0.450E-15	0.307E-14	0.408E-14	0.749E-14	0.698E-14	0.453E-14	0.100E-12			
36	5288	θ Cen	148 47	-36 13	K0 III-IV	2.06	0.462E-15	0.317E-14	0.413E-14	0.758E-14	0.714E-14	0.471E-14	0.103E-12			
1	15	α And	358 19	28 55	B9 p	2.06	0.496E-15	0.885E-14	0.108E-13	0.196E-13	0.148E-13	0.137E-13	0.760E-13			
40	5563	β UMi	137 18	74 17	K4 III	2.08	0.607E-15	0.236E-14	0.327E-14	0.605E-14	0.634E-14	0.340E-14	0.132E-12			
46	6556	α Oph	96 38	12 35	A5 III	2.07	0.375E-15	0.610E-14	0.761E-14	0.136E-13	0.109E-13	0.941E-14	0.749E-13			
50	7121	σ Sgr	76 40	-26 20	B2 V	2.03	0.617E-15	0.113E-13	0.135E-13	0.250E-13	0.183E-13	0.175E-13	0.790E-13			
28	4534	β Leo	183 07	14 45	A3 V	2.14	0.369E-15	0.631E-14	0.785E-14	0.140E-13	0.112E-13	0.974E-14	0.721E-13			
23	3634	λ Vel	223 17	43 19	K5 Ib	2.21	0.662E-15	0.192E-14	0.264E-14	0.491E-14	0.548E-14	0.276E-14	0.140E-12			
3	168	α Cas	350 19	56 22	K0 II III	2.23	0.403E-15	0.244E-14	0.329E-14	0.606E-14	0.577E-14	0.357E-14	0.902E-13			
47	6705	γ Dra	91 02	51 29	K5 III	2.22	0.592E-15	0.198E-14	0.275E-14	0.511E-14	0.550E-14	0.285E-14	0.126E-12			
41	5793V	α CrB	136 39	26 49	A0 V	2.24	0.350E-15	0.639E-14	0.791E-14	0.141E-13	0.110E-13	0.993E-14	0.649E-13			
2	99	α Phe	353 49	-42 29	K0 III	2.40	0.355E-15	0.220E-14	0.288E-14	0.531E-14	0.507E-14	0.325E-14	0.786E-13			
54	8308	ε Peg	34 20	9 44	K2 Ib	2.39	0.425E-15	0.169E-14	0.236E-14	0.438E-14	0.458E-14	0.244E-14	0.932E-13			
44	6378D	η Oph	102 51	15 41	A2.5 V	2.42	0.268E-15	0.469E-14	0.584E-14	0.104E-13	0.831E-14	0.726E-14	0.525E-13			
57	8781	α Peg	14 12	15 02	B9.5 III	2.48	0.271E-15	0.494E-14	0.611E-14	0.108E-13	0.859E-15	0.769E-14	0.502E-13			
8	911	α Cet	314 50	3 58	M2 III	2.53	0.621E-15	0.144E-14	0.201E-14	0.375E-14	0.430E-14	0.206E-14	0.128E-12			
29	4662	γ Crv	176 27	-17 22	B8 III	2.58	0.293E-15	0.528E-14	0.647E-14	0.116E-13	0.893E-14	0.823E-14	0.471E-13			
39	5531	α Lib	137 42	-15 55	A m	2.75	0.202E-15	0.332E-14	0.414E-14	0.742E-14	0.596E-14	0.513E-14	0.402E-13			
7	897D	θ Eri	315 44	-40 26	A3 V	2.91	0.175E-15	0.290E-14	0.357E-14	0.648E-14	0.519E-14	0.445E-14	0.350E-13			

Table 5-10 gives detector response data for the 57 "navigational stars" listed in the Air Almanac. These are relatively bright stars with visual magnitudes ranging from -1.46 to +2.91. The table locates and identifies each star, gives its visual magnitude, v , and gives the response of each type of detector in amperes of detector output per square centimeter of effective collecting area. It is interesting to note that for a given star (a given line in the table), the response for different detectors may differ by a factor of 100 (equivalent to five stellar magnitudes). Clearly the data of Figures 5-4 and 5-6 must be compiled anew when a specific detector is selected. These figures serve only as a rough guide to required tracker characteristics. Figures 5-7a and 5-7b show the response curves of the photodetectors considered.

A given photomultiplier or image dissector may be available with a choice of photocathodes, giving, for example, S-1, S-4, S-11, or S-20 response. An analysis might point to a particular detector as the best choice for a given desired sensitivity.

The image dissector is the detector most often used in star trackers. If an image dissector with a certain response curve is chosen, data such as presented in Table 5-10 can be used to determine its signal-to-noise ratio for observation of a particular star through a particular optical system. The basic equation for the signal-to-noise ratio of a detector is derived from Reference 5-3 as

$$S/N = 4.9 \times 10^9 D (IT)^{\frac{1}{2}}$$

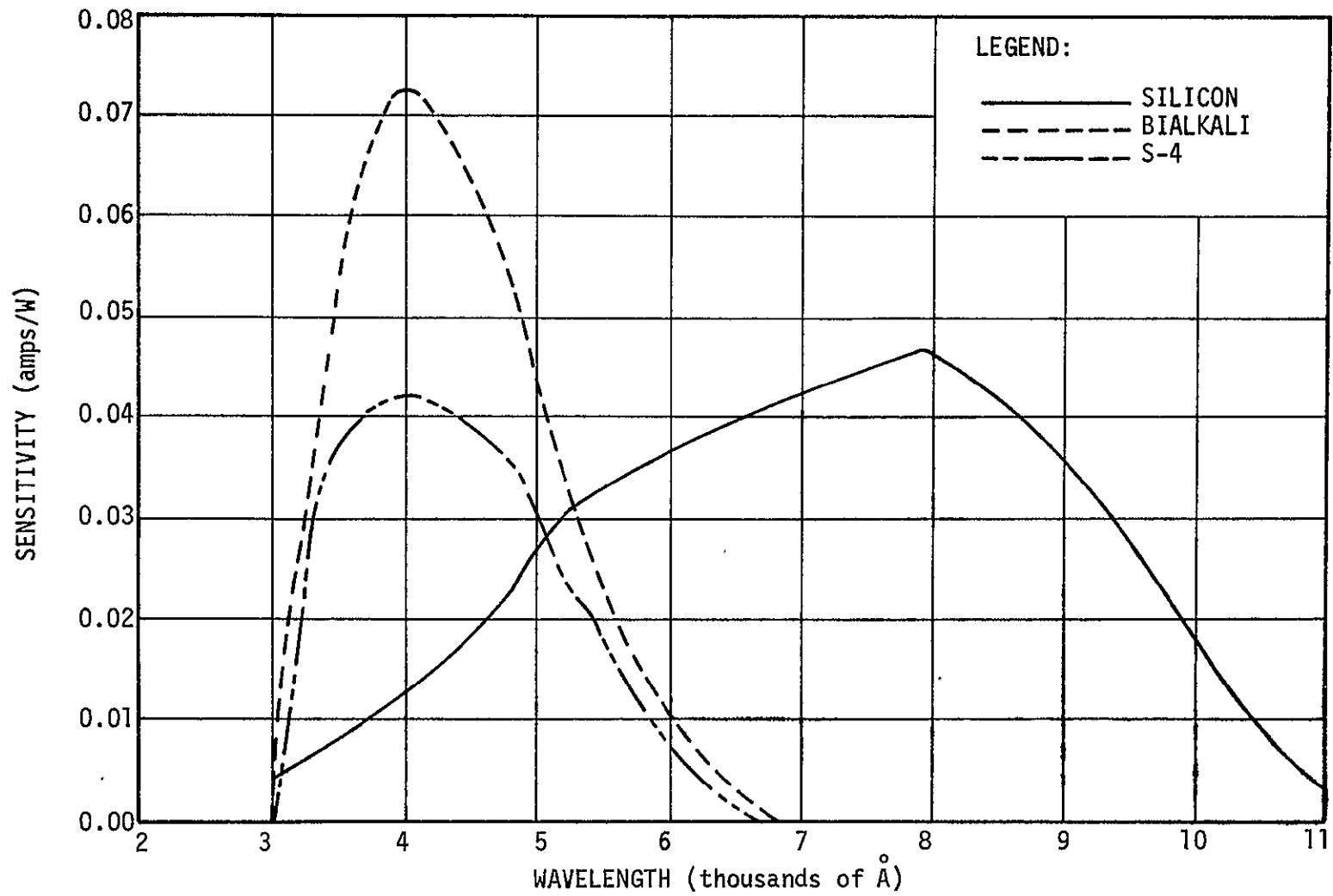


FIGURE 5-7a. SPECTRAL RESPONSE OF PHOTODETECTORS (from Reference 5-1)

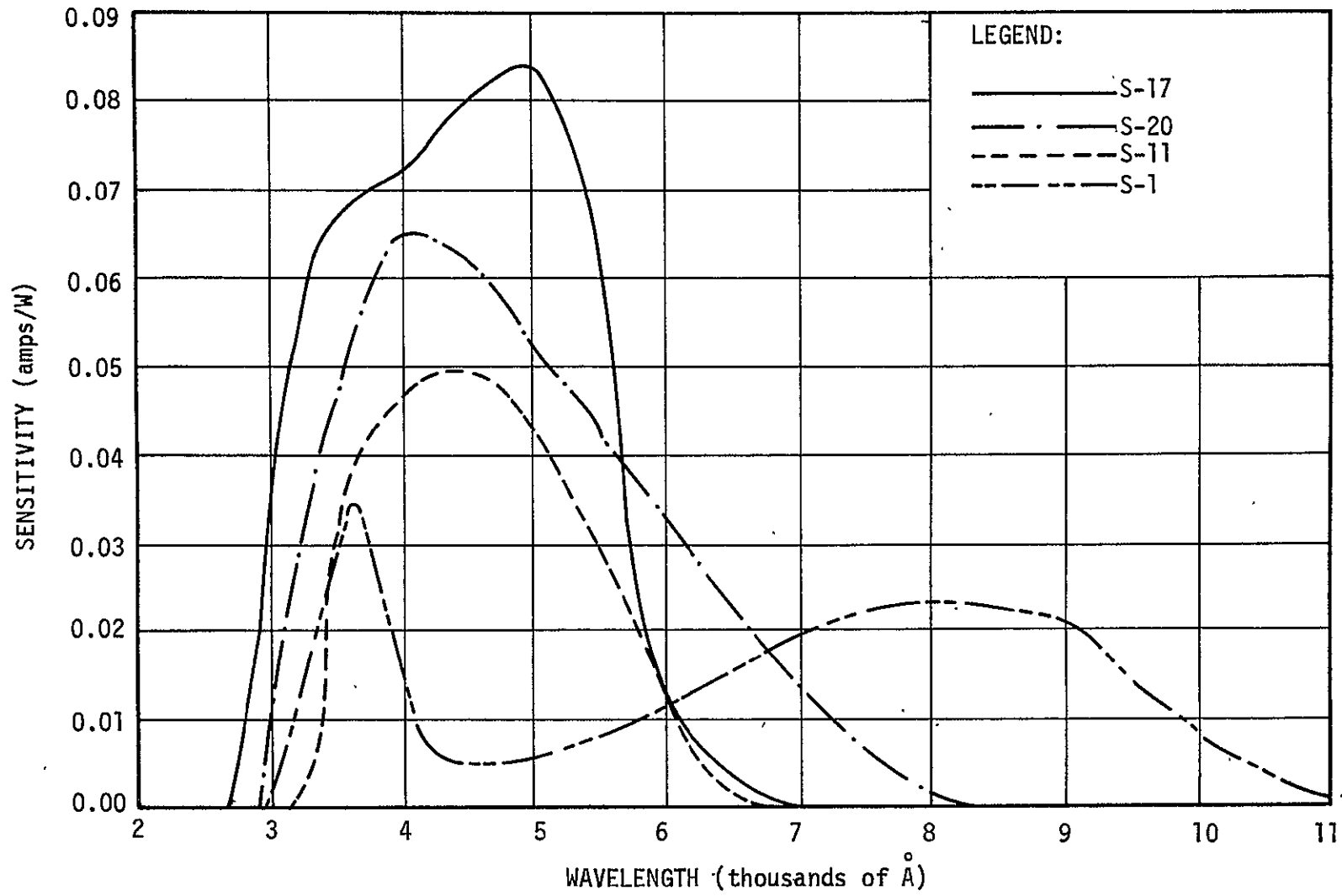


FIGURE 5-7b. SPECTRAL RESPONSE OF PHOTODETECTORS (from Reference 5-1)

where

D - diameter of the effective circular collecting aperture of the detector, in.

I - signal current for the detector, amps/cm² (Table 5-10)

T - signal integration time, sec.

A signal-to-noise ratio of the order of 10 is desirable for reliable operation. If the instrument is tracking a star, some degree of scanning is necessary to detect the direction of star motion; the shorter the required response time, the faster the instrument must scan and the smaller T becomes. In Reference 5-3, sample calculations for a specific image dissector indicate that T is inversely proportional to tracker bandwidth, being about 1/40 second at one cycle/sec. Thus, one may write

$$B = \frac{K_1}{T} = K_2 I$$

where

B - tracker bandwidth, cycles/sec

T - tracker integration time, sec

I - signal current, amps/cm².

The foregoing discussion shows how tracker response can be analyzed for given image dissectors and given stars. Since detectors and stars of interest have not yet been specified for HEAO-C, these calculations will not be taken further in the present study.

Fixed Star Trackers

Many star tracking devices have been developed for space applications and several have been proven in space. In the interest of economy and reliability, it would seem logical to find some instrument for the HEAO-C mission that could be used essentially "off-the-shelf", or at least one that could be used with minor modification. Six developers and manufacturers of star trackers were identified and extensive discussions ensued with the aim of finding a suitable tracker. Eventually it became clear that this approach is probably not practical. Instead, it will be necessary to develop a tracker for the specific requirements of HEAO-C, while drawing as much as possible on the techniques and components resulting from earlier tracker programs. The reasons for this are as follows:

- Any space-proven tracker is based on the technology of several years ago and includes techniques that would be considered obsolete in an instrument being designed today: for example, discrete electronic components arranged in cordwood modules, rather than integrated circuits. There exists a case for using the best of existing technology, which now makes it possible to design a better tracker.
- By the time an instrument has been delivered, installed, and proven its reliability by operating in space for a year or more, the manufacturer's production facility and qualification testing machinery have been dismantled. Recommencement of production and testing would not necessarily be cheaper than development of a new instrument.
- Any existing instrument has certain peculiarities associated with the spacecraft for which it was designed. Some trackers were designed to work in association with specialized data processing units, found only in their particular spacecraft; others contain elaborate electronics needed in their spacecraft, but not in the HEAO-C spacecraft. Some trackers require large heater powers or especially stable waveforms for their operation. Such peculiarities would impose special interface requirements on other parts of the HEAO-C spacecraft, and so eliminate much of the economy of using an existing tracker.

- No existing tracker quite meets the sensitivity/field of view requirements. A more sensitive photodetector or larger optical system would be required. In most cases this alone would compel redesign of the whole instrument.

Information on existing trackers is compiled in Table 5-11. This gives an indication of the state of the art, and shows that the technology does provide a good starting point for developing an instrument to meet HEAO-C requirements. Accuracies are not tabulated, since accuracy is a function of a number of variables as discussed in the text. All four trackers appear to be able to meet the accuracy requirements.

Tracker cost was discussed with the manufacturers. This is a sharp function of two variables: the extent to which an existing tracker must be modified to meet HEAO-C needs, and the qualification testing and supporting documentation required by NASA. The consensus on likely cost per tracker, for a program involving five to ten trackers, was in the \$100,000 to \$200,000 region.

ITT Boresighted Star Tracker (Ref. 5-4) - This instrument was flown in the first two OAO spacecraft. It is boresighted with the high-resolution spacecraft experiments. Designed for a 1-year lifetime, the tracker in OAO-2 is still operating after 18 months in orbit. Its photodetector, an electrostatically focussed image dissector with an S-20 spectral response curve, is matched with a 4.85-inch focal length, f/1.85 lens to cover a 3-degree square field of view. It scans with a limited field of view (10 arc-minutes) to reduce the effects of background noise. The detector can operate in the offset mode (tracking a star at a fixed angle to the optical axis), but offsetting occurs in discrete steps, increasing from 15 arc-seconds near the axis to 1 arc-minute near the edge of the field.

This tracker has successfully held the OAO-2 on a star of +6.6 visual magnitude. Tracker noise appears in telemetry records as the main source of a 2 arc-second jitter in spacecraft attitude. Superimposed

TABLE 5-11. FIXED STAR TRACKERS

Manufacturer	ITT, San Fernando, California	Hycon, Monrovia California	Bendix, Teterboro, New Jersey	Ball Brothers, Boulder Colorado
Designation	Boresighted star	HST 513	Fixed star tracker	Celestial attitude error sensor
Development status	Used in orbit	Prototype only	For launch late 1971	In qualification test
Vehicle	OA0-1,2,3	Aerobee	Fourth OA0 mission	Aerobee 150
Detector	Image dissector (S-20)	Image dissector	Image dissector	Image dissector (S-20)
Focal length	4.85 inches	3.0 inches	2.4 inches	2.0 inches
Aperture	f/1.85	f/0.87	f/0.7	f/0.75
Field of view	3 deg x 3 deg	8 degree diameter	8 deg x 8 deg	8 deg x 8 deg
Design sensitivity	+6	+3	+4	+4
Design bandwidth	0.5 hertz	5 hertz	1 hertz	5 hertz
Weight	9 lb (sensor) + 14 lb	9 pounds	14 pounds	10 pounds
Power	7 W (sensor) + 8 W (electronics)	12 watts	10 watts	9 watts
Dimensions	5 x 10 x 12 in. + 3 dia x 15 long	4 dia x 11 long	6 x 6 x 13 in.	5 dia x 11 long

on this is a long-term drift of 5 to 10 arc-seconds over times such as an orbital period. Accuracy could be improved with an image dissector with lower-distortion, electromagnetic rather than electrostatic deflection at a cost of a pound or two in weight. The manufacturers estimate total errors below 1 arc-minute for tracking off-axis stars. However, off-axis operation is limited by the finite offset step size (15 arc-seconds to 1 arc-minute); therefore, spacecraft pointing direction cannot be defined more finely than the step size.

In its OAO-2 configuration the tracker weighs 23 pounds. Of this, 9 pounds is due to the sensor package and 14 to the electronics, which uses quadruplicate circuitry to meet the lifetime requirement. Some of the electronics is used for processing ground commands and other signals related to selection of other trackers (the OAO spacecraft carries six additional trackers). This would not be useful or necessary in HEAO-C. However, attempts to remove unwanted parts within existing equipment may be more expensive than designing completely new equipment.

Hycon HST 513 (Refs. 5-3 and 5-5) - This instrument is an outgrowth of the manufacturer's work on star trackers for sounding rockets. However, it has not been advanced beyond the prototype stage and has not been flight-qualified. The HST 513 uses an image dissector with electromagnetic deflection, and, like the ITT tracker, it can be made to scan a limited (20 arc-minutes) region of its field of view. It has a 3-inch focal length, $f/0.87$ lens and its total field of view is 8 degrees in diameter; however, it is sensitive only to +3 magnitude and brighter stars.

The tracker can also operate in a television mode, scanning the entire field and generating voltages proportional to star x and y coordinates. In this mode it might be used as part of a star field mapping system as will be discussed later in this section.

TABLE 5-12. AVERAGE NUMBER OF STARS SEEN

Item	Data			
Tracker	ITT	Hycon	Bendix	Ball
Field	3° × 8°	8° dia.	8° × 8°	8° dia.
Sensitivity	+6	+3	+4	+4
Bandwidth	0.5 Hz	5.0 Hz	1.0 Hz	5.0 Hz
Average number of stars seen ¹	1.0	0.2	0.8	0.6
Bandwidth required for HEAO-C application ²	0.06 Hz	0.3 Hz	0.1 Hz	0.5 Hz

¹The average number of stars seen is computed assuming a visual response curve. Since tracker responses vary, it is only an approximate figure.

²Bandwidth required would permit detection of an average of 10 to 12 stars and a very high probability of detection of at least one star at all times.

The HST 513 could provide the attitude data required to hold a spacecraft within a few arc seconds of a star. When the star is offset from the axis, nonlinearities increase to several tens of arc seconds near the edge of the field, even if the best calibration and compensation methods are employed. Accuracy would probably always sufficient for HEAO-C control, provided compensation was effective.

The HST-513 was not designed for a specific vehicle and may not be readily modified using alternative lenses and alternative electronic modules.

Bendix Fixed Star Tracker (Ref. 5-6) - This instrument is being developed for the fourth OAO mission (projected launch date September 1971). It uses an image dissector (FW 143 tube) and scans an 8-degree square field of view with a 40-arc minute square instantaneous field. It is designed to select and track the brighter star in the field and is sensitive to magnitude +3.

Accuracy at null is better than 10 arc seconds. Specified accuracy for offset tracking is 5 percent (or up to 1.5 arc minutes) for offsets up to 30 arc minutes in one axis, and 10 percent (or up to 24 arc minutes) for offsets up to 4 degrees. However, the nonlinearities found within these tolerances are highly repeatable. With calibration and compensation, an accuracy of about 30 arc seconds would be expected. The tracker includes a protective shutter which closes when the tracker axis gets within 60 degrees of the Sun.

Ball Brothers Celestial Attitude Error Sensor (Ref. 5-7) - This tracker has been developed for pointing the Aerobee 150 sounding rocket. Several trackers are now being produced and qualification-tested. It uses an S-20 image dissector with a 2.0-inch focal length, f/0.75 lens and is sensitive down to +4 magnitude.

The tracker selects the brightest star in the 8-degree square field. This field can be command-limited to 2 or 4 degrees square. An upper threshold rejection circuit is being developed for a balloon flight application of this tracker; this would permit selection of the brightest star below some given level within the -1 to +4 magnitude range of the instrument.

Vibration and temperature changes limit accuracy to about 45 arc seconds for a star on the optical axis and 2 arc minutes near the edge of the field. Prelaunch and postlaunch calibration could reduce this to below 1 arc minute.

Required Improvements for HEAO-C Mission - Given a suitable star in the field of view, any of the four trackers described above could be calibrated and compensated to meet the HEAO-C accuracy requirements. This leaves the question of whether a suitable star would be seen in any pointing direction. Table 5-12 gives the average number of stars that would be seen by each tracker, based on the star population data of Figure 5-3 and assuming visual magnitude spectral response. With the large statistical variation in star density across the sky, none of these trackers would be able to see a star at all times. This can be corrected by reducing tracker bandwidth, integrating the noise over longer periods, and hence, increasing the limiting sensitivity of the tracker.

It was mentioned earlier that in the range of visual magnitudes from +1.0 to +4.7, a tracker sized to always see at least one star will detect 10 to 12 stars, on the average, over all parts of the sky. Thus the ITT tracker, which will now detect an average of one star in its field of view, must be made to detect about 12 times as many stars to ensure that it can always detect at least one star in any part of the sky. The number of stars N on the celestial sphere of a given magnitude M is given roughly by

$$\log_{10} N = 0.82 + 0.47 M$$

from which it can be shown that N is increased by a factor of 12 where tracker sensitivity goes from +6 to about +8.3, a change of sensitivity magnitude of 2.3. Since one magnitude corresponds to a brightness change by a factor of

$$(100)^{1/5} = 2.51 ,$$

the sensitivity will increase by

$$(2.51)^{2.3} = 8.3 .$$

It was shown earlier that for a given optical system and a given required signal-to-noise ratio, tracker bandwidth can be written

$$B = N_2 I$$

so that the bandwidth is reduced in the same proportion as the signal current produced by starlight. Thus in this case for an increase in sensitivity of 8.3 times the bandwidth is reduced from 0.5 to 0.006 hertz.

Similar calculations for the other three trackers result in the numbers given at the bottom of Table 5-12. Bandwidths as low as 0.06 hertz are quite acceptable to the rest of the system, since the star tracker is used only for periodic updating of a gyro attitude reference. Thus the figures indicate that in theory, any of the trackers could be made to meet the HEAO-C requirements.

It is possible that at the very low signal levels being sought, the B/T relation will break down due to other noise sources. Such sources include imperfectly shielded sunlight, electrical circuit interference, light scattering from particles around the spacecraft, and the dark current of the photodetector. These effects are complicated to treat analytically. However, personnel at ITT were of the opinion that the desired improvement of about two visual magnitudes might be attainable. ITT representatives also supplied a figure for photodetector dark current, expressed in equivalent radiant energy falling on the S-20 photocathode as 2×10^{-16} watts. According to Reference 5-3, the S-20 photocathode is characterized by a radiant sensitivity of 0.043 amp/W, resulting in a cathode dark current of 0.086×10^{-16} amps. This may be compared directly with Table 5-10, which gives signal current for stars down to magnitude +2.91. The bottom line of the table shows that an S-20 cathode receiving light from Theta Eridani generates a signal current of 0.519×10^{-14} amp/cm² of collecting area. The ITT tracker has a 2.65-inch (6.73-cm) diameter aperture; assuming a light transmission of 0.7, the signal current is

$$\frac{\pi(6.73)^2}{4} \times 0.7 \times 0.6 (9 \times 10^{-14}) = 13.0 \times 10^{-14} \text{ amps .}$$

The tracker sensitivity was to be improved to +8.3. If the tracker views a star with the same spectral curve as Theta Eridani, but fainter by

$$8.3 - 2.9 = 5.4 \text{ magnitudes,}$$

the signal output is

$$\frac{13.0 \times 10^{-14}}{(2.51)^{5.4}} = 8.9 \times 10^{-16} \text{ ampere}$$

which is still two orders of magnitude greater than the dark current of 0.086×10^{-16} ampere. This indicates that dark current will probably not be a limiting factor.

If the tracker was made to detect an average of 12 stars, a variable threshold would be adjusted to eliminate all but the brightest stars in any particular star field. Aging and changes in orbit can affect sensitivity by 0.5 magnitude or more, so the threshold would require occasional calibration with known stars.

It seems possible that any of the four trackers discussed could be made to meet HEAO-C requirements. It is not possible at this stage to determine what practical difficulties would be encountered in reducing bandwidth (increasing T), and in matching with other HEAO-C equipment an instrument originally designed for a different vehicle.

Gimballed Star Trackers

The problem of sensitivity and field of view of a star tracker can be eliminated by mounting the tracker on gimbals with large angular freedom. The optical part of the tracker can have a small field of view and gimbal rotation can bring the star to the optical axis, irrespective of spacecraft attitude. Therefore, accuracy is not limited by tracker nonlinearities. Since the tracker can be rotated through large angles, moderate sensitivity is sufficient and software is required to handle a relatively small number of stars. Several gimballed trackers are described below, characteristics are tabulated in Table 5-13.

TABLE 5-13. GIMBALLED STAR TRACKERS

Manufacturer	Kollsman, Syosset, New York	Kollsman, Syosset, New York	ITT, Monrovia, California	Bendix, Teterboro, New Jersey
Designation	KS-137	KS-199	SPARS	ATM star tracker
Development status	Used in orbit	Prototype only	Under development	In qualification testing
Vehicle	OAO-1, OAO-2	USAF (cancelled)	Classified	ATM
Detector	Photomultiplier (S-4)	Solid state (silicon)	Image dissector (S-20)	Image dissector (S-20)
Focal length	4.9 inches	3.12 inches	110 inches	6.8 inches
Aperture	f/1.4	f/1.25	f/31	f/4.5
Field of view	1 deg × 1 deg	1-degree diameter	10 arc minutes	1 deg × 1 deg
Gimbal freedom	±43 degrees	±55 degrees	±45/±135 degrees	±87/±40 degrees
Design sensitivity	+3	+1.8	+4	+2.4
Weight	24 + 19 + 8 lb	23 + 12 lb	30 + 10 lb	32 + 28 lb
Power	13 watts	3 watts	50 watts	9 + 15 watts
Dimensions	18 × 17 × 16 in + 16 × 11 × 4 in + 12 × 8 × 3 in	10 × 15 × 10 in + 7 × 9 × 8 in	15 × 15 × 15 in 700 in	13 × 17 × 14 + 6 × 13 × 18

Kollsman KS-137 (Ref. 5-8) - This tracker was developed for the Orbiting Astronomical Observatory (OAO) and has flown on the OAO-1 and OAO-2. Each OAO spacecraft carries six KS-137 trackers which together provide coverage of the entire sky. This ensures that despite Earth occultation and Sun position, the OAO trackers can always observe at least three stars to establish a three-axis reference for spacecraft alignment. More precise alignment is controlled by the ITT fixed boresighted tracker described earlier.

The KS-137 is based on an optical system and photomultiplier having an S-4 (Table 5-10) response. This combination has a 1- by 1-degree field of view and can accurately track stars down to about +3 magnitude. The scanning action necessary for tracking is provided by a pair of vibrating reeds arranged at right angles. Gimbal freedom amounts to ± 43 degrees. The gimbal angle pickoffs are so-called phasolvers, which use changes in capacitance to measure rotation. The phasolvers are more complex than the conventional optical encoders, and require several pounds of auxiliary electronics to provide highly stable ac waveforms. However, they are believed by the manufacturer to be more reliable than the conventional optical encoder. Pickoff accuracy is about 10 arc seconds per axis, or 30 arc seconds total.

The OAO spacecraft include a substantial amount of processing electronics designed to interface with the six KS-137 trackers and the ITT fixed tracker. This electronics carries out the coordinate transformations made necessary by the tracker mounting arrangements. Trackers mounted on the spacecraft surface are not necessarily aligned with spacecraft axes. The processing electronics also gives less weight to data from trackers which are momentarily pointed at large gimbal angles.

If used on HEAO-C spacecraft, either the Kollsman or the ITT tracker would have to be modified to match different processing electronics.

The merit of this tracker is its record of use in space. The OAO-2 has been in orbit nearly two years and telemetry indicates that after that time, at least four and possibly five of the six trackers are still operating.

Kollsman KS-199 (Ref. 5-8) - This tracker was developed for an Air Force application which failed to materialize. It has a 2.5-inch aperture Mangin optical system and a silicon (solid state) detector; the telescope has a 1-degree diameter field of view and is sensitive to about +1.8 magnitude (silicon). There are 82 stars in the celestial sphere which it can track. The solid-state detector is more reliable and much more compact than a photomultiplier; it is also capable of momentary exposure to direct sunlight without damage.

The optical system scans by means of a flexible fiber optics rod or 'wand' which is made to nutate by opposed pairs of electromagnets. The telescope is mounted on gimbals with ± 55 degrees of freedom, so that on the average it can view 20 percent of the sky containing 17 detectable stars.

Tracker accuracy is always better than 15 arc seconds per axis of 21 arc seconds total. This represents considerably higher accuracy than the 30-arc-second one-sigma performance of the KS-137. On the other hand, the first flight model of the KS-199 is not quite complete and of course no data exists on its performance under actual space conditions.

ITT SPARS [Space Precision Attitude Reference System

(Ref. 5-4) - This tracker is being developed by ITT for a military application. If the project continues as expected, the tracker will be space-qualified in time for HEAO-C use. Its optical system is based on the 3.5-inch aperture, 110-inch focal length, Questar telescope, which is to be modified by temperature- and vibration-isolation and by the introduction of quartz and Invar for certain components. The telescope field of view is 10 arc minutes and the instrument is to be sensitive to +4-magnitude stars.

Under laboratory conditions the tracker is accurate to a few arc seconds. Its limitation is gimbal reliability. The system is designed for a 3-sigma lifetime of a few weeks. However, later development work by ITT will be directed toward extending the lifetime to years.

At present the gimbal and telescope assembly weigh about 50 pounds and the electronics about 20 pounds. Both figures will be reduced in the course of development and Table 5-13 gives estimates of final figures.

Bendix ATM Star Tracker (Ref. 5-6) - As a backup supplier for the OAO program, Bendix produced a tracker similar to the Kollman KS-137 already described. Bendix is now using more advanced techniques to produce a star tracker for alignment of the ATM. With a 6.8-inch focal length optical system stopped down to f/6.8, the tracker can detect only stars brighter than +1.5 magnitude. However, the aperture is limited by lens hood design which in turn is limited by a requirement for pointing to within 5 degrees of the Earth. If this requirement is relaxed somewhat, the aperture can be increased to f/4.5 and the sensitivity increased by nearly a magnitude.

The tracker first searches a ± 2 -degree field and attempts to lock onto any star detected; if no star is seen, it searches a field of ± 5 degrees about one gimbal axis and ± 15 degrees about the other. Upon star acquisition, it switches automatically to its high-accuracy track mode. The gimbal pickoffs are optical encoders with 30 arc seconds resolution and the tracker is capable of meeting HEAO-C accuracy requirements.

HEAO-C STAR TRACKER

None of the fixed or gimballed trackers described are ideal for the HEAO-C requirements. However, they indicate that a good basis exists for developing a tracker to meet these requirements. A fixed tracker could be developed, using a large optical system together with long integration time (low bandwidth) to obtain sufficient sensitivity. Such a tracker would be a relatively compact device with no moving parts. However, it would be limited by the linearity and repeatability of image dissector deflection electronics. The accuracy requirement limits the field of view to less than 10 degrees, which in turn requires a sensitivity to at least +6- or +7-magnitude stars. This requires that ground software include a catalog of many thousands of stars and be accurate enough to avoid any errors in star identification. Because of the small tracker field of view, the reference stars must always lie close to the spacecraft axes and this simplifies the onboard conversion of tracker outputs to attitude errors.

Gimballed trackers require somewhat more complicated software on the spacecraft, but a much shorter star catalog on the ground and much less risk of errors in identification. The main objection that may be raised against gimbal trackers is the presence of moving

parts. However, the OAO experience does show that gimbals can be made to operate in space for long periods.

Since a decision on fixed versus gimballed star trackers for the HEAO-C mission cannot be made at this time, an allowance will be made for sufficient weight and volume for accomodation of gimballed trackers on the spacecraft. Table 5-14 projects the characteristics of a HEAO-C tracker based on the present state of the art. Two trackers will be used to provide periodic updating of a three-axis reference system. Total weight and power would included both the gimbal/telescope unit and the electronics package of a typical present-day tracker. The limiting magnitude and the gimbal freedom indicated are together sufficient to ensure that a least two stars are visible at all times. This makes it very likely that the system will be capable of providing the necessary updating, despite such limitations as Sun angle and Earth occultation.

TABLE 5-14. PROJECTED HEAO-C STAR TRACKER CHARACTERISTICS

<u>Item</u>	<u>Data</u>
Weight, lb	40
Power, W	25
Volume, overall, ft ³	2
Volume to accommodate, inside spacecraft, ft ³	1
Limiting star magnitude	+2.3
Number of stars visible	100
Gimbal freedom, deg	±50
Mission time, yr	1 to 2

An actual specification for a HEAO-C tracker must include the minimum permissible angle between the optical axis and the Sun (or the Earth). System design will include preparation of a practical updating scheme, taking into account experiment scheduling, gyro drift, computer processing of redundant attitude data, and orientation of the orbit to the solar vector. If additional trackers are required to allow for failures, the processing problem is compounded. These detailed investigations are considered outside the scope of the present study.

STAR MAPPER ATTITUDE SENSING SYSTEM

Control Data Corporation (CDC) has developed a family of star mappers capable of determining pointing direction without a priori information (Ref. 5-9). Their basic instrument uses a photomultiplier and a slowly rotating reticle with an elaborate pattern of slits. The photomultiplier generates pulses as star images intersect the slits. The system analyzes the pulses to determine the distances between pairs of stars; distances are matched to identify three stars. This is sufficient for 3-axis information. All processing is done by the CDC 469 computer, an LSI machine currently in the development stage and scheduled for delivery in 1971. The computer is to be constructed within a 4-inch cube, and to be capable of storing data on 200 stars. It can accept new star tables, which might be read in from the ground as different portions of the sky were examined. On the other hand, it might be possible to design a mapper with a field of view, sensitivity, and star catalog that will permit operating in any portion of the sky without table updating. Normal time for identification of an unknown star field is several seconds; attitude data can be updated at millisecond intervals thereafter. In a system designed for

the HEAO-C spacecraft, not only field of view and star catalog, but reticle slit pattern and rotation rate would have to be optimized to provide the desired accuracy and dynamic response.

Table 5-15 gives performance data for a classified system currently under development by CDC (Ref. 5-10). The field of view and sensitivity are sufficient for operation in any portion of the sky, and the accuracy is more than sufficient for the HEAO-C application. This system is scheduled for delivery in early 1971. The sensing head of an earlier mapper was test-orbited in the satellite ATS-3. In this experiment, telemetered data from the head was analyzed on the ground to determine satellite attitude to about 20 arc-seconds. It appears that the star mapper technology, as represented by CDC work, will be equal to HEAO-C requirements. Investigation has not identified state-of-the-art mappers by any other manufacturers.

A complete attitude sensing system includes the sensing head, the CDC 469 computer, and the three reference gyros described earlier. Solar sensors are not required. The gyros can supply rate data for initial detumble (despin), and once angular rates are low enough for star mapper operation, the spacecraft can be slewed in any desired direction for pointing at a desired target. Because star data is stored on board, ground control need not identify star patterns to provide an initial reference. Table 5-16 provides weight and power information for a complete system. Regarding reliability, CDC personnel believe the limiting factor to be the photomultiplier tube rather than the reticle drive motor. The best measure would be the inclusion of a second star mapper to provide a backup in the event of failure.

The sensing head requires protection from bright sources. In the case of the Earth and the Moon, electrical disabling is sufficient.

TABLE 5-15. CDC STAR MAPPER CHARACTERISTICS

<u>Item</u>	<u>Data</u>
Optical aperture, in. diam.	4
Dimmest star sensed	+5 magnitude
Field of view, deg	10 to 15
Dimensions (sensing head), in.	12 diam. by 18 long
(computer)	4 in. cube
Time to identify stars	Less than 1 minute
Time to update, msec	1
Accuracy (pitch), arc-sec rms	5
(yaw), arc-sec rms	5
(roll)(about optical axis), arc-min rms	1

TABLE 5-16. STAR MAPPER SYSTEM WEIGHT AND POWER BREAKDOWN

<u>Item</u>	<u>Weight (lb)</u>	<u>Average Power (W)</u>	<u>Power When Operating (W)</u>
Star mapping head	17	7	7
CDC 469 computer	3	10	10
Three reference gyros	3	30	30
Gyro electronics	3	3	3
Mounting hardware and local wiring	<u>8</u>	<u>-</u>	<u>-</u>
TOTAL	<u>34</u>	<u>50</u>	-

A shutter is recommended for Sun protection. Since it is boresighted with the X-ray telescope, the mapper will normally look at about 90 degrees to the Sun, but solar exposure could occur during the early phases of reference acquisition and slewing. If despin ended with the mapper looking too near the Sun, the gyros could be used to make a controlled turn through 40 or 50 degrees until the illumination level is low enough for the Sun shutter to open.

TELEVISION ASPECT SYSTEM

An allied system is the star field system, also represented by the product of one manufacturer. In this case, it is a star field sensor designed by Kollsman for Apollo guidance system alignment. The system was designed to detect +6 magnitude and brighter stars within a 10- by 10-degree field of view and to detect motion of some star that was automatically and arbitrarily selected. Development was discontinued when the requirement failed to materialize. The principle, however, remains valid. The system could be used to maintain lock in an established direction and to control reorientations without the aid of gyroscopes.

In considering systems of this kind, it should be remembered that the HEAO-C spacecraft may contain a television aspect device to telemeter star field information to the ground (Ref. 5-11). This type of data can be reduced to a manageable volume only by processing to eliminate blank areas, so that telemetered data is limited to the brightness and the coordinates of the stars seen. Data processed in this way is a potential source of precise attitude information. The principle is similar to that of the Kollsman star field motion sensor, with the advantage that a large part of the required equipment is already

on board the spacecraft. Because of this, and because it was never completed, the Kollsman instrument will not be discussed further; but the derivation of attitude data from the television aspect system will be briefly explored.

The television aspect system is required to determine stellar positions to 10 arc-seconds. A 1,024 by 1,024 element raster and a square ± 1.37 -degree field of view are envisaged, each picture element being 10 by 10 arc-seconds (Figure 5-8). The optical system, using a 6-inch aperture, is capable of much higher resolution than that stated above. However, a star image is so small that it normally appears in one picture element only.

In both field of view and accuracy, the television aspect system meets attitude sensing requirements. However, the manner in which attitude data can be extracted from the encoded star field on a real-time basis must be determined.

The extensive recent work on pattern recognition is pertinent here; numerous analog instruments have been devised for statistically analyzing the motion of complex images. In the present case, however, the type of image being handled is simple enough to permit straightforward digital processing.

The sensitivity and field of view of the television aspect system result in an average of five detectable stars in the field of view. The television system is expected to have an integration time of 1 second. Its output to the telemetering system consists of 15 data words that give the rectangular coordinates and brightness of the five brightest stars seen (Figure 5-8). A hypothetical processor will extract attitude data by comparing successive 15-word star field samples. The processing problem can be viewed as a search or scan process which manipulates one sample with respect to the other until coincidence is

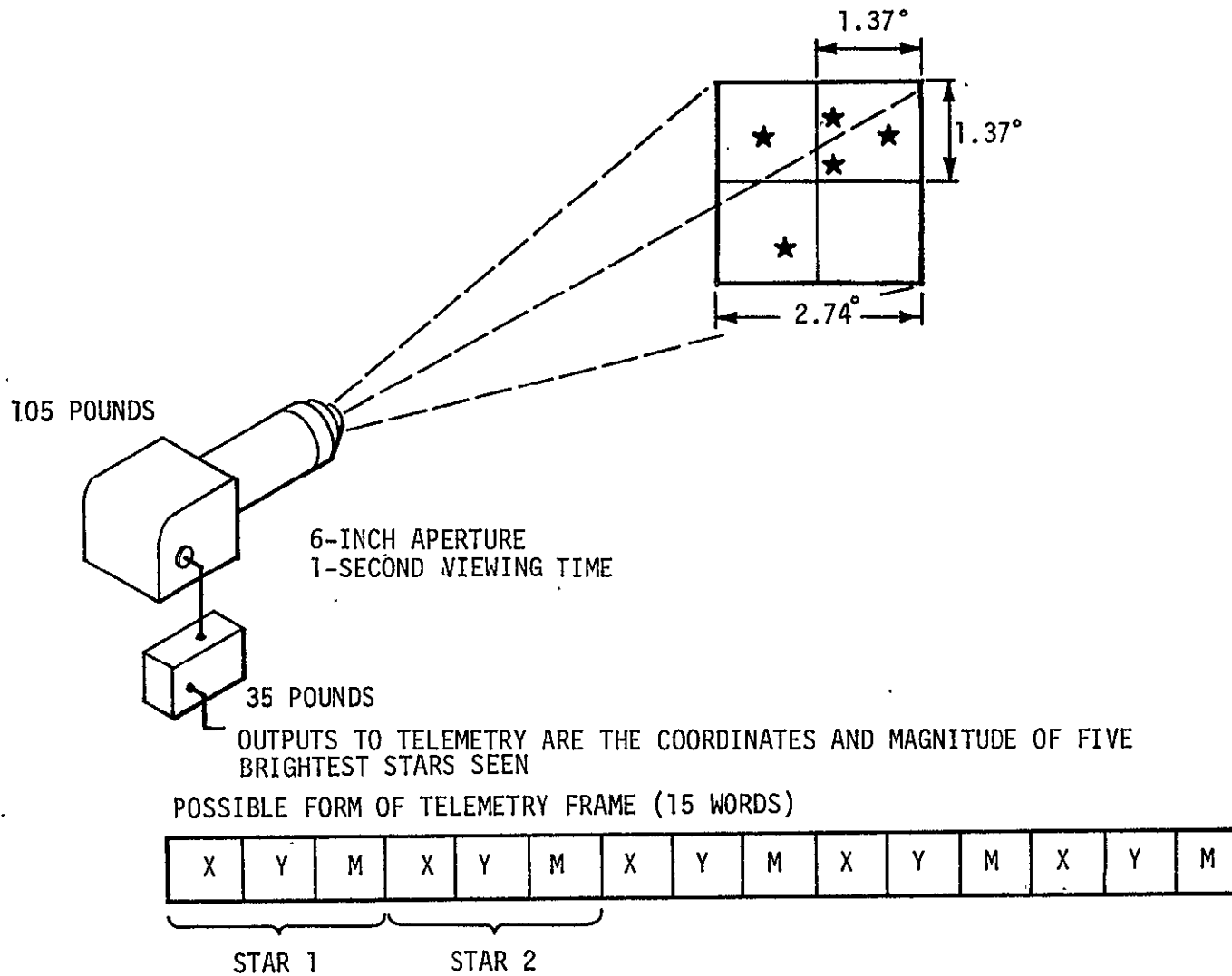


FIGURE 5-8. TELEVISION ASPECT SYSTEM

obtained for at least some fixed number of star images (such as three). The required manipulation, expressed in terms of translation and rotation of the star pattern, can be converted directly to pitch and yaw motions of the optical axis, and roll about this axis, respectively.

The difficulty of search is greatly dependent on the magnitude of possible sample-to-sample motion. Stabilization requirements include angular rates of 1 arc-second; but the usefulness of the system increases with its ability to handle higher angular rates. The search problem is greatly simplified if maximum sample-to-sample motion is small compared with the average distance between stars. For example, assuming that the search method starts by seeking the new position of the star nearest the center of the field of view, translation of this star is a close approximation to translation of the image for small angular motions. Rotation effects are small. If sample-to-sample motion is limited to $\pm n$ picture elements in each of the X and Y directions, the number of elements to be searched for the new position of the star is

$$(2n + 1)^2$$

arranged in a square centered on the previous star position. With random star distribution, the probability that this square does not contain one of the other stars is

$$\left[1 - \left(\frac{2n + 1}{1024} \right)^2 \right]^4 .$$

If the probability of no confusion between stars is to be 0.995, n is limited to 17, i. e., 1,225 squares are to be searched. Since the picture elements on a side are 10 arc-seconds, sample-to-sample motion in the 1-second integration time is limited to

$$\pm 170 \text{ arc-seconds/sec} = 0.047 \text{ deg/sec.}$$

This is large enough to cover residual motion within the rate gyroscope deadband following despin.

The practicality of completing the search process within the 1-second interval between star field samples must then be verified. The above discussion deals only with star field translations, which represent pitch and yaw motion. A 0.047-degree pitch or yaw displaces any star image by 17 picture elements. A roll (rotation about the optical axis) of the same magnitude has no effect on a star very near the axis, but displaces a star image at the edge of the field by

$$\frac{1,024}{2} \left(\frac{0.047}{57.3} \right) = 0.42 \text{ element.}$$

At most, this would be sufficient to move a star image into the adjacent picture element.

A simple search algorithm could establish translational motion by identifying a star near the optical axis and searching the surrounding 35 by 35 element square for its new position (Figure 5-9). This can be done by a comparison of first X- and then Y-coordinates for the five stars in the new sample to find one lying within the square. As shown earlier, the probability is 0.995 that any star found within the square is the one originally at its center. Star brightness comparisons can provide an additional guarantee against incorrect identification. The apparent displacement may be up to 17 elements. Of this, all but 0.42 element (or less) must be the result of true translation rather than rotation. Therefore, the position of any of the four remaining stars can be predicted to within one element of displacement, or within a 3 by 3 element square (Figure 5-10). The search algorithm can be completed by a search limited to this square. A similar 3 by 3 search on one other star, together with star brightness checks, confirms the

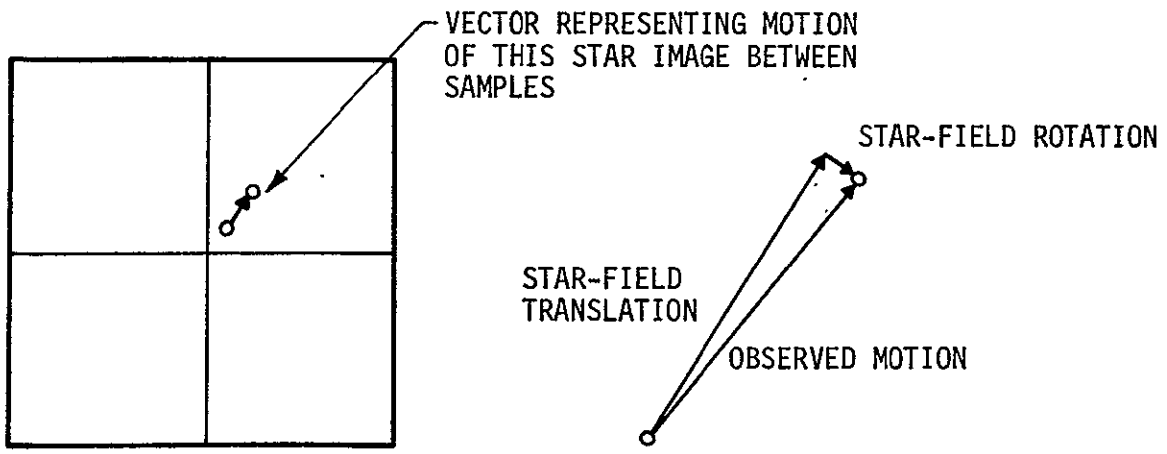
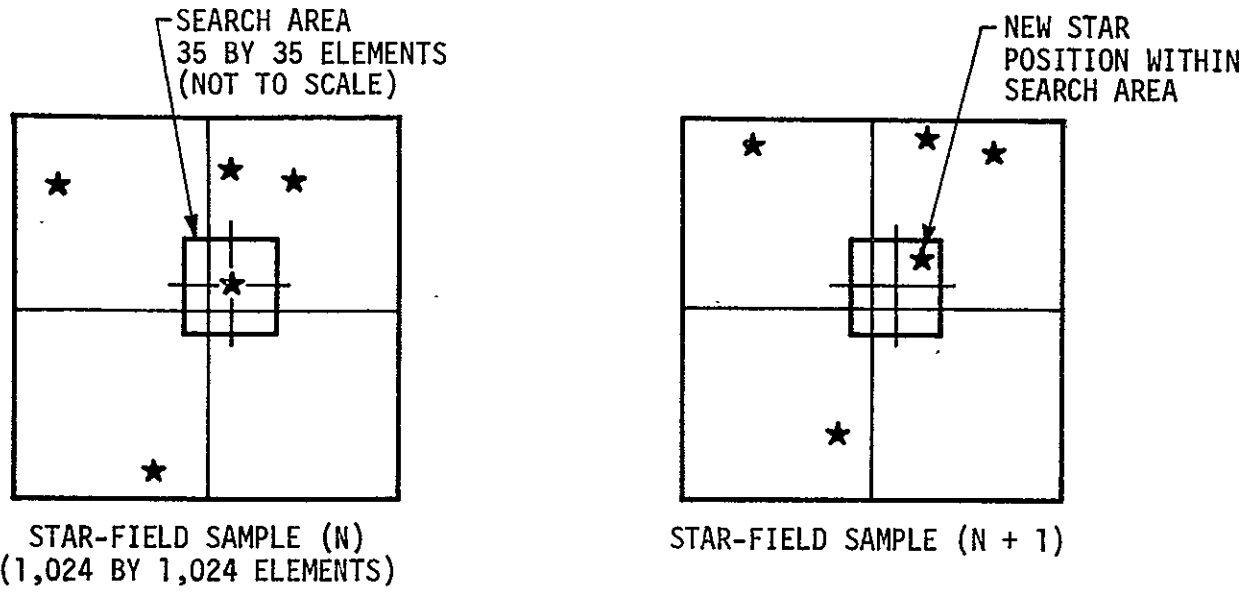
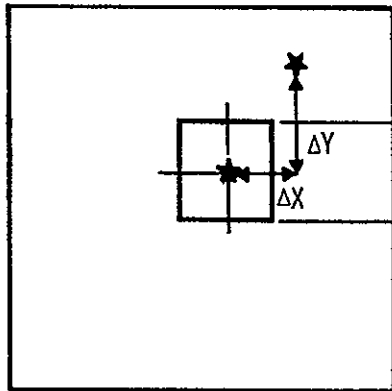


FIGURE 5-9. ESTIMATE OF STAR-FIELD TRANSLATION

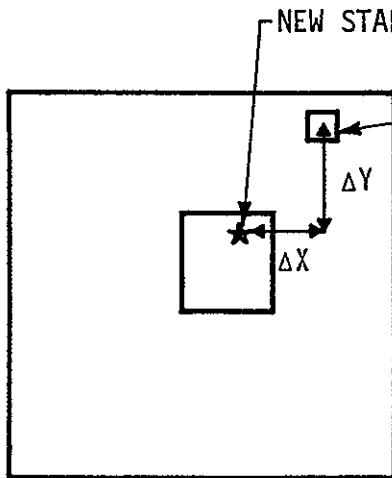


Y_b

Y_a

NOTE:

ΔX AND ΔY - STAR 2 POSITION WITH RESPECT TO STAR 1



NEW STAR 1 POSITION

3 BY 3 ELEMENT SEARCH AREA
(CENTERED ON DEDUCED NEW
STAR 2 POSITION FOR NO
ROTATION BETWEEN SAMPLES)

NOTE:

POSITION OF STAR 2 WITHIN 3 BY 3
AREA DETERMINES ACTUAL ROTATION

FIGURE 5-10. ESTIMATE OF ROTATION

data obtained. Star image displacements (in units of picture elements) are then converted into attitude error angles, taking into account star position within the field. Table 5-17 lists the operations required to derive attitude angles from the television system output. The stars that are nearest and farthest from the optical axis are best found by minimizing and maximizing the function

$$|X| + |Y|$$

rather than

$$X^2 + Y^2$$

since addition is much more rapidly carried out than multiplication. This reduces the first nine steps of Table 5-17 to less than 70 additions and subtractions. It may be possible to complete even the last step with additions and subtractions only, making total computing time very short for the basic procedure outlined.

TABLE 5-17. STAR FIELD ANALYSIS ALGORITHM

1. IDENTIFY STAR NEAREST OPTICAL AXIS IN Nth STAR FIELD SAMPLE
2. DEFINE 35 BY 35 ELEMENT SEARCH AREA CENTERED ON THIS POINT
3. FIND STAR IN THIS AREA IN (N + 1)th SAMPLE
4. CHECK MAGNITUDE TO CONFIRM STAR IDENTIFICATION
5. IDENTIFY STAR FARTHEST FROM OPTICAL AXIS IN Nth SAMPLE
6. DEFINE 3 BY 3 ELEMENT SEARCH AREA CENTERED ON THIS POINT
7. FIND STAR IN THIS AREA IN (N + 1)th SAMPLE
8. CHECK MAGNITUDE TO CONFIRM STAR IDENTIFICATION
9. USE MEASURED DISPLACEMENT OF THE TWO STARS TO CALCULATE STAR FIELD ROTATION AND TRANSLATION
10. OUTPUT ROTATION AND TRANSLATION SCALED TO EQUAL ATTITUDE ANGLE CHANGES.

This analysis of the star search problem is, of course, an elementary one, ignoring as it does such complications as noise, star entry and departure from the field of view, and the effects of double stars. An example of improvement would be a step which recorded rates of motion averaged over several previous samples and which ignored individual samples indicative of abnormal rates or accelerations. The algorithm is readily elaborated to include such cases. The spacecraft attitude control computer is currently expected to have a basic operation time of about 3 microseconds and a multiply/divide time of 60 microseconds. Such a machine would require less than 1 millisecond to apply a basic search algorithm of the kind proposed. In fact, the 1-second period between star field samples would allow application of a far more sophisticated procedure, if desired.

To be really useful, the system should also be able to handle slewing to new targets and new star fields. Slewing is controlled by gyros, which can point the spacecraft in the new direction to within about 0.1 degree; the television aspect system must correct this small remaining error and lock onto the new star field.

This can be done using the procedure outlined above, but there are two differences. One is that no previous star field sample is available. Instead, the system must use a star field description telemetered from the ground. This would consist of the usual 15 words of data describing the output of the television system for the case when the spacecraft is perfectly pointed. The other difference is that the 0.1-degree error corresponds to 37 picture elements; the area which must be searched contains

$$(2 \times 37 + 1)^2 = 5,625 \text{ elements.}$$

The search begins with the star which is nearest the center of the field in the 'previous' (telemetered) star field sample. The probability that no other star now lies within this area is given by the equation quoted earlier as 0.979. This means that in about one case out of fifty, or once a week on the average, the system would run the risk of identifying the wrong star. The error would become evident when the magnitudes of the five stars were compared with their telemetered values. One possibility at this stage would be an appeal for assistance from the ground. Human examination of the field telemetered by the television system would very quickly correct the error in star identification. It would, of course, be more convenient if the system could deal with the problem automatically. Various procedures for this can be devised; they could include carrying out a search process for all five stars. It would not be difficult to devise several possible processes for reliable identification, none of which would require more than a second of computing time. When the process was complete, star magnitudes would be checked for agreement with telemetered values. Agreement on all five magnitudes would provide good insurance against acceptance of an incorrect star identification.

Like the star tracker, the television aspect system requires an additional reference during occultation. As before, a pair of gyros is suggested for use during initial spacecraft despin and solar acquisition. If a degree of redundancy is to be provided, the use of a second television system may be considered. Since pointing does not require 10 arc-second accuracy and, since an even lower accuracy may be acceptable in the unlikely event of television system failure, the secondary television system may have a much smaller optical system. If basic resolution cell size is increased from 10 to 100 arc-seconds, with the aim of achieving a pointing precision not much worse than the desired 1 arc-minute, the focal length of the optical system can be reduced by a factor of 10 with a great reduction in weight. A weight of 50 pounds

is estimated for a secondary system of this kind. Table 5-18 lists the characteristics of the complete television aspect sensing system, which includes the usual solar sensors for initial solar acquisition, but excludes a redundant television aspect system.

TABLE 5-18. ATTITUDE SENSING WITH TELEVISION ASPECT SYSTEM

<u>Item</u>	<u>Weight (lb)</u>	<u>Average Power (W)</u>	<u>Power When Operating (W)</u>
Three reference gyros	3	30	30
Coarse Sun sensors and mounting	8	-	1
Fine Sun sensor	2	-	1
Electronics (gyros and Sun sensors)	4	5	5
Mounting hardware and local wiring	<u>5</u>	<u>-</u>	<u>-</u>
TOTAL	<u>22</u>	<u>35</u>	-

The merits of this attitude sensing system are its low weight and power consumption. The use of a given basic unit for two purposes, i. e., aspect sensing and attitude control, may be considered advantageous from the viewpoint of total development cost, or disadvantageous from the viewpoint of development risk. Only one basic instrument is required, but development difficulties affect two systems. An important factor is the extent to which the television system can be based on perfected or proven equipment.

The above discussion indicates that the television aspect system is a suitable source of fine attitude data as far as field of view, accuracy,

and data processing time are concerned. The real limitation of this attitude sensing scheme is its dependence upon a component (the television camera) which only one of the candidate experiment packages can provide. If another experiment package is selected, the weight of the television camera must be assigned to the weight budget of the attitude sensing system.

COMPARISON OF ALTERNATIVE SYSTEMS

This section summarizes the characteristics of the three attitude sensing systems described in previous sections.

Star Tracker System

This system is based on a tracker of single reference star which produces two-axis information; the initial pointing direction must be determined with help from the ground, but after that point gyro control is sufficiently accurate to slew to new positions and to pick up the appropriate reference star each time. The system has the appeal of appearing closest to the present state of the art.

Star Mapper System

This system uses special-purpose sensors to generate star field data and a special-purpose computer to generate three-axis information. In effect, it is the television aspect system described herein except that it uses special-purpose components. To a limited degree, its components have been proven. The star mapper system can operate entirely without ground control, since it contains sufficient stored data to identify any star field.

Television Aspect System

With a television camera included in the spacecraft experiment package, this system, as in the case of the star tracker system, requires initialization from the ground but can then operate automatically. The star field is analyzed to generate three-axis information, using a program in the spacecraft attitude control computer. This system makes efficient use of components assumed to be already available on board and, as such, it may be considered to represent low development risk.

Table 5-19 shows that weight and power differences between systems are only a small fraction of spacecraft weight. Therefore, the choice should be based on the probability that a given system can be successfully developed and reliably operated in space. The star tracker system will be tentatively selected for the baseline system, because of its closeness to the present state of the art. Technical developments in the other types of trackers (star mapper and star field sensor) should be monitored closely, however. As progress is made in these areas, one of the other attitude sensing systems may appear more attractive.

TABLE 5-19. COMPARISON OF ATTITUDE SENSING SYSTEMS

	<u>Weight (lb)</u>	<u>Power (W)</u>
Star tracker system	110	85
Star mapper system	34	50
Television aspect system	22	35

Comparison With HEAO-A Equipment

The HEAO-A spacecraft is externally similar to the HEAO-C, but the requirements of its experiments are entirely different. The HEAO-A attitude sensing and control system does have a pointing mode, but its principal mode of operation, the scan mode, involves continuous rotation about its z-axis, which is either aligned with or at some fixed angle to the solar vector. The rotation rate is in the region of 0.5 deg/sec.

The basic attitude sensing system proposed for the HEAO-A spacecraft (Ref. 5-12) includes the reference gyros, coarse and fine Sun sensors, and the star tracker found in HEAO-C. It also carries two other instruments, a specialized digital Sun sensor capable of measuring the angle of the z-axis from the Sun, and a star field mapper of the Control Data Corporation type. In both scan and pointing modes, the star tracker and the Sun sensors together provide three-axis attitude data accurate to about 1 degree; this is sufficient for attitude control requirements. The star mapper has no rotating reticle, and therefore operates only during spacecraft rotation. In the scan mode, the mapper provides pulses which can be analyzed on the ground for after-the-fact determination of attitude to 0.1 degree or better.

Table 5-20 shows that this represents a more elaborate complement of instruments than HEAO-C. In making any comparison of the selected attitude sensing systems, it should be borne in mind that a large amount of work, including collection of a great deal of information on star sensors and fairly detailed simulations, followed the HEAO-A and preceded the HEAO-C studies. Therefore, it may be appropriate to inquire how the system suggested for HEAO-C might be modified for HEAO-C use.

TABLE 5-20. COMPARISON OF HEAO-A AND HEAO-C
ATTITUDE SENSING EQUIPMENT

<u>HEAO-A</u>	<u>HEAO-C (Baseline)</u>	<u>HEAO-C Alternate, Adaptable to HEAO-A Needs</u>
Reference gyros	Reference gyros	Reference gyros
Coarse Sun sensors	Coarse Sun sensors	Coarse Sun sensors
Fine Sun sensor	Fine Sun sensors	Fine Sun sensors
Star tracker	Star trackers (2)	Star mapper
Digital (large-angle) Sun sensor		Computer (CDC 469)
Star mapper		

One piece of information obtained during HEAO-C work was knowledge of the existence of a Control Data Corporation program involving a star mapper and CDC 469 onboard computer, being developed for a system in which a spacecraft rotation rate of less than 1 revolution per hour provides all necessary scanning for on-board, real-time attitude determination. This system is expected to be flight-qualified in time for the HEAO-C mission. The star mapper is one of the three types of star sensors described as feasible for the HEAO-C mission. Without a motor-driven reticle, the star mapper/CDC 469 combination is ideally suited to determination and control of the spacecraft axis of rotation in the HEAO-A mission. In this primary mode of operation, the spacecraft does not depend upon any moving parts for attitude sensing. In the pointing mode, the spacecraft does require operation of the reticle motor, however.

In conclusion, the HEAO-C baseline system (using two single-star trackers) is not well suited for HEAO-A use; but a HEAO-C

system using the star mapper would be well adapted to HEAO-A requirements. The pointing direction of the mapper would be nominally 180 degrees away from the Sun, and the three reference gyros would provide attitude data during occultation. The coarse and fine Sun sensors would be best retained for initial orientation and later backup use.

Thus Table 5-20 includes a second HEAO-C system applicable to HEAO-A requirements.

Since HEAO-B has identical attitude sensing requirements to HEAO-A, the above discussion applies to HEAO-B also.

Comparison with HEAO-D Requirements

The scientific payload of the HEAO-D spacecraft generates disturbing torques which make precise three-axis control impracticable. At present there are two possibilities for HEAO-D attitude sensing requirements: either there is provision for later on-the-ground attitude determination only, or there is this plus sufficient attitude control to keep the solar panels oriented more or less toward the Sun.

In the first case, the star mapper alone is sufficient as a primary source of attitude data, since angular motion of the uncontrolled spacecraft provides the necessary scanning action. No reticle drive motor is required. One mapper plus three reference gyros provide attitude data at all times. If attitude control is required to meet solar power constraints, coarse and fine Sun sensors would provide angle data while the reference gyros would generate the rate signals needed for stabilizing the control loop. Table 5-21 compares the systems involved.

TABLE 5-21. COMPARISON OF HEAO-C AND HEAO-D
ATTITUDE SENSING EQUIPMENT

<u>HEAO-C Alternate</u>	<u>HEAO-D (No Attitude Control)</u>	<u>HEAO-D (Partial Attitude Control)</u>
Reference gyros	Reference gyros	Reference gyros
Coarse Sun sensors		Coarse Sun sensors
Fine Sun sensors		Fine Sun sensors
Star mapper	Star mapper	Star mapper
Computer (CDC 469)		

6. ATTITUDE CONTROL SYSTEM

This system has the function of maintaining the desired spacecraft attitude or orientation in the presence of disturbing torques. It must rotate the spacecraft to the desired attitude and apply the appropriate torques to maintain direction. It has to operate in four modes:

- Despin mode - The system eliminates residual angular motion following separation of the spacecraft from its launch vehicle. This is done using reference gyros to detect angular rates and gas jets to eliminate the rates. The spacecraft ends this mode with no net angular momentum. In all other modes control torques are provided by internal momentum exchange devices (control moment gyros) rather than by the gas jets.
- Acquisition mode - The spacecraft is first rotated so that its solar panels face the Sun and begin generating electricity. It then rotates about the sun line at a predetermined rate. The Sun direction is detected by coarse and fine solar sensors distributed over the body of the spacecraft. A star tracker looking about 90 degrees away from the Sun generates an output indicating star transits; star identification makes possible the establishment of a three-axis system.
- Slew mode - The spacecraft is slewed or rotated to point in a desired direction with respect to the stars.
- Pointing mode - The spacecraft holds this direction until commanded or programmed to slew to a new target.

The attitude control requirements for the HEAO-C spacecraft consist of attitude pointing accuracy, an attitude rate of change limitation while pointing at a target, and a large angle change, or slewing, capability. These requirements are

- The attitude control system shall have the capability of orienting the telescope lines of sight (spacecraft x-axis) to within ± 1 arc minute of the desired direction and maintaining this orientation during the viewing period. This is the pointing mode of spacecraft operation.
- In the pointing mode, the telescope lines of sight shall be confined within an error circle of less than 1 arc second in diameter during 1 second of time.
- In the pointing mode the spacecraft angular error about the telescope lines of sight shall be controlled to ± 5 arc minutes.
- The attitude control system shall have the capability of rolling the spacecraft about its z axis through 100 degrees during a period of one-third of an orbit (32 minutes).
- The attitude control system shall have the capability of turning the spacecraft through 360 degrees about the optical line of sight (spacecraft x axis) during the dark portion of any orbit. The dark period of the orbit varies from 21 minutes to 36 minutes for a 300-nautical-mile circular orbit inclined 35 degrees to the equator.

Figure 6-1 shows the orientation of the spacecraft principal body axes and the location of the center of mass. The principal mass moments of inertia of the spacecraft are

- About the x axis

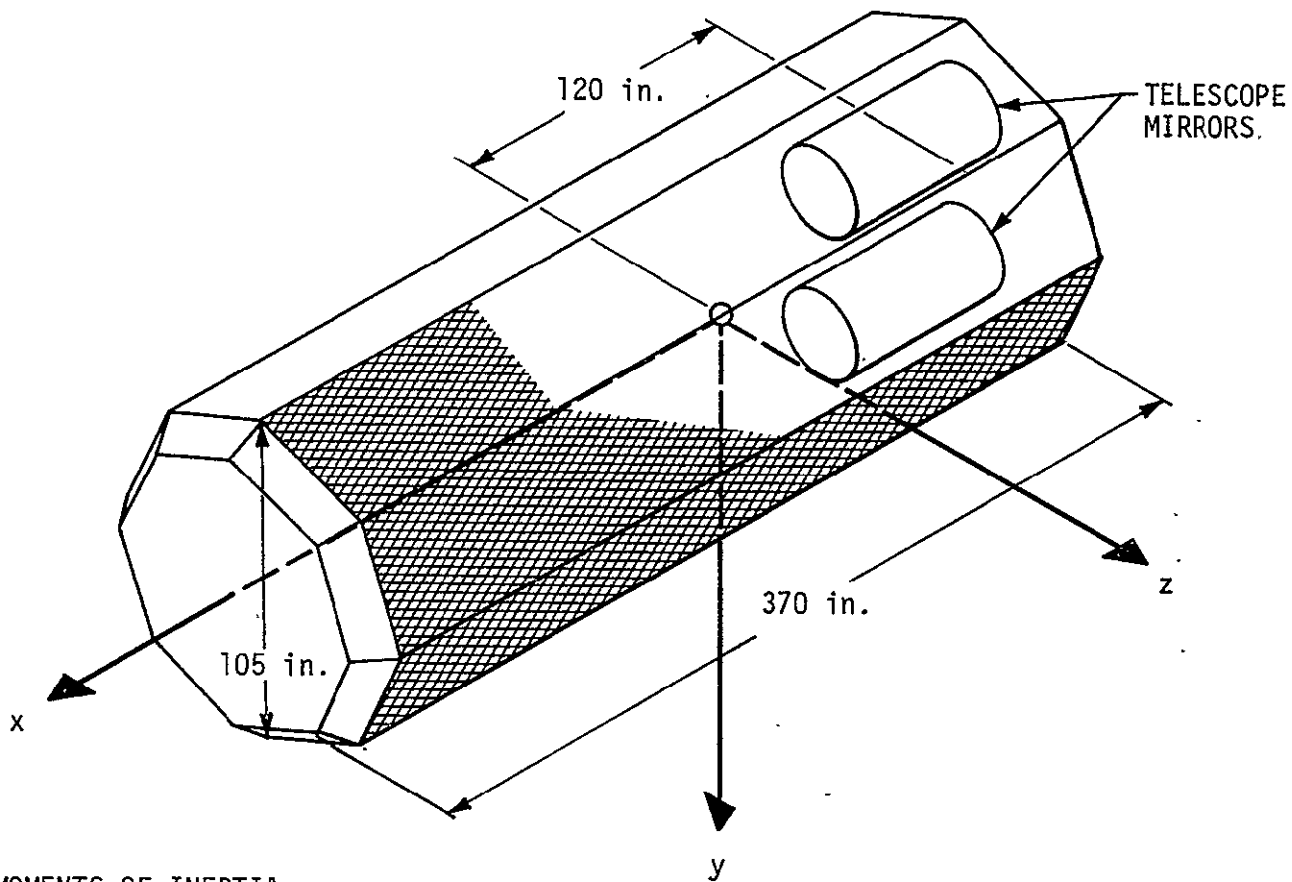
$$I_x = 4,600 \text{ slug-ft}^2$$

- About the y axis

$$I_y = 46,800 \text{ slug-ft}^2$$

- About the z axis

$$I_z = 47,300 \text{ slug-ft}^2.$$



MOMENTS OF INERTIA

$$I_x = 4,600 \text{ slug-ft}^2$$

$$I_y = 46,800 \text{ slug-ft}^2$$

$$I_z = 47,300 \text{ slug-ft}^2$$

FIGURE 6-1. HEAO-C SPACECRAFT PRINCIPAL AXES SYSTEM AND LOCATION OF CENTER OF MASS

DISTURBANCE TORQUES

Both external and internal disturbing torques will be acting on the orbiting HEAO-C spacecraft. A knowledge of the magnitudes and variations of these torques is required for the proper sizing of the attitude control system. The following disturbing torques have been identified for a spacecraft in a 300-nautical-mile Earth orbit.

- External
 - ▲ Gravity gradient
 - ▲ Aerodynamic
 - ▲ Magnetic
 - ▲ Solar radiation
- Internal
 - ▲ Movement of experiment detectors.

The largest disturbing torque acting on the spacecraft is the gravity gradient torque. This torque results from the fact that the mass moments of inertia of the spacecraft are not equal for all three principal axes. Gravity gradient tends to align the axis of minimum moment of inertia with the local vertical. The magnitudes of the maximum gravity torques are expected to be (Appendix A)

- $T_{xg} \text{ max} = \pm 0.001 \text{ ft-lbf}$
- $T_{yg} \text{ max} = \pm 0.077 \text{ ft-lbf}$
- $T_{zg} \text{ max} = \pm 0.076 \text{ ft-lbf}$.

Aerodynamic disturbing torque results from the fact that the center of pressure of the spacecraft surface and the spacecraft center of mass are not always aligned along the velocity vector. The maximum expected aerodynamic torque is expected to be (Appendix A)

$$T_a = 4.82 \times 10^{-4} \text{ ft-lbf}$$

or, about two orders of magnitude smaller than the maximum gravity gradient torque.

A magnetic disturbing torque will also be acting on the HEAO-C spacecraft. This torque results from the interaction of the natural magnetic moment of the spacecraft with the geomagnetic field. The magnetic torque acting on a magnetically clean spacecraft will be very small in comparison with the gravity gradient torque. However, the use of magnetic torquers, which is anticipated for the HEAO-C spacecraft, will induce fields on the spacecraft and magnetize ferrous objects including the optical bench if Invar is used for the bench material. This effect may be significant and the resulting disturbance torque cannot be estimated without a detailed analysis which is beyond the scope of the present study.

A solar radiation disturbance torque results from the fact that the centroid of the spacecraft area projected normal to the solar vector does not always lie on the solar vector from the spacecraft center of mass. The maximum expected solar radiation torque is (Appendix A)

$$T_s = 1.9 \times 10^{-4} \text{ ft-lbf}$$

which is the same order of magnitude as the maximum expected aerodynamic torque and three orders of magnitude smaller than the maximum expected gravity gradient torque.

Internal disturbance torques will be created when the experiment detectors are rotated or moved at the telescope focal planes. The magnitude of a typical disturbing torque is expected to be (Appendix A)

$$T_I = \pm 0.004 \text{ ft-lbf}$$

or about 5 percent of the maximum expected gravity gradient torque.

The analysis of disturbing torques indicates that, with the exception of the magnetic torque which has not been analyzed, gravity gradient is the only significant disturbing torque expected on the HEAO-C spacecraft. The magnitudes of maximum expected torques and momentums accumulated per orbit from these torques are listed in Table 6-1. These torques are discussed in more detail in Appendix A.

TABLE 6-1. MAXIMUM EXPECTED DISTURBANCE TORQUES AND MOMENTUMS ACCUMULATED PER ORBIT

Source	Torque (ft-lbf)			Momentum (ft-lbf-sec)		
	x Axis	y Axis	z Axis	x Axis	y Axis	z Axis
Gravity gradient (secular + cyclic)	0.001	0.077	0.076	3	220	220
Aerodynamic	0.000	0.000	0.000	-	-	-
Solar radiation	0.000	0.000	0.000	-	-	-
Internal component motion	<u>0.000</u>	<u>0.000</u>	<u>0.000</u>	<u>-</u>	<u>-</u>	<u>-</u>
TOTALS	0.001	0.077	0.076	3	220	220

SURVEY OF ATTITUDE CONTROL SYSTEMS

Attitude control systems can be broadly classified into two types. These are

- Passive attitude control systems
- Active attitude control systems.

In the passive attitude control system use is made of environmental forces to control the spacecraft attitude. Examples of these forces are gravitational force, aerodynamic pressure, and solar radiation pressure. In each of these cases the spacecraft is designed to be

inherently stable. Passive systems have limitations that allow only one axis to be aligned to a reference coordinate system and that allow the system no slewing capability. The attitude control requirements for the HEAO-C mission preclude the use of a passive attitude control system.

An active attitude control system requires a continual source of energy within the spacecraft as well as continual knowledge of the actual and desired orientations. Active attitude control systems typically used are reaction jets, flywheels, or control moment gyros. An active control system will be required if any of the following requirements are to be met:

- Stability about all axes in all regions of space
- Capability of changing attitude on command
- High accuracy of orientation.

The basic difference between active and passive systems is that any passive system has some known stable orientation whereas an active system must be provided knowledge of the actual and desired orientations. This information may be supplied by attitude sensing devices such as Sun sensors, star sensors, etc. Reaction jets systems have been used for attitude control on a number of spacecraft. The propellant used can range from compressed gas to liquid rocket fuel to ion or plasma sources, depending upon the mission. For short flight-time missions the propellant weight is tolerable, but for very long duration missions the propellant weight usually is excessive if fine pointing and continuous control is desired.

A reaction-wheel system or a control moment gyro (CMG) system should be a satisfactory method of providing attitude control on long duration missions. Such a system operates by means of angular momentum transfer from flywheels or CMGs to the spacecraft or vice versa. The advantages of using a reaction wheel or CMG system are:

- Efficient control of cyclic disturbances
- Ease in management and operation of desaturating devices for continuous disturbances.

Any steady torque over a long period of time or any large impulse will saturate this system, however, and some sort of desaturating procedure is necessary. This procedure must use reaction jets or some other form of actuator that either expells mass or reacts with something outside the spacecraft. Magnetic torquers may be used for momentum desaturation. A magnetic torquer is a device located on the spacecraft that produces a magnetic moment. This moment reacts with the Earth's magnetic field to produce a torque on the spacecraft. In order to produce a torque in the desired direction, a knowledge of the direction of the geomagnetic field vector is required. This information is provided by a three-axis magnetometer.

The advantages of magnetic torquers over reaction jets are:

- Magnetic torquers have higher reliability because they have no moving components.
- The weight of the magnetic torquers is less than the weight of a reaction jet system for a long duration mission.
- There is no risk of contamination of optical surfaces onboard the spacecraft by jet exhaust.

The disadvantages of magnetic torquers over reaction jets are:

- The Earth's magnetic field is not uniform around the Earth and is strongly influenced by solar flares and radiations. This introduces some uncertainty in the ability to produce the desired control torques at all times.
- The strength of the Earth's magnetic field decreases as the orbit altitude increases and hence the magnitude of control torque is lower at higher altitudes.

- The magnetic field produced by the torquers will magnetize ferrous objects on the spacecraft. Sensitive equipment will have to be located at some distance from the torquers. The reaction force produced by the magnetized objects will tend to oppose the torque produced by the torquers.

The problem of contamination of optical surfaces by reaction jets exhaust may be eliminated by using cold nitrogen gas for the propellant; however, a large amount of propellant would be required for the 2-year HEAO-C mission. Thus in spite of certain drawbacks of magnetic torquers they appear to be better suited than reaction jets for the HEAO-C mission.

From the preceding survey of different control systems it appears that a combination of momentum storing devices (reaction wheels or CMGs) and magnetic torquers are the best choice for the HEAO-C mission.

MOMENTUM STORAGE DEVICES

Two types of momentum storage devices were considered for the HEAO-C spacecraft; namely reaction wheels and CMGs. A reaction wheel device includes a rotor having a high mass moment of inertia that can be accelerated (or decelerated) by an electric motor. The torque accelerating the rotor causes a change in the magnitude of the rotor angular momentum and an equal but opposite change in the angular momentum of the spacecraft in which the rotor is mounted. A CMG, on the other hand, is a gimballed wheel rotating at a constant speed. This wheel provides an angular momentum of constant magnitude which can be oriented at various angles relative to the spacecraft in which it is mounted. A torque is imparted to the spacecraft by changing the direction of the gyro momentum vector. The relative advantages and disadvantages of the two devices are given below:

- Reaction Wheel Advantages

- ▲ Relatively simple - 1 degree of freedom about a single axis
- ▲ Minimum number of bearings results in low bearing friction and high reliability
- ▲ Requires a simple control law
- ▲ Highly accurate control can be achieved
- ▲ Continuous power requirement is moderate.

- Reaction Wheel Disadvantages

- ▲ Two levels of control are required -- one for accurate pointing and the other for slewing
- ▲ Peak power requirements are high.

- CMG Advantages

- ▲ Large maximum torques and a large range of torques can be provided
- ▲ Better bandwidth characteristics; i. e., more rapid response to small errors than a reaction wheel
- ▲ A more nearly linear approach to saturation than a reaction wheel, which becomes highly nonlinear as it approaches saturation.
- ▲ Higher drive motor efficiency. Since the CMG rotor speed is constant, its drive motor can be smaller and operate more efficiently, thereby minimizing weight and power requirements.

- CMG Disadvantages

- ▲ System operation is complex due to gyroscopic cross coupling effects and the required mechanical gimbaling

- ▲ More bearings are required than for a reaction wheel; therefore, bearing friction is greater and reliability is lower.
- ▲ The control laws which translate torque commands for each spacecraft axis into gimbal torque commands are complex.

System Capacity Requirements

The momentum storage system must have the capacity to provide control torques during the operation of the experiments in the spacecraft pointing mode and also to perform spacecraft slewing maneuvers. Table 6-1 lists the control torques required for the pointing mode and also the momentum capacity on each spacecraft axis if momentum were allowed to accumulate for an entire orbit. Simulation of spacecraft dynamics with periodic momentum dumping using magnetic torquers established that the total increase in momentum could be limited to slightly over 20 ft-lbf-sec; this accumulation could occur in any spacecraft axis. Therefore, a momentum storage capacity of 30 ft-lbf-sec per axis will be adequate for operation in the pointing mode. Slewing requirements increase the required capacity.

The spacecraft must be capable of slewing about the z-axis through an angle of 100 degrees in 32 minutes. This maneuver is performed by accelerating the spacecraft to some constant angular rate, permitting it to coast for a period, and then decelerating it to zero angular rate. The mathematical relationship for the angular momentum and torque required is given by:

$$H = \frac{Tt}{2} \left[\frac{(Tt)^2 - 4\theta I T}{2} \right]^{\frac{1}{2}} \quad (6-1)$$

where

- H - angular momentum accumulated at the end of the accelerating torque application, ft-lbf-sec
- T - torque applied to accelerate the spacecraft, ft-lbf
(Note: The torque is not necessarily applied during the entire maneuver period.)
- t - total maneuver time, sec
- θ - total angle of rotation of the spacecraft about the z-axis, radians
- I - Moment of inertia of the spacecraft about the z-axis, slug-ft².

Equation 6-1 applies to the case in which the magnitudes and durations of the accelerating and decelerating torques are equal. The relationship between the magnitude of applied torque and the momentum required for the HEAO-C spacecraft is shown in Figure 6-2. The values of the constants used in this plot were

- t = 1,800 seconds (2 minutes was allowed for damping of transients)
- $\theta = 1.75$ radians (100 degrees)
- I = 47,300 slug-ft².

It can be seen in Figure 6-2 that the angular momentum requirement decreases as the torque level increases. However, the decrease in angular momentum becomes very small as the torque level is increased above 1.0 ft-lbf. If a torque of 0.4 ft-lbf is applied for this maneuver, a momentum storage requirement of approximately 50 ft-lbf-sec will be required. This choice of requirements is well suited to the use of either reaction wheels or CMGs and is therefore selected for the z-axis slewing requirement.

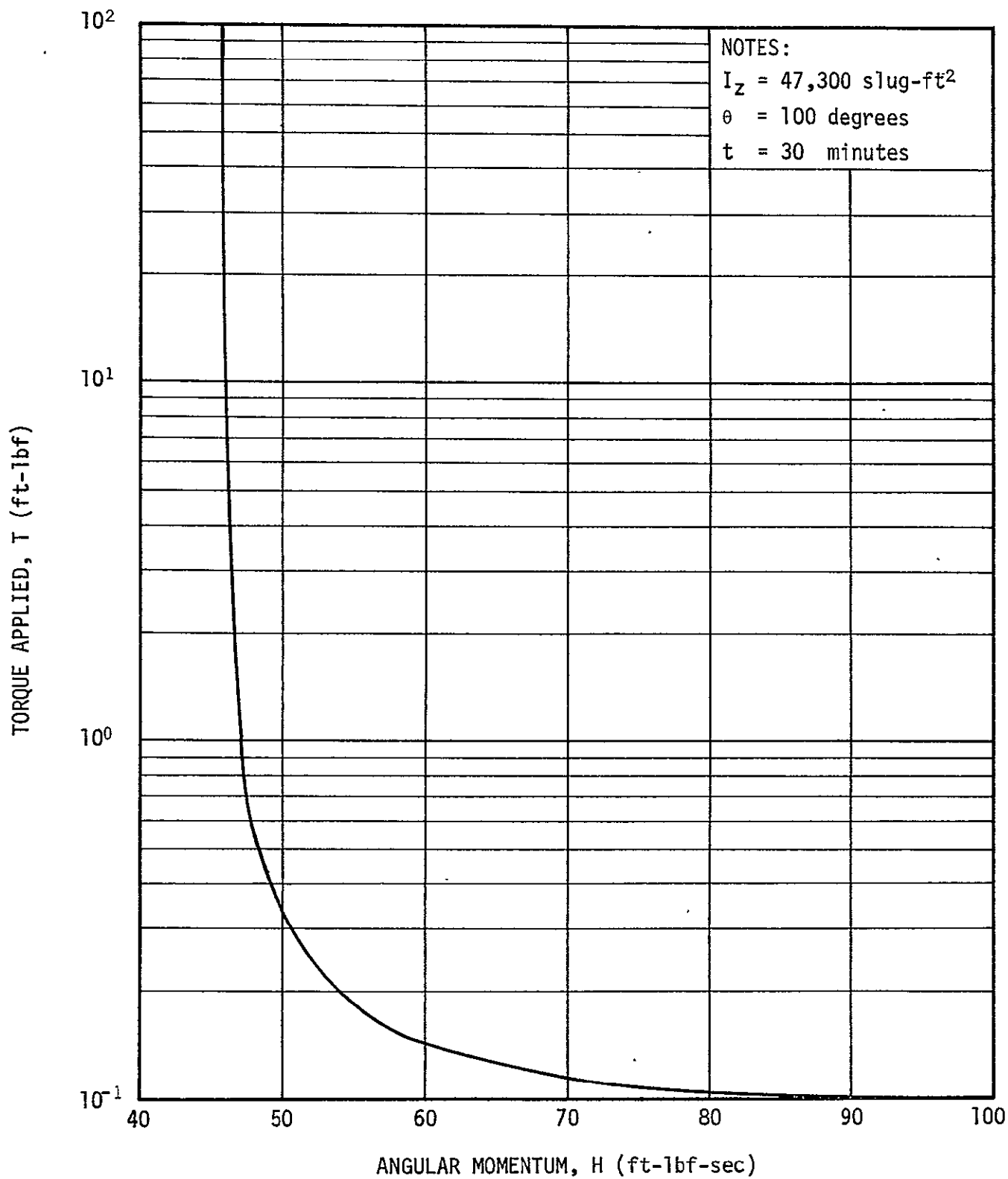


FIGURE 6-2. ANGULAR MOMENTUM REQUIRED FOR SLEWING THE SPACECRAFT ON z AXIS FOR DIFFERENT LEVELS OF APPLIED TORQUE

The imaging polarization experiment requires that the spacecraft be rotated through 360 degrees about the x axis. Because of electric power and possibly thermal control requirements, it is necessary that this maneuver be performed during the dark portion of the orbit. The maneuver might be performed as two 180-degree maneuvers or four 90-degree maneuvers. If two 180-degree maneuvers are performed, the maneuver time must not exceed 12 minutes to allow an experiment time of at least 9 minutes for the minimum duration nighttime period of 21 minutes. If four 90-degree maneuvers are to be performed, each must be completed in 3 minutes to allow three 3-minute observing periods during the minimum nighttime period.

The 90-degree maneuvers can be completed in 2.5 minutes, leaving 0.5 minute for transient damping, using a minimum torque of 1.3 ft-lbf. However, a relatively high momentum capacity of 98 ft-lbf-sec is required. A better choice is the use of a 2.0-ft-lbf torque, in which case a momentum capacity of only 60 ft-lbf-sec is required. The 180-degree maneuver can be made in 5 minutes, leaving 1 minute for transient damping, using a torque of 2.0 ft-lbf. The momentum requirement for this maneuver is 52 ft-lbf-sec. Therefore, a torque requirement of 2.0 ft-lbf and a momentum requirement of 60 ft-lbf-sec is established for the x-axis roll maneuver.

The torque and momentum requirements for overcoming disturbing torques in the pointing mode and for slewing the spacecraft are listed in Table 6-2. The y-axis torque and momentum requirements are less than those for the x- and z-axes because no slewing requirement has been specified for this axis. However, maneuver capability about this axis will be necessary in order to acquire sources. Maximum use of y-axis slew capability may be made when the spacecraft is reoriented to permit flare observations. Design momentum requirements for the x- and z-axes were increased from 90 and 80 to

TABLE 6-2. TORQUE AND MOMENTUM CAPABILITY REQUIREMENT FOR MOMENTUM STORAGE DEVICES

	Torque (ft-lbf)			Momentum (ft-lbf-sec)		
	x Axis	y Axis	z Axis	x Axis	y Axis	z Axis
Disturbing Torques	0.001	0.077	0.076	30	30	30
Slewing	2.0	0.0	0.4	60	0	50
Total Requirements	2.001	0.077	0.476	90	30	80
Values used for Sizing Control System	2.0	0.5	0.5	100	100	100

100 ft-lbf-sec to give a design margin over expected requirements and the y-axis momentum requirement was chosen as the same for uniformity. Since the x-axis torque requirement was significantly above the z-axis requirement, separate design requirements of 2.0 and 0.5 ft-lbf were chosen. The y-axis torque requirement was chosen as 0.5 ft-lbf for uniformity with the z-axis requirement.

Reaction Wheel Sizing

The weight of a reaction wheel system for three axis control consists of the weights of three momentum packages (rotor, motor, and housing), wiring, control electronics, and miscellaneous hardware. The power required by the system is the motor power plus the power dissipated by the electronics.

The weight of a rotor and housing is dependent upon the amount of momentum capability required of the system, while the motor weight is a function of the stall torque. The sizing equation giving rotor weight as a function of momentum, wheel radius, and rotor speed is

$$W_r = \frac{4,820 H}{R \omega_r} + 0.2 R^{1.4} \text{ lbm} . \quad (6-2)$$

where

W_r - rotor weight, lbm

H - angular momentum of the reaction wheel, ft-lbf-sec

R - rotor radius, in.

ω_r - rotor speed, radians/sec.

The housing weight is given by

$$W_h = 0.027 R^{2.75} \text{ lbm} . \quad (6-3)$$

The maximum power required from the motor occurs at maximum stored momentum or wheel speed, ω_{\max} . This relationship is

$$P = \frac{T_{\max} \omega_{\max}}{\eta} \quad (6-4)$$

where

- P - electric power input (peak), watts
- T_{\max} - maximum control torque needed, ft-lbf-sec
- η - conversion efficiency from electrical input power to motor shaft power. A value of 0.75 has been assumed.

Substituting the rotor speed ω_{\max} from Equation 6-4 into Equation 6-2 and combining with Equation 6-3, the total rotor plus the housing W_T , becomes

$$\begin{aligned} W_T &= W_r + W_h \\ &= \frac{4,820 H T_{\max}}{R^2 P \eta} + 0.2 R^{1.4} + 0.027 R^{2.75} \quad . \quad (6-5) \end{aligned}$$

For a given H, T_{\max} , P, and η , this equation has a minimum W_T for a particular reaction wheel radius R_0 and represents the optimum reaction wheel size. An additional 20 percent weight is added to the weight obtained from Equation 6-5 to account for the spin motor and electronics to give the total single axis unit weight. The x-axis torque and momentum requirements are

$$T_x = 2.0 \text{ ft-lbf}$$

$$H_x = 100 \text{ ft-lbf-sec} \quad .$$

Figure 6-3 is a plot of the x-axis system weight as a function of rotor radius for several peak power levels. The maximum allowable peak power was chosen as 100 watts because a lower value would significantly increase system weight and a higher value would reduce system weight at a rapidly diminishing rate. The x-axis system weight is 135 lbm for a peak power of 100 watts.

The y- and z-axes torque and momentum requirements are

$$T_y = T_z = 0.5 \text{ ft-lbf}$$

$$H_y = H_z = 100 \text{ ft-lbf-sec}$$

Figure 6-4 is a plot of the system weight for either the y- or z-axis as a function of rotor radius for peak powers of 50 and 100 watts. For a peak power of 100 watts, system weight is 60 lbm for each axis.

Total system weight and peak power for all three axes is 255 lbm and 300 watts. The average power requirement is estimated on the basis of computer simulation of spacecraft dynamics with control moment gyros to be one-fifth of the maximum, or 60 watts.

Control Moment Gyro Sizing

The weight of a control moment gyro consists of the weights of rotor, gimbals, gimbal torquer, rotor spin motor, associated electronics, and miscellaneous hardware. The power required by the CMG and its associated electronics is for the

- Spin motor and drive electronics
- Gimbal actuator and drive
- Gimbal position and rotor speed sensing elements and interface circuits.

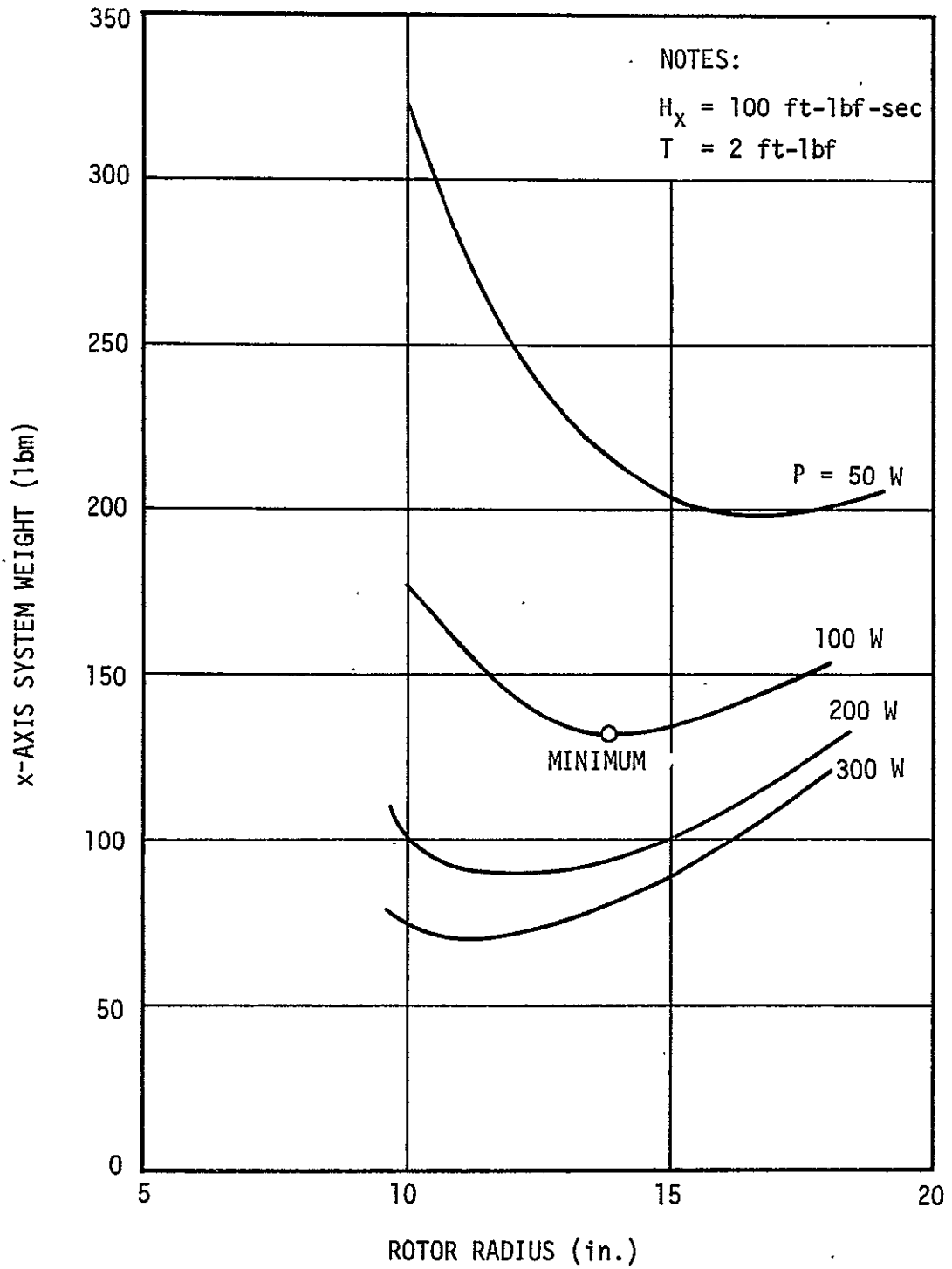


FIGURE 6-3. x-AXIS REACTION WHEEL WEIGHT AS A FUNCTION OF ROTOR RADIUS FOR VARIOUS PEAK POWER LEVELS

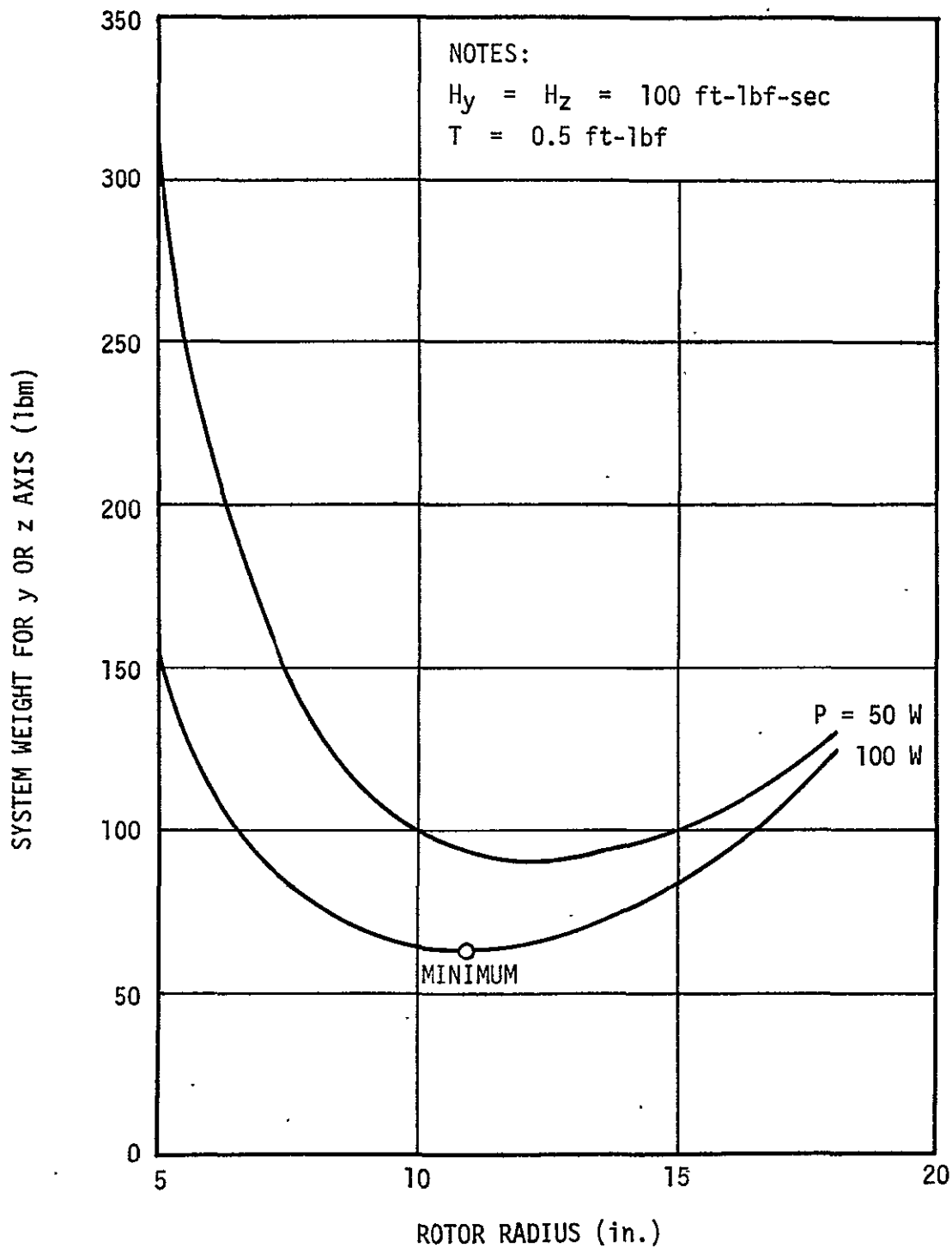


FIGURE 6-4. REACTION WHEEL WEIGHT AS A FUNCTION OF ROTOR RADIUS FOR EITHER THE y OR z AXIS

The power required is generally a constant level, determined mainly by the spin motor and electronics, plus peak levels of short duration that are required by the gimbal actuators when they are producing control torques. A survey of hardware produced by several manufacturers indicates that the peak power requirement is typically 4 to 8 times the average power requirement.

A large number of CMG configurations may be formulated from the two basic building blocks, the single gimbal and the double gimbal CMG, through the use of different combinations and orientations of the gyros. Each of the configurations has its own characteristics, momentum envelope and control laws for implementations. In this study four types of basic configurations were considered and compared for weight, power requirement, redundancy, and momentum utilization. These configurations are:

- Three single degree of freedom gyros (single gimballed)
- Three pairs of single degree of freedom gyros (also called twin gyros or scissored pairs)
- Three two degree of freedom gyros (double gimballed)
- Four single gimbal gyros (also called 4-FACS).

The system utilizing three scissored pairs of single degree of freedom gyros was chosen as the baseline configuration. Characteristics of other CMG configurations that were considered are given in the appendix. Although the three scissored pair configuration is heavier and requires more power than any of the other CMG systems considered, its other advantages are believed to more than offset these disadvantages:

- Negligible cross coupling between axes when operating in the pointing mode. This permits the application of the desired torques in all axes without the production of unwanted torques.

- The control law is very simple.
- The system is redundant and control could be maintained in the event of failure of one gyro on each axis.

A control moment gyro system of three scissored pairs of gyros was simulated in the computer simulation of the spacecraft dynamic response to disturbing torques and control torques.

Figure 6-5 shows the arrangement for three scissored pairs of gyros. This arrangement consists of six constant speed, single degree of freedom gyros which are used in pairs to provide three momentum vectors aligned with the three vehicle axes. The rotors of two gyros of a pair spin in opposite directions; they are driven to equal and opposite gimbal angles to produce a torque aligned along one vehicle axis.

In this arrangement cross-coupling is avoided during the pointing mode, when the spacecraft body rates are small, at the expense of requiring six gyros. When the spacecraft is slewed, however, the spacecraft body rates are large, and there is cross-coupling between axes. Another advantage of this arrangement over other CMG configurations is that it allows large gimbal angles so that a major portion of the momentum stored in the gyros is available for transfer to the vehicle. Gimbal angles greater than 60 degrees are possible but are undesirable since the gimbal rate required is a cosine function of the gimballed angle. Thus at a gimbal angle of 60 degrees the required gimbal rate for a constant output torque is twice the rate required when the gimbal angle is zero. This will result in a higher torquer power requirement and the application of a greater load on gimbal bearings. Other advantages of this arrangement, as stated previously, is its very simple control law and redundancy.

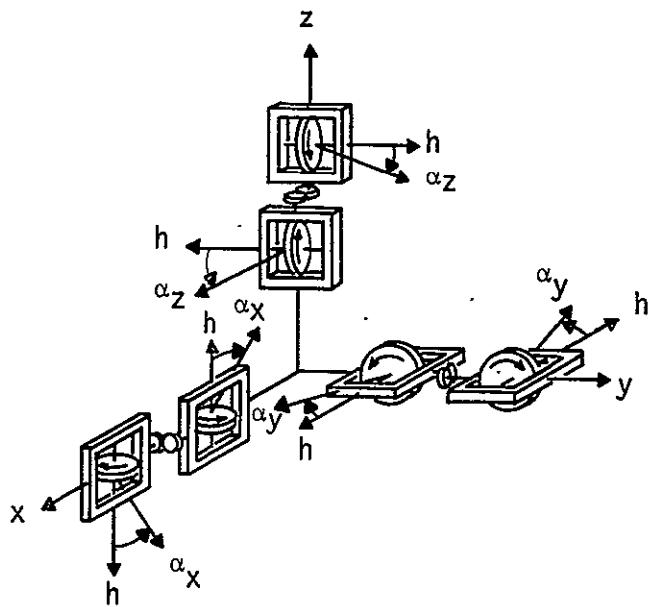


FIGURE 6-5. THREE PAIRS OF SINGLE DEGREE OF FREEDOM GYROS (SCISSORED PAIRS)

If all of the six gyros are assumed to have the same rotor angular momentum, then the momentum in each axis (Figure 6-5) can be expressed as

$$\begin{aligned} H_x &= 2h \sin \alpha_z \\ H_y &= 2h \sin \alpha_x \\ H_z &= 2h \sin \alpha_y \end{aligned} \quad (6-6)$$

The reaction torque exerted on the spacecraft by the gyro system can be obtained by differentiating the Equation 6-6

$$\begin{aligned} T_x &= \frac{-dH_x}{dt} = -2h \alpha_z \cos \alpha_z \\ T_y &= \frac{-dH_y}{dt} = -2h \alpha_x \cos \alpha_x \\ T_z &= \frac{-dH_z}{dt} = -2h \alpha_y \cos \alpha_y \end{aligned} \quad (6-7)$$

It is apparent from the above equations that the output torques are uncoupled.

For gyro gimbal angles limited to 60 degrees Equation 6-6 becomes

$$H_x = H_y = H_z \leq \sqrt{3} h \quad .$$

For a momentum storage requirement in each axis of 100 ft-lbf-sec.

$$h \geq \frac{100}{\sqrt{3}} = 58 \text{ ft-lbf-sec or } 60 \text{ ft-lbf-sec} \quad .$$

The weight and power required for a 60-ft-lbf-sec CMG is
(Refs. 6-1 and 6-2)

- Weight = 35 lbm
- Power = 10 watts average.

For a system of six gyros, the total system weight is 210 lbm. The average power requirement is 60 watts. The peak power requirement is estimated to be 220 watts, based on four units operating at peak power (50 watts each) and two units operating at average power.

Comparison of Wheels and CMG Configurations

A comparison of a reaction wheel momentum dumping system and the control moment gyro configurations that were considered is given in Table 6-3. The weight and power requirements for the reaction wheel system are greater than for any of the four CMG configurations considered, although only slightly greater than for the three scissored pair configuration. The reaction wheel system is attractive because of its simplicity and ease of operation; i. e., simple control law. The advantage of the three scissored pair CMG configuration over the reaction wheel system is its inherent redundancy plus the other advantages previously given. There is no redundancy in the reaction wheel system.

A comparison of the different CMGs configurations shows that the three two degree of freedom gyros (double gimballed) have the least weight and power requirements. The problem with double gimballed gyros is that they require a very complex control law. Without a special control law this configuration can have an inner gimbal lock at low momentum and also can result in hang up. Hang up is the condition in which the momentum vectors of all three gyros are aligned in the direction of a desired control torque. In this condition, the gyros cannot produce the desired torque. Because of these serious problems, the double gimballed configuration is not considered very attractive.

TABLE 6-3. COMPARISON OF REACTION WHEELS AND CMG CONFIGURATIONS FOR THREE AXIS CONTROL

Configuration	Angular Momentum Per Rotor (ft-lbf-sec)	Weight (lbm)	Power (W)		Momentum Utilization Percent of Total Momentum
			Average	Peak	
Three Reaction Wheels	100	255	60	300	33 each axis
Three Single Degree of Freedom Gyros (Single Gimballed)	70 (3 units)	120	36	150	67 each axis
Three pairs of Single Degree of Freedom Gyros (Scissored Pair)	60 (6 units)	210	60	220	33 each axis
Three Two Degree of Freedom Gyros (Double Gimballed)	40 (3 units)	120	30	140	100 all axes
Four Single Degree of Freedom Gyros (4 FACS)	100 (4 units)	180	52	208	25 in one axis 50 in two axes

The weight and power requirements for the three single degree of freedom gyros are about the same as those for the double gimballed gyros. The disadvantages of three single degree of freedom gyros are the presence of cross coupling between axes and they lack redundancy.

The four single degree of freedom gyros (4 FACS) configuration requires slightly less weight and power than the three scissored pair configuration. The disadvantage of four single degree of freedom gyros in the presence of cross coupling for gimbal angles other than 45 degrees.

After considering the advantages and disadvantages of each system and configuration, the three scissored pair CMG configuration was selected as a baseline momentum storage system. This comparison was not meant to be an analysis to determine the optimum configuration. It was intended only to identify a feasible system having no serious disadvantages. Further analysis and the inclusion of factors such as providing the required reliability not treated in depth in this study may make dictate the use of a different system.

Availability of Suitable Hardware

No space flight proven momentum storing devices in the capacity range of interest are presently available. The closest approximation appears to be the Model 100 control moment gyro developed and tested by Sperry's Phoenix Division. This gyro, which has an angular momentum capacity of 100 ft-lbf-sec, meets the momentum requirement for use in the four single degree of freedom gyro configuration, but is slightly oversized for the three scissored pair configuration. However, the weight, volume, and power requirements of these somewhat oversized units have been included in the HEAO-C spacecraft layout and weight and power summations. The salient features of Sperry Model 100 CMG are

- Angular momentum - 100 ft-lbf-sec
- Rotor speed - 7,850 rpm
- Maximum reaction torque - 50 ft-lbf
- Peak gimbal torque (direct drive) - 0.85 ft-lbf
- Maximum gimbal rate - 0.35 radian/sec
- Rotor diameter - 16 inches
- Envelope dimensions 25 by 20 by 18 inches
- Run up time - 2 hours
- Spin motor (induction type) power
 - ▲ Peak during run up - 60 watts
 - ▲ Steady operation - 13 watts
- Gimbal torquer power (permanent magnet, dc pancake, brush type)
 - ▲ Stall - 60 watts
 - ▲ Peak - 60 watts
 - ▲ Supply voltage - 28 Vdc
- Wear out life - greater than 2 years
- Reliability - 0.98 for 11,000 hours (excluding electronics)
- Weight
 - ▲ Total - 42.2 lbm
 - ▲ Gyro - 35 lbm
 - ▲ Electronics - 7.2 lbm.

It is proposed that the CMGs be spun up before launch, rather than in orbit. This saves electrical power and permits the CMGs to be used immediately for slewing the spacecraft toward the Sun. The CMG spinup power will never represent a load on the spacecraft power system, and the long spinup time will not affect spacecraft operations in

the critical period between arrival in orbit and alignment of the solar panels toward the Sun. Sperry representatives stated that the CMGs are quite capable of sustaining launch accelerations in the spinning condition.

DESATURATION OF MOMENTUM STORAGE DEVICES

Momentum storage devices require periodic dumping of momentum to prevent saturation. A torque source is required for momentum dumping; this torque may be provided by any convenient means such as reaction jets or reaction with the geomagnetic field. The required torque for the HEAO-C spacecraft will be provided by electromagnets, or magnetic torquers. Three torquers are used, one aligned with each spacecraft body axis. When the torquers are energized, they produce a magnetic moment that interacts with the geomagnetic field to produce a torque on the spacecraft.

The problems encountered in using the geomagnetic field are:

- The magnetic field is not uniform and varies in magnitude and direction as the spacecraft orbits the Earth.
- The torque generated is always normal to the geomagnetic field vector. Because of this inherent limitation on the direction of the generated torque, the component of the moment vector normal to the magnetic field vector can be desaturated, whereas the component along the magnetic field cannot be desaturated.

Magnetic Torquer Sizing

The long term effect of the secular component of gravity gradient torque acting on the spacecraft is the accumulation of angular momentum in the momentum storage device. The effect of other types of external and internal disturbance torques is cyclic, which result in no long-term momentum accumulation. Therefore magnetic torquers

are sized to produce a torque equal to the average gravity gradient torque and thereby to eliminate the angular momentum resulting from this disturbance.

The variation of secular gravity gradient torque is a sine squared waveform and therefore the average torque is half of the maximum torque. The maximum gravity torque is about 0.08 ft-lbf and therefore average gravity torque is 0.04 ft-lbf.

The magnetic moment generation capability of an electromagnet is

$$M = T/B_G \quad (6-8)$$

where

M - magnetic moment, ft-lbf/gauss

T - torque generated, ft-lbf

B_G - geomagnetic field strength, gauss .

The strength of Earth's magnetic field at an altitude of 300 nautical miles varies from a minimum of approximately 0.243 gauss at the geomagnetic equator to a maximum of approximately 0.485 gauss at the geomagnetic poles. The dipole model gives these same values for the poles and geomagnetic equator. Departures of the actual field from a dipole field are both regional and local. To take into account the effect due to these anomalies and other effects resulting from solar activity, a value of 0.20 gauss is used for the geomagnetic field for sizing the electromagnet. The required maximum torque magnetic moment from Equation 6-8 is

$$M = \frac{0.04}{0.20} = 0.20 \text{ ft-lbf/gauss } (2,700 \text{ amp-m}^2)$$

This magnetic moment is produced if the maximum current is supplied to the torquer. If a smaller current is supplied, the magnetic moment and resulting torque is lower.

The volume of the core for an electromagnet is given by

$$V = \frac{4\pi \times 10^{-3} \times M}{B_C} \quad (6-9)$$

where

V - volume of core, m³

M - magnetic moment generated by the electromagnet, amp-m²

B_C - flux in the core, gauss.

For a given maximum value of magnetic moment to be generated, the core volume is minimum when B_C is maximum; i. e., the saturation value of B_C for the core material. Thus a core material which has a very high saturation flux should be used to minimize the required core volume and hence core weight. The core material should retain minimum residual magnetism when the magnetizing force is removed; i. e., low coercive force, so that moments can be easily controlled.

The criteria for the selection of core material are

- Low density of the material
- High saturation flux
- Low coercive force.

Table 6-4 gives the physical and magnetic characteristics of three magnetic materials that are suitable on the above basis.

TABLE 6-4. PROPERTIES OF FERRO-MAGNETIC MATERIALS

Name	Alloy (%)	Density (gram/cm ³)	Coercive Force (oersted)	Saturation Value of B _c (gauss)
Permendur	50 Co 50 Fe	8.3	2.00	24,500
AEM 4750	48 Ni 52 Fe	8.2	0.07	16,000
M-50 Silicon-iron	0.40 Si 99.60 Fe	7.85	1.00	20,500

The power mass product for the windings of the electromagnet solenoid is given by

$$PW_{\text{sole}} = 4\pi H^2 \ell \sigma \rho V \quad (6-10)$$

where

- P - power, W
- W_{sole} - mass of solenoid, kg
- H - magnetizing force, amp/m
- ℓ - length of the electromagnet, m
- σ - resistivity of the winding wire, ohm-m
- ρ - density of winding wire, kg/m³
- V - volume of the core, m³

Aluminum wire is selected for the solenoid windings as the product of $\sigma \rho$ is minimum for aluminum wire.

In the electromagnet design the length-to-diameter ratio of the core is a dominating factor. The higher the ratio, the smaller is the end effect. For a very high ratio, the end effect approaches zero and the effective permeability of the core approaches the true permeability. In practice the length of the core is determined by the dimensions of the spacecraft for internally mounted electromagnets. For the HEAO-C spacecraft, an electromagnet 90 inches long can be accommodated inside the spacecraft along the minimum dimension axes.

Knowing the volume of the core needed from Equation 6-9, the diameter of the circular core section can be determined as

$$d = \frac{4}{(4V/\pi l)^{\frac{1}{2}}} \quad (6-11)$$

where

- d - diameter of core, m
- V - volume of core, m³
- l - length of core, m.

The total weight of the electromagnet (excluding insulation, mounting, etc.) is given by

$$W_T = W_{\text{core}} + W_{\text{sole}} \quad (6-12)$$

where

- W_T - total weight of the electromagnet, kg
- W_{core} - weight of core, kg
- W_{sole} - weight of solenoid, kg.

Equation 6-12 can be written as

$$W_T = V\rho_{\text{core}} + W_{\text{sole}} \quad (6-13)$$

where

V - volume of core, m^3

ρ_{core} - density of core, kg/m^3 .

Substituting the values of V and W_{sole} from Equation 6-9 and Equation 6-10 into Equation 6-13 gives

$$W_T = \frac{4\pi \times 10^{-3} M}{B_C} \rho_{\text{core}} + \frac{4\pi l \sigma \rho V H^2}{P} \quad (6-14)$$

Putting the value of V from Equation 6-9 into Equation 6-14 gives

$$\begin{aligned} W_T &= \frac{4\pi \times 10^{-3} M}{B_C} \rho_{\text{core}} + \frac{16\pi \times 10^{-3} l \sigma \rho M H^2}{B_C P} \\ &= K_1 \frac{M}{B_C} + \frac{K_2 M H^2}{B_C P} \end{aligned} \quad (6-15)$$

where

K_1 - a constant equal to $4\pi \times 10^{-3} \rho_{\text{core}}$

K_2 - a constant equal to $16\pi^2 \times 10^{-3} l \sigma \rho$,

For a given core material the flux density in the core B_C is dependent upon the magnetizing force H . This relationship can be expressed as

$$H = f(B_C) . \quad (6-16)$$

Equation 6-15 can now be expressed as .

$$W_T = K_1 \frac{M}{B_C} + \frac{K_2 M [f(B_C)]^2}{B_C P} \quad (6-17)$$

For an electromagnet the maximum value of M is a design requirement and is fixed. Similarly, the maximum power P available for the production of M is also limited. Thus in Equation 6-17 the only variable is B_C . The weight of the electromagnet for the production of M for the power available can be minimized from Equation 6-17.

The minimum weights of electromagnets using cores of materials listed in Table 6-4 have been calculated using Equation 6-17 and the hysteresis curves for these core materials. In these calculations the value of the maximum moment used was 2,700 amp-m² and maximum power available was limited to 10 watts. For these values the minimum weights of the electromagnets and the corresponding values of H and B_C are given in Table 6-5. The values of H and B_C listed in Table 6-5 were used in Equations 6-9 through 6-11 for calculations of weight and core diameters of torquers using the three different core materials. These values are given in Table 6-6.

In Table 6-6 it is shown that the minimum weight electromagnet has a permendur core. The disadvantage of using permendur as a core material is that it has a larger coercive force and a larger hysteresis loss than the other two materials. Hysteresis introduces some indetermination in the dipole moment, since the resultant dipole is not exactly related to the instantaneous applied field. However, this problem can be eliminated by placing a magnetic sensor near the middle point of the electromagnet and comparing its reading with that of a boom mounted three-axis magnetometer. The internal magnetometer senses

TABLE 6-5. MINIMUM WEIGHT OF ELECTROMAGNET FOR
THREE CORE MATERIALS

Material	Weight of the Electromagnet (lbm)	Magnetizing Force H (oerstead)	Flux Density B_c (gauss)
Permendur	31	17	20,000
AEM 4750	51	30	14,000
M-50 Silicon-iron	40	21	16,000

TABLE 6-6. COMPARISON OF CORE MATERIALS

	Permendur	AEM 4750	M-50 Silicon Iron
Weight of one electromagnet, lbm	31	51	40
Weight of core	29	44	37
Weight of solenoid for 10-watt power	2	7	3
Weight of three equal size Electromagnets, lbm	93	153	120
Maximum Power (for three-electromagnets), watts	30	30	30
Length of Electromagnet, in.	90	90	90
Diameter of core, in.	1.21	1.46	1.36

the magnetic field due to the electromagnet. The torquers are nulled by utilizing torquer current to adjust the internal field to conform within close tolerances to the field sensed by the external magnetometer. The torquer current is then switched off until desaturation is again required.

Availability of Suitable Hardware

Electromagnets will be designed to fit in the available space and produce the magnetic moments required for the HEAO-C mission. No attempt will be made to use available hardware for this application.

Magnetometers will be required onboard the spacecraft for sensing the magnitude and direction of the geomagnetic field. A three-axis magnetometer, will be mounted on a 20-foot boom away from the spacecraft to sense the essentially "undisturbed" geomagnetic field in the three spacecraft body axes.

The geomagnetic field inside the spacecraft is distorted due to the presence of the magnetic moments of the electromagnets and induced magnetic moments in the optical bench and in other ferrous objects. Information on this distorted field is the basis of proper operation of the magnetic torquers, because the magnetic moments of the electromagnets react against this distorted field.

Two electromagnets are located at the upper end of the spacecraft (Stations 363 and 366) and the third is located in the middle of the spacecraft (Station 146). Therefore, two types of magnetometers are needed to provide the required information of the magnetic field near the coils.

- A two-axis magnetometer located at the middle of the two electromagnets
- A single-axis magnetometer located at the middle of the single electromagnet.

When the electromagnets are off, some residual magnetism is left in the electromagnets and spacecraft components. For nulling this residual magnetism, the information obtained from the two magnetometers located near the electromagnets is used along with the information of the magnetometer located on the boom. Corrective actions for demagnetization are taken until the geomagnetic field sensed in all axes by the three magnetometers are within acceptable limits.

The magnetometers manufactured by Dalmo-Victor and used on the OAO spacecraft can be used on the HEAO-C spacecraft. This magnetometer measures the geomagnetic field along each of the vehicle axes and converts this to a dc voltage. This magnetometer weighs 6.5 lbm and requires a power of 1.76 watts. The performance characteristics of this Fluxgate magnetometer are

- Range - $\pm 6,000$ gamma (± 0.6 gauss)
- Sensitivity - 4.167×10^{-10} Vdc/gauss
- Dimensions - 100 gamma (1×10^{-3} gauss)
- Frequency response - 280 cycles.

Computer Simulation

In order to determine the feasibility of using magnetic torquers to provide momentum dumping torques, a computer program was written to simulate the desaturation of the momentum storage devices. The geomagnetic field was modeled as a dipole moment through the center of the Earth inclined at 11 degrees to the axis of rotation. The program calculates the geomagnetic field components in the spacecraft principal body axes as the spacecraft orbits the Earth. Since gravity gradient torque is the predominant disturbance acting on the spacecraft, this was the only disturbance that was included in the computer simulation.

The equations derived in Reference 6-2 for gravity torques are used for computing the magnitude and direction of these torques for each orbital position of the spacecraft. The angular momentum imparted

to the spacecraft by gravity torques is than computed and stored in the momentum storing device. The only characteristic of the storage device that is modeled is its ability to hold momentum, so it could be either a reaction wheel or CMG system. When the magnitude of stored angular momentum exceeds a predetermined value, the magnetic torquers are energized for momentum desaturation. For the present simulation this limit was arbitrarily selected as 30 ft-lbf-sec. Magnetic torques for desaturation are applied continuously until the stored momentum drops below an arbitrarily selected limit of 10 ft-lbf-sec. At this time the magnetic torquers are switched off until stored angular momentum again exceeds 30 ft-lbf-sec.

Each of the three equal size electromagnets used in the program is capable of producing a maximum magnetic moment of 0.2 ft-lbf/gauss (2,700 amp-m²) The control law used for the generation of magnetic moments for the efficient desaturation of stored momentum is given in the appendix.

Three cases of different spacecraft orientations were simulated. Each orientation will result in maximum gravity gradient momentum accumulation in one of the principal spacecraft axes. The complete simulation results are discussed in the appendix. The momentum storage history for all three cases is similar to the plot shown in Figure 6-6. Maximum momentum accumulation is less than 50 ft-lbf-sec for this case, but slightly exceeds 50 ft-lbf-sec in another case. This is an increase of about 20 ft-lbf-sec after the desaturation procedure was initiated at a level of 30 ft-lbf-sec. From these results, it was concluded that total momentum accumulation can be limited to less than 30 ft-lbf-sec by initiating the desaturation procedure at a level of less than 30 ft-lbf-sec. In this manner an additional accumulation of about 20 ft-lbf-sec would be permitted after beginning the desaturation procedure, as in the simulations, but the maximum total momentum

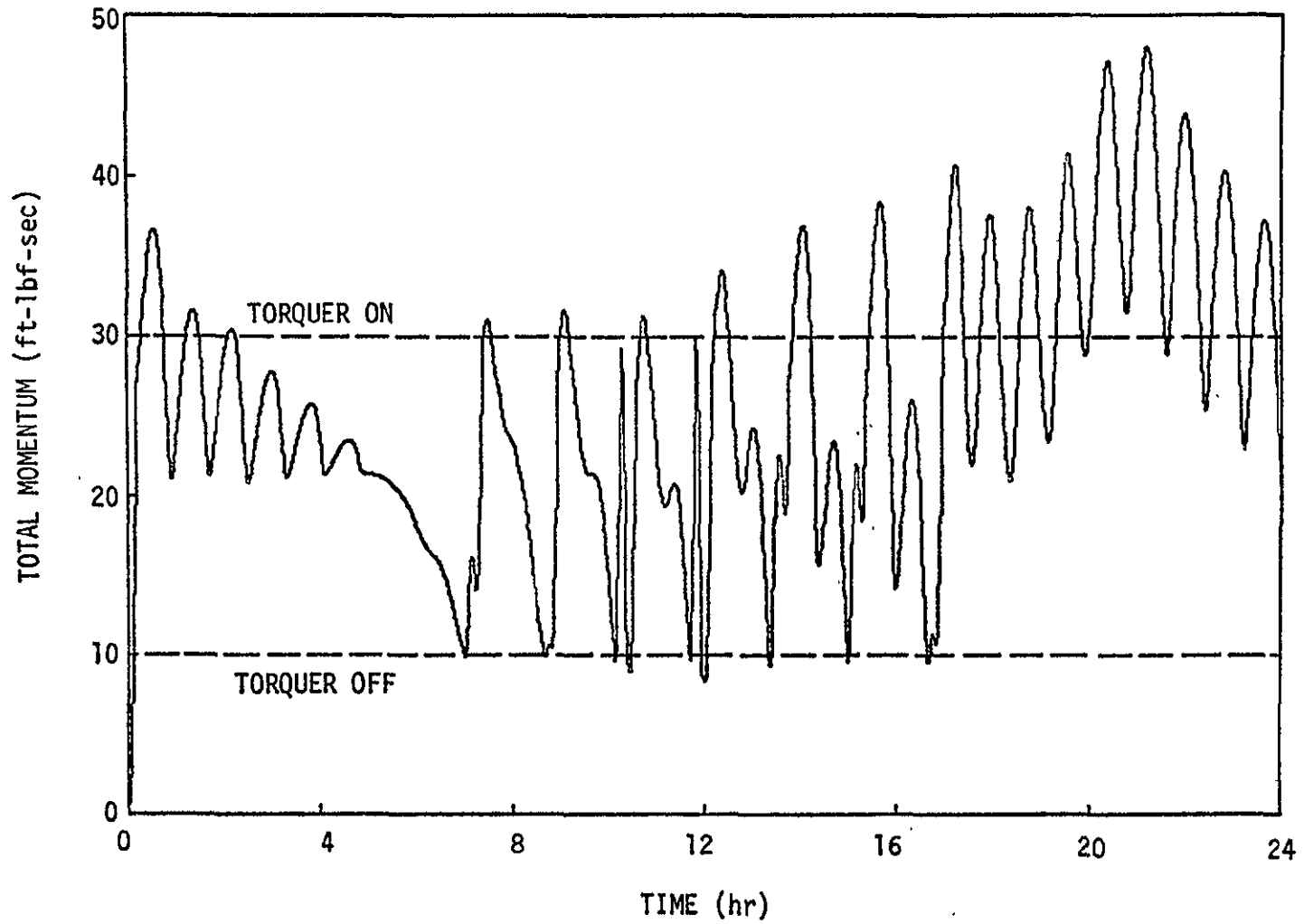


FIGURE 6-6. TOTAL MOMENTUM STORED IN THE MOMENTUM STORAGE DEVICE FOR CASE II

accumulation would be limited to 20 to 25 ft-lbf-sec. Since the accumulated momentum can occur on any spacecraft axis, depending upon orientation and orbit parameters, it is necessary to provide the maximum required capacity for each spacecraft axis.

Major conclusions from the simulation may be summarized as

- The total stored momentum can be maintained at a level of less than 30 ft-lbf-sec.
- The maximum level of stored momentum can occur along any of the spacecraft principal axes.
- The maximum magnetic moment capacity of each torquer, 0.2 ft-lbf/gauss (2,700 amp-m²) is adequate for momentum dumping.

SUMMARY OF SYSTEM OPERATION

In the HEAO-C attitude control system, control moment gyros provide control torques for fine pointing control and for large and small angle slewing. Magnetic torquers provide momentum dumping of the CMGs by creating torques on the spacecraft which cause the CMGs to react in a manner to decrease their stored momentum. A block diagram of the attitude control system is shown in Figure 6-7.

In the pointing mode the system operates essentially as two nearly independent control loops. Loop 1 consists of magnetic torquing coils and associated electronics, including connections to the central spacecraft computer. These coils can be energized to generate a magnetic moment in a desired direction which reacts against the geomagnetic field to apply a torque to the spacecraft. The operation of this loop has already been discussed and analyzed.

Loop 1 contains no means of sensing attitude error; this is a function of control loop 2. Loop 2 includes reference gyros which provide a source of attitude data and additional equipment for correcting

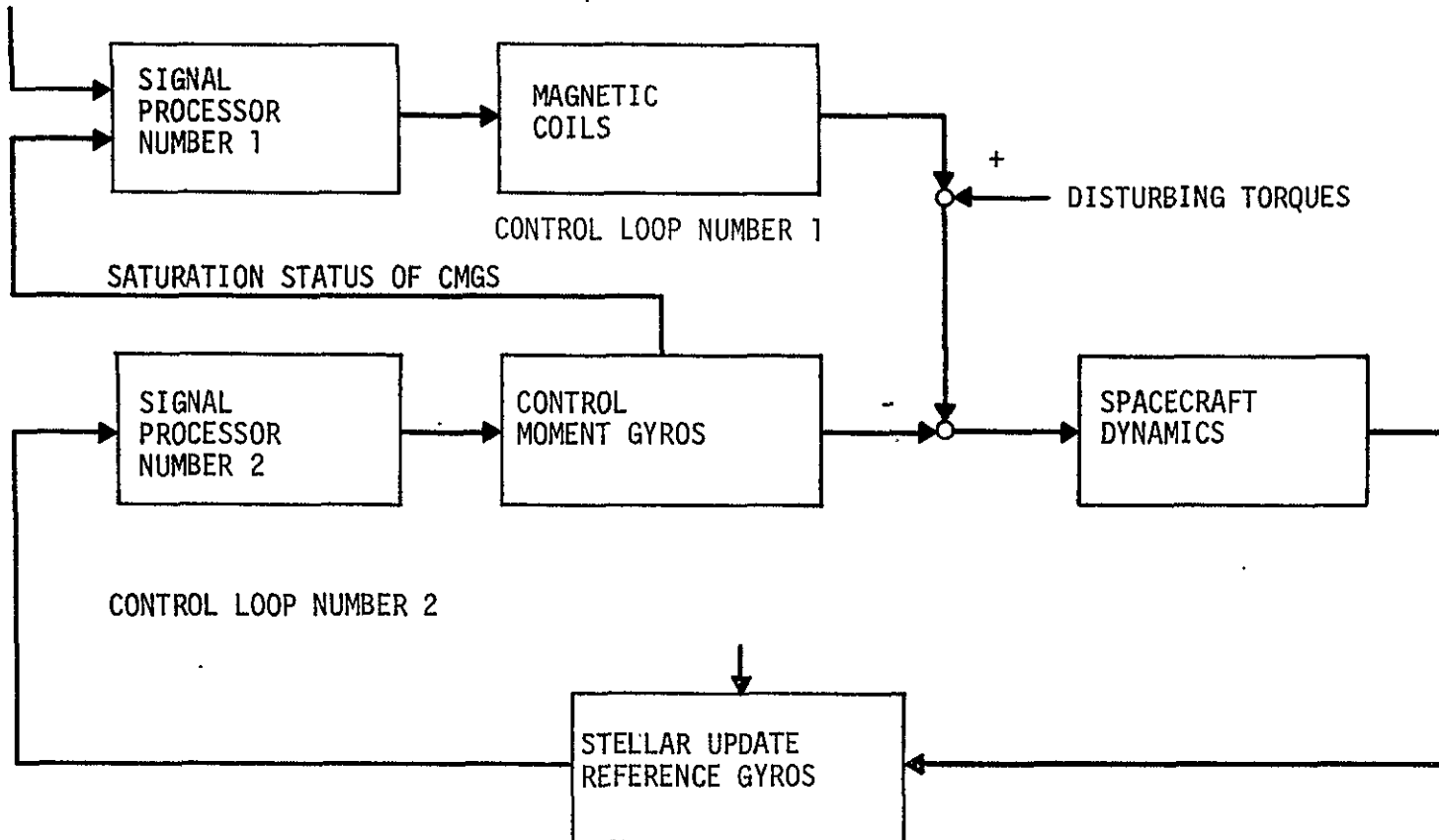
GEOMAGNETIC FIELD
MEASUREMENTS

FIGURE 6-7. ATTITUDE CONTROL SYSTEM

for gyro drift by reference to known stars. Star trackers provide reference sources for updating the gyros. Here only the gyros will be considered a part of the loop, and it will be assumed that gyro accuracy is maintained by whatever external corrections may be required.

Loop 2 also includes an additional torquing device: the CMG. A pair of CMGs are provided for each spacecraft axis. Each CMG consists of a constant-speed rotor mounted in a gimbal; gimbal rotation results in a precession torque. Rotation is effective only up to 90 degrees, so that the CMG is limited in the torque time product, or angular momentum, that it can impart to the spacecraft. The CMG can be regarded as a device capable of generating torque by storing momentum, up to some maximum or saturation level.

Control loop 2 is subject to external torques from two sources: from the magnetic coils of loop 1 and from such natural causes as gravity gradients. If total external torque acting on the loop is always of the same sign, the CMGs will eventually saturate. However, if the secular component of torque is zero, that is, if the torque continually changes sign so that its time integral tends to zero, saturation will never occur. This indicates the function of loop 1: isolation of loop 2 from secular torques. Loop 1 includes provisions for monitoring the saturation status of the CMGs, and a continuous attempt is made to generate magnetic coil torques tending to desaturate the CMGs. Control laws and performance simulations for both loops of the system are presented earlier in this report. The CMGs must have sufficient momentum capacity to avoid saturation during periods when the geomagnetic field is unfavorably oriented.

To a large extent the behavior of the two control loops can be analyzed separately. Thus when loop 2 is analyzed, it is assumed that loop 1 is successfully operating to isolate the spacecraft from secular

torques and thereby keeping the CMGs below their saturation limits. Loop 1 can then be regarded as merely another source of disturbing torque, and the system can be designed to accept this without excessive attitude disturbance just as it accepts gravity gradient and other torque disturbances of natural origin. CMG desaturation is, then, a continuous process rather than one involving periodic perturbations.

CMG CONTROL LOOP COMPONENTS

Reference Gyros

The reference gyros are used during all four modes of attitude control. In each mode it is possible to operate with separated, single-axis gyros. In each axis, there is a gyro and associated electronics; for ease of temperature control and convenience, the three gyros and their associated electronics are mounted in a single package. Figure 6-8 shows the essentials of one axis of the gyro package. The other axes are identical. The gyro itself is a nulling, rate-sensing device. Angular motion produces precession torques within the gyro; motion is detected by the pickoff and nulled by applying current to the torquer. The current required to null gyro motion is proportional to precession torque and hence to angular rate. The torquer signals may be either analog or digital in form.

Integration of the rate output provides angle information. The gyro is, however, subject to drift, which appears as a spurious gyro output; this is allowed for by drift calibration of the gyro and generation of a compensating voltage at the integrator input. Calibration may be based on a combination of preflight, laboratory measurements, and in-orbit checks using stellar references. The compensating voltage may be constant or a function of time or other parameters. The performance obtained from the gyro package depends in large part on the skill with which drift is analyzed and corrected.

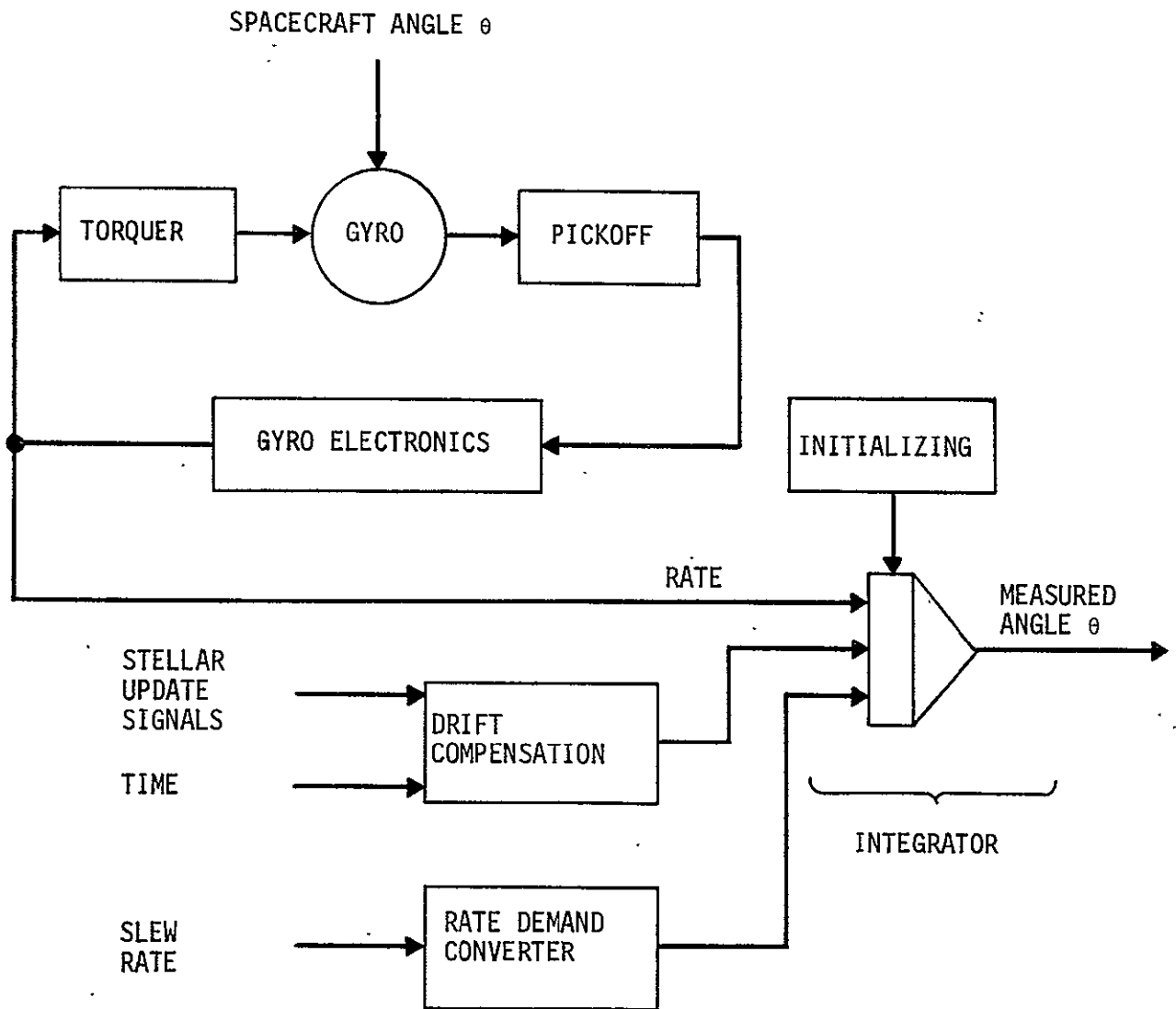


FIGURE 6-8. REFERENCE GYRO COMPONENTS (ONE AXIS ONLY)

In the slewing mode, a signal representing slew rate is received by the rate demand converter. Here the signal is converted to whatever form (analog or digital, parallel or serial) and scaling are compatible with the integrator. The gyro circuitry also includes provisions for setting a zero condition in the integrator when the desired angle is reached and zero rate is to be maintained. The design and operation of the circuitry for these functions is a complex area of study which will not be developed here. Many standard methods exist for drift compensation and rate integration.

The response of the complete control loop is very slow (of the order of cycles per minute) due to the great inertia of the spacecraft. On this time scale the reference gyro appears as a virtually instantaneous source of attitude data. However, the gyro pickoff and electronics introduce noise. The reference gyro loop of Figure 6-7 can, therefore, be represented as a black box in which noise is added to angle information.

Another question is the choice of actual hardware. The specifications for the spacecraft gyros are quite stringent; they must operate continuously for a 2-year (20,000 hour) mission, and they must be useful in all four operating modes. The latter requirement implies a large dynamic range. In the despin mode, reference gyros must measure spacecraft angular rates as high as 3.0 deg/sec. Because the system is nonlinear, the gyros do not need to accurately measure rates as high as 3.0 deg/sec, but they must be capable of accepting such rates without damage. Accurate rate measurement is required in the 0.001 to 0.100 deg/sec region for precise slew mode operation. The gyros must also have random drifts below 0.1 deg/hr for pointing mode operation.

The operating life requirement implies the use of gas rather than ball bearings for the gyro rotors. There are several commercially available gas bearing gyros said to be qualified for 50,000 hours of operation and capable of meeting the specified drift and dynamic range requirements. Table 6-7 gives manufacturer data for one such instrument. The criterion for selection of a specific gyro may be the adequacy of evidence that the gyro will in fact operate for the required length of time. Data on long-duration operation of gyros in space is sparse. Gas bearing gyros were used in the inertial reference unit of the OAO-2; however, one gyro failed after 200 days. This is of course an extremely long lifetime from the standpoint of most gyro applications.

Redundant gyros can be included on the spacecraft at a small cost in weight. A basic package containing three gyros and the necessary electronics for torqueing, initializing, drift compensation, integration, and analog/digital conversion should weigh not more than about 10 pounds.

Signal Processor

Figure 6-7 shows the signal processor No. 2 receives angle error information from the reference gyro electronics, and generates torque demands for the control moment gyros. Simulation results indicate that the signal processor can contain separate and independent channels for the three axes. The processor contains circuits for the following functions:

- Suppression of electrical noise originating in the reference gyro pickoff and electronics
- Introduction into the control equation of the damping and other compensating terms needed for stable behaviour
- Application of well-defined limits to the torque demand to avoid control moment gyro saturation
- Matching the form (analog or digital) and scaling of the reference gyro output to the control moment gyro input.

TABLE 6-7. REFERENCE GYRO CHARACTERISTICS

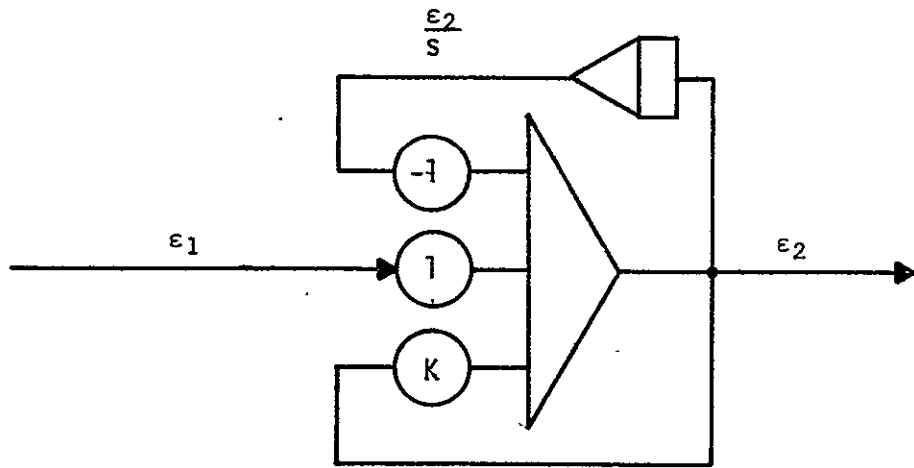
<u>Item</u>	<u>Data</u>
Manufacturer	Kearfott Division of Singer-General Precision, Inc., Wayne, New Jersey
Designation	Gas bearing gyro, C70 2590 003
Weight, lb	1.0
Length, in.	3.2
Diameter, in.	2.1
Short-term random drift ($1-\sigma$), deg/hr	0.001
Long-term (run-to-run) drift ($1-\sigma$), deg/hr	0.01
Heatup power, W	80 at 115 V
Heatup duration (typical), min	4
Spinup power, W	15 at 26 V 3 ph. 800 Hz
Spinup duration, sec	25
Heater power while running, W	0 or 25 (on/off)
Spin power while running, W	7.5 at 26 V 3 ph. 800 Hz
Torquer capacity, deg/sec	3.06

Information on the noise content of the input to the signal processor is not available at this stage. It will be assumed to take the form of white noise of unlimited bandwidth, and for simulation purposes a simple low-pass filter (single time constant) will be used. In later work, selection of the reference gyro and associated electronics will define the noise much more precisely. More detailed analysis of control moment gyro behaviour will define the limits of acceptable noise, and it will become possible to design an optimum noise filter.

It will be shown later that satisfactory system response can be obtained if the processor introduces a damping term of the form $1 + ts$ (torque proportional to error rate). An integral term may be added to eliminate steady-state error in the presence of disturbing torques, although this is not essential for the pointing accuracies now required. Thus the signal processor includes a low-pass filter, a rate-generating circuit, and an integrator. Its transfer function is

$$G \left(1 + t_1 s + \frac{1}{t_2 s} \right) .$$

Theoretically, perfect rate information can be obtained by differentiation of the error angle signal; however, differentiation tends to be avoided in actual hardware because of noise enhancement, dynamic range requirements, and other problems. Figure 6-9 shows a 'rate' circuit from standard analog computer practice; Figure 6-10 shows the complete signal processor for one axis, as represented in the HEAO-C simulation. The low-pass noise filter is followed by circuits to generate rate and integral terms. The last circuit applies a limit to the output signal, which represents torque demand. It should be noted that the amplifiers shown merely amplify and do not invert the signal. The spacecraft could perform these functions using operational



NOTES:

$$\epsilon_2 = \epsilon_1 - \frac{\epsilon_2}{s} + K \epsilon_2$$

$$\epsilon_2 (1 - K) + \frac{\epsilon_2}{s} = \epsilon_1$$

$$\frac{\epsilon_2}{s} \approx \epsilon_1 \text{ IF } K \approx 1$$

THE AMPLIFIERS DO NOT INVERT

FIGURE 6-9. CIRCUIT TO GENERATE APPROXIMATE RATE

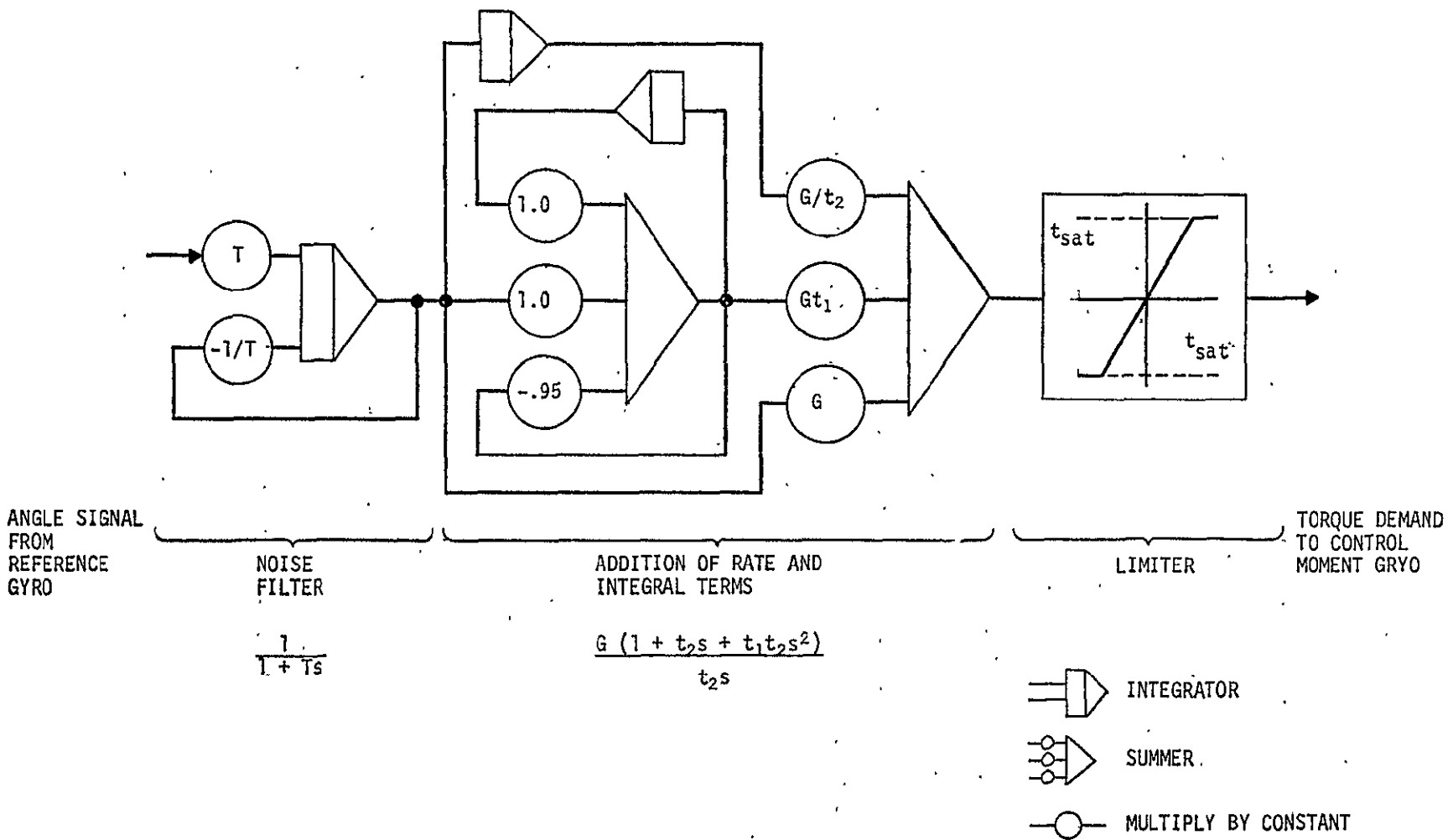


FIGURE 6-10. SIGNAL PROCESSOR

amplifiers of the kind employed in analog computers; alternatively, digital techniques could be used, as was in fact done in the simulation.

The signal processor, then, contains three circuits equivalent to that of Figure 6-10. Both input and output are low-level signals; consequently the circuitry is physically compact and does not dissipate more than a few watts of heat. It may be convenient to incorporate the signal processor into the reference gyro package, or perhaps to mount it at the control moment gyros.

Control Moment Gyros

The instantaneous torque demands of the attitude control system control system are met by the control moment gyros (CMGs). The CMG consists basically of a rotor spinning at constant speed, mounted in gimbals which allow controlled rotation of the spin axis in a plane normal to the spin axis. The result is a precessional torque about the output axis given by

$$T_{\text{CMG}} = \dot{\alpha} H \cos \alpha$$

where $\dot{\alpha}$ is the angular rate of the gimbal and H is the angular momentum of the CMG rotor. Thus a torque demand represents a demand for a certain gimbal angular rate. Torque is very nearly proportional to α when α is small. The CMG becomes gradually less effective as α approaches 90 degrees, where torque about the output axis is zero.

For reasons given earlier the scissored pair CMG configuration has been assumed in HEAO-C simulation. However, most of the simulation work would be directly applicable if certain other CMG arrangements were chosen. In most cases the major difference is in the control law relating demand torque to gimbal rate; some CMG arrays require fairly complex control laws to produce the desired torques.

The Sperry CMG used as a basis for this work has a gearless direct drive torquer; this is capable of lower torque than gears, but is more reliable for a long mission. Figure 6-11 shows the dynamics of the rotor, gimbal and torquer and Table 6-8 lists the constants of Figure 6-11 as supplied by Sperry. This information provides a basis for detailed simulation. Most of the quantities indicated in Figure 6-11 are determined by the mechanical and electrical design of the package. However, the gain K_O , which determines overall bandwidth, is normally set as desired for the intended application. It is necessary to determine suitable values of this gain for the HEAO application, so that the CMG package can be included in a simulation of the attitude control system. Selection of gain is mainly a matter of balancing response requirements or bandwidth (calling for high gain) against the restrictions of noise and saturation limits.

Before undertaking the analysis required to determine the gain K_O , it is desirable to replace the dynamics of Figure 6-11 by a simplified representation. This can be done if the response to only certain types of inputs is considered. This analysis will apply to test inputs of the following general type:

- Sine wave torque demand
- Frequency of a few Hz
- Peak amplitude of a few ft-lbf.

For example, suppose that the signal processor produces a torque demand

$$T = T_O \sin \omega t$$

where

$$T_O - 10 \text{ ft-lbf}$$

$$\omega - 20 \text{ rad/sec.}$$

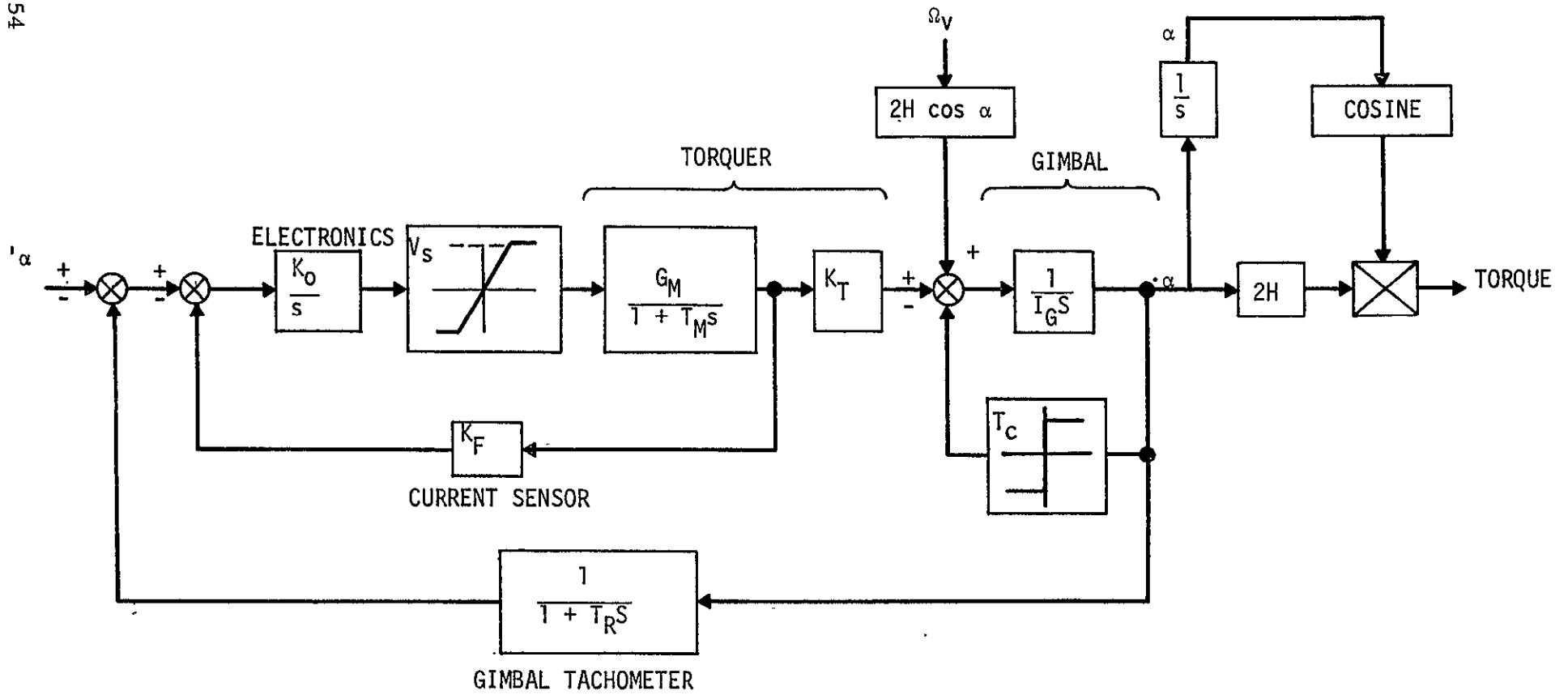


FIGURE 6-11. DYNAMICS OF CMG SCISSORED PAIR CONFIGURATION

TABLE 6-8. CMG DYNAMICS

<u>Symbol</u>	<u>Name</u>	<u>Value</u>	<u>Units</u>
$\dot{\alpha}_C$	Gimbal Rate Command	--	rad/sec
$\dot{\alpha}$	Gimbal Rate	--	rad/sec
I_M	Torquer Motor Current	--	amps
T_M	Torque Motor Torque	--	ft-lbf
$\dot{\alpha}_L$	Gimbal Rate Limit	0.1	rad/sec
K_O	Gain	*	V/rad
V_S	Supply Voltage Limit	27 (NOM)	V
G_M	Torque Motor Conductance ($1/R_M$)	0.066	mhos
T_M	Torque Motor Time Constant (L_M/R_M)	0.005	sec
K_F	Current Feedback Gain	0.04	rad/amp-sec
K_T	Torque Motor Torque Constant	1.2	ft-lbf-sec
T_C	Coulomb Torque	0.05	ft-lbf
I_e	Equivalent Gimbal Inertia = $I_g + H^2/K$	0.4	slug-ft ²
I_g	Real (no speed) Gimbal Inertia	0.2	slug-ft ²
H	Gyro Angular Momentum	100	ft-lbf-sec
K	Gyro Output Axis Torsional Spring Constant	50,000	ft-lbf-rad
α	Gyro Gimbal Angle	--	radian
T_R	Gimbal Angle Tachometer Time Constant	0.002	sec
Ω_v	Vehicle Rate	--	rad/sec

*This parameter is adjusted to achieve the desired loop dynamic response.

The demand frequency $\omega/2\pi$ will be shown to be well within the CMG bandwidth. Therefore, the demanded torque is correctly generated by rotation of the CMG gimbals in accordance with

$$\alpha = \frac{T_o}{2H} \sin \omega t$$

where H is equal to 100 lb-ft-sec for each CMG rotor, giving

$$\alpha = 0.05 \sin \omega t \text{ rad/sec.}$$

The maximum gimbal angular excursion is

$$\begin{aligned} \int \dot{\alpha} dt &= -\frac{0.05}{\omega} \cos \omega t = 0.0025 \text{ radian (max)} \\ &= 0.143 \text{ degree} \end{aligned}$$

Gimbal angular acceleration is

$$\frac{d\dot{\alpha}}{dt} = \frac{\omega T_o}{2H} \cos \omega t$$

requiring that each gimbal torquer produce a torque

$$T_G = \frac{I_G \omega T_o}{2H} \cos \omega t$$

or, since the effective moment of inertia of each gimbal is given in Table 6-8 as 0.4 slug-ft²,

$$T_G = 0.4 \cos \omega t \text{ ft-lbf.}$$

The peak torque of 0.4 ft-lbf is eight times the coulomb torque T_c (Table 6-8). The system will, therefore, spend nearly all its time in

the linear region. In addition, it will be shown later that this test input will not drive the CMG torquer supply voltage to the limit (V_s) of 27 volts. Therefore, the response of the system to this input can be approximated quite well by a model which excludes the nonlinearities V_s and T_c .

The motion of a rigid spacecraft acted upon by this torque is described by .

$$\ddot{\theta} = \frac{T_o}{I_s} \sin \omega t \quad \text{rad/sec}^2$$

$$\dot{\theta} = \frac{T_o}{I_s \omega} \cos \omega t \quad \text{rad/sec}$$

$$\theta = - \frac{T_o}{I_s \omega^2} \sin \omega t \quad \text{rad.}$$

In the spacecraft moment of inertia is $I_s = 47,000 \text{ slug-ft}^2$, the maximum spacecraft angular rate is

$$|\dot{\theta}_{\max}| = \frac{T_o}{I_s \omega} = \frac{1}{94,000} \frac{\text{rad}}{\text{sec}} = 2.2 \frac{\text{arc sec}}{\text{sec}}$$

and the maximum spacecraft angular excursion is

$$|\theta_{\max}| = \frac{T_o}{I_s \omega^2} = 0.11 \text{ arc sec.}$$

Even for rotation about the minimum moment of inertia axis, spacecraft angular rates are several orders of magnitude below CMG gimbal rates. Therefore, the spacecraft remains almost fixed in inertial space. This indicates that the vehicle rate Ω in Figure 6-11 may be omitted.

These steps have simplified the dynamics somewhat. It is also possible to eliminate some of the time constants shown in Figure 6-11. The values of the torque motor time constant T_M , and the gimbal angle tachometer time constant T_R are 0.005 and 0.002 seconds respectively (Table 6-3); therefore, they will not have significant effects on performance at frequencies well below 30 and 80 hertz respectively. These are an order of magnitude higher than the frequencies of interest. Therefore, for the cases of interest, these time constants can be regarded as zero.

Figure 6-11 may now be redrawn as Figure 6-12a which is entirely linear, and can be simplified further into Figure 6-12b. This is a simple second-order system with a natural frequency

$$\omega_o = \left(\frac{G_M K_T K_o}{I_G} \right)^{\frac{1}{2}} \text{ rad/sec}$$

and a damping ratio

$$\zeta = \frac{K_F I_G \omega_o}{2K_T} .$$

The gain K_o is adjusted for the desired system bandwidth:

$$K_o = \left(\frac{I_G}{G_M K_T} \right) \omega_o^2$$

or, using the data in Table 6-3,

$$K_o = 5.1 \omega_o^2 \text{ V/rad}$$

also

$$\zeta = 0.0067 \omega_o .$$

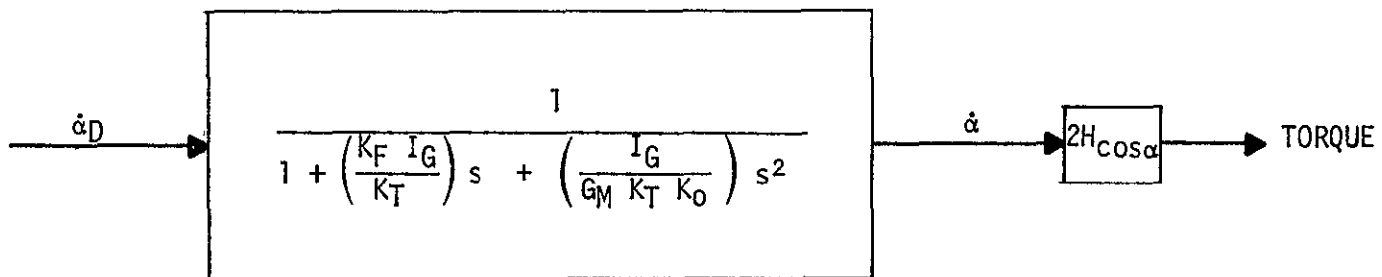
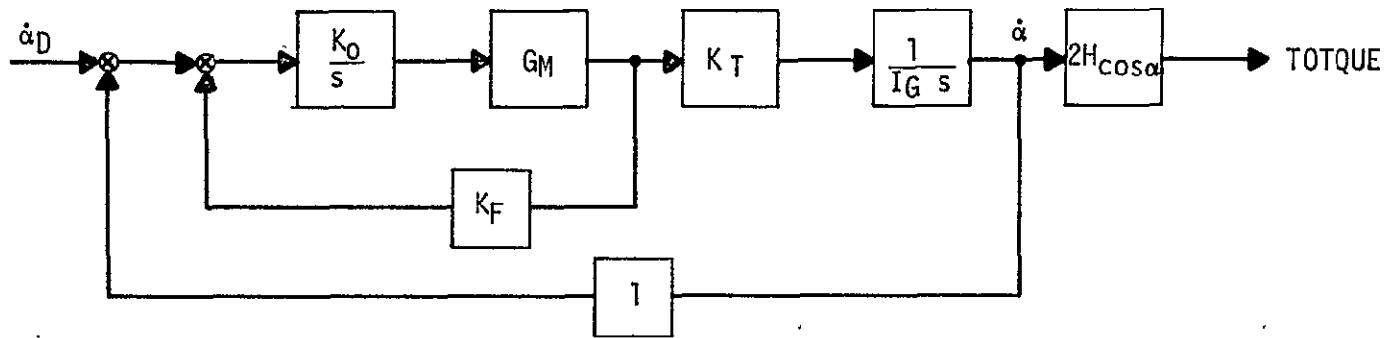


FIGURE 6-12. SIMPLIFIED CMG DYNAMICS

For $\omega_0 = 31.4$ rad/sec (5 hertz), this gives $K_0 = 5040$ and $\zeta = 0.21$. This damping factor is low and it might be desirable to increase it by changing K_F . Figure 6-13 shows the behaviour of the transfer function.

A high K_0 gives large CMG bandwidth, but also increases the likelihood that the amplifier output will reach the voltage saturation limit (Figure 6-11). The relationship between the demanded gimbal rate $\dot{\alpha}_D$ and the amplifier output voltage x is found from Figure 6-12(a) to be

$$\frac{x}{\dot{\alpha}_D} (s) = \frac{I_G s}{G_M K_T} \left(\frac{\dot{\alpha}}{\dot{\alpha}_D} \right) = 5.1 s \left(\frac{\dot{\alpha}}{\dot{\alpha}_D} \right).$$

For input signals well within the system bandwidth ($\omega \ll \omega_0$), the system closely follows input demand, i. e.,

$$\left| \frac{\dot{\alpha}}{\dot{\alpha}_D} \right| = 1 \text{ approximately;}$$

hence

$$\left| \frac{x}{\dot{\alpha}_D} \right| = 5.1 \omega \frac{V}{\text{rad/sec}}$$

approximately for this frequency regime. Figure 6-14 shows the behaviour of $|x/\dot{\alpha}_D|$ over the whole frequency range (note that $5.1 = 14.2$ dB). If $|\dot{\alpha}/\dot{\alpha}_D|$ includes adequate damping it will never greatly exceed 1 in the operating region of the system. Thus $|x/\dot{\alpha}_D|$ will never be much greater than about 6ω .

It is now possible to determine the condition for voltage saturation. A torque demand

$$T = T_0 \sin \omega t$$

NOTES:

1. $\zeta = 0.08$ FOR $\omega_0 = 12.6$ rd/s (2 Hz)
2. $\zeta = 0.2$ FOR $\omega_0 = 31.4$ (5 Hz)
3. $\zeta = 0.4$ FOR $\omega_0 = 62.8$ (10 Hz)
4. -40 dB/DECADE

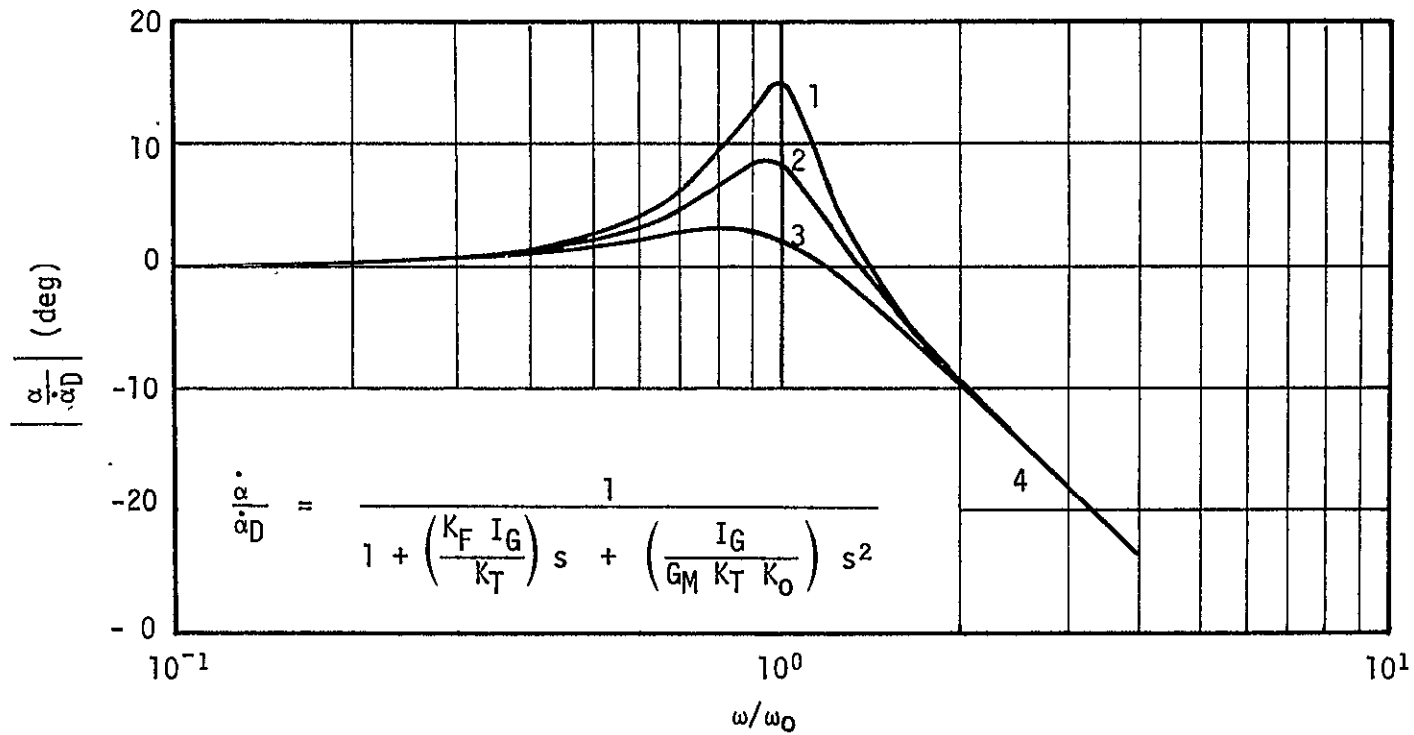


FIGURE 16-13. TRANSFER FUNCTION OF SIMPLIFIED CMG

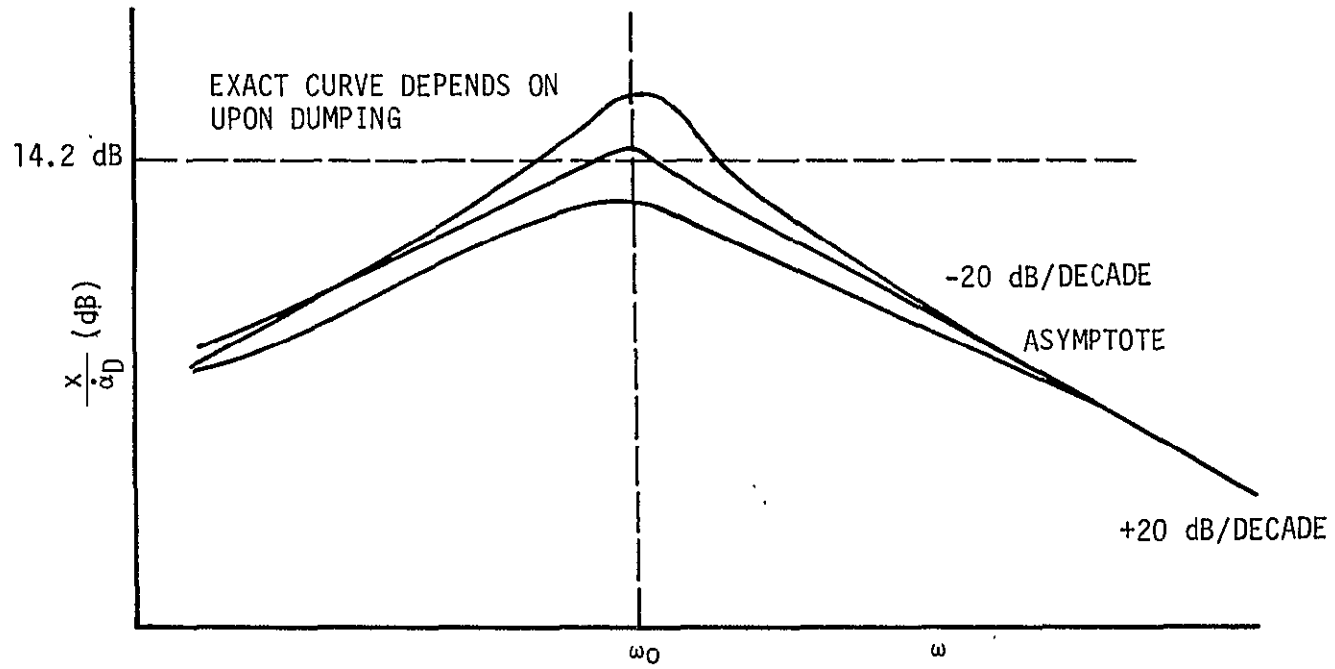


FIGURE 6-14. BEHAVIOUR OF SATURATION FUNCTION

results in a peak gimbal rate demand

$$\dot{\alpha}_D = \frac{T_O}{2H}$$

and a voltage

$$x = \left| \frac{x}{\dot{\alpha}_D} \right| \frac{T_O}{2H}$$

or approximately

$$x \approx 6 \frac{\omega T_O}{2H} \text{ volts}$$

and if it is required that

$$x < V_S$$

the maximum acceptable torque is

$$T_O = \frac{H V_S}{3\omega}$$

which, substituting values from Table 6-8, gives the condition for saturation

$$\omega T_O \geq 900 \text{ (lb-ft)} \times \text{(rad/sec)} .$$

In the spacecraft pointing mode the highest frequencies of interest are a few radians per second; the torques required for HEAO-C operation in this mode are never more than a few ft-lbf. The ωT_O product therefore will never be greater than about 100, so saturation will not occur. This justifies the assumption made earlier that the nonlinearity V_S would not affect CMG performance in the pointing mode. Pointing mode behaviour can, therefore, be based on the purely linear representation of Figure 6-12.

CMG voltage and torque limits could be reached during slew mode operation, if, for example, the attitude control system demanded a step change in spacecraft angular rate $\dot{\theta}$. A step change in $\dot{\theta}$ corresponds to a demand for infinite CMG torque and hence infinite $\dot{\alpha}$. The maximum voltage V_s would result in an initial gimbal acceleration

$$\frac{d\dot{\alpha}}{dt} = \frac{V_s G_M K_T}{I_G} = 5.1 \text{ rad/sec}^2.$$

The CMG becomes less and less effective as α approaches 90 degrees. To maintain proper control it is desirable to limit α to perhaps 70 degrees. If the gimbal maintained the acceleration calculated above, α would reach 70 degrees in less than 0.7 second. In addition, power requirements for the two CMGs in the scissored pair would surge to

$$\frac{2 V_s^2}{G_M} = 96 \text{ watts}$$

imposing an unacceptable burden on the spacecraft power supply. To avoid both saturation and power surge problems, the torque demand applied to each CMG pair is limited to a few ft-lbf by the nonlinear circuit in the signal processor (Figure 6-10). This will prevent saturation even for the slewing mode. The nonlinearity V_s need not appear in the simulation of the attitude control system.

The above analysis has shown that the only important nonlinearity at the top end of the torque curve is that provided within the signal processor. However, the coulomb torque T_c , was mentioned earlier as providing a small nonlinearity at the bottom end. This tends to set a lower limit on the torque which can be applied to the gimbal. This limit cannot be directly represented unless the dynamics

of the complete CMG are simulated. Discussion with Sperry representatives revealed that the effect of T_c is augmented by certain other nonlinearities not shown in Figure 6-11; these include the effect of bit quantization in digital portions of the electronics. Experiments by Sperry indicated that all such nonlinearities could be fairly well represented by a dead zone on CMG gimbal rate in the region of ± 0.005 deg/sec. With a rotor momentum of 100 lb-ft-sec per CMG, this corresponds to an output torque dead zone T_D of about ± 0.02 ft-lbf. A dead zone on torque is easily simulated without any representation of CMG dynamics. This is done by interposing between the signal processor and the CMG a unit with the function

$$T_{CMG} = 0 \text{ if } |T'_{CMG}| < T_D$$

and

$$T_{CMG} = T'_{CMG} \text{ if } |T'_{CMG}| \geq T_D$$

where T'_{CMG} is the signal processor output and T_{CMG} is the signal actually applied to the CMG.

The CMG introduces one other nonlinearity: a limit on α or on stored momentum. Figure 6-15 shows the CMG in a form suitable for simulation with the simplified dynamics of Figure 6-12 and a dead zone and an α limit added. The $\cos \alpha$ factor is omitted in the pointing mode because in this mode the system never approaches saturation and α is normally limited to a fraction of a degree. In the loop diagram of Figure 6-7, Figure 6-15 represents the elements of the CMG block.

SPACECRAFT DYNAMICS SIMULATION

Basic Equations

The preceding sections have described the hardware blocks of CMG control loop. In each case it has been possible to treat the system

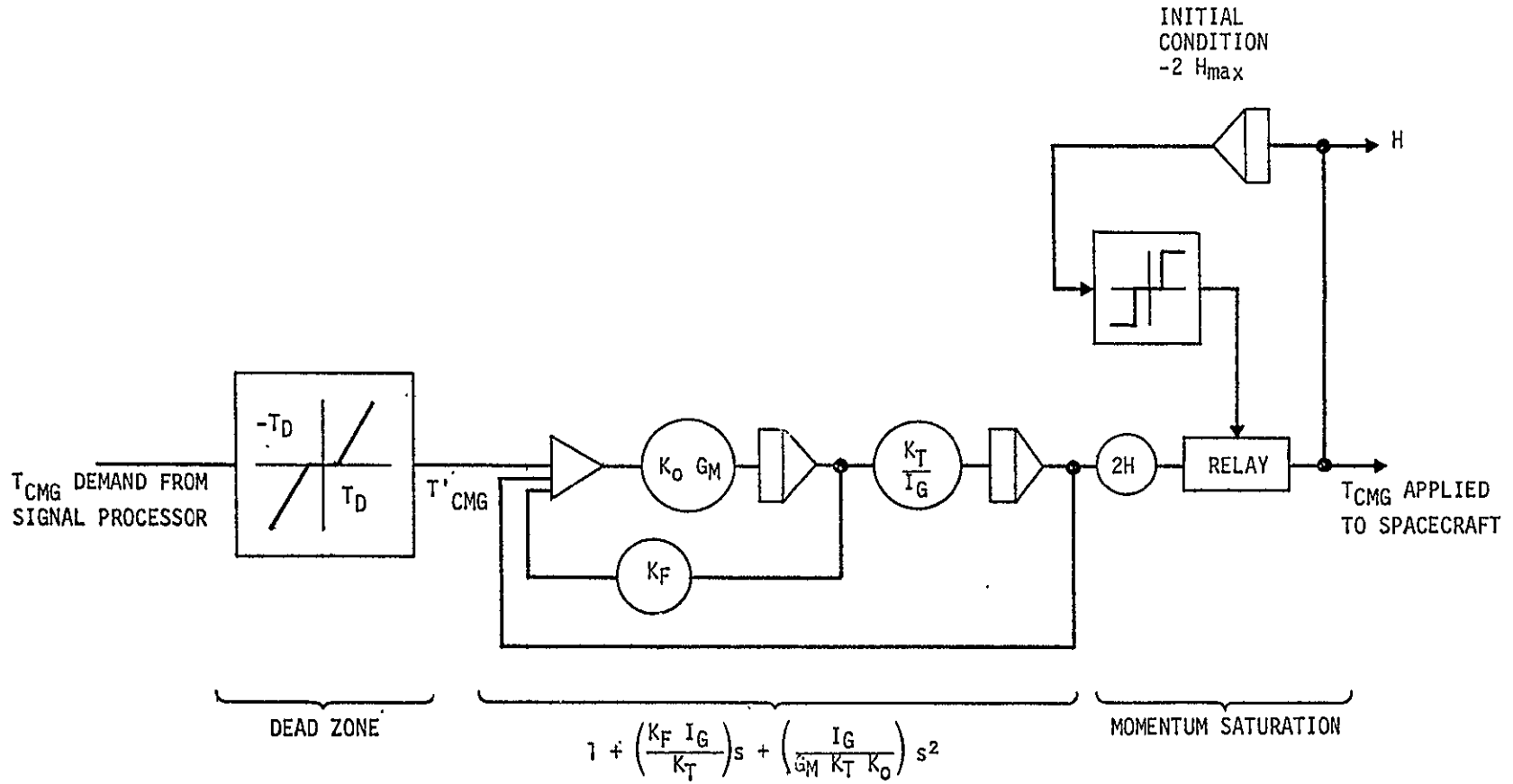


FIGURE 6-15. CMG ARRANGED FOR SIMULATION

as a combination of three single-axis systems. When spacecraft dynamics are considered, it becomes necessary to consider coupling between the axes unless angular rates are very small. The basis of the spacecraft dynamics are the Euler equations for a rigid body acted upon by torques:

$$I_x \ddot{\theta}_x = T_x + (I_y - I_z) \dot{\theta}_y \dot{\theta}_z$$

$$I_y \ddot{\theta}_y = T_y + (I_z - I_x) \dot{\theta}_x \dot{\theta}_z$$

$$I_z \ddot{\theta}_z = T_z + (I_x - I_y) \dot{\theta}_x \dot{\theta}_y$$

where

I - mass moment of inertia about the spacecraft body axes

$\dot{\theta}$ - angular rate about the spacecraft body axes

$\ddot{\theta}$ - angular acceleration about the spacecraft body axes

T - torque in the spacecraft body axes.

Several sources of torque exist. Disturbing torques originate within and outside the spacecraft; control torques are intentionally generated by the CMGs; and unwanted cross-coupling torques occur due to gyroscopic effects. The latter torques appear as soon as a CMG pair acquire some net stored momentum. For example, consider the x-axis CMG pair which, when no x-axis torque is demanded, will in general represent a stored momentum vector lying along the x axis. If now the spacecraft rotates about the y or z axis, rotation of the x-axis momentum vector results in torques about the z or y axis respectively.

The use of CMGs in scissored pairs ensures that the net momentum vector of each pair lies entirely along the axis with which that pair is associated. Scissored pairs also cancel out the reaction

torques generated when the torquers rotate the CMG gimbals, since the two torquers rotate in opposite directions. Lack of perfect matching between the components of a scissored pair would in fact result in small cross-coupling effects. These have not been analyzed here because such mismatching would be expected to be extremely small, and because in the most critical mode of operation (the pointing mode) angular rates are very low and any cross-coupling effects correspondingly small.

The Euler equations can now be written:

$$I_x \ddot{\theta}_x = T_{x\text{CMG}} + T_{x\text{EXT}} + H_y \dot{\theta}_z - H_z \dot{\theta}_y + (I_y - I_z) \dot{\theta}_y \dot{\theta}_z \quad (6-18)$$

$$I_y \ddot{\theta}_y = T_{y\text{CMG}} + T_{y\text{EXT}} + H_z \dot{\theta}_x - H_x \dot{\theta}_z + (I_z - I_x) \dot{\theta}_x \dot{\theta}_z \quad (6-19)$$

$$I_z \ddot{\theta}_z = T_{z\text{CMG}} + T_{z\text{EXT}} + H_x \dot{\theta}_y - H_y \dot{\theta}_x + (I_x - I_y) \dot{\theta}_x \dot{\theta}_y \quad (6-20)$$

Here terms of the form $H\dot{\theta}$ represent the cross-coupling effects of stored momentum discussed above. Torques external to the CMG loop ($T_{x\text{EXT}}$ etc.) include the effects of the magnetic coil momentum dumping system.

The attitude control system is closed-loop because T_{CMG} is a function of θ . The reference gyros detect θ , the signal processor uses the θ signal to generate a T_{CMG} demand, and the CMG electronics drive the gimbals to whatever rates are required to meet this demand. The signal processor converts θ to T_{CMG} by implementing for each axis the equation

$$\frac{T_{\text{CMG}}}{I} = -a \int \theta dt - b\theta - c\dot{\theta}.$$

The minus signs result in negative feedback; the $\dot{\theta}$ term provides damping. The positive constants a, b, c have been chosen to give the same response in each axis, that is,

$$a_x = a_y = a_z \frac{\text{arc-sec/sec}^2 \text{ acceleration}}{\text{arc-sec} \cdot \text{sec integral of error}} \text{ or } \text{sec}^{-3}$$

$$b_x = b_y = b_z \frac{\text{arc-sec/sec}^2 \cdot \text{acceleration}}{\text{arc-sec error}} \text{ or } \text{sec}^{-2}$$

$$c_x = c_y = c_z \frac{\text{arc-sec/sec}^2 \text{ acceleration}}{\text{arc-sec/sec error rate}} \text{ or } \text{sec}^{-1} .$$

The system behaves similarly to a second-order system having a natural frequency

$$\omega = \sqrt{a} \text{ rad/sec (or } f = 2\pi\sqrt{a}\text{)}$$

and a damping ratio

$$\zeta = \frac{c}{2\omega}$$

In most of the HEAO-C simulation runs, these were set at $\omega = 0.2 \text{ rad/sec}$ and $\zeta = 0.7$. These values were found to give satisfactory system response. The integral or a term gradually eliminates steady state error in the continued presence of an external disturbing torque. It was found that a setting of $a = 0.001$ was small enough to avoid destabilizing the system, but large enough to eliminate steady-state errors within a couple of cycles.

Simulation Results

The spacecraft and CMG control loop was simulated using the Continuous System Modeling Program (CSMP) written by IBM for use on their 1130 digital computer. The input to this program is a description of a network of elements of the type found in an analog computer. The program automatically develops differential equations to describe the behaviour of the networks, and then numerically integrates the equations and plots the results. CSMP has provisions for rapid and easy change of system parameters, so that it is possible to carry out a short simulation run, observe system response, and immediately rerun with changed data. CSMP was found to be a useful and effective tool for the HEAO-C simulation.

The purpose of the simulation was to determine the spacecraft response to typical disturbing torques. Gravity gradient torque changes would act so slowly that the spacecraft response could not be easily plotted as a function of time. For this reason disturbing step torques of the magnitude of the average torque imparted to the spacecraft by the electromagnet torques coils were used in the stability simulation.

CMG Representation - To determine the simplest permissible representation of the CMGs, a single-axis simulation was programmed with the CMG bandwidth at 5 hertz and this was compared with system response for infinite CMG bandwidth. It was found that the plotted results were indistinguishable. On this basis, the CMG representation was reduced to that shown in Figure 6-16, where only certain nonlinearities are taken into account as discussed earlier. The quantities indicated by numbers and the symbols used in Figure 6-16 are identified in Table 6-9.

Cross-Coupling Effects - Equations 6-18 through 6-20 provide a basis for simulation. It is interesting to compare the magnitudes of the terms of these equations. Because angular rates are small, it

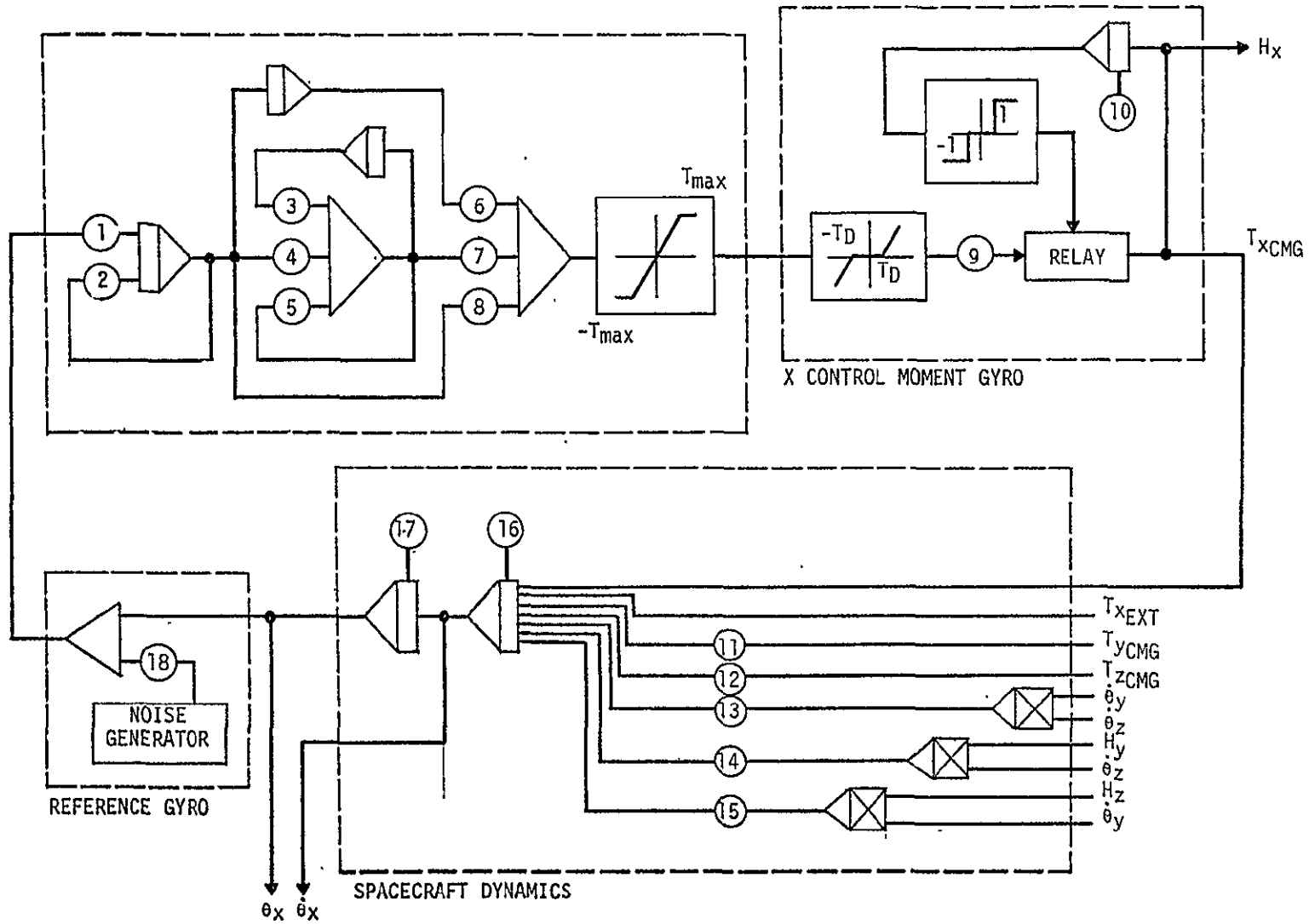


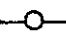



FIGURE 6-16. REPRESENTATION OF ONE AXIS OF A THREE-AXIS SIMULATION

TABLE 6-9. KEY TO FIGURE 6-16

①	$T =$ time constant of noise filter
②	$-1/T$
③	-1.0
④	1.0
⑤	-0.95
⑥	a_x
⑦	c_x
⑧	b_x
⑨	$2I_w =$ total rotor inertia of CMG
⑩	$-H_{\max} =$ maximum permissible stored momentum
⑪	Depends upon misalignment of y-axis CMG
⑫	Depends upon misalignment of z-axis CMG
⑬	$(I_y - I_z)/I_x$
⑭	$1/I_x$
⑮	$1/I_x$
⑯	Initial x-axis rate
⑰	Initial x-axis angle
⑱	Depends upon desired noise amplitude
	Summer (adds variables)
	Integrator (n gives initial condition)
	Multiply by constant
	Multiply two variables

may be anticipated that the last term in each of the three equations will be relatively small. To determine the relative importance of these terms, two cases were run, one based on the full equations and the other omitting terms of the form $H\dot{\theta}$ and $\dot{\theta}_x \dot{\theta}_y$. Since the simplified equations contain no cross-coupling terms, they permit reduction of the simulation to single-axis cases.

Both cases consisted of an x-axis torque step of 0.03 ft-lbf, with no other disturbance. To produce cross-coupling effects, substantial initial stored momenta were included. Table 6-10 compares the single-axis with the more precise three-axis simulation. The results never differ by more than 0.05 percent. This excellent agreement becomes less surprising if one compares typical numerical values for the quantities

$$T_{CMG} + T_{EXT}$$

and

$$H_y \dot{\theta}_z - H_z \dot{\theta}_y + (I_y - I_z) \dot{\theta}_y \dot{\theta}_z$$

which do, in fact, differ by three or four orders of magnitude for this case. This indicates that for the pointing mode, where required torques are in the 0.01 to 0.1 ft-lbf region and the resulting angular rates are of the order of 0.1 arc sec/sec, the single-axis simulation gives an excellent approximation. This results in a three-fold saving in computer time. On the other hand, slewing mode behaviour involves rotation through large angles at substantial rates and must, therefore, be studied using the full three-axis simulation.

Iteration Step Size - The next simulation runs were carried out with the object of identifying a suitable iteration step size. A small step results in high accuracy at the expense of long computing time;

TABLE 6-10. SIGNIFICANCE OF CROSS-COUPLING TERMS

Time (sec)	x-Axis Angle (arc sec)	
	Three-Axis Simulation	One-Axis Simulation
0.000	0.0000	0.0000
5.000	0.3750	0.3750
10.000	1.4999	1.5000
15.000	3.3744	3.3750
20.000	5.9982	6.0000
25.000	8.5772	8.5798
30.000	8.6621	8.6637
35.000	7.2962	7.2974
40.000	6.4192	6.4214
45.000	5.9622	5.9633
50.000	5.2436	5.2433
55.000	4.3912	4.3913
60.000	3.7605	3.7608
65.000	3.2881	3.2878
70.000	2.8179	2.8174

NOTE: Initial Stored Momenta $H_x = 60$ lb-ft-sec
 $H_y = -40$
 $H_z = 20$

Iteration Step Size, 0.5 sec

The 3-axis simulation includes the effects of cross coupling, whereas the 1-axis simulation does not.

generally a suitable step is somewhat smaller than the smallest time constant in the system. In these runs the smallest time constant was the tracker noise filter (1 second). A series of runs with step sizes of 0.1, 0.2, 0.5 and 1 second indicated that a 0.2-second step would give step-originated errors below 0.1 percent. This was one-fifth of the smallest time constant. This ratio was preserved in all later runs.

The example used in the step size comparison was response of the system to step torques about all three axes. Figure 6-17 shows response for the y axis; this plot was produced by automatic plotting of all four runs, superimposed, the effect of step size changes being indistinguishable on this scale. Response about the other axes is quite similar and is shown in Table 6-11 for the $\Delta t = 0.1$ second case. The torques used were of the same order of magnitude as typical magnetic coil torques; it is seen that the spacecraft undergoes very small excursions. The maximum motion of the pointing axis, determined as

$$(\theta_y^2 + \theta_z^2)^{\frac{1}{2}},$$

is less than 9 arc seconds. The results indicate that the system is stable with the settings used, and that it can satisfactorily control the spacecraft in the pointing mode against gravity gradient torques.

Noise Filter Time Constant - Noise in the attitude signal was discussed earlier. A low-pass noise filter with a 1-second time constant has been used in most simulation runs. Figure 6-18 shows the effect of time constants of 0.5, 1, and 2 seconds by comparing responses to a 0.03 ft-lbf torque step. For each time constant, cases with two damping ratios are shown to illustrate the ability of increased damping to suppress oscillations. If the time constant is as long as 2 seconds,

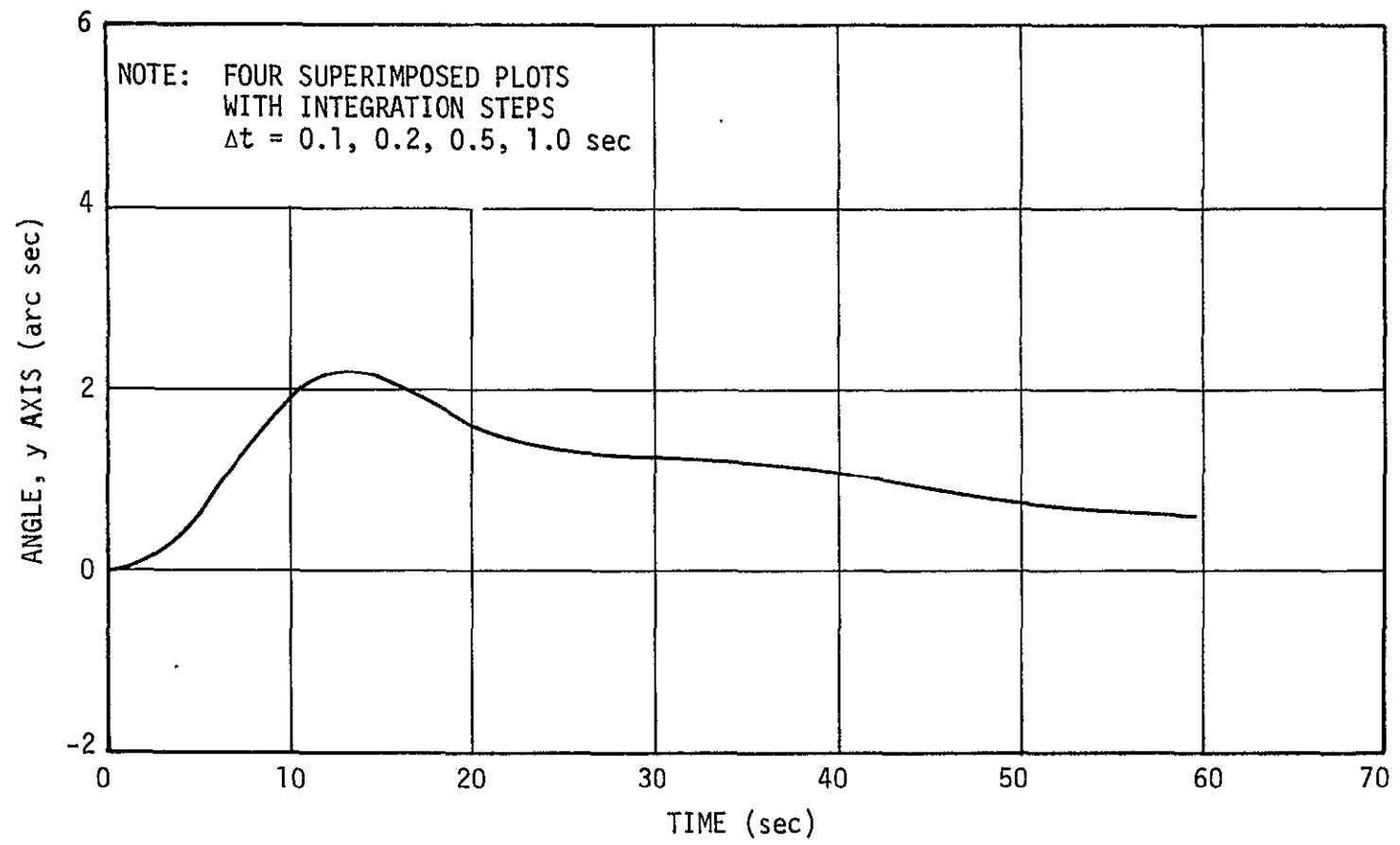


FIGURE 6-17. EFFECT OF INTEGRATION STEP SIZE ON CONTROL SYSTEM RESPONSE

TABLE 6-11. CMG CONTROL SYSTEM RESPONSE TO STEP TORQUES IN ALL AXES

<u>Time</u> <u>(sec)</u>	θ_x <u>(arc sec)</u>	θ_y <u>(arc sec)</u>	θ_z <u>(arc sec)</u>
0.000	0.0000	0.0000	0.0000
5.000	0.3859	0.6236	0.1244
10.000	1.6067	1.8934	0.4668
15.000	3.7166	2.1426	0.8735
20.000	6.6098	1.6201	0.9998
25.000	8.8909	1.3216	0.9597
30.000	8.5183	1.2475	0.9526
35.000	7.1583	1.1801	0.7988
40.000	6.4366	1.0708	0.5719
45.000	5.9574	0.9105	0.4956
50.000	5.1374	0.7489	0.4971
55.000	4.2845	0.6516	0.4179
60.000	3.7087	0.5878	0.3094

NOTE: No Initial Rates

No Tracker Noise

Step Torque Sizes:

$$T_{x_{ext}} = 0.03 \text{ lb-ft}$$

$$T_{y_{ext}} = 0.05 \text{ lb-ft}$$

$$T_{z_{ext}} = 0.01 \text{ lb-ft}$$

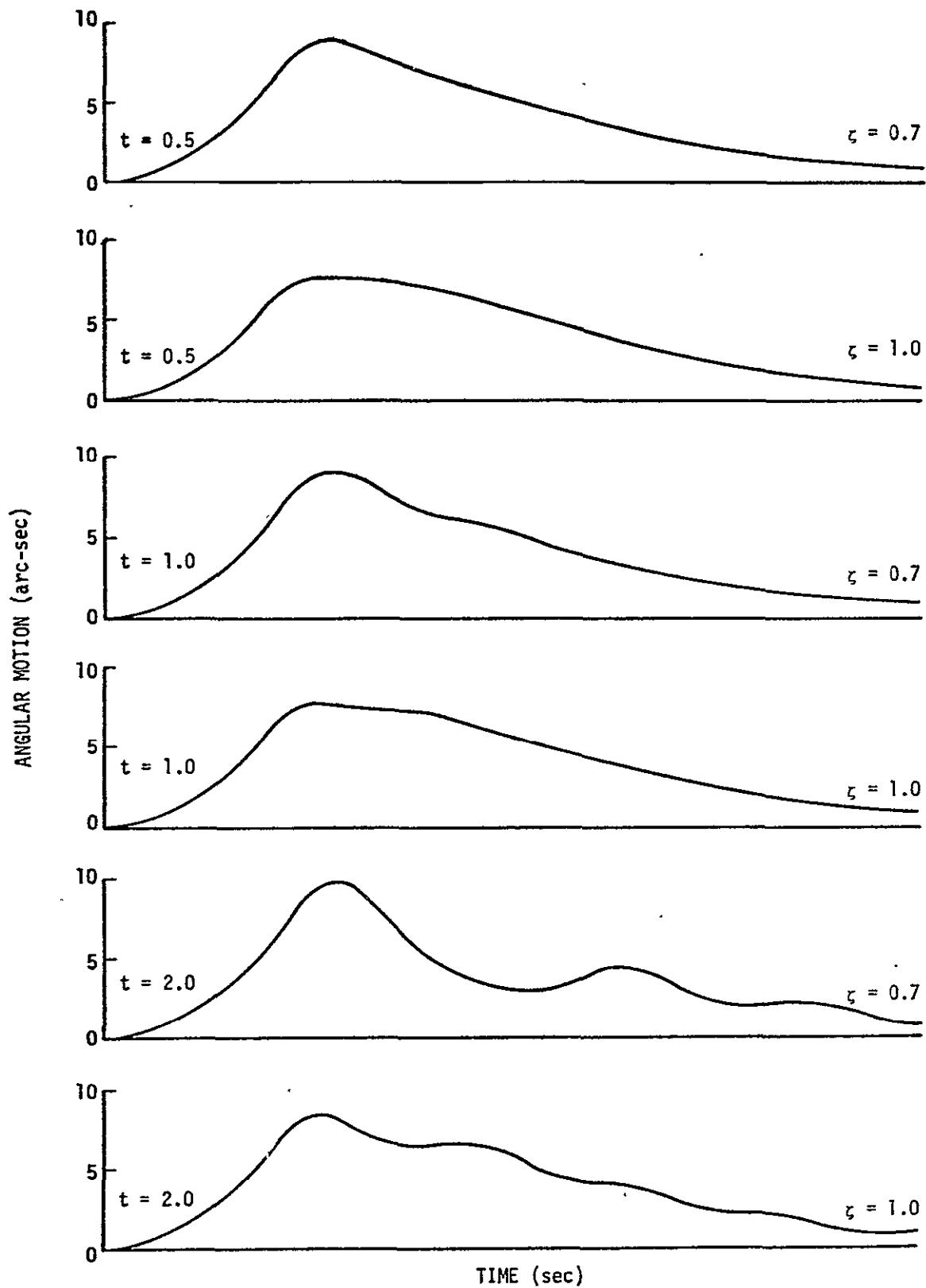


FIGURE 6-18. CONTROL SYSTEM RESPONSE TO A 0.03 FT-LBF TORQUE STEP FOR DIFFERENT NOISE FILTER CONSTANTS AND DAMPING RATIOS

a damping ratio even higher than 1 may be desirable. In the design of an actual system, the noise filter would probably be more complicated than a single time constant and the required compensation would probably also be more complicated than a simple increase in the damping ratio. Figure 6-18 merely illustrates general trends. It is expected that a noise filter time constant of 0.5 second would in fact give ample filtering.

CMG Misalignment - Another effect investigated in the simulation was sensitivity to misalignment of the CMGs. Misalignment was represented in the simulation by supplying to each axis some fraction of the control torques being demand from the CMGs in the other two axes. In the physical system this could be due to CMG mounting errors, asymmetries within CMG pairs, or other causes.

Table 6-12 compares two runs for the full three-axes simulation, with disturbing step torque of 0.03 ft-lbf. In the first case, stored momentum on all three-axes results in cross-coupling, which causes very small y- and z-axis disturbances that can be neglected. The y-axis angle stays within the system dead zone, so the y-axis CMG does not change its stored momentum. In the second case, a misalignment of 3 degrees results in y- and z-axis excursions which are much larger but still less than 1 arc second. The x-axis response is almost unchanged.

Three degrees is a very large misalignment for a properly constructed system. It can be concluded that alignment of CMG torques is not at all critical.

Large Angle Rotation - Discussion so far has been limited to small angular excursions. It is of interest to determine whether the simulation will continue to perform properly when angular motion is

TABLE 6-12. CONTROL SYSTEM RESPONSE TO AN x-AXIS DISTURBANCE TORQUE OF 0.03 ft-lbf WITH A 3-DEGREE MISALIGNMENT OF THE CMG

(1) With Perfect CMG Alignment

Time (sec)	Angle (arc sec)			Stored Momentum lb-ft-sec	
	x axis	y axis	z axis	x axis	y axis
0.000	0.0000	0.0000	0.0000	60.0000	-40.0000
5.000	0.3750	-0.0003	-0.0005	60.0000	-40.0000
10.000	1.4999	-0.0021	-0.0042	60.0000	-40.0000
15.000	3.3744	-0.0073	-0.0142	60.0000	-40.0000
20.000	5.9982	-0.0173	-0.0336	60.0000	-40.0000
25.000	8.5772	-0.0335	-0.0648	59.9900	-40.0000
30.000	8.6621	-0.0530	-0.1018	59.9751	-40.0000
35.000	7.2962	-0.0708	-0.1352	59.9710	-40.0000
40.000	6.4192	-0.0863	-0.1633	59.9708	-40.0000
45.000	5.9622	-0.1007	-0.1889	59.9674	-40.0000
50.000	5.2436	-0.1141	-0.2120	59.9626	-40.0000
55.000	4.3912	-0.1258	-0.2315	59.9596	-40.0000
60.000	3.7605	-0.1360	-0.2478	59.9574	-40.0000

TABLE 6-12. Concluded

(2) With 3 Degrees CMG Misalignment

Time (sec)	Angle (arc sec)			Stored Momentum lb-ft-sec	
	x axis	y axis	z axis	x axis	y axis
0.000	0.0000	0.0000	0.0000	60.0000	-40.0000
5.000	0.3750	-0.0003	-0.0005	60.0000	-40.0000
10.000	1.4999	-0.0021	-0.0042	60.0000	-40.0000
15.000	3.3744	-0.0073	-0.0142	60.0000	-40.0000
20.000	5.9982	-0.0173	-0.0336	60.0000	-40.0000
25.000	8.5851	0.0063	-0.0251	59.9900	-40.0000
30.000	8.6983	0.1903	0.1397	59.9749	-40.0000
35.000	7.3371	0.4909	0.4196	59.9704	-40.0000
40.000	6.4533	0.7730	0.7067	59.9702	-40.0000
45.000	5.9827	0.8303	0.8362	59.9667	-40.0184
50.000	5.2403	0.7389	0.7807	59.9618	-40.0225
55.000	4.3757	0.6572	0.6853	59.9589	-40.0226
60.000	3.7478	0.5899	0.6075	59.9567	-40.0238

NOTE: No Noise

0.03 ft/lb Torque About x-Axis

Initial Stored Momentum $H_x = 60$ lb-ft-sec $H_y = -40$ $H_z = 20$

Iteration Step Size = 0.5 sec.

large, and if so, whether the CMG/star tracker system being simulated remains effective at large angles.

Table 6-13 shows the behaviour of the control system during rotation through a large angle. The spacecraft has an initial x-axis rate of 1 deg/sec (3,600 arc sec/sec) and an initial x-axis stored momentum of -100 ft-lbf-sec, equal to the saturation level. This saturation effectively disables the x-axis control loop, so that rotation continues at nearly constant rate. The only y- and z-axis disturbances are cross-coupling effects due to stored momentum.

The initial z-axis stored momentum of 100 ft-lbf-sec, together with the x-axis rate, results in a y-axis torque amounting to

$$100 \times \frac{1}{180/\pi} = 1.75 \text{ ft-lbf.}$$

at the beginning of the simulation. This torque results in a maximum y-axis disturbance of only 41 arc seconds or 0.11 degree. This disturbance torque is more than an order of magnitude greater than typical gravity gradient torques; since the system is operating in its linear region, gravity torques alone would be expected to contribute much less than 0.1 degree to the y-axis disturbance.

This conclusion is of particular interest in connection with the use of the CMG system in the HEAO-A spacecraft. It will be remembered that the HEAO-A rotates continuously at a rate of 0.6 deg/sec or less, compared with the 1 deg/sec of the present case. In addition, in the HEAO-A mission, the required control accuracy of the spacecraft axis is only 1 degree. The simulation results suggest that a CMG system may be well able to meet these requirements.

TABLE 6-13. LARGE ROTATION, SHOWING MOMENTUM INTERCHANGE

Time (sec)	Angle (arc sec)		Stored Momentum (lb-ft-sec)		
	x axis	y axis	x axis	y axis	z axis
0.000	0.0000	0.0000	-100.0000	0.0000	100.0000
2.000	7186.1250	- 15.8736	-100.0000	0.1191	99.9995
4.000	14366.5058	- 57.7794	-100.0000	1.3299	99.9568
6.000	21543.7383	-111.6824	-100.0000	4.4584	99.8062
8.000	28716.8906	-163.6335	-100.0000	8.4537	99.4708
10.000	35885.8907	-211.2602	-100.0000	12.4489	98.8815
12.000	43040.8047	-254.4501	-100.0000	16.4441	98.0230
14.000	50211.7188	-293.0366	-100.0000	20.4392	96.9322
16.000	57368.7813	-326.7855	-100.0000	24.4344	95.6729
18.000	64522.1563	-355.3936	-100.0000	28.4296	94.3061
20.000	71672.0002	-378.4999	-100.0000	32.4247	92.8701
22.000	78818.5626	-395.7009	-100.0000	36.4199	91.3734
24.000	85962.0783	-406.4520	-100.0000	40.4150	89.8005
26.000	93102.7658	-410.6303	-100.0000	44.4101	88.1247
28.000	100240.8439	-407.4241	-100.0000	48.4053	86.3215
30.000	107376.5158	-396.4398	-100.0000	52.4044	84.3778
32.000	114510.0158	-377.1391	-100.0000	56.3955	82.2936
34.000	121641.5627	-348.9462	-100.0000	60.3907	80.0795
36.000	128771.4845	-311.2449	-100.0000	64.3858	77.7505
38.000	135899.8754	-263.3804	-100.0000	68.3809	75.3202
40.000	143027.0629	-204.6614	-100.0000	72.3759	72.7970

TABLE 6-13. Continued

Time (sec)	Angle (arc sec)		Stored Momentum (lb-ft-sec)		
	<u>x axis</u>	<u>y axis</u>	<u>x axis</u>	<u>y axis</u>	<u>z axis</u>
42.000	150153.3128	-134.3638	-100.000	76.3710	70.1835
44.000	157279.0004	- 52.9729	-100.0000	79.7903	67.4777
46.000	164404.7503	28.1815	-100.0000	81.2719	64.6860
48.000	171531.0041	94.0530	-100.0000	81.2293	61.8478
50.000	178657.9378	136.0013	-100.0000	80.5668	59.0224
52.000	185784.6878	153.5452	-100.0000	80.1963	56.2491
54.000	192910.5316	152.8425	-100.0000	80.6749	53.5188
56.000	200034.6879	143.2595	-100.0000	82.1757	50.7735
58.000	207156.5941	133.6761	-100.0000	84.4375	47.9317
60.000	214275.9691	129.6142	-100.0000	86.9907	44.9259
62.000	221392.7816	132.4064	-100.0000	89.3759	41.7320
64.000	228507.2504	140.8490	-100.0000	91.2998	38.3780
66.000	235619.5941	148.9840	-100.0000	92.6905	34.9301
68.000	242730.0941	155.9173	-100.0000	93.6577	31.4647
70.000	249838.8441	159.0101	-100.0000	94.3992	28.0387
72.000	256946.0003	158.1906	-100.0000	95.1027	24.6731
74.000	264051.4382	154.7245	-100.0000	95.8790	21.3515
76.000	271155.0632	150.4125	-100.0000	96.7421	18.0344
78.000	278256.8757	146.8097	-100.0000	97.6306	14.6795
80.000	285356.9758	144.7504	-100.0000	98.4501	11.2591
82.000	292455.0633	144.2543	-100.0000	99.1171	7.7698

TABLE 6-13. Concluded

<u>Time</u> <u>(sec)</u>	<u>Angle</u> <u>(arc sec)</u>		<u>Stored Momentum</u> <u>(lb-ft-sec)</u>		
	<u>x axis</u>	<u>y axis</u>	<u>x axis</u>	<u>y axis</u>	<u>z axis</u>
84.000	299551.5633	144.8046	-100.0000	99.5814	4.2304
86.000	306646.4383	145.6175	-100.0000	99.8417	0.6720
88.000	313739.8132	146.0790	-100.0000	99.9244	-2.8743
90.000	320831.7508	145.9829	-100.0000	99.8971	-6.3869

Table 6-13 shows that initial stored momentum consists of -100 ft-lbf-sec along the x and 100 ft-lbf-sec along the z axis. As the spacecraft rotates about the x axis, the stored momentum vector remains fixed in inertial space since the system is a conservative one. In spacecraft axes, the z-axis momentum vector gradually rotates in the y-z plane until after 90 degrees of rotation it is aligned close to the y axis. This is consistent with theory and confirms the proper operation of the three-axis simulation, which shows y-axis and z-axis stored momenta to vary as the sine and the cosine of time, respectively. This also shows that in a HEAO-A application, the stored momentum vectors and hence the CMG gimbal angles must oscillate continuously.

For convenience the case used maximum stored momenta of 100 ft-lbf-sec. A CMG becomes ineffective at large gimbal angles and a limit of 60 to 70 degrees is common. If stored momentum for a scissored pair is

$$H_s = 2H \sin \alpha = 100 \text{ ft-lbf-sec},$$

and if α is limited to 65 degrees, H or rotor momentum must be

$$H = \frac{100}{2 \sin 65 \text{ deg}} = 55 \text{ ft-lbf-sec}.$$

and the gimbals oscillate continuously between ± 65 degrees from their zero position. According to one CMG manufacturer (Sperry-Phoenix), such oscillation will not reduce reliability.

Star Tracker Capture from Slew - During the mission the spacecraft must perform numerous slewing maneuvers to switch from one target (pointing direction) to another. It is shown later that a slew rate in the region of 0.03 deg/sec is convenient. An interesting question is whether the star tracker/CMG control loop is capable of initiating

control and stabilization from this slewing rate. Figure 6-19 shows motion about the y axis with an initial rate of 0.028 deg/sec (100 arc sec/sec) at 0.28 degrees from the zero position. The required pointing accuracy of 1 arc minute is reached in less than 90 seconds; the maximum overshoot is only about 0.3 degree.

This performance is satisfactory provided the overshoot is not enough for the tracker to inadvertently view another star. The problem of spacings between stars is analyzed in Section 5 of this report, where it is suggested that the tracker be capable of searching areas as small as ± 0.15 degree; this is small enough for single-star identification in the most congested regions of the sky. In the great majority of pointing directions, a much larger search area would be small enough to contain only one detectable star, and in these cases the performance indicated in Figure 6-19 would be acceptable. In congested areas, it would be necessary to improve the performance with reduced overshoot, perhaps by increasing damping.

To avoid the necessity of control system damping changes, it may be better to provide separate means for reducing rate at the end of slew so that the star tracker/CMG loop has a smaller rate to contend with. Removal of about four-fifths of slew rate would be sufficient.

It is interesting to observe the behaviour of the x and z axes during y-axis capture from the slew rate. In the run of Figure 6-19 and Table 6-14 there was no initial velocity about the x or z axis and no disturbing torque about any axis. In the absence of cross-coupling these axes would have remained undisturbed. However, Equations 6-18 through 6-20 indicate two cross-coupling terms for each axis. To observe cross-coupling, substantial initial stored momenta (60 lb-ft-sec each) were set about the x and z axes. These gave rise to

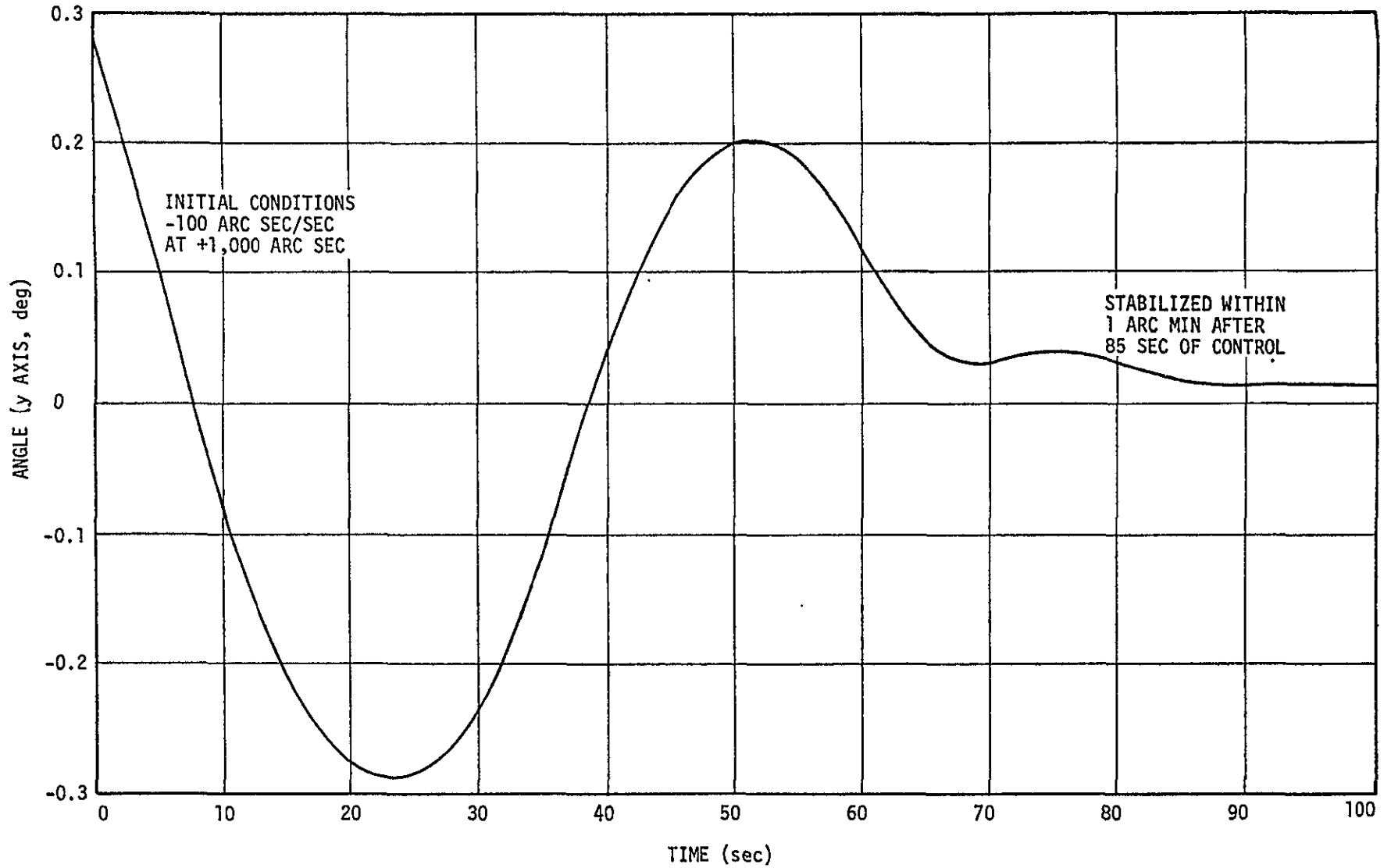


FIGURE 6-19. REFERENCE STAR CAPTURE FROM SLEW RATE

TABLE 6-14. REFERENCE STAR CAPTURE FROM SLEW RATE

Time (sec)	Angle (arc sec)			Stored Momentum (lb-ft-sec)	
	<u>x axis</u>	<u>y axis</u>	<u>z axis</u>	<u>x axis</u>	<u>y axis</u>
0.000	0.0000	1000.0001	0.0000	60.0000	0.0000
5.000	-12.8308	391.3230	- 3.3973	60.0118	- 9.9880
10.000	-45.8094	- 287.3236	- 1.8368	60.2186	- 3.6354
15.000	-57.2744	- 752.4847	10.1057	60.5928	6.3526
20.000	-34.3825	- 997.2865	12.8724	60.8020	16.3405
25.000	-10.2633	-1024.2426	9.2231	60.8189	26.3285
30.000	8.1105	- 833.9401	7.7004	60.8188	36.3163
35.000	29.3365	- 426.6107	7.3234	60.7584	46.3042
45.000	59.5154	533.8717	-11.7266	60.3434	36.1465
50.000	47.6624	713.3327	-17.6720	60.1411	26.1585
55.000	24.9856	674.7681	-13.1849	60.0056	16.1705
60.000	1.4605	425.9021	-10.0794	60.1016	8.3770
65.000	-27.8062	170.9113	- 1.8307	60.2273	15.6629
70.000	-36.0922	116.9246	9.3994	60.4414	23.8013
75.000	-15.2638	143.1025	5.3593	60.5050	22.8477
80.000	8.0581	110.5543	- 4.6773	60.4485	20.2178
85.000	10.4769	62.0763	- 2.6692	60.3665	21.3709
90.000	0.9435	52.6225	4.0356	60.3638	22.9595
95.000	- 7.9303	54.9087	2.9435	60.3809	22.7199
100.000	- 8.6800	46.4554	- 1.9309	60.4195	22.1788

appreciable $H\dot{\theta}$ terms and hence to the angular motion shown in Table 6-14. X-axis motion is greatest because of the small moment of inertia about this axis; but maximum motion is only about 1 arc minute and both axes stabilize quite well in a short time. Table 6-14 also traces the buildup of stored momentum in the x and y axes. The x axis starts with 60 ft-lbf-sec and this barely changes while the axis suppresses cross-coupling disturbances. In the y axis, stored momentum reaches a maximum of 46 ft-lbf-sec or 46 percent of saturation. The initial spacecraft angular momentum about the y axis is

$$I_y \dot{\theta}_y = 46,800 \times \frac{100}{3,600 \times 57.3} = 22.6 \text{ ft-lbf-sec}$$

and the y axis stored momentum approaches this value as the spacecraft stabilizes.

Conclusions - The most important result of the simulation work done so far is the identification of practical system parameters resulting in satisfactory performance. System operation in the pointing mode results in angular excursions of the order of 10 arc seconds or less. This indicates that total spacecraft pointing error will consist almost entirely of error in attitude measurement, due to reference gyro drift and star tracker nonlinearities.

ACQUISITION MODE

In the acquisition mode, the spacecraft aligns its z axis with the solar vector and then rotates about this axis until star tracker data provides a three-axis reference. The spacecraft is then able to slew to any desired direction. The acquisition process is subject to several constraints which will now be discussed.

The most important constraint is the duration of the sunlit portion of the orbit, which may be as short as 60 minutes. Passage into the Earth's shadow would interrupt the acquisition process; within an hour, then, the spacecraft must align itself with the Sun, develop the desired z-axis rotation, and collect enough star tracker data to establish a reference. In a following discussion on the slewing mode, it is shown that rotation of the spacecraft through 180 degrees about the high moment of inertia axes (y and z) may require 30 minutes if the control moment gyros are used. This would account for half the sunlit period. Therefore, the gas jet (despin) system is used rather than the CMGs. This can align the spacecraft toward the Sun and develop a suitable z-axis rate in a total time of not more than 5 minutes, leaving at least 55 minutes for collection of the x-axis star tracker data.

With the spacecraft in continuous rotation, the x-axis tracker points toward Earth nearly half the time on the average. To ensure that useful data is collected, the spacecraft should execute at least one complete revolution during the 55-minute period; then at least 25 minutes of useful data will be obtained. This establishes a lower limit on the scan rate about the z axis, amounting to

$$\frac{360}{55 \times 60} = 0.11 \text{ deg/sec.}$$

Suppose now that the tracker is of the fixed (non-gimballed) type similar to the existing trackers of Table 5-11. For the HEAO-C mission, it has a field of view limited to 5 degrees in diameter, because with a larger field, nonrepeatable nonlinearities would make it impossible to achieve the required 1 arc minute control accuracy. Without additional filtering, the tracker has a typical bandwidth of

5 hertz and is capable of acquiring a star within its field in not more than 1 second. To permit the tracker to make useful measurements, a star should remain within the field for 1 second to ensure acquisition, plus several tracker time constants to permit accurate measurement of star position and brightness. A total time of 1.5 seconds appears ample. Thus if a star crosses the center of the field, angular rate can be no higher than

$$\frac{5}{1.5} = 3.3 \text{ deg/sec} .$$

If the star passes 2 degrees from the center of the field, this rate is reduced to

$$\frac{2 \times 2 \sin \left[\cos^{-1} \left(\frac{2}{5/2} \right) \right]}{1.5} = 1.6 \text{ deg/sec} .$$

Thus the z-axis scan rate must lie between this and the lower limit of 0.11 deg/sec. The 2-degree off-axis restriction limits the diameter of the effective field to 4 degrees.

The dynamic range of the z-axis reference gyro must be considered also. When the spacecraft operates in the slewing mode, angular rates are in the 0.01 to 0.10 deg/sec range. It is convenient if the acquisition mode rate is about the same. Therefore the rate will be tentatively set close to the lower limit, at 0.15 deg/sec.

It is estimated that the tracker views the sky for at least 25 minutes, in which time it scans a strip of length

$$25 \times 60 \times 0.15 = 225 \text{ degrees} .$$

This is greater than a horizon-to-horizon scan of 180 degrees. Due to orbital motion, such a large scan may or may not be possible, depending upon initial conditions. This total scan might be the sum of two scans, interrupted by an Earth occultation. To be conservative in the absence of detailed calculations, it will be assumed that a single uninterrupted scan lasts for at least 150 degrees. The area scanned is

$$4.0 \times 150 = 600.0 \text{ square degrees}$$

or about 1/70 of the celestial sphere. On average, this area contains seven stars brighter than +4 magnitude, 20 brighter than +5, and 60 brighter than +6. The numbers vary considerably depending on the portion of sky viewed.

The reference about the z axis is to be established using star tracker data together with a computer-generated map of the region being scanned. The time and date are the only information needed to produce the map. During the 1.5 second or more which a star spends in its field of view, the tracker can measure its brightness to ± 0.5 magnitude or better and measure its angle about the z axis to one part in several hundred of the field of view. Since a ground-based computer can predict star angle to the z axis, these two pieces of information may be sufficient for confident identification of the first star seen. When a second star is detected, the spacing between stars provides another piece of information. It appears that if the tracker is sensitive enough to detect a minimum of three stars, very reliable identification is possible. As soon as identification is made, information on position about the z axis at a given time is transmitted to the spacecraft.

In Section 5 it was shown that the star tracker will be sensitive to at least +6 magnitude stars. Thus 60 or more stars may be

detected. It will be convenient if the star tracker includes a magnitude gate which can be set to reject stars fainter than, for example, +4 so that star identification is not confused by an excess of data.

It appears that a fixed star tracker suitable for the spacecraft pointing mode will also meet acquisition mode requirements. It is also possible to use a gimballed star tracker for acquisition of a desired reference star.

In the acquisition mode the gimballed instrument has the great advantage that it is not restricted to scanning the strip 90 degrees away from the sun. Instead, it can be set at some angle where the star pattern viewed is most easily identified. In fact, the lower sensitivity and small field of view of the gimballed tracker make such setting necessary to ensure that sufficient stars are detected. The smaller field of view (typically one rather than five degrees in diameter) reduces the upper limit on scan rate, but a rate of 0.15 deg/sec is still suitable. The basic acquisition procedure is the same as that outlined for the fixed tracker.

SLEWING MODE

In the pointing mode the spacecraft is stabilized about all three axes. In the slewing mode the spacecraft rotates about one or two axes to align the viewing experiments with a new target. For convenient operation, the spacecraft should be able to observe several targets in succession without real-time ground control, slewing from each target to the next on the basis of internally stored data. The purpose of the present analysis is to determine whether this slewing can be made sufficiently accurate for reliable identification and acquisition of a new reference star without ground control. Expected slewing errors will be determined for a typical case and compared with the requirements for reliable star identification.

The Slew Maneuver

Slewing of the spacecraft from one target to another is performed using the control moment gyros. Slewing may be about either y or z, or both spacecraft axes. When the spacecraft slews to a new position, identification of a new set of reference stars confirms correct positioning. Star identification depends upon specifying a small "target box" within the field of view, inside which the star is to appear for each of the two star trackers. Each tracker must be made to search this box only, and the box must be small enough to contain only the guide star. If the slewing error can be limited to less than half the width of the box (Figure 6-20), the requirements for onboard target shifting can be met.

The basic slewing case considered will involve travel to a target in one of the most densely populated portions of the sky. Such regions are quickly located by reference to a star atlas such as Reference 6-3; the locality of Aldebaran is a good example. From a study of several such regions, it is concluded that a box size of 0.3 by 0.3 degree is sufficiently small for even such worst cases. In other parts of the sky, the box could be several degrees in extent and the slewing accuracy requirement would be proportionately less stringent. The magnitude of the reorientation was arbitrarily taken as 10 degrees about each of the spacecraft y and z axes. This magnitude is considered to be significantly larger than a typical reorientation maneuver.

Slewing torques will be generated by the scissored CMG pairs provided for each spacecraft axis; there will be one maneuver of 10 degrees about the y axis, followed by one of the same magnitude about the z axis. In general, a deliberate slew about the x axis or pointing direction is not required as a part of the slew. Each maneuver will consist of acceleration of the spacecraft to a constant angular velocity

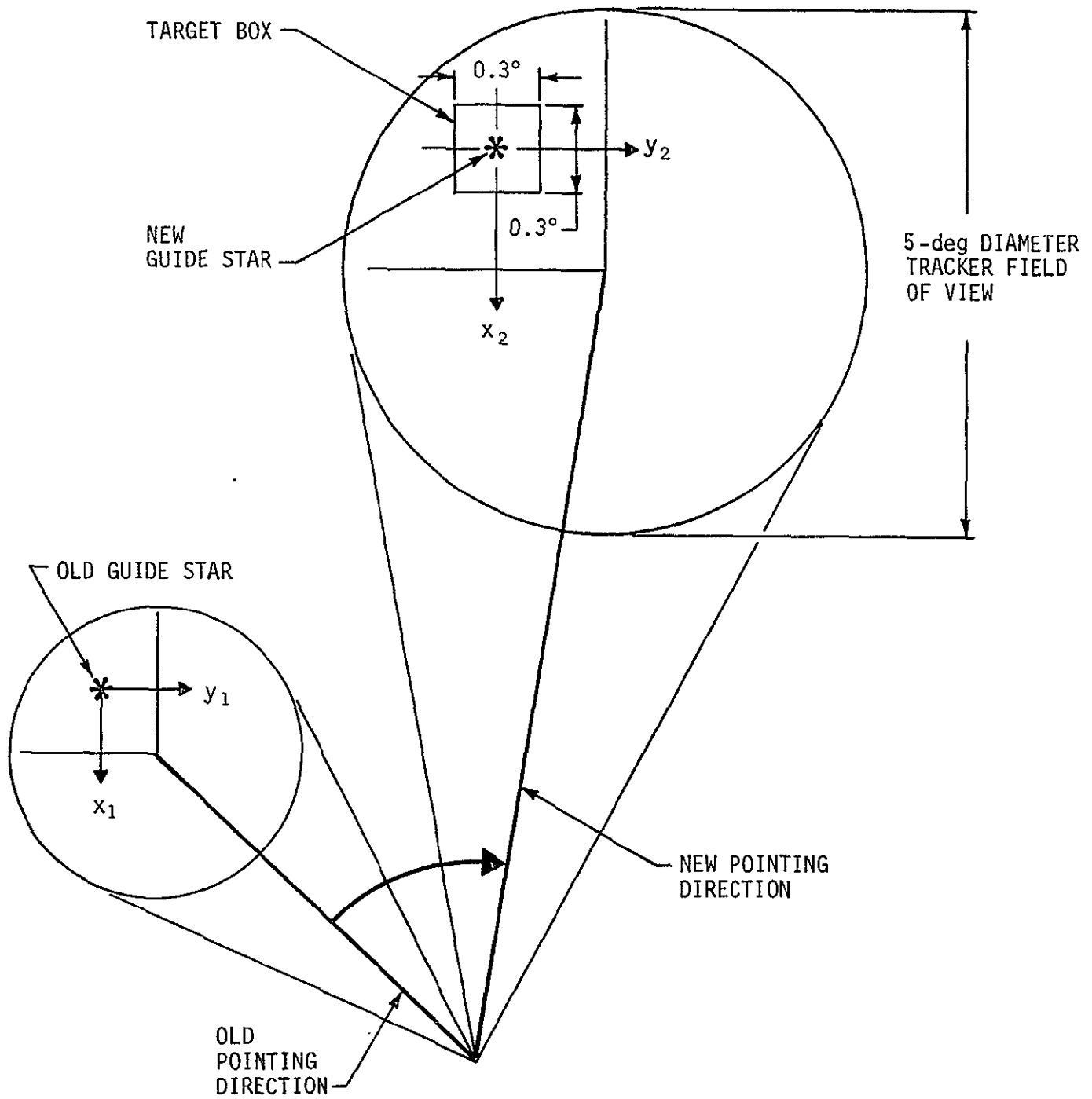


FIGURE 6-20. SLEWING MANEUVER

by application of a predetermined torque, followed by coast to some angle specified for each slew, followed by deceleration at the same torque to zero angular velocity. If the torque and acceleration/ deceleration are fixed, specification of the angle at end of coast is sufficient to specify the total angular travel. The angle at end of coast and the attainment of zero angular velocity will be measured by integration of the reference gyro outputs.

Figure 6-21 shows in simplified form how slewing is mechanized for the y axis. Normally, the mode selector is switched to HOLD and the reference gyro maintains spacecraft attitude. When slewing is scheduled, the following sequence of events occurs:

1. The desired angle to end of coast is read into the logic unit.
2. The mode selector is switched to SLEW.
3. The gyro electronics demand maximum CMG torque until the desired angular rate is attained.
4. The logic unit generates an angle demand and the spacecraft coasts until gyro output indicates that this is satisfied.
5. The logic generates a zero rate demand and the CMGs respond with maximum torque until this is satisfied.
6. While the y axis holds at zero rate, the logic unit transmits a signal to the z axis where a similar procedure is followed. However, the z axis logic unit completes the operation by returning both y- and z-axis mode selectors to the HOLD positions and initiating the star tracker acquisition mode.
7. The star tracker attempts to acquire the new guide star and verify its brightness and location within the tracker field of view. If it is successful, the mode selector transfers the attitude hold role to the reference gyro, a clock is started, and observations proceed for a predetermined time until the next slew.

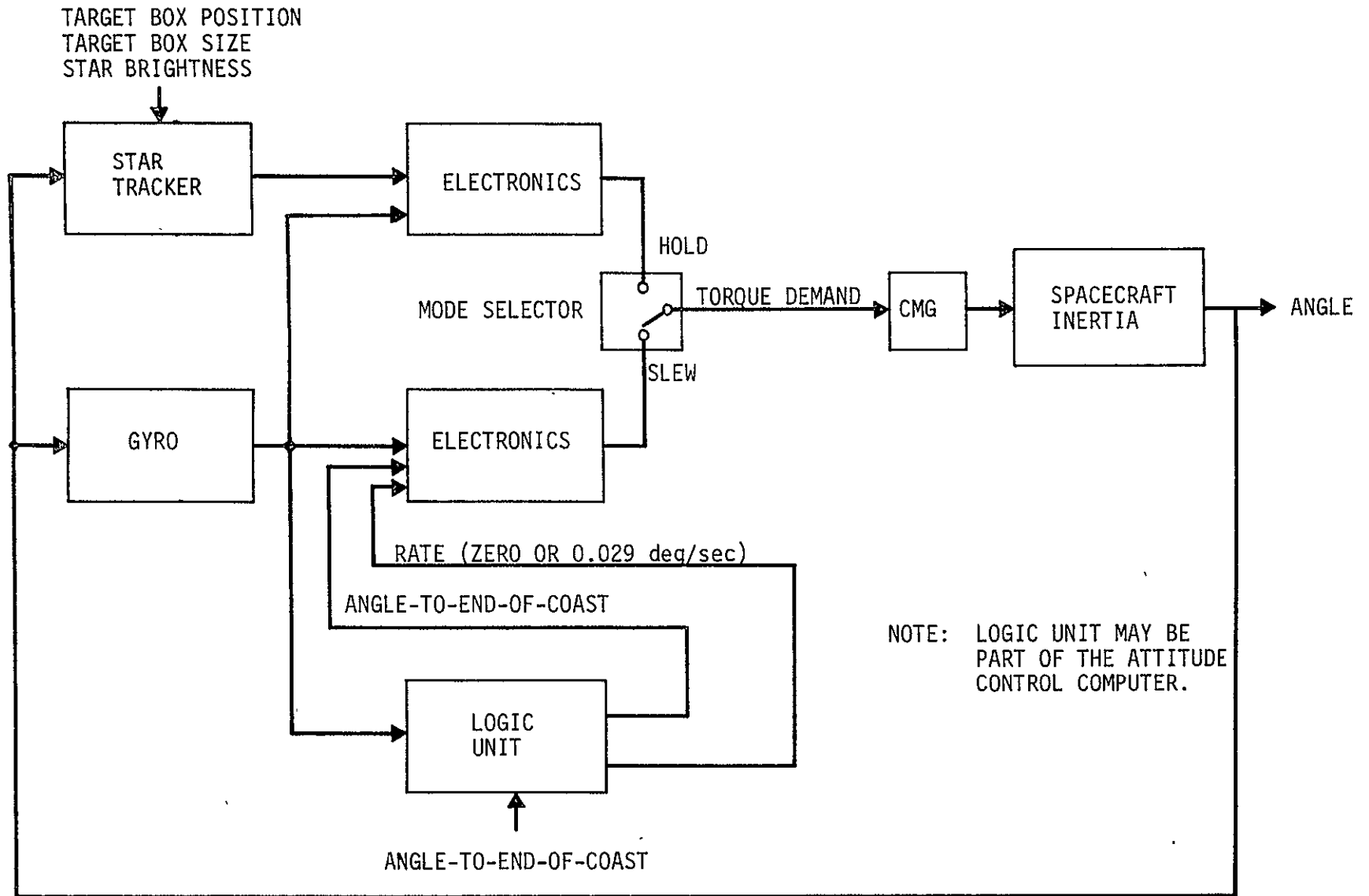


FIGURE 6-21. SLEWING MECHANISM (y AXIS)

If star identification is unsuccessful, the system may hold the first star found and transmit a LOST signal to the ground so that spacecraft attitude can be determined by examining the star field seen via the television aspect system. An alternative would be solar acquisition.

The above procedure represents only one way of mechanizing the slewing process. A survey of techniques used on actual spacecraft might show some other procedure to be more accurate or otherwise superior. No attempt has been made to compare different procedures or to identify the best one; the above serves merely as one example.

The CMGs have limited momentum capacity and are, therefore, limited in the angular rate they can give the spacecraft. A high angular rate and fast slew would ease the reference gyro drift requirement, but would leave less control moment gyro capacity remaining to deal with cyclic torque components imperfectly attenuated by the magnetic coil system. At this point it is assumed that both the y and z axis CMG pairs have available a reserve capacity of 25 lb-ft-sec per pair for slewing. Simulation of the magnetic torque CMG momentum dumping procedure indicates that this momentum reserve can be easily maintained for each spacecraft axis.

The moments of inertia of the spacecraft are somewhat less than 50 000 slug ft² about both the y and z axes. This means that the CMGs can generate a spacecraft angular rate of 0.0005 radian/sec. The next question is the time required by the CMGs to develop this rate; this is a function of their torque capacity. They may use either geared or direct drive torquers; geared torquers are capable of much higher torque, but they also exhibit backlash, friction, and other disadvantages from which the direct drive is free. The direct drive can generate about 1 lb-ft of torque; this is believed to be adequate for HEAO-C requirements, so that direct drive will be assumed. To leave a comfortable

performance margin, the slewing analysis will be based on a figure of 0.5 lb-ft torque total for a CMG scissored pair which is only 0.25 lb-ft per CMG or one-quarter the capacity of the torquer. The corresponding angular acceleration of the spacecraft is 10^{-5} rad/sec².

At a torque level of 0.5 lb-ft, the y axis CMG pair can develop the full spacecraft angular rate in 50 seconds. During this time, the spacecraft rotates through 0.72 degree. At this point the CMG pair reaches its momentum limit and rotation of its gimbal ceases; that is, no further torque is applied. In a 299-second coasting period, the spacecraft rotates through a further 8.56 degrees. At this point the logic unit, which monitors gyro output, generates a zero-angular-velocity command and the CMGs apply a torque of -0.5 lb-ft for 50 seconds. During deceleration, the spacecraft travels through a further 0.72 degree bringing total travel about the u axis to 10.0 degrees. Figure 6-22 shows the operation graphically. It is followed by a similar operation about the z axis, resulting in a total displacement from the original position of about 14 degrees. For both axes, the torque level of 0.5 lb-ft and the slew rate of 0.0005 rad/sec (0.029 deg/sec) are constants written into the onboard attitude control program. The angle at end of coast (9.28 degrees in the case of the y axis) determines the magnitude of slew and is calculated to allow for probable deceleration time. The calculation is done on the ground and the resulting requirement stored in the onboard attitude control program.

Slewing Errors

Several sources of error in the slewing maneuver can be identified; the following major sources will be considered in an analysis of these errors:

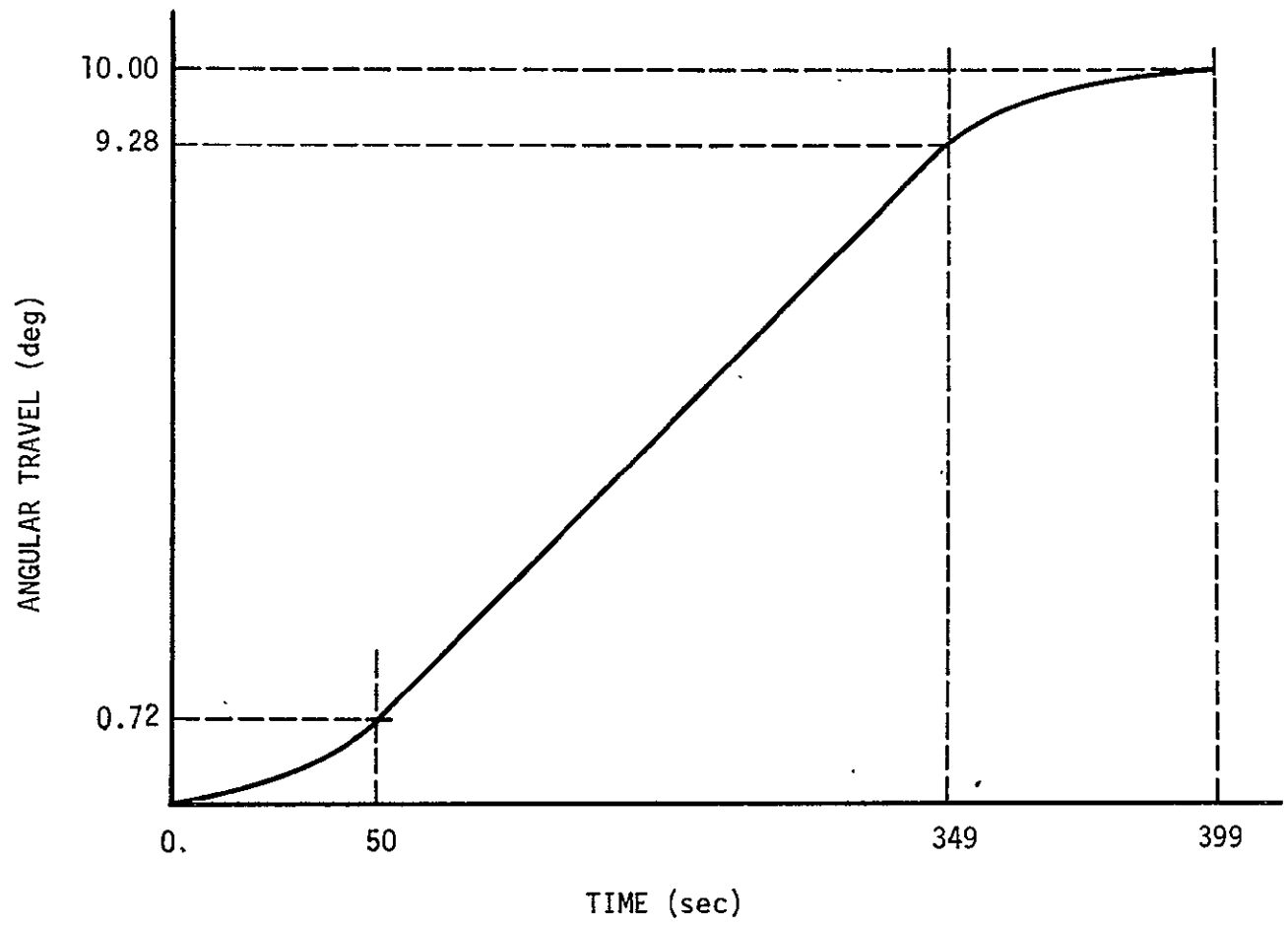
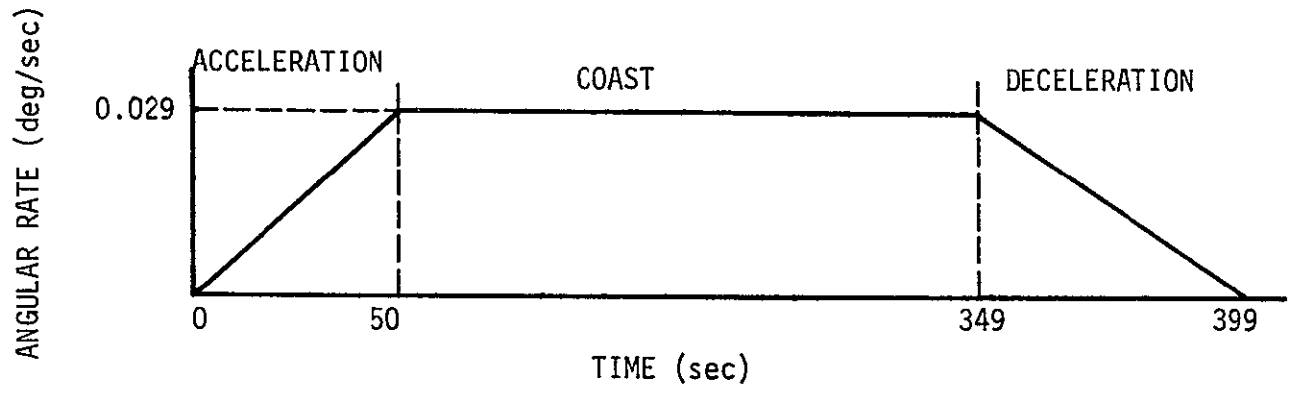


FIGURE 6-22. TEN-DEGREE SLEW

- Initial position about the x axis
- Initial position about the y axis
- Reference gyro drift during the maneuver
- CMG torque
- CMG transient.

No attempt will be made to analyze minor factors such as bit quantization, electronic integrator drift, gyro resolution, or angular velocity at the start of the slewing maneuver.

Initial Position About the X-Axis - Slewing is initiated by the reference gyro, which demands the rates and angles required for slewing. At the moment of control transfer, the spacecraft will in general have some positional error about each axis. The x axis control loop is required to maintain position about the x axis to within ± 5 minutes of arc; this requirement is taken as a 3-sigma value of initial position error. This error contributes to total slewing error in two ways.

First, if the old reference star is not at the center of the x axis tracker field of view, an x rotation appears to the tracker as a motion about the y and z axes. This cross-coupling would significantly affect system accuracy in the pointing mode. It is therefore taken into account by the spacecraft computer which combines data from all three axes, provided by the x axis tracker and a second tracker located on the z axis, to determine the actual angle about each individual axis. These angles are stored in the computer and, therefore, have no effect on slewing accuracy.

A second effect of error about the x axis does not seriously alter pointing mode performance and therefore is not considered in that mode. It does have an impact on slewing accuracy, however. An x rotation of 5 minutes of arc (0.083 degree), which is allowable in the pointing mode, results in a tilt of the y axis of the same amount.

Therefore slewing occurs, not about the nominal, but about the new y axis position. For a 10-degree slew, the resulting error is

$$\sin^{-1} [(\sin 10 \text{ deg}) (\sin 0.083 \text{ deg})] = 0.0167 \text{ degree} .$$

Initial Position About the Y-Axis - The y axis control loop is required to maintain an accuracy of ± 1 minutes of arc or 0.0167 degree. This is taken as a 3-sigma value and adds directly to other y axis slewing errors.

Reference Gyro Drift - During slew about the y axis, the y axis reference gyro ensures that the desired rates and angles are attained and the x and y axes gyros operate to maintain zero angular rate about their respective axes. Gyro drift, expressed in units of angular rate, normally consists of a predictable and regular rate which can be allowed for plus a smaller, random component with some maximum 3-sigma value, D deg/sec. In a total slewing time t , the rotation about each axis is Dt . The rotation about the y axis adds directly to other sources of error; rotation about the x axis changes the y axis pointing direction by an angle Dt in the yz plane; and rotation about the z axis changes y axis direction by Dt in the yx plane.

Each of these changes in y axis direction occurs linearly during the time t , so that the average effect is a change $Dt/2$. With a slew through 10 degrees the effect on final end of slew position is

$$\sin^{-1} [(\sin Dt/2) (\sin 10 \text{ deg})]$$

or approximately

$$\frac{\pi}{180} \times 10.0 \times Dt/2 \text{ radians}$$

since the angles involved are small.

The reference gyros not only control slewing, but in the pointing mode, they also enable the y-z and the x axis star trackers to reacquire their guide stars after Earth occultation. With maximum occultation time of 0.6 hour, and a target box 0.30 degree by 0.30 degree square, error in two axes must not exceed

$$\frac{0.15 \text{ deg}}{0.6 \text{ hr}} = 0.25 \text{ deg/hr.}$$

or, for one axis,

$$\frac{0.25}{\sqrt{2}} = 0.18 \text{ deg/hr.}$$

Since this value cannot be exceeded, it can be regarded as a 3-sigma value. This is the gyro drift performance that is available to control slewing.

During a slew through 10 degrees, the y-axis gyro measures angular travel at the end of 349 seconds (Figure 6-22). Its drift error at this time is

$$\left(\frac{349}{3600}\right) (0.18) = 0.0175 \text{ degree.}$$

The x- and z-axis gyros operate (in the hold mode) throughout the slew, so that their drift is given by

$$\frac{Dt}{2} = \left(0.18\right) \left(\frac{399}{3600}\right) \left(\frac{1}{2}\right) = 0.00999 \text{ degree (each)}$$

and their contributions to error about the y-axis are each

$$\left(\frac{\pi}{180}\right) (10.0) (0.00999) = 0.0017 \text{ degree.}$$

CMG Torque - Since the reference gyro measures angle at end of coast, it does not matter how long the spacecraft takes to reach coasting speed. However, the end-of-coast angle specified must be calculated based on some assumed rate of CMG deceleration. If the CMG is regarded as a constant-gain device with a simple first-order time constant, uncertainties in deceleration time and deceleration travel are two-fold: uncertainties in actual torque level and uncertainties in the time constant.

Torque commands applied to the CMG are met by its internal feedback loops; a change in CMG gain would be due to the aging of certain internal electronic components. One percent is a safe figure for such variations. For deceleration through a given angular velocity, the distance travelled will also vary by 1 percent or in this case 0.0072 degree.

CMG Transient - The magnitude of the effective CMG time constant is a function of mechanical and electrical scale factors but it also covers static friction and dead zone effects; these nonlinearities make analysis of the actual transient a complex matter. It is suggested that in the course of CMG development it will be possible to predict the transient shape to an accuracy of at worst 20 percent (3-sigma). This is believed to be a conservative figure. The CMG bandwidth is at least 3 hertz, corresponding to an equivalent time constant no greater than

$$t = \frac{1}{2\pi f} = 0.054 \text{ second}$$

to which may be added the gyro constant which is typically 0.006 second, making a total of 0.060 second. The uncertainty corresponds to 0.012 second (20 percent) in both torque-on and torque-off times, or a total of 0.024 second for the complete deceleration process. This results in a residual velocity upon arrival at the target position of

$$\begin{aligned}\dot{\theta}_r &= \ddot{\theta} \times \Delta T = 0.024 \times 10^{-5} = 2.4 \times 10^{-7} \text{ rad/sec} \\ &= 1.4 \times 10^{-5} \text{ deg/sec}\end{aligned}$$

and this velocity must be nulled by the star tracker-CMG loop to maintain lock on the star. It also results in an uncertainty in distance travelled during deceleration which amounts to

$$\frac{0.024 \text{ sec}}{50 \text{ sec}} \quad 0.72 \text{ deg} = 0.00035 \text{ degree.}$$

The slewing errors expected for the y axis are summarized in Table 6-15. Identical figures apply to the z axis. The total slewing error is much smaller than the 0.15-degree half-width of the target box. The 3-sigma gyro drift of 0.18 deg/hr corresponds to a 1-sigma figure of 0.06 deg/hr. Gyros with much better performance are commercially available. Table 6-7 describes one suitable instrument, which, because of gas spin bearings, is quite capable of running for the required 2-year mission time. This makes it possible for the spacecraft to carry out both functions, post-occultation reacquisition of the guide star, and slewing to new stellar targets using internal stored information, without real-time ground control. Nonreal-time verification of spacecraft attitude is available from telemetered star field data for each new position.

TABLE 6-15. Y-AXIS SLEWING ERROR BUDGET

<u>Error Source</u>	<u>Error (deg)</u>
Initial position, x	0.0167
Initial position, y	0.0167
Gyro drift, y	0.0175
Gyro drift, x	0.0017
Gyro drift, z	0.0017
CMG torque	0.0072
CMG transient	<u>0.0004</u>
Expected 3-sigma value of total error*	0.0304

*Assuming:

1. Errors have a mean of 0 and a normal distribution.
2. Errors are statistically independent.

Additional Considerations

The above analysis of slewing performance has not taken into account several factors, all of which show the analysis to be a conservative one.

- Much of the uncertainty in gyro drift, CMG torque, and CMG transients is assumed to be due to component aging. These gradual changes could be identified and followed by telemetry and nonreal-time analysis, and could be taken into account in determining the magnitude of the commanded angle-to-end-of-coast.
- The position at start of slew has been assumed unknown, within a ± 1 minute of arc range. In fact the instantaneous position could be measured and taken into account by the system to improve slewing accuracy.
- The size of the target box has been assumed of fixed size, this size having been fixed by examination of the most densely populated portions of the sky. System reliability would be further increased at the expense of data volume by making box size a variable specified separately for each slew. In the great majority of cases a much larger box would suffice to ensure correct star identification.
- The accuracy analysis has been carried out for a 10-degree slew only. Larger slews could be subject to larger errors, but these would remain within box limits. The experimental program might be planned so that densely populated areas would be approached by a short and highly accurate slew from a nearby X-ray target, rather than by a less accurate long slew.

Table 6-16 lists the data to be stored for each slew to a new target. No number is assigned to individual slews, which are simply executed in the order in which they are stored in the onboard computer program. The duration for which a given attitude is held between slews may be specified at any value from 1000 seconds to 16,000 seconds in 1000-second steps; the angle of slew may be up to 80 degrees in 0.01-degree increments, so that a single slew may bring the spacecraft to

TABLE 6-16. SLEWING DATA REQUIREMENTS

Duration of observation, sec	1000 to 16,000	1000	16	4
y slew, deg	0.01 to 80.0	0.01	8000	13 + sign bit
z slew, deg	0.01 to 80.0	0.01	8000	13 + sign bit
Box center (x), deg	0.0 to 3.0	0.05	60	6 + sign bit
Box center (y), deg	0.0 to 3.0	0.05	60	6 + sign bit
Box side length, deg	0.2 to 2.0	0.1	19	5
Maximum magnitude	-1.0 to +6.5	0.5	16	4
Magnitude range	0.5 to 2.0	0.5	4	2

NOTE: Number of bits required to specify each slew = 57 bits.

anywhere over one-half of the celestial sphere. The target box may be centered anywhere within the field of view of the tracker and the size of the box itself may be varied over a wide range. Maximum magnitude specifies the upper limit of star brightness; this, plus magnitude range, specify the brightness range within which the new guide star should lie. A total of 57 bits are required for each slew; for a typical observational program involving 5,000 targets, this would be equivalent to 15,000 19-bit words.

GAS THRUSTOR SYSTEM

System Design

The basic spacecraft attitude control system, using magnetic coils and control moment gyros (CMG), is designed to operate at low torque levels and to minimize stored angular momentum. When the HEAO-C spacecraft separates from its launch vehicle at the beginning of the mission, it has some residual angular momentum which is best eliminated by a relatively high-torque system so that the spacecraft solar panels can be quickly oriented toward the Sun. Until solar orientation is achieved, the spacecraft must rely on internal (battery) power.

The detailed logic of despun and solar acquisition has not been analyzed, because these details have very little effect on overall HEAO weight and performance. Well-established logic schemes have been demonstrated in existing spacecraft and this area presents no new problems.

HEAO work has been based on a maximum initial angular rate of 3 deg/sec or 0.052 radian/sec. The maximum moment of inertia of the spacecraft is somewhat less than 50,000 slug ft² (y axis). If the angular momentum vector is oriented entirely along this axis, it

will have a magnitude of 2,600 lb-ft-sec. Jet Propulsion Laboratory experience with the Ranger and Mariner series of spacecraft has shown that a specific impulse of 60 seconds can be expected of a system which expands nitrogen through a nozzle of large area ratio. If the moment arm of the control jets is known, the amount of gas required can be estimated. The y axis jets are located at opposite ends of the spacecraft, about 15 feet from the center of gravity on either side. This gives a first approximation of gas consumption as

$$\frac{2600}{60 \times 15} = 2.89 \text{ lb .}$$

However, typical despun logic does not necessarily give minimum gas consumption. The present system may require as much as 50 percent more than the theoretical amount of 4.3 pounds; this is because available thrust may not always be directed in the most efficient way relative to the instantaneous angular momentum vector.

The spacecraft must then rotate toward the Sun. It will be shown below that 1.9 pounds of gas are sufficient for a 180-degree turn about the y or z axis in less than 200 seconds. If a substantial further margin is allowed, a total nitrogen weight of 10.0 pounds should be sufficient for both requirements. The assumed angular rate of 3 deg/sec is high for so large a vehicle, and so it is probable that in fact a substantial amount of nitrogen would remain unused. It could presumably be used in a backup mode for slewing or solar reacquisition at a later time in the mission.

Because of the large size of the spacecraft and the low jet thrusts desired, the system is divided into two self-contained modules located at opposite ends of the spacecraft. Each module includes a

nitrogen tank, six control valves for the x, y, and z axes, and six jets, together with the usual valves, filters, and transducers as will be described shortly.

Each module, then, contains 5.0 lb of nitrogen. This can be stored at 200 atmospheres in a 10.5-inch diameter tank. A titanium tank of about this size was used in a similar role on Mariner 4 and would be appropriate here. Table 6-17 gives a weight breakdown of the complete system; Figure 6-23 shows the components of one module, and Figure 6-24 shows how the jets are connected to the attitude control system to generate the desired couples. Nitrogen tank weight is based on the use of a standard titanium alloy such as Ti-6Al-4V, with a 0.12-inch wall to give a substantial safety factor and with a 20 percent allowance for weld beads, connection boss, etc. Two squib valves, one normally open (NO) and the other normally closed (NC), control gas flow to the pressure regulator; the latter reduces gas pressure to some value convenient for the jets and their control valves. The best pressure level would be chosen following an investigation of such factors as required gas line size and the transient response of both the regulator itself and the slugs of gas residing in the lines. Actual attitude control systems of this kind have generally used pressures of the order of 100 lb/in². A filter is provided to protect the regulator and control valves from minute fragments which the squib valves might possibly inject into the gas stream. Tank pressure, regulator output pressure, and tank temperature are telemetered. Provision is also made for telemetering squib valve signals to verify reception of the open and close commands. If desired, the signals at the jet control valves could be telemetered also.

TABLE 6-17. GAS SYSTEM WEIGHT BREAKDOWN (TWO UNITS)

<u>Item</u>	<u>Weight (lb)</u>
Tank (one 10.5-in. diameter Titanium)	7.5
Nitrogen	5.0
Two Squib Valves	0.6
Fill Valve and Filter	0.3
Tank Temperature Transducer	0.2
Two Pressure Transducers	0.5
Filter	0.3
Regulator	1.0
Lines	2.9
Six Electric Valves	3.0
Six Jets	2.0
Wiring Harness	2.5
Mounting Hardware	<u>3.2</u>
Total for One Unit	29.0
Second Identical Unit	<u>29.0</u>
TOTAL FOR SYSTEM	<u><u>58.0</u></u>

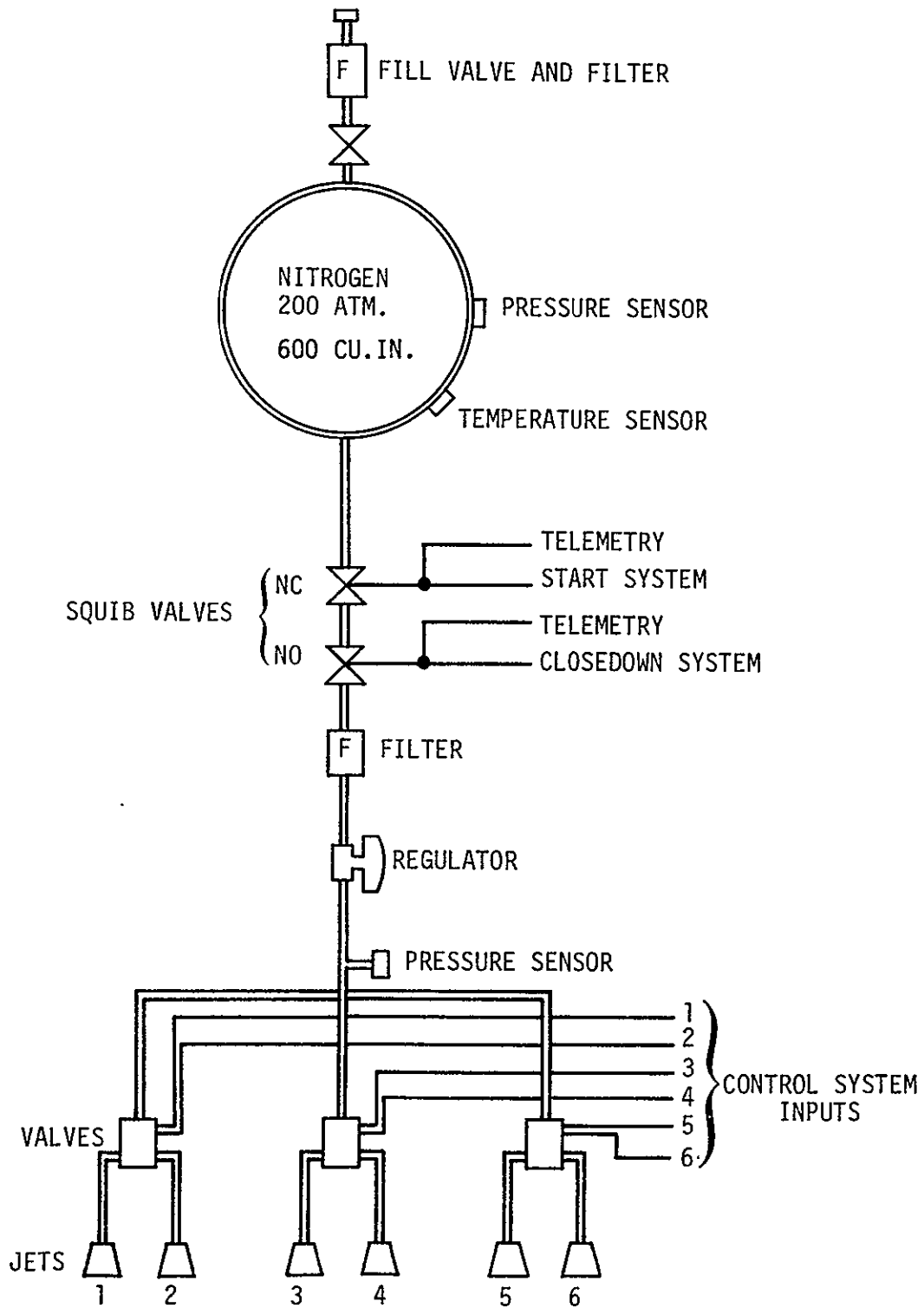


FIGURE 6-23. GAS THRUSTOR UNIT (ONE OF TWO)

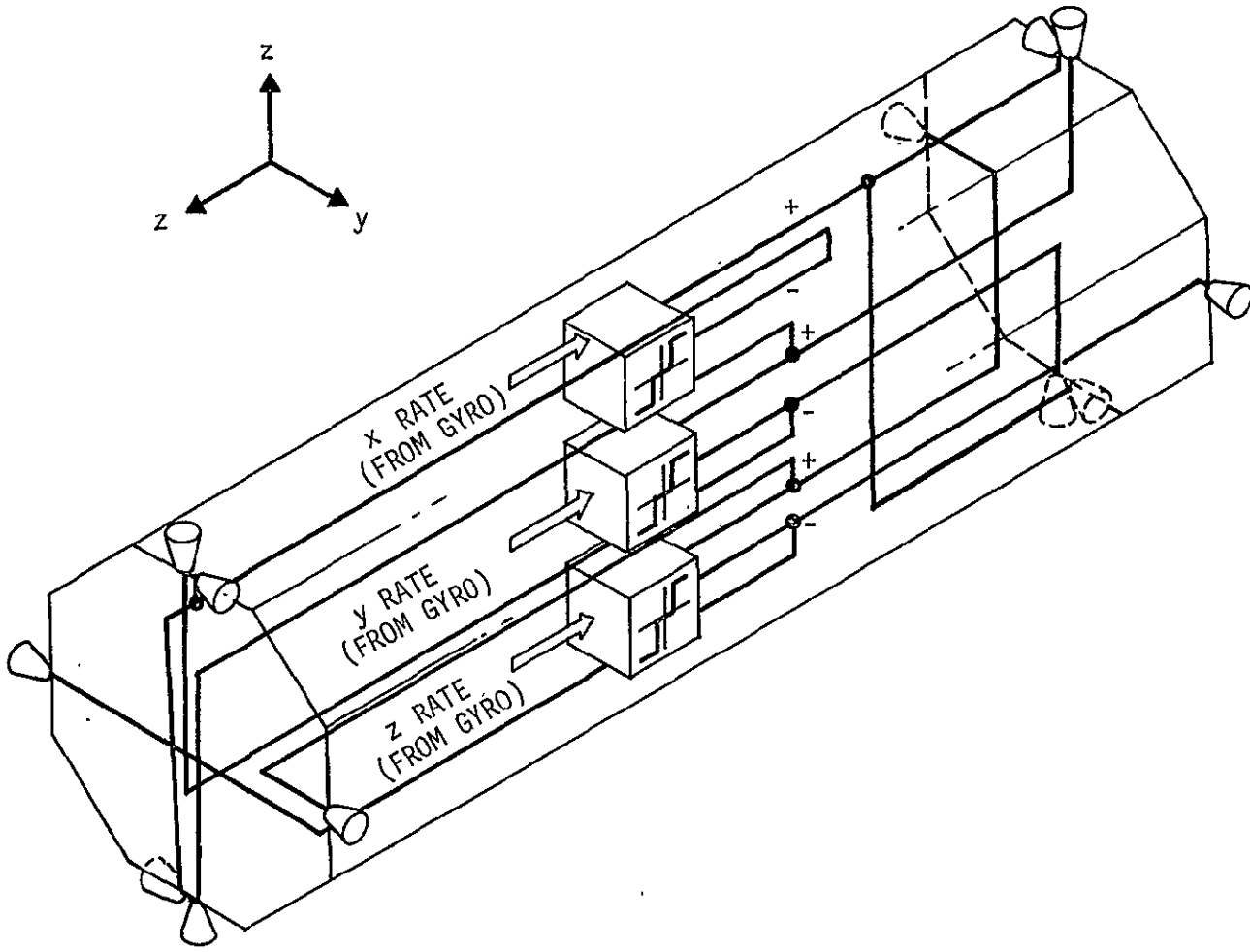


FIGURE 6-24. GAS THRUSTER SYSTEM MECHANIZATION (FOR TWO-UNIT SYSTEM)

W

The total of 58 pounds for the two modules represents a very small fraction of total spacecraft weight. The use of hydrazine rather than nitrogen would have resulted in a specific impulse higher by about a factor of four, with a proportionate reduction in propellant weight; however, the overall system weight saving would have been small. Because of the small weight penalty, nitrogen is chosen for greater convenience in handling and loading the system.

Required Thrust Level - The required system thrust level is of interest. A single set of reference gyros will be used for measurement of angular rate during despin and also for an attitude reference in the pointing mode. The first application requires acceptance of relatively high angular rates; the second requires attainment of low gyro drift rate. The Kearfott gyro described in Table 6-7 is suitable for both roles. It can accept an angular rate as high as 3.06 deg/sec for 30 seconds. This limitation is imposed by heat dissipation in the gyro torquer. The heat generated would be approximately the same if the gyro experienced a rate falling uniformly from 3.06 deg/sec to zero in a period of 60 seconds. To provide a margin of safety, the gas system will be tentatively sized to reduce this rate to zero in only 30 seconds. The required angular acceleration is

$$\ddot{\theta} = \frac{0.052}{30} = 0.0017 \text{ radian/sec}^2$$

and if this occurs entirely about the y axis (highest moment of inertia), the required thrust for each jet on this axis is

$$\frac{50,000 \times 0.0017}{2 \times 15} = 2.8 \text{ lb}$$

since this axis has two jets each with a moment arm of 15 feet. The system is most conveniently mechanized if the same thrust is used on the x axis. For this axis the moment arm is only 4.3 feet and the moment of inertia 4600 slug-ft². The use of two jets results in an angular acceleration of

$$\theta = \frac{2 \times 2.8 \times 4.3}{4600} = 0.0052 \text{ radian/sec}^2$$

If the system threshold is set at zero angular rate, the actual angular rate attained will depend largely on the system time constant. This is for all practical purposes equal to the time constant of the jet valves. From data on other similar valves, this is estimated at not more than 0.03 second. Multiplied by system angular acceleration, this indicates a residual rate of 0.0029 deg/sec or 10.5 seconds of arc/sec for the case of the y axis and 0.0089 deg/sec or 32.4 seconds of arc/sec for the x axis. These levels are low enough for a convenient transition to reference gyro attitude control. This suggests that the thrust and acceleration suggested are a reasonable compromise. A lower acceleration would of course give lower residual angular velocity, but would also require longer for despin and would impose a greater heat load on the gyro torquer.

System specific impulse is based on the assumption of constant nitrogen temperature (68°F). During continuous discharge of gas, the nitrogen tends to cool as its potential energy (pressure) is converted to kinetic energy in the jet nozzles. Eventually an analysis should be carried out to determine the line and valve size and nozzle design required to prevent a serious drop in temperature and hence in specific impulse. If this occurred, it might be necessary to use relatively

large nozzles with electrical heating. Any electrical power requirement arising here would be small because of the short time required for despin.

A quick calculation indicates a jet orifice diameter of about 0.14 inch for 2.8 pounds thrust. With an expansion ratio of 50 to 1 for a highly efficient nozzle, the maximum cone diameter would be only 0.99 inch and the entire nozzle could be machined from a block of metal occupying less than 2 in³.

The location of all jets at the ends of the spacecraft presents a possible cross-coupling problem. The x-axis jets would ideally be located at the longitudinal station containing the spacecraft center of gravity; at present, any misalignment of the x-axis jets will result in a spurious torque about the y or z axis. It should not be difficult to maintain jet alignment of 0.5 degree or approximately 0.01 radian; this would result in a couple about the y axis of

$$2 \times 2.8 \times 0.01 \times 15 = 0.84 \text{ lb-ft}$$

which is less than the available y-axis control torque by a factor of more than 100. This suggests that the cross-coupling effect will not be a major problem.

Rotation Toward Sun - When despin is complete, the spacecraft is rotated toward the Sun. Suppose that this requires a full 180 degrees of rotation about the y axis. Then if the appropriate jets are first operated for 10 seconds, the spacecraft will develop an angular velocity

$$\begin{aligned}\dot{\theta}_y &= \ddot{\theta} t = 0.017 \text{ rad/sec} \\ &= 0.97 \text{ deg/sec}\end{aligned}$$

and will cover, during acceleration, a distance of

$$\begin{aligned}\theta_y &= \frac{1}{2} \ddot{\theta} t^2 = 0.085 \text{ radian} \\ &= 4.9 \text{ degrees.}\end{aligned}$$

If it then coasts for 176 seconds the spacecraft will rotate through 170.2 degrees, at which point 10 seconds of deceleration will bring total travel to 180 degrees in a time of 196 seconds. This time is satisfactorily short, and gas consumption for two 2.8-pound jets each thrusting for 20 seconds total is only

$$\frac{2 \times 2.8 \times 20}{60} = 1.87 \text{ pounds.}$$

Single-Unit Version - The complete jet system is designed in two independent units. If it is thought that any reliability advantage is not worthwhile, the system could be designed instead as a single module mounted at one end of the spacecraft, with six jets and six valves providing three-axis control. In the thrust regions of interest, hardware weight is only very slightly sensitive to rate of gas flow, so most components would weigh about the same as for a single unit. Only the tank, nitrogen, and tank mounting hardware would be heavier and as Table 6-18 shows, there would be a reduction of net weight from 58 to 43 pounds.

Such a system would not generate balanced couples; each operation of a jet would result in translation as well as rotation of the spacecraft. The net translation occurring during gas system operation would depend on the detailed history of despin and rotation toward the Sun. But whatever that history, the effect can never reach

TABLE 6-18. GAS SYSTEM WEIGHT BREAKDOWN (SINGLE UNIT)

<u>Item</u>	<u>Weight (lb)</u>
Tank (One 13-inch diameter Titanium)	15.0
Nitrogen	10.0
Two Squib Valves	0.6
Fill Valve and Filter	0.3
Tank Temperature Transducer	0.2
Two Pressure Transducers	0.5
Filter	0.3
Regulator	1.0
Lines	2.9
Six Electric Valves	3.0
Six Jets	2.0
Wiring Harness	2.5
Mounting Hardware	<u>5.0</u>
SYSTEM TOTAL	<u><u>43.3</u></u>

the result of discharging the full 10-pound nitrogen supply through a nozzle aligned through the spacecraft center of gravity. Even in this hypothetical case the spacecraft, weighing approximately 15,000 pounds, would undergo a net velocity change of only

$$\frac{10 \times 60}{15,000} \times 32.2 = 0.78 \text{ ft/sec}$$

which would result in changing future orbital position by less than 1 mile. Orbit position is not at all critical to HEAO-C operations. Even a shift of several miles would be unimportant. Therefore, the single-unit system is quite acceptable from this standpoint.

Use in Slewing Mode

Earlier it was shown that the CMGs are limited in torque to about 2 lb-ft/axis. At some points in the experimental program it is desirable to make several observations of an x-ray source with the spacecraft in positions 90 degrees apart about the x axis or optical axis. These measurements are to be carried out entirely during a Sun occultation period, so that the spacecraft can be reoriented toward the Sun as soon as it emerges from the Earth's shadow. With the torques available from the CMGs it is not easy to slew sufficiently rapidly to leave much observing time. Therefore, it is of interest to determine to what extent the gas jet system could be used in a fast slewing role.

It would be desirable to carry out three observations, 90 degrees apart, and to travel a further 90 degrees to the original orientation within 21 minutes. The x-axis jets can accelerate the spacecraft at 0.0052 radian/sec². In 4 seconds, they can bring angular velocity from

0 to 1.20 deg/sec; during this time the spacecraft would rotate through 2.40 degrees. Seventy-one seconds of coasting would allow for rotation through a further 85.2 degrees, and deceleration to zero rate would bring total rotation to 90 degrees and total time to 79 seconds. If an additional 30 seconds is allowed for the CMG control system to damp slewing rates below 1 second of arc/sec, the total maneuver time for four 90-degree maneuvers in 7.3 minutes. This leaves a time of 4.6 minutes for each of the three observations, which is almost twice as long as the times permitted with CMG maneuvering.

Gas consumption is found by dividing total impulse by specific impulse, the total thrusting time being 8 seconds.

$$\begin{aligned} \text{Total Impulse} &= 2 \times 2.8 \times 8 \text{ lb-sec} = 45 \text{ lb-sec} \\ \text{Specific Impulse} &= 60 \text{ seconds} \\ \text{Gas Used} &= 0.75 \text{ pounds.} \end{aligned}$$

Initial operations are unlikely to leave enough gas for more than one or two 90-degree fast slews; a single complete rotation requires four such maneuvers. If fast slew capability was strongly desired, hydrazine could be used in place of nitrogen. If the total weight for the two units was increased from 58 to 150 pounds, the system could contain at least 80 pounds of hydrazine. Hydrazine has about four times the specific impulse of nitrogen, so this would be enough for

$$\frac{80 \times 4}{0.75} = 427 \text{ 90-degree fast slews}$$

or for 106 complete rotations with observations at 90-degree intervals. It would be necessary to investigate the possible effect of jet plume on the optical equipment to ensure that the exhaust would disperse satisfactorily without interfering with observations. In this respect,

hydrazine is one of the least offensive rocket propellants due to the low temperature and molecular weight of its exhaust.

If the gas system is used for despin and initial orientation, it needs to operate only for a short time at the beginning of the mission. If it is designed to be useful later in the mission, its reliability and lifetime become a matter for concern and it may be necessary to use a more complicated configuration than Figure 6-23 indicates. Suitable arrangements of redundant valves and other long-life features have been successfully developed for planetary spacecraft where operating lifetimes of years are required.

HEAO-B AND -D MISSIONS

Attitude Control Requirements

The attitude control requirements for the B mission are the same as for the A mission:

- Attitude hold of the spacecraft scan axis (z) to within one —degree of the desired direction in the scan mode
- A scan rate of the spacecraft about the z axis of 0.1 rpm.

There is no requirement for attitude control of the HEAO-D spacecraft for operation of the experiment payload.

Orbits and Mass Characteristics

The B mission launch date is 1975 and the orbit will be a 200-nautical-mile circular orbit inclined at an angle of 28.5 degrees to the equator. The D mission launch date is 1977 and the orbit will be a 300-nautical-mile circular orbit inclined at an angle of 35 degrees to the equator.

The mass moments of inertia about the principal spacecraft axes are approximately:

- HEAO-B: $I_x = 3,900 \text{ slug-ft}^2$
 $I_y = 46,000 \text{ slug-ft}^2$
 $I_z = 46,300 \text{ slug-ft}^2$

- HEAO-D: $I_x = 3,600 \text{ slug-ft}^2$
 $I_y = 36,100 \text{ slug-ft}^2$
 $I_z = 36,300 \text{ slug-ft}^2$.

The significant disturbing torques expected to be acting on the HEAO A, B, C, and D spacecraft are listed in Table 6-19. The estimated magnitudes of these torques are also given in this table.

Suitability of Mission A System for B and D Missions

HEAO-B Mission - The attitude control system for mission A consists of:

- A RCS unit: This is primarily used for acquisition and reorientations of the scan axis.

- A flywheel rotating at a constant speed: The axis of the flywheel is along the scan axis and the angular momentum is 2,000 ft-lbf-sec. The flywheel provides some stability to the scan axis.

- Magnetic torquers: Magnetic torquers are used for the attitude and rate control of the scan axis in the scanning mode and for attitude control of the optical axis in the pointing mode. The magnetic torquers are sized to provide control torques equal to gravity torques.

Table 6-19 shows that the disturbance torques expected for mission B are much larger than mission A. This is due primarily to

TABLE 6-19. DISTURBANCE TORQUES ACTING ON THE HEAO SPACECRAFT FOR MISSIONS A, B, C, AND D

	<u>HEAO-A</u>	<u>HEAO-B</u>	<u>HEAO-C</u>	<u>HEAO-D</u>
Launch Date	1974	1975	1976	1977
Altitude (n.mi)	200	200	300	300
Maximum Torques (ft-lbf)				
Gravity Gradient	0.070	0.080	0.080	0.060
Aerodynamic ¹	0.007	0.008	0.0004	0.0016
Magnetic ²	0	0.132	0	16.3

¹Aerodynamic torques for missions A and B were taken as 10% of the maximum gravity gradient torque. Aerodynamic torques for missions C and D were calculated based on average 2σ atmospheric density for the launch year date. The center of pressure and center of mass for the D spacecraft were assumed to be the same as those for the C spacecraft.

²Magnetic disturbance torque for the B mission is caused by magnetization of the magnetic shields and the resulting interaction with the Earth's field. Magnetic disturbance on the D mission is caused by the reaction of the magnetic moment of the magnetic spectrometer experiment coil with the Earth's field.

the magnetic disturbance torque on B. If it is assumed that the spacecraft of mission B has a flywheel similar to that of the mission-A spacecraft, and assuming further that a disturbance torque of 0.20 ft-lbf (magnetic plus gravity torque) is acting normal to the scan axis, then the scan axis of the spacecraft will deviate 1 degree in less than 4 minutes. Without the flywheel the scan axis of the spacecraft under the same conditions will deviate 1 degree in about 40 seconds. From this it can be seen that though the flywheel is able to provide some stability to the scan axis, it is not enough to meet the B mission requirements or to justify the weight (240 lbm) and power (55-watt average) requirements. Therefore the HEAO-A attitude control system is not expected to fulfill the HEAO-B mission requirements.

The use of two very strong Alvarez electromagnets, for experiments use only, poses a very serious problem in the use of magnetic torquers for attitude control. The presence of the magnetic field due to the Alvarez electromagnets and the induced magnetic moment in the spacecraft components will degrade the performance of the magnetic torquers. Furthermore the size of the magnetic torquers for mission B will be larger than that of mission A because of large disturbance torques. This large size of the magnetic torquers will have strong magnetic field and this in turn may require additional shielding of the spacecraft components near the vicinity of the magnetic torquers.

From the above analysis it appears that an extensive study is required to determine the feasibility of magnetic torquers for mission B.

Attitude control by use of reaction control system (jet thrusters) can of course be achieved at the cost of excessive weight penalty in terms of propellant weight required for two years mission.

A combination of magnetic torquers and reaction control system may look attractive and should be investigated.

HEAO-D Mission - Since the HEAO-D mission payload will include the single coil magnetic spectrometer experiment (Ref. 6-4), the axis of this coil will tend to align itself with the geomagnetic field vector \vec{B} . It is assumed that the coil axis will coincide with the spacecraft longitudinal, or x axis. The only presently identified requirement for spacecraft attitude control on the D mission is possibly to maintain the sides of the spacecraft on which the solar panels are mounted toward the Sun. This amounts to single axis (x axis) attitude control.

A large flywheel on the y axis of the HEAO-D spacecraft might be useful in limiting roll about the x axis. However, an additional attitude control subsystem such as reaction jets would also be required for initial alignment and for periodic adjustments. A simpler system would utilize only reaction jets to provide control about the x axis. Since the disturbing torques about this axis are small, the propellant requirements would not be excessive.

Control torques about the x axis could not be provided by magnetic torquers as long as the x axis were aligned with the geomagnetic field vector \vec{B} . As mentioned above the magnetic spectrometer experiment will exert a large torque, perhaps as much as 16 ft-lbf, to align the x axis with B. However the result may be oscillation of the x axis about \vec{B} (Ref. 6-4). In this case magnetic torquers on the y and z axes could periodically exert control torques about the x axis. Fine control about the x axis would not be required, also disturbing torques about the x axis are expected to be minimal. This system is believed to be more appropriate for the HEAO-D mission than the use of a HEAO-A type flywheel.

REFERENCES - Section 6

- 6-1. Nichol, K. C., "Research and Investigation on Satellite Attitude Control - Part I" and "Investigation of Space Vehicle Attitude Control Techniques - Part II", Technical Report AFFDL-TR-64-168, Air Force Flight Dynamics Laboratory, Wright Patterson Air Force Base, Ohio, March 1965
- 6-2. Steputis, Fred J., "Advanced Astronomy Mission Concepts - Volume III", Subsystem Design, Martin Marietta Corporation Denver, Colorado, April 1969

7. THERMAL CONTROL ANALYSIS

The objectives of the thermal control analysis described herein were to

- Evaluate the capability of the thermal control concept proposed in Reference 7-1 to maintain the temperature levels and thermally-induced deformations of the proposed HEAO-C experiment packages within acceptable limits
- Establish an overall thermal control concept, incorporating the experiment thermal control system proposed in Reference 7-1, for maintaining all spacecraft systems and subsystems within acceptable operating temperature limits.

Based on the results of a preliminary analysis, it was concluded in Reference 7-1 that excessive misalignment of the mirror and detector assembly axes, caused by thermally-induced bending of the spacecraft during orbit, would preclude mounting the mirror assemblies and experiment packages directly to the spacecraft structure. Hence, the experiment thermal control concept illustrated schematically in Figure 7-1 was proposed. In this concept, the mirror assemblies and experiment packages are mounted to a common truss structure, referred to as the "optical bench", which is constructed of Invar to reduce dimensional changes caused by temperature excursions. The optical bench is connected to the spacecraft only at its ends. After orbit insertion, the bench is decoupled from the spacecraft structure at the nonviewing end. This prevents the thermal bending of the spacecraft from deflecting the optical bench. The limited number of contact points also facilitates control of the bench temperature within narrow limits.

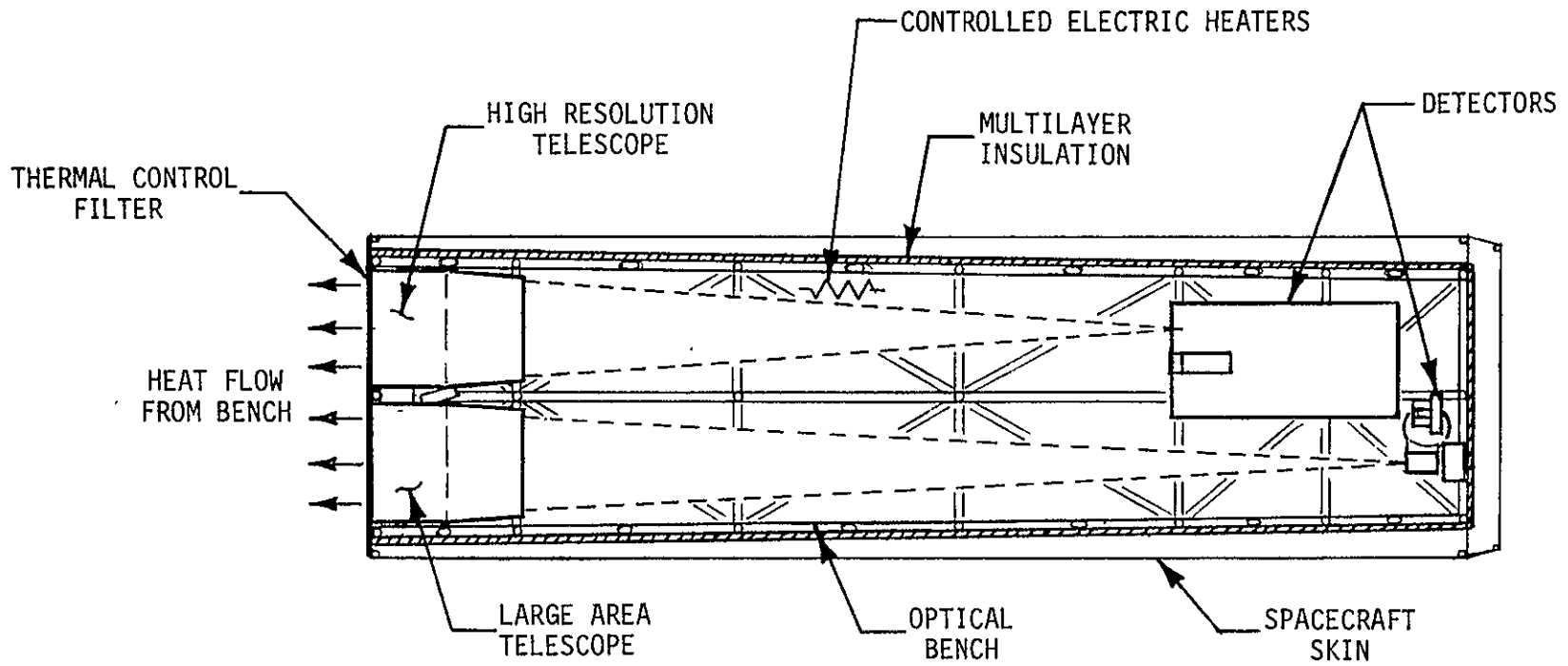


FIGURE 7-1. PROPOSED HEAO-C THERMAL CONTROL SCHEME

The optical bench, except for the viewing end, is completely enclosed by highly-efficient multilayer insulation. A thin "thermal control filter" is located in front of the viewing end to increase the thermal resistance between the mirrors and the space environment. Virtually all heat generated by the experiment packages inside the optical bench is transferred to the thermal control filter, from which it is ultimately radiated to space. Thus, the optical properties of the thermal control filter are of paramount importance in determining the operating temperatures of the mirrors and experiment packages inside the optical bench. The thermal control filter is designed to reject the maximum possible heat dissipation from inside the bench under most severe environmental heating conditions, while maintaining the bench temperature at an acceptable level. Small electrical heaters inside the optical bench will be activated to supply heat inside the bench when experiment heat dissipation rates are less than maximum.

Most subsystems are located between the optical bench and the outer spacecraft structure. Heat generated by these subsystems is radiated to space by the spacecraft skin. The mosaic crystal was assumed to be in the extended position, with the angle between the centerline of the spacecraft and the plane of the mosaic crystal equal to 50 degrees.

THERMAL DESIGN REQUIREMENTS

Optical Bench

The primary thermal design requirements of the HEAO-C experimental package, as specified in Reference 7-1, are:

- Control of the focal plane of the high resolution mirror to within ± 0.004 -inch axial displacement and ± 0.01 -inch lateral displacement
- Maintenance of parallelism of the optical axes of the two telescopes to within ± 1 -arc minute.

The approach that was followed in establishing the design goal for acceptable operating temperature limits of the optical bench was to determine the temperature limits corresponding to each of the design requirements described above, and then to adopt the most stringent of these limits as the design goal. First, the requirement which limits the maximum axial displacement, ΔL_f , of the focal plane to ± 0.004 inch dictates that the mean bench temperature, T_m , must remain within the limits of $70^\circ\text{F} \pm 16^\circ\text{F}$. These limits were estimated from the relation

$$L_f = L_f \alpha_b (T_m - T_o) \quad (7-1)$$

where

- L_f - the focal length of the high resolution mirror, 312 inches
- α_b - the thermal expansion coefficient of Invar, 8×10^{-7} in/in $^\circ\text{F}$
- T_o - the mean temperature of the optical bench during calibration (assumed to be 70°F).

The design requirement which limits the lateral displacement, δ , of the focal plane to ± 0.01 inch dictates a maximum difference between the mean hot side and cold side temperatures of the optical bench of 19.3°F . This requirement may be explained with the aid of Figure 7-2, which illustrates the thermal bending of the optical bench. The displacement of the bench axis δ is related to the lateral temperature difference ΔT by the relation

$$\delta = \frac{\alpha_b L_b^2 \Delta T}{2D} \quad (7-2)$$

where

L_b - optical bench length, 360 inches

D - optical bench mean diameter.

Substituting the appropriate values of δ , L_b , α_b and D into Equation 7-2 and solving for ΔT yields the maximum allowable lateral temperature difference of 19.3°F or $\pm 9.6^\circ\text{F}$.

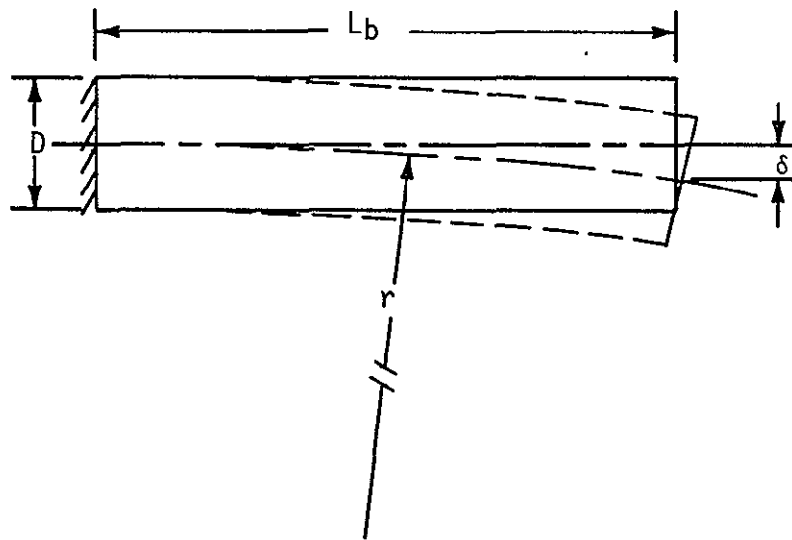


FIGURE 7-2. ILLUSTRATION OF THERMALLY INDUCED BENDING OF THE OPTICAL BENCH

Thus, the thermally induced lateral movement of the focal plane relative to the detector assembly will be controlled to within ± 0.01 inch provided the temperatures of all points on the optical bench are maintained within the limits of $\pm 9.6^\circ\text{F}$ around some reference temperature level. Now, assuming that the coefficient of thermal expansion, α_b , is invariant with temperature, the thermally induced bending of the optical bench is dependent on the temperature difference across the

bench, ΔT , rather than on the selected reference temperature level. However, when the other thermal design requirements are taken into consideration, i. e., allowable axial displacement of focal plane and acceptable telescope temperatures, it becomes essential to choose a reference temperature level that is equivalent to the temperature of the optical bench during preflight calibration, T_0 . Assuming T_0 is 70°F , the acceptable temperature limits of all points on the optical bench for satisfactory control of thermally induced lateral displacement of the focal plane become $70^\circ\text{F} \pm 9.6^\circ\text{F}$.

From a thermal design standpoint, maintaining parallelism of the optical axes of the two telescopes within ± 1 arc minute depends primarily on control of the mirror temperatures to within acceptable limits. The Cervit mirrors are held by annular rings of Invar, whose coefficient of thermal expansion is approximately eight times larger than that of Cervit. Therefore, a decrease or increase in temperature from the design point will result in a tightening or loosening, respectively, of the Invar rings on the mirrors, resulting in an angular deflection of this mirror contour. An accurate determination of the acceptable mirror temperature limits would require a rather detailed structural analysis to account for the interactions between the Invar support rings and the Cervit mirrors subject to a specified temperature distribution. Such an analysis is beyond the present scope of work. Therefore, the mirror operating temperature limits recommended in Reference 7-1 ($70^\circ\text{F} \pm 10^\circ\text{F}$) were adopted as requirements for the present study.

From a collective consideration of all of the cases considered above, it is apparent that a sufficient, but not necessary, condition for satisfaction of all of the thermal design constraints of the optical bench is maintenance of the temperatures of all points within the optical bench, including telescopes, experiment packages, and truss members, within

the limits of $70^{\circ}\text{F} \pm 9.6^{\circ}\text{F}$. Therefore, a thermal design goal was established to control the entire optical bench assembly to within the temperature limits of $70^{\circ}\text{F} \pm 9.6^{\circ}\text{F}$.

Spacecraft Structure

The primary thermal design requirements of the spacecraft structure call for minimization of solar panel operating temperatures and of temperature gradients within the spacecraft's aluminum framework. The former requirement exists because of the inherent decrease in power conversion efficiency of solar cells with increasing operating temperature. Although the power supply was designed based on a conservatively high estimate of average operating temperature, methods of reducing the solar panel temperature will result in an increased margin of power availability.

It is important to minimize temperature gradients within the spacecraft structure to reduce thermally induced bending to the maximum extent possible. The spacecraft is designed to provide adequate clearance between the outer structure and the optical bench even with thermally induced deflections corresponding to a conservatively high lateral temperature difference of 366°F . (This maximum lateral temperature difference was predicted from a simplified thermal analysis during the early stages of conceptual design.) However, minimization of thermally induced bending is desirable to reduce reliability penalties that must accompany the cyclic deformation of the spacecraft over a long duration (2-year mission) as it continuously travels into and out of the Earth's shadow.

Experiments and Subsystems

The required heat dissipation rates and allowable temperature limits of the HEAO-C experiments and subsystems are presented in

Table 7-1. Unless noted otherwise, the listed heat dissipation rates are average values that must be rejected continuously. The allowable temperature limits of 14 to 86°F for the experiment sensor packages were prescribed in Reference 7-1. Thermal design of the solid state detector package, a critical problem area, was not treated in the present scope of work.

The thermal design approach for the optical bench consisted of specification of optical properties of the thermal control filter which would result in rejection of the maximum expected heat dissipation from inside the optical bench under the most severe environmental heating conditions, while maintaining the bench at an acceptable temperature level. For conditions of less than maximum heat dissipation by the experiments, small electrical heaters inside the optical bench would be activated to maintain the required temperature levels therein. Examination of Table 7-1 reveals that the maximum possible heat dissipation requirement inside the optical bench will be 35 watts, and will occur when all experiments except the high resolution image detector are activated simultaneously. (The high resolution image detector and the high resolution crystal spectrometer cannot be operated simultaneously.)

Concerning heat dissipation outside the optical bench, the thermal model considered all of those components listed in Table 7-1 that are to be located outside the bench to be operating continuously, including the electronics module for the high resolution image detector (19 watts). The latter electronics module was assumed to be operational in the thermal model although its associated experiment package inside the optical bench is assumed to be deactivated, as discussed previously. This assumption permitted simulation of the maximum heat dissipation requirements both inside and outside the thermally isolated optical

TABLE 7-1. HEAT DISSIPATION REQUIREMENTS FOR HEAO-C
EXPERIMENTS AND SUBSYSTEMS

<u>Components</u>	<u>Number of Units</u>	<u>Heat Dissipation per Unit (W)</u>	<u>Allowable Temperature Limits (°F)</u>
<u>Experiments</u>			
High Resolution Image Detector	1	13.5**	14 to 86
Electronics Module	1	19.0	160 max
High Resolution Crystal Spectrometer	1	21.0*	14 to 86
Large Area Image Detector	1	1.0*	14 to 86
Electronics Module	1	13.5	160 max
Multiple Polarimeter	1	1.0*	14 to 86
Electronics Module	1	8.6	160 max
Solid State Detector	1	2.0*	14 to 86 ^{††}
Electronics Module	1	6.2	160 max
Mosaic Crystal	1	0.0	Unknown
Electronics Module	1	0.5	160 max
Flare Detectors			
Coarse Detectors	4	1.0	Unknown
Fine Detectors	1	0.0	Unknown
Electronics Modules	5	6.4	160 max

* Inside optical bench

** Inside optical bench, but not operated simultaneously with high resolution crystal spectrometer

† Increases to 130 watts per unit for approximately 12 minutes per orbit

†† Exterior surface

TABLE 7-1 - Continued

<u>Components</u>	<u>Number of Units</u>	<u>Heat Dissipation per Unit (W)</u>	<u>Allowable Temperature Limits (°F)</u>
<u>Experiments</u>			
Scintillation Counter	1	11.0	14 to 86
Monitor Proportional Counter Electronics Module	1	1.0	14 to 86
	1	8.0	160 max
Flat Crystal Spectrometer Electronics Modules	1	2.0*	14 to 86
	2	7.5	160 max
<u>Subsystems</u>			
Aspect Detector Electronics Module	1	8.0*	14 to 86
	1	6.0	160 max
Data Management Computer	1	145.0	0 to 120
Charger-Battery-Regulator Modules	9 (7 active)	70.0	-20 min; 0 to 32 preferred
Load Distributor	2	30.0	-40 to 120
Tape Recorders	4 (1 active)	15.0	0 to 130
S-Band Decoder/Transmitter	2	30.0	160 max
Diagnostic Logic	1	3.0	160 max
Command Decoder	1	4.0	160 max
Signal Conditioner	1	8.0	160 max

TABLE 7-1 - Concluded

<u>Subsystems Component</u>	<u>Number of Units</u>	<u>Heat Dissipation per Unit (W)</u>	<u>Allowable Temperature Limits (°F)</u>
Command Receiver	2	0.4	160 max
S-Band Power Amplifier	2	15.0 [†]	160 max
Multiplexer	1	5.0	160 max
Solar Combiners	7	15.0	-85 to 374
Star Tracker	3	10.0	0 to 140
Diplexer	1	10.0	160 max
Electromagnetic Control Torquers	3	7.0	-30 to 120
Reference Gyros	3	10.0	0 to 140
Magnetometer	1	6.0	-30 to 120
Power Combiner	1	--	160 max
Switching Network	2	--	160 max

bench with the same thermal model. Since the optical bench is almost perfectly isolated from its surroundings by multilayer insulation, this assumption yields valid temperature predictions for maximum heat dissipation rates both inside and outside the bench, although these two conditions will not exist simultaneously during an actual flight.

ANALYTICAL APPROACH

Determination of Environmental Heating Rates

Environmental heating rates of the external surface of the HEAO-C spacecraft were predicted using the Lockheed 140 Node Heat Rate Program (Ref. 7-2). Heating rates were determined for the four spacecraft/orbit orientations illustrated in Figure 7-3. The prescribed orbital altitude was 300 nautical miles, and the prescribed angle of inclination of the orbit plane to the equator was 35 degrees. Cases I and II (Figure 7-3) considered the spacecraft to be oriented broadside-to-the Sun with the angle β^1 equal to 58.5 and 0 degrees, representing the maximum and minimum durations of direct solar illumination, respectively. Case III considered the spacecraft longitudinal axis to be tilted 15 degrees toward the Sun, continuously, with the angle β equal to 58.5 degrees. This case represents the requirement for continuous 15 degree off-axis viewing, and yields the most severe continuous heat rejection requirement for the optical bench thermal control filter. Case IV considered the spacecraft longitudinal axis to be tilted 30 degrees toward the Sun, with the angle β equal to 58.5 degrees. It is noted that the orientation represented by Case IV will occur only during approximately one orbit per day. Because of the large thermal inertia of the spacecraft, only those structural elements

¹The angle β is the angle between the Earth-Sun line and the orbit plane, measured in a plane perpendicular to the orbit plane.

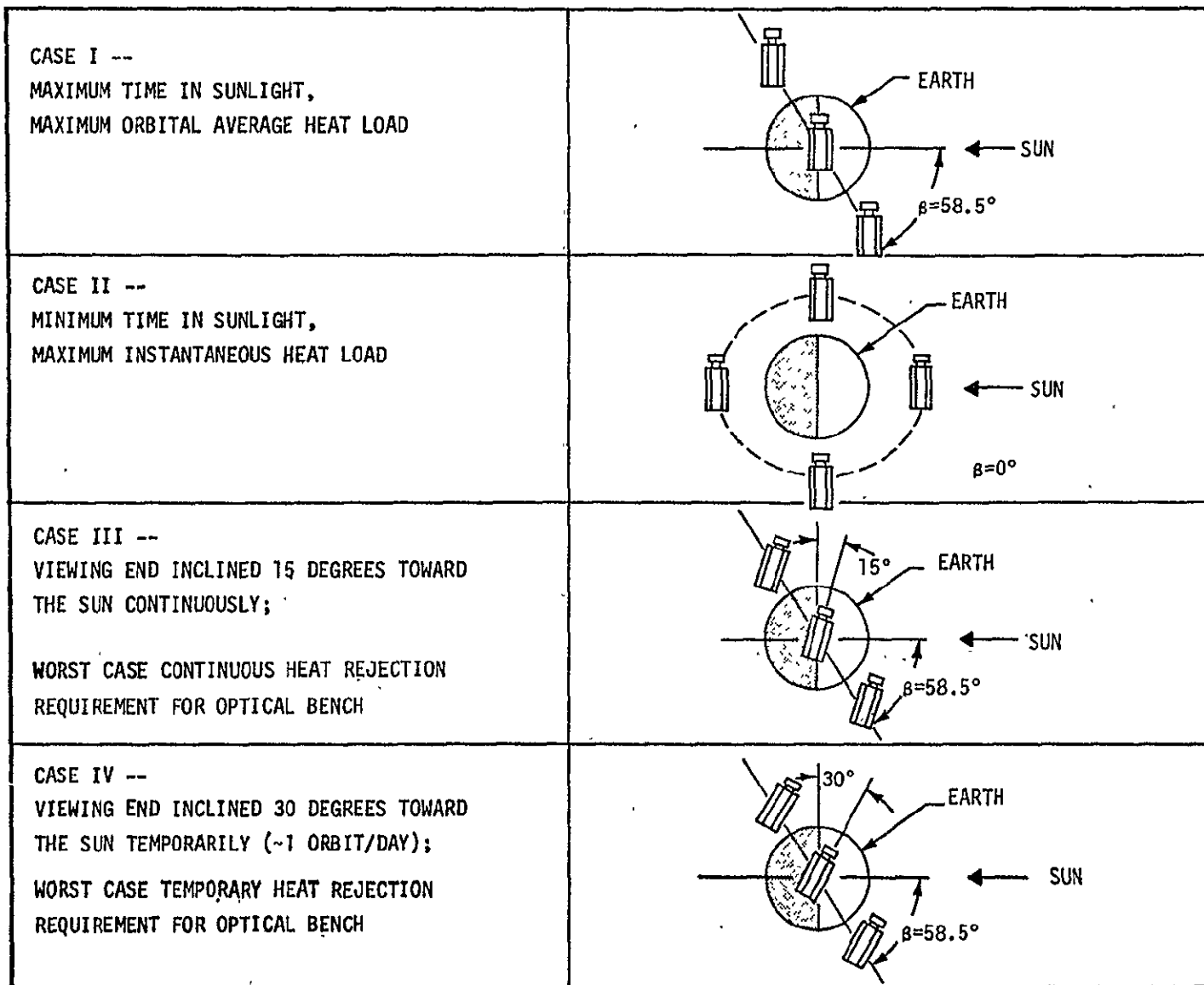


FIGURE 7-3. SPACECRAFT ORBIT/ORIENTATIONS CONSIDERED IN THERMAL ANALYSIS

near the exterior surfaces will exhibit a substantial deviation in temperature response characteristics due to the temporary 30-degree off-axis orientation. Values of solar absorptivity, α_s , and infrared emissivity, ϵ , assumed in this analysis for the external surfaces are listed in Table 7-2. The optical properties of the solar panels were taken from Reference 7-3. The solar absorptivity of 0.71 takes into account the fact that a fraction of the incident solar energy is converted into electrical energy when the solar cells are active, and is not available to increase the internal energy (temperature) of the material. The values of α_s (0.22) and ϵ (0.24) of the spacecraft side panels and top end correspond to Fuller Aluminum Silicon Paint (171-A-152) as described in Reference 7-4. This less emissive thermal control coating was selected after a preliminary analysis considering Z-93 ($\alpha_s = 0.35$, $\epsilon = 0.85$) as the coating for these spacecraft skin surfaces resulted in predicted minimum temperatures of some of the components that were below the allowable limits presented in Table 7-1. Components having predicted temperatures below the limit were control moment gyros, redundant CBR modules, magnetic coils, star trackers, and reference gyros. Of course, if other considerations indicate a strong desirability for utilizing a highly emissive surface coating, e.g., Z-93, other thermal design alternatives for elevating selected subsystem operating temperatures (added insulation, louvers, equipment relocation, etc.) should be investigated.

TABLE 7-2. ASSUMED OPTICAL PROPERTIES OF EXTERNAL SURFACES

<u>Surfaces</u>	<u>α_s</u>	<u>ϵ</u>
Solar Panels	0.71	0.82
Spacecraft Side Panels and Top End (Station 370)	0.22	0.24
Thermal Control Filter	0.4	0.06
Monitor Proportional Counter Face	0.4	0.06
All Other External Surfaces	0.5	0.5

The assumed optical properties of the thermal control filter ($\alpha_s = 0.4$, $\epsilon = 0.06$) are representative of aluminized Mylar, the filter material recommended in Reference 7-1.

The optical properties of the exposed face of the monitor proportional counter are also representative of a thin layer of aluminized Mylar. Aluminized Mylar was selected to cover the face of the monitor proportional counter because it satisfies the requirement for raising the thermal resistance between the experiment and the space environment and is also transparent to X-rays in the applicable energy range of 0.2 to 4.0 KeV.

Optical properties of the few remaining external surfaces, i. e., the viewing faces of the scintillation counter, aspect detector, mosaic crystal spectrometer, star tracker and magnetometer were undefined at the time of this study. In the absence of any better definition of the optical properties of these surfaces, a rather arbitrary assumption was made that they were covered by a fictitious coating having medial values of α_s (0.5) and ϵ (0.5).

The environmental heat source constants used in the analysis were:

- Solar Constant - $429 \frac{\text{Btu}}{\text{hr/ft}^2}$
- Earth Albedo - 0.3
- Earth Emission - $68 \frac{\text{Btu}}{\text{hr/ft}^2}$

These values represent nominal environmental heating conditions. It is important to note that deviations of the environmental constants due to seasonal variations, variations in cloud cover and measurement

uncertainties would result in significant changes in predicted orbital heating rates and temperature responses. These deviations should be accounted for through performance of a sensitivity analysis during a later phase of the spacecraft design.

Prior to prediction of the environmental heating rates, the spacecraft external configuration was transformed into a thermal model that was compatible with the orbital heat rate simulation program, as illustrated in Figure 7-4. The exposed surfaces of the spacecraft were represented by a total of 57 surface nodes. The thermal control filter, located at the viewing end of the optical bench, and the mosaic crystal spectrometer, which protrudes ahead of and shades the viewing end, were represented by two surface nodes each. The remaining exposed instrument faces were represented by one surface node each. The nodal representations of all other exposed surfaces were as shown in Figure 7-4.

Evaluation of Spacecraft Temperature Response

The temperature response of the entire spacecraft to the predicted environmental heating rates was evaluated through utilization of the Chrysler "CINDA" digital computer program (Ref. 7-5). In this solution technique, the physical system is first transformed into an equivalent thermal resistance-capacitance network which is input to the CINDA program. The program then employs finite difference techniques to solve for the transient temperature response of the nodal network, subject to input boundary heating conditions.

For the CINDA model described herein, the HEAO-C spacecraft was divided into a total of 363 nodes. Of these, 57 nodes were coincident with the 57 surface nodes considered in the orbital heat rate simulation described previously. In addition, 180 nodes represented the optical bench structure and multilayer insulation, as

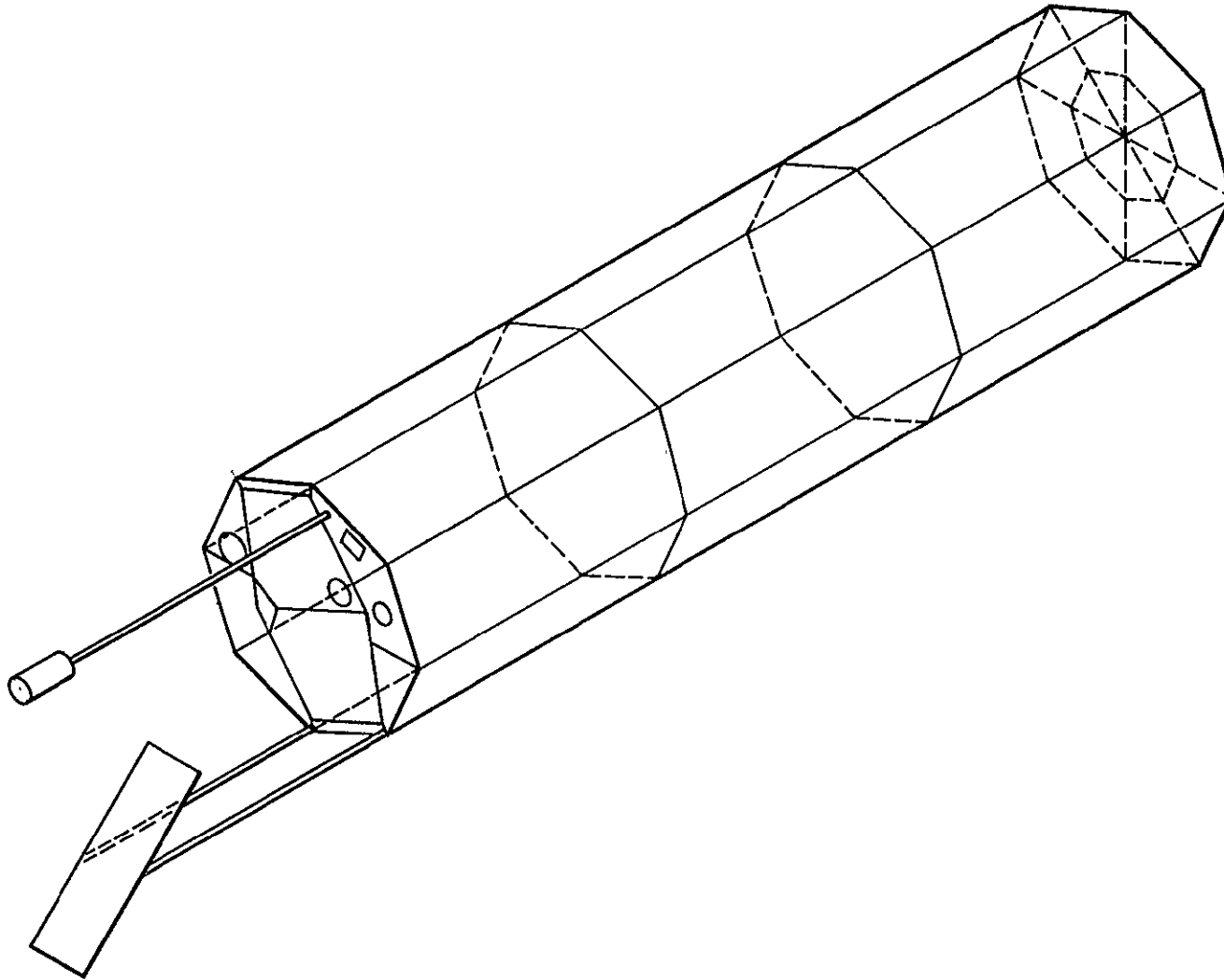


FIGURE 7-4. NODAL REPRESENTATION USED IN THERMAL MODEL TO DETERMINE SPACECRAFT ORBITAL HEATING RATES

illustrated in Figure 7-5. The insulation thickness was 1.5 inches, as prescribed by thermal design personnel from American Science and Engineering, the agency responsible for the study (Ref. 7-1). Calculation of the equivalent thermal resistance between optical bench nodes in the longitudinal direction required special consideration because of the complexity of the truss geometry. The equivalent resistance network in the longitudinal direction between two typical optical bench nodes for the selected nodal geometry (Figure 7-5) is illustrated in Figure 7-6. The equivalent thermal resistance between typical nodes i and j , as derived from electrical network theory, is given by

$$R_{ij} = \frac{R_B \left(\frac{R_2 R_A}{R_2 + R_A} + \frac{R_C R_5}{R_C + R_5} \right)}{R_B + \frac{R_2 R_A}{R_2 + R_A} + \frac{R_C R_5}{R_C + R_5}}, \quad (7-3)$$

where

$$R_{A, B, C} = \frac{R_1 R_3 + R_1 R_4 + R_3 R_4}{R_{4,3,1}}. \quad (7-4)$$

All individual resistances in Equation 7-4 are computed from the standard relation

$$R = \frac{\Delta x}{kA} \quad (7-5)$$

where

Δx - conductive path length

k - thermal conductivity

A - cross-sectional area normal to heat flow.

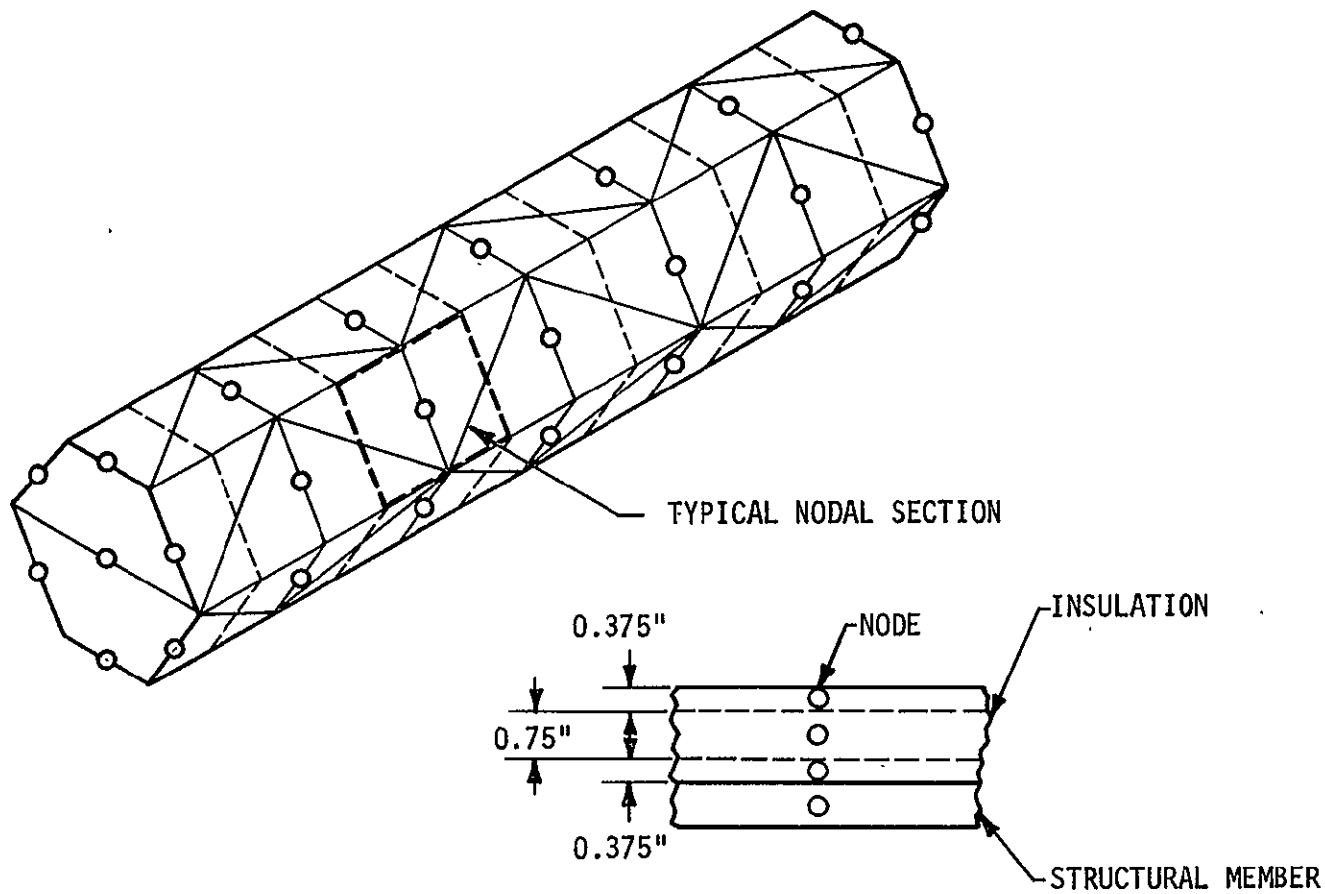


FIGURE 7-5. ILLUSTRATION OF NODAL REPRESENTATION OF THE OPTICAL BENCH AND MULTILAYER INSULATION

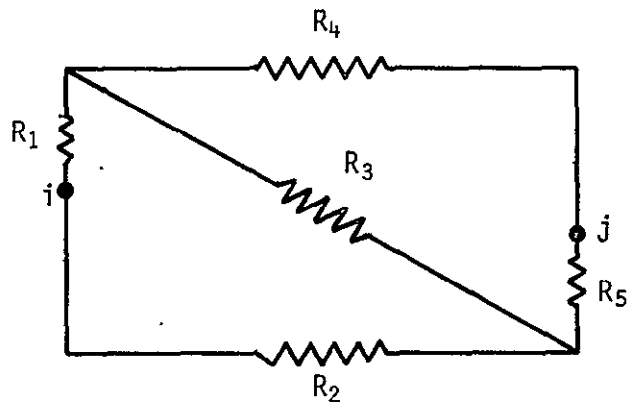


FIGURE 7-6. EQUIVALENT RESISTANCE NETWORK BETWEEN TWO NODES

Thermal resistances between optical bench nodes in the circumferential direction were determined simply from Equation 7-5, since preliminary calculations showed that parallel conduction paths could be considered negligible in the circumferential direction.

The experiment locations within the optical bench were shown previously in Figure 2-1. Each independent experiment module and each associated electronic package was represented by a single node, with the exception of the mirrors of the large area and the high resolution telescopes. Each of the telescope mirrors was simulated by a thick-walled cylinder with a cylindrical opening in the center which had a cross-sectional area equivalent to that of the aperture of the actual mirror. These hollow cylinders were divided into equal nodes along the telescope axis to more accurately determine the temperature gradient in this direction.

The proposed spacecraft structure is of the skin and stringer type as illustrated previously in Figure 4-7. With this configuration all of the structural supports contact the external skin. In the thermal model the composite skin and stringer wall structure was simulated by a thermally equivalent nodal network. The individual thermal capacitances of the structural support members and of the skin panels were lumped together in the calculation of the thermal capacitances of the equivalent skin panel nodes. In the calculation of the equivalent thermal conductances between skin panel nodes, the actual material cross-sectional areas normal to the appropriate heat flow paths were utilized.

Additional assumptions and guidelines employed in the temperature response predictions of the spacecraft were as follows:

- Thermal properties used for the spacecraft skin and structure were those of 6061 T6 aluminum (Ref. 7-6)

- ▲ Density, $\rho = 169 \frac{\text{lbm}}{\text{ft}^3}$

- ▲ Specific heat, $C_p = 0.23 \frac{\text{Btu}}{\text{lbm} \cdot ^\circ\text{F}}$

- ▲ Thermal conductivity, $K = 96.8 \frac{\text{Btu}}{\text{hr} \cdot \text{ft} \cdot ^\circ\text{F}}$

- Thermal properties used for the optical bench structure were those of Invar (Ref. 7-7)

- ▲ Density, $\rho = 504 \frac{\text{lbm}}{\text{ft}^3}$

- ▲ Specific heat, $C_p = 0.123 \frac{\text{Btu}}{\text{lbm} \cdot ^\circ\text{F}}$

- ▲ Thermal conductivity, $K = 6.05 \frac{\text{Btu}}{\text{hr} \cdot \text{ft} \cdot ^\circ\text{F}}$

- Thermal properties assumed for the composite solar panel structure were derived from the solar panel configuration of the Orbital Workshop (Ref. 7-8) as depicted in Figure 7-7.
- A 0.5-inch thickness of multilayer insulation was assumed to be located directly behind the solar panels to provide added thermal isolation of the optical bench on the warm side of the spacecraft and to shield the subsystems located there from the warm solar panels.
- Infrared emissivity values assumed for the internal surfaces of the spacecraft are as follows

	<u>ϵ</u>
▲ Inside surface of spacecraft panels	0.85
▲ Outside surface of optical bench insulation	0.03
▲ Inside surface of optical bench insulation	0.9
▲ Outside surface of solid-state detector	0.03
▲ All other components	0.9

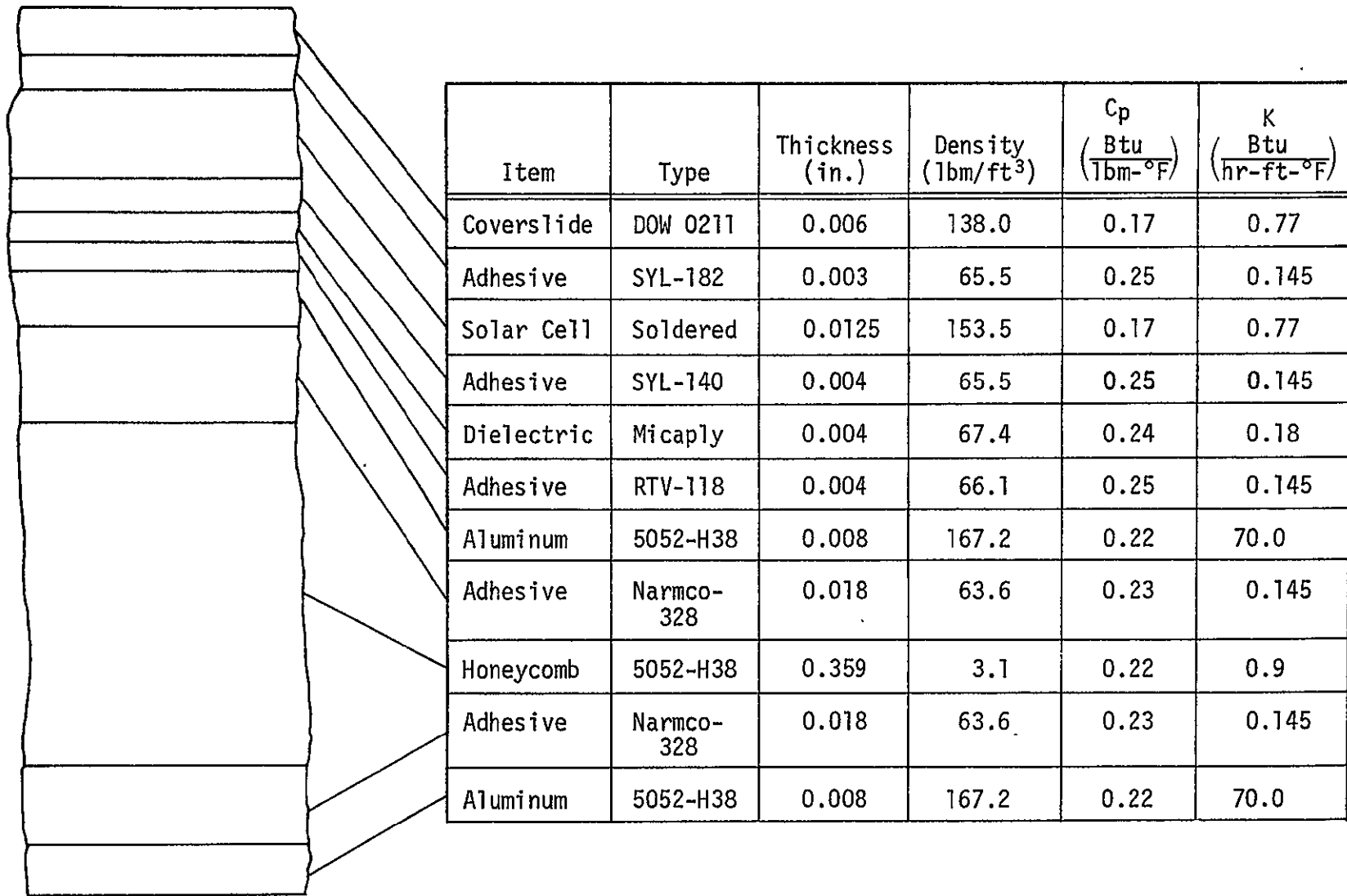


FIGURE 7-7. STRUCTURAL MODEL ASSUMED IN DERIVATION OF THERMAL PROPERTIES OF HEAO-C SOLAR PANELS

- The assumed contact conductance value for heat transfer between Invar members and the insulation surrounding the optical bench was 30 Btu/hr-ft²-°F (Ref. 7-9).
- Thermal properties assumed for the multilayer insulation are as follows
 - ▲ Thermal conductivity, K (normal) = $2.5 \times 10^{-5} \frac{\text{Btu}}{\text{hr-ft-}^\circ\text{F}}$
 - ▲ Thermal conductivity, K (parallel) = $3.0 \times 10^{-2} \frac{\text{Btu}}{\text{hr-ft-}^\circ\text{F}}$
 - ▲ Density, $\rho = 2.5 \frac{\text{lb}_m}{\text{ft}^3}$
 - ▲ Specific heat, $C_p = 0.3 \frac{\text{Btu}}{\text{lb}_m\text{-}^\circ\text{F}}$.
- Gray-body interchange factors required in the calculation of radiation conductances between nodes inside the spacecraft were evaluated by the digital computer program described in Reference 7-10.
- Each of the subsystem components outside the optical bench was considered to be attached to the spacecraft skin via four cylindrical mounts. The diameters of these mounts were assumed to be 1 inch for the larger components, and 0.5 inch for the smaller components. The contact conductance between the mounts and the skin was assumed to be 3,000 Btu/hr-ft²-°F. Small components with small internal heat generation rates were assumed to be isolated from the skin by insulative mounts to prevent them from becoming too cold.

The thermal model described above was input into the Chrysler CINDA program. The temperature responses of the 363 nodes were then calculated by the program for a simulated period of 50 hours (approximately 31 orbits) after orbit insertion, considering the entire spacecraft to be at an initial temperature of 70° F.

The estimated weights of the various items included in the thermal control system are presented in Table 7-3.

TABLE 7-3. THERMAL CONTROL SYSTEM WEIGHT

<u>Item</u>	<u>Weight (lb)</u>
Multilayer Insulation Surrounding Optical Bench (1.5 in.)	203
Multilayer Insulation Behind Solar Panels	72
External Thermal Control Coating	80
Internal Thermal Control Coating	80
Heaters Inside Optical Bench	<u>10</u>
TOTAL	<u><u>445</u></u>

DISCUSSION OF RESULTS

Spacecraft Oriented Broadside-to-Sun

Cases I and II of Figure 7-3 illustrate the broadside-to-Sun spacecraft orientation with the angle β equal to its maximum and minimum values of 58.5 degrees and 0 degree, respectively. The predicted orbital histories of the incident environmental heat flux on the thermal control filter and of the resulting filter temperature are presented in Figures 7-8 and 7-9 for Cases I and II, respectively. Since the filter is oriented parallel to the solar vector, it receives no solar flux for orientation Cases I and II.

It is noted from Figures 7-8 and 7-9 that the thermal control filter undergoes rather large temperature excursions during orbit, between the extremes of approximately 55°F and 99°F. Temperatures

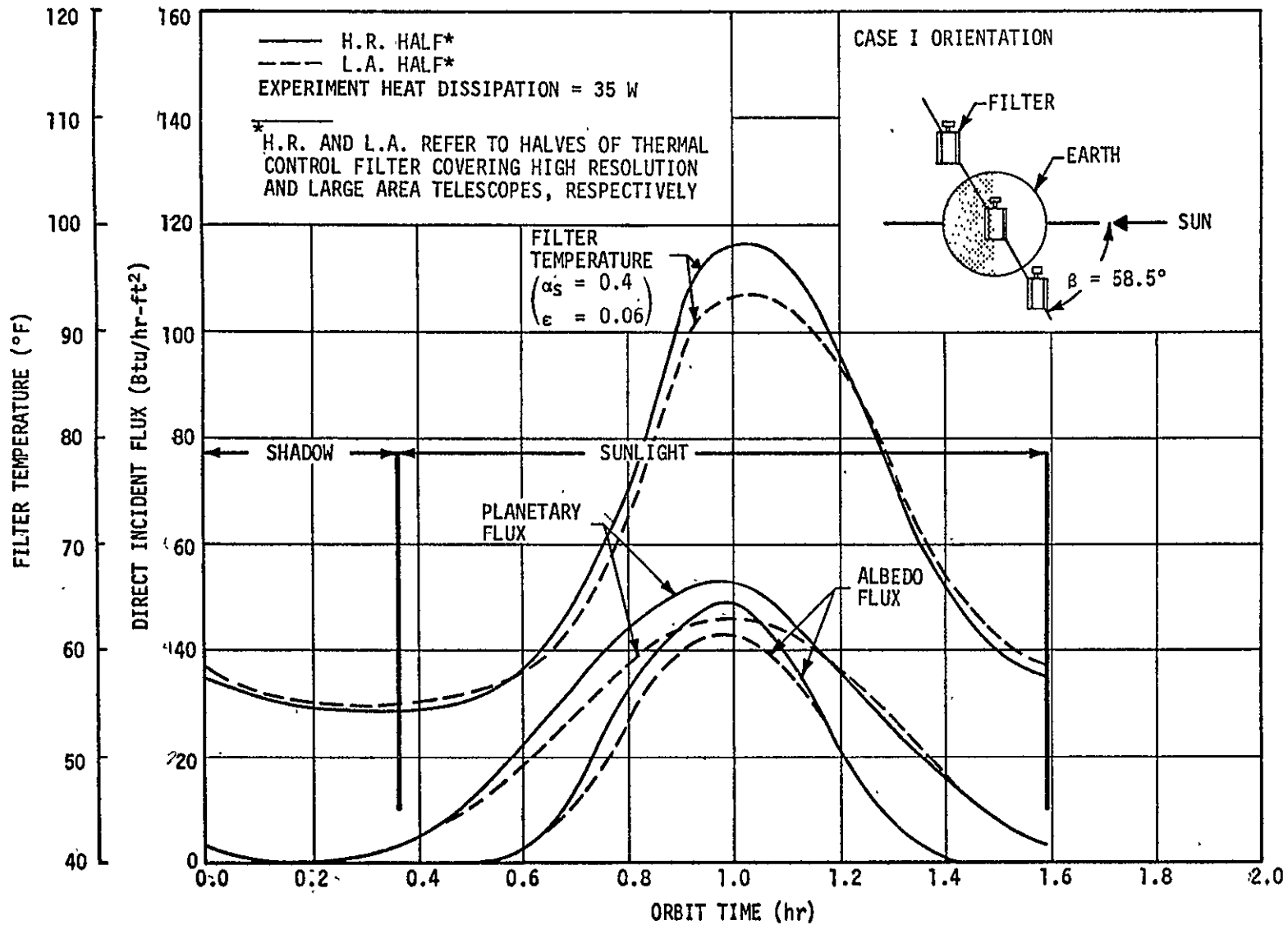


FIGURE 7-8. DIRECT INCIDENT HEAT FLUX ON THERMAL CONTROL FILTER DURING ORBIT AND RESULTING FILTER TEMPERATURE RESPONSE FOR CASE I ORIENTATION

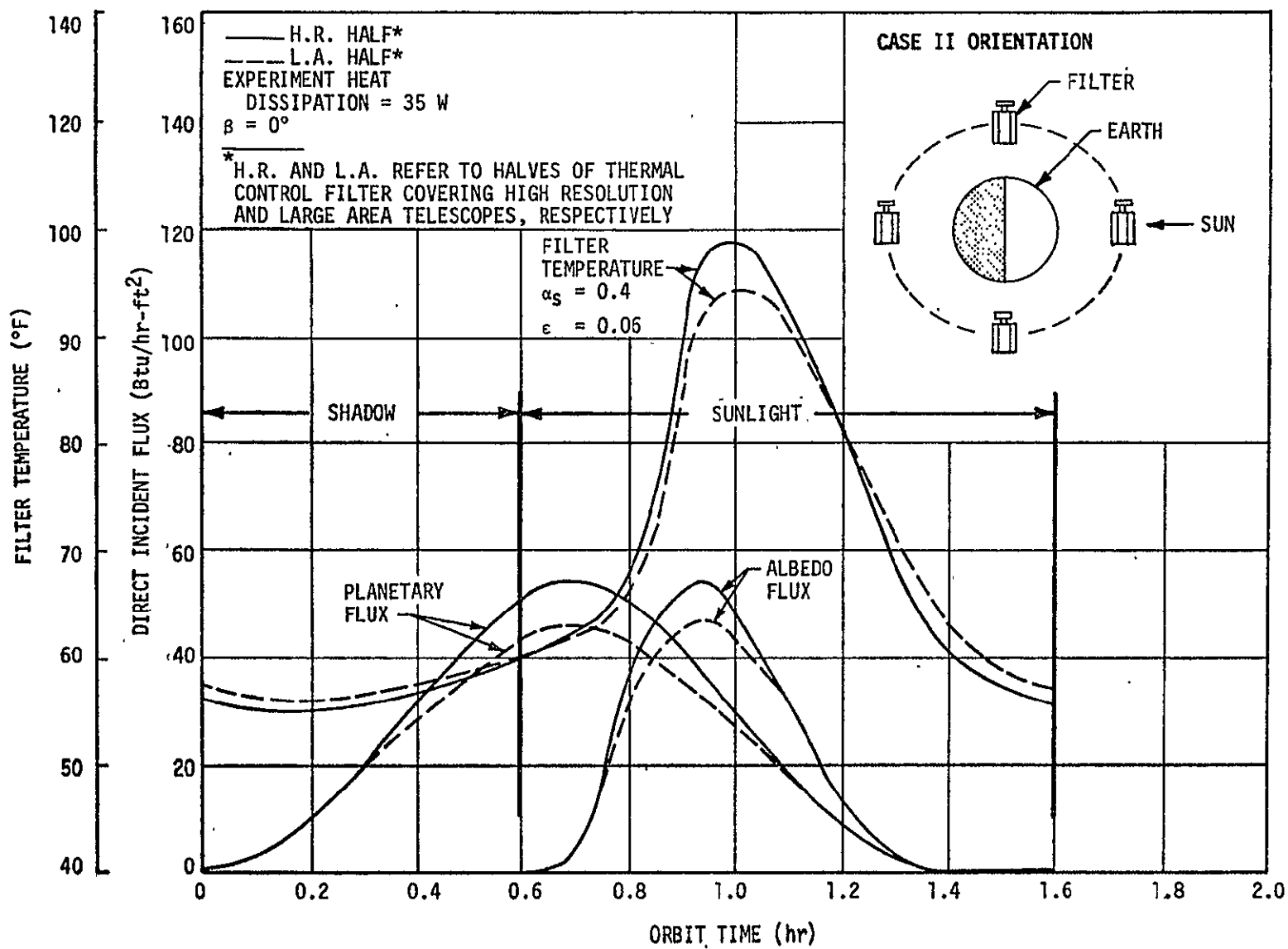


FIGURE 7-9. DIRECT INCIDENT HEAT FLUX ON THERMAL CONTROL FILTER DURING ORBIT AND RESULTING TEMPERATURE RESPONSE FOR CASE II ORIENTATION

of the half of the filter covering the high resolution (H. R.) telescope are generally greater than those of the half covering the large area (L. A.) telescope because of greater shading of the latter half by the extended mosaic crystal. Although the operating temperature levels of the experiment packages inside the optical bench are dependent on the operating temperature range of the filter, the large temperature excursions experienced by the filter during orbit will not be experienced by the components inside the bench. This is because of the thermal resistance between the filter and components and the large thermal inertia of the components. This fact is illustrated by the results presented in Figures 7-10 and 7-11.

Figure 7-10 illustrates the predicted operating temperature envelope of the optical bench truss structure after 50 hours in orbit for Cases I and II. Careful examination of the predicted temperature responses of the massive optical bench structure and of the experimental packages inside the bench indicated that they were very near cyclic equilibrium after the simulated 50 hours in orbit. As shown in Figure 7-10, the optical bench structure remains within the allowable temperature limits of $70^{\circ}\text{F} \pm 10^{\circ}\text{F}$ after being spaceborne for 50 hours, and exhibits very small transient variations in temperature during orbit. The temperature shown in Figure 7-10 for each longitudinal station along the optical bench represents the average value of the members at that cross section. However, the results of the thermal analysis indicate that at any instant the temperatures of the various truss members will be uniform to within 1°F at the viewing end of the optical bench, and within approximately 0.2°F at any other cross section along the length of the bench. Therefore, thermal bending of the optical bench due to lateral temperature differentials will be extremely small.

The predicted operating temperature envelopes of the telescope mirrors after 50 hours in orbit for Cases I and II are presented in

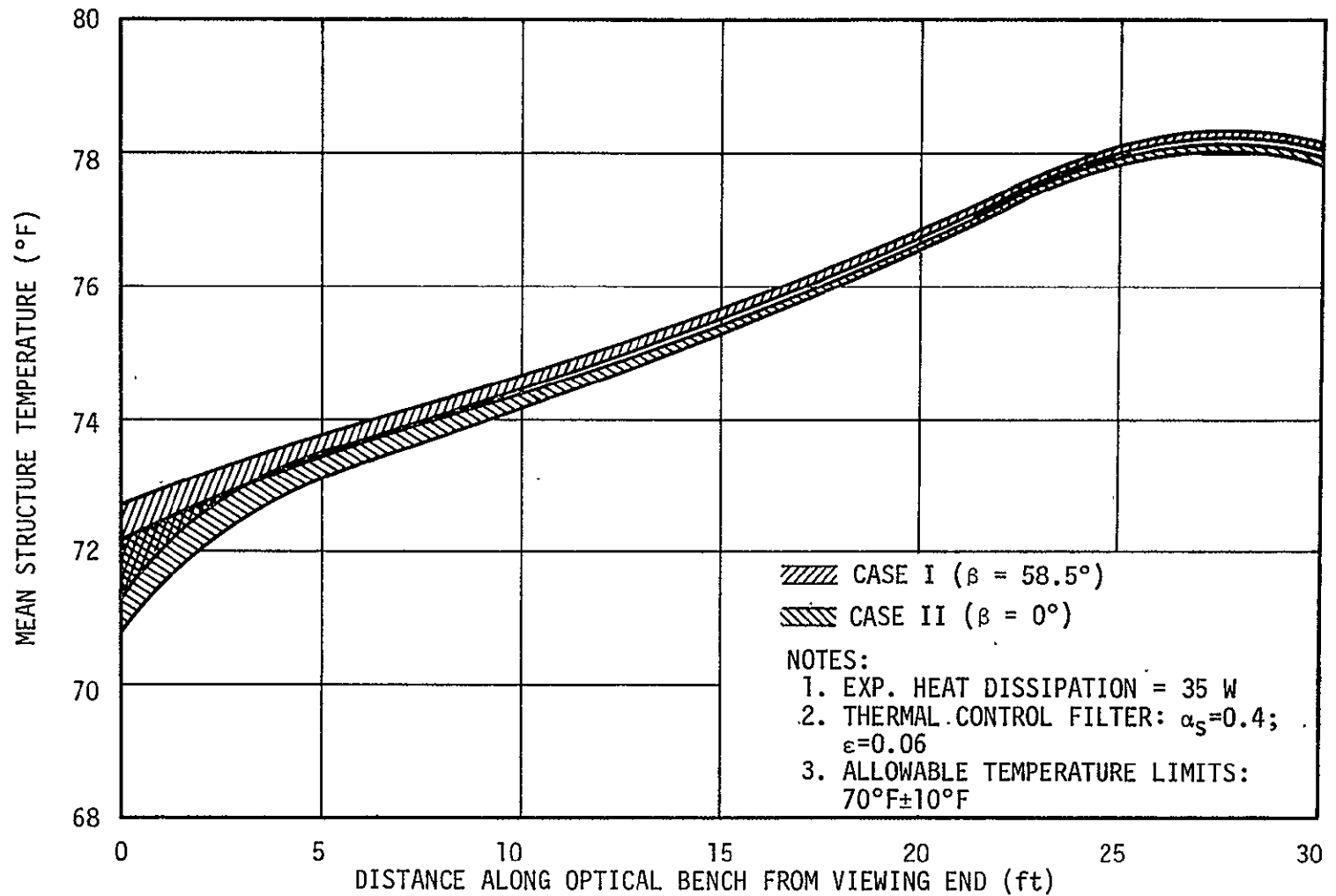


FIGURE 7-10. PREDICTED TEMPERATURE ENVELOPE OF OPTICAL BENCH STRUCTURE WITH SPACE-CRAFT ORIENTED BROADSIDE TO SUN (CASES I AND II)

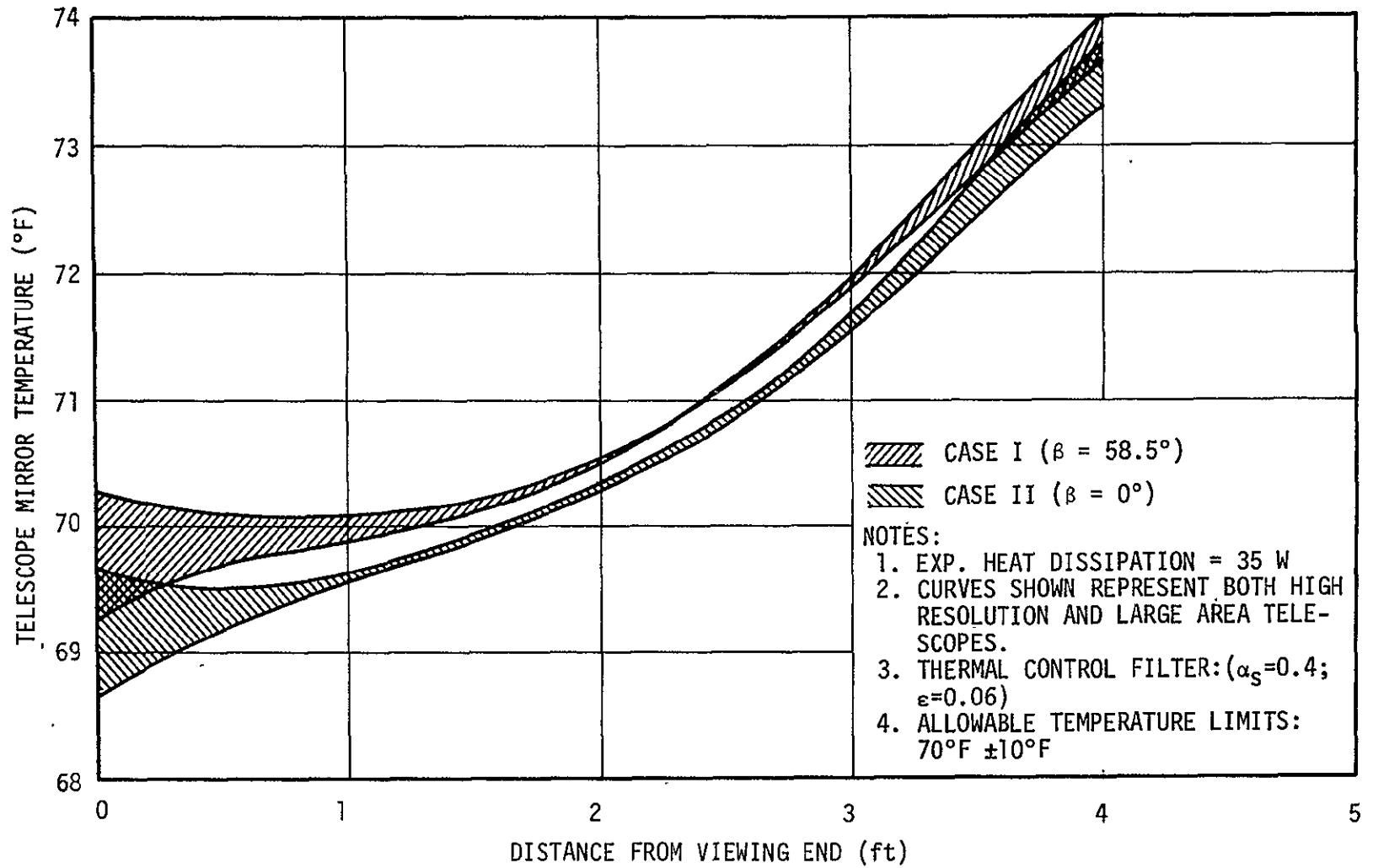


FIGURE 7-11. PREDICTED TEMPERATURE ENVELOPE OF TELESCOPE MIRRORS WITH SPACECRAFT ORIENTED BROADSIDE TO SUN (CASES I AND II)

Figure 7-11. As shown in this figure, the predicted axial temperature differential between the viewing ends and the aft end of the mirrors is approximately 5°F. The operating temperatures of both telescope mirrors are predicted to remain well within their allowable limits of 70°F ± 10°F. It is noted that the telescope mirror temperature distributions are very stable during orbit, as illustrated by the narrow width of the temperature envelopes, with a maximum transient variation at the viewing end of approximately 1°F.

The predicted operating temperature extremes of the experiments and system components for Cases I and II are compared with their allowable temperature limits in Table 7-4. Examination of Table 7-4 reveals that the predicted operating temperatures of all experiments and system components remain within their allowable limits. The experiment and component locations are depicted in Figures 2-1 and 3-2. The acceptable operating temperature predictions presented in Table 7-4 were obtained only after a few design interactions on the thermal control coating properties and insulation thicknesses.

The predicted orbital temperature histories of the spacecraft solar panels and the backside panel are presented in Figures 7-12 and 7-13 for Cases I and II of Figure 7-3, respectively. The predicted maximum surface temperature of the center solar panel is approximately 220°F for Case I ($\beta = 58.5$ degrees) and approximately 210°F for Case II ($\beta = 0$ degree). Comparison of these predicted maximum solar panel temperatures with those of other spacecraft, e. g., Skylab-A (212°F maximum) and HEAO-A (190°F maximum), reveals that the HEAO-C configuration analyzed herein would be subject to a relatively large power conversion penalty due to the high solar panel temperatures. Moreover, the predicted temperature of 220°F exceeds the recommended maximum value of 212°F which is

TABLE 7-4. PREDICTED EXPERIMENT AND SUBSYSTEM OPERATING TEMPERATURE EXTREMES

<u>Experiments</u>	TEMPERATURE, °F		
	$\beta = 0$ deg	$\beta = 58.5$ deg	Allowable
Scintillation Counter	69	70	14 to 86
Monitor Proportional Counter	32 to 33	31 to 32	14 to 86
Monitor Proportional Counter Electronics	91 to 92	96	160 Max.
Mosaic Crystal	-56 to -60	-71 to -75	Unknown
H.R. Crystal Spectrometer	79	79	14 to 86
H.R. Image Detector	79	79	14 to 86
H.R. Image Detector Electronics	93	94	160 Max.
Solid State Detector	86 to 87	86 to 87	14 to 86 [†]
Solid State Detector Electronics	50	49	160 Max.
L.A. Image Detector	80	80	14 to 86
L.A. Image Detector Electronics	61 to 62	60	160 Max.
Multiple Polarimeter	79	79	14 to 86
Multiple Polarimeter Electronics	50 to 53	44 to 45	160 Max.
Flat Crystal Spectrometer	70	70	14 to 86
Flat Crystal Spectrometer Electronics	22 to 24	5 to 6	160 Max.
Fine Flare Detector	72 to 73	73 to 74	Unknown
Fine Flare Detector Electronics	85	89	160 Max.
Coarse Flare Detectors (2; fwd. end)	- 2 to - 3	-19 to -20	Unknown
Coarse Flare Detectors (2; aft. end)	12 to 14	-18 to -27	Unknown
Coarse Flare Detector Electronics (2; fwd. end)	32 , 41	18 , 28	160 Max.
Coarse Flare Detector Electronics (2; aft. end)	54 , 62	42 , 51	160 Max.
<u>System Components</u>			
Charger Battery Regulator Modules (9)	29 to 65*	12 to 47*	-20 Min.
Load Distributor (2)	33 , 42	18 , 27*	160 Max.
Control Moemnt Gyros (6)	16 to 89*	0 to 93*	-40 to 120
Tape Recorders (4)	20 to 29*	5 to 14*	0 to 130
Switching Network (2)	21 to 25	7 to 9	160 Max.
Power Combiner	21 to 23	5 to 6	Unlimited
S-band Decoder/Transmitter 1	11 to 15	- 4 to - 1	160 Max.
S-band Decoder/Transmitter 2	39 to 42	25 to 27	160 Max.
Command Decoder	50	38	160 Max.
Signal Conditioner	87 to 88	77 to 78	160 Max.
Command Receiver 1	32 to 33	19 to 20	160 Max.
Command Receiver 2	24 to 26	11 to 12	160 Max.
S-band Power Amplifier 1	41 to 55	28 to 44	160 Max.
S-band Power Amplifier 2	67 to 81	56 to 70	160 Max.
Computer	83 to 84	69 to 70	0 to 120
Gas Bottle and Valves (2)	34 , 4	19 , -13	Unknown
Multiplexer	30 to 32	18 to 19	160 Max.
Solar Combiners (7)	84 to 174*	90 to 177*	-85 to 374
Aspect Detector	73	73 to 74	14 to 86
Aspect Detector Electronics	85	89	160 Max.
Electromagnetic Control Torques (3)	-8, 8, 20	-20, -23, 3	-30 to 120

*Signifies that variations are primarily due to location, rather than to transient effects

[†]Refers to exterior surface

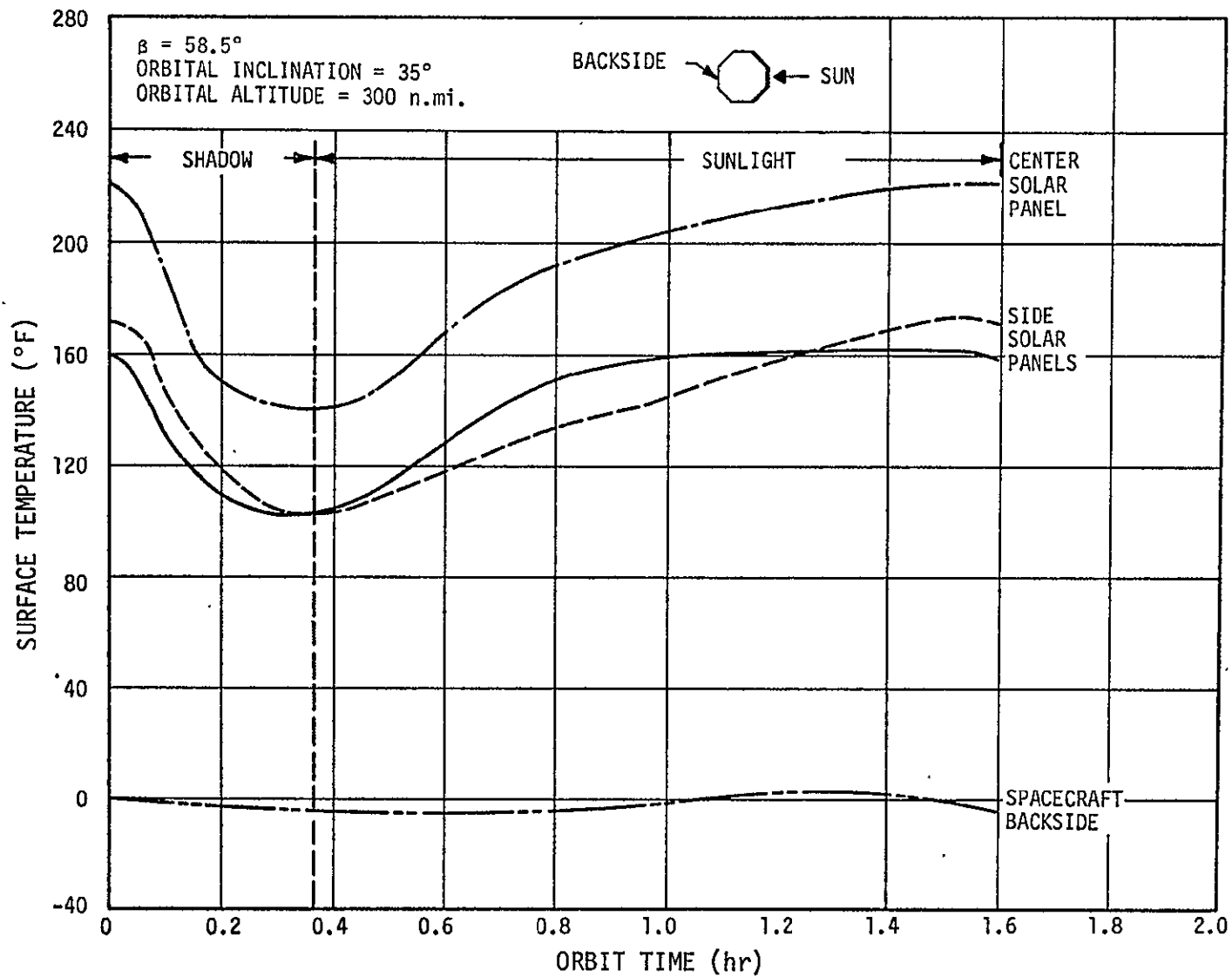


FIGURE 7-12. PREDICTED SOLAR PANEL AND SPACECRAFT BACKSIDE TEMPERATURE HISTORIES DURING ORBIT FOR CASE I ORIENTATION

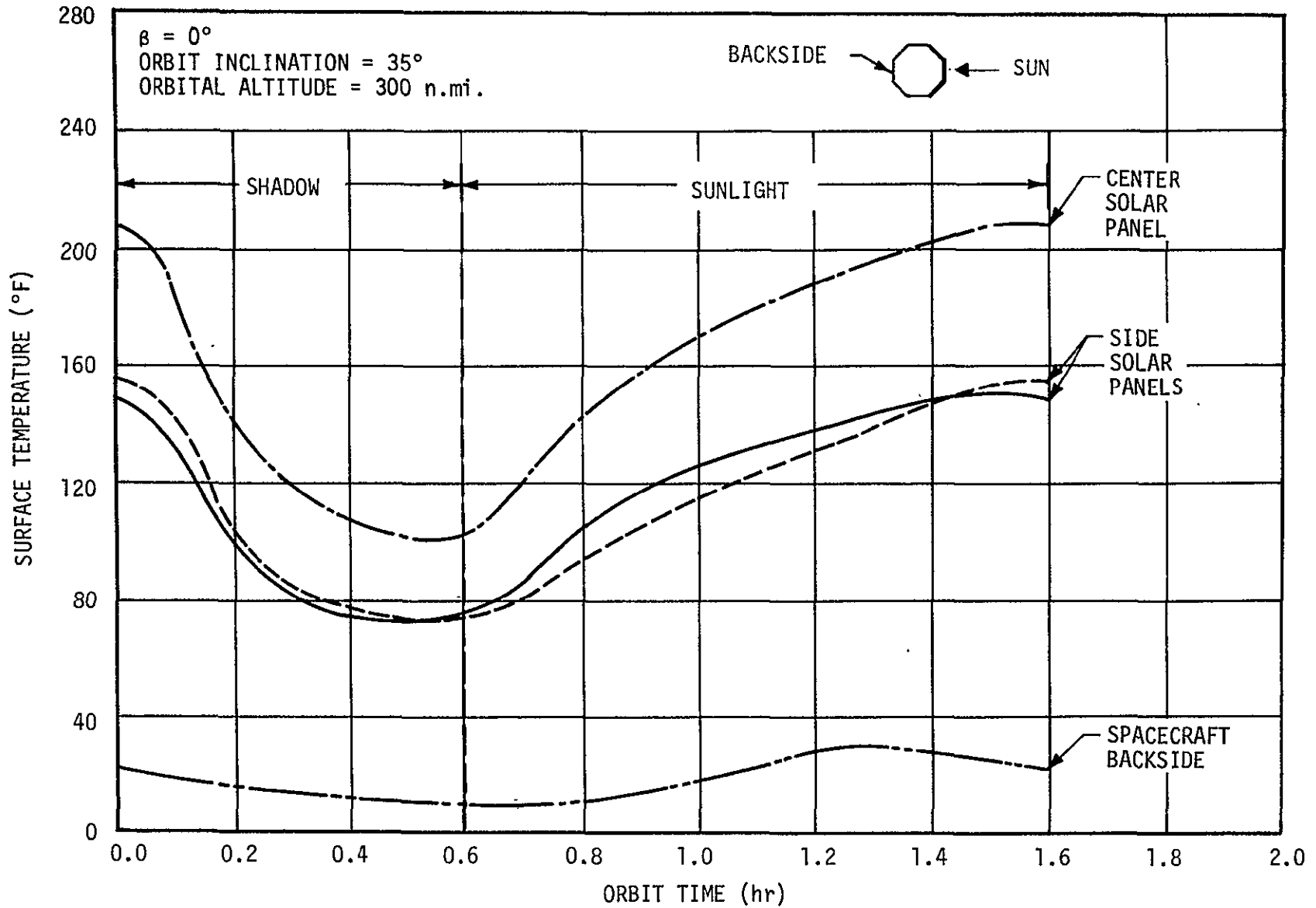


FIGURE 7-13. PREDICTED SOLAR PANEL AND SPACECRAFT BACKSIDE TEMPERATURE HISTORIES DURING ORBIT FOR CASE II ORIENTATION

based on previous experience with Apollo Telescope Mount (ATM) solar cell modules (Ref. 7-11). These relatively high predicted solar panel temperatures result primarily from the thicknesses of multilayer insulation located directly behind the solar panels (0.5 inch) and surrounding the optical bench (1.5 inches), which block radiative heat transfer from the solar panels to the backside of the spacecraft.

It is also important to note that the predicted solar panel temperature histories presented in Figures 7-12 and 7-13 represent nominal environmental heating conditions. Off-nominal variations in pertinent parameters, e.g., solar, albedo, and planetary environmental constants, solar absorptivity, emissivity, and power conversion efficiency values, could result in even higher solar panel surface temperatures. Therefore, it will be important in subsequent studies to investigate possible "worst case" boundary heating conditions to insure prediction of the maximum expected solar panel surface temperature. Moreover, alternate designs and thermal control methods for reducing the solar panel surface temperature should be investigated. The following design alternatives for reducing solar panel temperatures are recommended for investigation:

- Selection of a spacecraft orientation having no solar panel positioned exactly perpendicular to the solar vector. This would provide reduced solar panel temperatures, hopefully without incurring an excessive penalty in available power. This method would take advantage of the tradeoff between reduced power output with reduced projected area and increased power output with reduced solar panel temperature.
- Elimination of the separate 0.5-inch thickness of multilayer insulation which was assumed to be directly in contact with the backsides of the solar panels. This would permit slightly increased heat transfer from the backsides of the solar panels and would lower the solar panel temperatures to some extent. If this modification is adopted, additional insulation might have to be added to the 1.5-inch insulation thickness surrounding the optical bench to protect the bench

structure and experiments therein. In addition, individual shielding of the subsystems adjacent to the warm solar panels may be required.

- Incorporation of circumferential heat pipes into the spacecraft skin to efficiently conduct heat from the solar panels to the backside of the spacecraft and thereby reduce the solar panel temperatures. It is noted, however, that reduction of the solar panel temperatures using this method will only be accomplished at the expense of raising the heat rejection temperature of the components located at the backside of the spacecraft.
- Folding out of the two side solar panels to provide increased heat rejection by radiation from their backsides and improved heat conduction from the center solar panel. The anticipated effect would be an approximate equilization of the temperature response of all three panels, and reduction of the temperature level of the center panel.
- Folding out of the center solar panel or employing a corrugated surface design for the center panel to reduce the angle of solar incidence and the surface temperature level.
- Employing a thermal capacitor, incorporating a suitable phase change material, directly behind the solar panels to absorb heat during the sunlit fraction of the orbit and to reject it during the shaded fraction. This addition would reduce both the level of solar panel temperature and the fluctuation of temperature during orbit.

The predicted orbital history of the surface temperature differential, between the center solar panel and the backside of the spacecraft structure ΔT_{\max} is presented in Figure 7-14 for Cases I and II. The temperature difference between these two locations is the maximum for any two points separated by 180 degrees on the circumference of the spacecraft. The parameter ΔT_{\max} is important in determining the lateral deflection, or "hot dogging", of the spacecraft structure due to thermal stresses. From Figure 7-14 it can be seen that the maximum predicted value of ΔT_{\max} during orbit is approximately

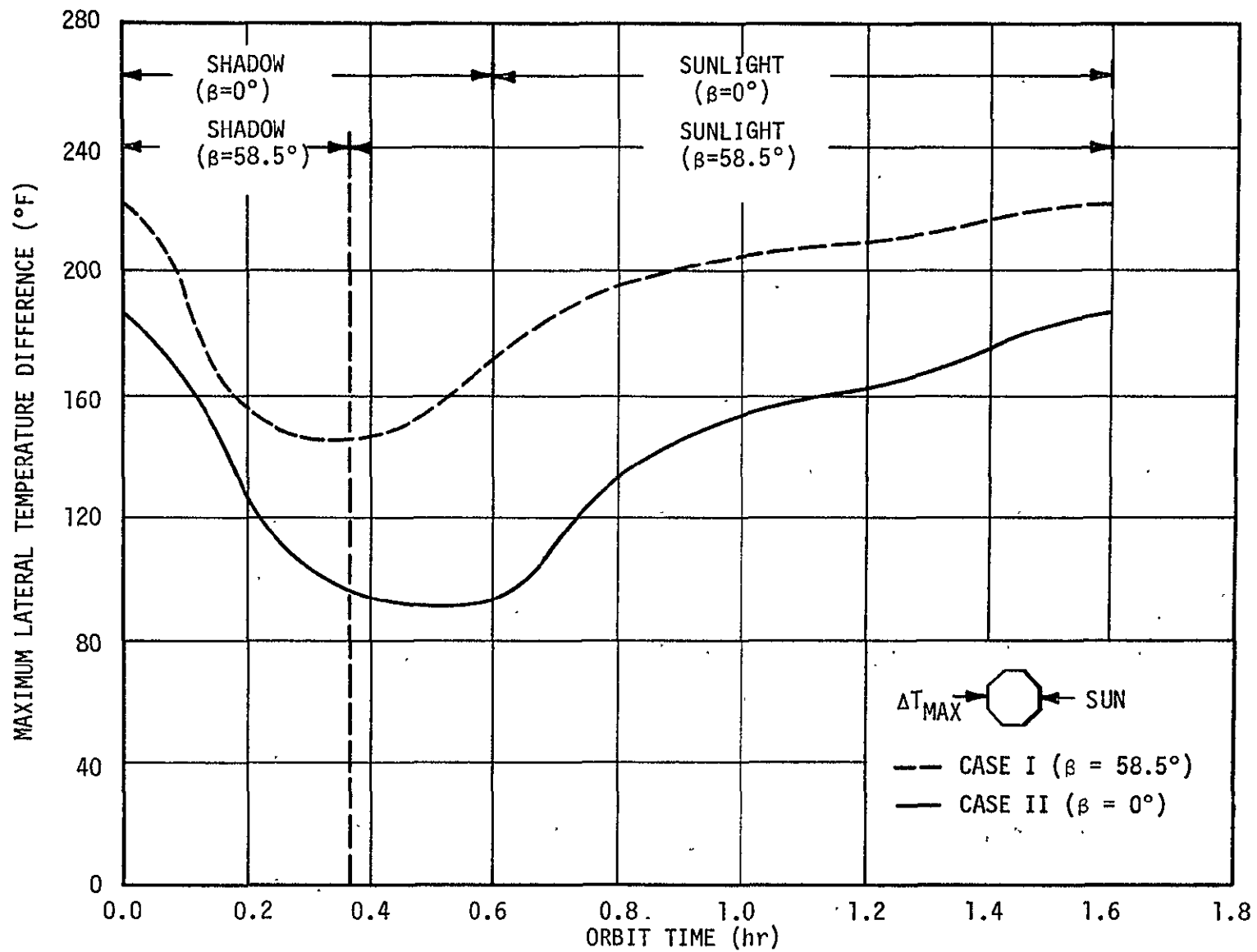


FIGURE 7-14. ORBITAL HISTORY OF MAXIMUM LATERAL TEMPERATURE DIFFERENCE ACROSS HEAO-C SPACECRAFT

220°F. Since the spacecraft structure was initially designed to permit a lateral deflection limits resulting from a ΔT_{\max} of 366°F (Section 4), it is obvious that the actual lateral deflection of the spacecraft structure will be well within the established limits.

Spacecraft Axis Inclined 15 Degrees Toward the Sun

Another design requirement for the HEAO-C spacecraft is to have the capability to view sources located as much as 15 degrees off the normal to the solar vector. These sources are to be viewed for an indefinite period of time. This pointing mode is illustrated as Case III in Figure 7-3; it provides the worst case continuous heat rejection requirement for the thermal control filter, since the filter is oriented 15 degrees toward the Sun.

The predicted orbital histories of the incident environmental heat flux on the thermal control filter and of the resulting temperature response of the filter after cyclic equilibrium are presented in Figure 7-15 for the Case III spacecraft orientation. As shown in Figure 7-15, the predicted filter temperature cycles between the values of 128°F and 212°F for this case.

Figures 7-16 and 7-17 present the predicted longitudinal temperature distributions of the optical bench structure and of the telescope mirrors, respectively, after a simulated orbit time of 69 hours. In performing the thermal modeling of the Case III orientation, it was assumed that the entire spacecraft was at a uniform initial temperature of 70°F prior to being subjected to the predicted environmental heat fluxes. The maximum predicted bench and mirror temperatures are 153°F and 174°F, respectively; both of which greatly exceed the upper limit of 80°F.

Examination of the predicted spacecraft temperature response revealed that the temperatures of the optical bench and telescope mirrors were still climbing after the simulated 69 hours in the Case

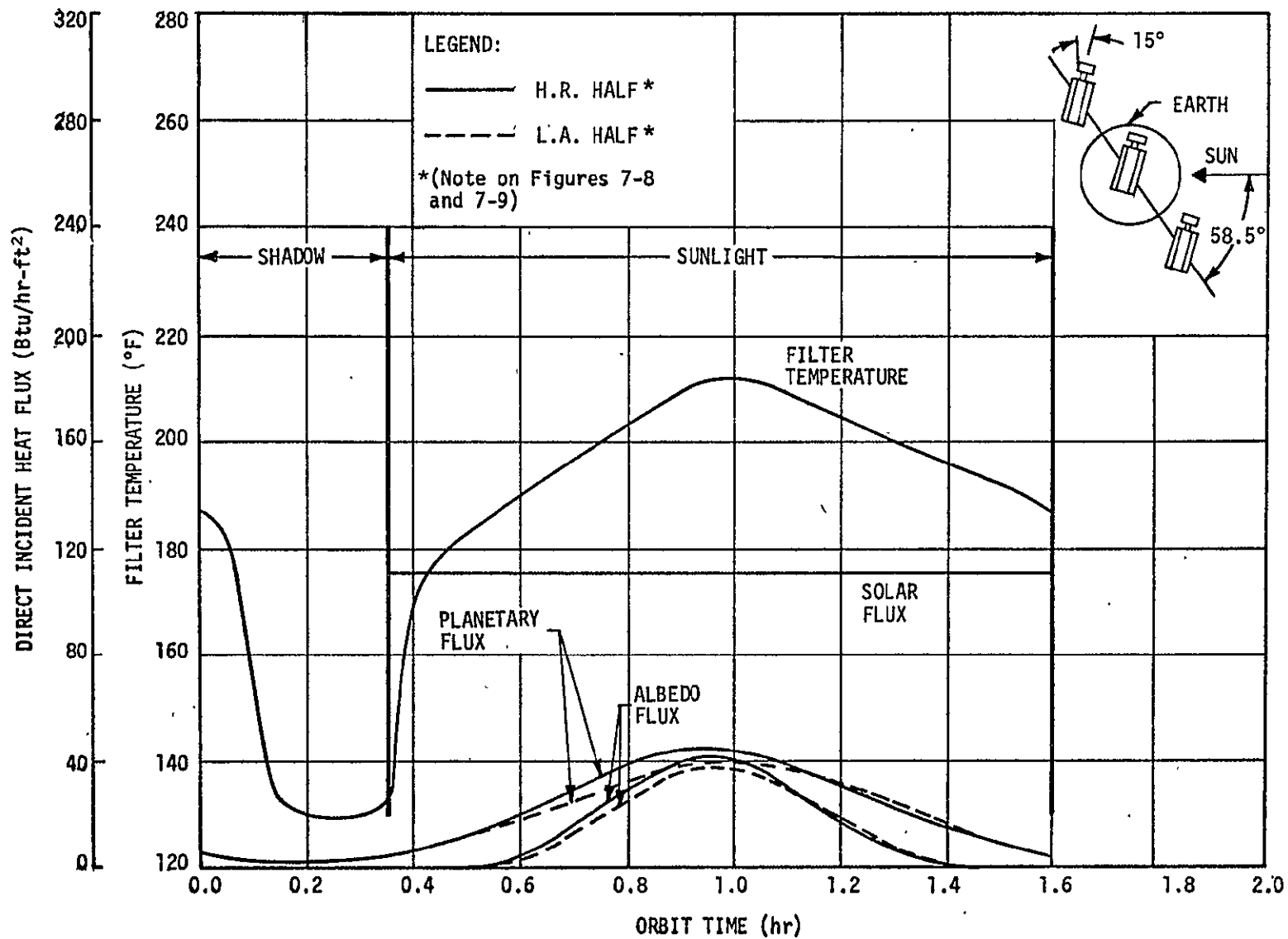


FIGURE 7-15. DIRECT INCIDENT HEAT FLUX ON AND TEMPERATURE OF THE THERMAL CONTROL FILTER DURING ORBIT WITH SPACECRAFT END INCLINED 15 DEGREES TOWARD SUN (CASE III)

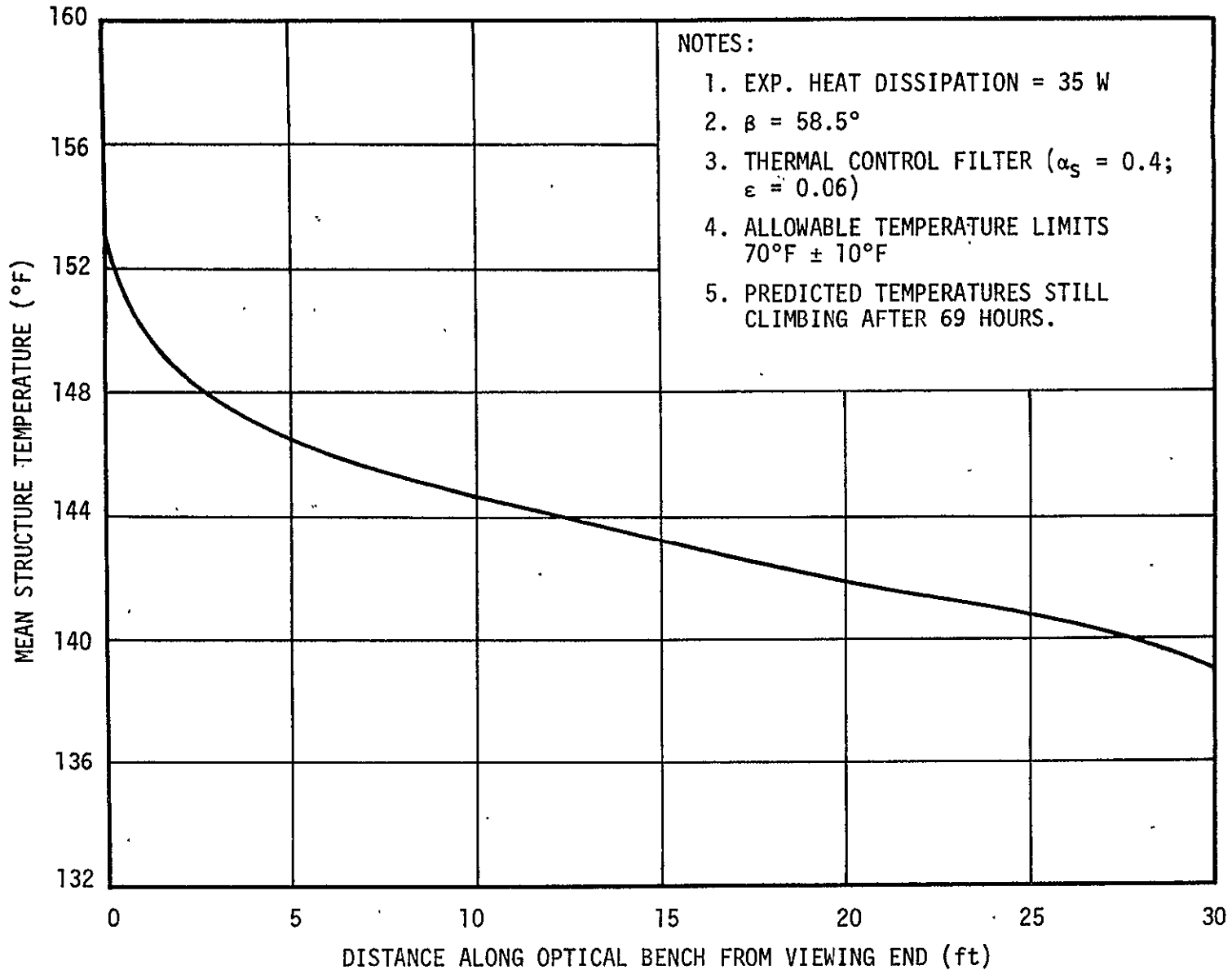


FIGURE 7-16. PREDICTED LONGITUDINAL DISTRIBUTION OF OPTICAL BENCH STRUCTURE TEMPERATURE AFTER 69 HOURS IN ORBIT WITH SPACECRAFT AXIS INCLINED 15 DEGREES TOWARD THE SUN (CASE III)

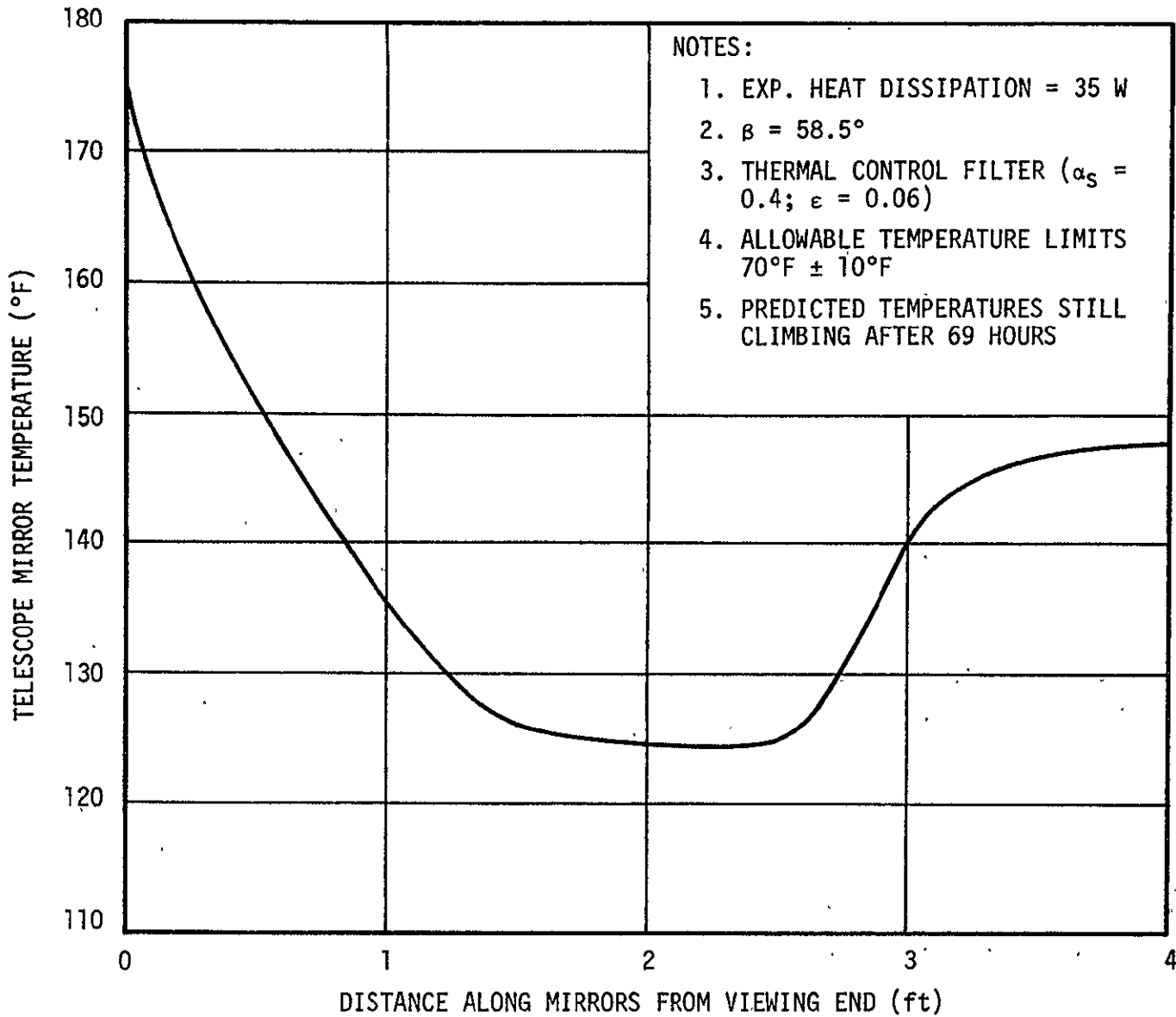


FIGURE 7-17. PREDICTED LONGITUDINAL DISTRIBUTION OF TELESCOPE MIRROR TEMPERATURES AFTER 69 HOURS IN ORBIT WITH SPACECRAFT AXIS INCLINED 15 DEGREES TOWARD THE SUN (CASE III)

III pointing mode. The slow temperature responses of these items result primarily from their large thermal capacitances. The temperatures of the viewing ends of the optical bench structure and of the telescope mirror tend to follow the orbital average temperature of the thermal control filter, which is approximately 184°F for Case III. These bench and mirror temperatures would continue to rise to slightly above the average filter temperature because of the experiment heat load which must be rejected from the bench.

Predicted temperatures of other experiment packages inside the optical bench after the simulated 69 hours of orbit time ranged up to 150°F, and were still rising. The predicted temperature of components located outside the optical bench were essentially unchanged from those predicted for the Case I orientation. The predicted maximum temperature of the center solar panel was approximately 215°F for the Case III pointing mode, as shown in Figure 7-18. This temperature is 5 degrees cooler than was predicted for the broadside-to-Sun (Case I) orientation.

From the results of the spacecraft thermal analysis for the Case III pointing mode, it is apparent that the maximum temperature limits of all components inside the optical bench would be exceeded if an aluminized Mylar thermal control filter were utilized with no Sun shade. Therefore, successful thermal control of the experiments during the Case III orientation will be achieved only if the optical characteristics of the thermal control filter are modified to reduce the absorbed solar energy or if a Sun shade is deployed.

Spacecraft Axis Inclined 30 Degrees Toward the Sun

One of the HEAO-C spacecraft design requirements is to provide a capability to view sudden flares of X-ray emissions at pointing angles between the spacecraft axis and the solar vector as small as 60 degrees (30 degrees off the normal broadside-to-Sun orientation).

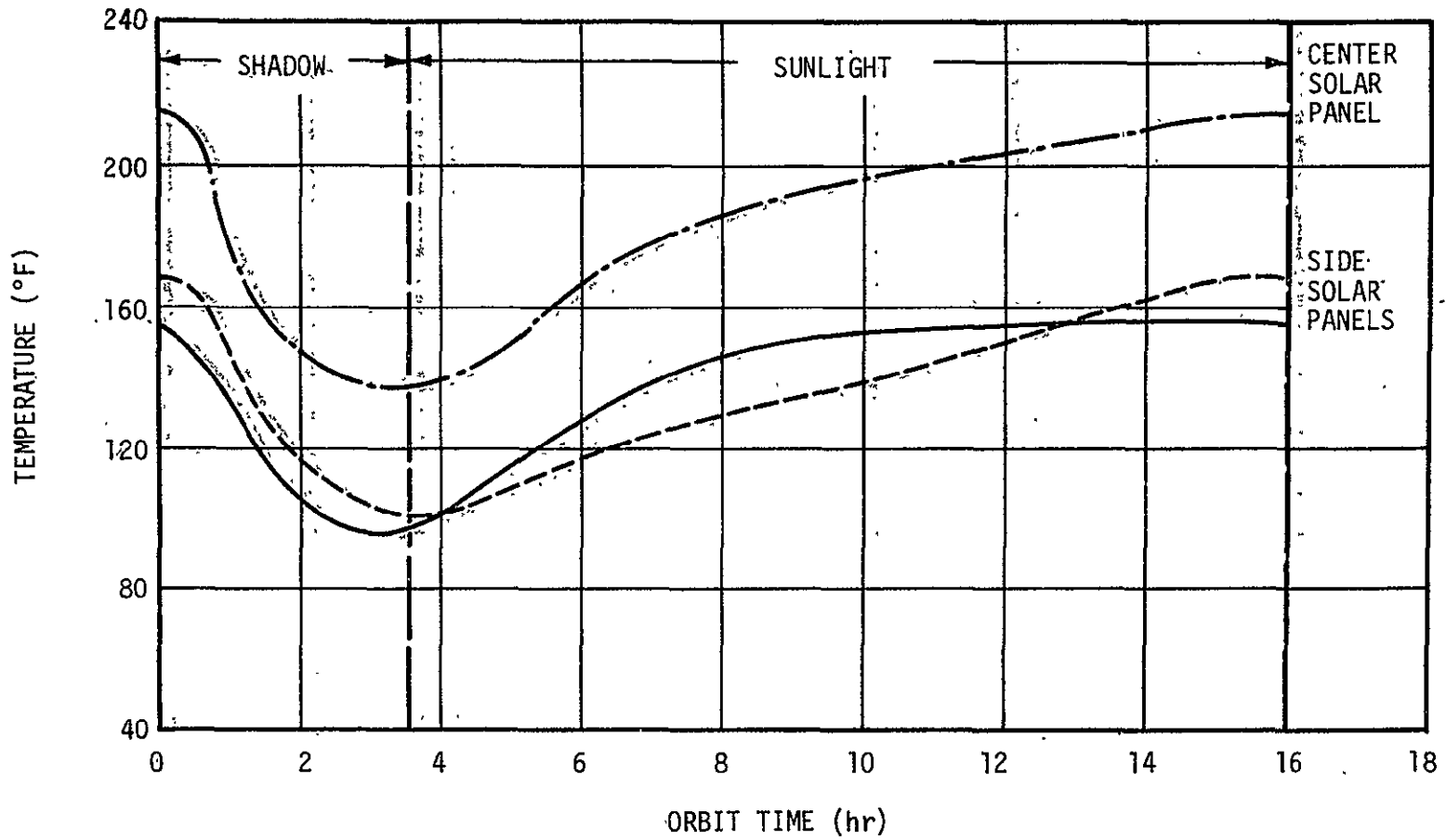


FIGURE 7-18. PREDICTED SOLAR PANEL TEMPERATURE HISTORY DURING ORBIT WITH THE SPACECRAFT AXIS INCLINED 15 DEGREES TOWARD THE SUN (CASE III)

Therefore, occasions may arise when the viewing end of the spacecraft is temporarily inclined toward the Sun as much as 30 degrees. This orientation is illustrated by Case IV of Figure 7-3. The maximum duration of the Case IV orientation is estimated to be one orbit per day.

The predicted histories of the incident environmental heat flux on the thermal control filter and of the resulting filter temperature for Case IV is presented in Figure 7-19. In producing the results presented in Figure 7-19, it was assumed that after being in orbit for 50 hours broadside to the Sun, the spacecraft axis is shifted 30 degrees toward the Sun at the time in orbit when the spacecraft emerges from the Earth's shadow, and that this attitude is maintained for a period of one orbit. As shown in Figure 7-19, the predicted thermal control filter temperature rises rapidly to a maximum value of 215°F as a result of the filter being exposed to direct sunlight for approximately 77 percent of the orbit. However, additional calculations revealed that the temperature history of the filter will return to its normal cyclic pattern, illustrated previously in Figure 7-8, within the next orbit following the shift back to the normal broadside-to-Sun (Case I spacecraft orientation).

The effects of the temporary shift of the spacecraft axis to the Case IV orientation on the temperature distributions of the optical bench and of the telescope mirrors are illustrated by the results presented in Figures 7-20 and 7-21. Figure 7-20 presents the predicted longitudinal temperature distribution of the optical bench structure at its maximum level during 50 hours of orbit prior to the 30-degree off-axis shift, at its maximum level during the orbit in which the spacecraft axis is inclined 30 degrees, and during the period of heat soak following the return to the normal (Case I) orientation. Twenty hours (12 orbits) of heat soak after return to the broadside-to-Sun

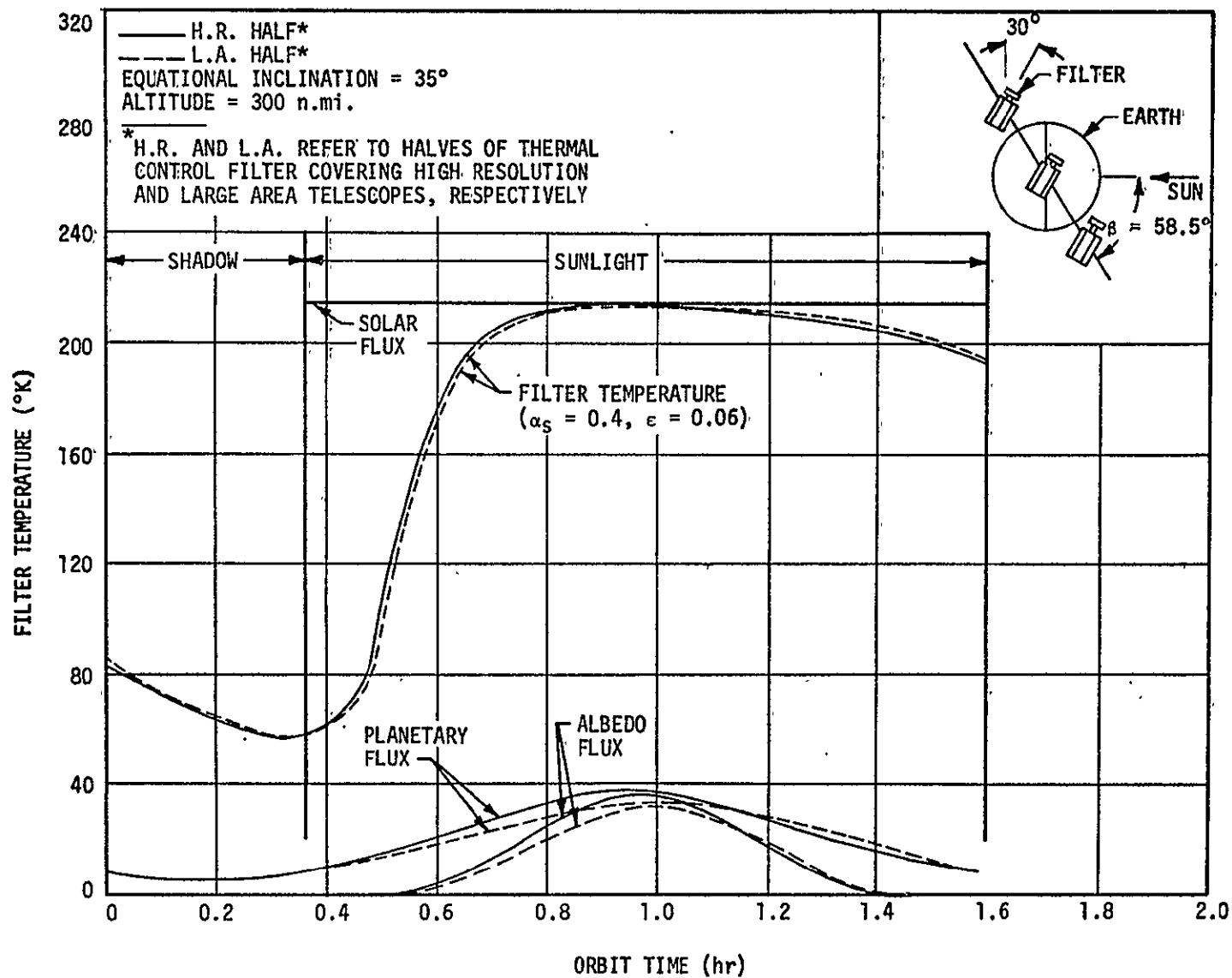


FIGURE 7-19. DIRECT INCIDENT HEAT FLUX ON THERMAL CONTROL FILTER AND RESULTING TEMPERATURE RESPONSE DURING ORBIT WITH SPACECRAFT VIEWING END INCLINED 30 DEGREES TOWARD SUN (CASE IV)

VII

7-46

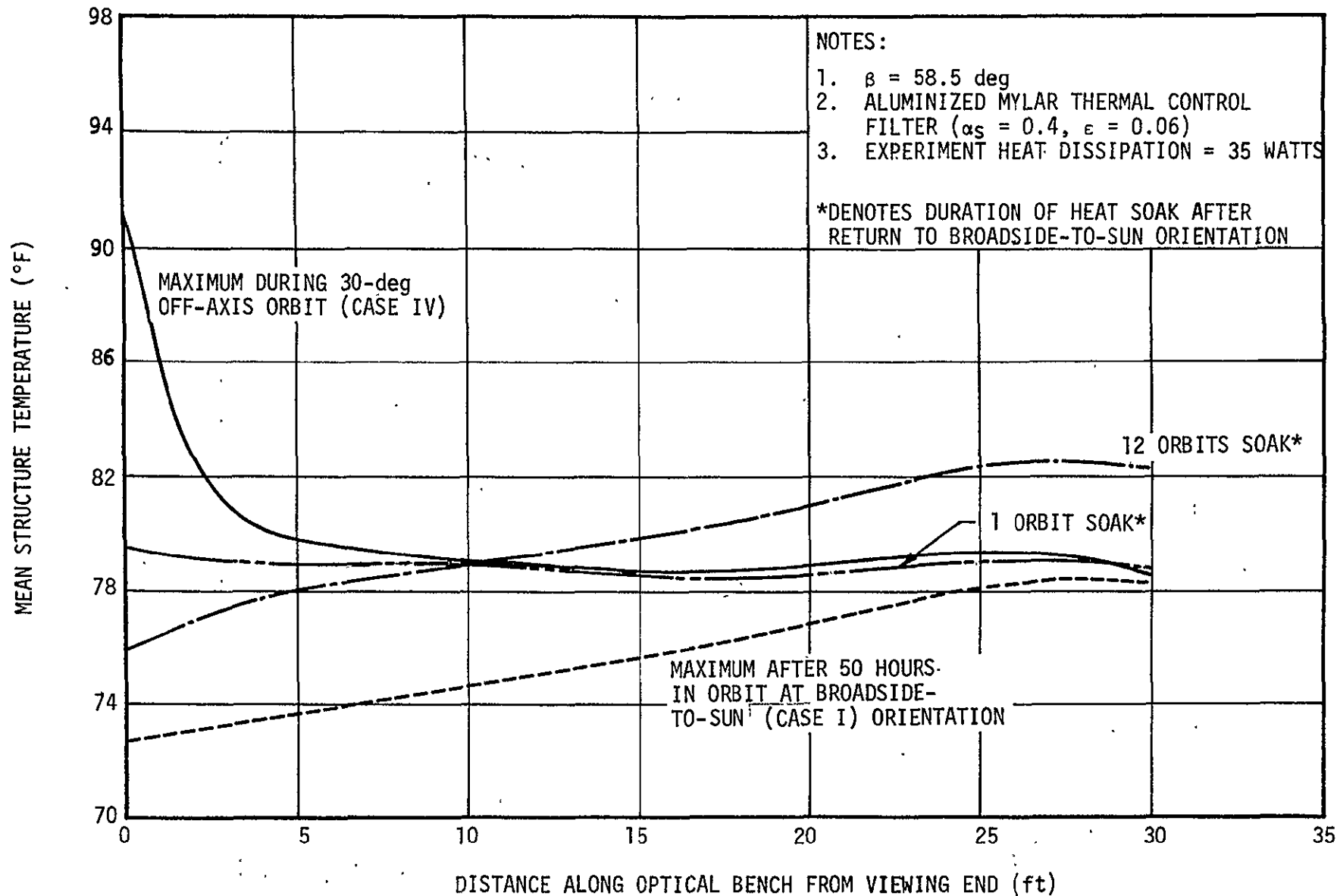


FIGURE 7-20. TRANSIENT EFFECTS ON OPTICAL BENCH STRUCTURE TEMPERATURE RESULTING FROM 30-DEGREE OFF-AXIS SHIFT FOR ONE ORBIT (CASE IV)

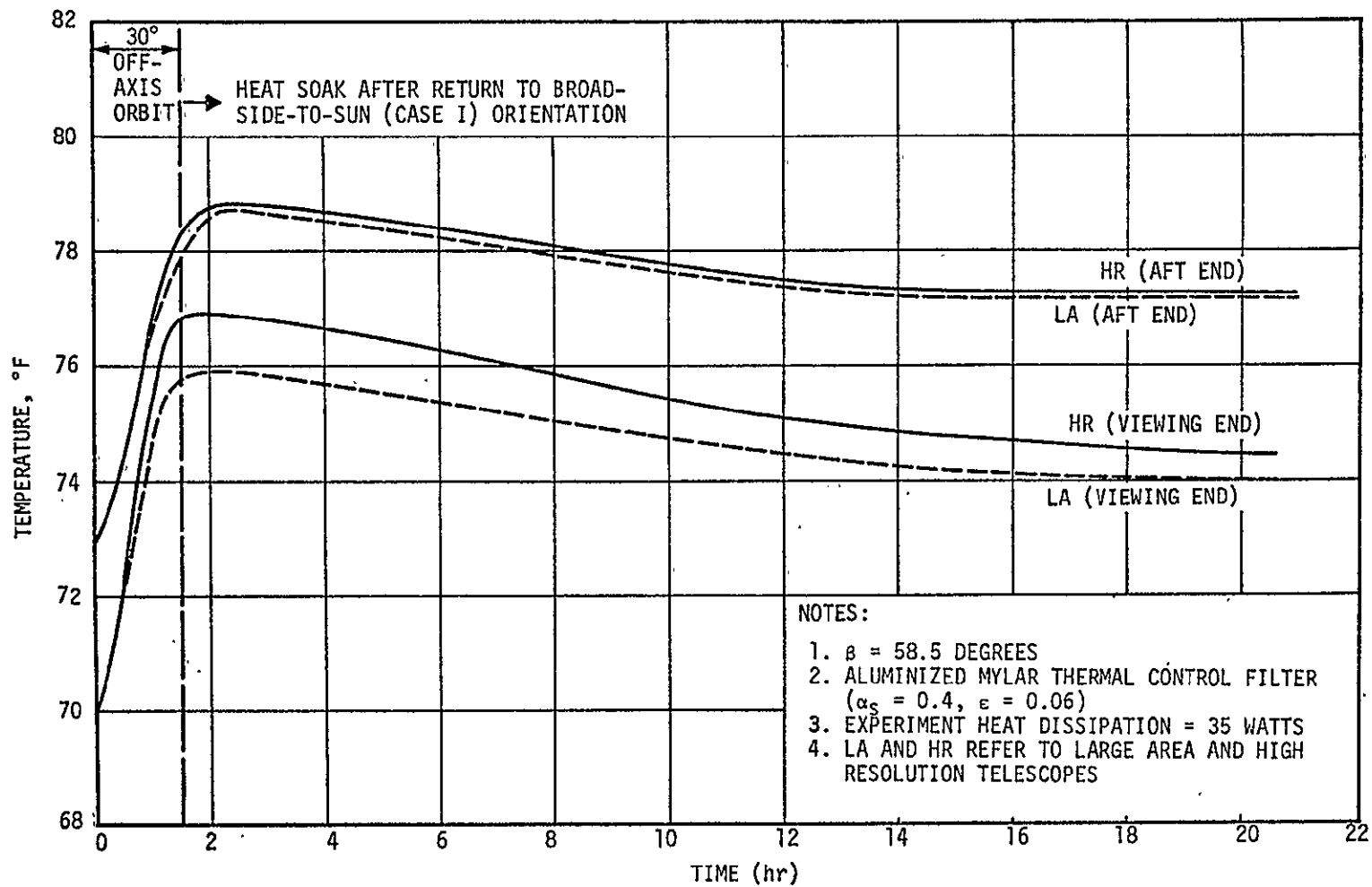


FIGURE 7-21. TRANSIENT EFFECTS ON TELESCOPE MIRROR TEMPERATURES OF 30-DEGREE OFF-AXIS SHIFT TOWARD THE SUN FOR ONE ORBIT (CASE IV)

(Case I) orientation were simulated by the thermal model. As shown in Figure 7-20, the predicted optical bench temperature near the viewing end rises above its allowable upper limit of 80°F to a maximum value of approximately 91°F during the 30-degree off-axis orientation. The predicted temperature response of the aft end of the optical bench continues to rise during the period of heat soak to a level of approximately 82.5°F after 20 hours (12 orbits) of heat soak. The extended period of temperature rise of the aft end results from the fact that heat generation from the detectors continues while the temperature differential between the aft end and the viewing end (which is the driving force for heat transfer) decreases due to the temporary 30-degree off-axis shift. Extrapolation of the predicted temperature-time curve representing the thermal response of the aft end of the optical bench indicated that the temperature at this location would reach a maximum value of approximately 83.5°F after a period of approximately 40 hours of heat soak.

Figure 7-21 illustrates the predicted effect of the temporary shift of the spacecraft axis to the Case IV orientation on the telescope mirror temperature history. The predicted transient temperature histories of the viewing and aft ends of both the L. A. and H. R. telescopes are presented for the orbit during which the spacecraft axis is canted 30 degrees and for the period of heat soak following the return to the broadside-to-Sun (Case I) orientation. The initial temperatures of 70°F and 73°F at the viewing and aft ends of the telescopes represent the predicted temperatures of those respective locations at the time in orbit when the spacecraft emerges from the Earth's shadow after being spaceborne for a period of 50 hours in the Case I orientation. It is noted from Figure 7-21 that the telescope temperatures will rise very rapidly after the viewing end of the spacecraft is inclined 30 degrees

toward the Sun, although the predicted telescope temperatures remain within the prescribed limits of $70^{\circ}\text{F} \pm 10^{\circ}\text{F}$. The aft ends of both telescopes are predicted to reach a maximum temperature level of approximately 77°F at the end of the Case IV orbit, while the viewing end of the L. A. telescope simultaneously reaches a predicted peak temperature of 76°F . The large area telescope temperature was predicted to be slightly lower than that of the H. R. telescope because of the shading provided by the extended mosaic crystal.

Figure 7-21 also illustrates that the telescopes will require a long period of heat soak to return to their normal temperature levels following the sudden shift to the Case IV orientation. This predicted slow temperature response results from the large thermal inertia of the telescopes and from the relatively small temperature differential between the telescopes and the thermal control filter during the heat soak period.

Predicted temperature histories of the solar panels during the Case IV orientation are not illustrated herein since the environmental heat flux incident upon the solar panels in the 30-degree off-axis orientation, and the resulting temperature response, will be less severe than for Cases I, II, and III described previously.

THERMAL CONTROL OF HEAO-B AND HEAO-D SPACECRAFT

The objectives of this segment of the investigation are to examine the thermal control requirements of the HEAO-B and HEAO-D spacecraft, to identify potential problem areas and to suggest approaches for accomplishing the thermal control objectives. The conclusions presented herein are based on spacecraft and experiment descriptions that were transmitted from NASA/MSFC to Teledyne Brown Engineering.

HEAO-B Mission

The arrangement of candidate experiments considered for the HEAO-B spacecraft is depicted in Figure 7-22. The spacecraft will be oriented predominantly broadside to the Sun throughout its orbital lifetime of two years. The spacecraft will be placed in a 200-nautical mile altitude circular orbit at an inclination of 28.5 degrees to the equator. Following the preferred mission sequence, the spacecraft will first perform a galactic scan for a period of one month which will be followed by a celestial scan for the next six months. A pointing mode will then be maintained for the remainder of the two-year mission. During the galactic and celestial scan modes, the spacecraft will spin at a rate of approximately 0.1 rpm about its scan axis, which will be aligned within 1 degree of the solar vector during the celestial scan mode and within a few degrees of the galactic plane axis during the galactic scan mode. In the pointing mode the spacecraft will be despun, and the instruments will be pointed at a selected positions on the celestial plane, with target selection at a given time limited by the solar offset angle.

The overall objective of the thermal control system is to maintain the absolute temperatures and the thermally-induced deformations of the system components to within acceptable limits. A general guideline, which was adhered to in the preliminary design of the HEAO-A and HEAO-C spacecraft, is that all internal spacecraft components shall be maintained within the operating temperature limits of 14°F to 86°F, unless otherwise specified. Examination of the thermal control requirements of the HEAO-B candidate experiments indicates that the magnetic spectrometer experiment and the focusing X-ray experiment will pose the most critical thermal control requirements. All other

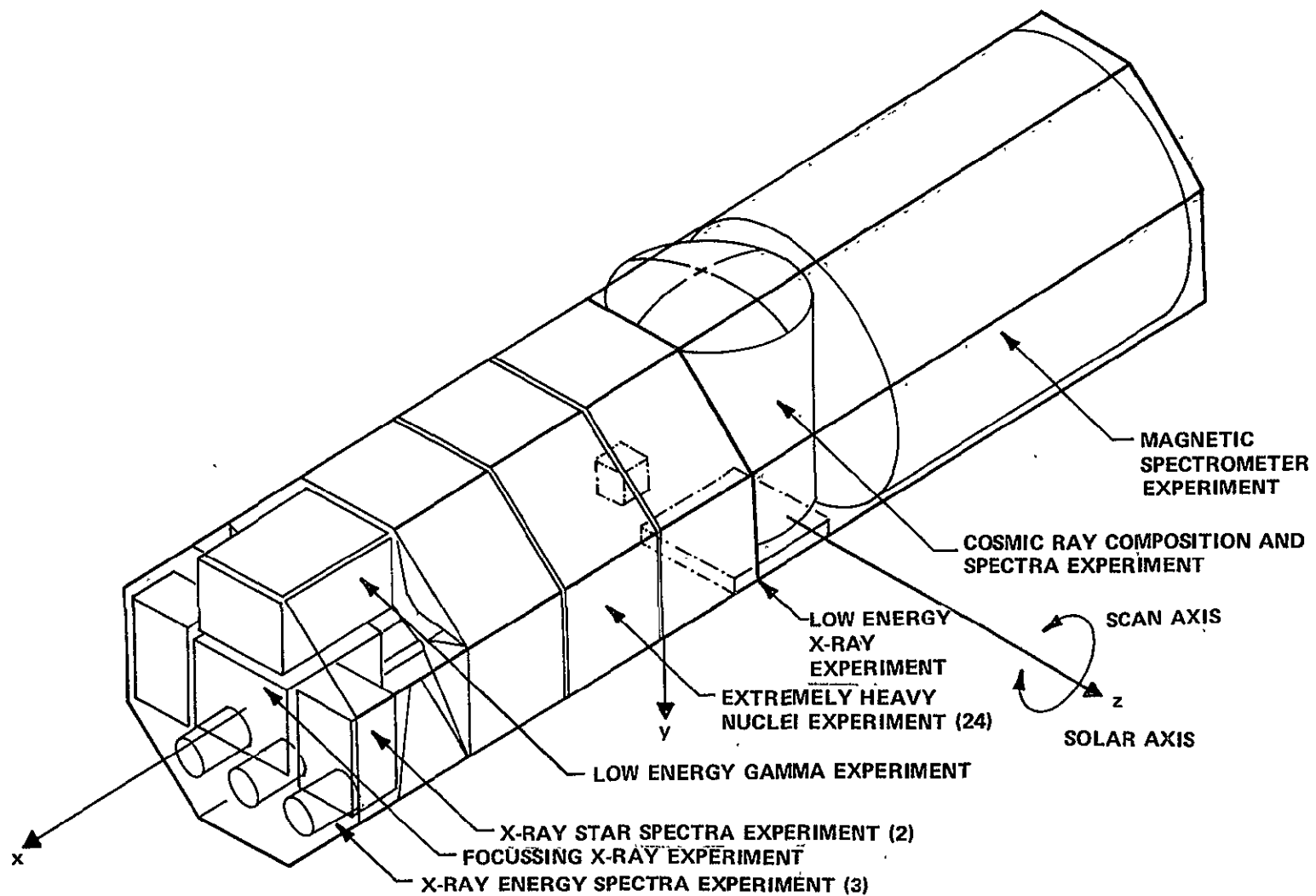


FIGURE 7-22. HEAO-B EXPERIMENT ENVELOPE

experiments should operate satisfactorily if their average operating temperatures are maintained within the guideline limits of 14°F to 86°F, which will present no apparent difficulty.

Magnetic Spectrometer Experiment - The magnetic spectrometer experiment, described in Reference 7-12, contains a superconducting magnet having two coils that are submerged in liquid helium to maintain a coil temperature of approximately 4°K. Because of the long (1 to 2 years) mission duration of HEAO-B, the prevention of complete boiloff of the liquid helium is an extremely difficult, but necessary, thermal control requirement. Reference 7-12 proposes a simple open-cycle thermal control scheme wherein a highly-effective dewar is filled with a sufficient amount of liquid helium (889 pounds for a one-year mission) to permit experiment operation for the desired lifetime based on a predicted total heat leak rate (206 mW for a one-year mission).

The dewar thermal protection system is designed to isolate the helium from the environment with a minimum heat leak into the helium storage vessel. The total heat leak rate of 206 mW is composed of heat leaks of 16.8 mW through the superinsulation, 189 mW through the tank supports and 0.2 mW through plumbing components. Protection from thermal radiation between the outside and inside tank walls is provided by a combination of passive and active shielding. Passive shielding consists of multiple layers of doubly aluminized Mylar with a layer density of approximately 67 layers per inch inside the evacuated annulus. Passive shielding alone would require an excessively large insulation thickness to reduce the heat leak through the insulation to the design level of 16.8 mW. For this reason, it is proposed in Reference 7-12 to add intermediate, actively cooled radiation shields inside the annular space, which are cooled by the

effluent helium vapor. Thus, the refrigerating capacity of the vaporized helium is used to reduce the temperature levels of the intermediate shields.

It is obvious that successful operation of the experiment using this thermal control concept will require careful analysis, development and testing of the proposed vapor cooling concept and of low heat leak structural supports for the helium vessel. It is important to note that the required initial weight of stored helium increases from 889 pounds to 2,027 pounds as the desired experiment lifetime is increased from one to two years, as reported in Reference 7-12. Correspondingly, the outside tank dimensions must be increased from 71-inch diameter and 69.6-inch length to 91.5-inch diameter and 90-inch length as the experiment lifetime is increased from one to two years. These increases in weight and size of the magnetic spectrometer experiment will impact the arrangement of the other experiments if a two-year experiment lifetime is desired.

An alternate approach for thermal control of the magnetic spectrometer experiment which would possibly result in a weight savings and increased experiment lifetime would utilize a closed cycle refrigeration system. According to Reference 7-13, miniature refrigerators which utilize reciprocating machinery to execute the Brayton or Claude cycle are under development for application to operating conditions similar to those required by the magnetic spectrometer experiment. To achieve the required reliability, a novel approach is used in compressor design wherein the pistons are rotated as well as reciprocated. This permits the use of ports to control gas flows and clearance seals to limit leakage. Electromagnetic actuators drive the pistons. The relatively few moving parts are completely supported on self-acting gas bearings, thus eliminating rubbing or sliding surfaces as in conventional reciprocating refrigerators.

Figure 7-23 shows the estimated weight of a closed-cycle refrigerator system as a function of temperature and cooling load (Ref. 7-13). Assuming a maximum total cooling load of 1 watt and an evaporator temperature of 4°K, Figure 7-23 indicates a total refrigeration system weight of approximately 300 lbm, including the weight of the power supply, power conditioning equipment, refrigerator and space radiator. Preliminary calculations indicate that the total heat leak into the helium tank can be maintained below a maximum of 1 watt with a thickness of superinsulation of approximately 5 to 6 inches, without using the effluent vapor cooling scheme proposed in Reference 7-12. This insulation requirement calculation is based upon the heat leak component through the tank supports to be 0.189 watt, as estimated in Reference 7-12.

Therefore, the utilization of a closed cycle refrigeration system could result in a maximum weight savings of approximately 589 lbm compared with the proposed stored helium concept, based on an experiment lifetime of one year. Realization of this maximum weight savings would require elimination of the entire 889 lbm of stored helium as specified in Reference 7-12. Since it would probably be desirable to keep the coil submerged in a small amount of liquid helium, even with the closed cycle refrigeration system, the maximum weight savings could not be fully realized. However, the weight savings to be gained from using a closed cycle refrigeration system becomes more significant when an experiment lifetime of two years is considered. This is because the refrigeration system weight is virtually independent of experiment lifetime (unless reliability considerations dictate a redundant system), whereas the required weight of stored helium for the concept proposed in Reference 7-12 more than doubles as the experiment lifetime is increased from one to two years.

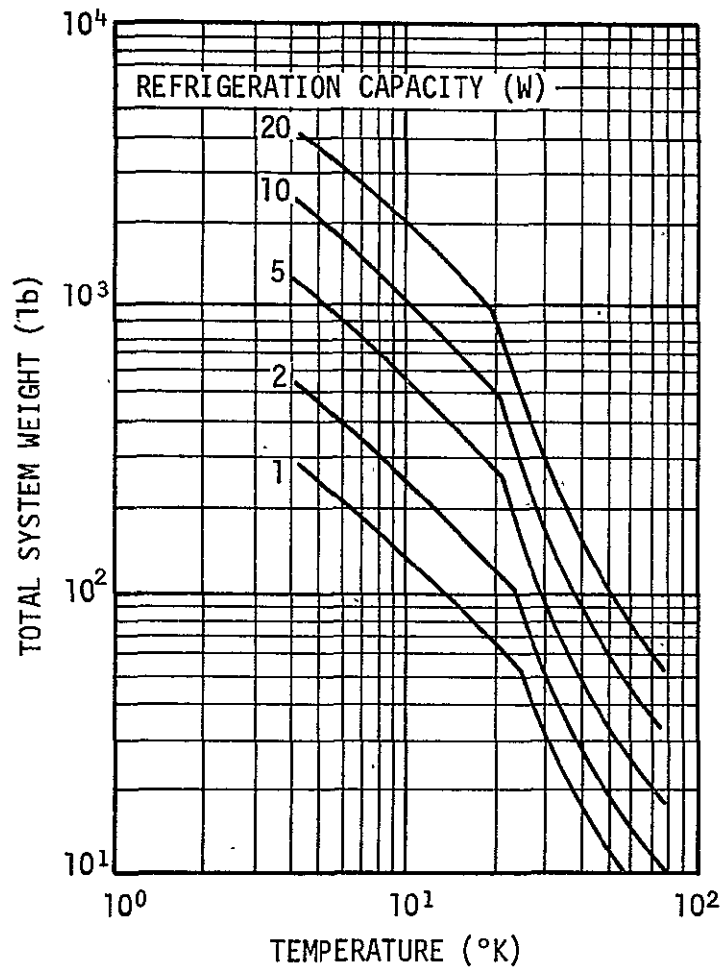


FIGURE 7-23. ESTIMATED WEIGHTS OF CLOSED-CYCLE SPACEBORNE REFRIGERATION SYSTEMS

In a comparison of the relative merits of a closed cycle refrigeration system versus the proposed stored helium concept, one must first establish whether a proven mechanical refrigeration system will be available by the desired launch date. Reference 7-12 is not conclusive in this regard. In addition, the potential weight savings of the closed cycle refrigeration system must be traded against the apparent improvement in simplicity of the stored helium concept. However, the proposed utilization of effluent helium vapors for active cooling of the radiation shields tends to degrade the simplicity and reliability of the stored helium concept due to the additional control requirements and the increased possibility of vapor leakage into the evacuated annular space occupied by the multilayer insulation. Infiltration of the multilayer insulation by helium vapors would result in reduced experiment lifetime due to degraded insulation performance and increased boiloff. Since isentropic efficiencies of the mechanical refrigeration system components are expected to be in the range of 80 percent (Ref. 7-13) the power requirement is not expected to be large enough to impose a critical requirement on the power supply.

Focusing X-Ray Experiment - There are two areas of concern relative to the thermal effects on the operation of the focusing X-ray experiment:

- Effects of thermally induced deformations of spacecraft structure on the experiment focal plane tolerances
- Thermally induced structural distortion of the grazing incidence X-ray mirrors inside the viewing package.

The former effect arises primarily because of the experiment's long length (~26 feet). The experiment will likely be calibrated in the laboratory where the mounting structure will have a particular temperature distribution. After the experiment becomes operational in

space, uneven environmental heating of the structure will result in a temperature distribution which may be considerably different from that at which the experiment has been calibrated. The relative deflections of the structural members resulting from the new temperature distribution could cause an excessive change in the location of the focal plane.

Since the magnitudes of the thermally induced deflections will be proportional to the coefficient of thermal expansion of the experiment mounting structure, consideration of a structural material which is relatively insensitive to temperature gradients, e. g., reinforced plastic or Invar, will be advantageous. An approach for controlling the focal plane position would consist of utilizing a low-expansion material in the construction of a mounting structure, similar to the HEAO-C optical bench, which is thermally and mechanically independent from the primary spacecraft structure. The criticality of minimizing thermal gradients in the experiment mounting structure would then be reduced drastically. An alternative approach would be an active focusing system to reposition the detectors to the focal plane in the event of excessive thermally induced deformations. An active system is undesirable, however because of its inherent reliability penalties. Moreover, it would not solve the problem of defocusing due to X-ray mirror distortions.

Excessive variations in the temperature levels of the mirrors or of their supporting structure would result in distortions of the mirror contours which would cause defocusing. Moreover, nonuniform circumferential or axial temperature distributions are both conditions which could lead to excessive distortions of the mirror contours and defocusing. Therefore, considerable care must be taken in the thermal design of the mirror package to insure that both the levels and gradients of mirror temperature remain within acceptable limits during orbit.

The mirrors are particularly susceptible to large excursions in temperature due to their nearness to the constantly changing environment. Utilization of a thin thermal control filter between the mirrors and the environment, similar to the HEAO-C concept, would reduce the transient temperature excursions of the mirrors. Small resistance heaters may be required to maintain the mirror temperatures during periods of exposure to deep space. Undesirable circumferential or axial temperature gradients in the mirrors or in their supporting structure could be eliminated through the integration of heat pipes into their structure. The heat pipes would conduct excess heat almost isothermally from potential hot spots to cooler locations on the mirror structure, thus maintaining a uniform mirror temperature distribution.

HEAO-D Mission

The proposed experiment arrangement for the HEAO-D spacecraft is illustrated in Figure 7-24. Of the experiments shown, only the magnetic spectrometer experiment poses unusually difficult thermal control requirements. The configuration of this experiment to be considered for the HEAO-D mission differs from that considered for the HEAO-B mission since only one coil (rather than two) is to be considered for HEAO-D.

In addition to the thermal control considerations discussed previously for this experiment, the single coil arrangement impacts the spacecraft thermal control system drastically, since a constant spacecraft orientation is no longer possible. This is explained by the fact that the electromagnetic field generated by the coil is not cancelled by that from a second coil. Hence, the magnetic field of this experiment interacts with the Earth's magnetic field, causing continuous reorientation of the spacecraft. This phenomenon will require either solar panels

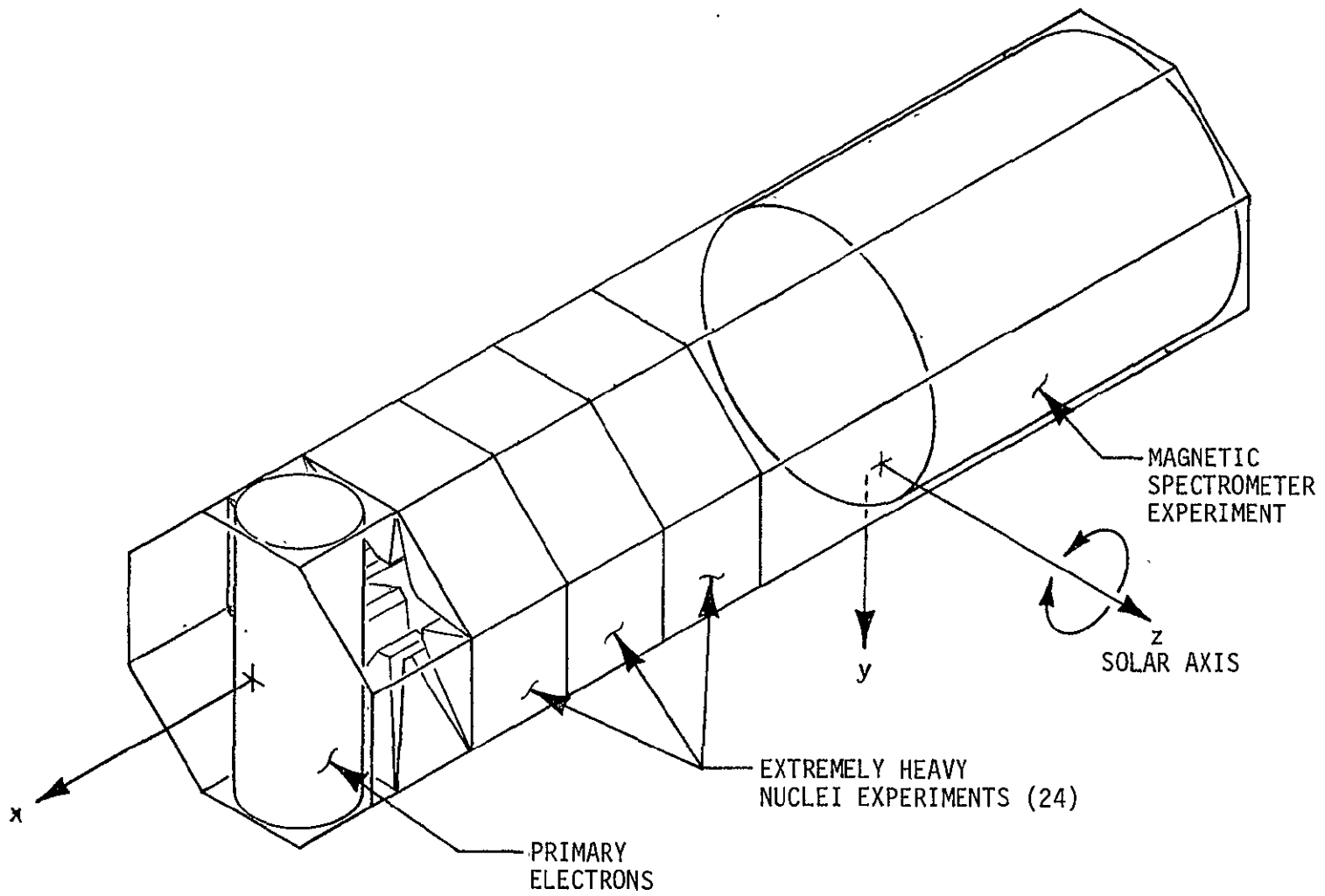


FIGURE 7-24. EXPERIMENT LOCATIONS ON THE HEAO-D SPACECRAFT

mounted over the entire spacecraft skin or moveable solar panels. Because of the inherently large absorptivity of solar panels, the former arrangement would result in an excessively warm ($\approx 150^{\circ}\text{F}$) spacecraft. Moveable solar panels would be difficult to control considering the rapidity of the spacecraft reorientation, and would consume a relatively large amount of power for repositioning devices alone. In addition, the design of a feasible thermal control system to maintain the spacecraft experiments and subsystems within required temperature limits under the conditions of constantly changing spacecraft orientation could prove to be a difficult task.

CONCLUSIONS

Based on the results of the HEAO-C thermal analysis described herein, the following conclusions about this mission may be drawn:

- The thermal control concept proposed in Reference 7-1 will maintain the experiments inside the optical bench within their allowable temperature and thermal deflection limits using an aluminized Mylar thermal control filter during the broadside-to-Sun (Cases I and II of Figure 7-3) orientations.
- A modified thermal control filter and/or a deployable Sun shade will be required to maintain the optical bench temperature below the allowable limit for orientation Cases III and IV (Figure 7-3) with the viewing end inclined 15 degrees toward the Sun continually or 30 degrees toward the Sun for one orbit per day.
- Design modifications will be required to prevent the surface temperature of the center solar panel from exceeding the recommended upper limit of 212°F during the Case I, broadside-to-Sun, orientation (220°F predicted). Modifications which are recommended for investigation include:
 - ▲ Folding out of the side solar panels to permit more efficient heat rejection from their backsides and thus to provide an improved path of heat conduction from the center solar panel.

- ▲ Incorporation of circumferential heat pipes into the spacecraft skin to efficiently conduct excess heat from the solar panels to the cooler backside of the spacecraft.
- ▲ Incorporation of a phase change material into the honeycomb substrate of the solar panels to act as a thermal capacitor. Excess heat would be absorbed by the phase change process during the sunlit portion of the orbit and would be rejected to space while the spacecraft is in the Earth's shadow.
- ▲ Specification of a spacecraft orientation in which the center solar panel is not oriented exactly perpendicular to the solar vector. An evaluation of the trade-off between the reduction in solar panel temperature and the reduction in the available power due to decreased projected area will determine whether this concept is beneficial.
- The remaining subsystems can be maintained within their allowable operating temperature limits using conventional thermal control techniques.
- The predicted transverse temperature difference across the spacecraft (220°F predicted) is well within the design limit of 366°F, and hence the thermally-induced bending of the spacecraft structure will be within design limits.

The following potential problem areas and subjects for further investigations have been identified for the HEAO-B and HEAO-D missions.

- HEAO-B Mission
 - ▲ Limiting the liquid helium boiloff of the magnetic spectrometer experiment to the design values is based upon the use of vapor cooled intermediate radiation shields and low heat leak structural supports. These components will require careful analysis, development and testing to insure proper operation.
 - ▲ The use of a closed cycle refrigeration system for cooling of the magnetic spectrometer experiment should be investigated.

- ▲ Thermal control of the focusing X-ray experiment within narrow limits is expected to pose some problems.
- HEAO-D Mission
 - ▲ Prevention of liquid helium boiloff from the magnetic spectrometer experiment will be difficult, as in the HEAO-B mission.
 - ▲ The single coil configuration of the magnetic spectrometer experiment proposed for this mission will greatly affect spacecraft attitude. This is expected to pose added thermal control problems.

REFERENCES - Section 7

- 7-1. "Technical Proposal for a Large Orbiting X-Ray Telescope for the HEAO", Publication No. 2410-I, American Science and Engineering, Cambridge, Massachusetts, May 1970
- 7-2. Newby, T. S., "Heat Rate Computer Program -- User's Manual", TXA-1954, Lockheed Missiles and Space Company, Sunnyvale, California, October 26, 1966
- 7-3. Simmons, C. V., "Saturn IB Orbital Workshop Solar Array Thermal and Performance Analysis", Teledyne Brown Engineering Report ASD-ASTN-1006, September 1969
- 7-4. Breuch, R. A., "Handbook of Optical Properties for Thermal Control Surfaces", LMSC-A847882, Vol. III, Lockheed Missiles and Space Company, Sunnyvale, California, June 1967
- 7-5. Gaski, J. D., "Chrysler Improved Numerical Differencing Analyzer", Technical Note AP-66-15, Chrysler Space Division, New Orleans, Louisiana, April 30, 1966
- 7-6. Aluminum Standards and Data, Second Edition, The Aluminum Association, New York, N. Y., December 1969
- 7-7. Metals Handbook, 8th Edition, Vol. 1, American Society for Metals, Metals Park, Ohio, 1961
- 7-8. Dendy, N. C., "Orbital Workshop Solar Array System Thermal and Performance Analysis for Sky Lab and Solar Inertial Latitude", Teledyne Brown Engineering Report ASD-ASTN-1147, May 1970
- 7-9. Fried, E. and Costello, F. A., "Interface Thermal Contact Resistance Problem in Space Vehicles", ARS Journal, October 26, 1961
- 7-10. Ponder, C. A., "Computer Program for Calculating Geometric Shape Factors and Gray Body Interchange Factors Between Diffuse Gray Surfaces", Technical Report HSM-R588-70, Chrysler Space Division, Huntsville, Alabama, March 1970

REFERENCE - Concluded

- 7-11. Horton, H. N., "Engineering Evaluation Test Report Investigation of Solder Joint Failures on ATM Solar Cell Modules", Astrionics Laboratory, NASA/Marshall Space Flight Center, Huntsville, Alabama, December 20, 1968
- 7-12. Alvarez, L. W., "Superconducting Magnetic Spectrometer Experiment for HEAO", UCBSL No. 374, University of California, Berkeley, California, May 29, 1970
- 7-13. Breckenridge, R. W., "Spaceborne Refrigeration Systems", Arthur D. Little, Inc., Cambridge, Massachusetts, Presented at Cryogenics and Infrared Detection Systems Conference, Frankfurt, W. Germany, April 17-18, 1969

8. ELECTRICAL POWER SYSTEM

DESIGN REQUIREMENTS

The design requirements for the HEAO-C electrical power system have been derived from the operational requirements of the experiments and spacecraft and, in many cases, are supplemented by design goals in excess of the requirements. The general design requirements are:

- Delivery of adequate electrical power to the using loads
- Delivery of regulated 28 volt dc power to the using loads
- Operation in a circular Earth orbit of 300 nautical miles altitude inclined at 35 degrees to the equator
- Continuous operation through solar illumination angles of 0 to ± 15 degrees and operation for one orbit per day with the solar illumination angle as large as ± 30 degrees
- Lifetime of one year

The general design goals are:

- Lifetime of two years
- Modular design
- Use of low cost, highly reliable, proven components.

The specific design requirements and goals are defined in the following paragraphs.

Electrical Power Load Requirement

The loads to be supplied with electrical power are delineated in the following list.

- Experiments
- Attitude sensing system
- Attitude control system
- Communications and data handling system
- Thermal control system.

The electrical power requirements of the individual elements of the experiments are listed in Table 8-1. Included in this listing is the identification of the combination of experiment elements which, when operated simultaneously, present the maximum experiment power requirements. Because the frequency and duration of use of the combinations of elements is not predictable, no power profile or composite average power load requirement has been established.

The electrical power requirements of the individual elements of the attitude sensing system are listed in Table 8-2. The total peak and average powers are listed in this table. All components of this system operate continuously except for the Sun sensors, which are used only for initial Sun acquisition. If attitude reference is lost at some point in the mission, the Sun sensors would probably be required again.

The electrical power requirements of the individual elements of the attitude control system are listed in Table 8-3. The total peak and average powers required are listed in this table. As indicated, the peak power load is primarily associated with operation of the control moment gyros. The CMGs for which these loads were sized are the Sperry Model 100 units, which produce 100 ft-lbf-sec of angular momentum. Although units of smaller capacity would be adequate for the subject mission, as discussed in Section 6, the Sperry units are sized because they represent the closest size in proven hardware. The conceptual HEAO-C spacecraft design includes six CMGs; average power is 15 watts per unit and peak power is 60 watts per unit. The peak CMG

TABLE 8-1. EXPERIMENTS POWER REQUIREMENTS

<u>Load Element</u>	<u>Power Required (W)</u>	
	<u>Element</u>	<u>Combination for Max. Exp. Power</u>
High Resolution Telescope		
H.R. Image Detector	13.5	13.5
H.R. Image Detector Electronics Module	19.0	19.0
H.R. Crystal Spectrometer	21.0	--
H.R. Experiment Transport Mechanism	6.0	--
Transmission Grating	6.0	--
Filter Wheel	6.0	--
Large Area Telescope		
L.A. Image Detector	1.0	1.0
L.A. Image Detector Electronics Module	13.5	13.5
Multiple Polarimeter	1.0	1.0
Multiple Polarimeter Electronics Module	8.6	8.6
Solid State Detector	2.0	2.0
Solid State Detector Electronics Module	6.2	--
L.A. Experiment Transport Mechanism	6.0	--
Mosaic Crystal	6.0	--
Mosaic Crystal Electronics Module	0.5	--
Mosaic Crystal Deployment Structure	6.0	--
Flare Detectors		
Course Detectors (4)	4.0	4.0
Course Detectors Electronics Modules (4)	25.6	25.6
Fine Detector	1.0	--
Fine Detector Electronics Module	6.4	--
Scintillation Counter		
Monitor Proportional Counter	1.0	1.0
Monitor Proportional Counter Electronics Module	8.0	8.0

TABLE 8-1 - Concluded

<u>Load Element</u>	<u>Power Required (W)</u>	
	<u>Element</u>	<u>Combination for Max. Exp. Power</u>
Flat Crystal Spectrometer	2.0	2.0
Flat Crystal Spectrometer Electronics Modules	15.0	15.0
Computer	145.0	145.0
Aspect Detector	8.0	8.0
Aspect Detector Electronics Module	6.0	<u>6.0</u>
TOTAL		284.2

TABLE 8-2. ATTITUDE SENSING SYSTEM POWER REQUIREMENTS

<u>Load Element</u>	<u>Power Required (W)</u>	
	<u>Average</u>	<u>Peak</u>
Star Trackers (2)	50	50
Reference Gyros (3)	30	30
Coarse Sun Sensor (8)	-	1
Fine Sun Sensor	-	1
Gyro and Sun Sensor Electronics	<u>5</u>	<u>5</u>
TOTALS	85	87

TABLE 8-3. ATTITUDE CONTROL SYSTEM POWER REQUIREMENTS

<u>Load Element</u>	<u>Power Required (W)</u>	
	<u>Average</u>	<u>Peak</u>
Control Moment Gyros (6)	90	225*
Electromagnetic Control Torquers (3)	20	30
Magnetometers (3)	5	5
Gas Despin System	<u>-</u>	<u>5</u>
TOTALS	115	265

*Power requirements are for six 100 ft-lbf-sec angular momentum gyros.

power requirement shown in Table 8-3 is an estimate assuming that three units are drawing average power and that three units are drawing peak power. CMGs would be spun up prior to launch using ground support power.

The electrical power requirements of the individual elements of the communications and data handling system are listed in Table 8-4. The total peak and average powers required are listed in this table. The peak power load is primarily associated with the operation of the S-band traveling wave tube power amplifiers during data transmission.

The electrical power requirements of the individual elements of the thermal control system are listed in Table 8-5. The total peak and average powers required are listed in this table. Bench heaters are required to maintain the optical bench within the design temperature range when the power being used by the bench experiments drops below 35 watts.

The total electrical power required to be supplied to all spacecraft load elements is listed in Table 8-6. The total peak and average powers required are listed in this table. The total peak power listed in the table will occur only if the peak control moment gyro requirement and data transmission are performed simultaneously. If the total peak power does occur its duration will not exceed approximately 6 minutes per orbit.

The design requirements for electrical power to be delivered to the loads including a 10% contingency are listed below.

- Peak power = 1141 watts
- Average power = 705 watts

TABLE 8-4. COMMUNICATIONS AND DATA HANDLING SYSTEM
POWER REQUIREMENTS

<u>Load Element</u>	<u>Power Required (W)</u>	
	<u>Average</u>	<u>Peak</u>
Command Receivers (2)	<1	<1
Command Decoder	<1	<1
Signal Conditioner	8	8
Multiplexer	5	5
Tape Recorders (4)	8	25
S-Band Decoder/Transmitters (2)	60	60
S-Band Power Amplifiers (2)	58	260
Beacon Transmitters	<u>8</u>	<u>8</u>
TOTALS	147	366

TABLE 8-5. THERMAL CONTROL SYSTEM POWER REQUIREMENTS

<u>Load Element</u>	<u>Power Required (W)</u>	
	<u>Average</u>	<u>Peak</u>
Optical Bench Heaters	<u>10</u>	<u>35</u>
TOTALS	10	35

TABLE 8-6. TOTAL HEAD-C POWER REQUIREMENTS

<u>Load Element</u>	<u>Power Required (W)</u>	
	<u>Average</u>	<u>Peak</u>
Experiments	284	284
Attitude Sensing System	85	87
Attitude Control System	115	265
Communications and Data Handling System	147	366
Thermal Control System	<u>10</u>	<u>35</u>
Subtotal	641	1037
Contingency (10 percent)	<u>64</u>	<u>104</u>
TOTALS	705	1141

Other Design Requirements

Other design requirements are as follows:

- Output Voltage - The voltage supplied to the wiring loads will be direct current 28 ± 4 volts.

- Orbital Periods - The period of the 300 n. mi. altitude circular orbit is 95.7 minutes. The daytime-nighttime extremes are:
 - ▲ 74.7 minutes day
 - ▲ 21.0 minutes nightand
 - ▲ 60.1 minutes day
 - ▲ 35.6 minutes night

- Solar Illumination Angle - The requirement is that the spacecraft be capable of continuous operation at an attitude where the solar vector makes an angle with the middle solar panel from 90 degrees to 75 degrees, and that the spacecraft be capable of operating for one orbit per day at an attitude where the solar vector angle to the middle solar panel is as low as 60 degrees. It is desirable that the spacecraft be capable of operation with the solar vector as low as possible.

- Lifetime - The minimum lifetime is one year and a two year lifetime is desirable.

- Modular Design - Maximum use of modular, interchangeable hardware with maximum commonality is a design goal.

- Component Selection - Maximum use of low cost, highly reliable, proven components is a design goal with preference being given to those components previously qualified through testing and/or actual flight use.

DESIGN APPROACH

Two basic design approaches were formulated and investigated. These two approaches differed primarily in the type of power source employed; one used solar cell modules and the other used radioisotope thermoelectric generators. Both approaches were pursued through the development of conceptual design block diagrams.

Solar Cell Module Approach

The conceptual solar cell module system, shown in Figure 8-1 consists of the following major elements.

- Solar Cell Modules - used to transform solar energy into prime electrical power
- Solar Combiners - used to combine the solar cell modules electrical power output for routing to the charger-battery-regulator modules
- Charger-Battery-Regulator Modules - used to provide orbital daytime/nighttime electrical power conversion and storage, and load voltage regulation
- Load Power Distributors - used to route electrical power to the spacecraft loads and to provide load sharing and isolation.

During the daylight portion of the orbit, the solar cell modules mounted on the spacecraft's external structure are illuminated and develop electrical energy. The electrical energy developed by the modules is combined by the solar combiners, which also provide isolation between modules whose electrical outputs are at different voltage levels. The combined electrical energy is supplied to the charger-battery-regulator modules, where it is regulated and routed first to the load distributors and then to the using loads.

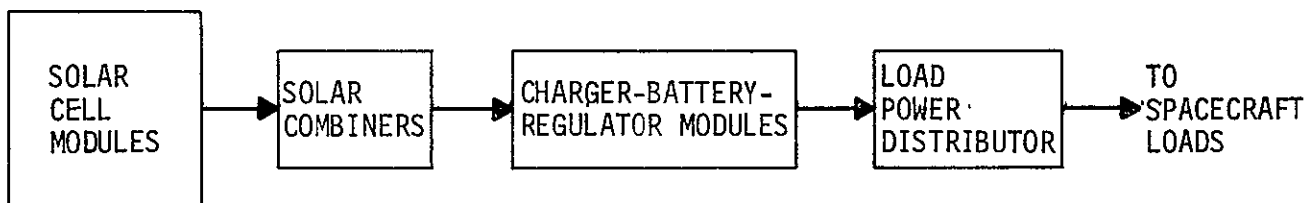


FIGURE 8-1. SOLAR CELL MODULE SYSTEM CONCEPT

Input electrical energy in excess of that required to satisfy the using loads is routed through battery chargers to batteries at a rate suitable for charging. If the input electrical energy is less than that required to satisfy the using loads, it is augmented by energy from the batteries. During the nighttime portion of the orbit, the electrical energy required by the using loads is supplied solely by the batteries.

Critical aspects of the solar cell module design approach include the following:

- Sizing, configuration, and placement for the solar cell modules with respect to solar illumination angles
- Variation of solar cell module electrical energy and voltage output with temperature
- Solar combiner isolation of solar cell modules
- Battery sizing with respect to depth of discharge and resultant battery operating life
- Load sharing and equalization of load distributors
- Overall system reliability.

Radioisotope Thermoelectric Generator Approach

The conceptual radioisotope thermoelectric generator system, shown in Figure 8-2, consists of the following major elements.

- Radioisotope Thermoelectric Generators - used to provide prime electrical power
- Regulators - used to regulate prime electrical power voltage and to isolate radioisotope thermoelectric generators from using loads
- Load Power Distributors - used to route electrical power to the using loads and to provide load sharing and isolation.

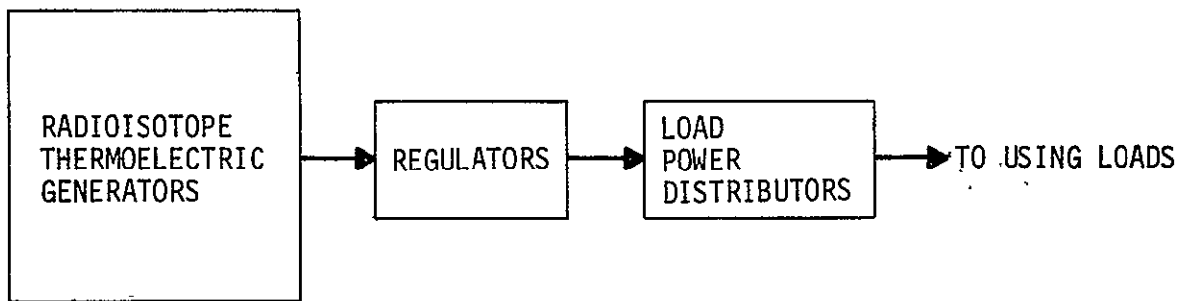


FIGURE 8-2. RADIOISOTOPE THERMOELECTRIC GENERATOR SYSTEM CONCEPT

The radioisotope thermoelectric generators, mounted external to the spacecraft, develop the electrical energy which is routed, through regulators, to the load distributors and using loads. Critical aspects of the radioisotope thermoelectric generator design approach include the following:

- Sizing, configuration, and placement of the radioisotope thermoelectric generators with respect to heat dissipation, radiation shielding, and spacecraft drag
- Isolation of radioisotope thermoelectric generators from using loads by regulators
- Load sharing and equalization of load distributors.

SPECIFIC SOLAR CELL MODULE SYSTEM DESIGN

The specific solar cell module system design proposed is shown in block diagram form in Figure 8-3. The system consists of the following major elements.

- 84 Solar Cell Modules - organized in 7 symmetrical sections of 12 modules each
- 7 Solar Combiners - one used for each solar cell module section
- 9 Charger-Battery-Regulator Modules - 7 used (one each) for the solar combiners plus 2 in passively redundant configurations
- 2 Load Distributors - 1 used with 4 charger-battery-regulator modules and 1 used with 3 charger-battery-regulator modules.

The following paragraphs describe the analyses involved in the system and component selection and sizing.

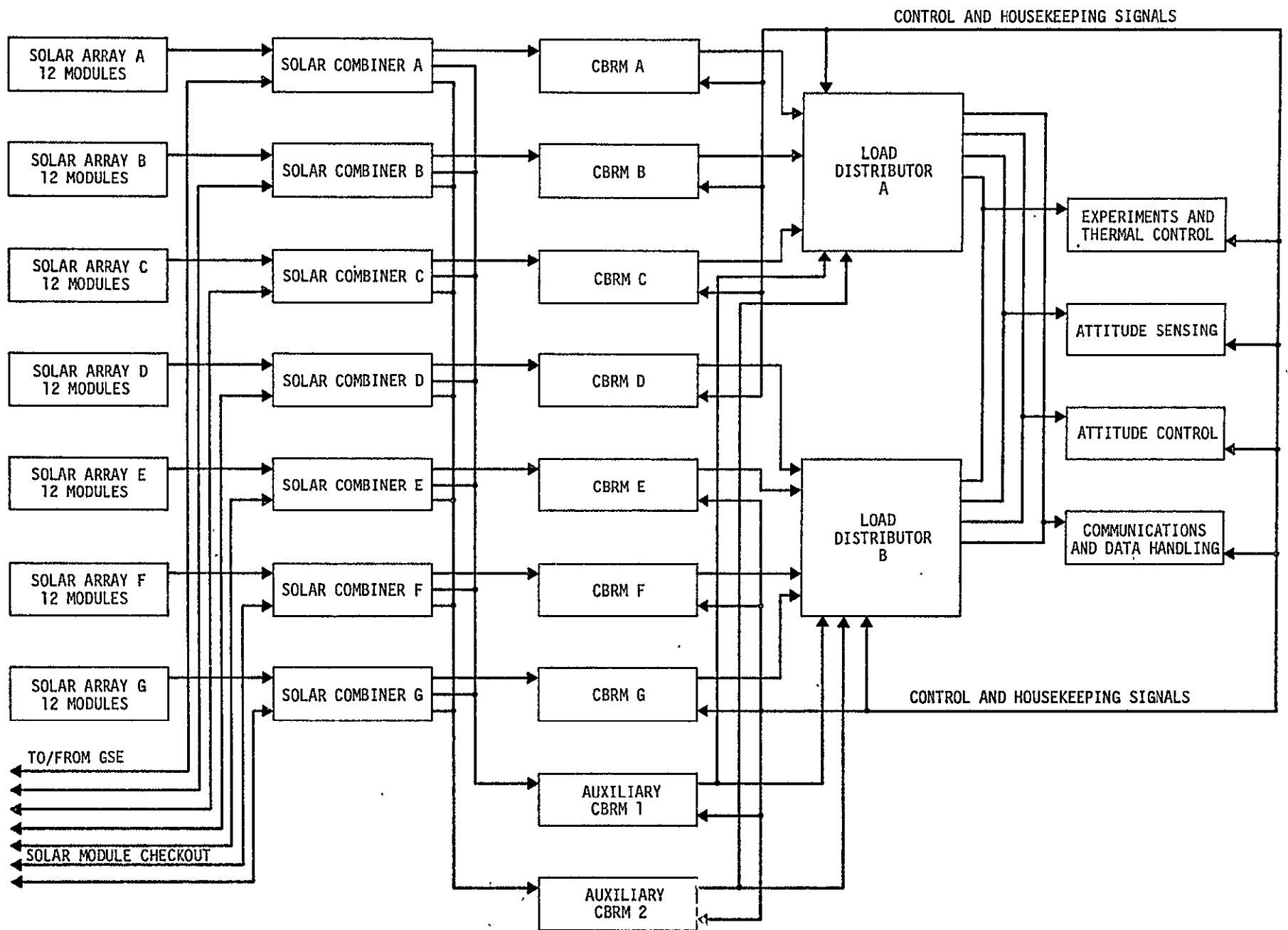


FIGURE 8-3. ELECTRICAL POWER SYSTEM BLOCK DIAGRAM

System Performance Factor

The system performance factor is the ratio of solar cell module output power to delivered load power. This factor includes the losses contributed from straight-through delivery of load power and from battery charging. As shown in Figure 8-4, power delivered directly from the solar cell modules to the using loads is reduced by the transmission losses L_T between the solar cell modules and the charger-battery-regulator modules, the regulator losses L_R , and the distribution losses between the charger-battery-regulator modules and the using loads L_D . Power delivered from the batteries is reduced by the regulator losses L_R and the distribution losses L_D between the charger-battery-regulator modules and the using loads. Power used to charge the batteries is reduced by the transmission losses L_T between the solar cell modules and the charger-battery-regulator modules, the battery charger losses L_{BC} and the charging losses L_B .

The power delivered from the batteries and consequently the solar cell module power required to replace it are functions of the ratio of orbital daytime duration to orbital nighttime duration. The period of the HEAO-C orbit is 95.7 minutes. The daytime duration of the orbit ranges from 74.7 to 60.1 minutes; there is a corresponding range of orbital nighttime duration of 21.0 to 35.6 minutes.

The specific power losses for the components described in detail in later paragraphs are as follows:

- Transmission losses - 7%
- Regulator losses - 11%
- Distribution losses - 10%
- Battery charger losses - 8%
- Battery charging losses - 24%

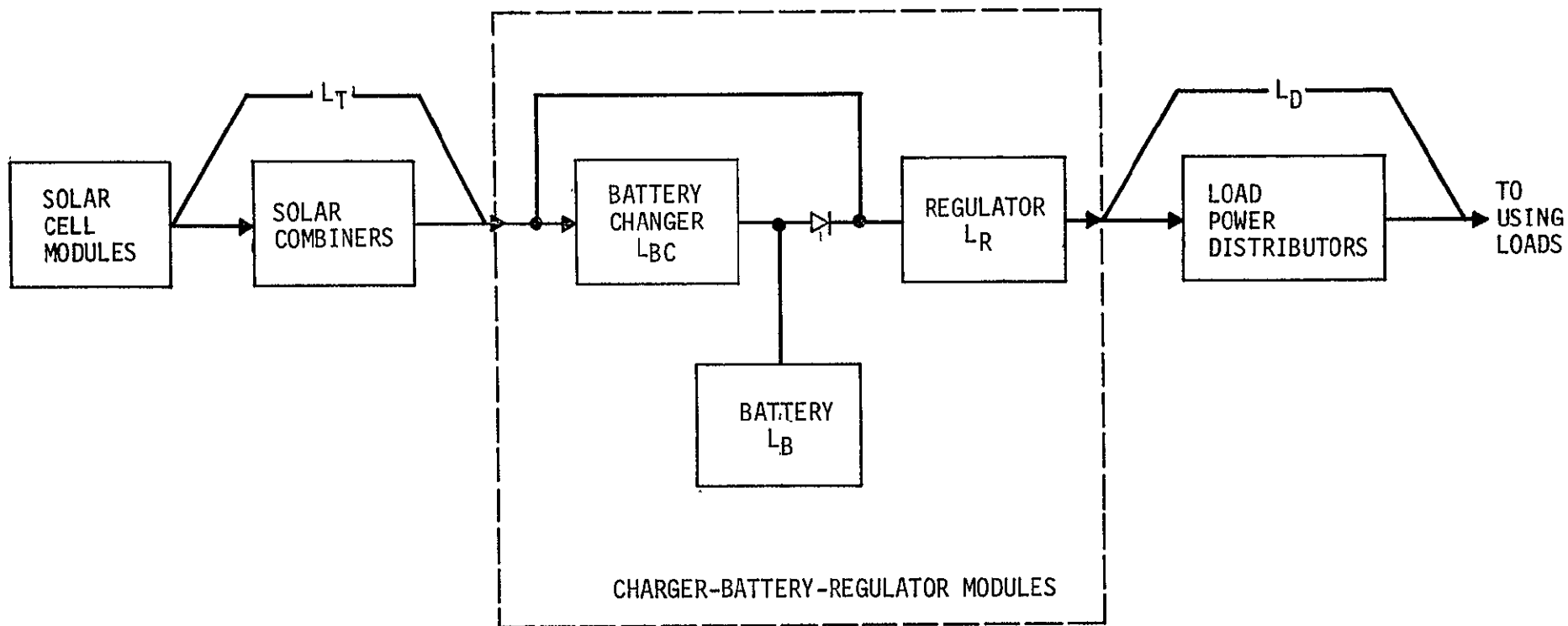


FIGURE 8-4. POWER LOSSES DIAGRAM

Using these values the power losses are described below:

- Straight-through losses = $7\% + 11 + (0.93) + 10\% (0.83) = 25.5\%$
 Straight-through efficiency = 74.5%
- Battery power losses = $11\% + 10\% (.89) = 19.9\%$
 Battery power efficiency = 80.1%
- Battery charging losses = $7\% + 8\% (0.93) + 24\% (.86) = 35.1\%$
 Battery charging efficiency = 64.9% .

The average power required from the solar cell modules P_{SM1} to satisfy the average load power P_L during the daytime portion of the orbit is defined by:

$$P_{SM1} = P_L / 0.745 = 1.34 P_L.$$

The average power required from the batteries P_B to satisfy the average load during the nighttime portion of the orbit is defined by:

$$P_B = P_L / 0.801 = 1.25 P_L.$$

The electrical energy withdrawn from the batteries E_B to satisfy the average load during the nighttime portion of the orbit is defined by:

$$E_B = P_B \frac{\text{Orbital Dark Minutes}}{60}$$

$$= 1.25 P_L \frac{\text{Orbital Dark Minutes}}{60}.$$

The average power required to replace the electrical energy withdrawn from the batteries P_B during the daytime portion of the orbit is defined by:

$$P_R = \frac{(E_B) (60)}{\text{Orbital Day Minutes}}.$$

The average power required from the solar cell modules to charge the batteries P_{SM2} is defined by:

$$P_{SM2} = P_R / 0.649 = 1.54 P_R.$$

The total average power required from the solar cell modules P_{SMT} is defined by:

$$\begin{aligned} P_{SMT} &= P_{SM1} + P_{SM2} \\ &= 1.34 P_L + 1.54 P_R \\ &= 1.34 P_L + 1.54 \frac{(EB) (60)}{\text{Orbital Day Minutes}} \\ &= 1.34 P_L + 1.54 \left[1.25 P_L \frac{\text{Orbital Dark Minutes}}{\text{Orbital Day Minutes}} \right] \\ &= 1.34 P_L + 1.93 P_L \frac{\text{Orbital Dark Minutes}}{\text{Orbital Day Minutes}}. \end{aligned}$$

The system performance factor PF_S is defined by:

$$PF_S = \frac{1.34 P_L + 1.93 P_L \frac{\text{Orbital Dark Minutes}}{\text{Orbital Day Minutes}}}{P_L}$$

The system performance factor as a function of the nighttime/daytime ratio of the 300 nautical mile, 35° inclination orbit is shown in Figure 8-5. As shown, the system performance factor varies between 1.88 and 2.48 (relating to system efficiencies of 53.2% and 40.3%) for the range of orbital nighttime/daytime ratios from 0.281 (21.0 minute nighttime/74.7 minute daytime) to 0.592 (35.6 minute nighttime/60.1 minute daytime).

Solar Cell Module Sizing

The average power required from the solar cell modules to supply the using loads is defined by:

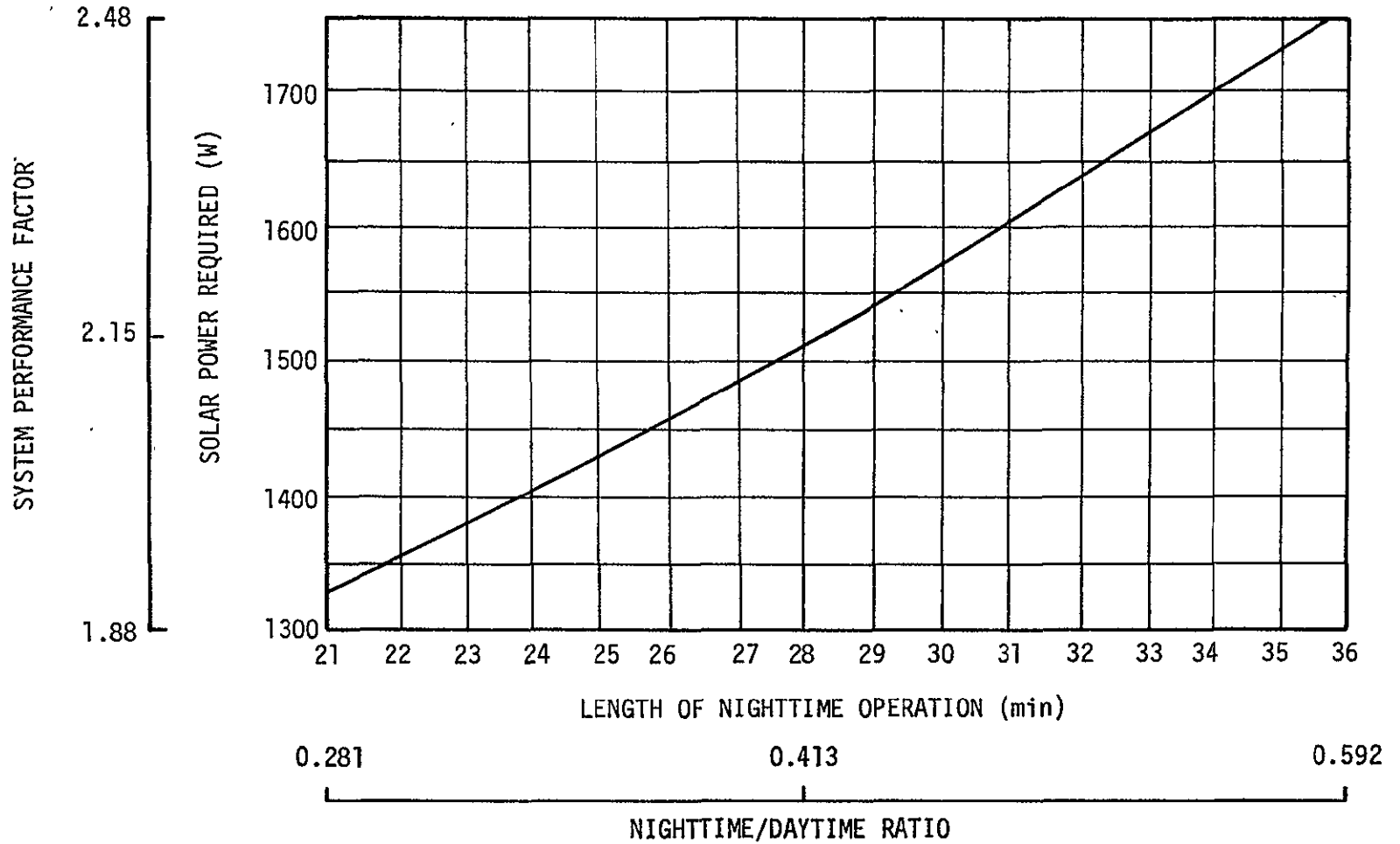


FIGURE 8-5. SYSTEM PERFORMANCE FACTOR AS A FUNCTION OF ORBITAL NIGHTTIME DURATION

$$P_{SMT} = (P_L) (PF_S)$$

Based upon the average load power requirement of 705 watts, the required average solar cell module power varies between 1325 watts (21.0 minute nighttime/74.7 minute daytime) and 1748 watts (35.6 minute nighttime/60.1 minute daytime) as shown in Figure 8-5.

The solar cell modules were considered in two mounting configurations. One mounting configuration placed the solar cell modules flush along three sides of the octagonal spacecraft, as shown in Figure 8-6. The other mounting configuration folded-out panels of the solar cell modules are shown in Figure 8-7. In each configuration, 84 solar cell modules were employed with 28 mounted on each panel.

In the basic observation mode, the solar cell modules are oriented so that the angle between the solar vector and the perpendicular to the middle solar panel is not greater than 15 degrees. This orientation may exist continually. In the flare observation mode, the spacecraft turns farther off the solar vector, but the solar vector angle is limited to 30 degrees from the perpendicular to the middle of the solar panel. This orientation exists for a maximum duration of one orbit per day. Orientations with solar vector angles of greater than 30 degrees are special case considerations which may be restricted to orbital nighttime operation to eliminate the impact on electrical power.

With the flush mounted solar cell module configuration, the solar cell module power availability profile varies as a function of orbital nighttime/daytime durations and solar vector angles, as shown in Figure 8-8. The power availability profiles for the folded-out solar cell module configuration is shown in Figure 8-9. The curves

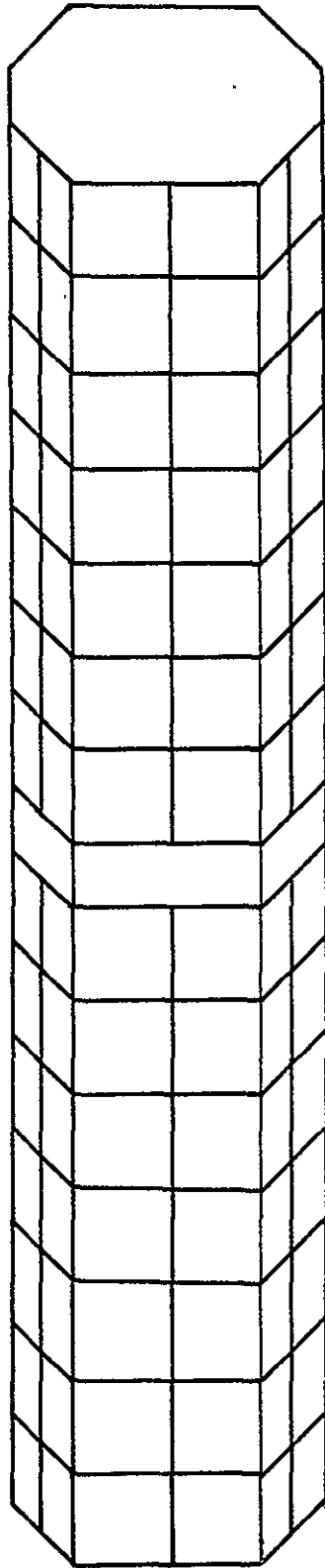


FIGURE 8-6. FLUSH MOUNTED SOLAR CELL MODULE CONFIGURATION

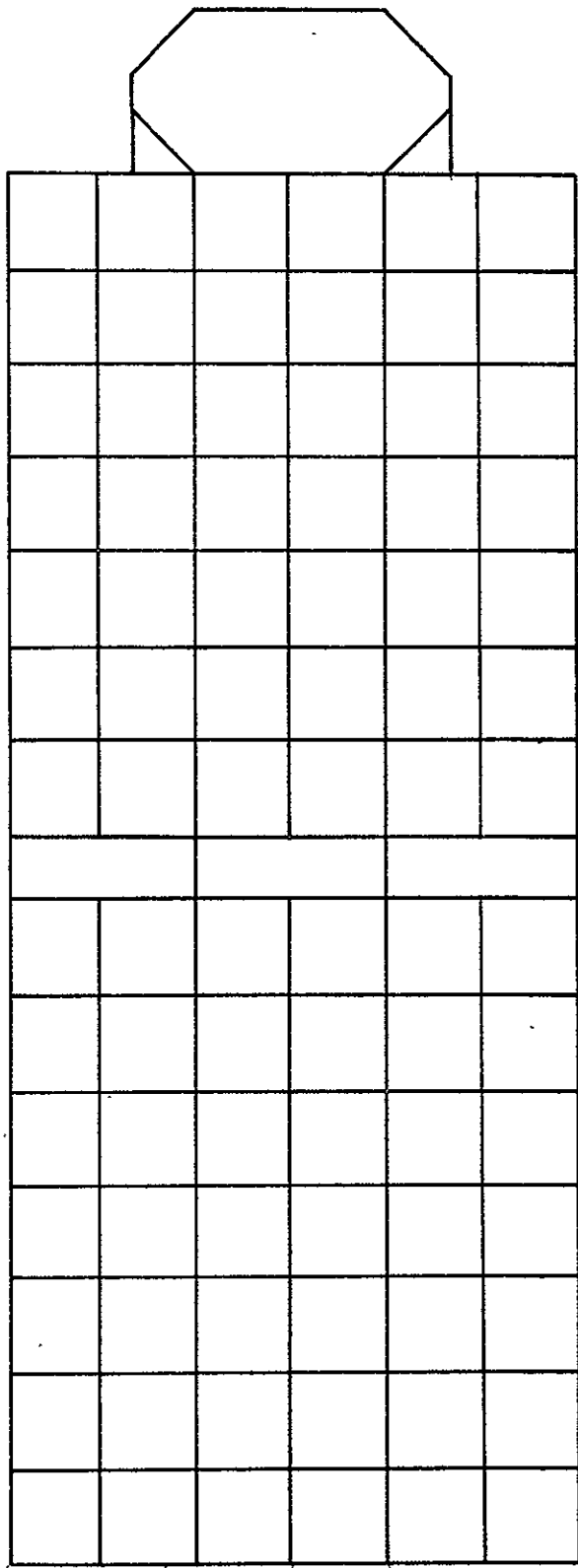


FIGURE 8-7. FOLDED-OUT SOLAR CELL: MODULE CONFIGURATION

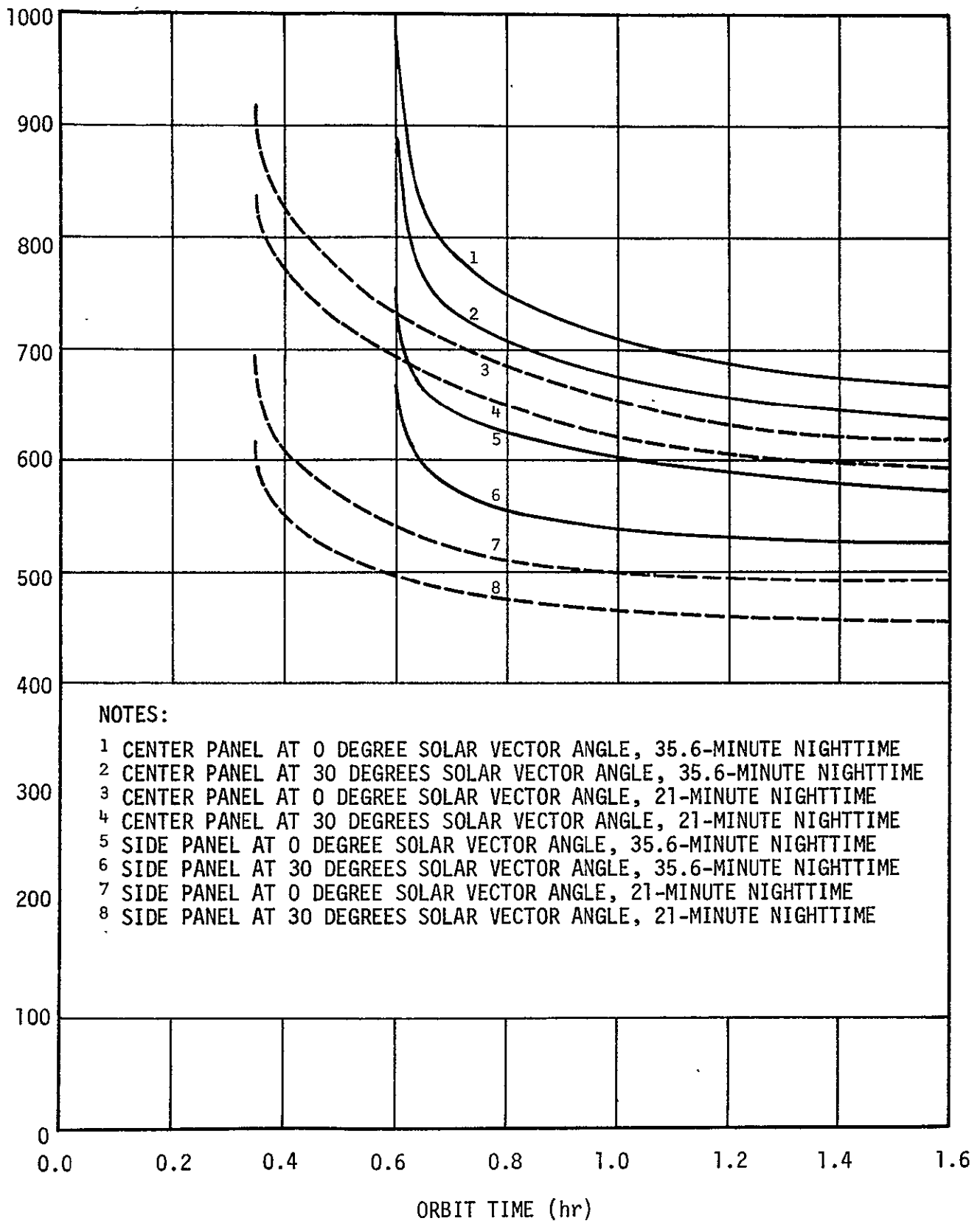


FIGURE 8-8. SOLAR CELL MODULE POWER AVAILABILITY FOR THE FLUSH MOUNTED CONFIGURATION

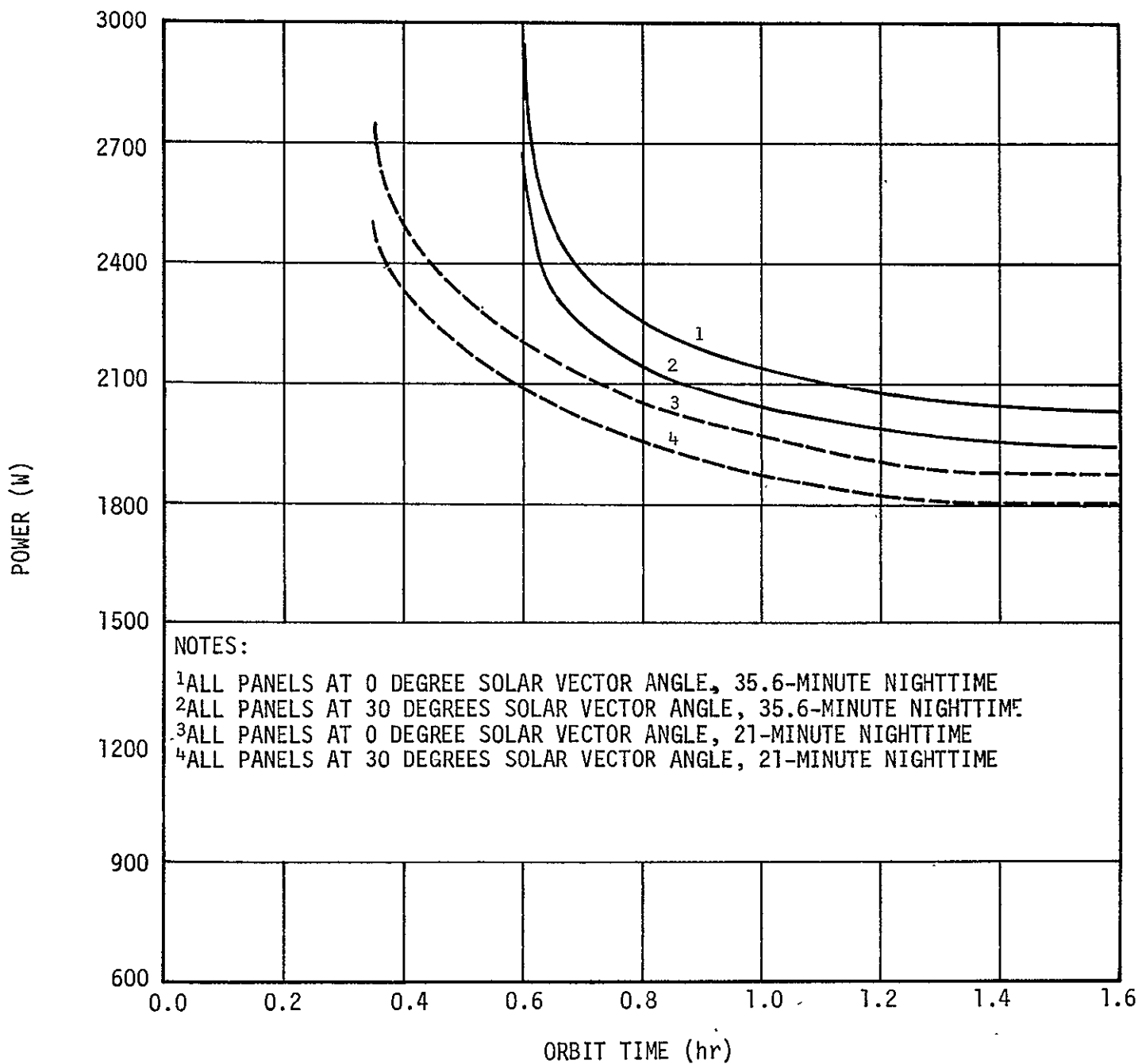


FIGURE 8-9. SOLAR CELL MODULE POWER AVAILABILITY FOR THE FOLDED-OUT CONFIGURATION

in Figure 8-8 are for single panels, but the curves in Figure 8-9 are for all three panels.

The average solar power available is determined by calculating the areas under the curves of Figures 8-8 and 8-9 and dividing this area by the duration of the orbit daytime period. The results are given for the flush mounted configuration in Figure 8-10 and for the folded-out configuration in Figure 8-11. The effect of the degradation of the solar modules with time in orbit is shown in Figures 8-10 and 8-11 by a reduction in power output of 5 percent per year. The average power is greater when the nighttime orbit period is longer because in the shorter daytime period, the solar modules do not get so hot and therefore produce more power per unit of time.

By comparison of the power required and the power available, the power margin is determined. Figure 8-12 shows the power margin in terms of solar cell module power as a function of the orbital nighttime duration, solar vector angles, and time in orbit for the flush mounted configuration. Figure 8-13 shows the power margin in terms of solar cell module power as a function of orbital nighttime duration, solar vector angles, and time in orbit for the folded-out configuration.

As shown in Figure 8-12, the solar cell module power available with the flush mounted configuration after two years does not satisfy that required for orientation of 15° and 30° off the solar vector. Figure 8-12 further indicates, however, that the deficiencies occur only during the longer nighttime orbits. The deficiency at 15° occurs only for orbits with nighttimes in excess of 34.3 minutes which are estimated to occur approximately 10 percent of the time. The deficiency at 30° occurs only for orbits with nighttimes in excess of 30 minutes, which are estimated to occur approximately 35 percent of the time.

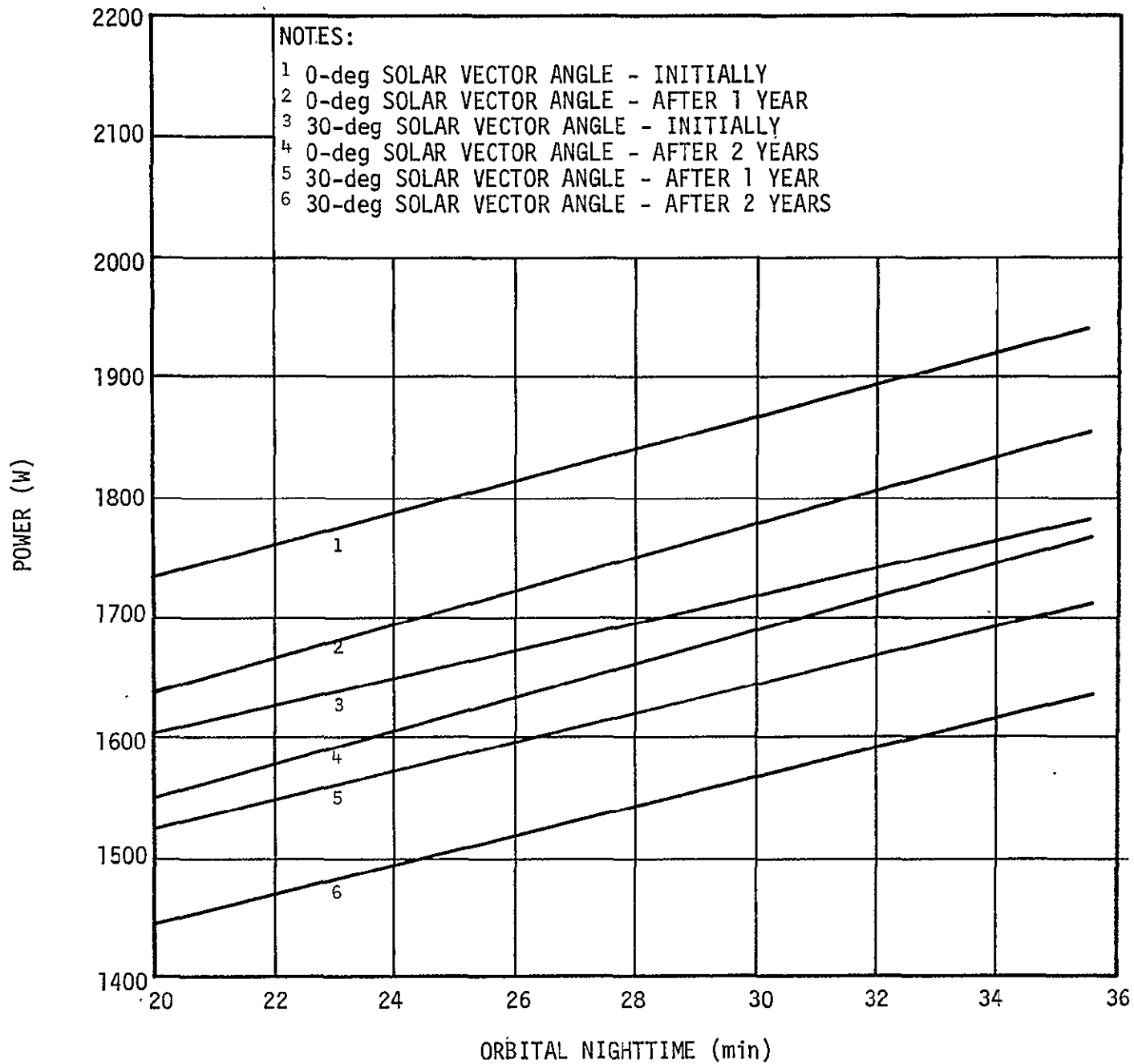


FIGURE 8-10. SOLAR CELL MODULE AVERAGE POWER AVAILABILITY FOR THE FLUSH-MOUNTED CONFIGURATION

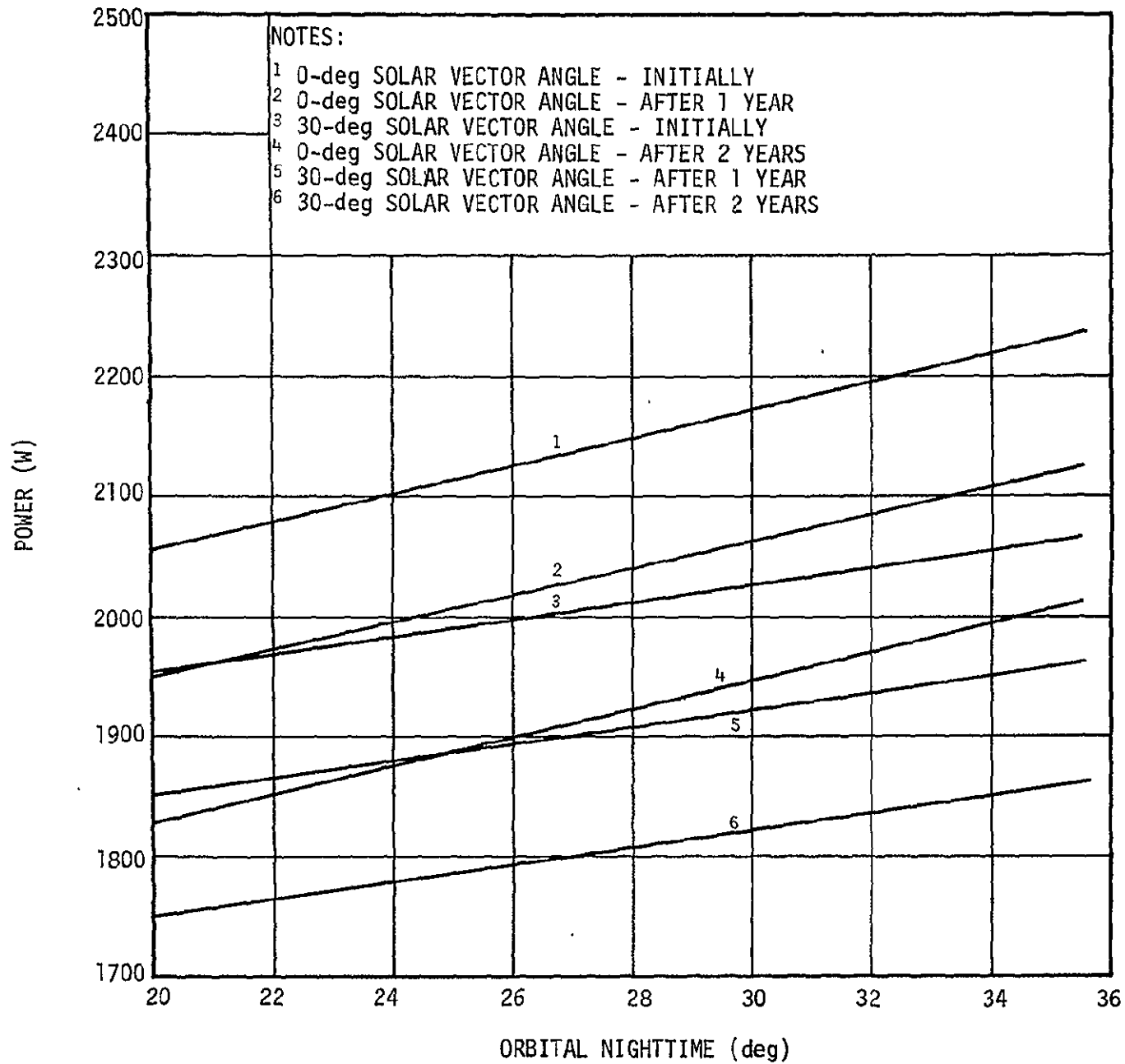


FIGURE 8-11. SOLAR CELL MODULE AVERAGE POWER AVAILABILITY FOR THE FOLDED-OUT CONFIGURATION

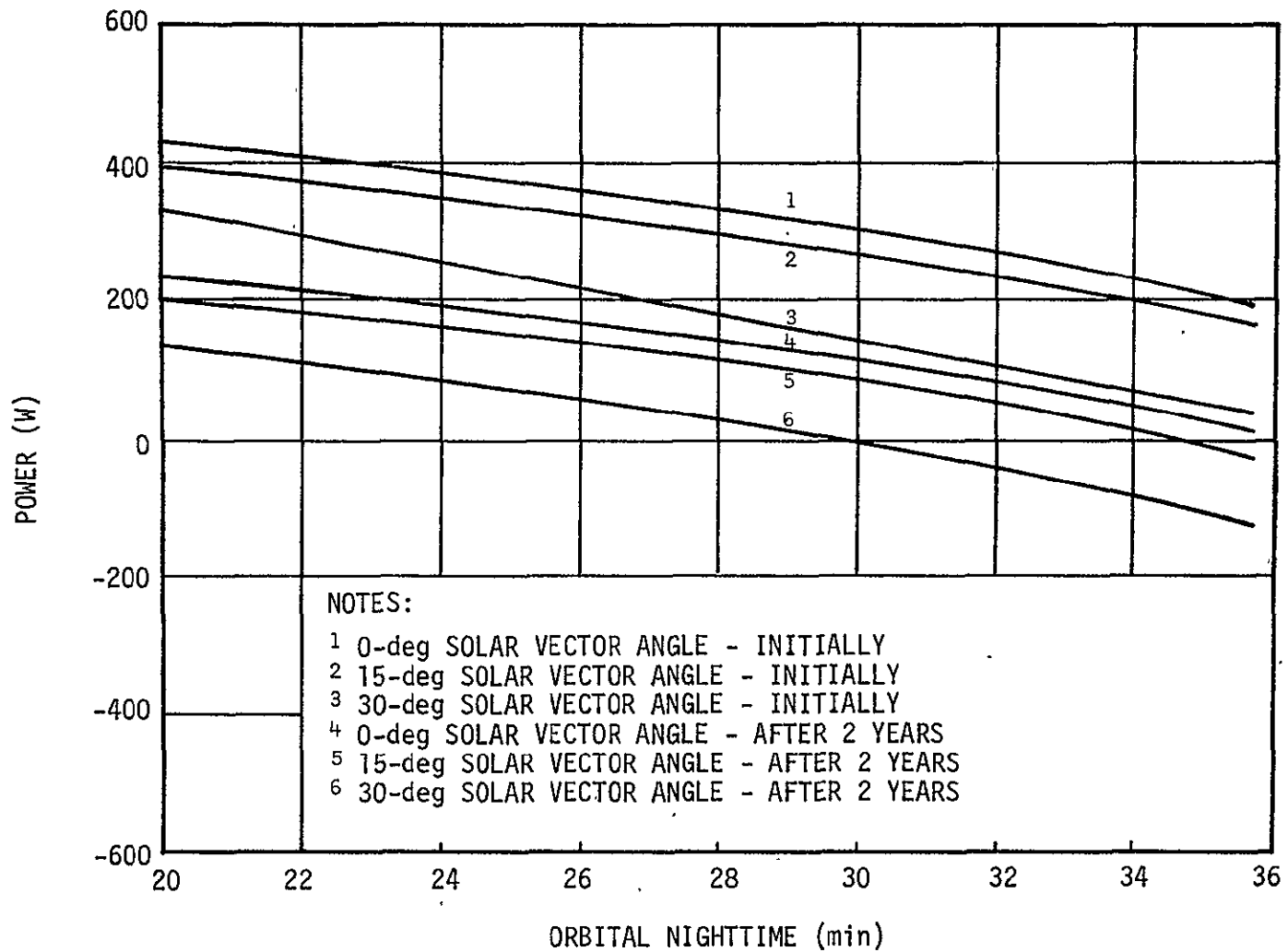


FIGURE 8-12. SOLAR CELL MODULE POWER MARGIN FOR THE FLUSH-MOUNTED CONFIGURATION

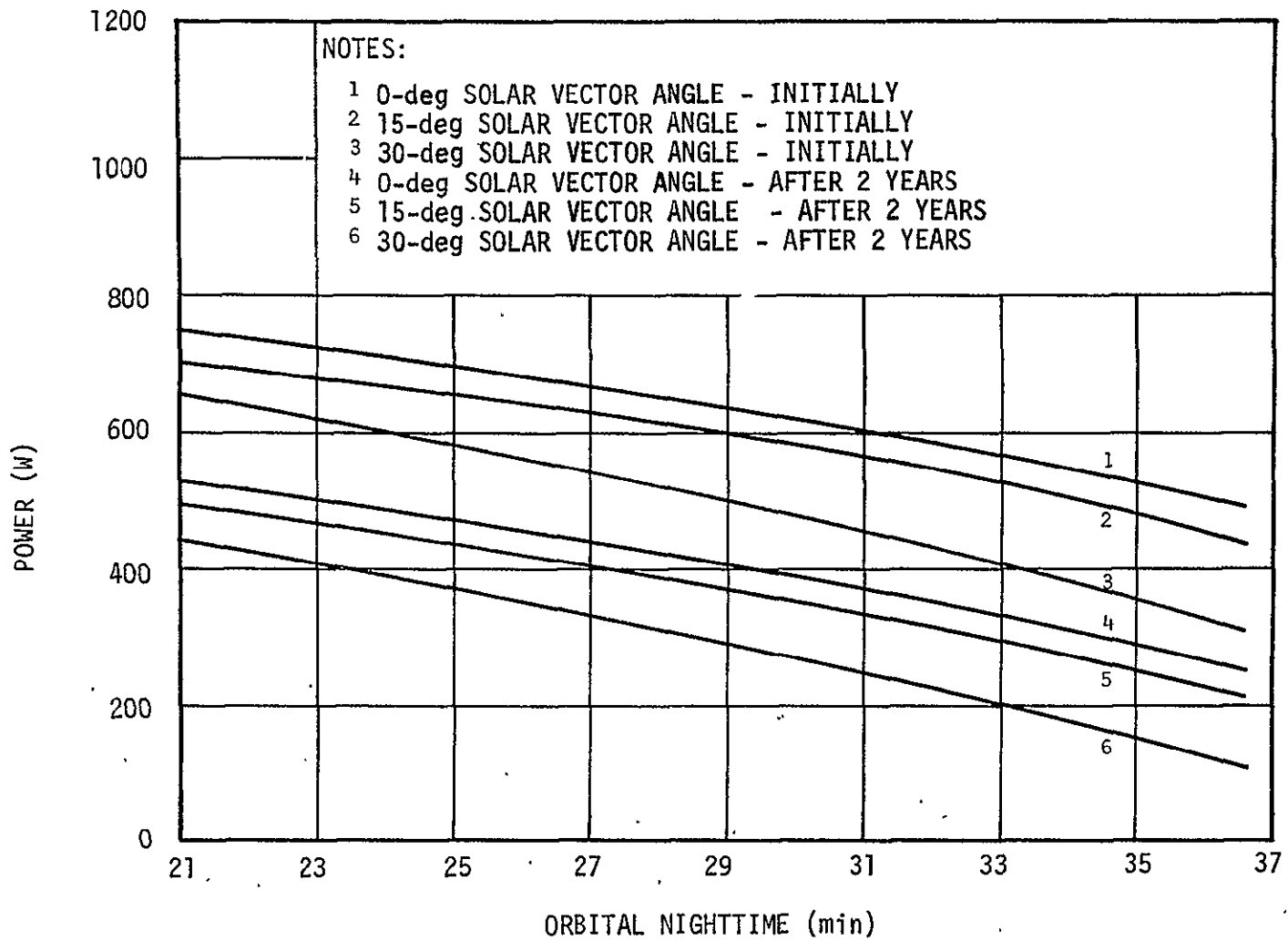


FIGURE 8-13. SOLAR CELL MODULE POWER MARGIN FOR THE FOLDED-OUT CONFIGURATION

Further, these deficiencies occur after two years of operation, the end of the design goal operational lifetime.

Charger-Battery-Regulator Module Sizing

The number of charger-battery-regulator modules required is determined as a function of the allowable battery depth of discharge which, in turn, is a function of lifetime. Figure 8-14 shows the typical relationship between battery depth of discharge and cyclic life. Based upon the one 1 year design requirement cyclic life of approximately 5,500 cycles and the two year design goal cyclic life of approximately 11,000 cycles, a maximum permissible depth of discharge of 15 percent has been chosen.

The number of charger-battery-regulator modules required is defined by the following relationship.

$$\begin{aligned} \text{Number} = & \frac{\text{Average Load} \times \text{Orbital Nighttime Period in Hours}}{\text{Regulator Efficiency} \times \text{Distribution Efficiency} \times 28 \text{ V}} \\ & \times \frac{1}{\text{Depth of Discharge}} \\ & \times \frac{1}{\text{Ampere-Hours per Charger-Battery-Regulator Module}} \end{aligned}$$

With the average required load power of 705 watts, the longest orbital nighttime of 35.6 minutes, regulator efficiency of 89 percent, distribution efficiency of 90 percent, depth of discharge of 15 percent and 20 ampere-hours battery capacity, the number of charger-battery-regulator modules required is seven.

With seven charger-battery-regulator modules, the depth of discharge of the batteries as a function of the orbital nighttime duration is shown in Figure 8-15. With an average depth of discharge of approximately 10 percent as shown in Figure 8-15, the battery cyclic life is

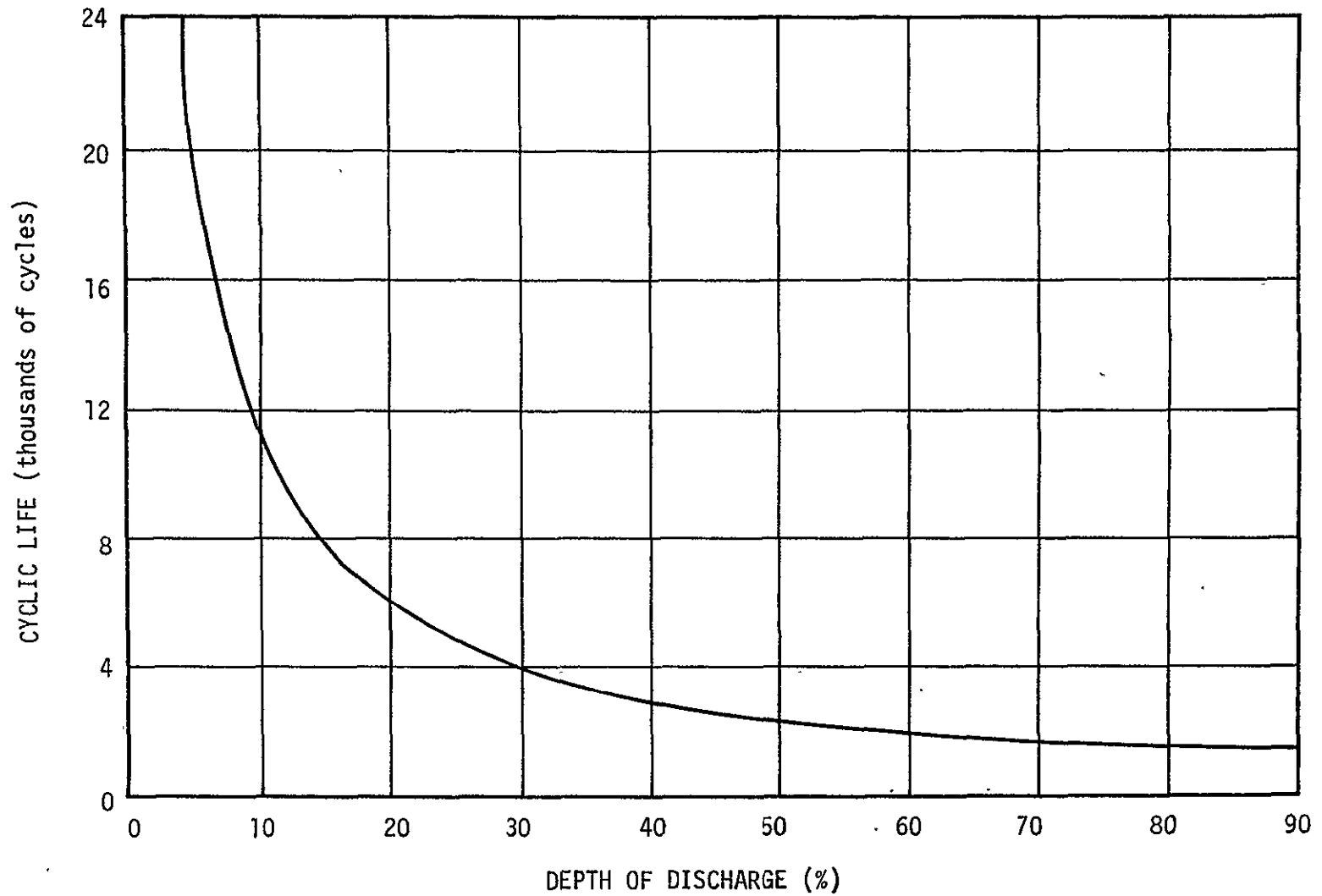


FIGURE 8-14. BATTERY CYCLIC LIFE AS A FUNCTION OF DEPTH OF DISCHARGE

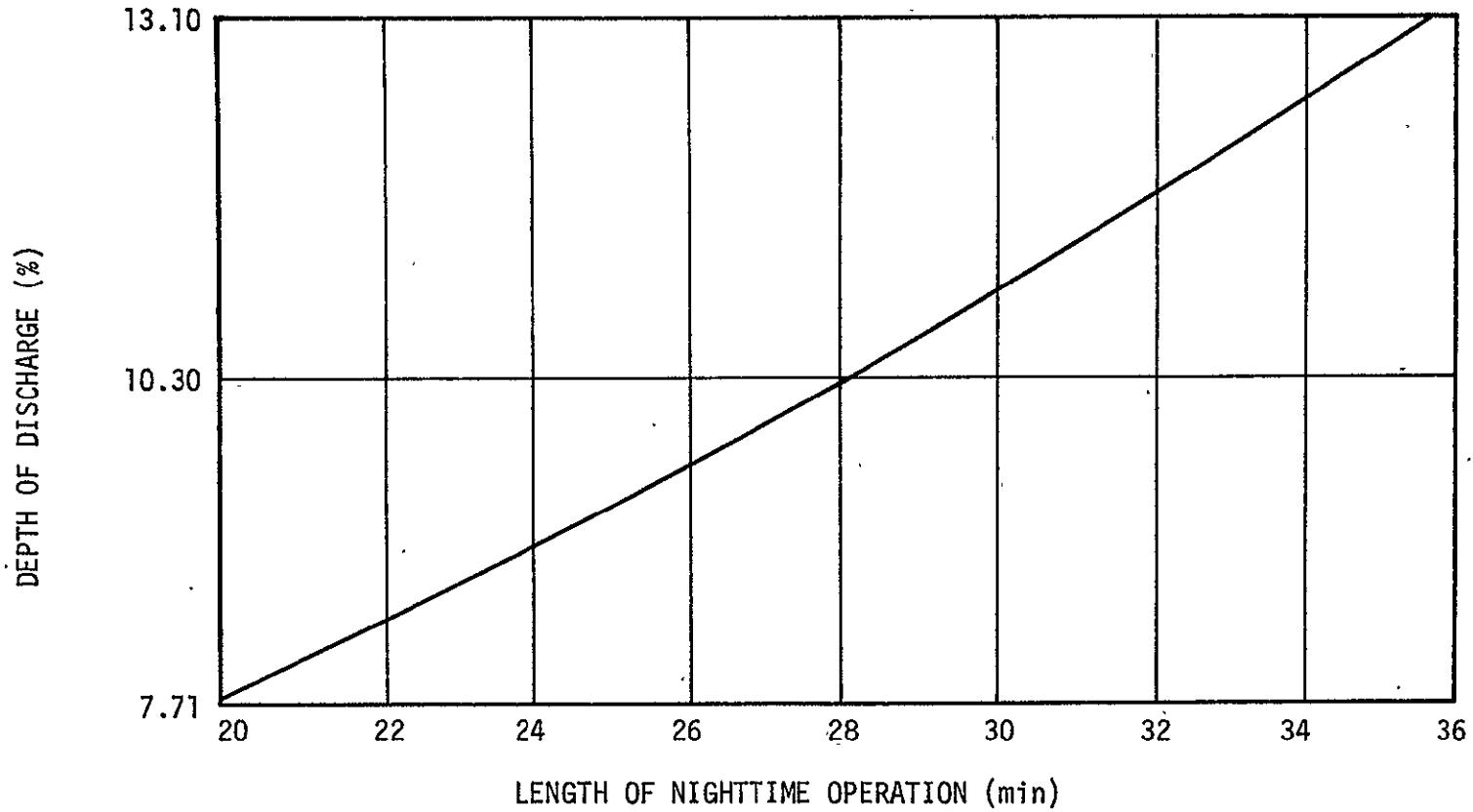


FIGURE 8-15. DEPTH OF DISCHARGE AS A FUNCTION OF ORBITAL NIGHTTIME DURATION

projected to be approximately 11,000 cycles or two years.

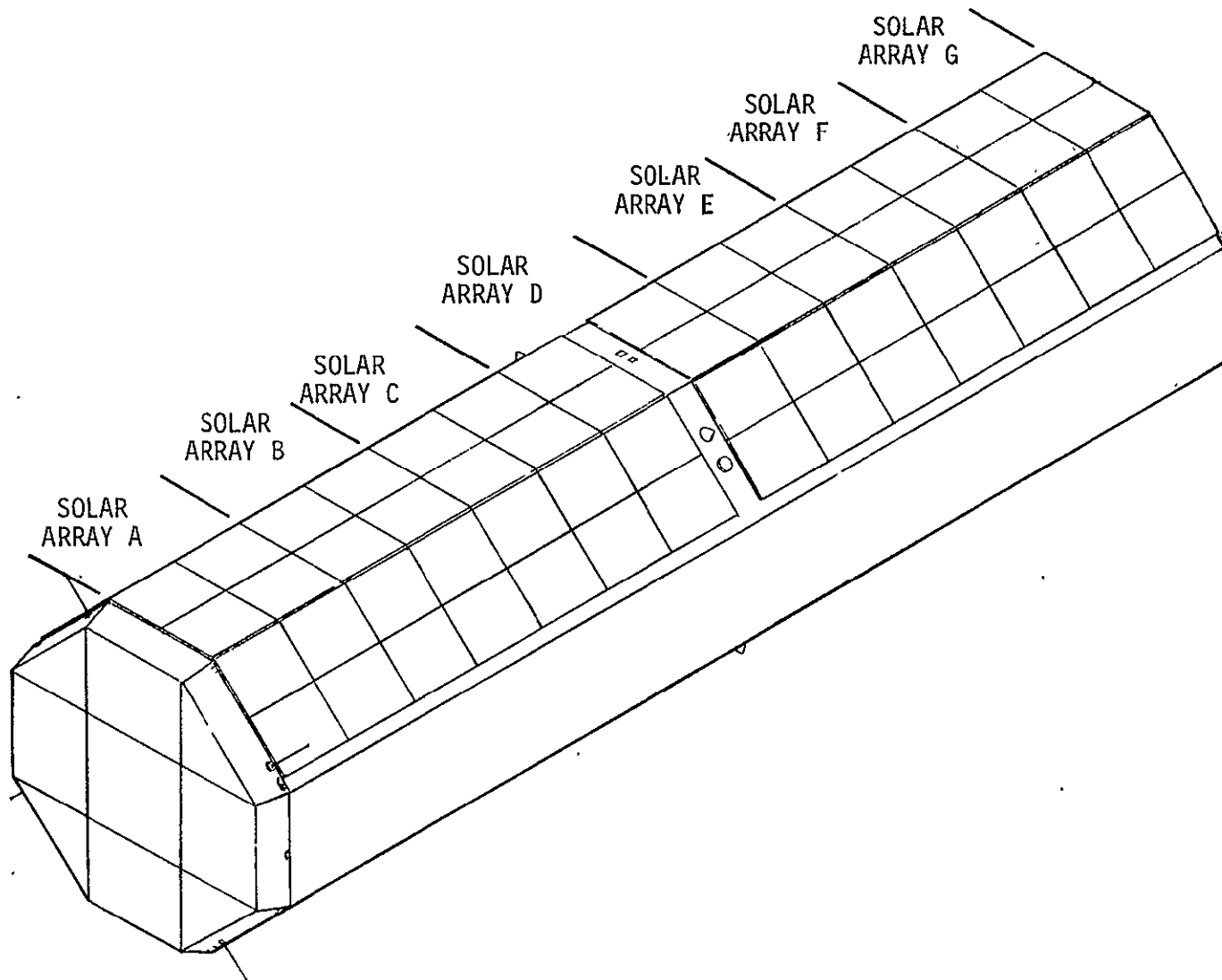
The depths of discharge of Figure 8-15 have been derived assuming that adequate solar cell module power will be generated to satisfy both the load power and battery charging requirements. As shown in Figure 8-12, if the flush mounted configuration is used, less than the required power is generated late in the second mission year when the solar vector angle is 15 to 30 degrees. The maximum depth of discharge that will be required under these conditions is approximately 18 percent.

Reliability Considerations

The system configuration of Figure 8-3 employs the symmetrical sectioning of the solar cell modules shown in Figure 8-16. Each section supplies electrical power to a redundantly circuited solar combiner. By virtue of using symmetrical solar cell module sections, the solar combiners can be of identical design. In addition, the sectioning minimizes the currents handled by the solar combiners and, as a result, reduces the blocking diode losses. Also, the sectioning provides convenient access to the solar cell modules for pre-launch checkout and fault isolation.

Each solar combiner is discretely connected to a separate charger-battery-regulator module; therefore, there is no single catastrophic system failure point from the solar modules through the charger-battery-regulator modules. Two load distributors are used to accommodate parallel power distribution for redundancy and power loss minimization.

Two auxiliary charger-battery-regulator modules are included in a passively redundant state. They may be employed to replace failed modules or to augment the normally active modules during



8-35

FIGURE 8-16. SOLAR PANEL SECTIONING

periods of predictably heavy load power requirements. If employed on such an occasion (as might be required for a unique experiment operation requiring gross misorientation with the solar vector), they could be connected to help supply the load by discharge of their batteries and then be disconnected and recharged at times when an excess of solar cell module power was available.

Thermal Considerations

All components of the electrical power system, except the solar cell modules and solar combiners are mounted on the side of the spacecraft opposite the sun. The solar cell modules will experience temperatures near or slightly in excess of their desirable design limit of 212°F. This condition will require special design considerations with respect to the solar cell interconnections. The relatively high temperatures which will be experienced by the solar combiners will not be in excess of their allowable operating temperatures and will, in fact, tend to improve the performance and reduce the losses of the diodes used. All of the components on the "cold" side of the spacecraft will be maintained within their operating temperatures. The batteries of the charger-battery-regulator modules will be heated by self-contained thermal strips to a temperature of 0° to 15°F to enhance their lifetimes.

Component Descriptions

The components proposed for use in the electrical power system and upon which the analyses were based are Apollo Telescope Mount (ATM) type hardware. A description of these components is given in Reference 8-1. A power system weight breakdown is given in Table 8-7.

TABLE 8-7. POWER SYSTEM WEIGHT

<u>Component</u>	<u>Weight (lb)</u>
Solar Combiners (7)	105
Charger-Battery-Regulator Modules (9)	990
Load Distributors (2)	60
Solar Cell Modules (84)	294
Cabling	<u>400</u>
TOTAL	1849

SPECIFIC RADIOISOTOPE THERMOELECTRIC GENERATOR SYSTEM DESIGN

The radioisotope thermoelectric generator system approach was not carried to the specific design stage for the below listed reasons.

- Radioisotope thermoelectric generators are constant power devices and their sizing must be based on the peak load power requirements resulting in radical oversizing for the major portion of the operational time.
- Radioisotope thermoelectric generators are inherently inefficient (approximately 6% efficient), resulting in large heat dissipation which would severely impact thermal control of the spacecraft.
- For purposes of thermal control and temperature differential, it is normally necessary to mount radioisotope thermoelectric generators external to the spacecraft. This would produce increased spacecraft drag and reduce the orbital lifetime of the spacecraft.

- Extensive shielding must be employed to control radiation from radioisotope thermoelectric generators to levels which will not cause interference with the experiments.
- Disposal of the radioisotope thermoelectric generators create significant spacecraft design and launch, orbit, reentry and recovery problems.

CONCLUSIONS

A solar cell module system is proposed to supply the required electrical power. Either the flush mounted or the folded-out solar cell module configuration will generate adequate electrical power. With the flush mounted configuration, battery depths of discharge will exceed 15 percent under worst case conditions of orbital nighttime length, solar vector off-orientation, and time in orbit. The maximum worst case battery depth of discharge is predicted to be approximately 18 percent. With either configuration, special consideration must be given to proper solar cell modules and thermal control design to assure proper operation at the highest temperatures achieved.

It is concluded that the penalty of additional drag and increased complexity associated with the use of folded-out solar cell modules outweigh the advantages of providing increased power to maintain the battery depth of discharge below 15 percent. It is further concluded that the penalty of periodic battery depth of discharge in excess of 15 percent is not sufficient to disqualify the use of the flush mounted solar cell modules configuration.

9. COMMUNICATIONS AND DATA HANDLING SYSTEM

The HEAO-C communications and data handling system consists of two basic parts; i. e., the part that applies to the experiments and the part that is a spacecraft system and interfaces with the experiment package. This study was concerned primarily with the latter part.

DESIGN REQUIREMENTS

The communications and data handling system is required to perform the following functions:

- Timing generation -- basic clock generation for the spacecraft and experiments with 0.1-millisecond resolution and 0.1-millisecond-accuracy capability
- Data handling -- spacecraft data acquisition, conversion, and formatting, experiment data interface, and spacecraft and experiment data multiplexing
- Data storage -- spacecraft and experiment data storage for transmission to ground stations
- Data transmission -- spacecraft and experiment data transmission to ground stations
- Command handling -- reception, decoding, and routing of spacecraft and experiment commands
- Beacon transmission -- VHF beacon generation and transmission
- Status transmission -- real-time spacecraft and experiment status transmission.

The baseline study criteria were as follows:

- A generated data bit stream rate of 27.5 kbits/sec
- Circular orbit, 35-degree inclination, 300-nautical-mile altitude
- One-year lifetime required, two-year lifetime goal
- Minimum weight and power
- Maximum use of low cost, highly reliable, proven components.

DESIGN APPROACH

The communications and data handling system was grouped into the following subsystems; timing, data handling, command handling, and beacon and status transmission. The design approaches for each are discussed in the following paragraphs.

Timing Subsystem

The timing subsystem's requirement of 0.1-millisecond-time resolution dictates the use of a 10 kilohertz clock. The requirement for time accuracy of 0.1 millisecond dictates periodic update of the clock from a ground station having compatible update capability. Manned Space Flight Network (MSFN) ground stations were chosen to be used for this function, since Satellite Tracking and Data Acquisition Network (STADAN) stations do not have the required clock accuracy. The MSFC ground stations selected are listed below

- Hawaii
- Guam
- Ascension
- Grand Canary.

In the design approach, a central spacecraft oscillator provides the source from which all spacecraft and experiment timing is derived.

The frequency of the oscillator must be chosen to be compatible with the various clock rates required. The stability of the oscillator was assumed to be no worse than 3 parts in 10^9 per day.

Data Handling Subsystem

The data bit stream rate provided for storage and transmission is 27.5 kbits/sec; this consists of 25 kbit/sec of experiment data and 2.5 kbits/sec of spacecraft systems status data. Spacecraft data, therefore, will be acquired, converted, and multiplexed into its pre-assigned format position in the basic 25 kbit/sec stream from the experiment package.

Storage of the data must be adequate to accommodate the amount of data generated between data transmissions. It must also have the means of inputting data at one rate (generation) and outputting data at a higher rate (for transmission).

Transmission of the data is proposed to be performed primarily to STADAN ground stations and secondarily to the previously listed MSFN ground stations. The STADAN ground station selected for use are:

- Tananarive
- Quito
- Santiago
- Johannesburg
- Rosman
- Orroral.

Using the STADAN ground stations, data will be transmitted simultaneously over two S-band links at 200 kbits/sec/link. Using the MSFN ground stations, data will be transmitted over a single S-band link at 500 kbits/sec.

Command Handling Subsystem

Commands to the spacecraft and experiments will be supplied through the STADAN ground stations' 148 megahertz up-link. This link has a 400 bit/sec data rate. Upon receipt of the commands, they will be decoded and routed to their required spacecraft and experiment address. If not intended for immediate use, they will be stored.

Beacon and Status Transmission Subsystem

Beacon and status transmission will be performed with the STADAN ground stations over the 36-megahertz link. Command acknowledgements and real-time status will be transmitted at a low data rate. As a beacon function, this link will be used with the Mini-track network to establish the spacecraft's orbital parameters.

DESIGN ANALYSIS

The following analyses were performed using the selected STADAN and MSFN ground station contact masks to define the performance characteristics for the communications and data handling system components.

Ground Station Contact

Contact time with the six STADAN ground stations previously listed, as a function of orbit number, is shown in Figure 9-1 by the solid line enclosing the shaded area. The dashed line indicates the contact time with the six STADAN ground stations plus the four MSFN stations previously listed. As shown in Figure 9-1, orbit numbers 4, 19, and 34 have no contact time with MSFN ground stations, and orbit number 24 has no contact time with the STADAN ground stations. The data for these plots were calculated using a Teledyne Brown Engineering

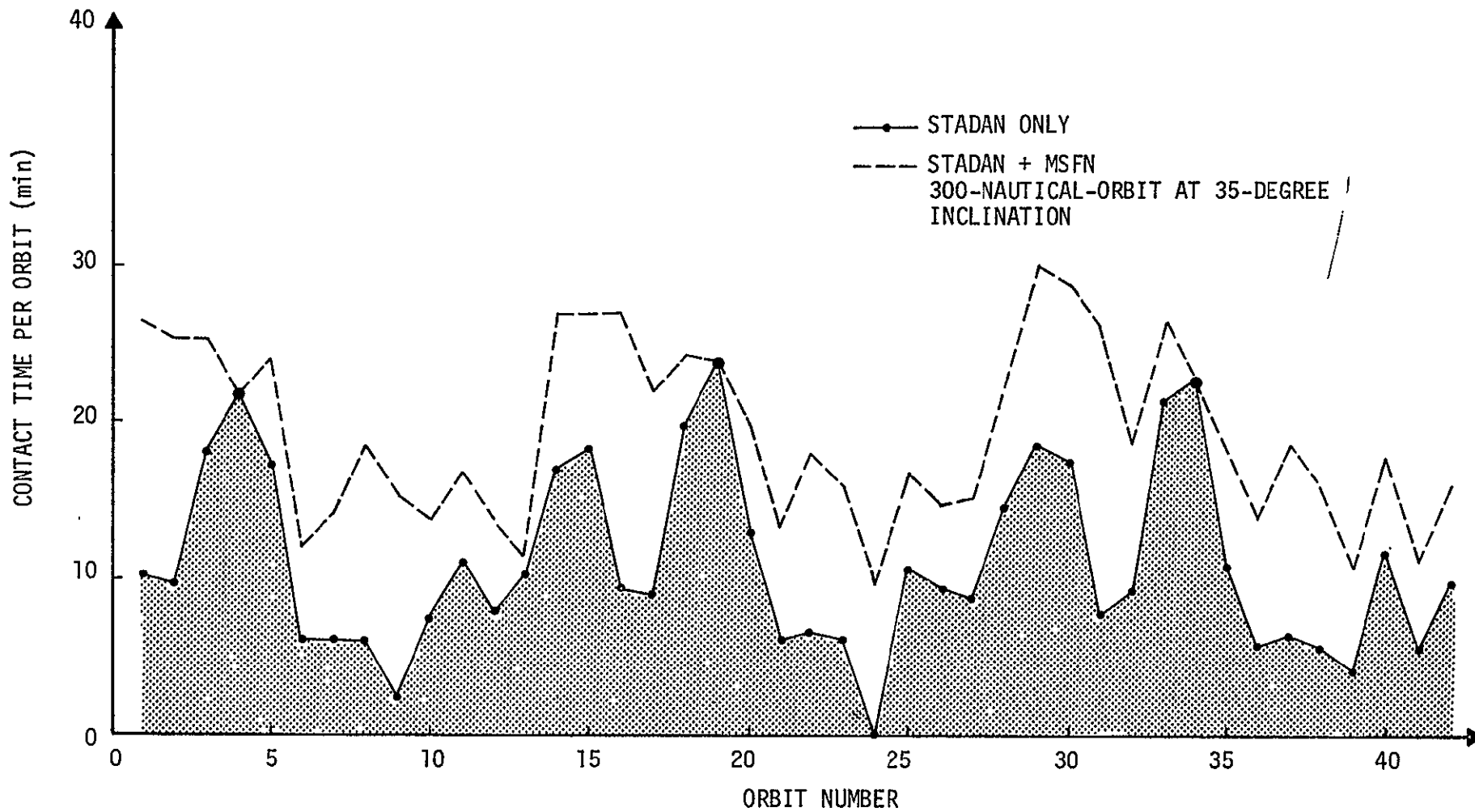


FIGURE 9-1. GROUND STATION CONTACT TIME PROFILE

computer program with simplified station mask characteristics provided by Goddard Space Flight Center.

Oscillator Update

The requirement for 0.1-millisecond time accuracy and the use of a clock with a stability of 3 parts in 10^9 per day dictates contact with an MSFN ground station three times daily or once every five orbits. As indicated in Figure 9-1, contact with an MSFN ground station occurs nearly every orbit, which satisfies the clock update requirement.

Data Accumulation

At a data stream rate of 27.5 kbits/sec, data will accumulate at a rate of approximately 158 Mbits/orbit. With 200 kbits/sec/link, dual link data transmission to the six previously listed STADAN ground stations only, the data accumulation (storage) profile through 40 orbits is as shown in Figure 9-2 (top). Figure 9-2 also shows the data accumulation profile for the STADAN stations plus MSFC Hawaii, the STADAN stations plus MSFN Guam, the STADAN stations plus MSFN Ascension, and the STADAN stations plus MSFC Grand Canary. In Figure 9-2, the ground stations are identified as follows:

- Tananarive - 1
- Quito - 2
- Santiago - 3
- Johannesburg - 4
- Rosman - 5
- Orroral - 6
- Hawaii - 8
- Guam - 9
- Ascension - 10
- Grand Canary - 11.

The maximum data accumulation encountered (data storage required) is approximately 300 megabits. The two recorders proposed for use

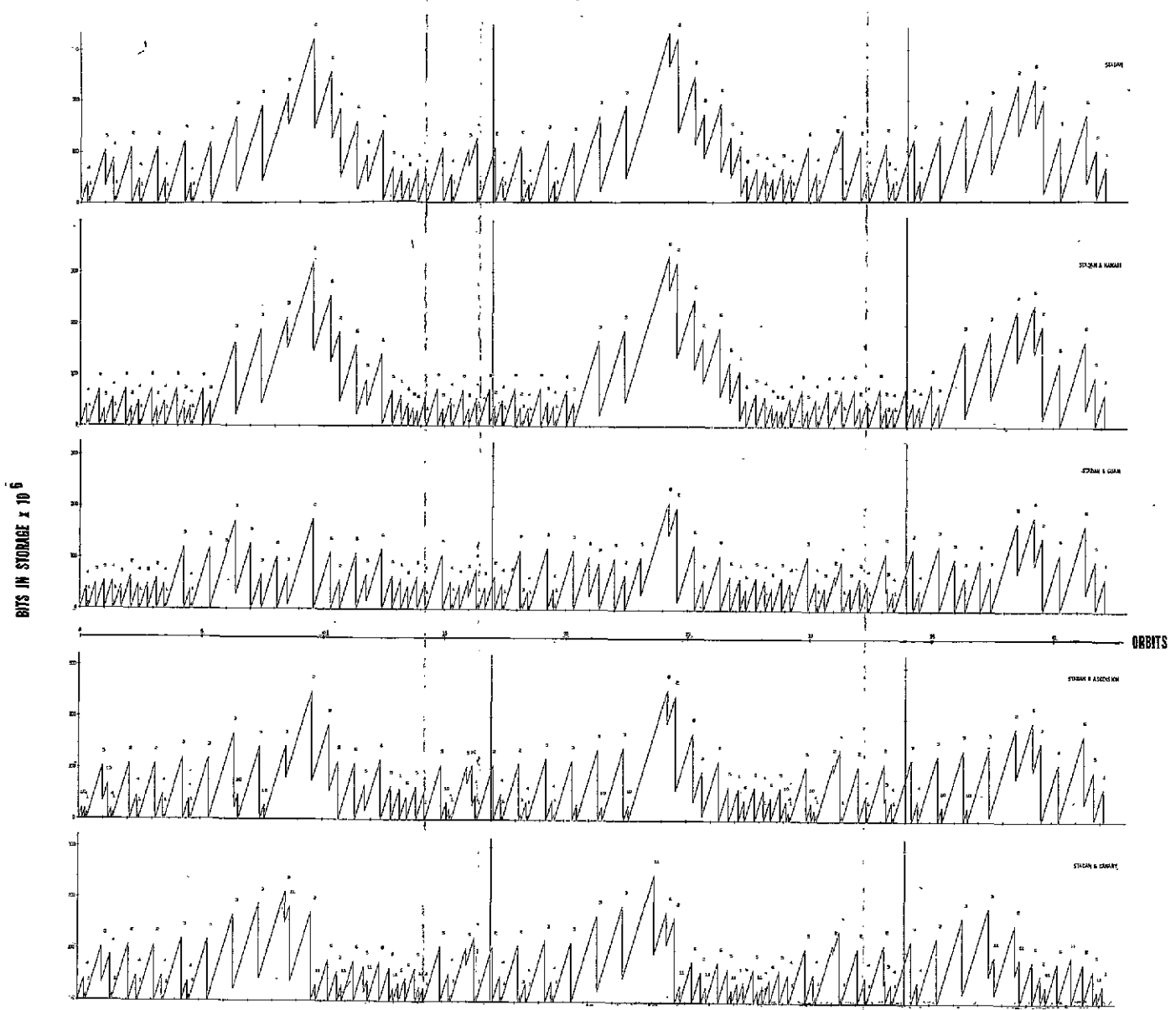


FIGURE 9-2. DATA ACCUMULATION PROFILE

FOLDOUT FRAME 1

9-7/9-8

FOLDOUT FRAME 2

have a combined storage capability of 864 megabits (432 megabits per recorder). The maximum data storage requirement can therefore be accommodated even with less ground station contact time than the baseline six STADAN stations provide with no MSFN contact. The capacities of two additional recorders, which act as redundant units are not included in the 864 megabit capacity quoted above.

Command Capability

Approximately 4,000 commands per orbit can be supplied to the spacecraft. This number is based upon a 12-bit command word repeated three times, a 6 minute average contact time with STADAN ground stations per orbit as indicated in Figure 9-1, and a 400 bit up-link data rate. Though the command capability requirement in terms of both numbers and usage is not presently defined, it appears that adequate command communication capability is available.

SPECIFIC SYSTEM DESIGN

The block diagram of the communications and data handling system is shown in Figure 9-3. The interface with the experiment package is indicated by the dashed line.

Timing Subsystem

The timing subsystem consists of the spacecraft oscillator and S-band receiver. The oscillator consists of the base frequency oscillator and frequency dividers required to derive the clock signals which are routed to the using elements of the spacecraft and experiments. The S-band receiver is used for the reception and demodulation of clock update signals, which are then routed to the oscillator.

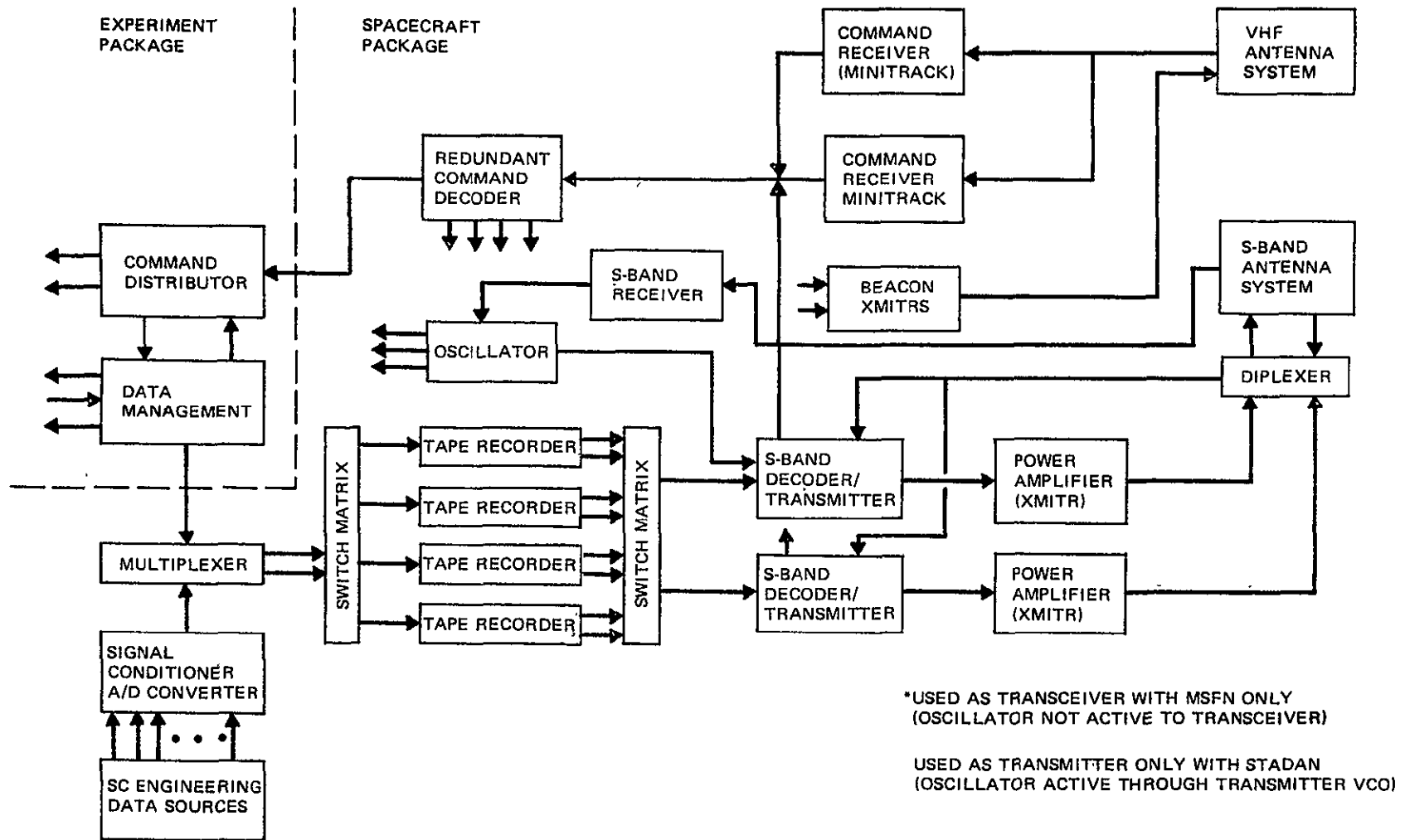


FIGURE 9-3. COMMUNICATIONS AND DATA HANDLING SYSTEM

Data Handling Subsystem

The data handling subsystem consists of all the elements involved in the acquisition, conversion, formatting, multiplexing, storage, and transmission of data. Data from spacecraft sources is signal conditioned, converted to digital form, and multiplexed with the experiment data. The resultant data stream is applied, through a switch matrix, to digital tape recorders. Four dual-track magnetic tape recorders are used for data storage. One recorder will accept the two channels of digital information continuously until the end of the tape reel is reached. At this time, the recorder control will automatically shut off the first machine and start the record mode of a second unit. When ground station contact is made, the full recorders will be switched sequentially to the payback mode. This mode continues until the tape dump is complete, even if more than one ground contact is required.

The output from the recorders is applied, through the switch matrix, to the S-band decoder/transmitters. Their outputs are amplified by traveling-wave-tube amplifiers and routed to the antenna system for transmission to the ground stations. The S-band decoder/transmitter, when operating with a STADAN station, receives its VCO locking signal from the spacecraft oscillator. When operating with an MSFN station, it receives its VCO locking signal from an S-band uplink.

Command Handling Subsystem

The command handling subsystem consists of the VHF antenna system, the VHF receivers, and the command decoder. The decoder provides for the decoding and routing of the commands and, if required, provides storage for spacecraft commands. Experiment commands are routed directly to the experiment data handling facilities, which provide for their storage and control.

Beacon and Status Transmission Subsystem

The beacon and status transmission subsystem consists of the VHF transmitter and antenna system. It transmits beacon signals and real-time spacecraft and experiment status data that is routed to it from the data handling subsystem.

COMPONENT DESCRIPTIONS

The components recommended are not intended to represent optimum selection, but define the hardware used in the design approaches and analyses. A system weight breakdown is given in Table 9-1.

Magnetic Tape Recorders

Since the tape recorder has moving parts, it is the least reliable element in the entire data system. Several methods by which the recording system reliability may be improved are redundancy, machine selection, and operational techniques.

The baseline on-board data storage system consists of four dual-track magnetic tape recorders. The 27.5 kilobits of data generated within the spacecraft each second are divided equally between two recorder tracks, requiring a capability of 13.75 kbits/sec for each track. At a recording bit density of 10,000 bits/inch, a recording tape speed of 1.375 inch/sec is required. Playback speed is determined by the 200 kbits/sec limit of each STADAN downlink. This leads to a playback speed of $200,000/10,000 = 20$ inch/sec. The playback-to-record ratio then is 14.55. Playback will be done with the tape moving in the opposite direction to the record mode. No rewinding operations are thus required, minimizing tape system wear and power requirements.

TABLE 9-1. COMMUNICATIONS AND DATA HANDLING SYSTEM WEIGHT

<u>Item</u>	<u>Weight (lb)</u>
S-Band Antenna (4)	4
Stitching Network (2)	20
Multiplexer	8
S-Band Decoder/Transmitter (2)	72
Command Receiver (2)	2
Beacon Transmitter (2)	2
S-Band Power Amplifier (2)	36
Tape Recorder (4)	60
VHF Antenna (4)	4
Signal Conditioner	3
Command Decoder	6
Power Combiner	10
Miscellaneous Hardware	20
Cabling	<u>80</u>
TOTAL	<u><u>327</u></u>

The recorder selected should be a proven model with a very high mean-time-between-failure (MTBF) figure. The unit recommended at this time is the Leach 2000 series recorder. This recorder offers several desirable features for the HEAO system: it was designed specifically for satellite use, advertised MTBF is greater than 14,000 hours, and in addition, the high density digital recording (HDDR) option is available, which allows for digital recording at packing densities of 10,000 bits/inch/track. The reel capacity is 21,600 inches, providing a data storage capacity of 216 Mbits/track, or 432 megabits for the two-track unit. Total recorder (4 units) capacity is 1,728 megabits.

Use of two data tracks per recorder offers several advantages. These include lower system power demand, increased data storage capability, less tape wear, and increased redundancy. These advantages are gained at negligible increases in weight and unit power demand. The four-recorder system would require only one two-channel tape machine to be on line recording at any given time. The other three would be in a standby mode, except during ground station contact when one machine at a time would be in a playback mode.

If one of the four tape machines fails, no mission degradation occurs. The main result would be that system storage capacity would drop from 1,732 to 1,296 megabits. Should two of the four tape units fail, again no direct mission impact will result. In this case, data storage capacity drops to 864 megabits.

If three out of four tape units fail, the ability to record while dumping data will be lost. This will cause an average loss of less than 10 percent of the total data. In addition, data storage capacity will drop to 432 megabits. Should all tape recorders fail, the system could still transmit real-time data rather inefficiently during approximately 6 percent of the total orbital time.

Signal Conditioner

The equipment converts analog operational data into a form suitable for input to the digital multiplexer unit. The signal conditioner will attenuate the analog signals to basic system voltage levels, multiplex them, and convert them into digital form.

Two units will be required: a commutator and an analog-to-digital converter. The equipment cannot be completely defined before "housekeeping" signals to be monitored are determined; however, the Teledyne Telemetry Model 378 commutator and the AD-610 analog-to-digital converter are typical of the hardware available for this application.

Antennas

Two separate antenna arrays are required for the communication and data handling system: an S-band array used with the telemetry transmitter and a VHF array shared by the Minitract transmitter and the command receiver.

The S-band antenna array will consist of four radiating elements, mounted symmetrically around the circumference of the vehicle at 90-degree intervals. Detailed design of the antenna system will be possible only after the vehicle configuration is finally defined, with optimum methods of feed, polarization, and phasing determined empirically. Although final selection of a radiating element is not possible at this time, it is believed that the antenna would be physically similar to the Electronic Resources Model 03-44-00010.

The VHF antenna array will consist of four VHF quarter-wave stub elements spaced at 90-degree intervals about the spacecraft cross section. This array will be used for both transmitting and receiving. A notch filter will be used to provide isolation between the 148 megahertz receivers and the 136 megahertz transmitters. The VHF antenna

elements will project approximately 22 inches from the spacecraft skin. The antenna would have a spring in its base which would erect the antenna after shroud separation.

Transmitters

Two S-band transmission links and one VHF transmission link are required in the spacecraft. The recommended S-band units are EMR Model 3620-05. These transmitters are rated at 20 watts.

The VHF beacon transmitter recommended for HEAO is Spacecraft Model T400. This unit has been flown on Pegasus 1, 2, and 3, Saturn I, OGO 1 and 2, and several other scientific satellites. It is designed to operate in the 136 megahertz band at up to 2 watts output. It has phase modulation capability, with a modulation sensitivity of 2 radians/V.

Command Receiver

The VHF receivers operate continuously in the 148 megahertz region. The AVCO model AED-301A receiver is recommended for this application. This model has flown on the OSO-H, ISIS, and SERT-II spacecraft.

Command Decoder

The command decoder accepts the command words from the command receiver, decodes the words into individual commands, and relays either the commands or control signals to the appropriate destination. The unit takes action on a command only if the status data from the hardware being addressed is correct. The decoder acknowledges receipt of commands by returning the signal through the beacon transmitter.

Although the specific configuration of the command decoder cannot be determined until final determination of the command requirements, a typical AVCO command decoder designed to interface with the AED-301A receiver can be used for preliminary design purposes

CONCLUSIONS

The communications and data handling system proposed will satisfy the requirements for timing generation, data handling, command handling, and beacon and status transmission. By using the previously listed STADAN and MSFN ground stations, adequate contact can be made to accommodate command transmission, data transmission, and clock update. It is proposed that the STADAN stations be employed for data transmission and the MSFN stations for clock update.

Upon firm establishment of operational procedures and sequences, and definition of definite data rates and formatting, it is recommended that maximum design priority be given to integration of the experiments and spacecrafts commands and data handling systems.

10. CONCLUSIONS

STUDY CONCLUSIONS

It is concluded from this study that the HEAO-C mission can be performed within the established guidelines. The conceptual spacecraft design presented in this report meets all requirements with two exceptions:

- When the middle solar panel is perpendicular to the solar vector, its maximum temperature exceeds the allowable limit.
- When the viewing end of the spacecraft is inclined toward the sun by as much as 15 degrees, the maximum allowable temperatures of the optical bench and the telescope mirrors are exceeded.

It is believed that these problems can be solved with additional study.

The structural design will support the optical bench and other loads during launch without deflecting to violate the 107.27 inch allowable dynamic envelope. The "Lord type" vibration mounts will provide vibration damping during launch between the optical bench and the spacecraft structure. They will not restrict or interfere with spacecraft operation in orbit; however, the effects of outgassing on the experiments has not been investigated. Decoupling the optical bench from the spacecraft structure at the non-viewing end after orbit insertion will permit thermal deflection of the spacecraft without deflection of the optical bench.

The spacecraft attitude reference will be provided by three reference gyros which will be updated using a system of two star trackers. Fixed star trackers may not provide the combination of field of view and sensitivity to permit viewing in any direction. This question was not analyzed in depth in this report. However, gimballed star trackers will permit the required pointing capability, and for this reason their use was allowed for in establishing the spacecraft weight and power requirements.

Spacecraft attitude control and slewing will be accomplished using a system of three scissored pairs of control moment gyros. Momentum desaturation of the gyros will be accomplished with magnetic torquers that produce momentum desaturating torques on the spacecraft by reacting with the geomagnetic field. If the optical bench is constructed of Invar, its magnetic properties must be taken into account in the operation of the magnetic torquers. Suitable coil switching procedures have not yet been investigated.

Simulation of the control moment gyro system indicates that a pointing accuracy of ± 30 arc seconds about each spacecraft axis can be achieved. The majority of this error is expected to be caused by sensor errors, rather than spacecraft motion due to control moment gyro activity.

Thermal analysis of the HEAO-C spacecraft indicates that all system components and experiments can be maintained within prescribed limits for the two cases investigated in which the spacecraft was broadside to the sun. However, in two other cases in which the viewing end of the spacecraft was inclined toward the sun, the telescope mirrors and the optical bench members received excessive solar radiation and became too hot. It is believed that this problem can be solved by changing the thermal properties of the thermal control filter, which covers the viewing end of the optical bench, and/or by adding a sun shade to this end of the spacecraft. Thermal analysis also indicates that in the baseline configuration, the middle solar panel will exceed its maximum allowable operating temperature. A likely solution to this problem is the folding out of the two side solar panels. An added bonus in this case would be the availability of additional solar power.

The electrical power system will provide an adequate power supply for the HEAO-C spacecraft during the first year. At the end of

the second year adequate power is still available when the spacecraft z axis is aligned with the solar vector and when the z axis is up to 15 degrees off the solar vector, except for those orbit orientations having maximum nighttime durations. At the beginning of the mission, adequate power is available for indefinite spacecraft operation with the z axis up to 30 degrees off the solar vector. By the end of the second year, however, spacecraft operation at 30 degrees off the solar vector will result in a deeper battery discharge depth for unfavorable orbit orientations, which are expected to occur about one-third of the time. The maximum depth of discharge is not expected to exceed 18 percent, however, and this condition is believed to be acceptable, since this discharge does not occur on each orbit and the greater depth of discharge occurs only at the end of the second year. The capacity of the present design of the electrical power system for the HEAO-C spacecraft is considered to be barely adequate, since a growth in power required would place severe limitations on the maximum deviation from the solar vector.

The present design of the communications and data handling system will provide adequate storage capacity for experiment and system status data. The STADAN stations will provide adequate contact time for transmission of all generated data as well as the required spacecraft system and experiment commands. The STADAN stations cannot provide the required spacecraft clock update signals however, and selected MSFN stations will be used for this function. MSFN stations will also be capable of receiving data transmissions from the spacecraft.

The overall study conclusion is that the primary problem area is thermal control of the telescope mirrors and optical bench during unfavorable sun orientation angles. It is believed, however, that a

solution to this problem will be found with additional study. It will also be necessary to lower the maximum temperature of the middle solar panel and it is highly desirable to provide an additional margin of electrical power. Both of these problems can be solved with additional study.

SYSTEM CAPABILITY MARGINS

As a result of the analyses performed in the conceptual system designs, some conclusions may be drawn concerning the margins of system capabilities in excess of the requirements. The 3-axis pointing error of ± 30 arc minutes that is estimated to be achievable on the basis of computer simulations gives a margin of 30 arc seconds about two axes and a margin of 4.5 arc minutes about the viewing axis. Maneuver capability meets the requirements and could be increased if desired by the use of larger control moment gyro units.

The maximum temperatures calculated for the optical bench and telescope mirrors after 50 hours in orbit for Cases I and II were 78°F and 74°F , respectively. This gives margins of 2°F and 6°F for these units, since the maximum allowable temperature is 80°F . This margin is believed to be too small at this early stage of spacecraft design. The excessively high temperatures for the Cases III and IV will require system modifications which are expected to also provide greater margins for the Cases I and II.

The electrical power margins were presented in Figure 8-12. Margins are adequate for initial conditions, but are not considered adequate throughout the mission lifetime. A growth in the power requirement would require a redesign of the solar module array.

SYSTEM FLIGHT COMMONALITY

As a result of analyses conducted during the present study and knowledge gained about the HEAO-A, -B, and -D missions, certain tentative conclusions may be drawn about the use of the same type of equipment on different missions. The same type of solar cell modules and charger battery regulator modules are believed to be suitable for all four missions. Some spacecrafts may require fold-out panels or panels located on many spacecraft sides, but the same type of hardware can probably be used. The same basic communications and data handling system is believed to be suitable for all four missions. The data handling functions will vary somewhat on different missions but the basic data storage and transmission functions are expected to be the same. The same type of transmitters, receivers, tape recorders, and switching matrices should be adequate for all missions.

Simulation results indicated that the HEAO-C attitude control system could also be used on the HEAO-A and HEAO-B missions. Although a less sophisticated system would probably suffice for the A mission, a system having improved pointing accuracy will probably be needed for the B mission. Therefore the HEAO-C system could also be used on both the A and B missions or only on the B mission, depending upon a more detailed determination of requirements and the A mission system capabilities. The attitude control requirements of the HEAO-D mission have not been established; however, it is not expected that the systems used on the other missions will be suitable.

The HEAO-A attitude sensing system is expected to be applicable to the HEAO-B mission also and possibly to the HEAO-D mission, but not to the HEAO-C mission. The HEAO-C mission attitude sensing system would be suitable to the pointing phases of the A and B missions, but not to the survey phases.

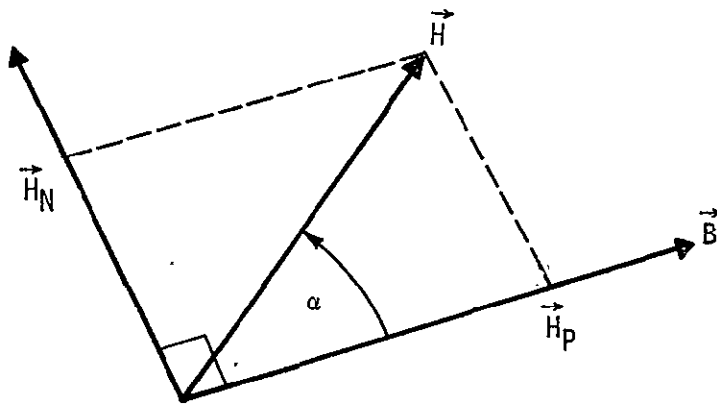
Since the thermal control requirements differ greatly on each mission, it is not expected that the system for one mission would be entirely suitable for any other mission.

APPENDIX A. COMPUTER SIMULATION RESULTS OF MOMENTUM DUMPING

MOMENTUM DUMPING CONTROL LAW

The spacecraft control moment gyros, or any other momentum storage devices used, will be desaturated using the control torque produced by the magnetic torquers. When the stored momentum in the CMGs exceeds a predetermined value (30 ft-lbf-sec in the simulations), the magnetic torquers are energized and control torques are produced for desaturation. When the stored momentum falls below a preset limit (10 ft-lbf-sec in the simulations), the magnetic torquers are deenergized. The magnetic torquers produce torques directly on the spacecraft. The direction of these torques is chosen to make the CMGs react to them in a manner that will reduce the stored momentum.

The schematic below shows the direction of the stored momentum vector \vec{H} inclined at an angle α with the Earth's magnetic field vector \vec{B} at any instant of time. \vec{H}_N is the component of \vec{H} normal to \vec{B} and \vec{H}_P is the component along \vec{B} .



The torque \vec{T}_M , produced by the interaction of the magnetic moment \vec{M} of the electromagnets with the Earth's magnetic field \vec{B} is given as:

$$\vec{T}_M = \vec{M} \times \vec{B} . \quad (A-1)$$

Equation A-1 shows that the torque produced will be normal to both \vec{B} and \vec{M} and that the maximum torque for given magnitudes of \vec{M} and \vec{B} is obtained when \vec{M} is normal to \vec{B} . Mathematically this condition is expressed as:

$$\vec{M} \cdot \vec{B} = 0 . \quad (A-2)$$

Multiplying both sides of Equation A-1 by \vec{B} gives

$$\vec{B} \times \vec{T}_M = \vec{B} \times (\vec{M} \times \vec{B}) . \quad (A-3)$$

Expansion of Equation A-3 gives

$$\vec{B} \times \vec{T}_M = B^2 \vec{M} - \vec{B} (\vec{M} \cdot \vec{B}) . \quad (A-4)$$

Using the relationship of Equation A-2, Equation A-4 can be expressed as

$$\vec{B} \times \vec{T}_M = B^2 \vec{M}$$

or

$$\vec{M} = \frac{\vec{B} \times \vec{T}_M}{B^2} . \quad (A-5)$$

Because the control torque produced by the magnetic torquers is always normal to \vec{B} , the component of stored momentum \vec{H}_N normal to \vec{B} can always be decreased by the proper production of magnetic torque. However, the component \vec{H}_P cannot be decreased by the magnetic torquers. Since the direction of the magnetic field vector

changes as the orbital position of the spacecraft changes, the momentum component that cannot be reduced at one time can be reduced at a later time. The proper direction of the control torque \vec{T}_N is opposite to \vec{H}_N . This torque will provide momentum in the opposite sense to that of the stored momentum component \vec{H}_N , and thereby desaturating the system momentum.

Mathematically the desired direction for \vec{T}_M can be expressed as a triple vector cross product of \vec{H} and \vec{B} as:

$$\vec{T}_M = K [(\vec{H} \times \vec{B}) \times \vec{B}] \quad (\text{A-6})$$

where K is some positive gain constant. Substituting the value of \vec{T}_M from Equation A-6 into Equation A-5 gives

$$\vec{M} = \frac{\vec{B} \times \vec{K} [(\vec{H} \times \vec{B}) \times \vec{B}]}{B^2} \quad (\text{A-7})$$

Equation A-7 can be expanded to

$$\vec{M} = \frac{K}{B^2} \{ \vec{B} \times [\vec{B} (\vec{H} \cdot \vec{B}) - B^2 \vec{H}] \}. \quad (\text{A-8})$$

Equation A-8 can be simplified to

$$\vec{M} = -K (\vec{B} \times \vec{H}). \quad (\text{A-9})$$

Expansion of Equation A-9 into component form gives

$$\begin{aligned} M_x &= -K [B_y H_z - B_z H_y] \\ M_y &= -K [B_z H_x - B_x H_z] \\ M_z &= -K [B_x H_y - B_y H_x] \end{aligned} \quad (\text{A-10})$$

where

- M_x, M_y, M_z - magnetic moments produced by the magnetic torquers in the corresponding spacecraft axes
- B_x, B_y, B_z - components of the Earth's magnetic field in x, y, and z axes of the spacecraft
- H_x, H_y, H_z - components of stored momentum in x, y, and z axes of the spacecraft.

All the quantities on the right-hand side of Equation A-10 are sensed on board the spacecraft and this information is available all the time. Whenever momentum dumping is required the magnetic torquers are energized. Each magnetic torquer placed on the spacecraft body axis generates a corresponding magnetic moment as expressed by Equation A-10.

In the momentum dumping simulation program, the required magnetic moments as calculated in Equation A-10 are provided. In actual practice these magnetic moment values could be provided by adjusting the current in the torquer coils. This procedure has not been addressed in this study. Investigation of implementation techniques may indicate that some time sharing program using a constant current would be desirable.

The characteristic feature of this momentum desaturation scheme is that the torque generated is a function of the angle α as shown below. The magnitude of the required control torque can be obtained from Equation A-6 after some simplification

$$T_M = K H B^2 \sin \alpha \quad (A-11)$$

Equation A-11 shows that when α is zero, no torque is produced and no momentum dumping is possible in this case. This is as expected because if in this case the magnetic torquers are energized, the torque produced is normal to both \vec{B} and \vec{H} and, therefore, instead of momentum dumping the magnetic torquers will add momentum. Whenever the value of α is large, a large \vec{T}_M will be generated which will dump a large fraction of the momentum.

In essence, the function, $\sin \alpha$, in Equation A-11 acts as a controller which assures that the system will dump the momentum and not add the momentum; i. e., the system will produce control torques and not disturbance torques.

SIMULATION RESULTS

A computer program written at Teledyne Brown Engineering was used for simulating the performance of magnetic torquers for momentum dumping of the spacecraft momentum storage devices. The basic functions of the simulation are given below:

- The program computes the gravity gradient torque in spacecraft body axes as the spacecraft orbits the Earth. The program has the capability to compute gravity torques for all orientations of the spacecraft in space and takes into account the effect due to orbital precession.
- The angular momentum imparted to the spacecraft by gravity gradient torques is computed and accumulated. It is assumed that this momentum is counteracted by some type of momentum storage device; therefore, there is no deviation of the spacecraft orientation in inertial space.
- When the level of momentum stored in the momentum storage device exceeds a predetermined value, the magnetic torquers are switched on for momentum dumping. In the present simulation results this limit was arbitrarily set at 30 ft-lbf-sec.

- The size (maximum magnetic moment capability) of each of the three electromagnets used in the program was 0.2 ft-lbf/gauss (2,700 amp-m²).
- Magnetic control torques are produced according to the control laws derived in the preceding section. The value of the gain constant K (Equation A-10) used is $0.03/B^2$ where B is magnitude of the Earth's field.
- The components of the Earth's magnetic field are computed in spacecraft body axes as the spacecraft orbits. The Earth's field is simulated by a dipole moment inclined 11 degrees with the Earth's axis.
- Control torques for momentum dumping are applied continuously until the total system momentum drops below a certain preset lower value, at which time the magnetic torquers are switched off. This preset value was 10 ft-lbf-sec for the current simulation.

The duration of each simulation was 24 hours. During this time the magnetic field of the Earth makes one revolution and the spacecraft will have encountered all possible values of the geomagnetic field vector for the orbit orientation. Three cases were simulated, each representing a different initial orientation of the spacecraft. Each case was selected to produce a maximum gravity torque on the spacecraft and so that one of the three axes would accumulate momentum continuously due to secular gravity torque. All cases are for a 300-nautical-mile-circular orbit inclined at an angle of 35 degrees to the Earth's equator.

- Case I

- ▲ The node line of the equatorial plane and the orbit plane is normal to the Sun line from the center of the Earth. In other words the Sun is at solstice (Figure A-1).
- ▲ The y axis of the spacecraft is oriented parallel to the node line. The orientation of x and z axes is such that they make an angle of 45 degrees with the

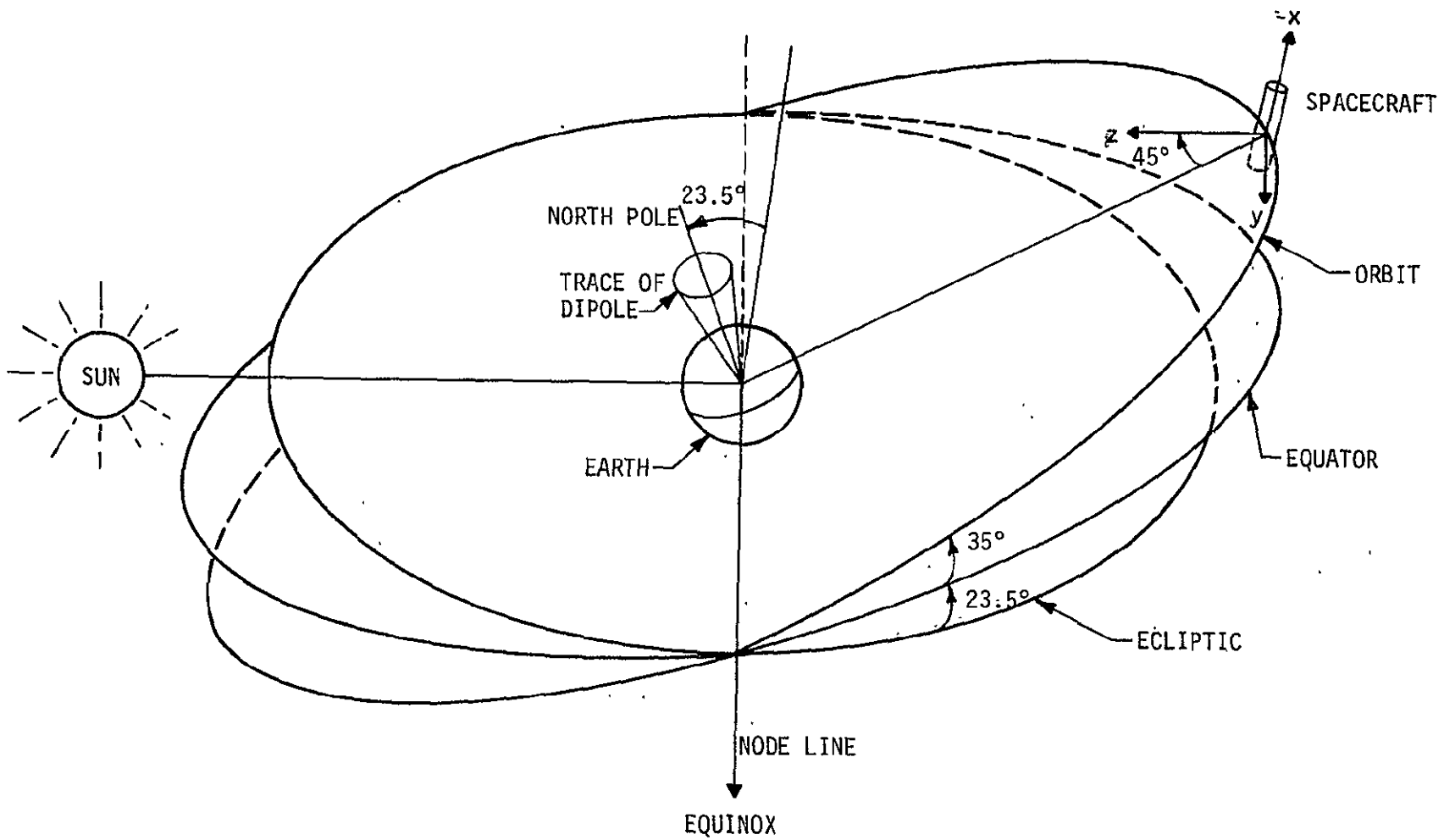


FIGURE A-1. CASE I SIMULATION - SECULAR TORQUE IN y AXIS

local vertical when the radius vector is normal to the node line. This spacecraft and orbit orientation causes all of the secular component of the gravity gradient torque to act in the y axis. Precession of the orbit plane from this orientation causes a portion of the secular torque component to act in the other two axes.

- ▲ The node line of the geomagnetic equatorial plane and the geographic equatorial plane is normal to the Sun line; i. e., this is coincident with the orbit plane node line at starting time (time = 0). The Earth's magnetic dipole is tilted 11 degrees from the geographic north towards the Sun at the starting time.

- Case II

- ▲ The orbital parameters are the same as in Case I except that the Sun is on the node line; i. e., the Sun is at Equinox (Figure A-2).

- ▲ The spacecraft z-axis points at the Sun. The orientation of the x and y axes is such that they make an angle of 45 degrees with the local vertical when this radius vector is normal to the node line. This spacecraft orientation causes all of the secular component of the gravity gradient torque to act in the z axis. Precession of the orbit plane from this initial orientation causes a portion of the secular torque component to act in the other two axes.

- ▲ The node line of the geomagnetic equatorial plane and the geographic equatorial plane is normal to the orbit plane node line at starting time. The Earth's magnetic dipole is tilted 11 degrees towards the Sun at starting time.

- Case III

- ▲ The parameters for this case are the same as for Case I except that the spacecraft x and y axes have been interchanged; i. e., the x axis is parallel to the node line and the y-axis is inclined at 45 degrees to the radius vector (Figure A-3). This spacecraft and orbit orientation causes all of the secular component of the gradient torque to act in the x axis. Precession of the orbit plane from this initial orientation causes a portion of the secular torque component to act in the other two axes.

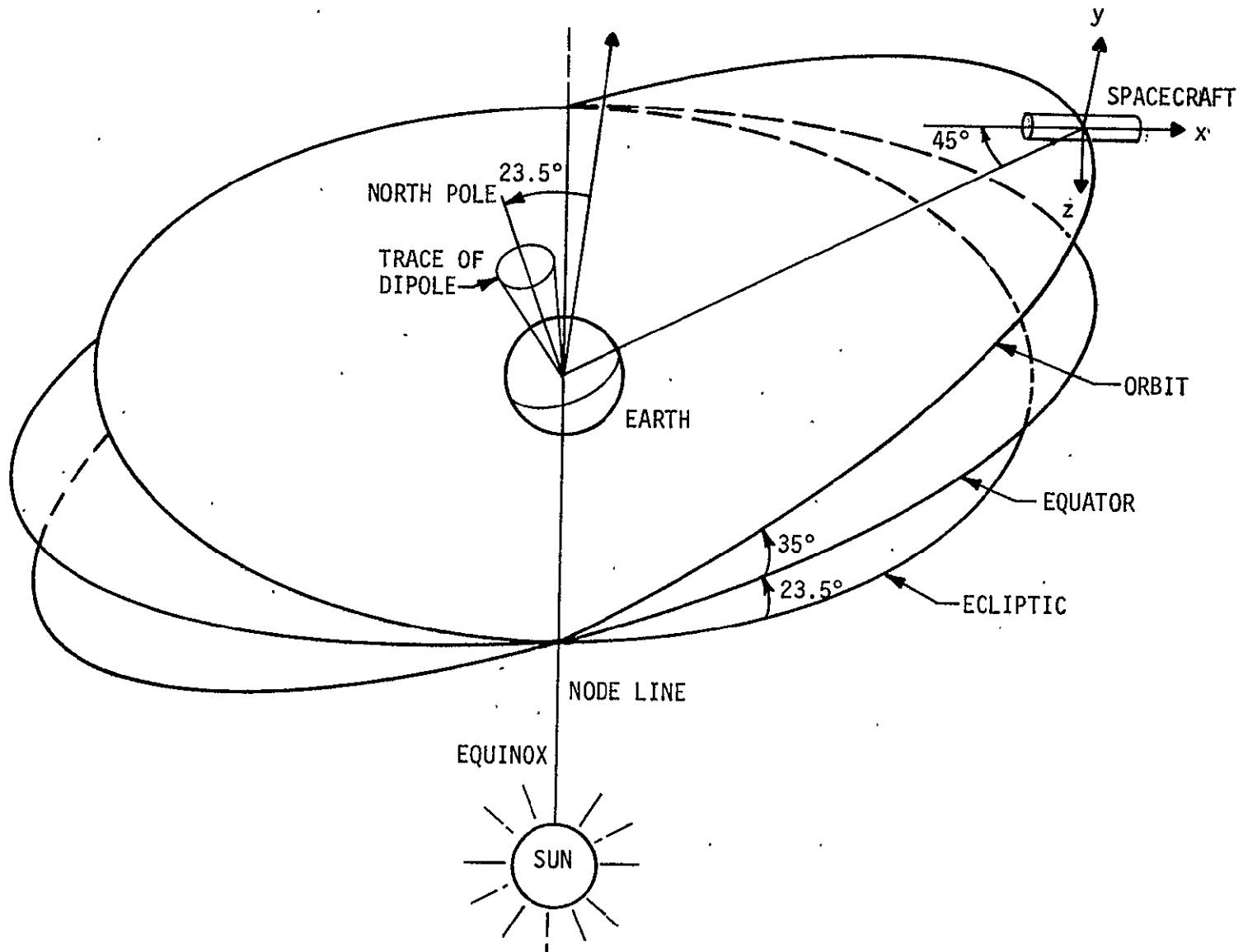


FIGURE A-2. CASE II SIMULATION- SECULAR TORQUE IN z AXIS

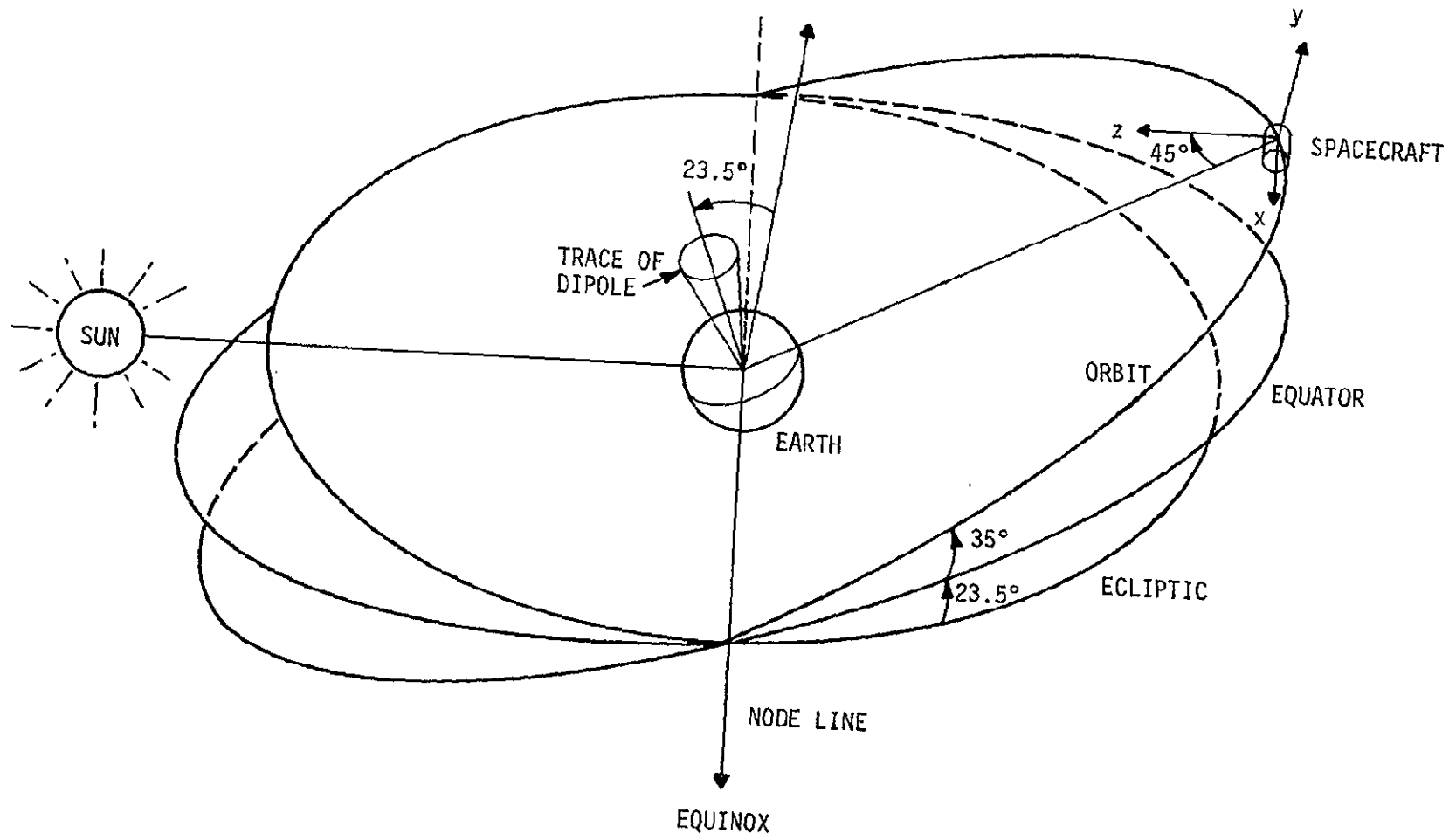


FIGURE A-3. CASE III SIMULATION - SECULAR TORQUE IN x AXIS

Figure A-4 through A-27 show the computer simulation results for Case I. Figures A-4 through A-6 are the profiles of the gravity gradient torques acting on the spacecraft body axes. The gravity torque is primarily cyclic in the x and z axes and is primarily secular in the y axis. Figures A-7 through A-9 show the momentum imparted to the spacecraft by the gravity torques. The total momentum due to gravity torque, as shown in Figure 10, builds up continuously and goes up to 3,300 ft-lbf-sec during 24 hours.

Figures A-11 through A-13 show the profiles of the magnitude of the Earth's magnetic field in the spacecraft axes. The Earth's magnetic field magnitude profile is shown in Figure A-14. The Earth's magnetic field varies from a minimum of 0.24 gauss to a maximum of 0.39 gauss for the present orbit.

Figures A-15 through A-27 show the performance of the magnetic torquers in dumping the stored momentum. Figures A-15 through A-17 show the profile of the components of the stored momentum in spacecraft axes. The stored momentum components at any time are less than 40 ft-lbf-sec in the x axis; less than 30 ft-lbf-sec in the y axis and less than 50 ft-lbf-sec in the z axis. Figure A-18 shows the profile of the total momentum stored in the momentum storage device. The total momentum stored at any time is less than 50 ft-lbf-sec. This indicates that the electromagnets are effective in momentum dumping.

Figure A-19 shows the component of the stored momentum normal to the geomagnetic B field. As expected the electromagnets are effective in keeping this component very small. However, the electromagnets cannot dump the component of the momentum parallel to B field, as shown in Figure A-20. Since both the B-field vector and the stored momentum vector changes their orientations as the spacecraft orbits the Earth, this component can be reduced. Notice the similarity

between Figures A-18 and A-20; the stored momentum consists essentially of that component parallel to the B-field vector. Figure A-21 is the profile of the angle between the total momentum vector and the B-field vector. From Figure A-21 it is seen that most of the time the angle is near 180 degrees. This means that most of the time the component normal to the B field is very small in comparison to the component parallel to the B field.

Figures A-22 through A-24 show the profile of the magnetic torques produced in spacecraft axes for momentum dumping. A comparison of these profiles with those in Figure A-4 through A-6 shows that these are in the opposite sense to that of the gravity torques. This is as expected.

Figures A-25 through A-27 show the profile of the magnetic moment generated by the three electromagnets. These profiles can be related to the power required for these electromagnets.

Figures A-28 through A-51 are computer data plots for the Case II simulation. In this case the secular gravity torque is primarily in the z axis instead of the y axis, as in Case I. Figure A-30 shows the profile of this secular gravity torque. The total momentum imparted to the spacecraft by gravity torque is shown in Figure A-34 to be 3,300 ft-lbf-sec in 24 hours. In Case II the magnetic field has been shifted by 90 degrees from its position in Case I. This fact is illustrated in the plots of the magnetic field for Case II, Figures A-35 through A-38, in which corresponding characteristics are displaced by 6 hours from those in plots for Case I.

Figures A-39 through A-51 show the performance of the electromagnets. In this case, the components of the stored momentum

are kept less than 40 ft-lbf-sec in the x axis; less than 50 ft-lbf-sec in the y axis; and less than 40 ft-lbf-sec in the z axis, as shown in Figures A-39 through A-41. The total momentum stored in the momentum storage device is kept less than 50 ft-lbf-sec as shown in Figure A-42. This indicates that the electromagnets are effective in keeping the stored momentum level less than 50 ft-lbf-sec in this case too.

Figures A-52 through A-75 are the computer data plots for the Case III simulation. In this case, the secular gravity torque is primarily in the x axis. Figure A-58 shows that a total momentum of 125 ft-lbf-sec is imparted to the spacecraft by gravity torques. Figures A-63 through A-75 show the performance characteristics of the electromagnets for this case. Figures A-63 through A-65 show that the components of the stored momentum are kept less than 20 ft-lbf-sec in the x axis, less than 40 ft-lbf-sec in the y axis, and less than 52 ft-lbf-sec in the z axis. Figure A-66 shows that the total stored momentum in the momentum storage device is kept less than 52 ft-lbf-sec. This again indicates the effectiveness of the electromagnets in keeping the stored momentum at a low level.

From the data presented, it is evident that the electromagnets are able to keep the stored momentum level below 52 ft-lbf-sec for Cases I, II, and III. It is believed that the maximum stored momentum for any spacecraft and orbit orientation can be maintained below 30 ft-lbf-sec by changing the levels at which the torquers are switched on and off. Therefore, this value was used in sizing the control system.

This simulation also indicates that the 30 ft-lbf-sec momentum vector is equally likely to occur in any direction in space. Another conclusion is that the magnetic moments of each torquer, 0.2 ft-lbf/gauss (2,700 amp-m²), are adequate for momentum dumping for the HEAO-C spacecraft.

NOT REPRODUCIBLE

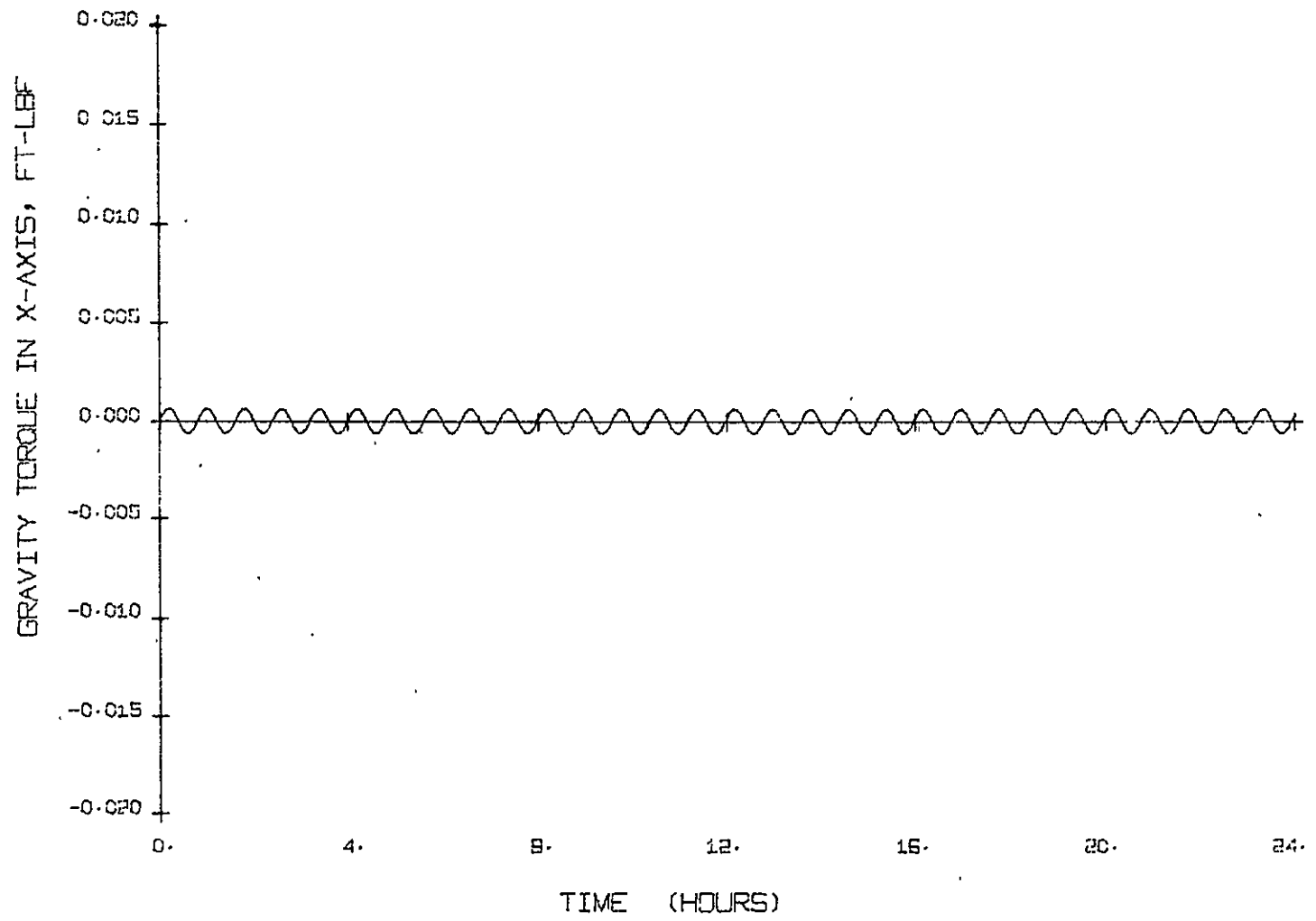


FIGURE A-4. GRAVITY GRADIENT TORQUE PROFILE IN THE x AXIS FOR CASE I

NOT REPRODUCIBLE

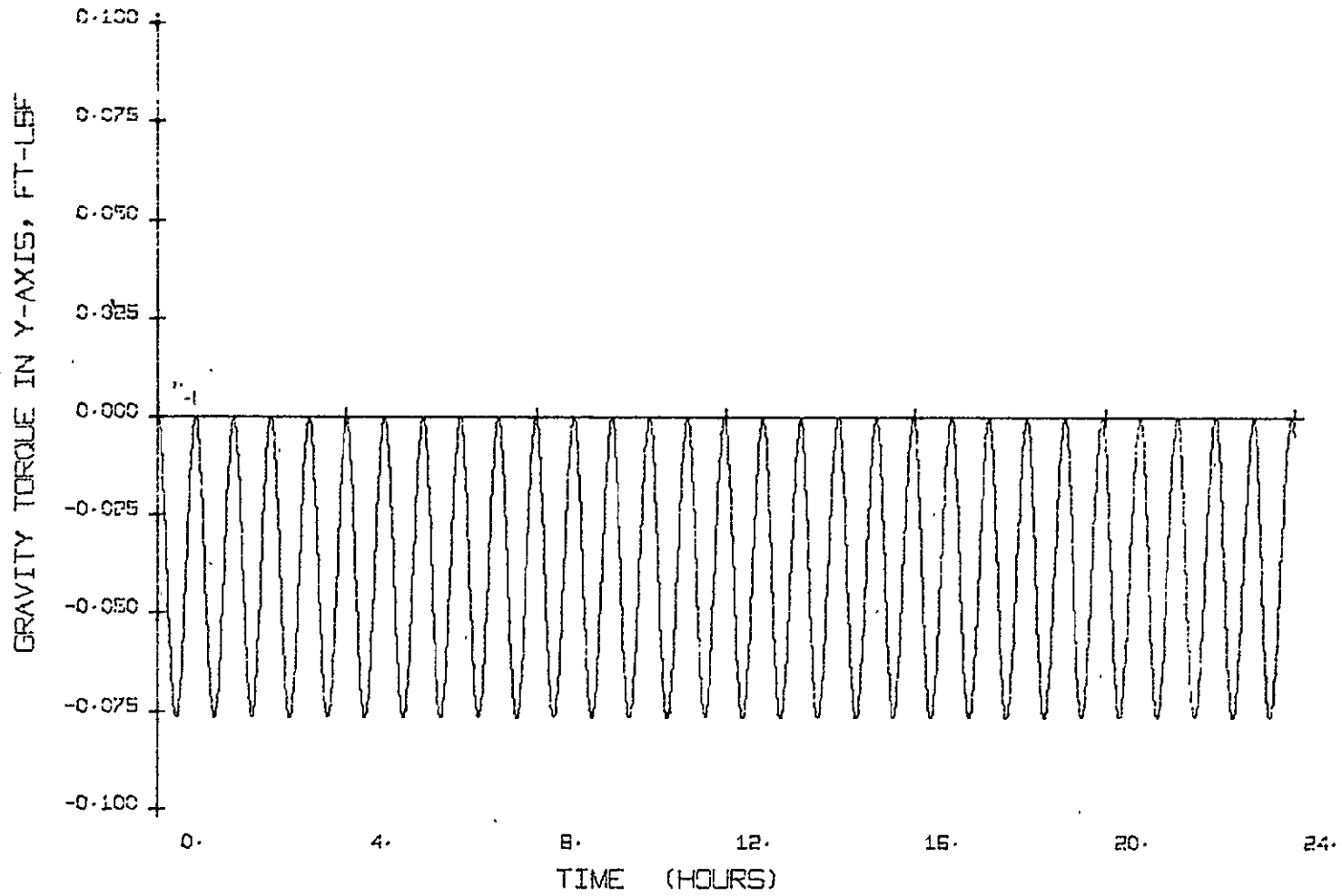


FIGURE A-5. GRAVITY GRADIENT TORQUE PROFILE IN THE y AXIS FOR CASE I

NOT REPRODUCIBLE

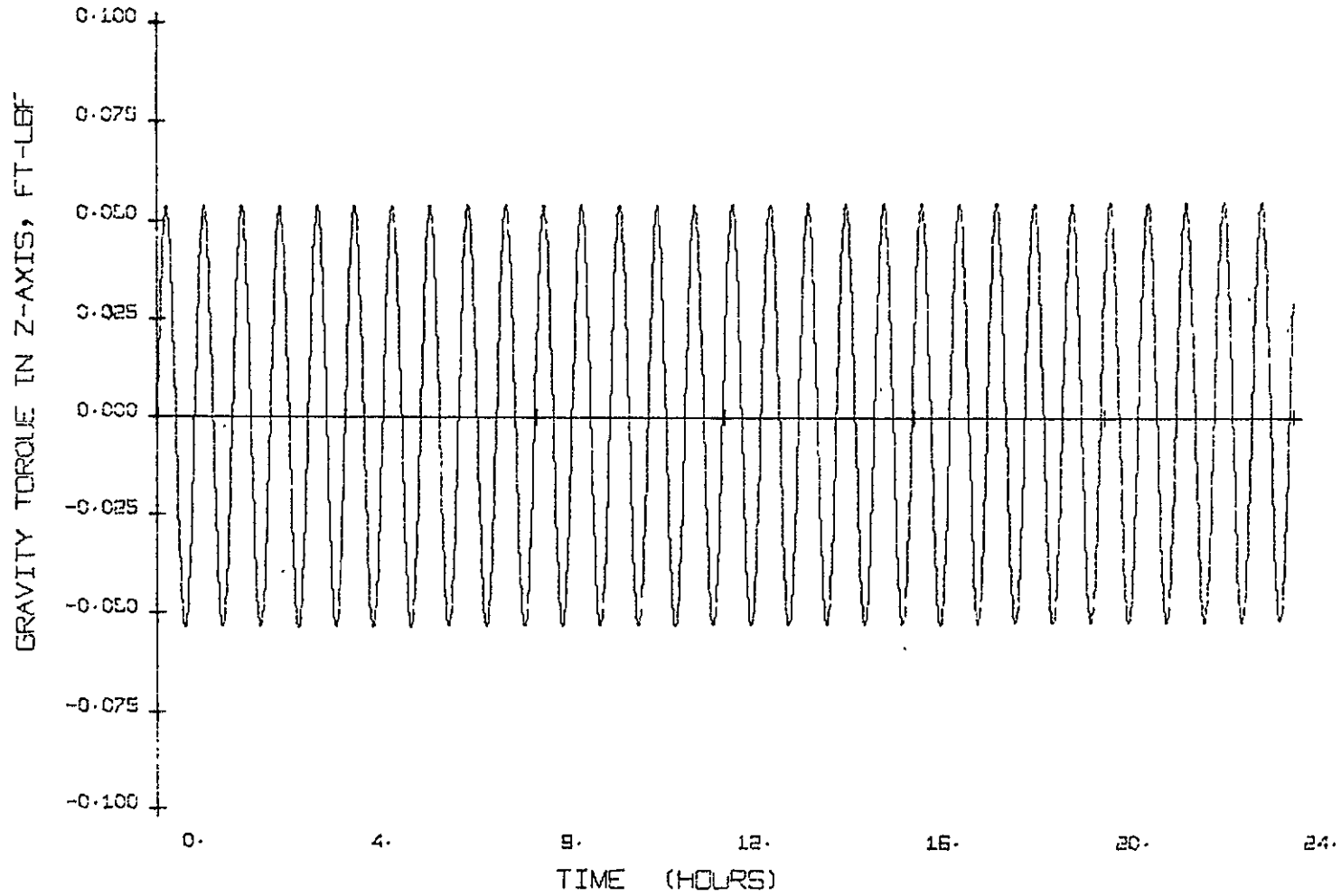


FIGURE A-6. GRAVITY GRADIENT TORQUE PROFILE IN THE z AXIS FOR CASE I

NOT REPRODUCIBLE

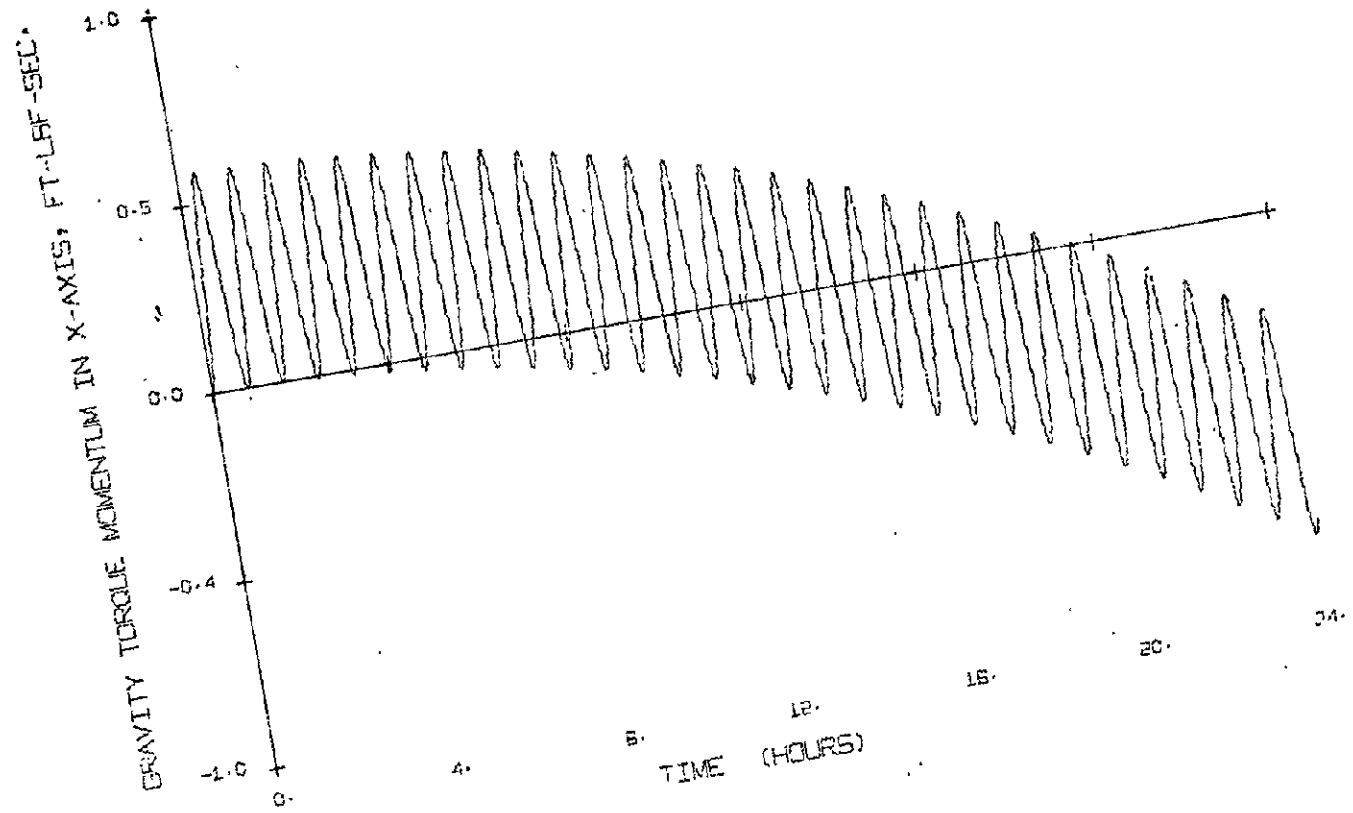


FIGURE A-7. GRAVITY TORQUE MOMENTUM IN THE X AXIS FOR CASE I

NOT REPRODUCIBLE

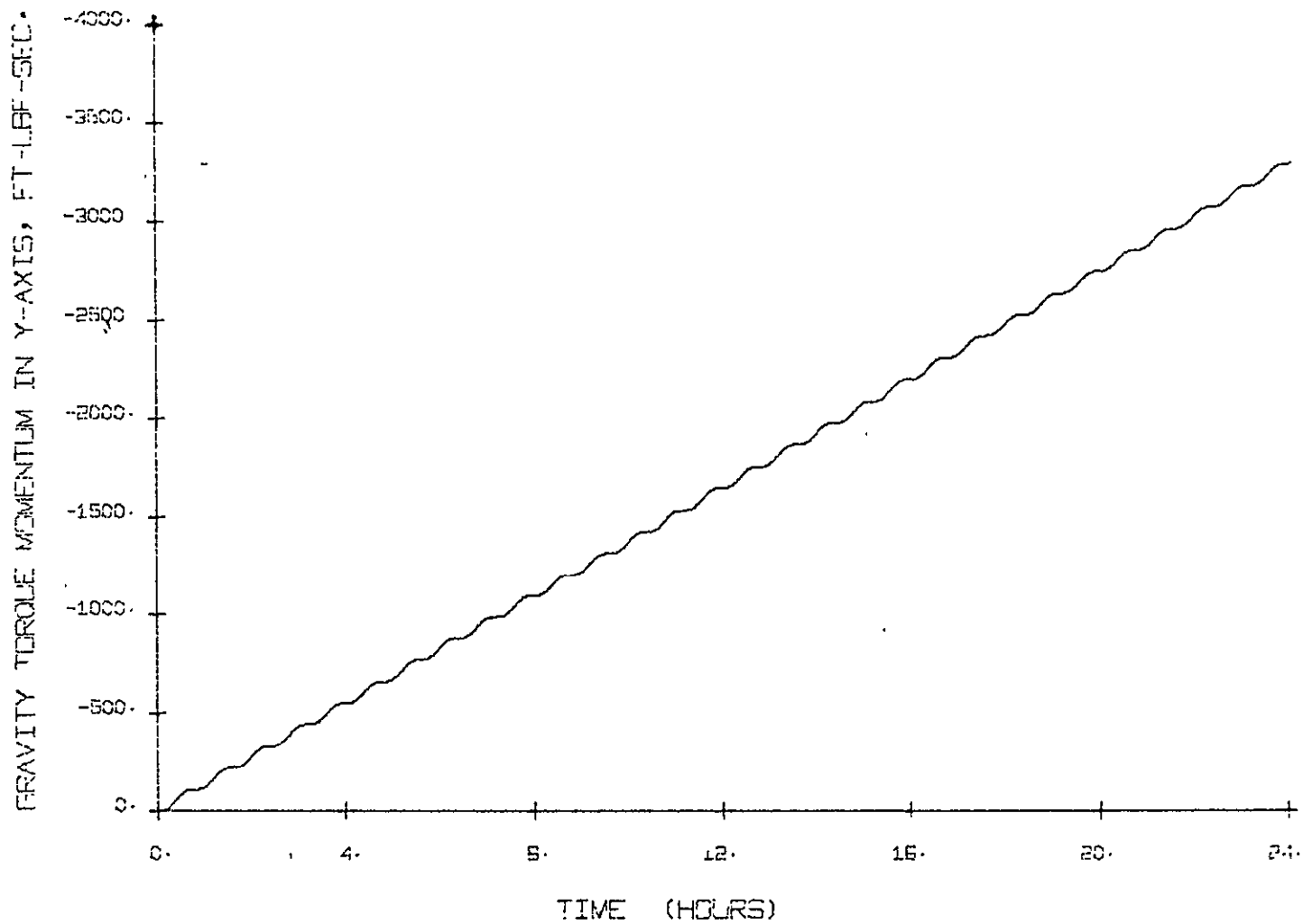


FIGURE A-8. GRAVITY TORQUE MOMENTUM IN THE y AXIS FOR CASE I

NOT REPRODUCIBLE

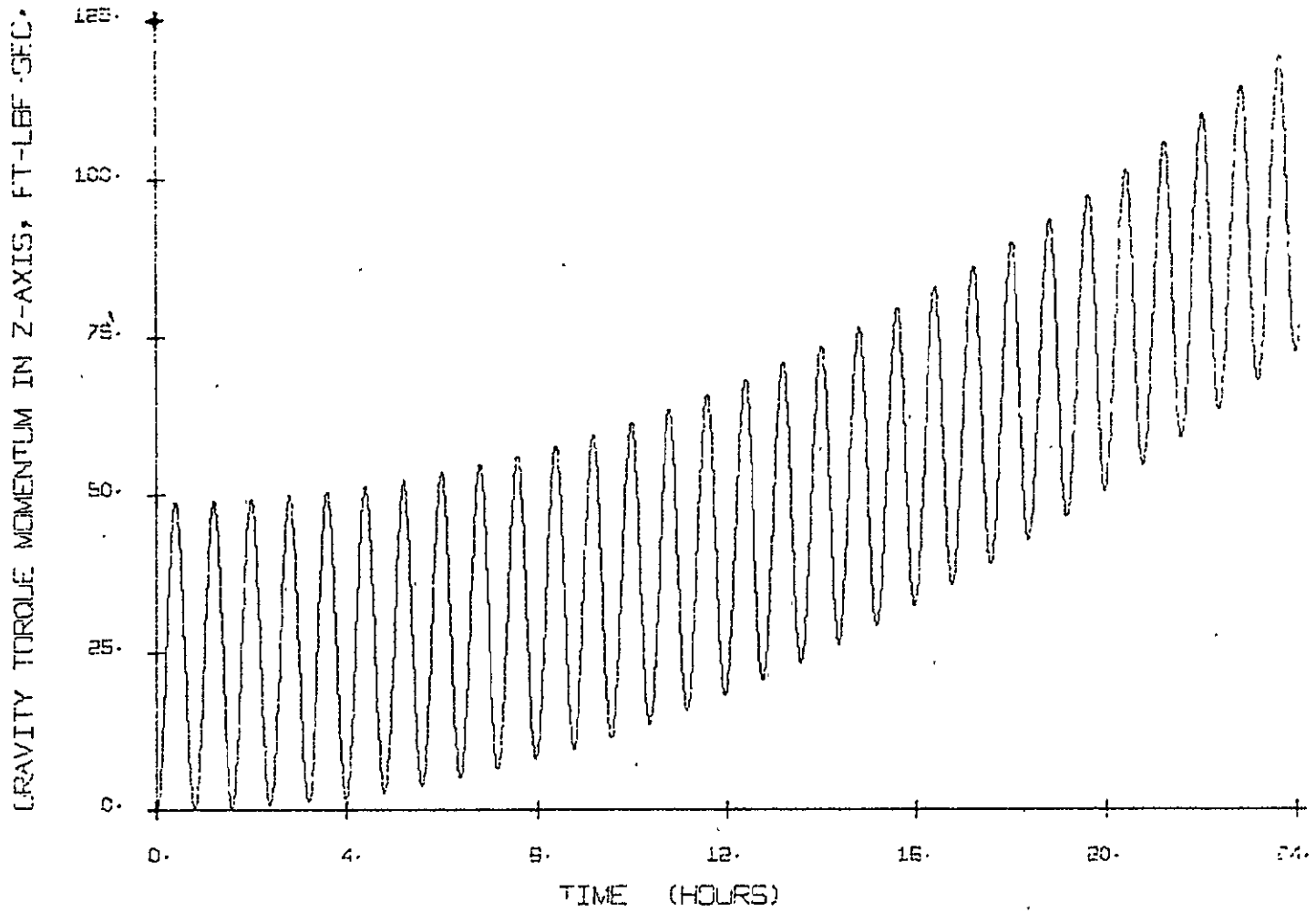


FIGURE A-9. GRAVITY TORQUE MOMENTUM IN THE z AXIS FOR CASE I

NOT REPRODUCIBLE

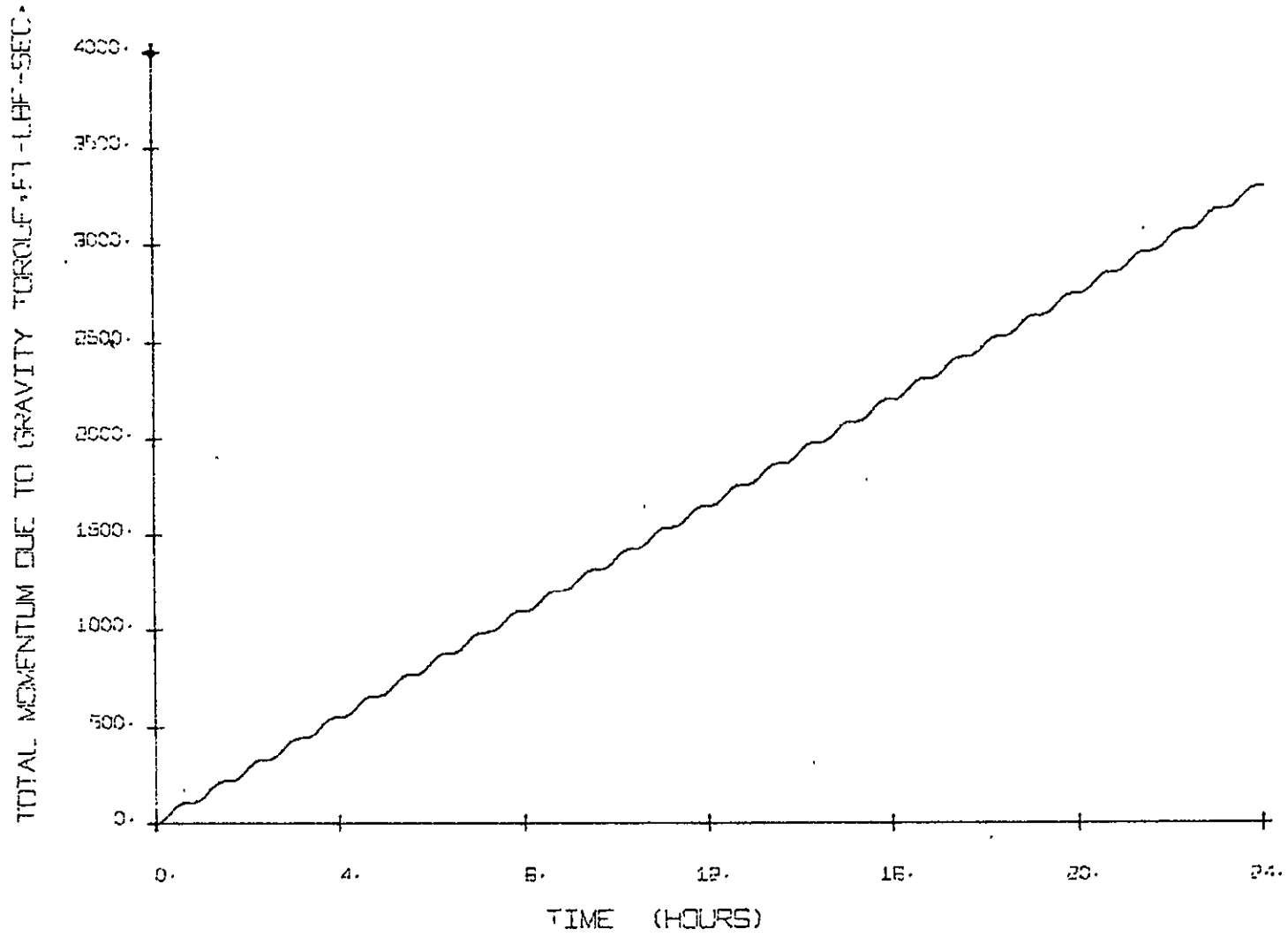


FIGURE A-10. TOTAL MOMENTUM DUE TO GRAVITY TORQUE FOR CASE I

NOT REPRODUCIBLE

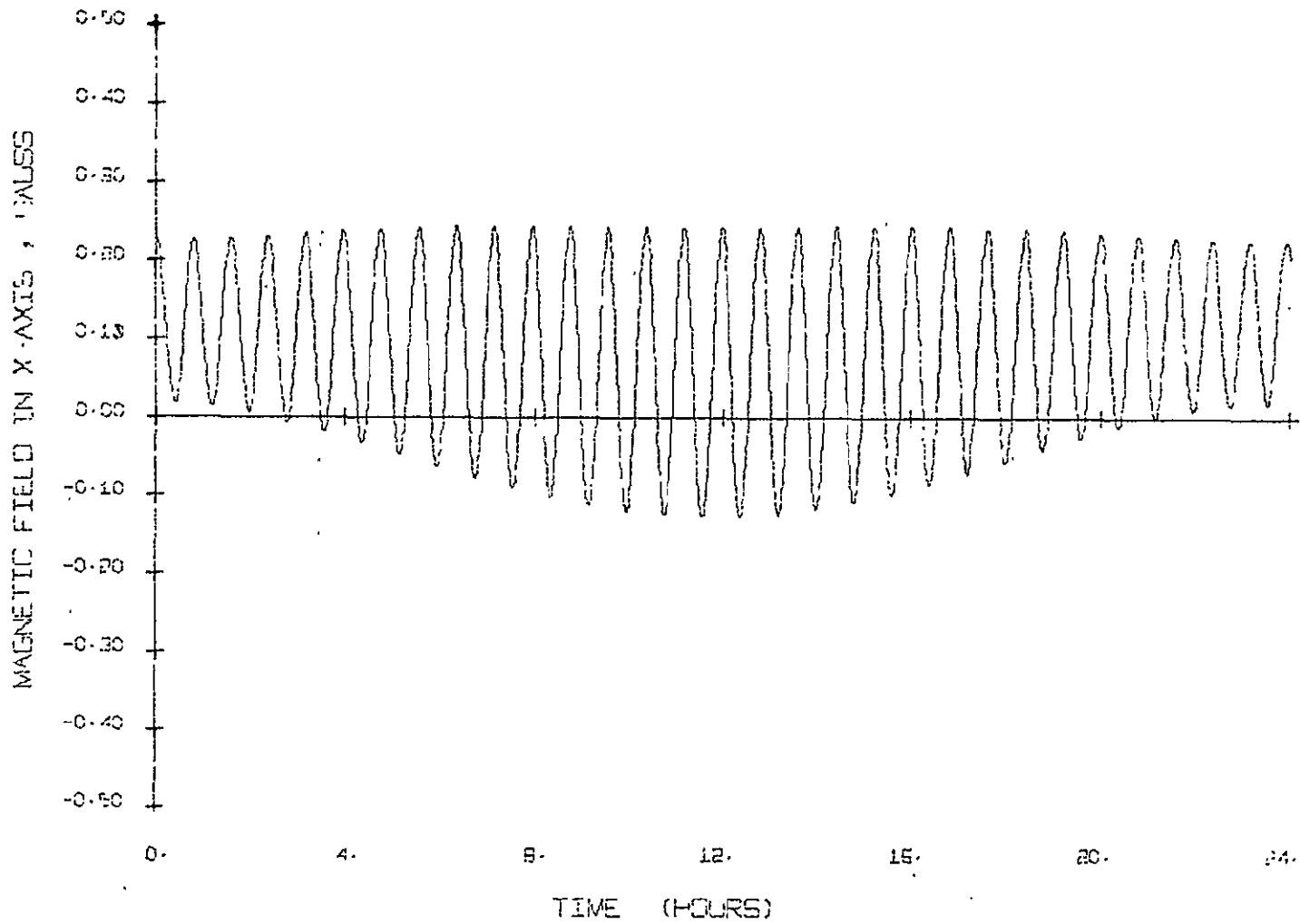


FIGURE A-11. COMPONENT OF THE EARTH'S MAGNETIC FIELD IN THE x AXIS FOR CASE I

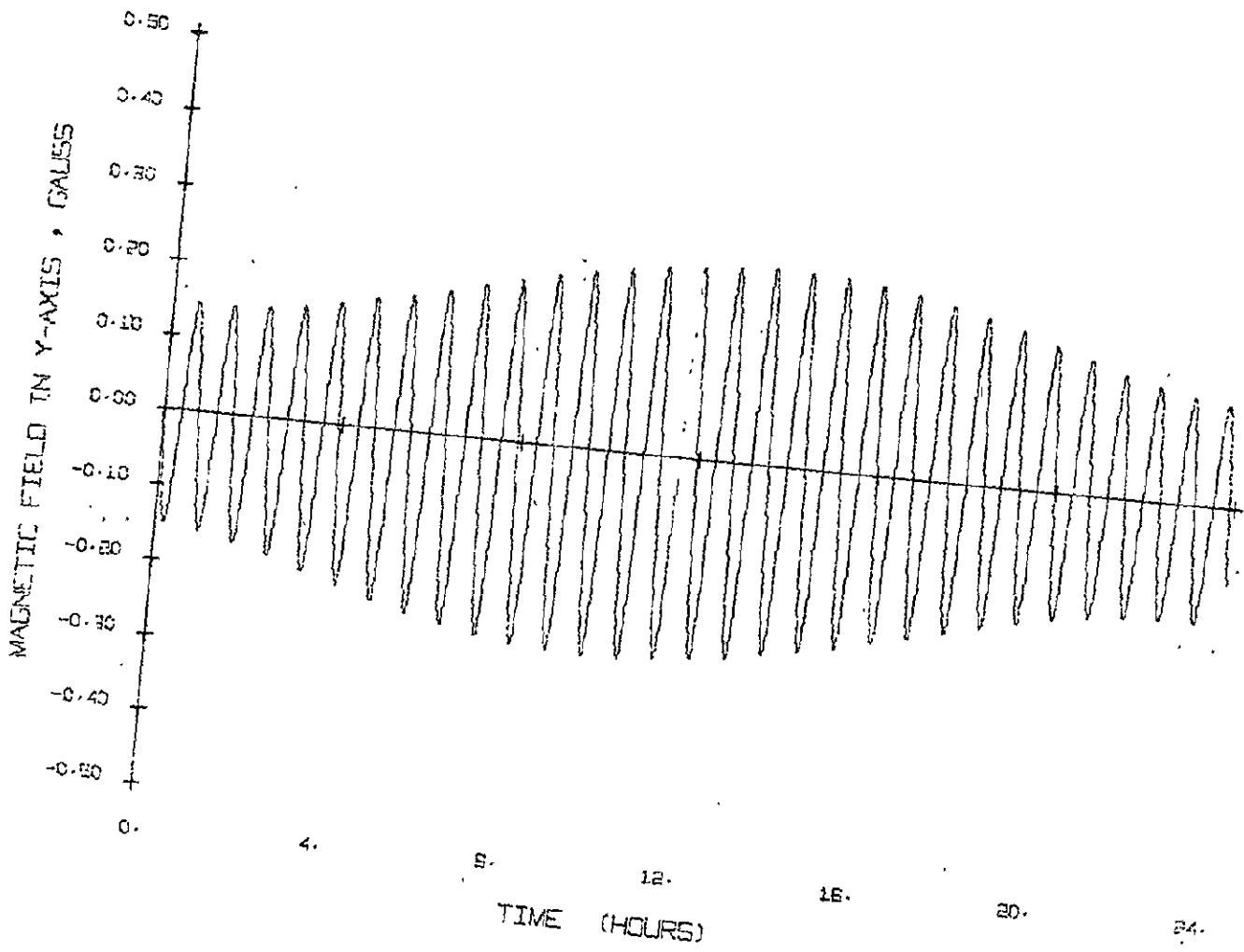


FIGURE A-12. COMPONENT OF THE EARTH'S MAGNETIC FIELD IN THE y AXIS FOR CASE I

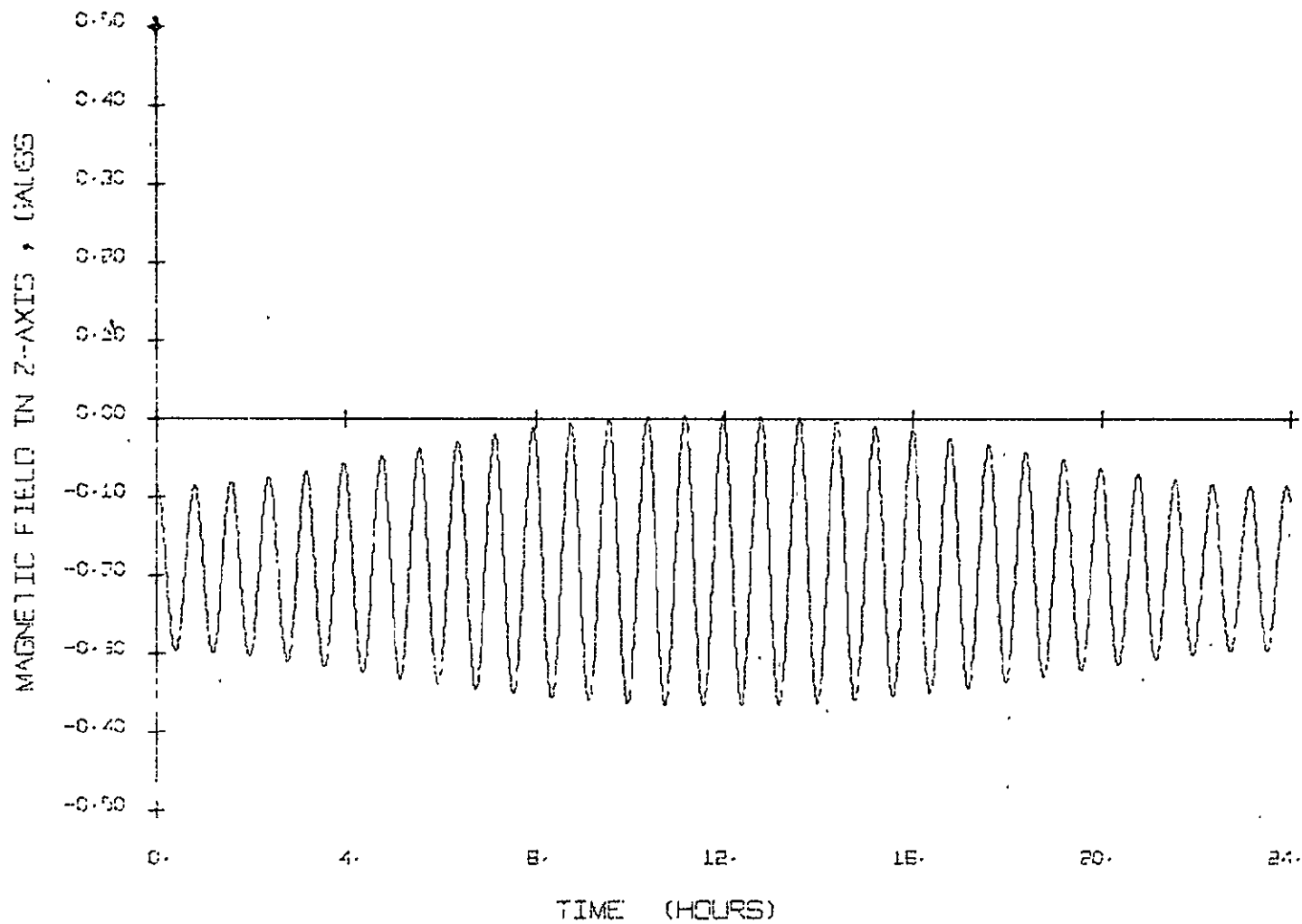


FIGURE A-13. COMPONENT OF THE EARTH'S MAGNETIC FIELD IN THE z AXIS FOR CASE I

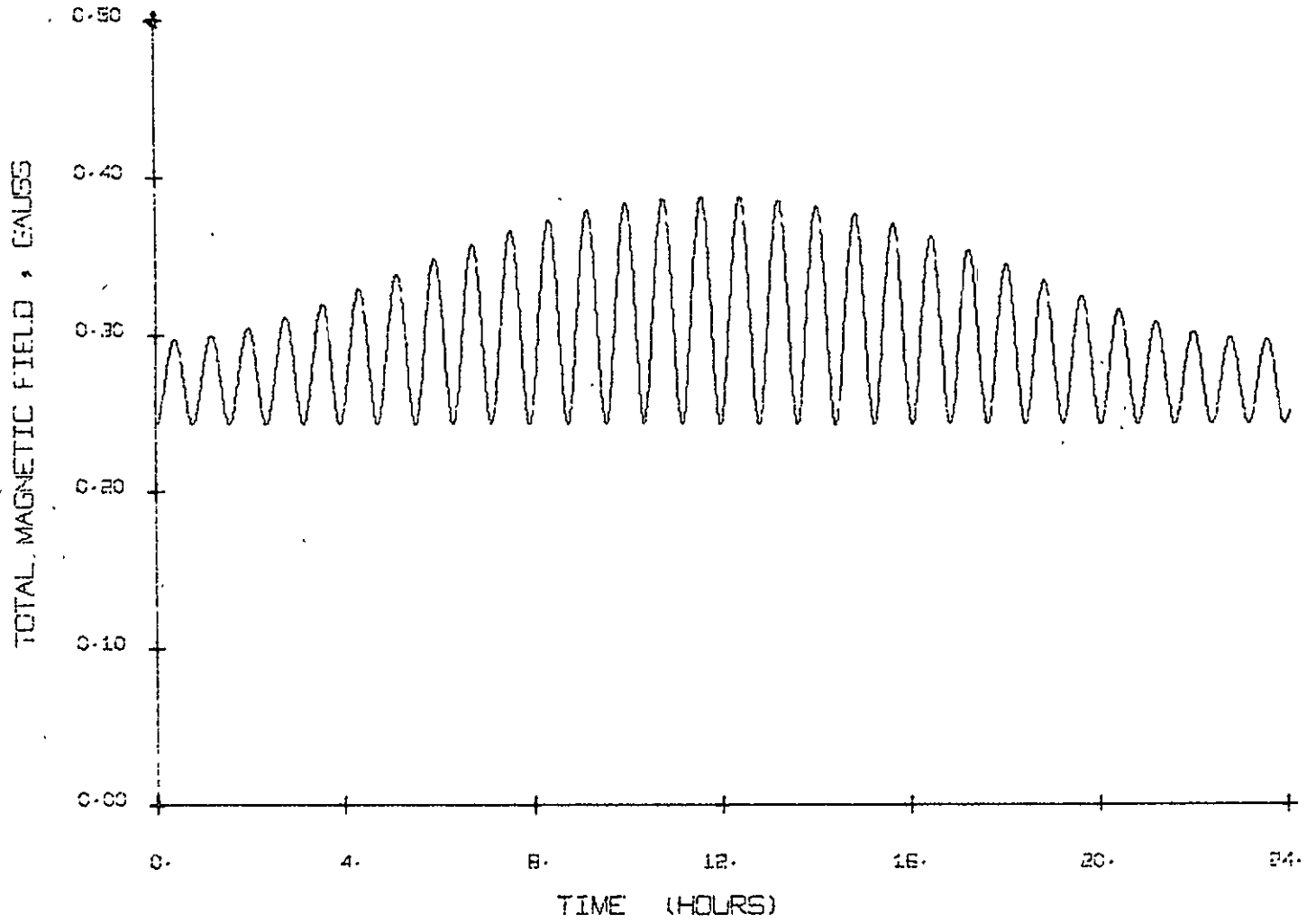


FIGURE A-14. EARTH'S MAGNETIC FIELD PROFILE FOR CASE I

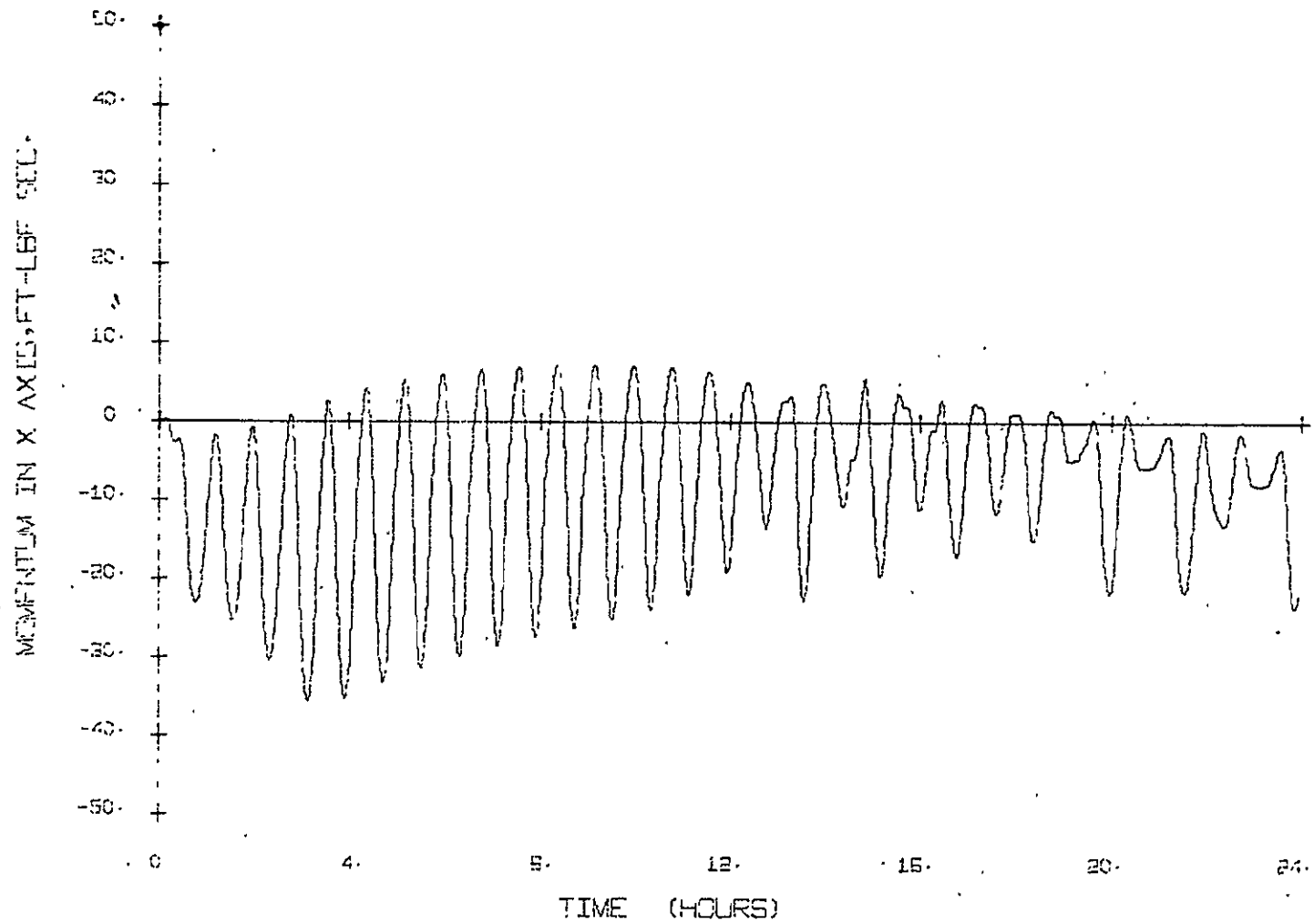


FIGURE A-15. COMPONENT OF STORED MOMENTUM IN THE x AXIS FOR CASE I

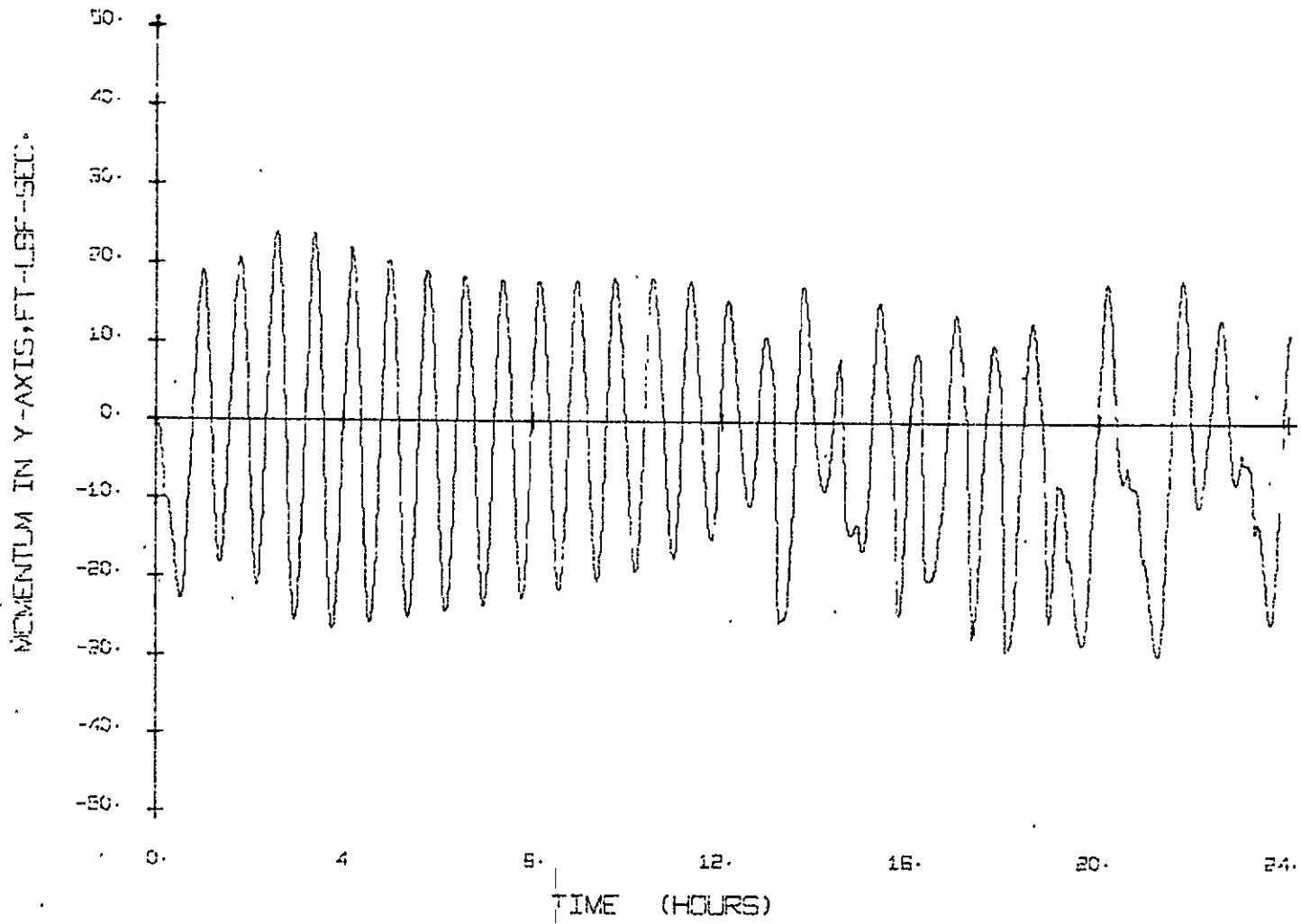


FIGURE A-16. COMPONENT OF STORED MOMENTUM IN THE y AXIS FOR CASE I

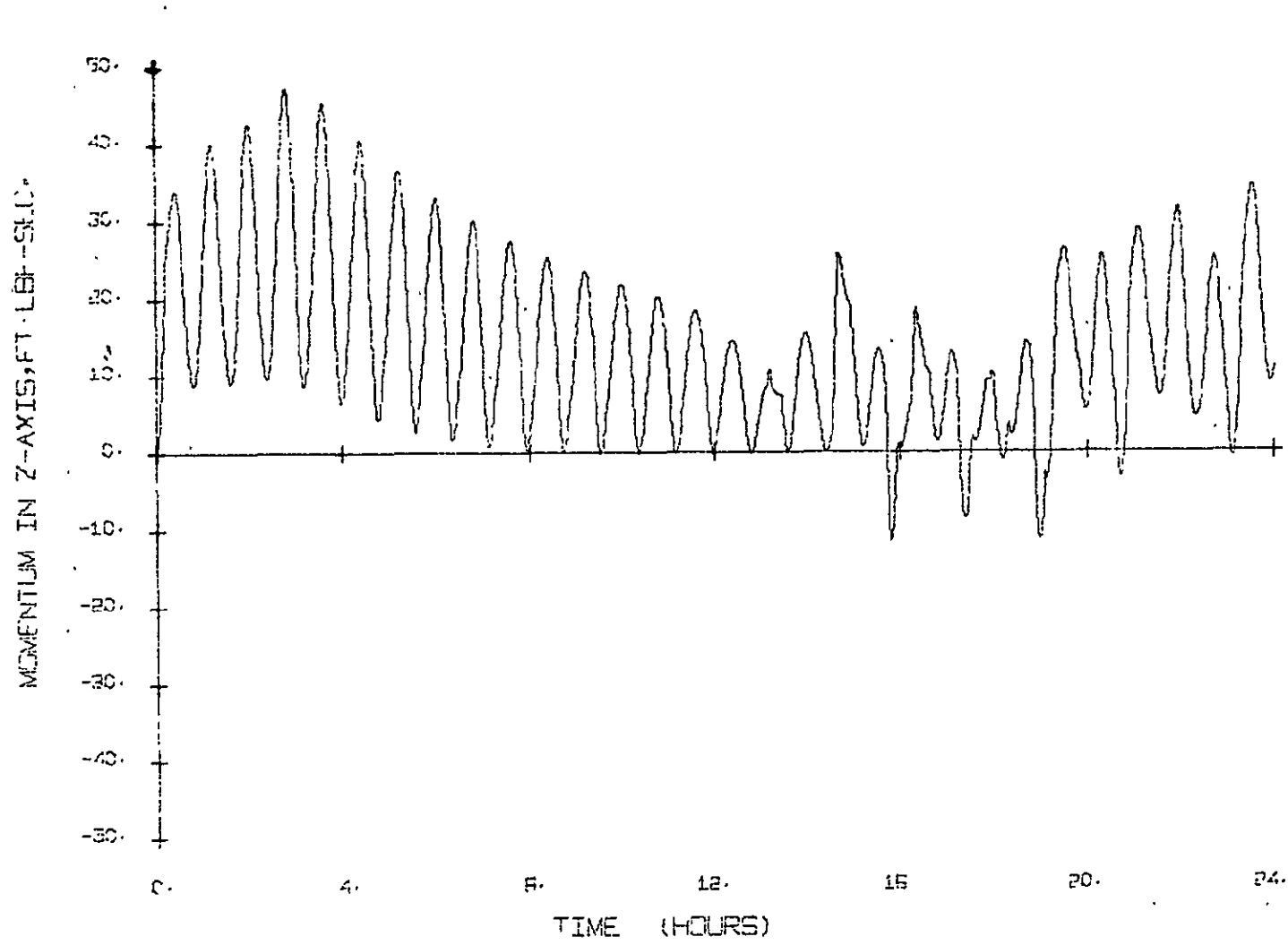


FIGURE A-17. COMPONENT OF STORED MOMENTUM IN THE z AXIS FOR CASE I

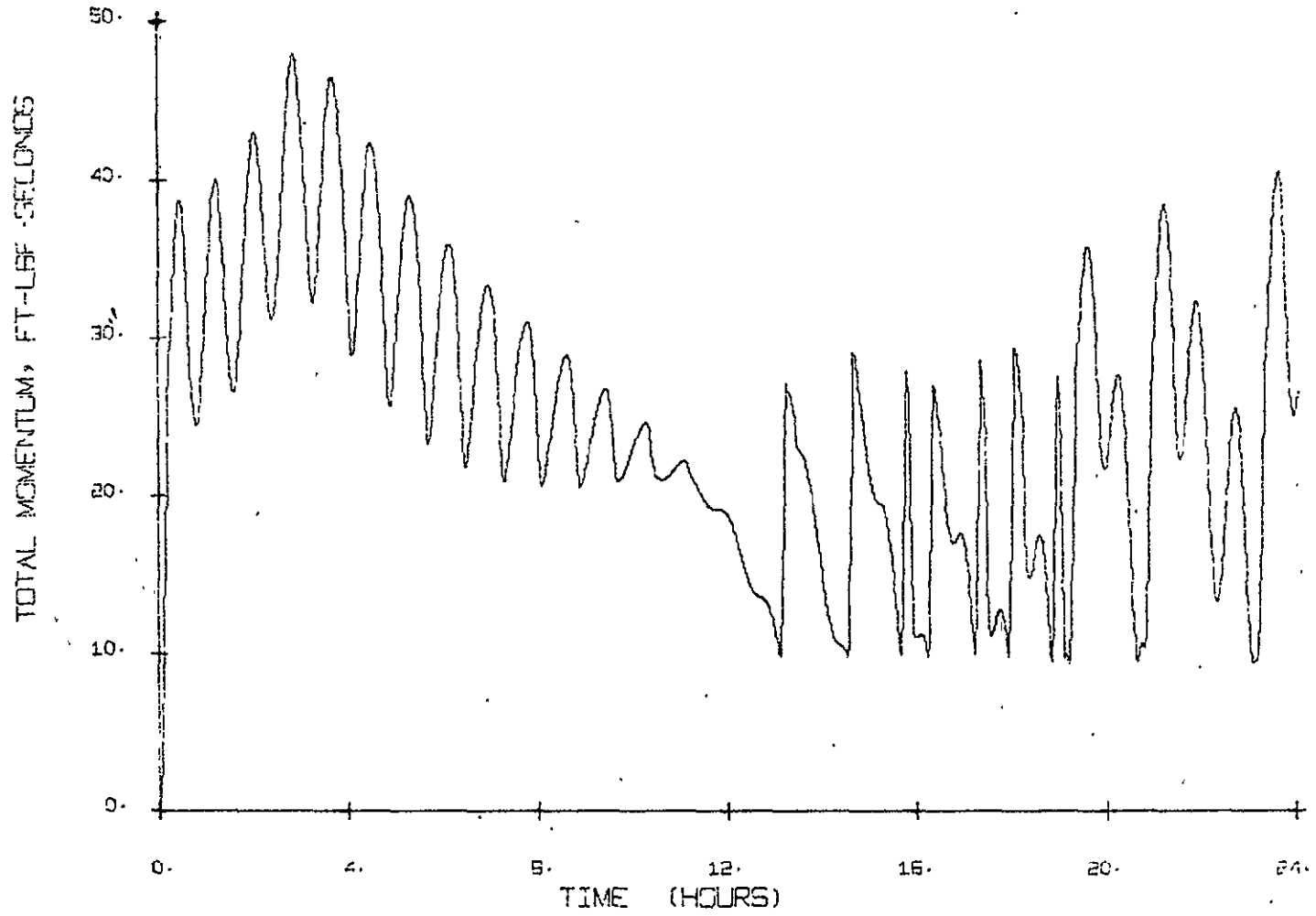


FIGURE A-18. TOTAL MOMENTUM STORED IN THE MOMENTUM STORAGE DEVICE FOR CASE I

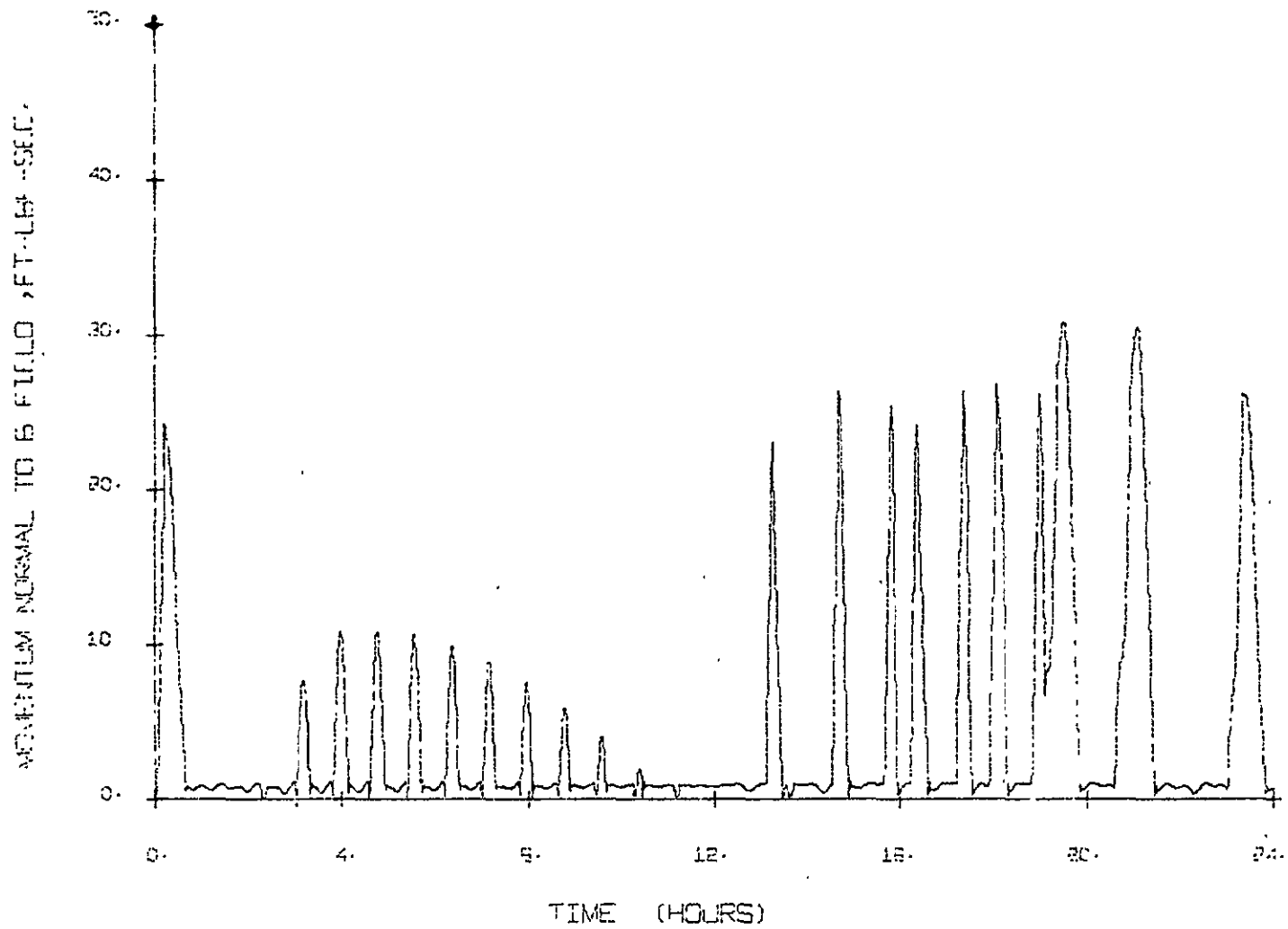


FIGURE A-19. COMPONENT OF STORED MOMENTUM NORMAL TO THE B-FIELD FOR CASE I

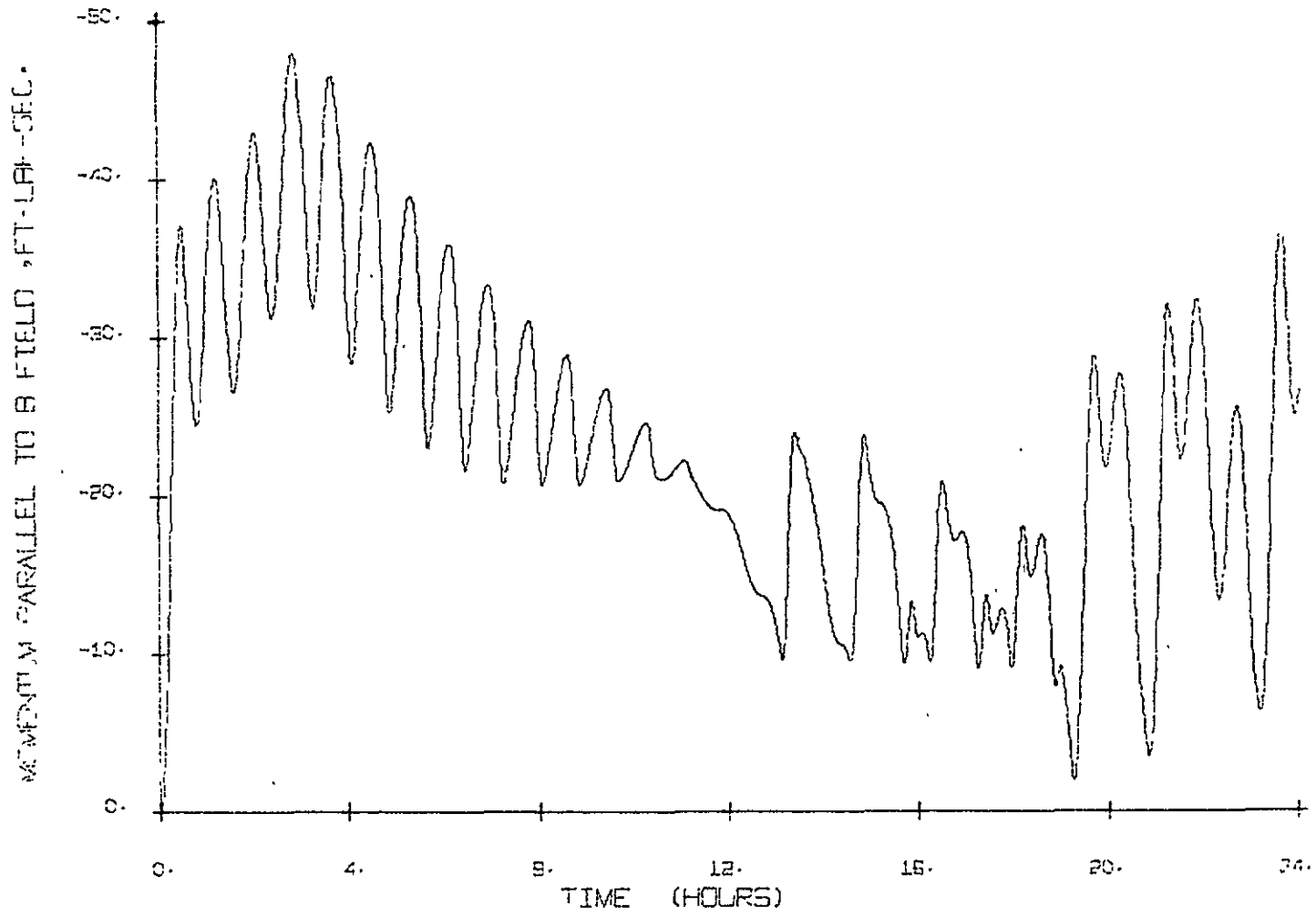


FIGURE A-20. COMPONENT OF STORED MOMENTUM PARALLEL TO THE B-FIELD FOR CASE I

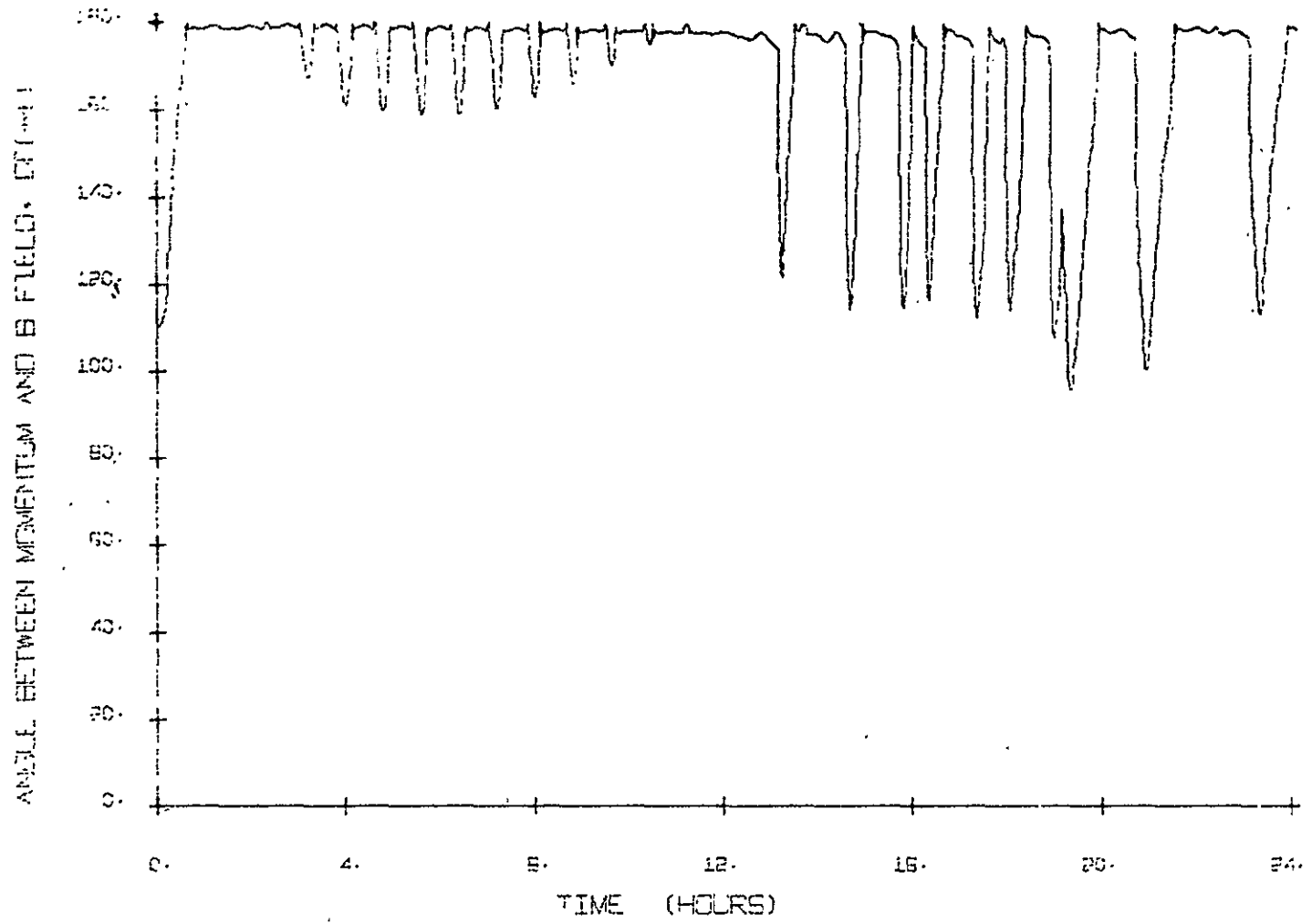


FIGURE A-21. ANGLE BETWEEN THE STORED MOMENTUM VECTOR AND THE B-FIELD VECTOR FOR CASE I

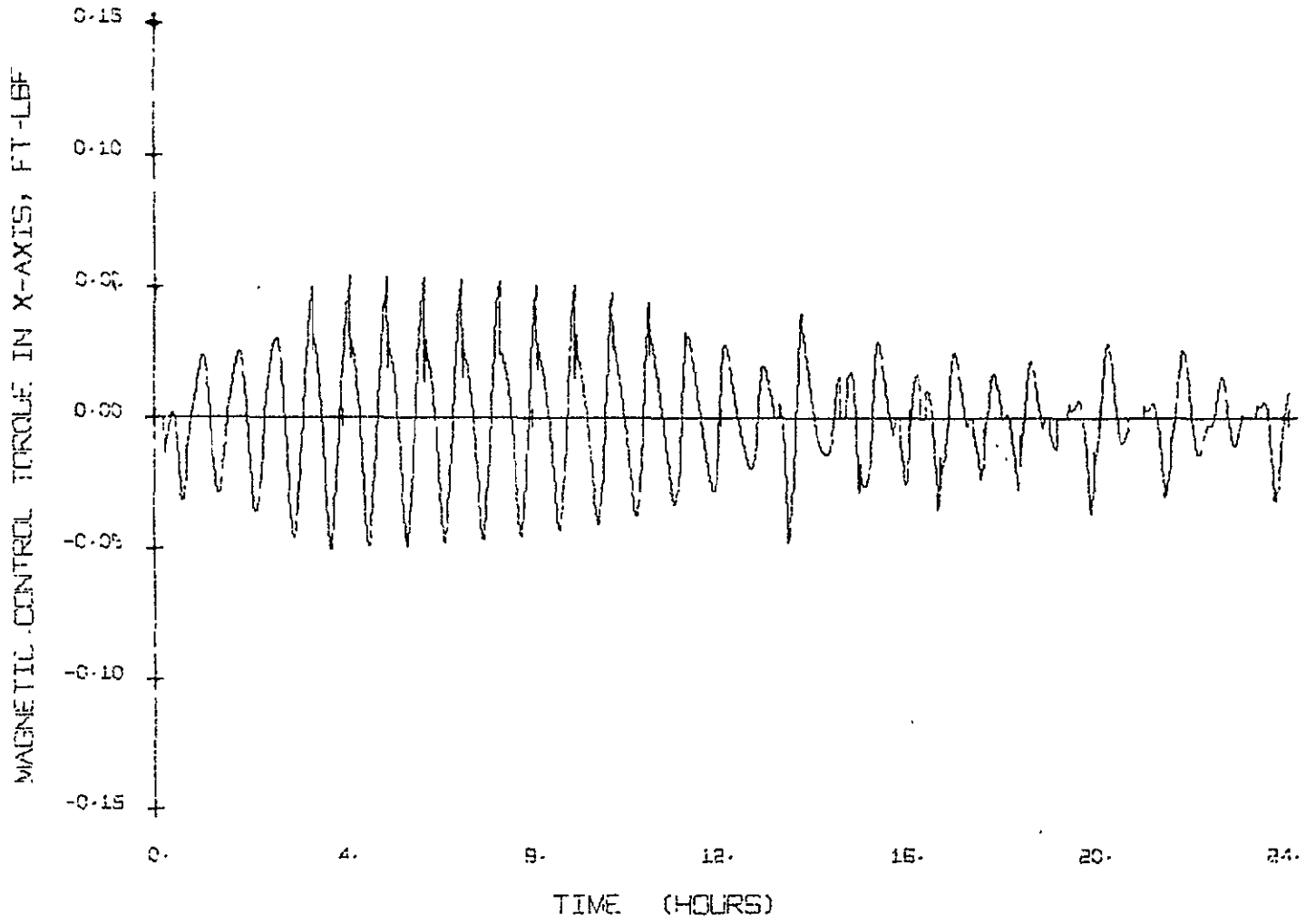


FIGURE A-22. MAGNETIC CONTROL TORQUE IN THE x AXIS FOR CASE I

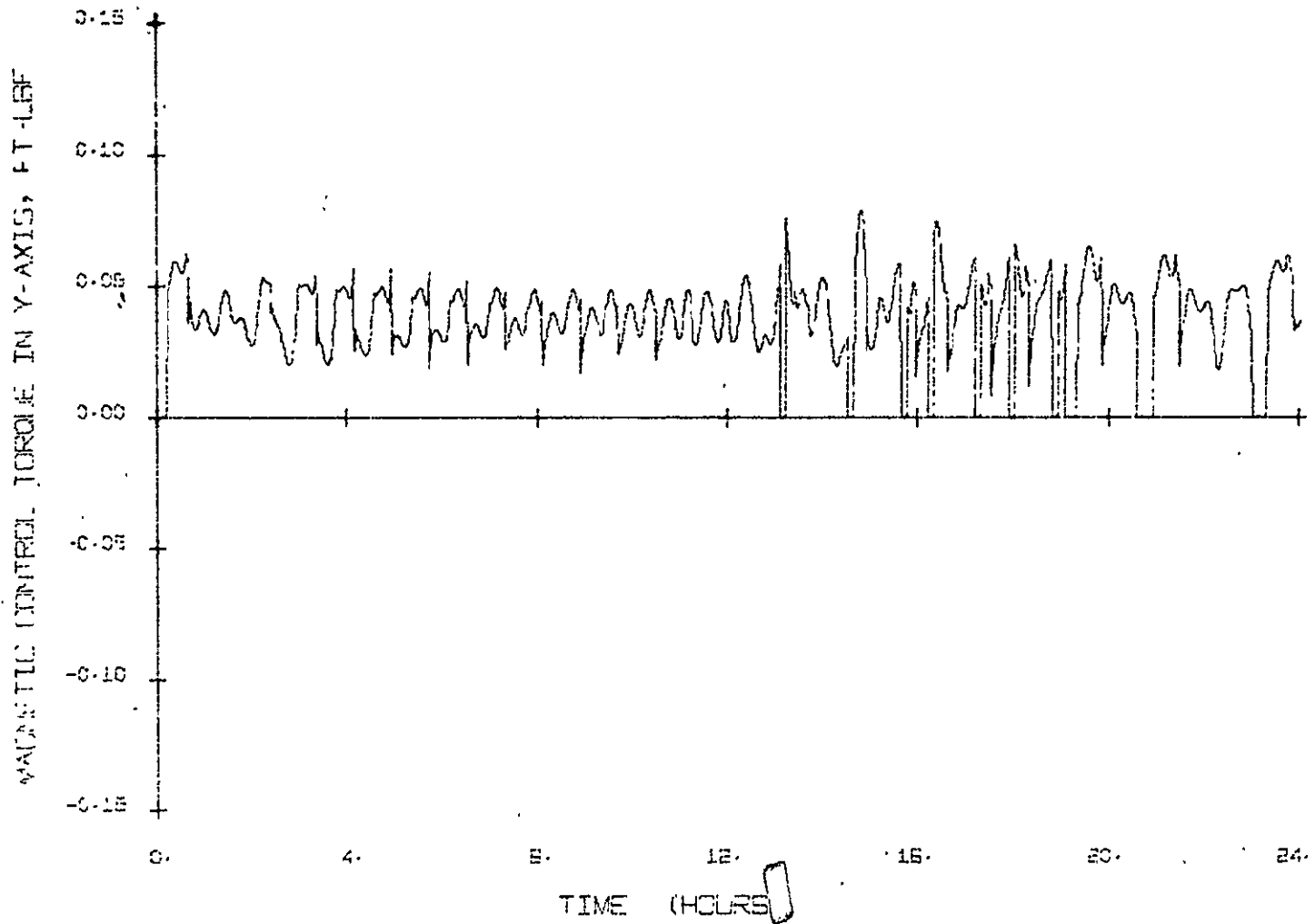


FIGURE A-23. MAGNETIC CONTROL TORQUE IN THE y AXIS FOR CASE I

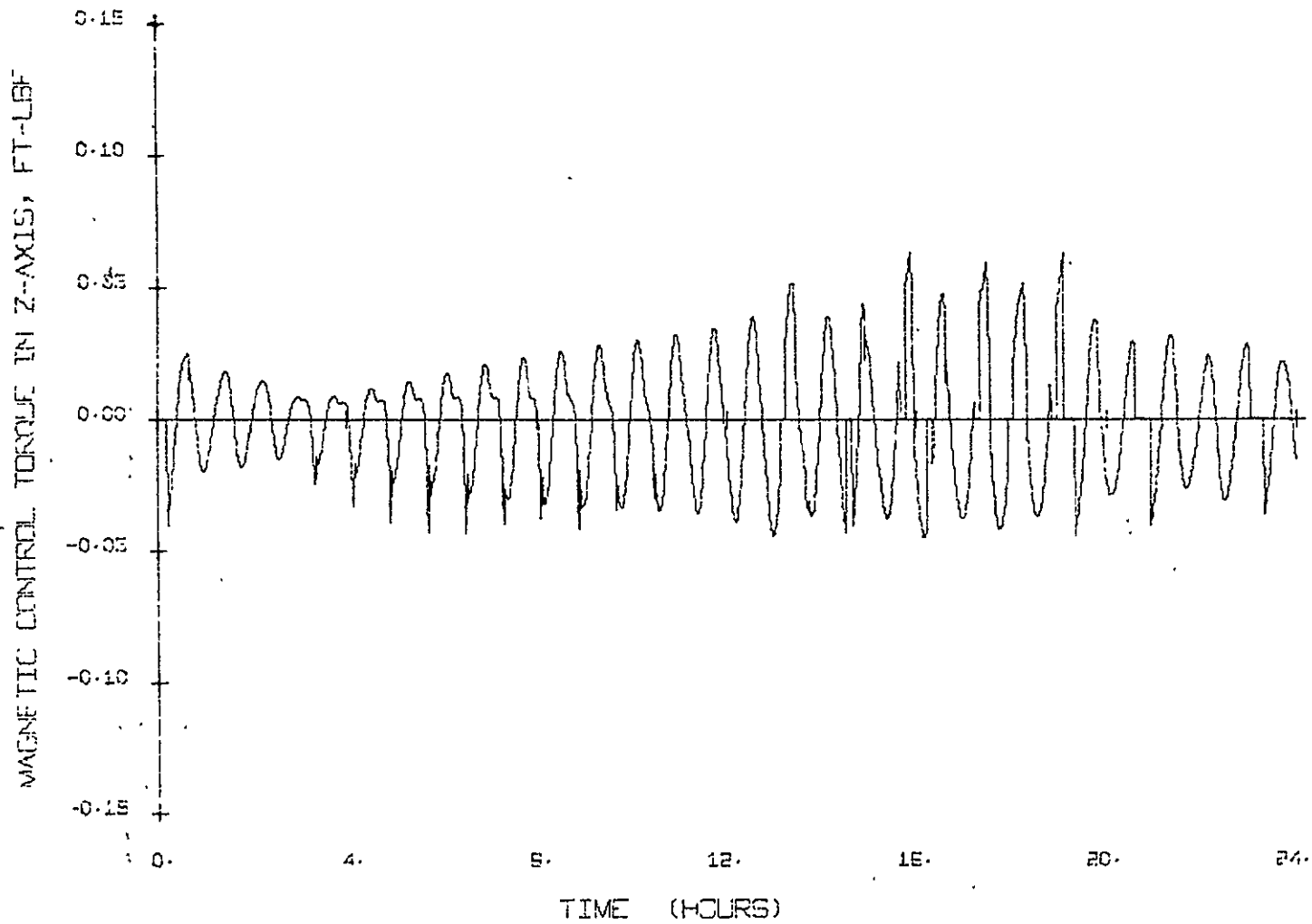


FIGURE A-24. MAGNETIC CONTROL TORQUE IN THE z AXIS FOR CASE I

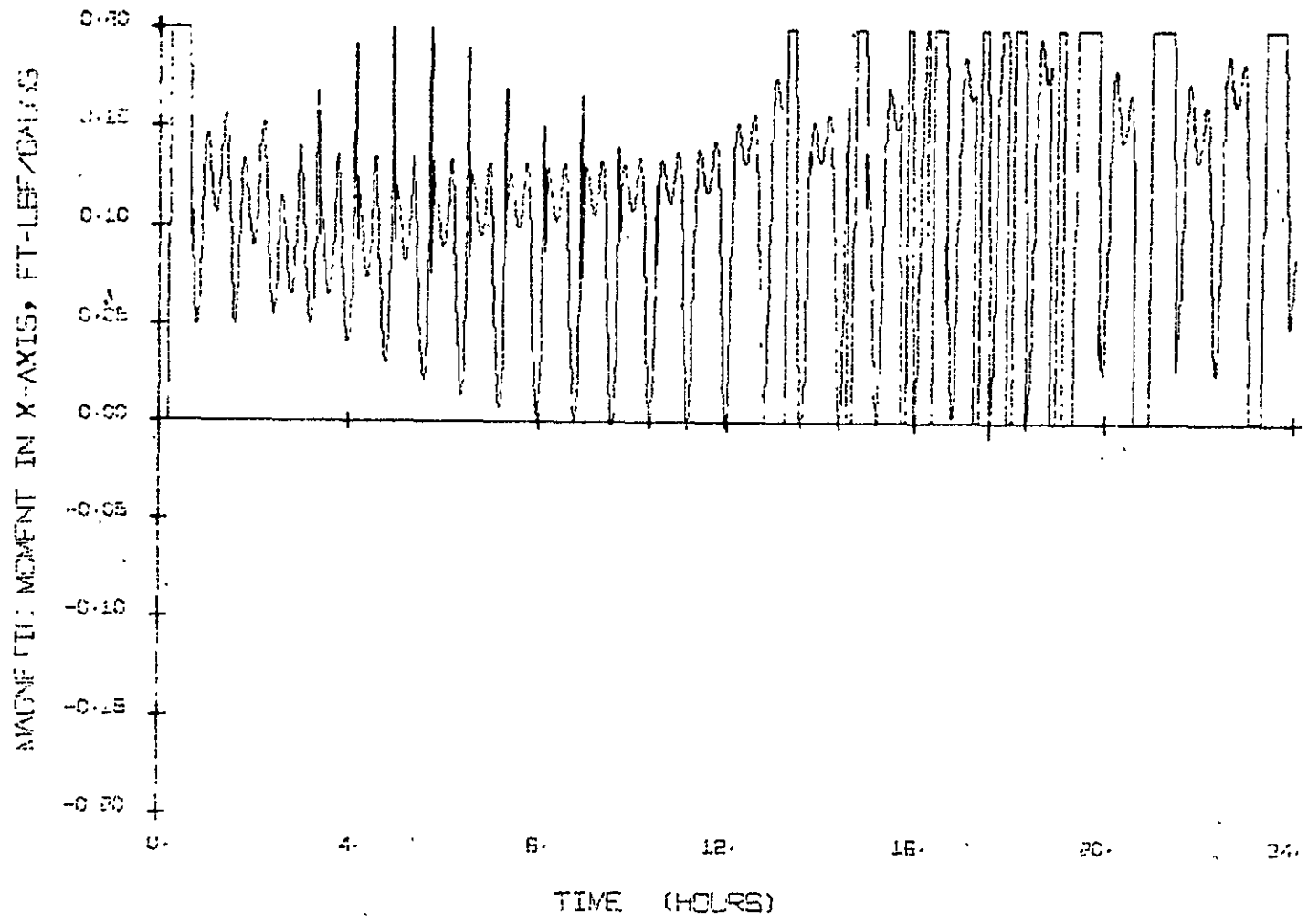


FIGURE A-25. MAGNETIC MOMENT PRODUCED BY THE x AXIS ELECTROMAGNET FOR CASE I

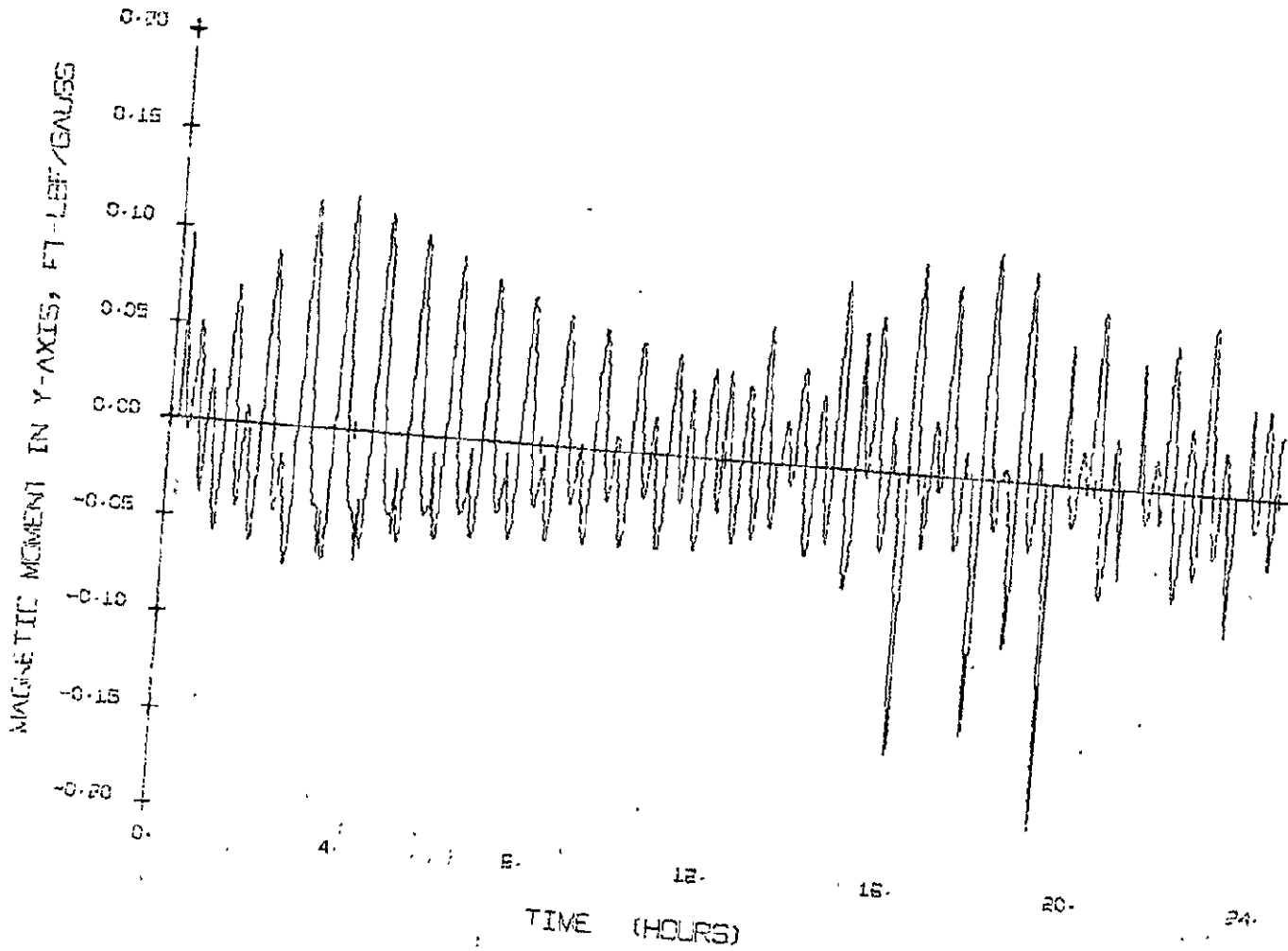


FIGURE A-26. MAGNETIC MOMENT PRODUCED BY THE y AXIS ELECTROMAGNET FOR CASE I

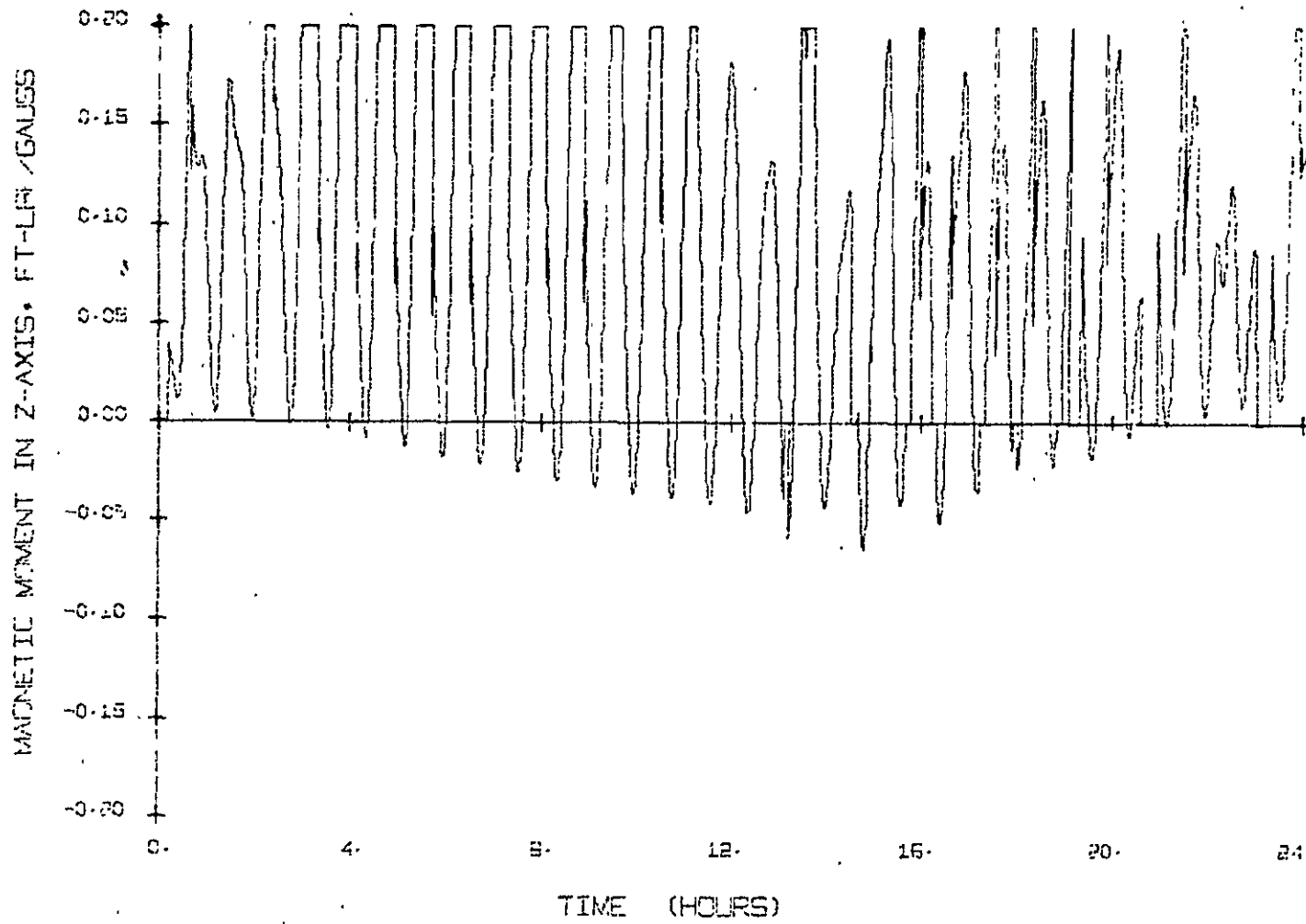


FIGURE A-27. MAGNETIC MOMENT PRODUCED BY THE z AXIS ELECTROMAGNET FOR CASE I

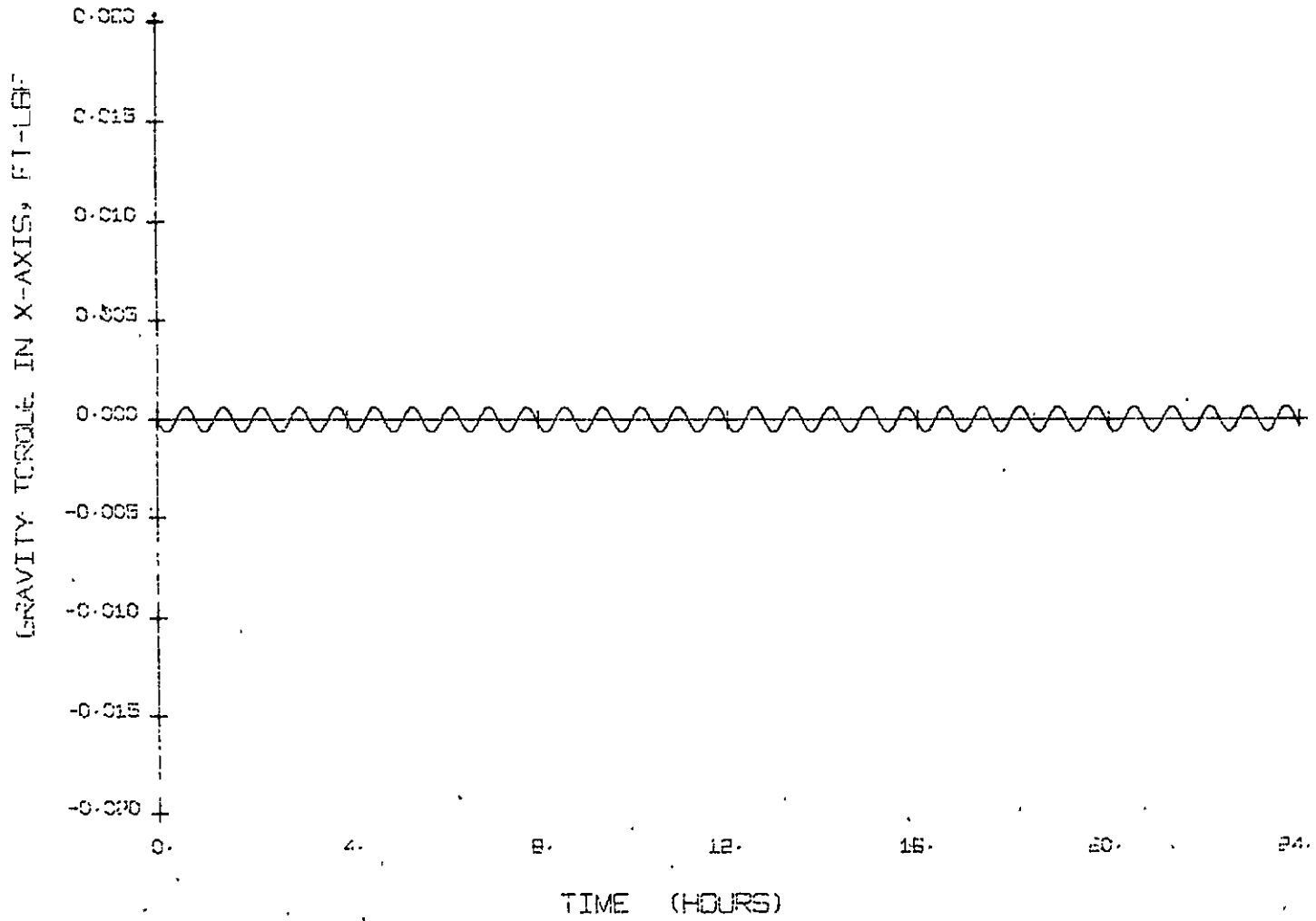


FIGURE A-28. GRAVITY GRADIENT TORQUE PROFILE IN THE x AXIS FOR CASE II

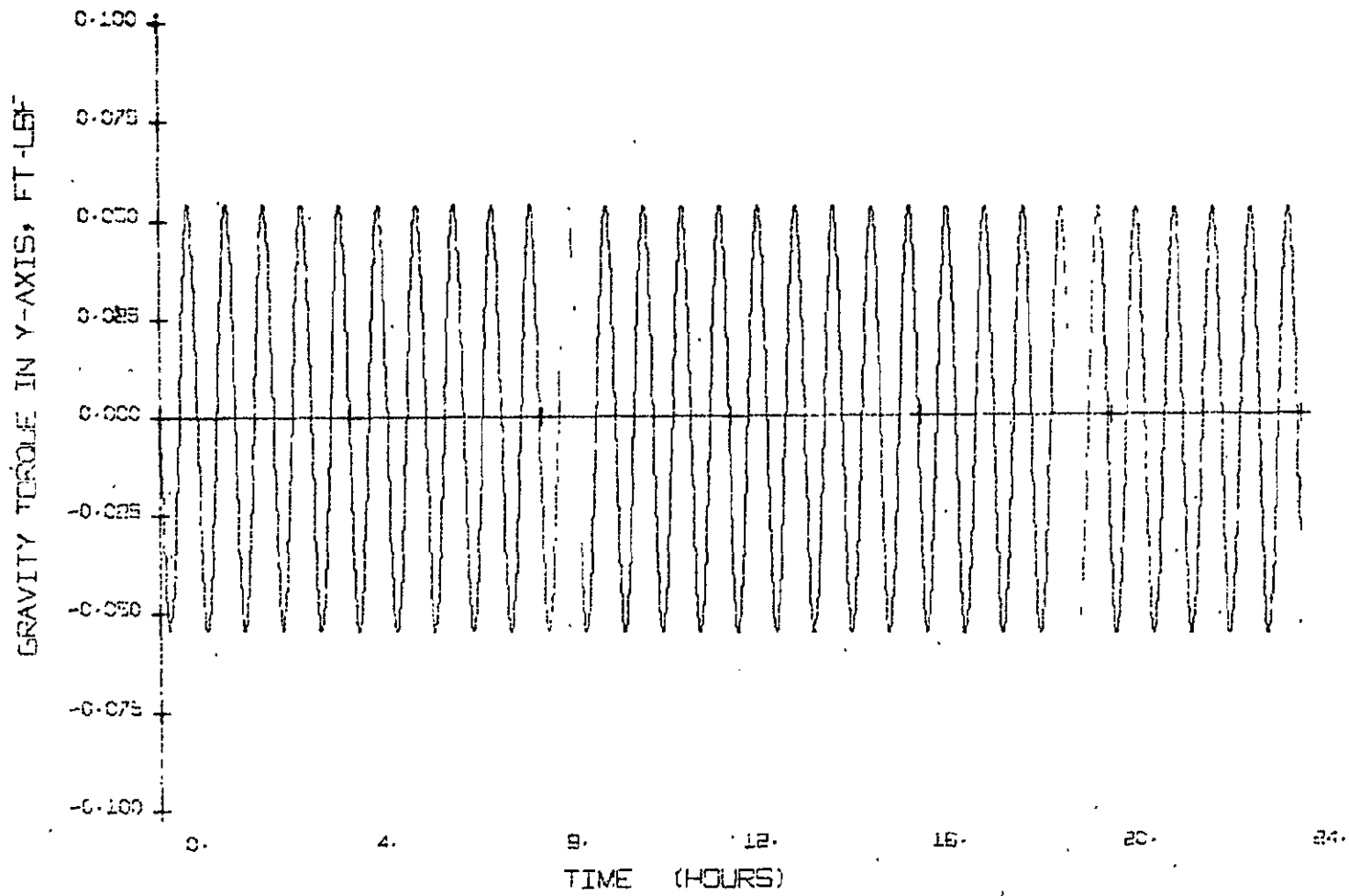


FIGURE A-29. GRAVITY GRADIENT TORQUE PROFILE IN THE y AXIS FOR CASE II

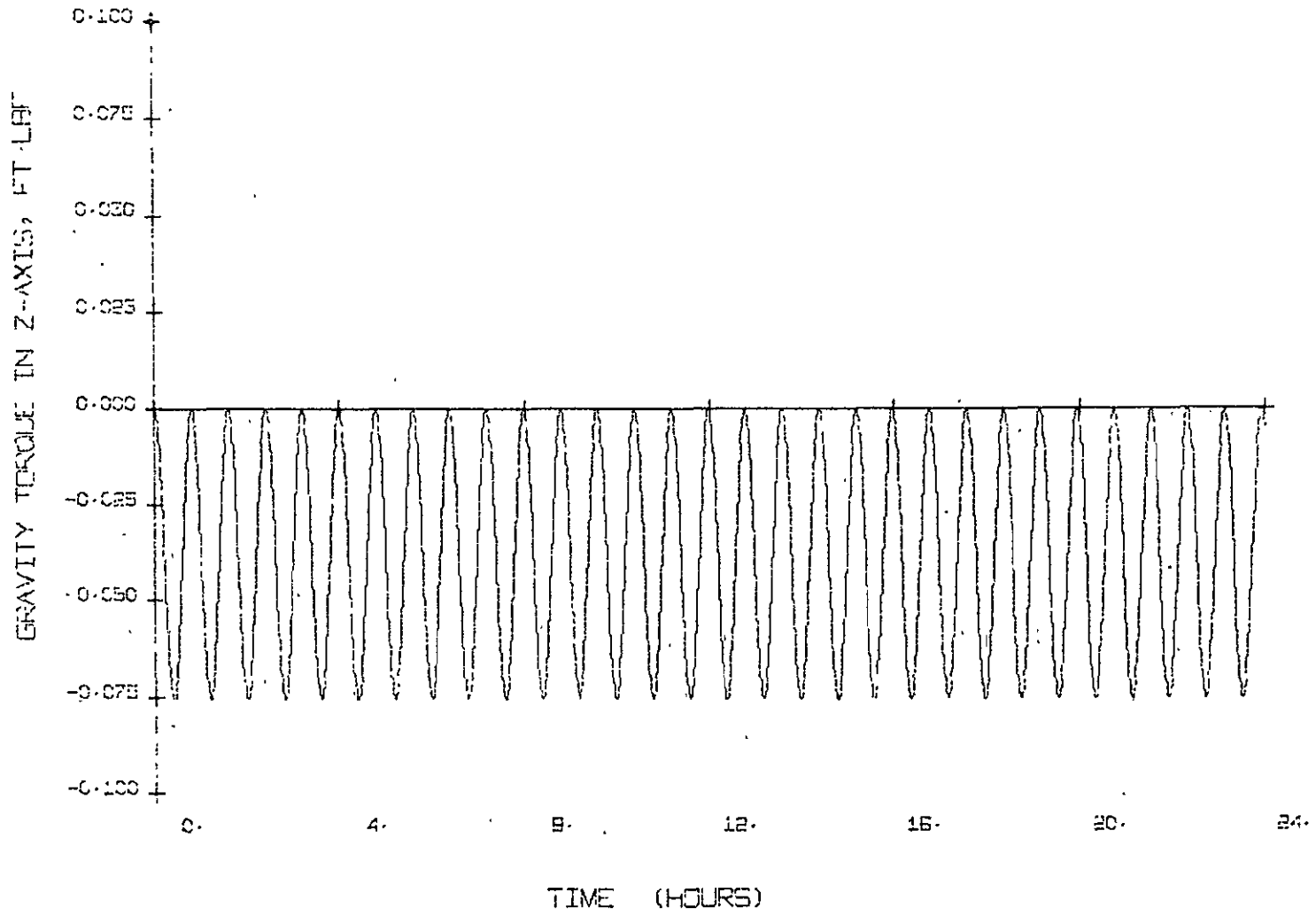


FIGURE A-30. GRAVITY GRADIENT TORQUE PROFILE IN THE z AXIS FOR CASE II

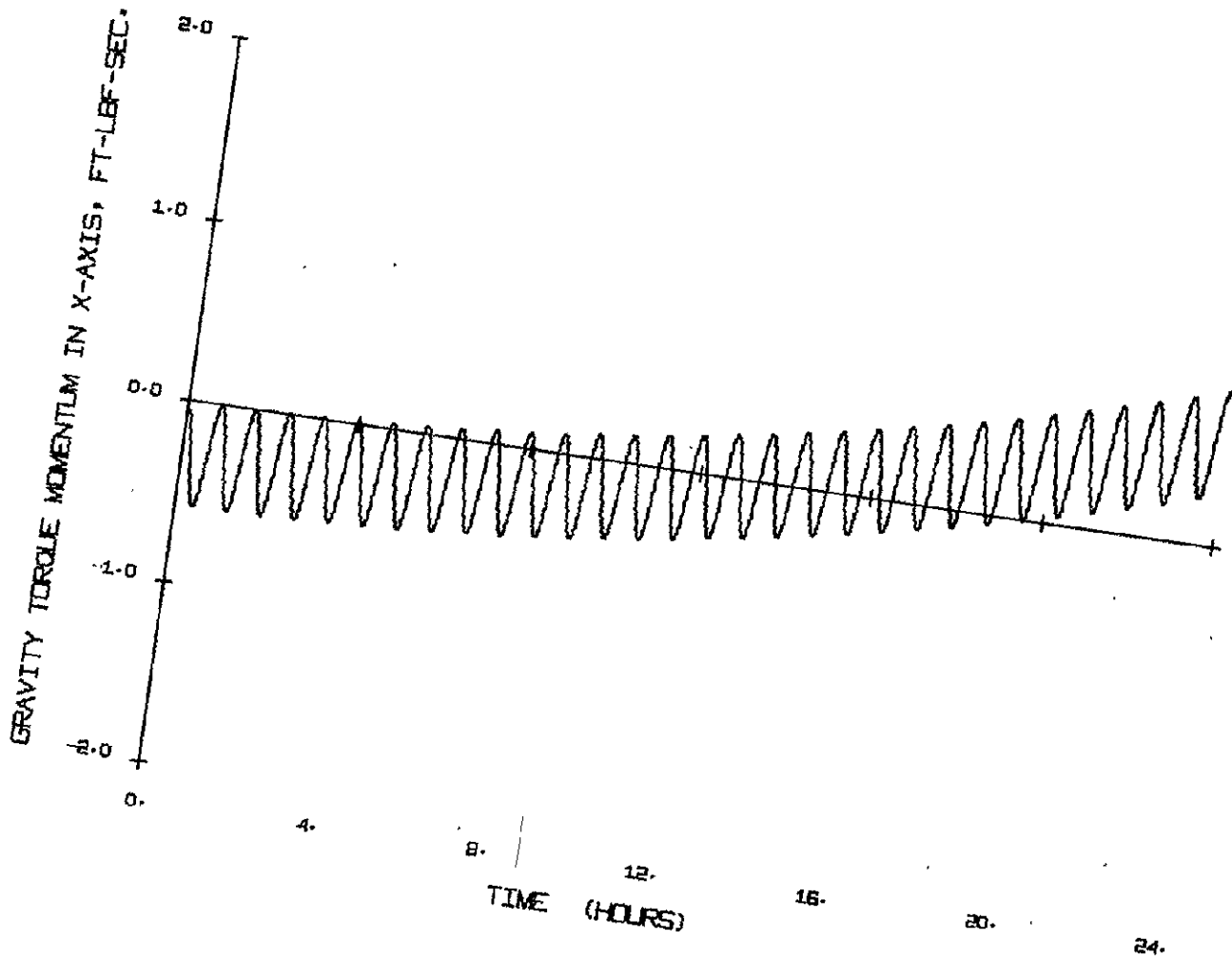


FIGURE A-31. GRAVITY TORQUE MOMENTUM IN THE x AXIS FOR CASE II

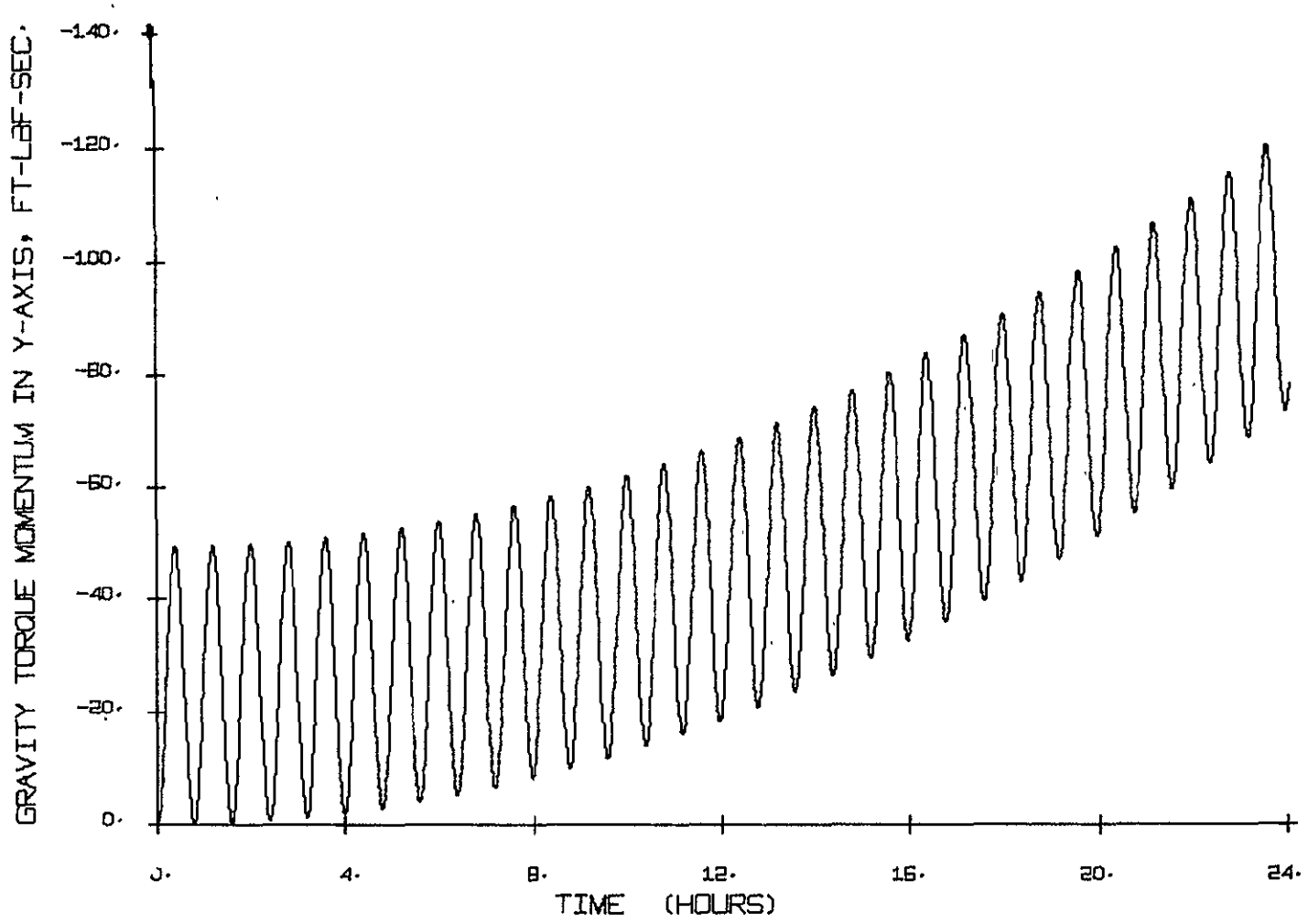


FIGURE A-32. GRAVITY TORQUE MOMENTUM IN THE y AXIS FOR CASE II

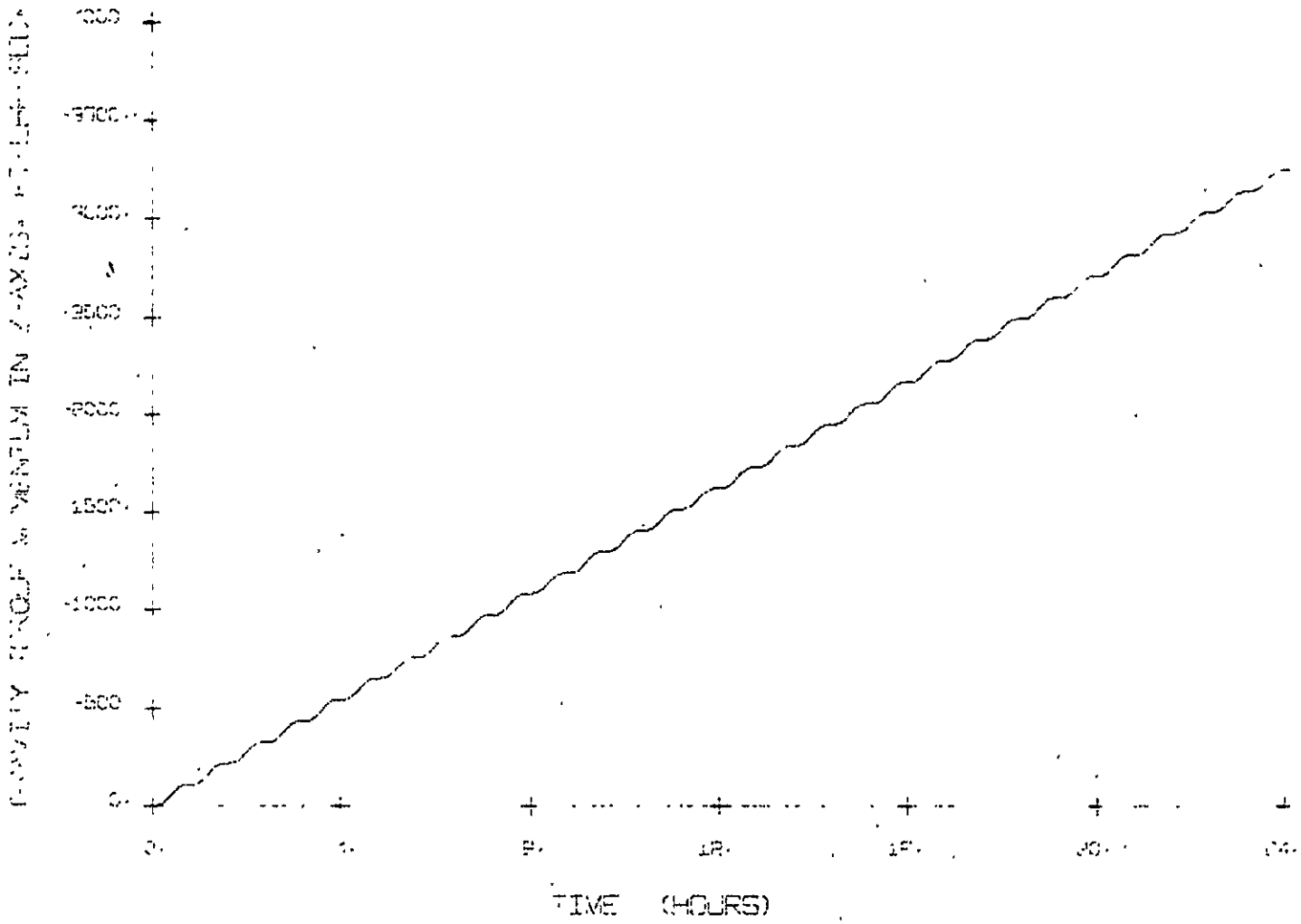


FIGURE A-33. GRAVITY TORQUE MOMENTUM IN THE z AXIS FOR CASE II

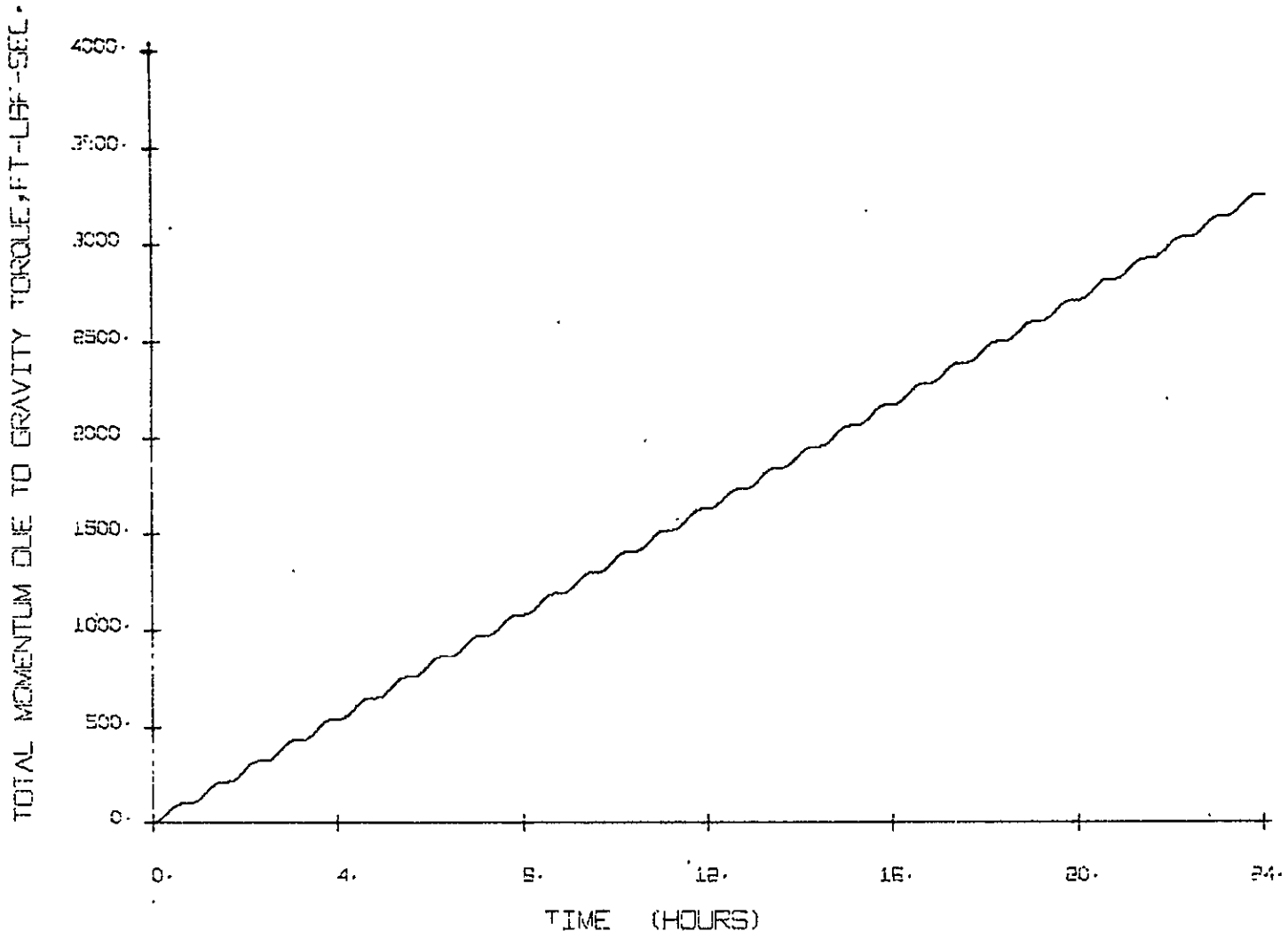


FIGURE A-34. TOTAL MOMENTUM DUE TO GRAVITY TORQUE FOR CASE II

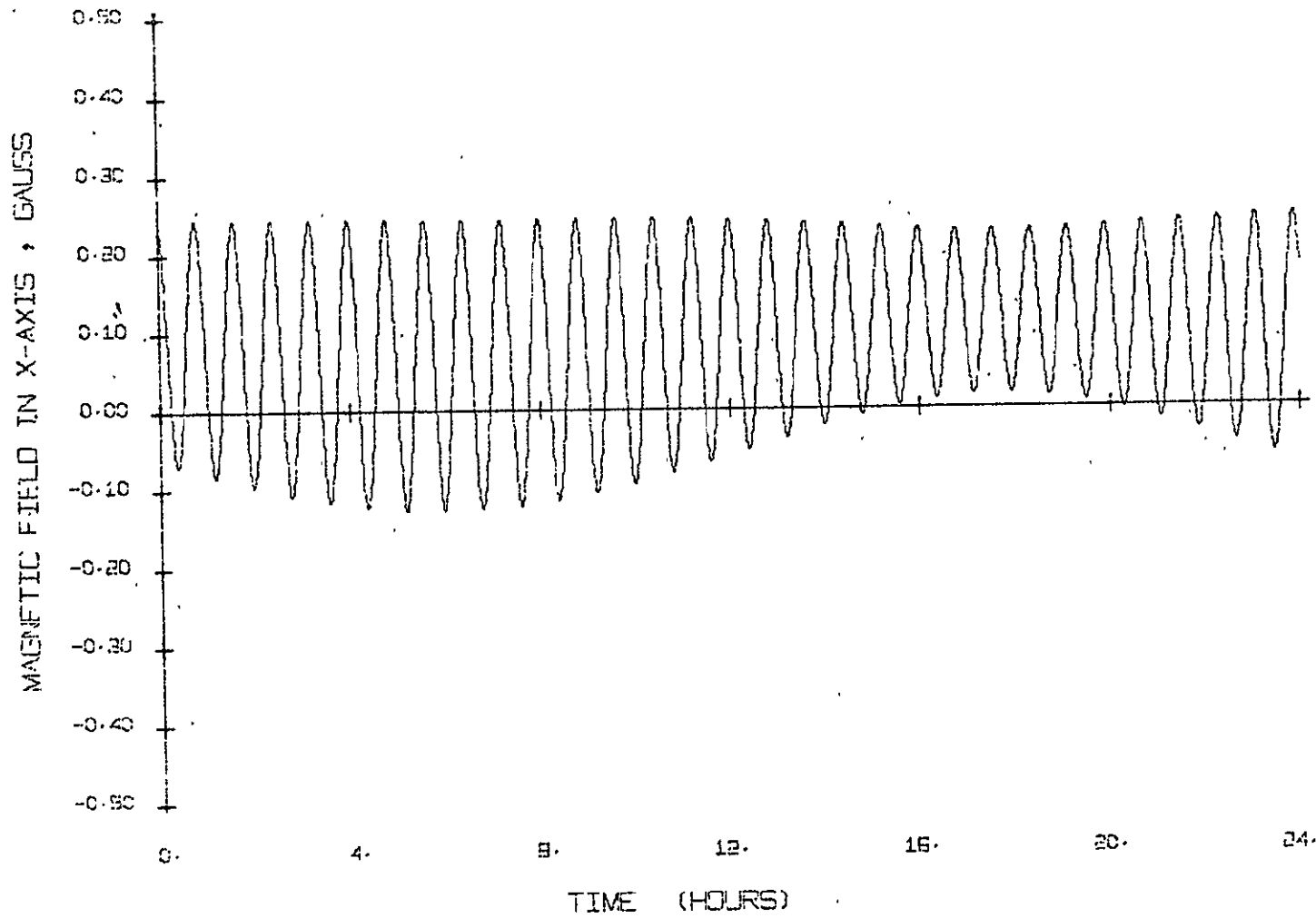


FIGURE A-35. COMPONENT OF THE EARTH'S MAGNETIC FIELD IN THE x AXIS FOR CASE II

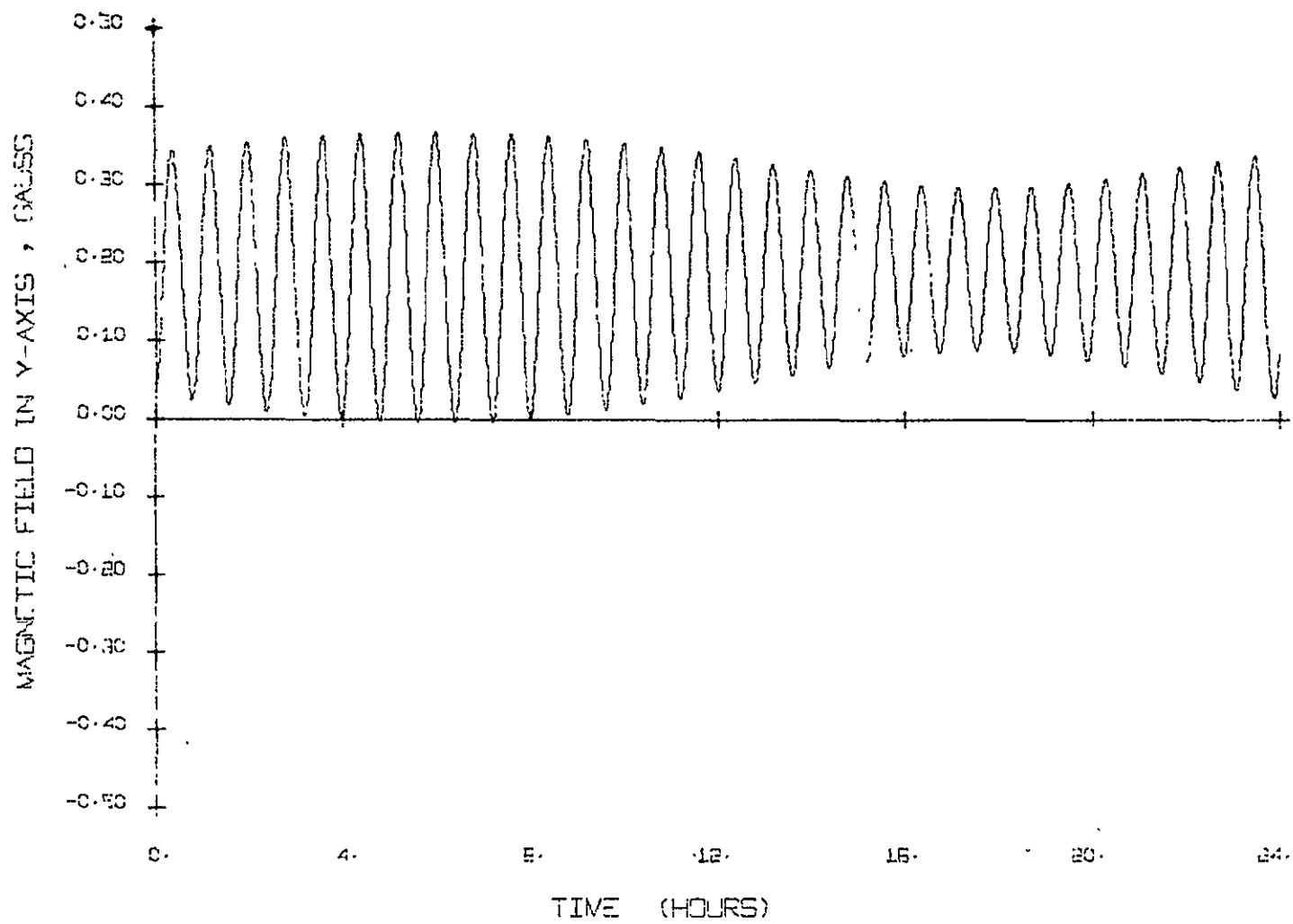


FIGURE A-36. COMPONENT OF THE EARTH'S MAGNETIC FIELD IN THE y AXIS FOR CASE II

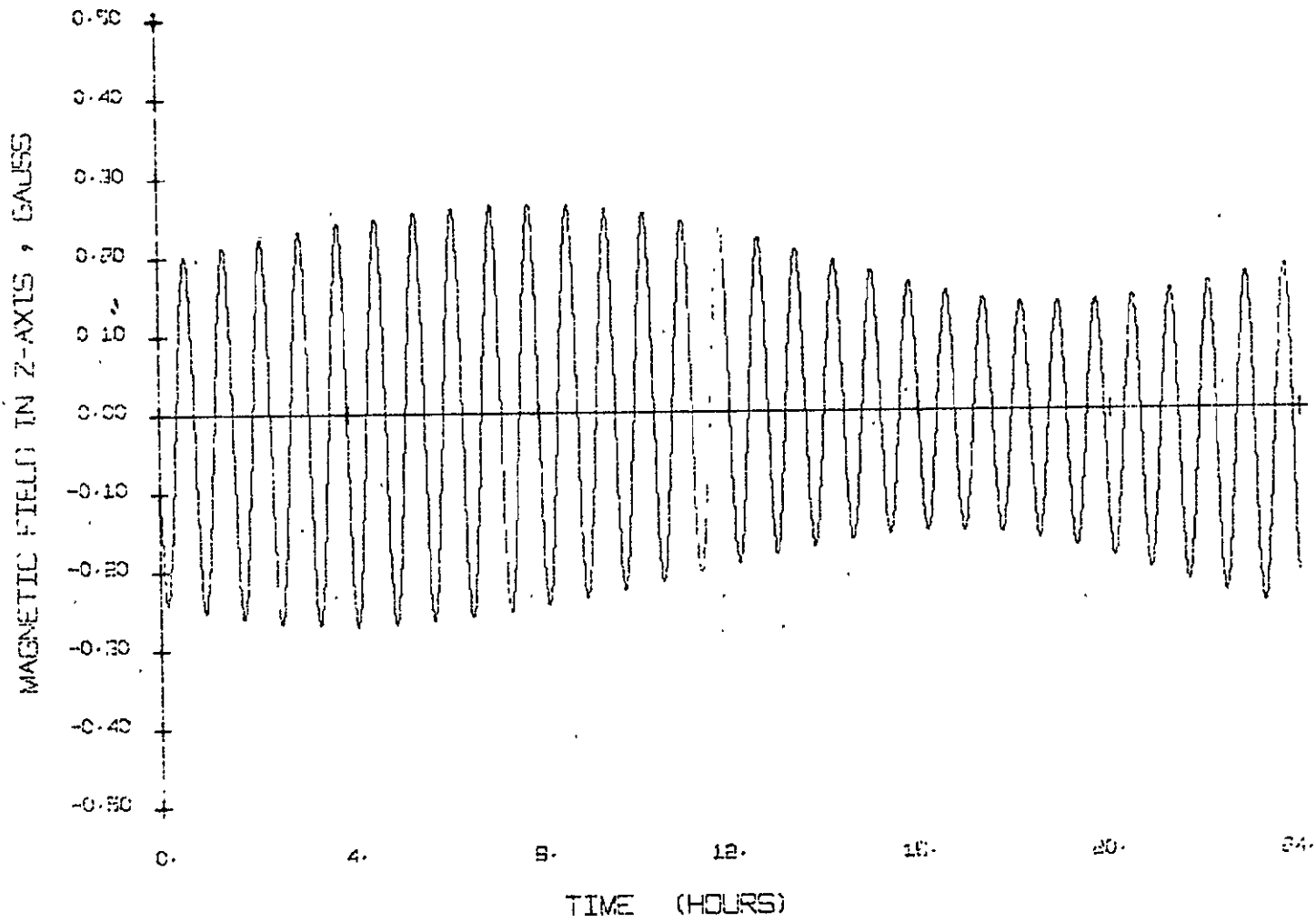


FIGURE A-37. COMPONENT OF THE EARTH'S MAGNETIC FIELD IN THE z AXIS FOR CASE II

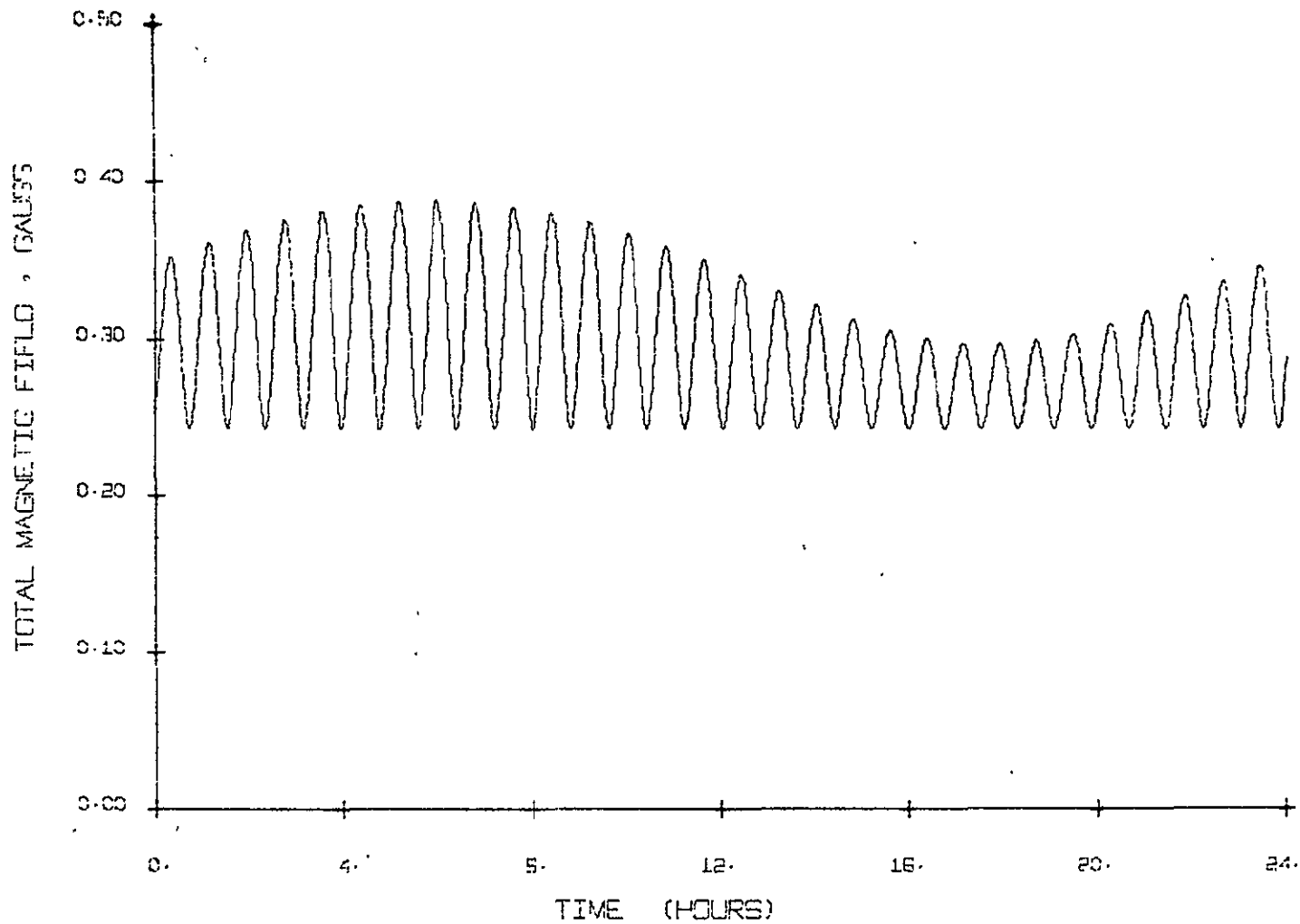


FIGURE A-38. EARTH'S MAGNETIC FIELD PROFILE FOR CASE II

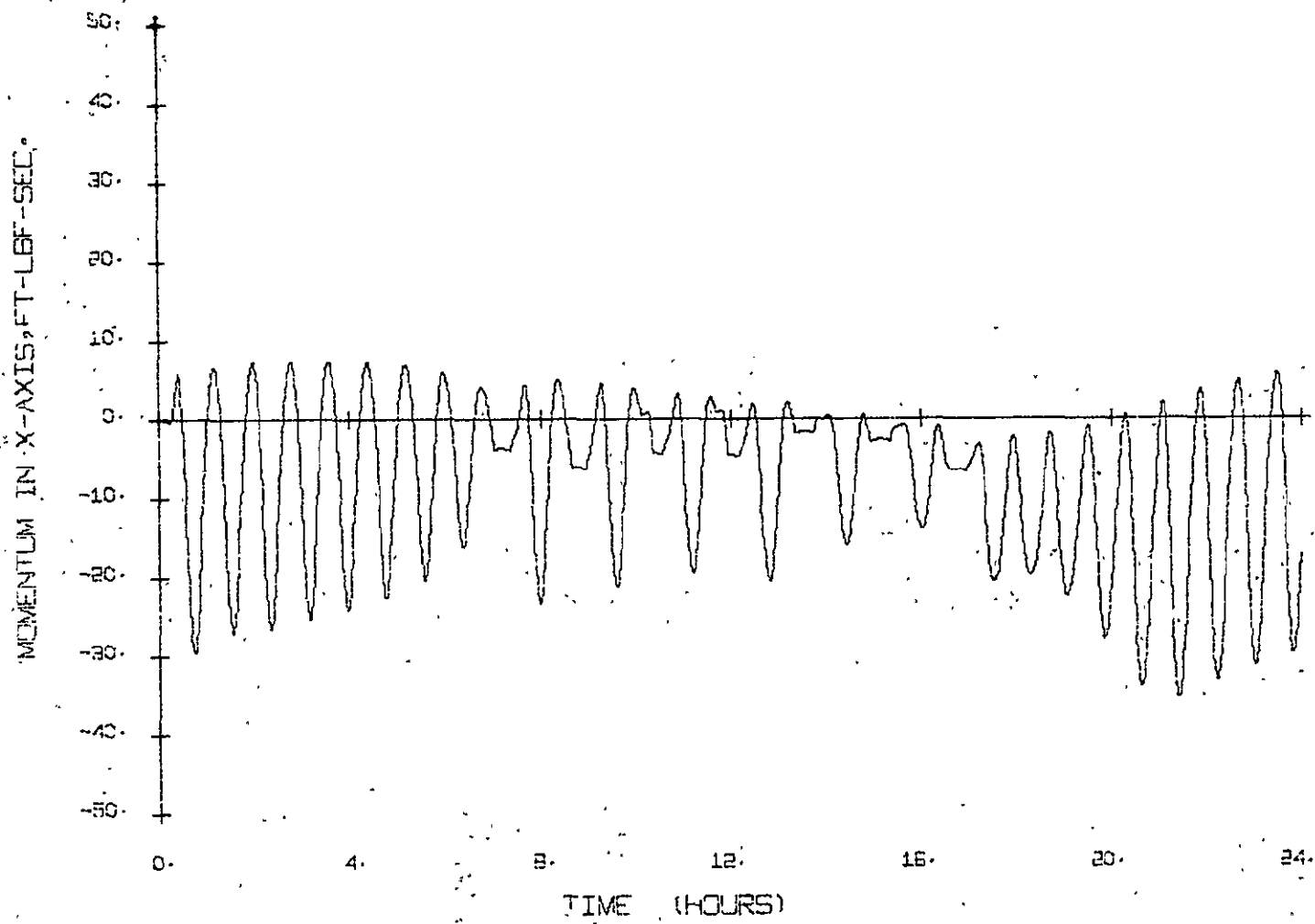


FIGURE A-39. COMPONENT OF STORED MOMENTUM IN THE x AXIS FOR CASE II.

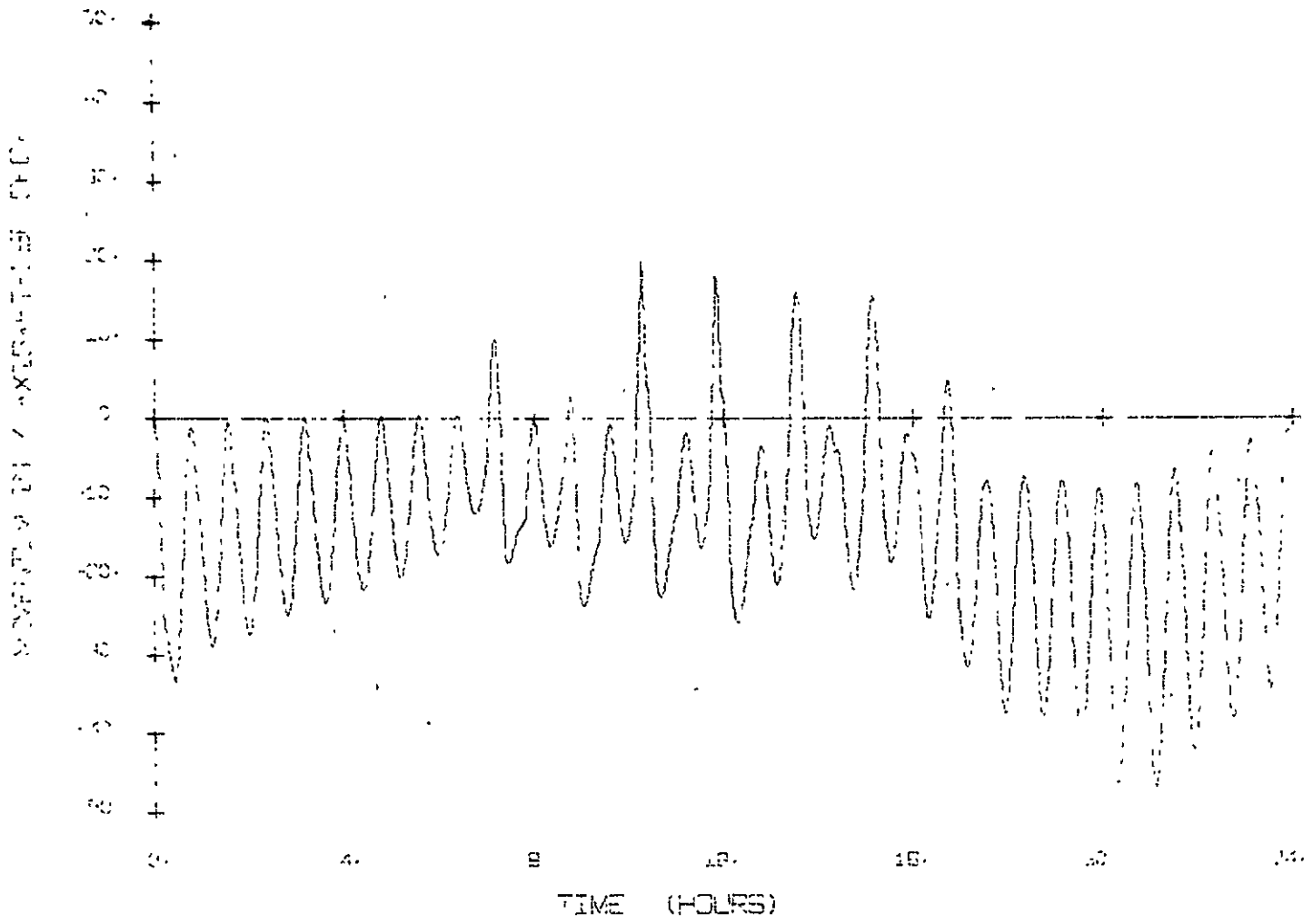


FIGURE A-40. COMPONENT OF STORED MOMENTUM IN THE y AXIS FOR CASE II

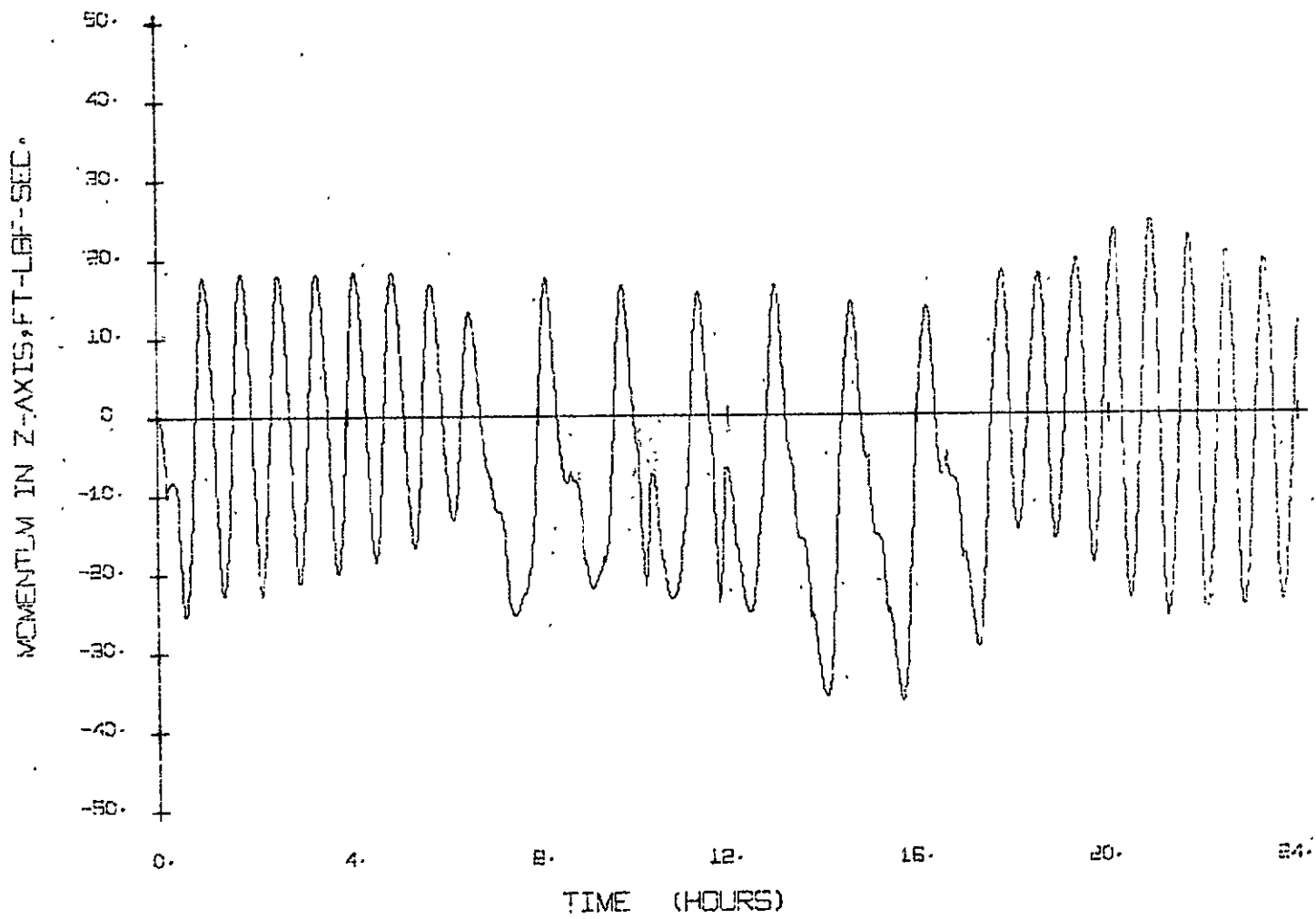


FIGURE A-41. COMPONENT OF STORED MOMENTUM IN THE z AXIS FOR CASE II

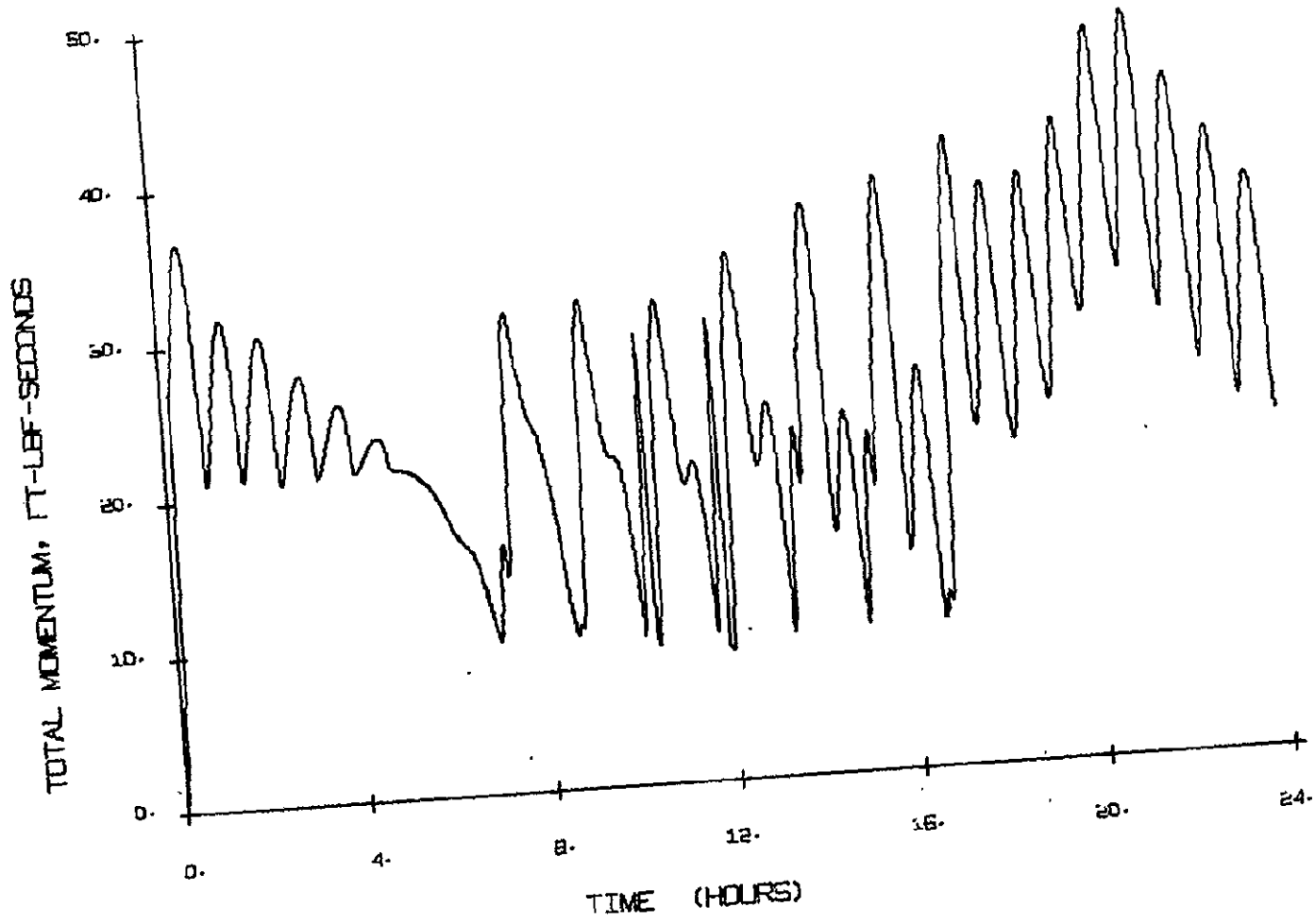


FIGURE A-42. TOTAL MOMENTUM STORED IN THE MOMENTUM STORAGE DEVICE FOR CASE II

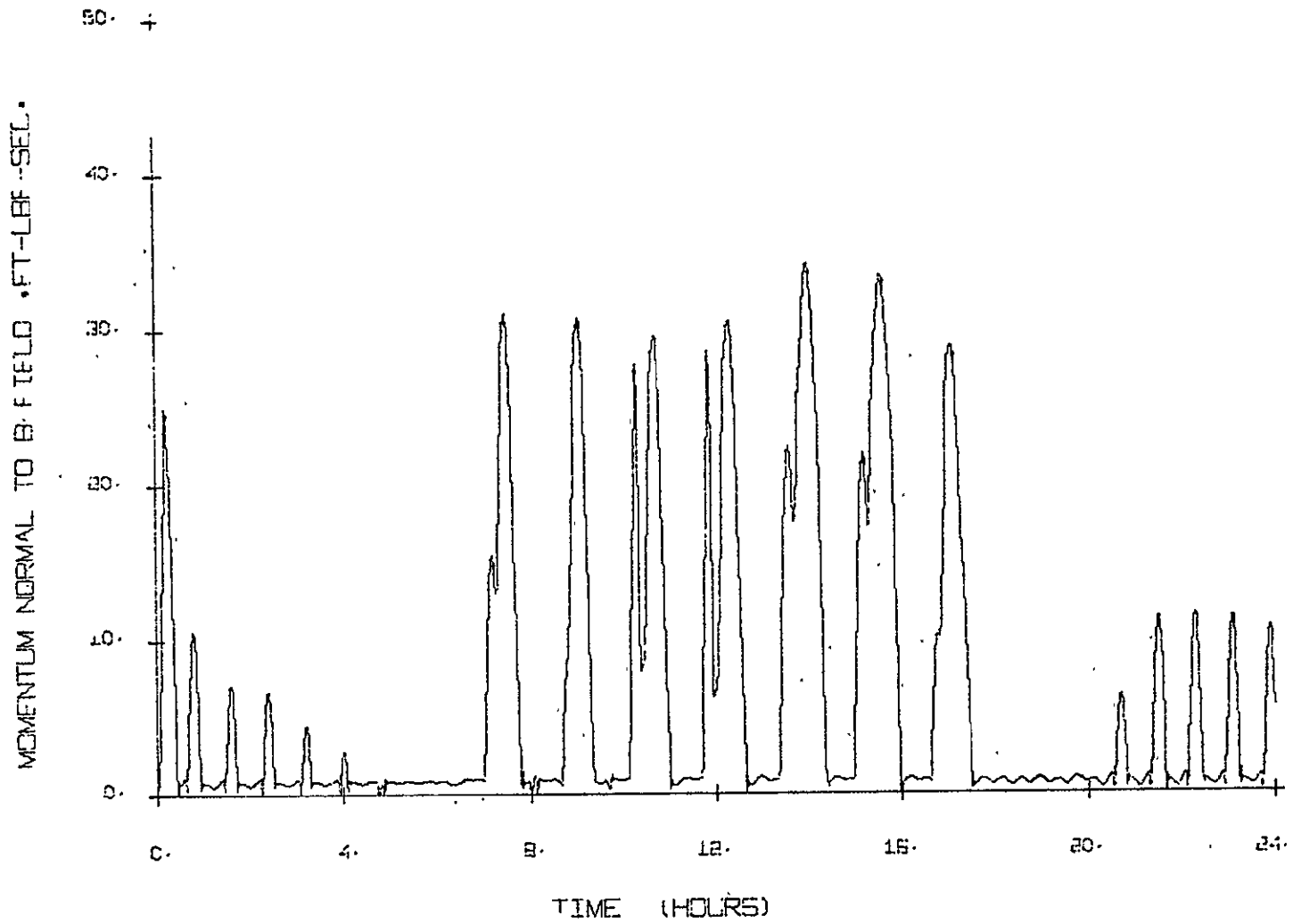


FIGURE A-43. COMPONENT OF STORED MOMENTUM NORMAL TO THE B FIELD FOR CASE II

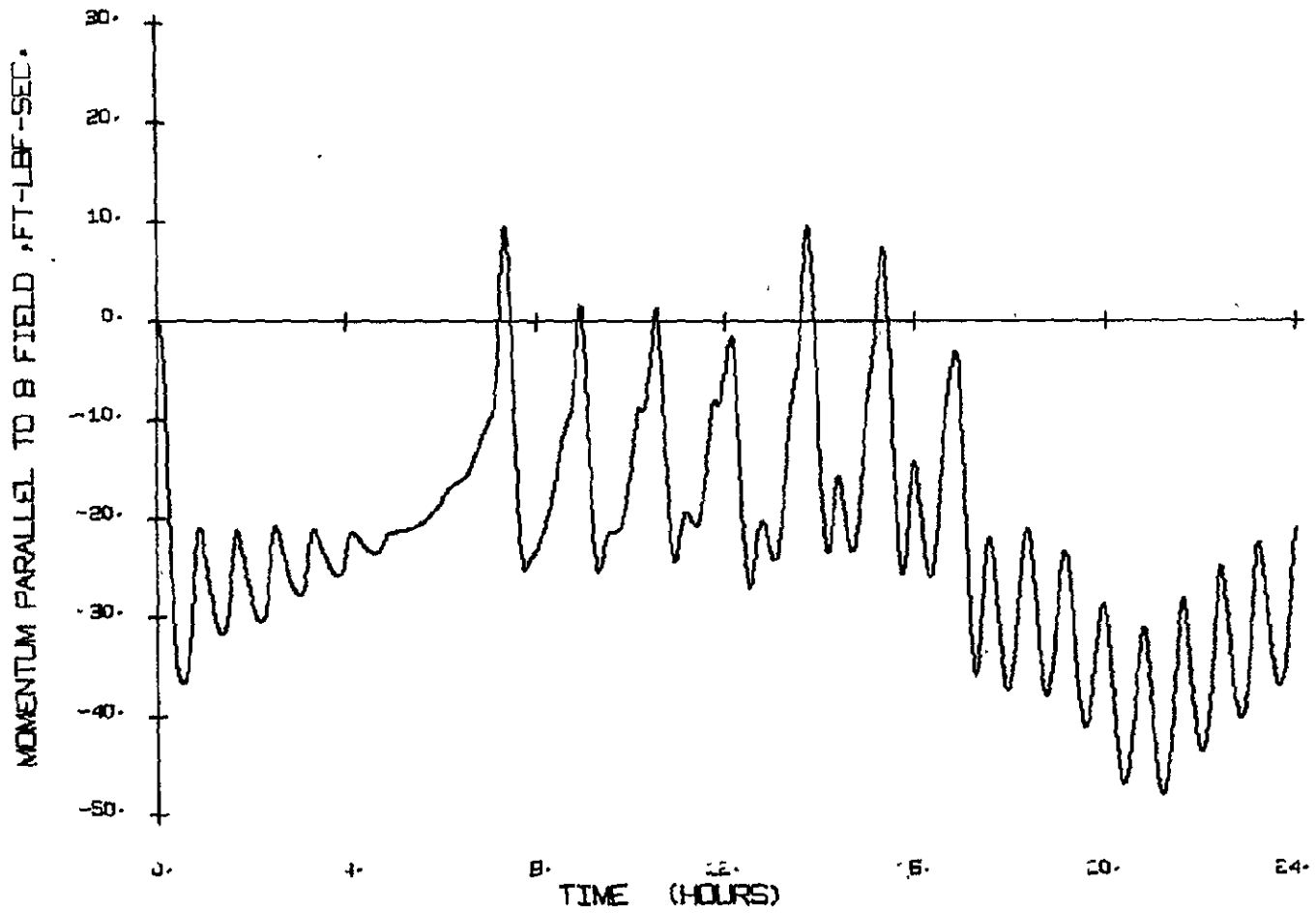


FIGURE A-44. COMPONENT OF STORED MOMENTUM PARALLEL TO THE B FIELD FOR CASE II

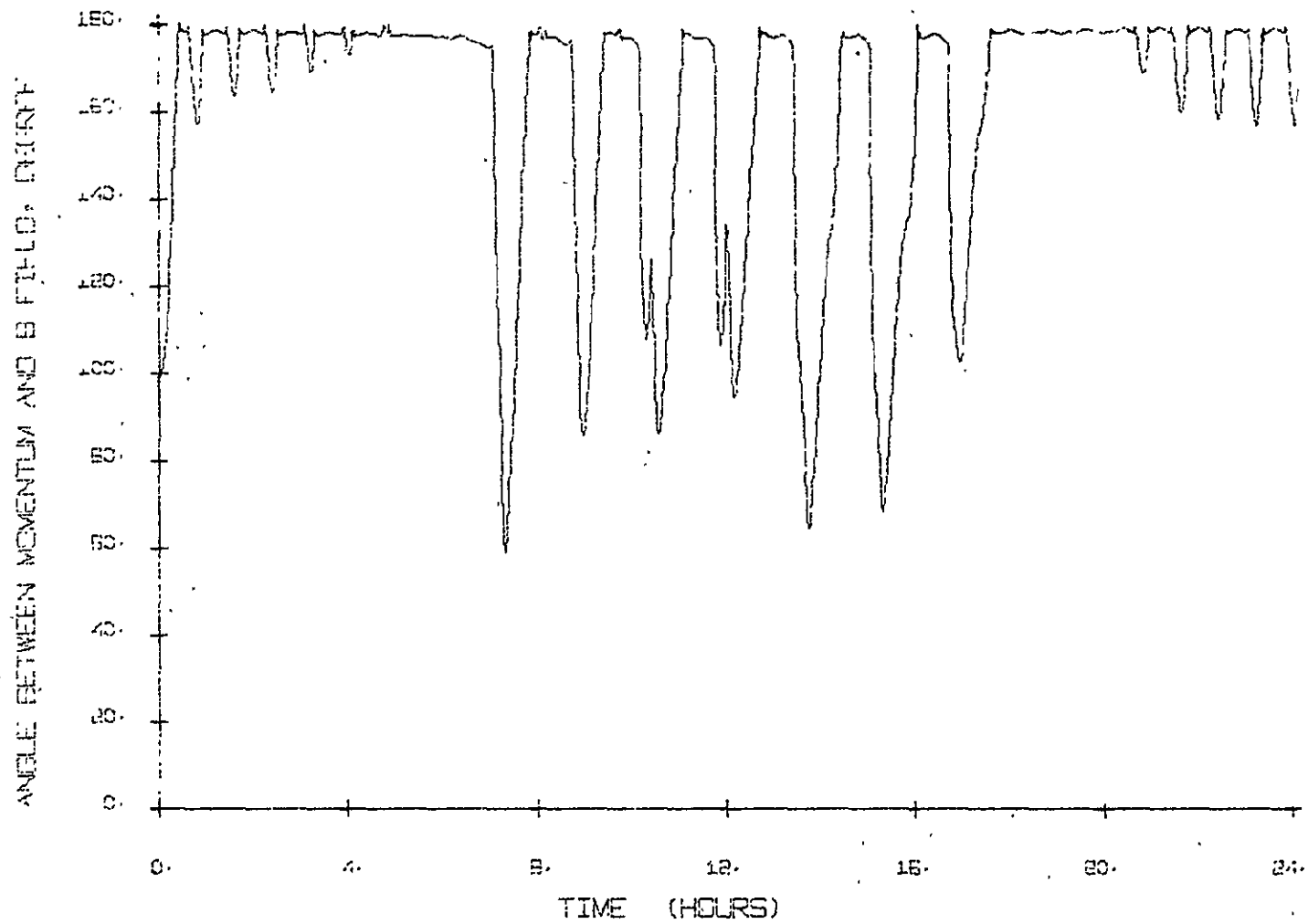


FIGURE A-45. ANGLE BETWEEN THE STORED MOMENTUM VECTOR AND THE B-FIELD VECTOR FOR CASE II

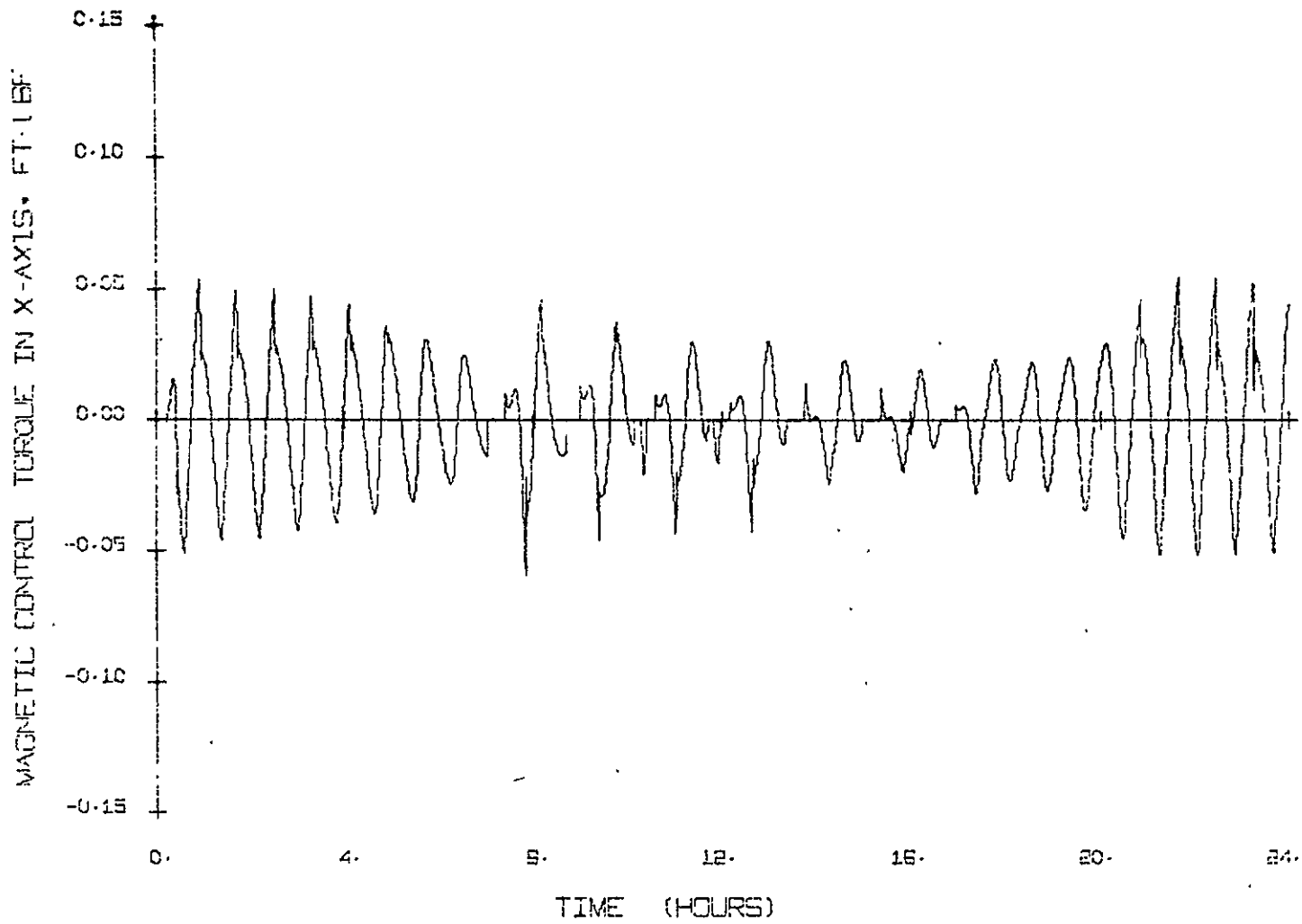


FIGURE A-46. MAGNETIC CONTROL TORQUE IN THE x AXIS FOR CASE II

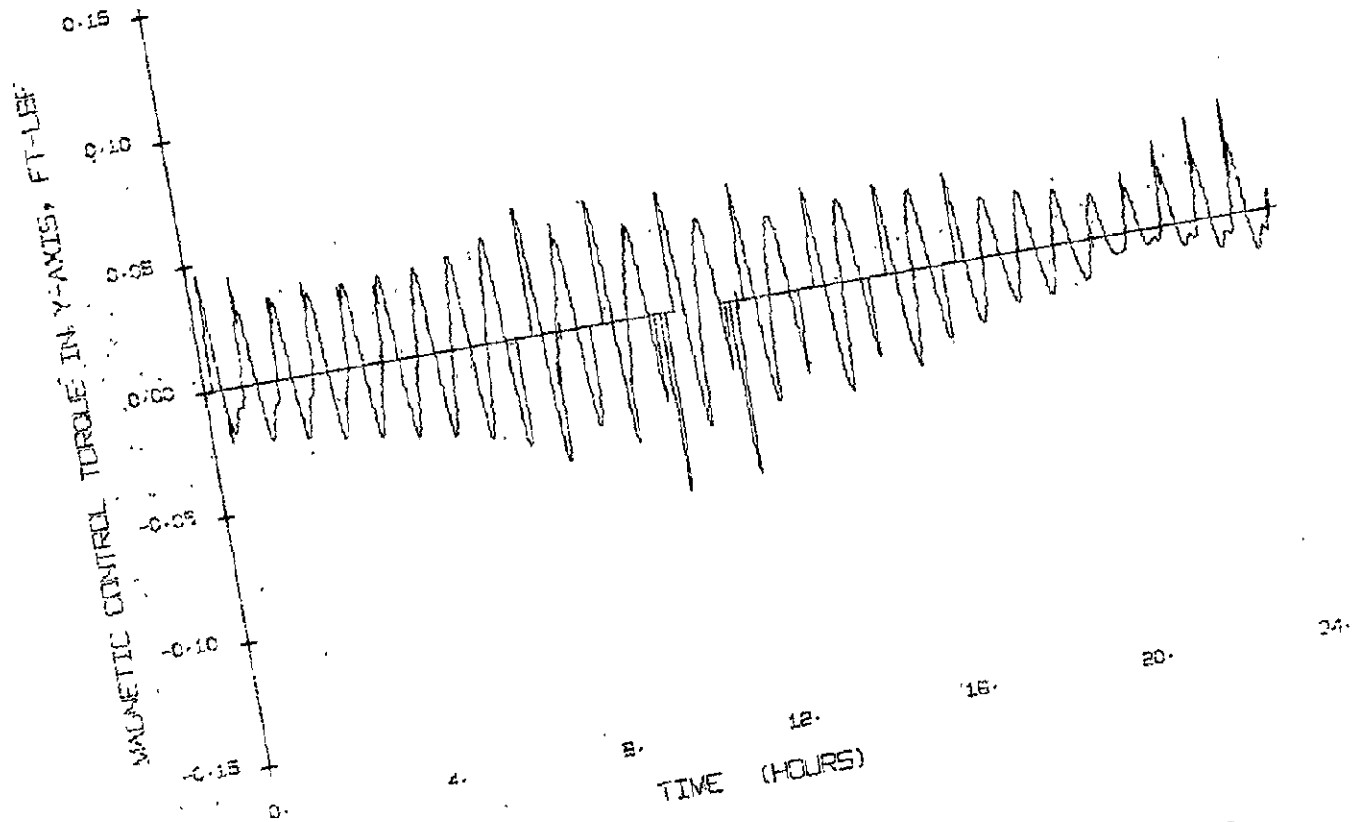


FIGURE A-47. MAGNETIC CONTROL TORQUE IN THE Y AXIS FOR CASE II

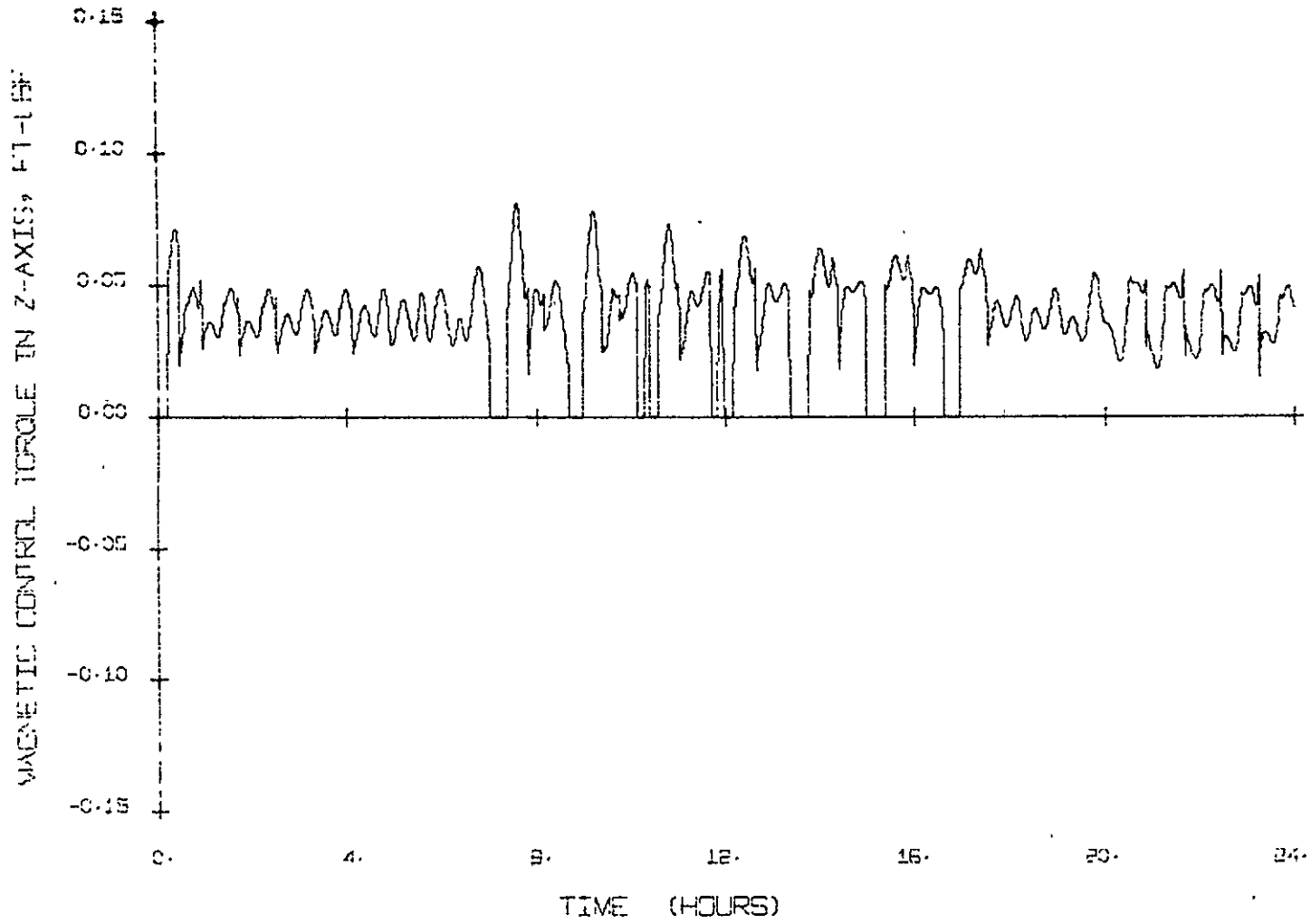


FIGURE A-48. MAGNETIC CONTROL TORQUE IN THE z AXIS FOR CASE II

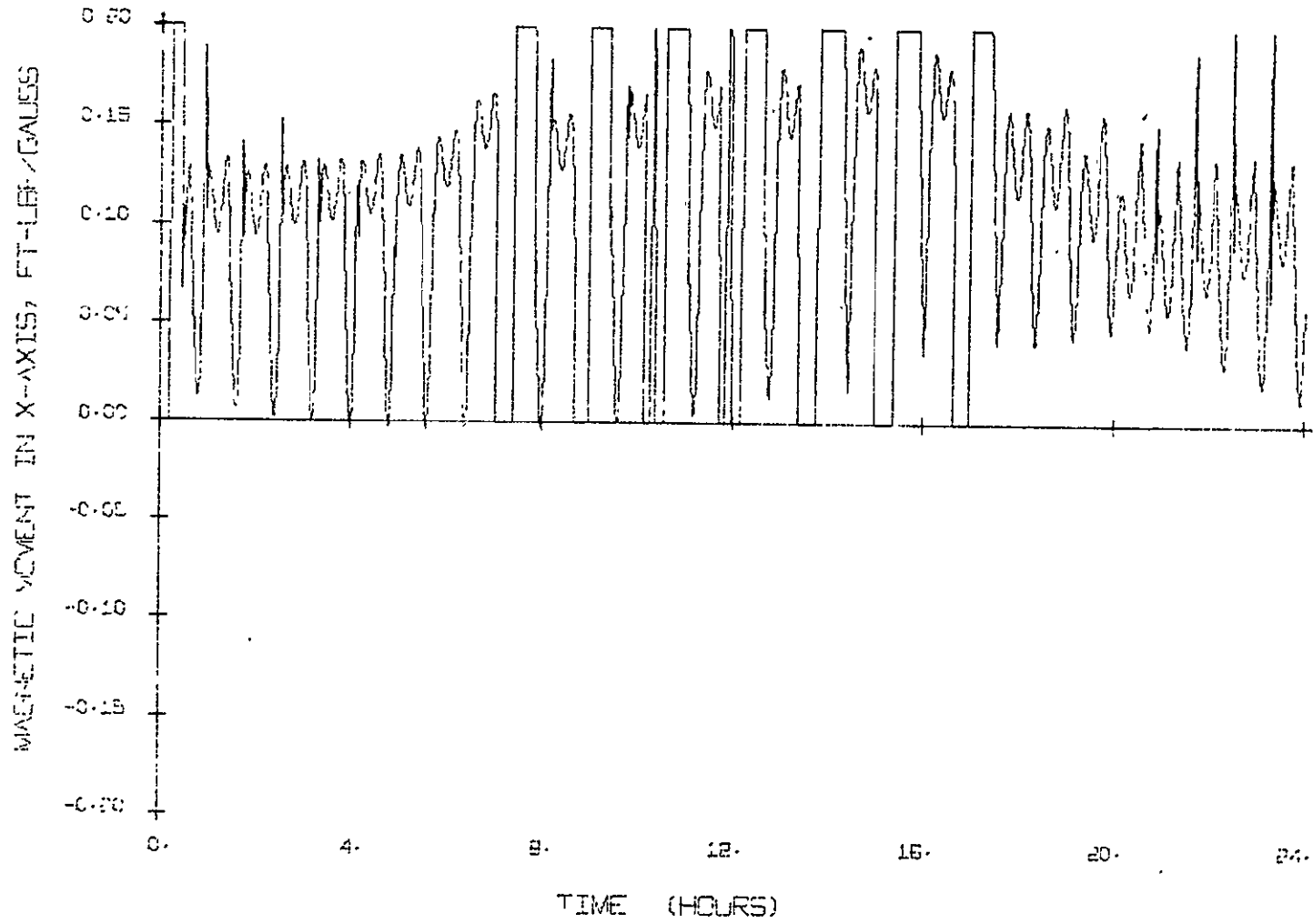


FIGURE 49. MAGNETIC MOMENT PRODUCED BY THE x-AXIS ELECTROMAGNET FOR CASE II

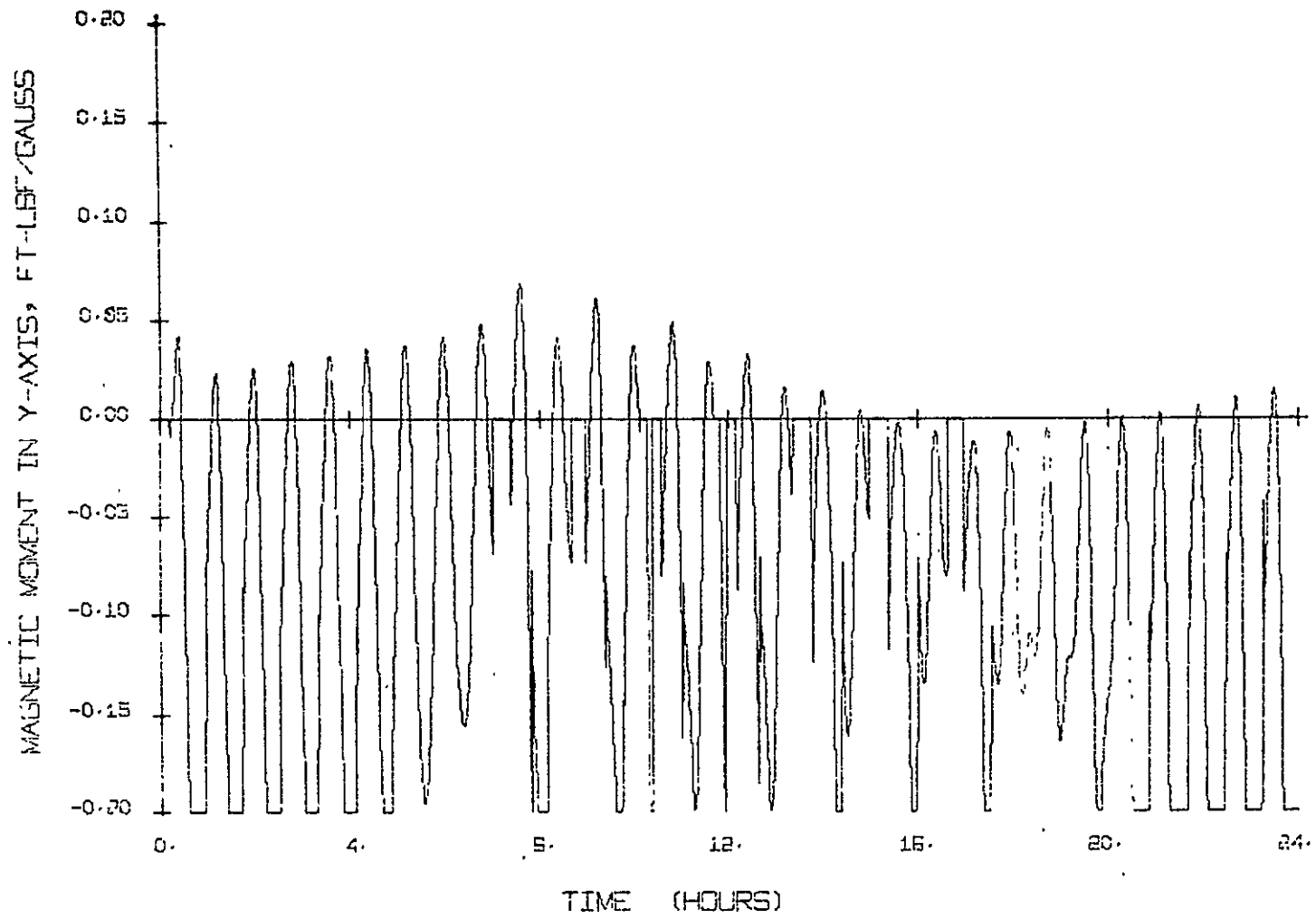


FIGURE A-50. MAGNETIC MOMENT PRODUCED BY THE y-AXIS ELECTROMAGNET FOR CASE II

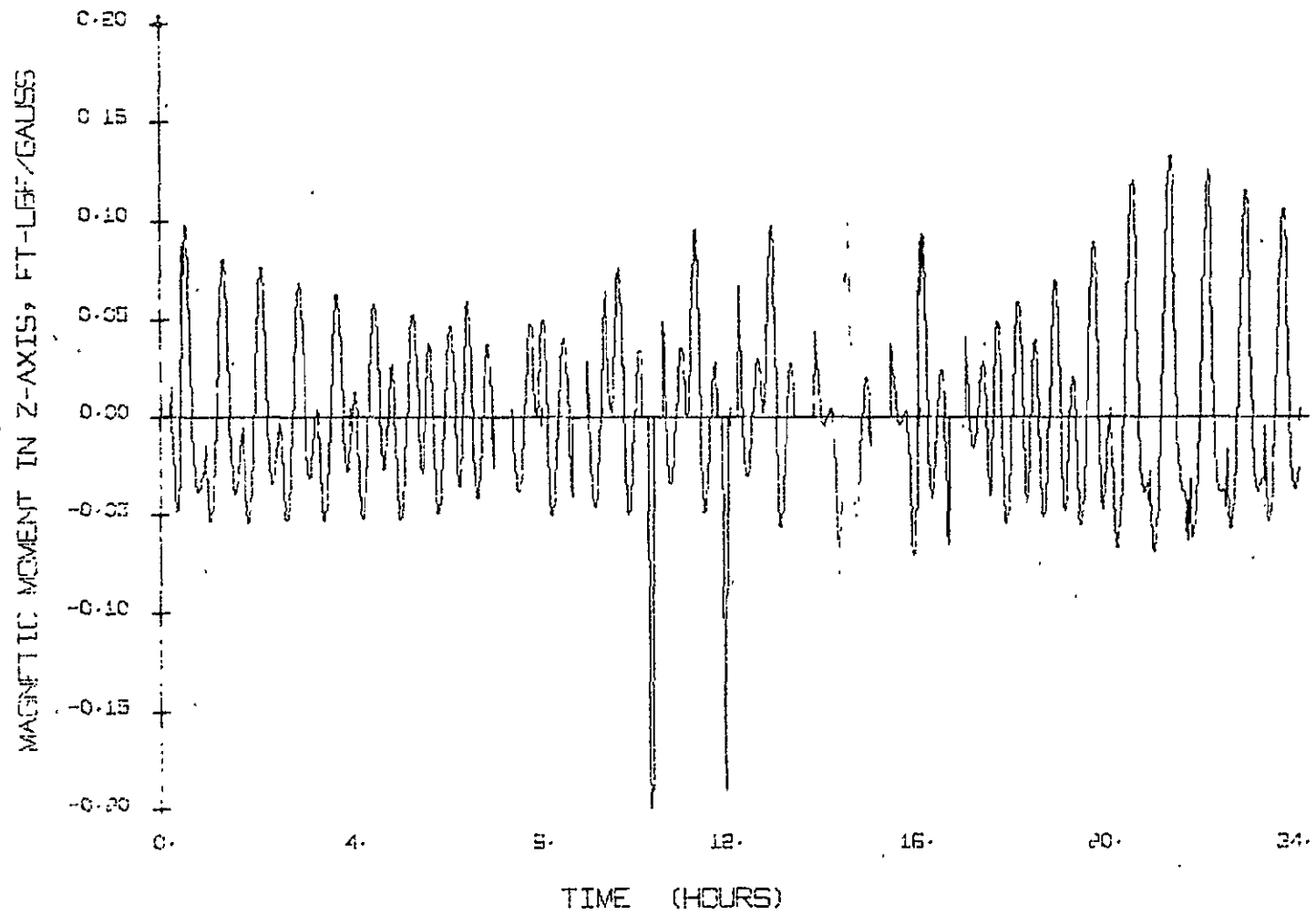


FIGURE A-51. MAGNETIC MOMENT PRODUCED BY THE z AXIS ELECTROMAGNET FOR CASE II

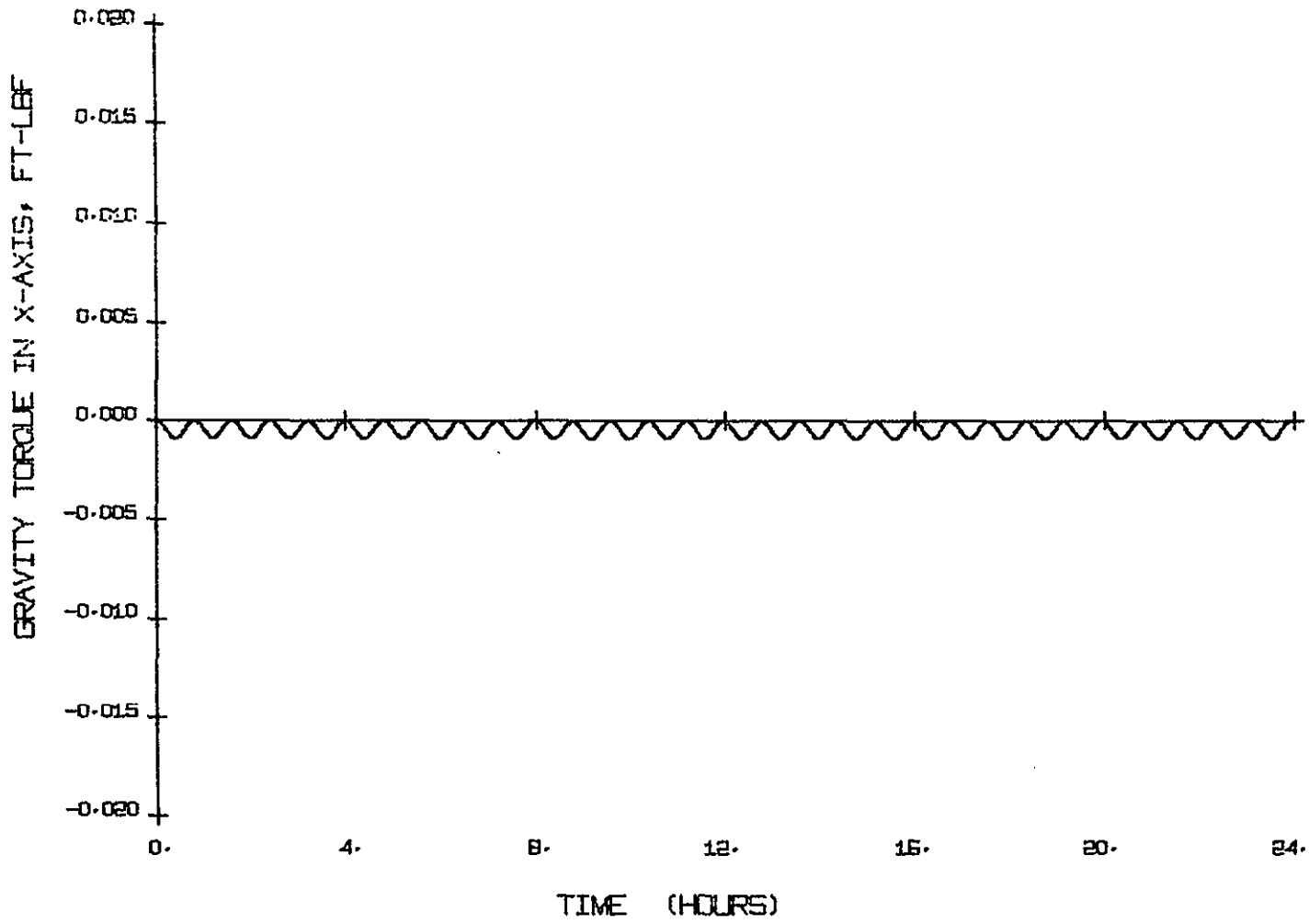


FIGURE A-52. GRAVITY GRADIENT TORQUE IN THE x AXIS FOR CASE III

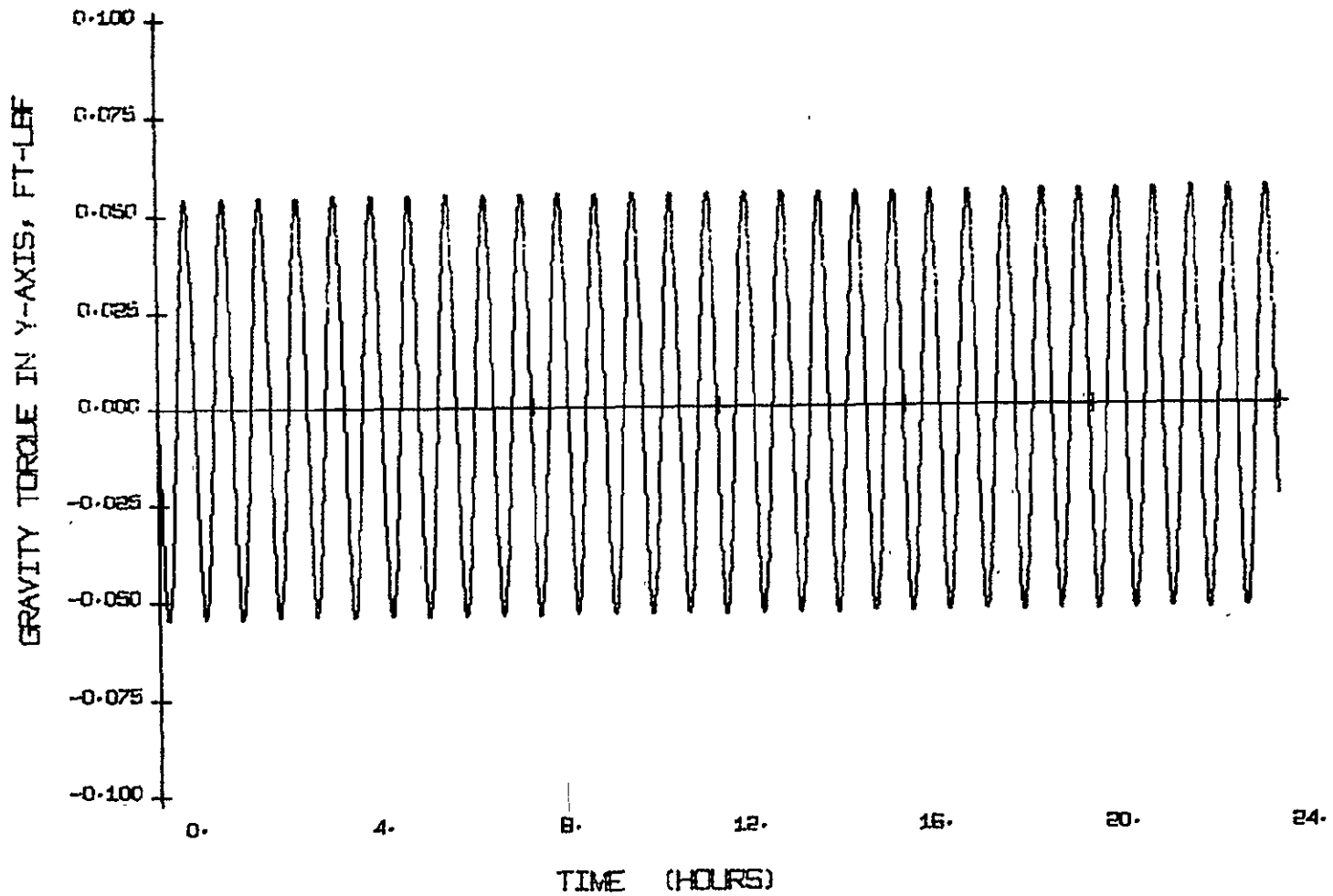


FIGURE A-53. GRAVITY GRADIENT TORQUE IN THE y AXIS FOR CASE III

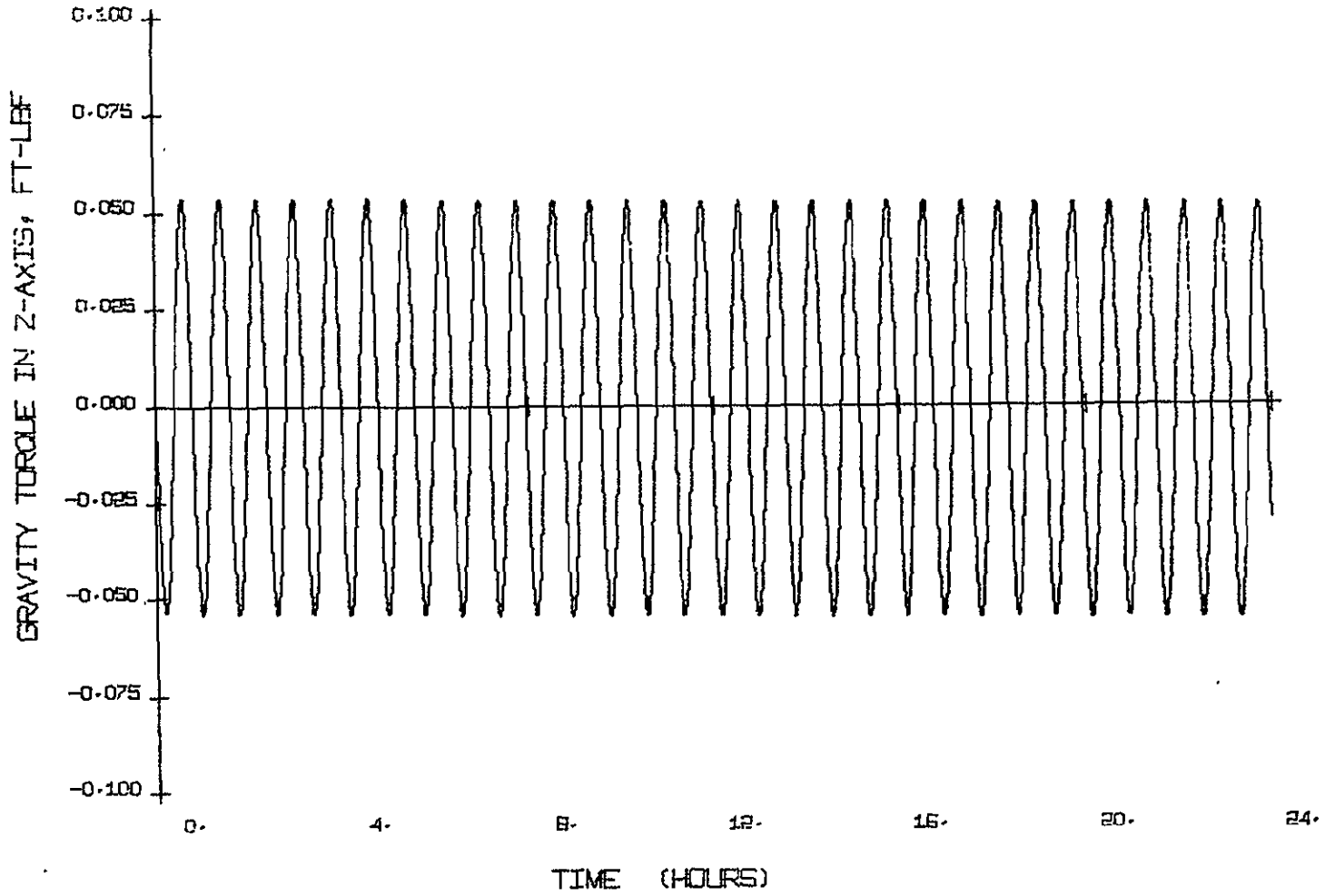


FIGURE A-54. GRAVITY GRADIENT TORQUE IN THE z AXIS FOR CASE III

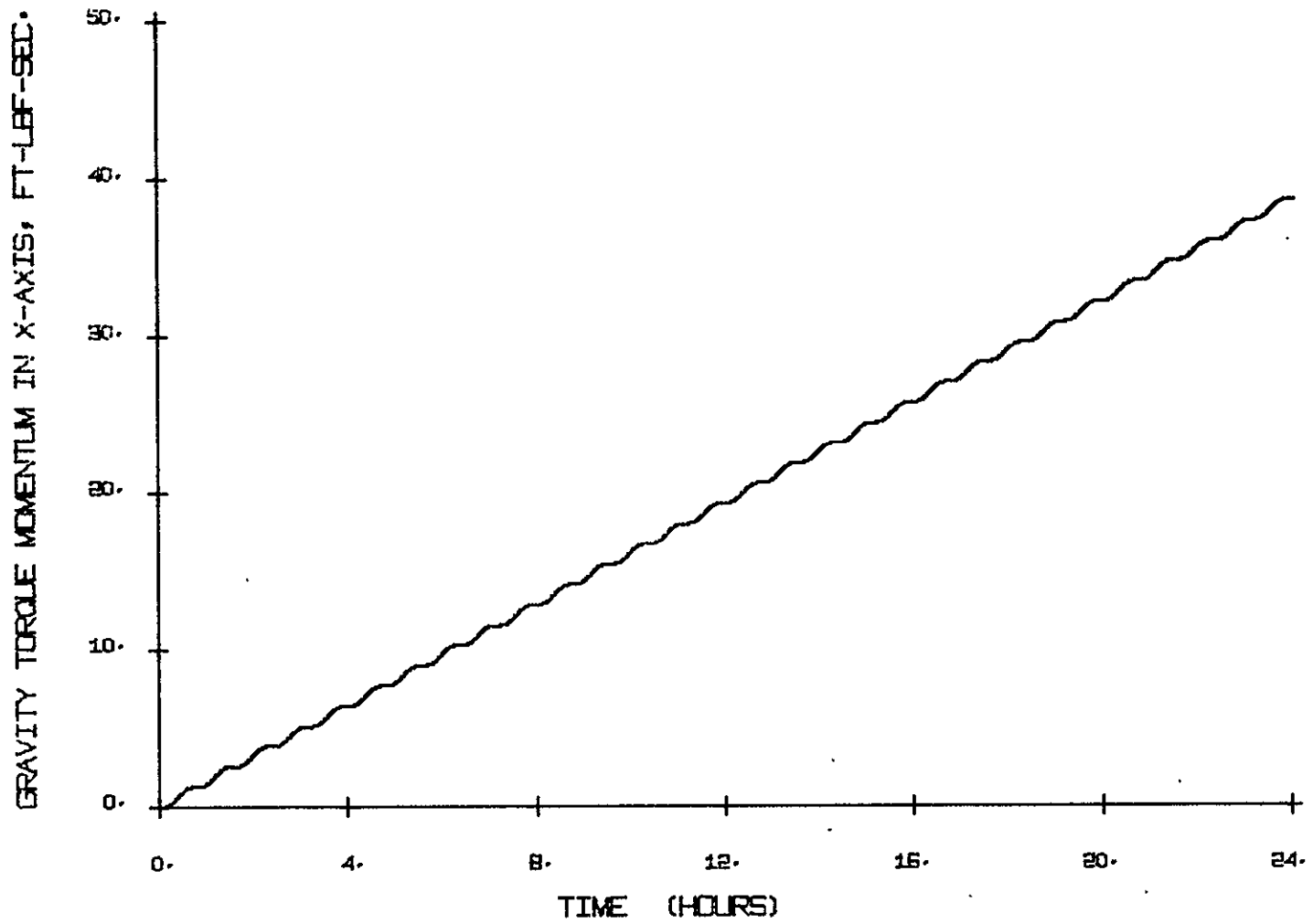


FIGURE A-55. GRAVITY TORQUE MOMENTUM IN THE x AXIS FOR CASE III

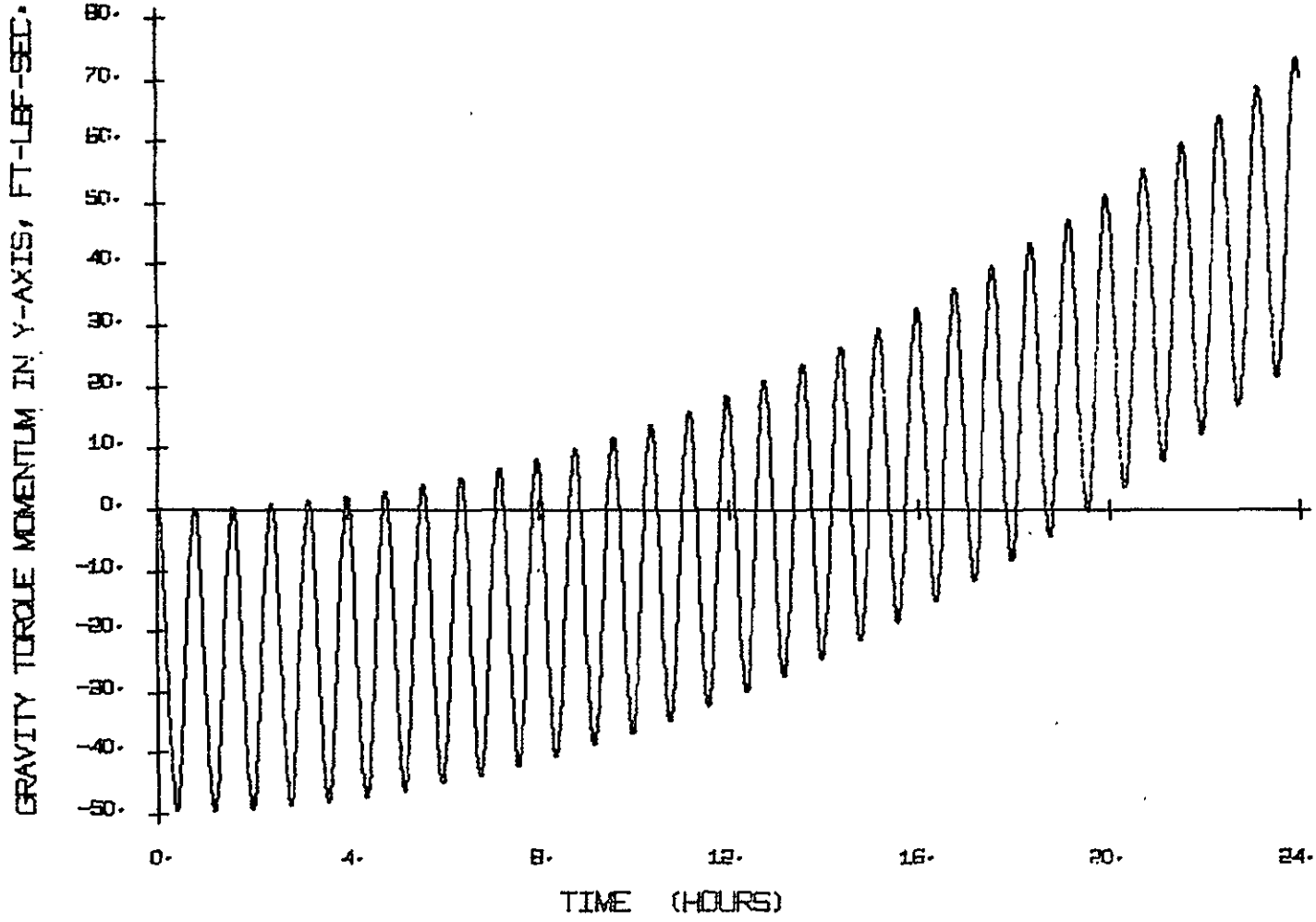


FIGURE A-56. GRAVITY TORQUE MOMENTUM IN THE y AXIS FOR CASE III

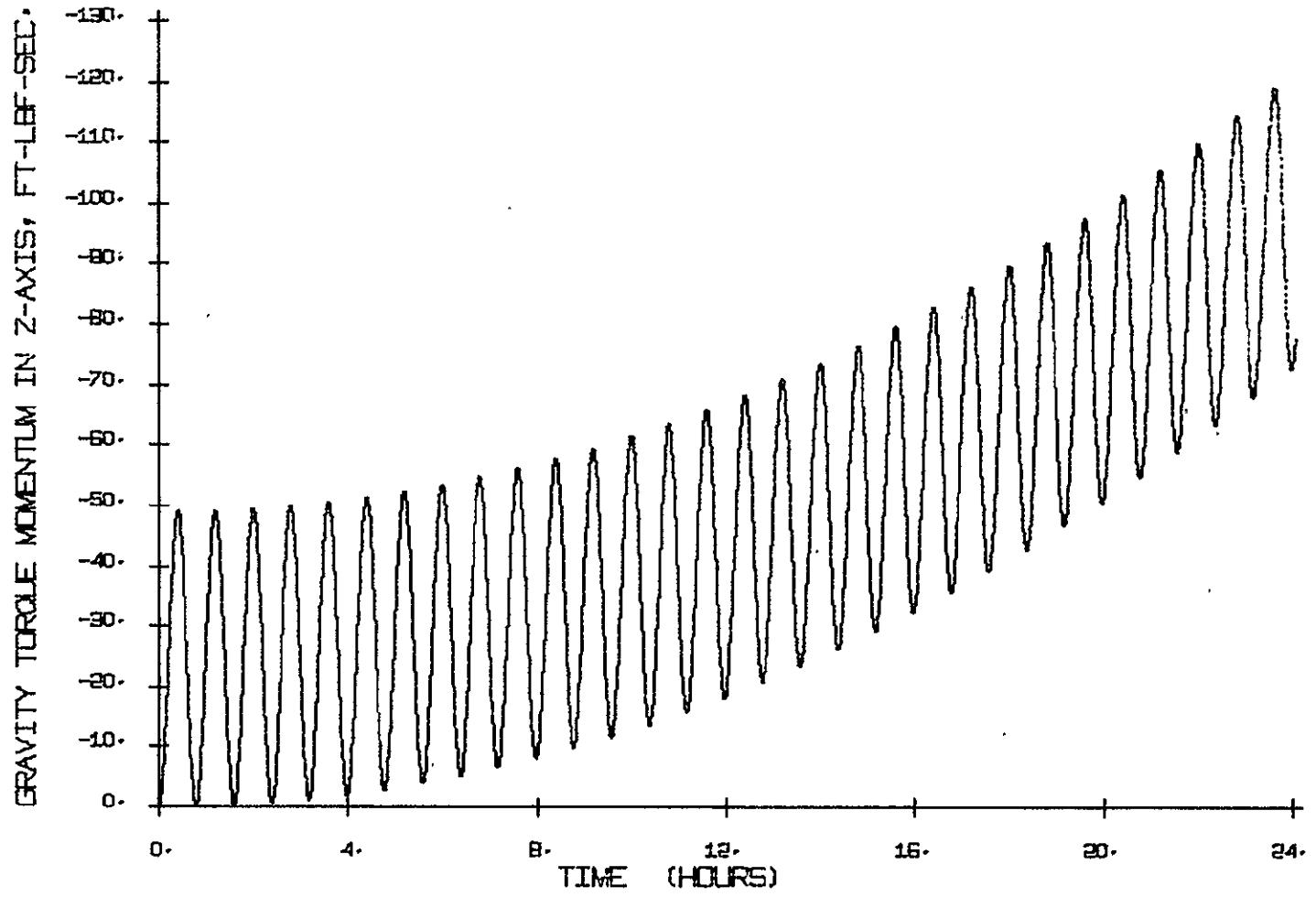


FIGURE A-57. GRAVITY TORQUE MOMENTUM IN THE z AXIS FOR CASE III

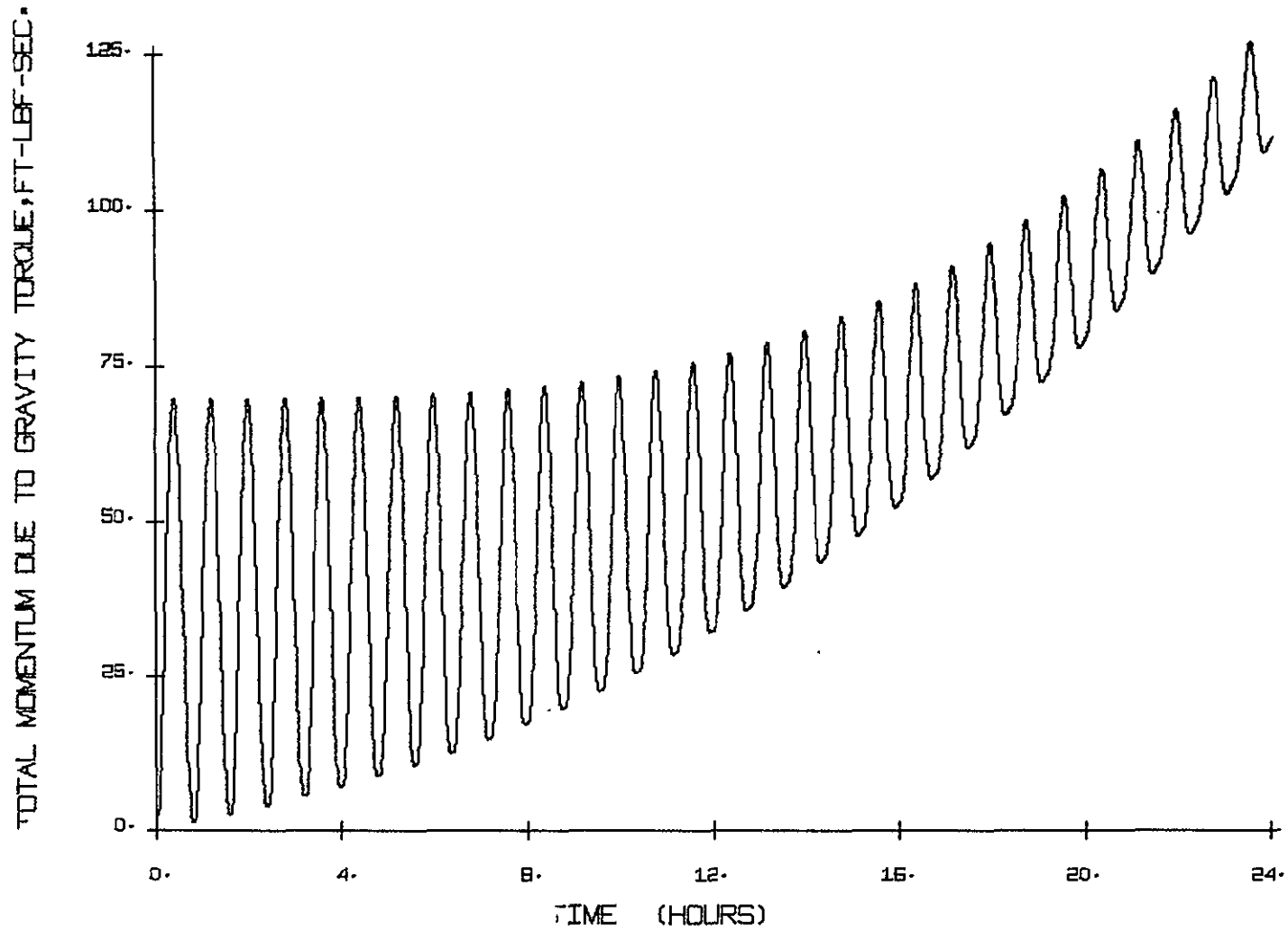


FIGURE A-58. TOTAL MOMENTUM DUE TO GRAVITY TORQUE FOR CASE III

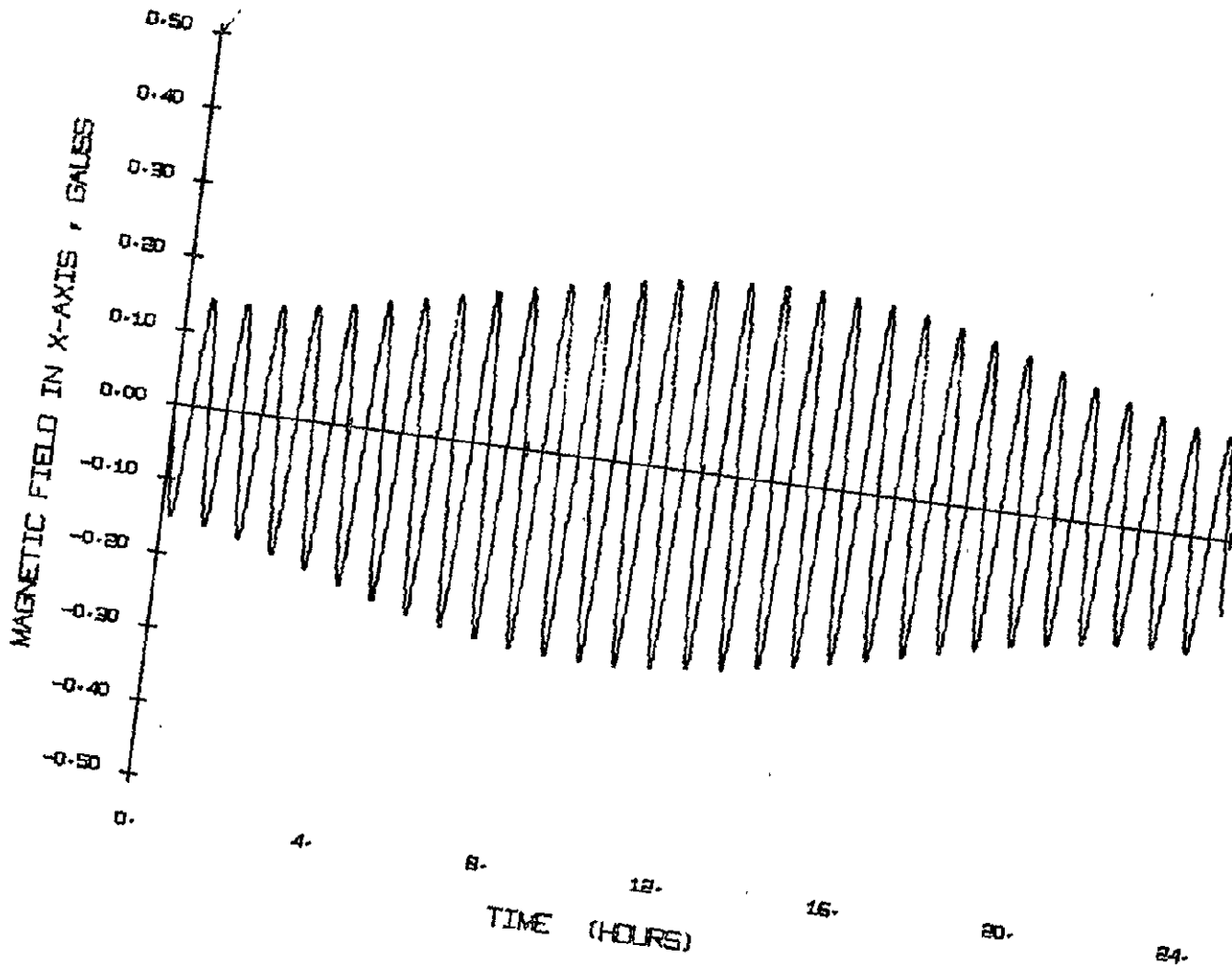


FIGURE A-59. COMPONENT OF THE EARTH'S MAGNETIC FIELD IN THE x AXIS FOR CASE III

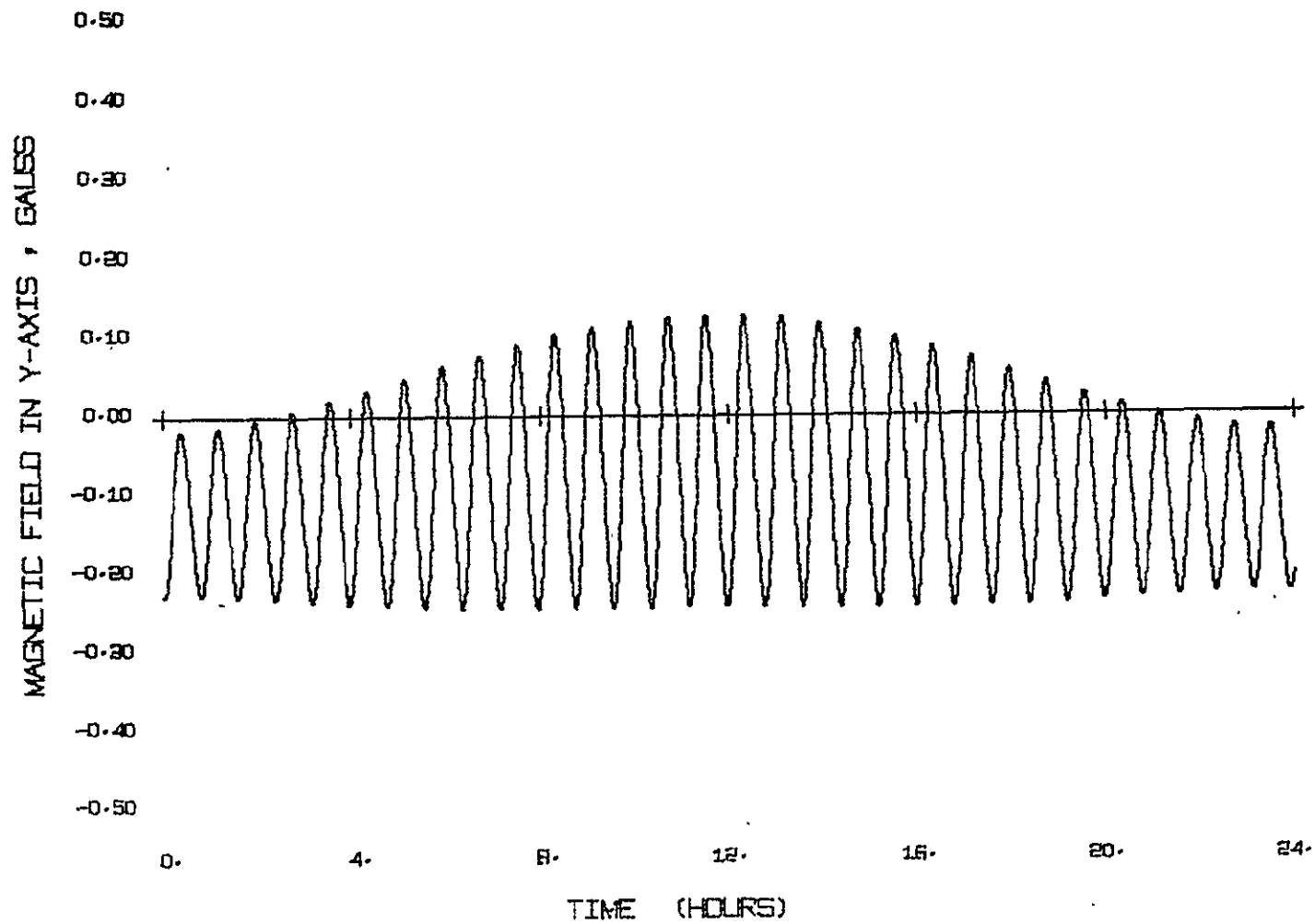


FIGURE A-60. COMPONENT OF THE EARTH'S MAGNETIC FIELD IN THE y AXIS FOR CASE III

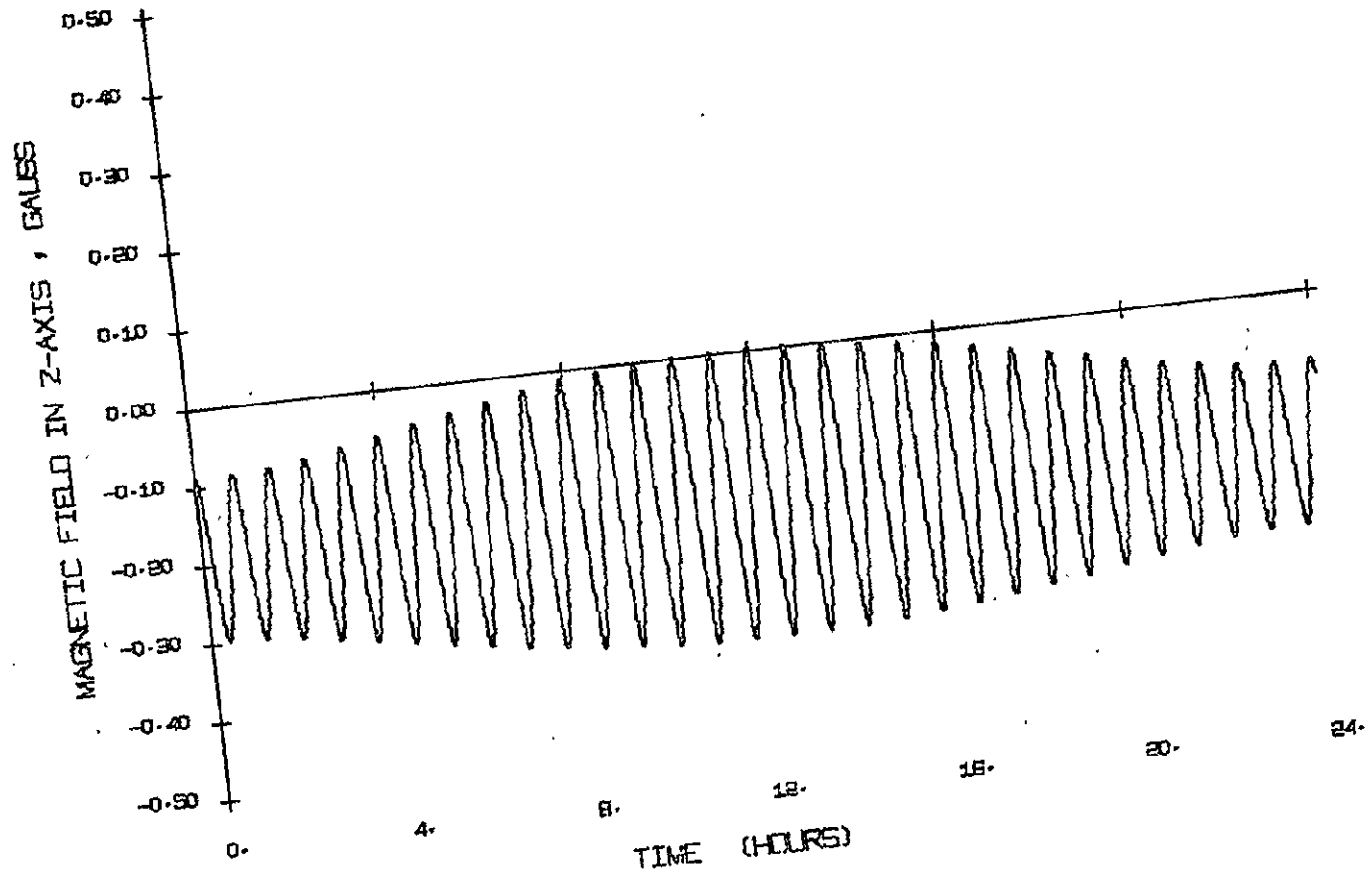


FIGURE A-61. COMPONENT OF THE EARTH'S MAGNETIC FIELD IN THE Z AXIS FOR CASE III

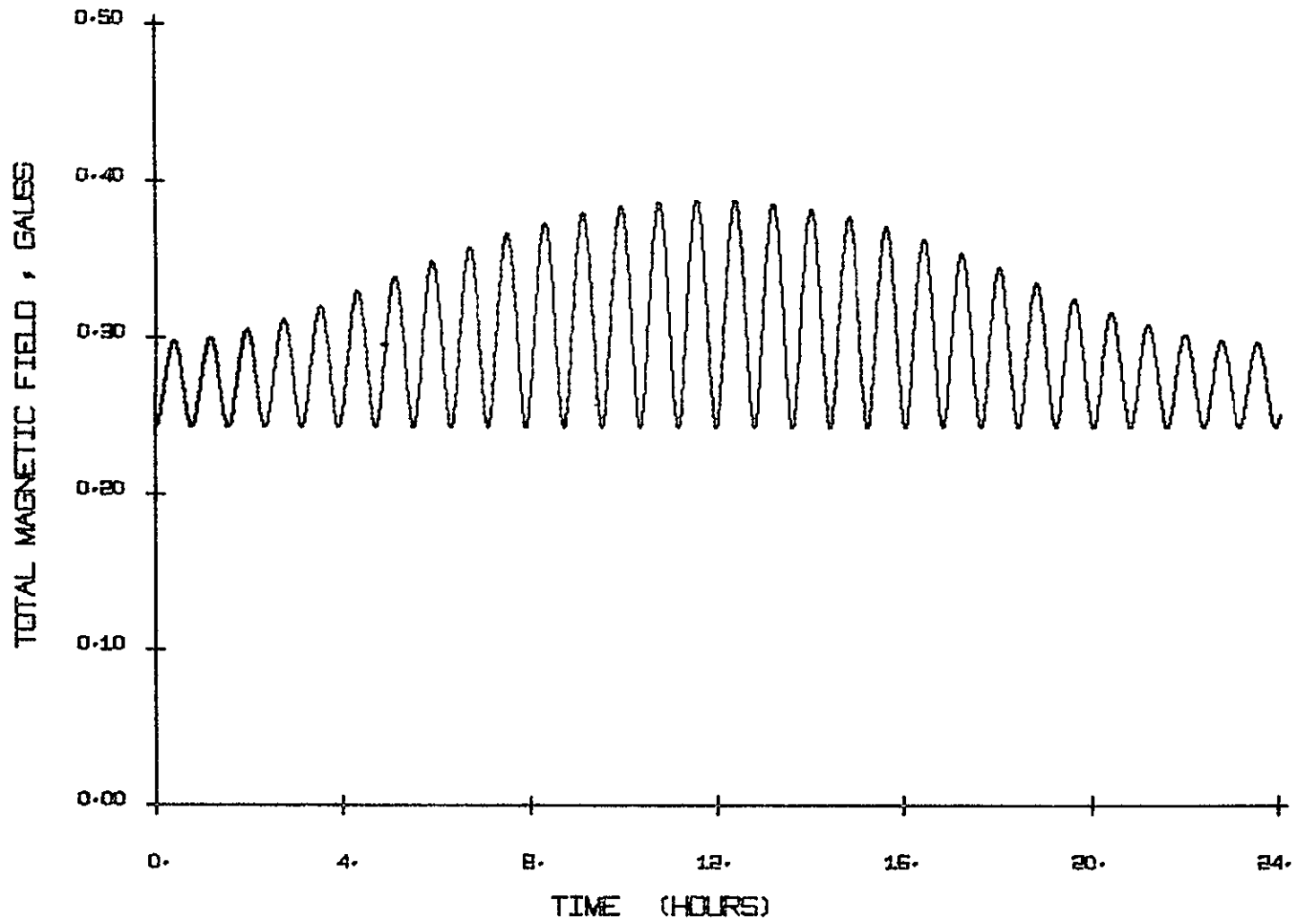


FIGURE A-62. EARTH'S MAGNETIC FIELD PROFILE FOR CASE III

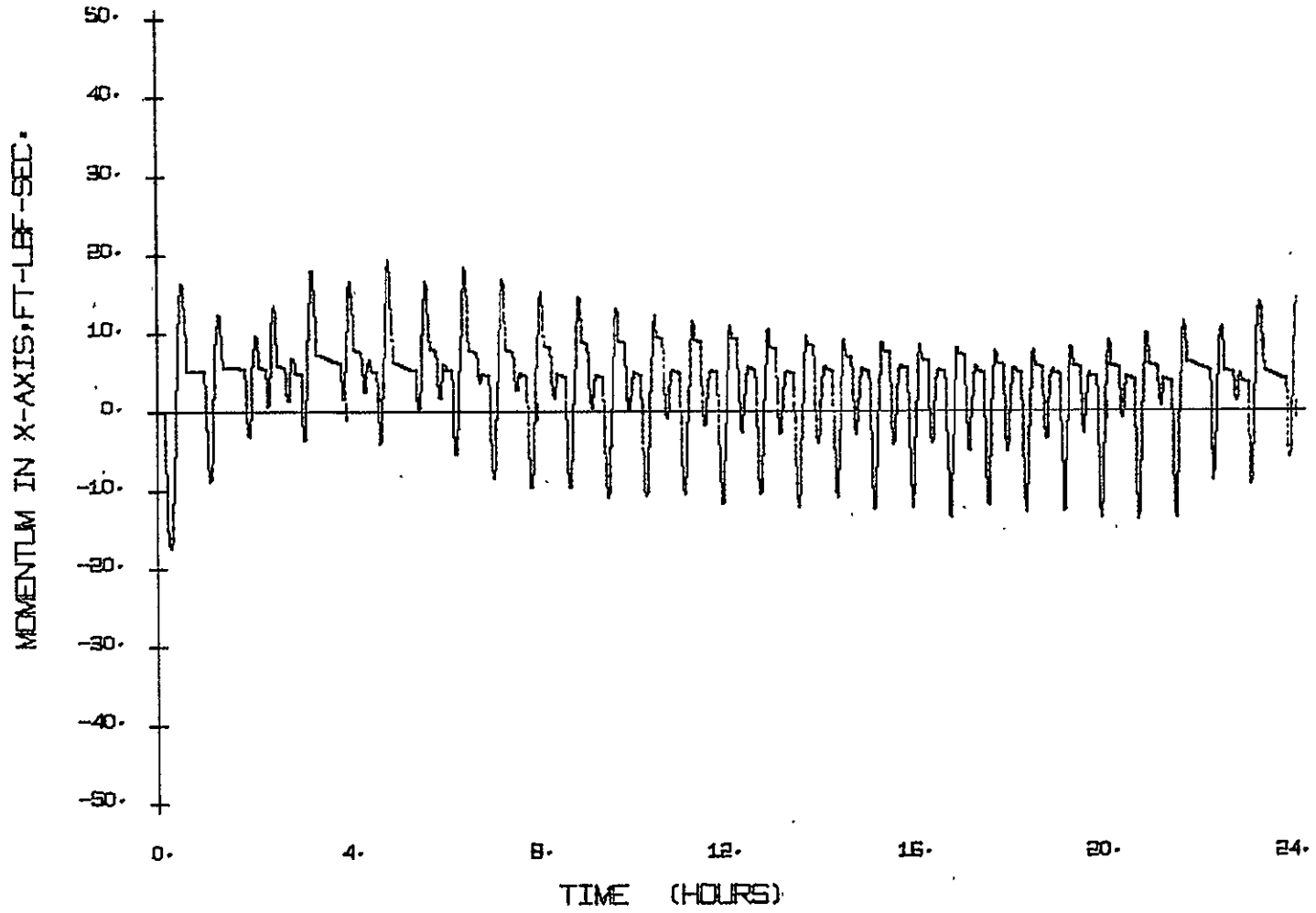


FIGURE A-63. COMPONENT OF STORED MOMENTUM IN THE x AXIS FOR CASE III

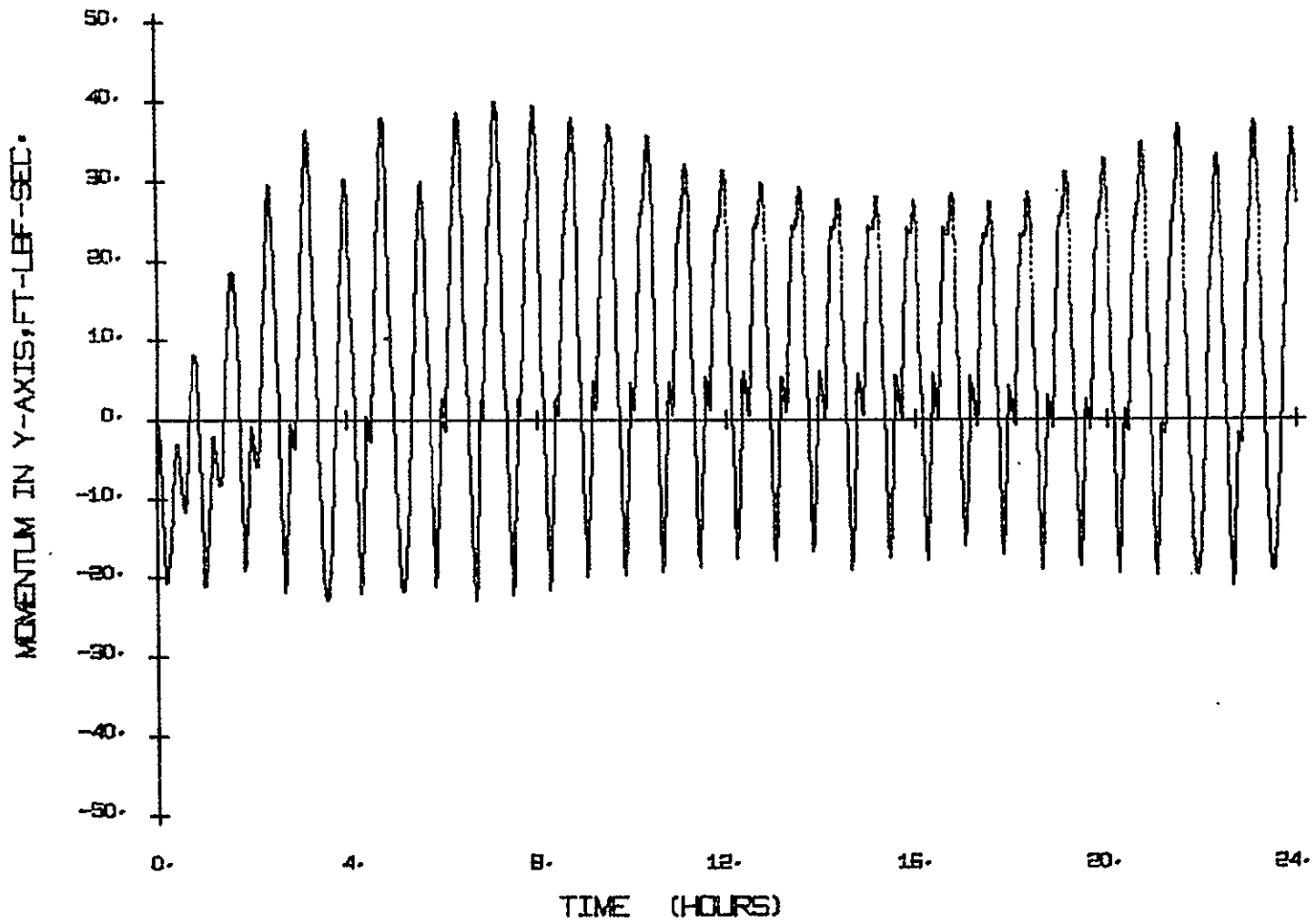


FIGURE A-64. COMPONENT OF STORED MOMENTUM IN THE y AXIS FOR CASE III

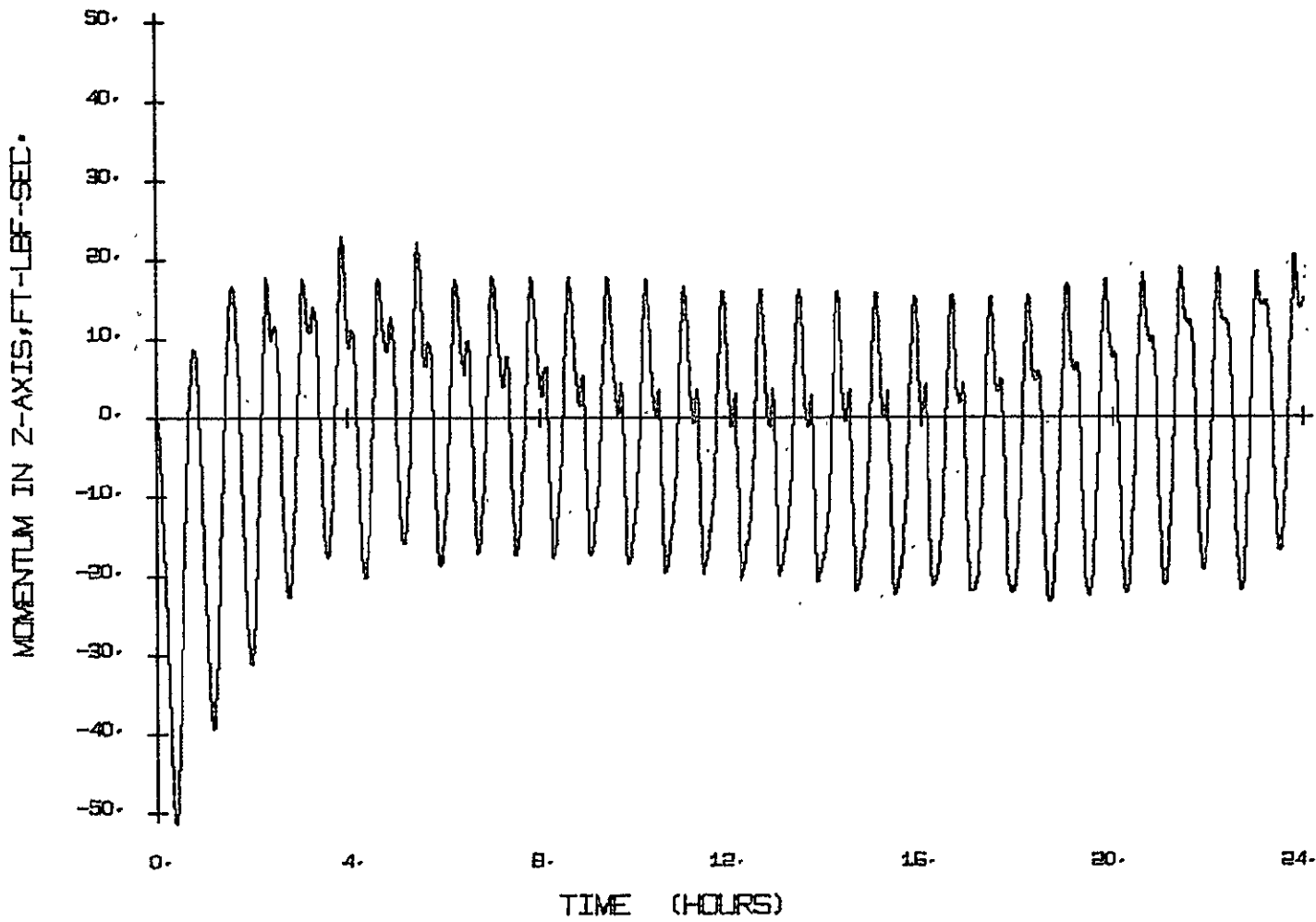


FIGURE A-65. COMPONENT OF STORED MOMENTUM IN THE z AXIS FOR CASE III

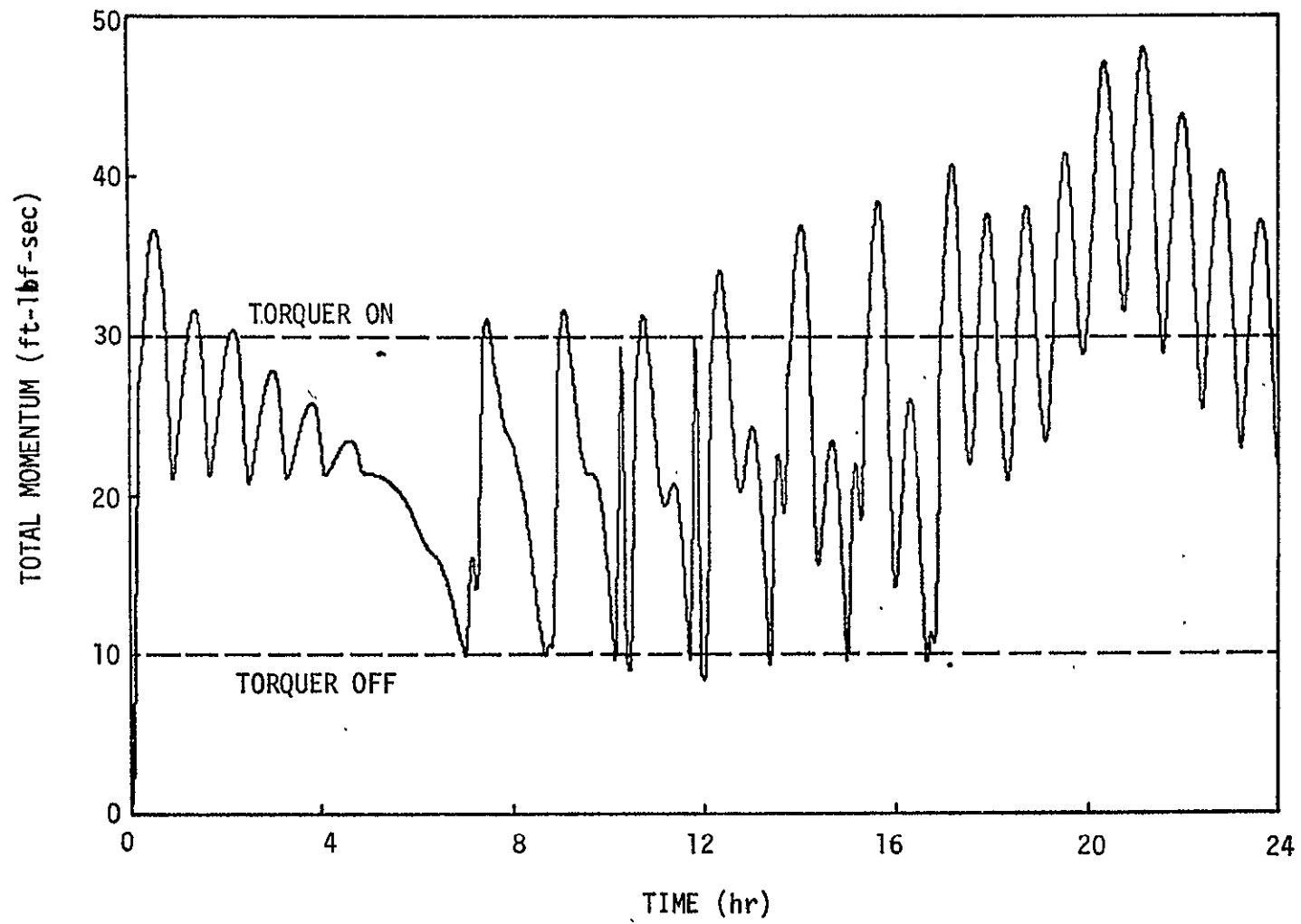


FIGURE A-66. TOTAL MOMENTUM STORED IN THE MOMENTUM STORAGE DEVICE FOR CASE III

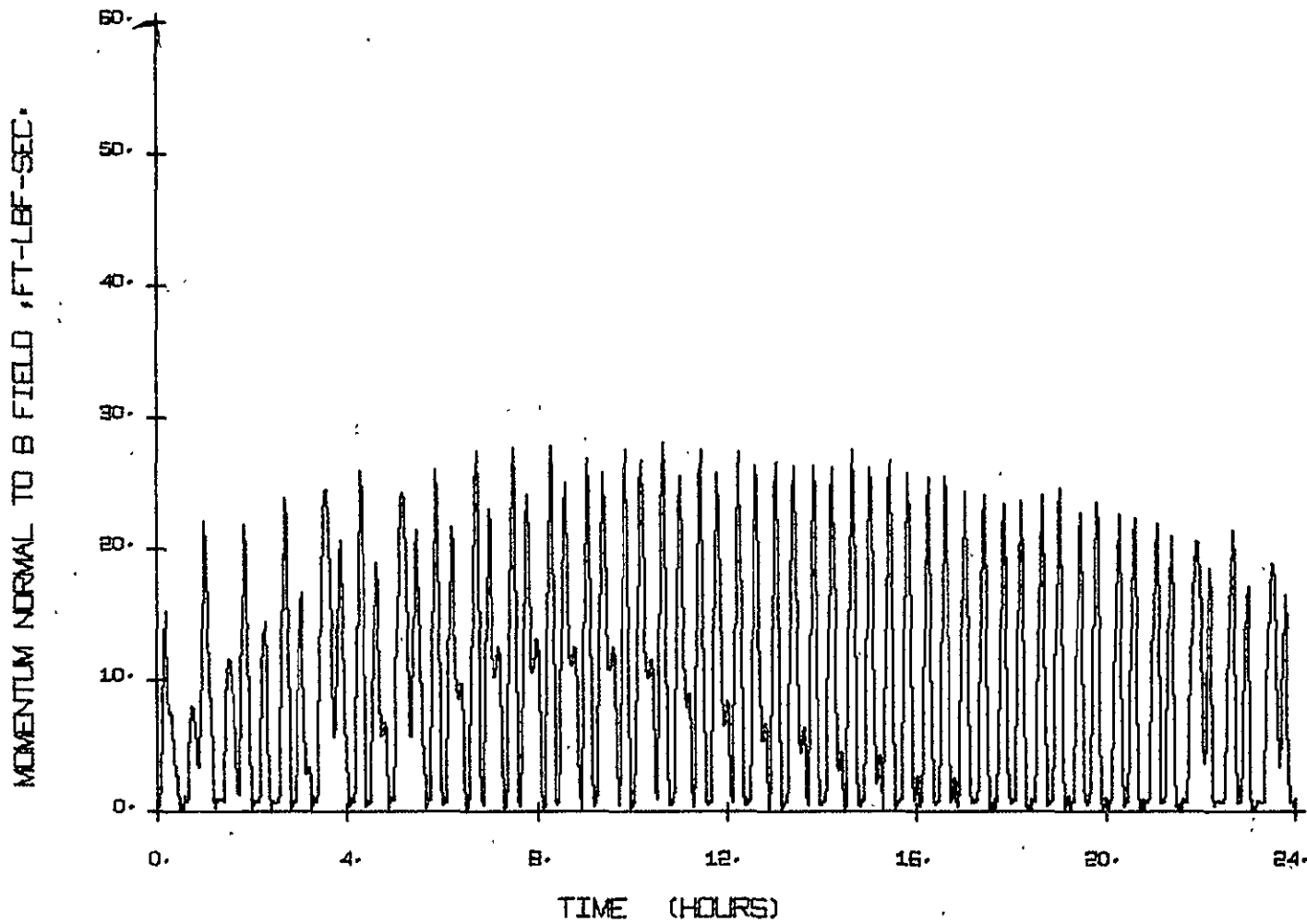


FIGURE A-67. COMPONENT OF STORED MOMENTUM NORMAL TO THE B FIELD FOR CASE III

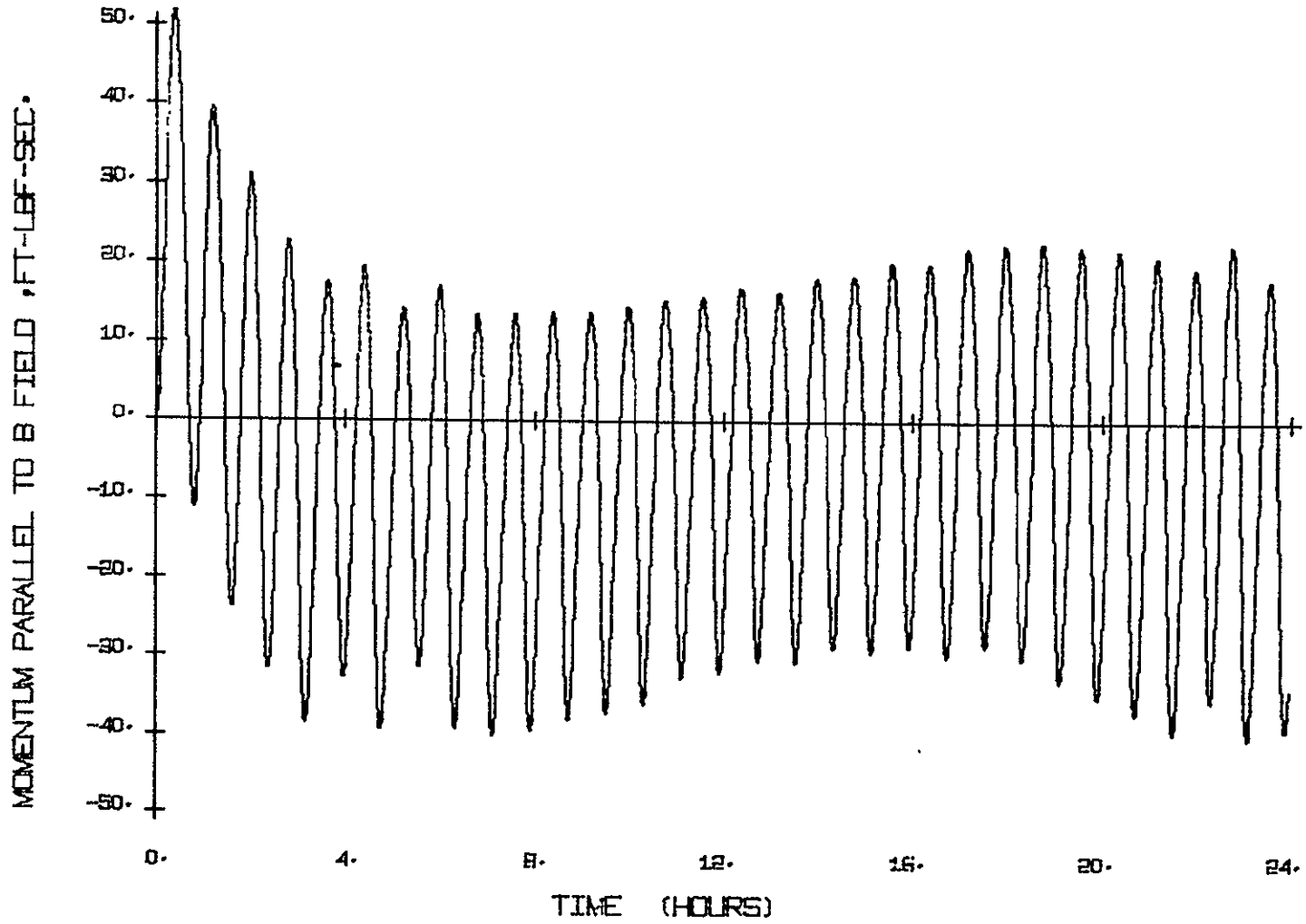


FIGURE A-68. COMPONENT OF STORED MOMENTUM PARALLEL TO THE B FIELD FOR CASE III

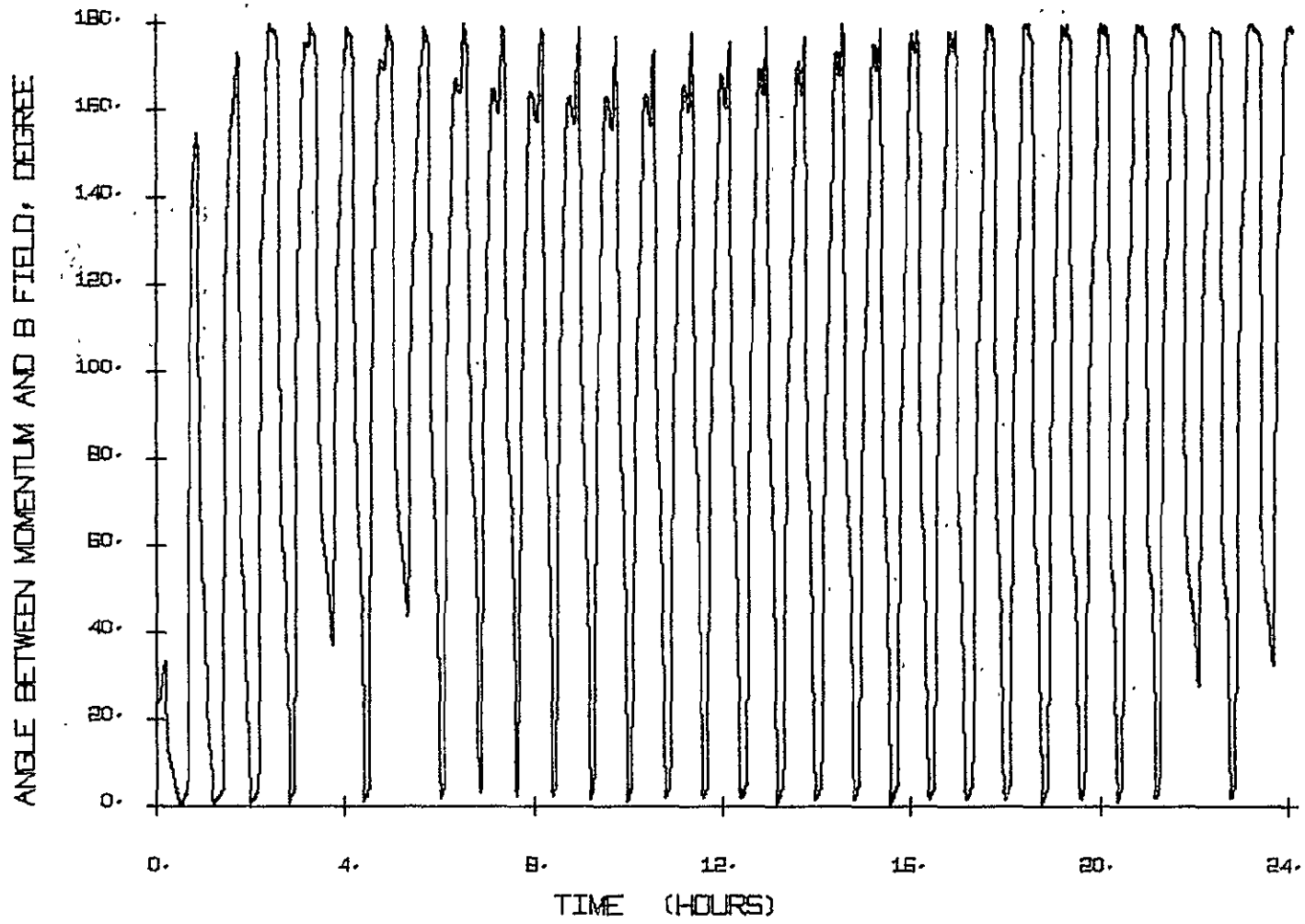


FIGURE A-69. ANGLE BETWEEN THE STORED MOMENTUM VECTOR AND THE B- FIELD VECTOR FOR CASE III

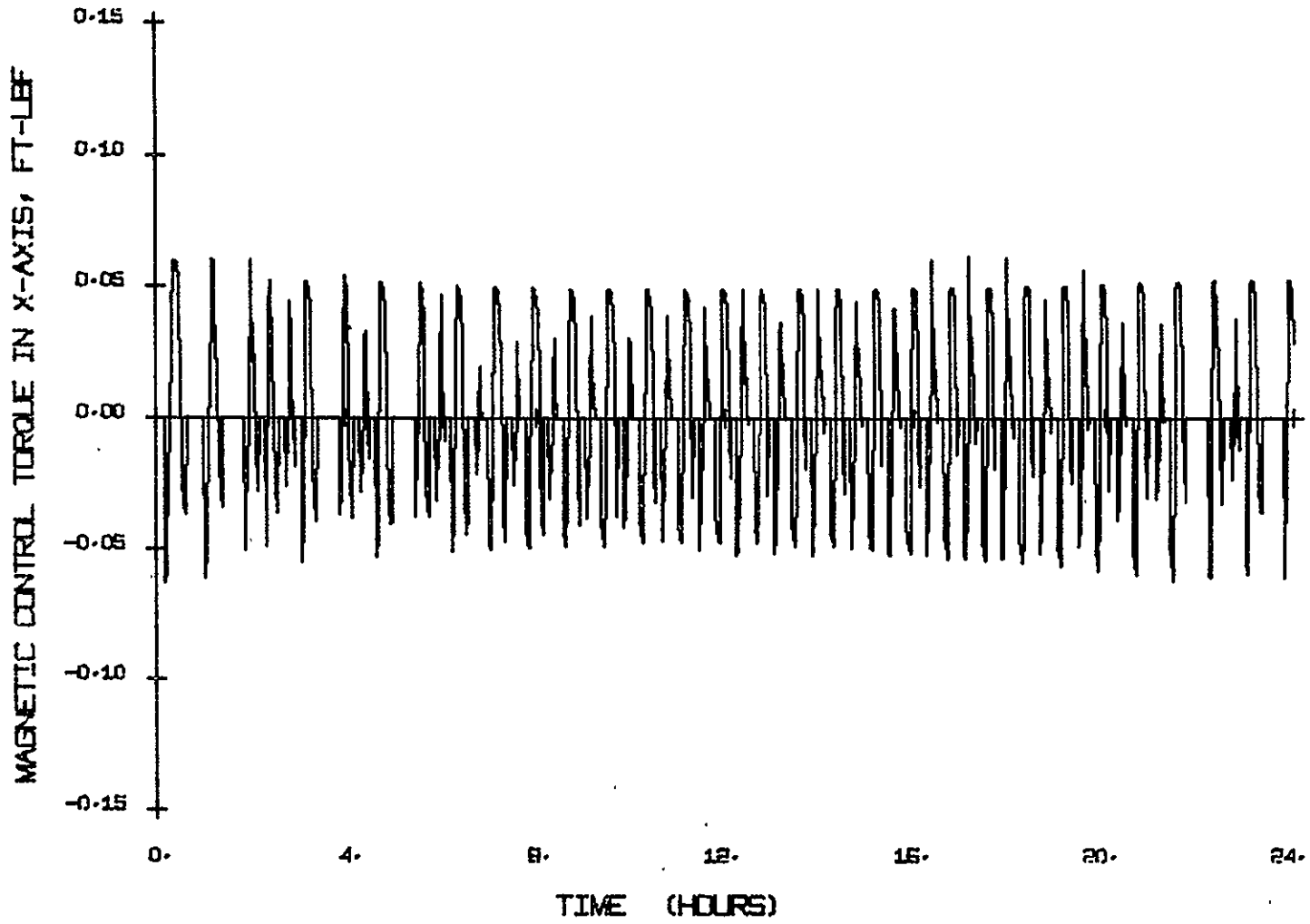


FIGURE A-70. MAGNETIC CONTROL TROQUE IN THE x AXIS FOR CASE III

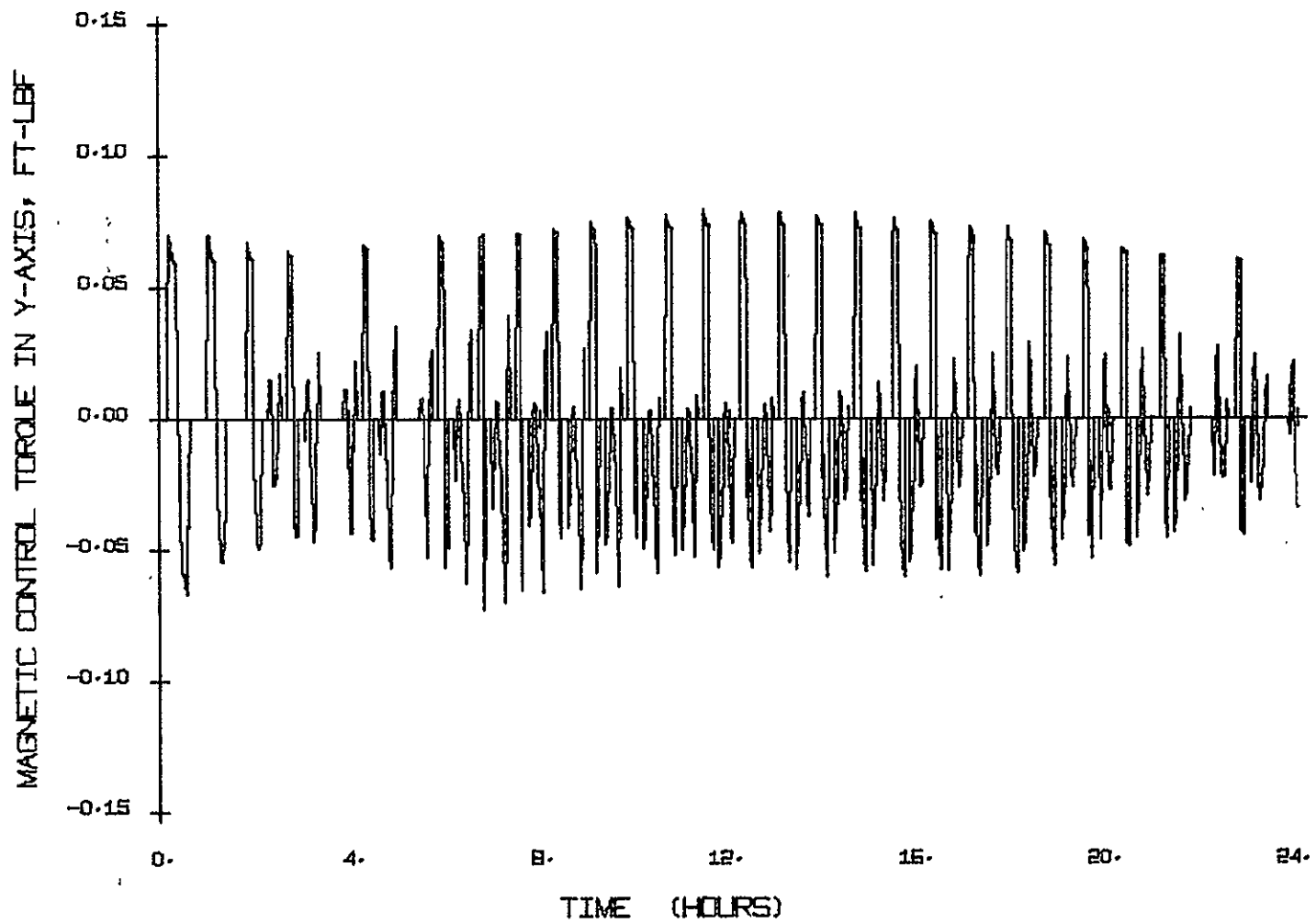


FIGURE A-71. MAGNETIC CONTROL TORQUE IN THE y AXIS FOR CASE III

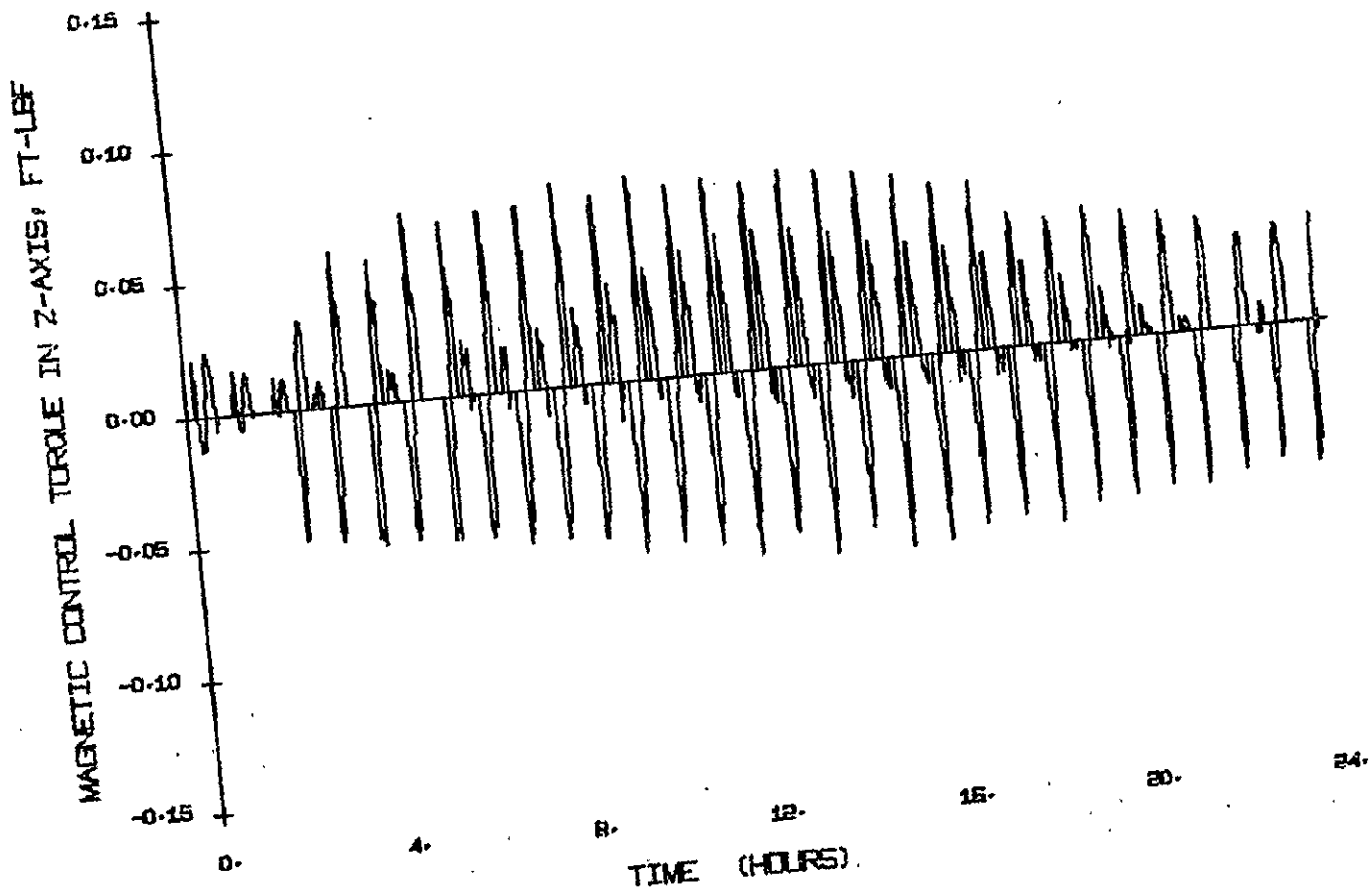


FIGURE A-72: MAGNETIC CONTROL TORQUE IN THE Z AXIS FOR CASE III

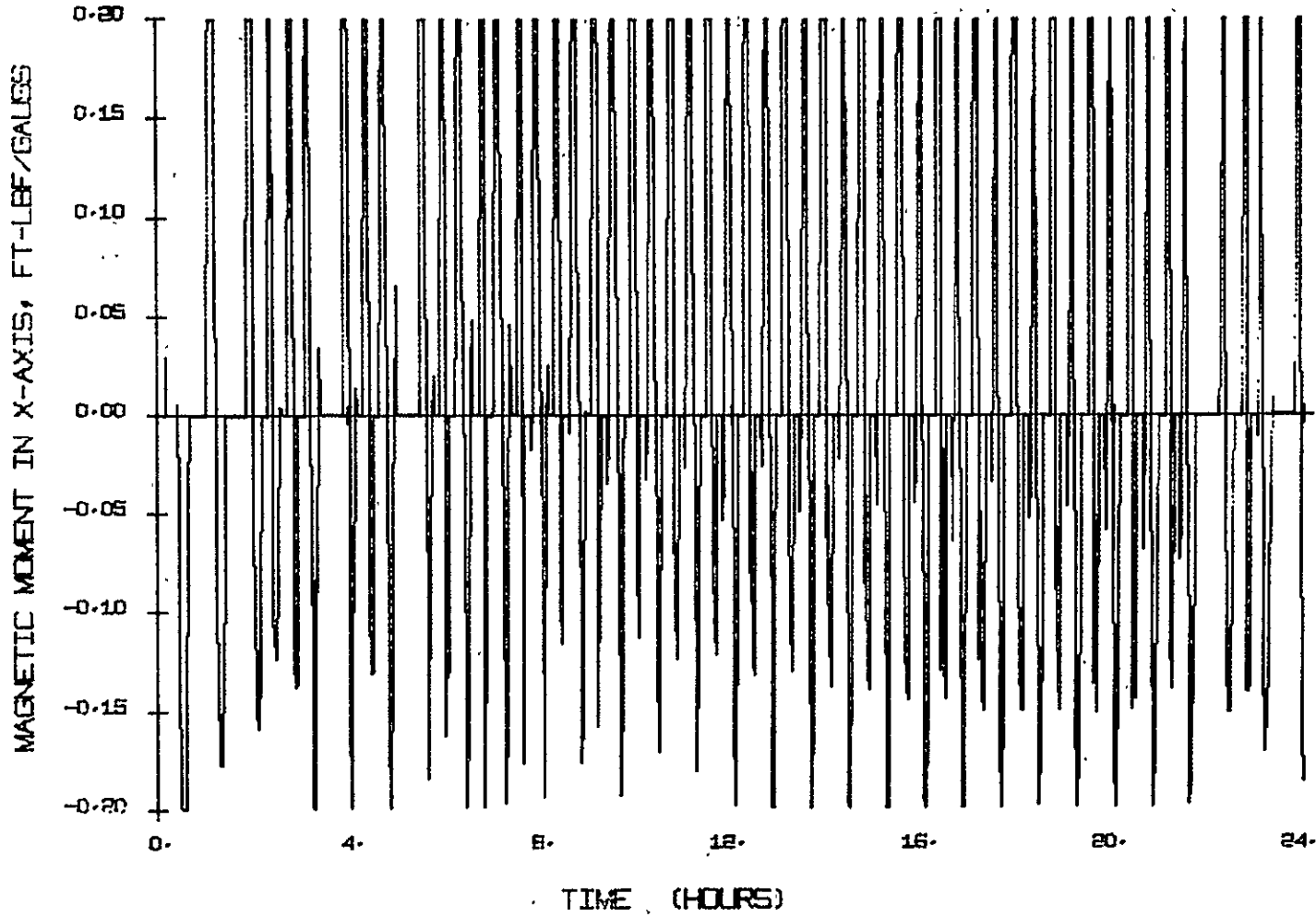


FIGURE A-73. MAGNETIC MOMENT PRODUCED BY THE X AXIS ELECTROMAGNET FOR CASE III

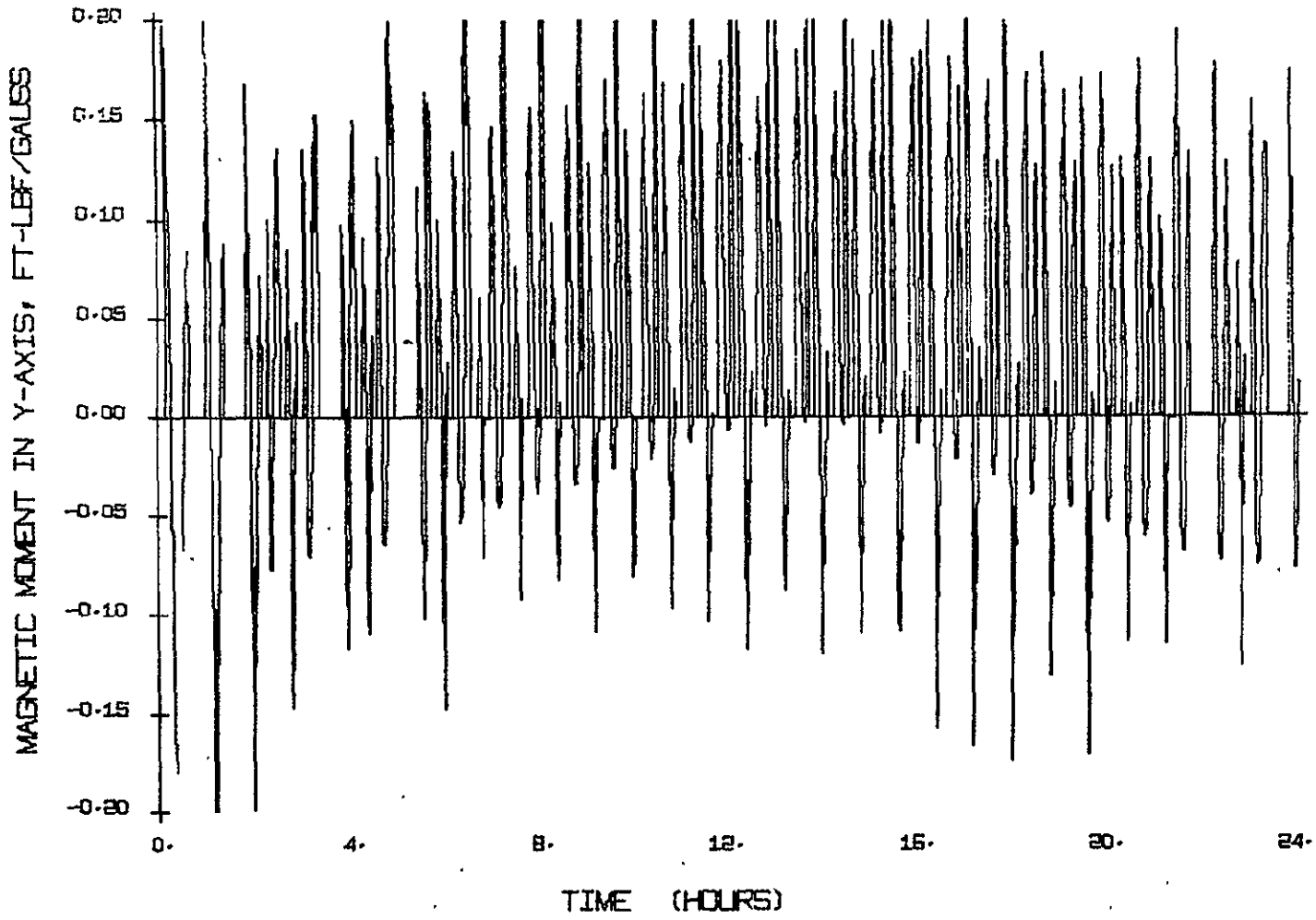


FIGURE A-74. MAGNETIC MOMENT PRODUCED BY THE y AXIS ELECTROMAGNET FOR CASE III

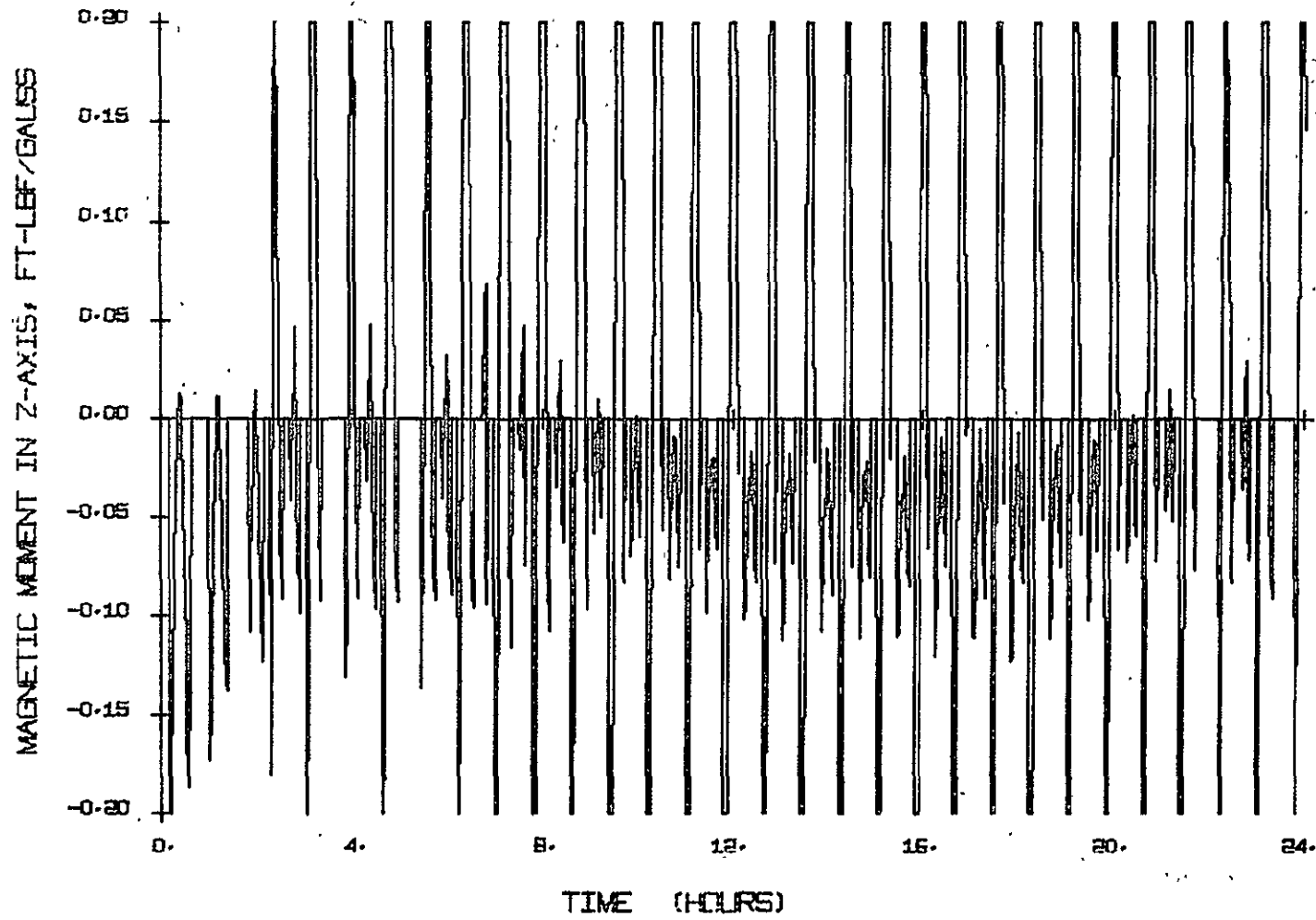


FIGURE A-75. MAGNETIC MOMENT PRODUCED BY THE z AXIS ELECTROMAGNET FOR CASE III

DISTURBANCE TORQUES

Both external and internal disturbance torques act on the orbiting spacecraft. A knowledge of these disturbance torques is required for the proper sizing of the attitude control system. The disturbance torques at a 300-nautical-mile Earth orbit are:

- External
 - ▲ Gravity
 - ▲ Aerodynamic
 - ▲ Magnetic
 - ▲ Solar radiation

- Internal
 - ▲ Internal machinery
 - ▲ Fuel or gas venting.

Each of these disturbance torques are analyzed below.

Gravity Torque

The maximum values of the gravity gradient torque in the spacecraft body axes, are obtained when one of the body axis is inclined at an angle of 45 degrees with the local vertical. The equations for these maximum torque conditions are:

$$(T_{xG})_{\max} = \pm \frac{3}{2} \frac{GM}{R^3} (I_y - I_z) \quad (A-12)$$

$$(T_{yG})_{\max} = \pm \frac{3}{2} \frac{GM}{R^3} (I_x - I_z) \quad (A-13)$$

$$(T_{zG})_{\max} = \pm \frac{3}{2} \frac{GM}{R^3} (I_y - I_x) \quad (A-14)$$

where

$(T_{xG})_{max}$, $(T_{yG})_{max}$, $(T_{zG})_{max}$	- maximum gravity gradient torques in x, y, and z axes respectively
GM	- gravitational parameter = 1.40766 $\times 10^{16}$ ft ³ /sec ²
R	- distance of the center of mass of the satellite from the center of the Earth, ft
I_x , I_y , I_z	- Spacecraft principal moments of inertia, ft-lbf-sec ²

Substituting the numerical values in the above three equations gives

$$(T_{xG})_{max} = \pm 0.001 \quad \text{ft-lbf}$$

$$(T_{yG})_{max} = \pm 0.077 \quad \text{ft-lbf}$$

$$(T_{zG})_{max} = \pm 0.076 \quad \text{ft-lbf.}$$

The variation of gravity gradient torque components is sinusoidal. In general the torques in any two axes are cyclic at twice the orbital frequency and accumulate zero net angular momentum, whereas the third axis torque is secular. This component causes angular momentum to be accumulated and creates a need for a momentum storage-type control system and for periodic desaturation of this system.

Aerodynamic Torque

An approximate aerodynamic torque acting on a spacecraft in a circular orbit is obtained using the following simplifications:

- A constant atmospheric density which is the average for plus two sigma conditions predicted for 1976 is used (Ref. A-1)
- A constant vehicle drag coefficient is used.

Aerodynamic force $d\bar{F}$ acting on a differential area dA can be expressed as

$$d\bar{F} = -\rho v^2 \{ (2 - f_n) (\bar{v} \cdot \bar{n})^2 \bar{n} + f_t (\bar{v} \cdot \bar{n}) [\bar{n} \times (\bar{v} \times \bar{n})] \} dA \quad (A-15)$$

where

- ρ - atmospheric density at the orbital altitude
- v - vehicle velocity relative to the surrounding atmosphere
- f_n - normal momentum interchange coefficient for free molecular flow
- \bar{v} - unit velocity vector
- \bar{n} - outward unit vector normal to the surface
- f_t - tangential momentum interchange coefficient for free molecular flow.

If the atmosphere is assumed to be nonrotating at a 300-nautical-mile-circular orbit altitude, then we have

$$v = 24,874 \text{ ft/sec}$$

and

$$\rho = 4.80 \times 10^{-16} \text{ slug/ft}^3.$$

The values of f_n and f_t have been taken as 0.8 and 1.0, respectively.

Aerodynamic torque \bar{T}_a is given by

$$\bar{T}_a = (\int d\bar{F}) \ell \quad (A-16)$$

where ℓ is the moment arm; i. e., distance between center of pressure and center of mass of the spacecraft.

Figure A-76 shows the location of the center of mass and center of pressure for the condition of angle of attack of 90 degrees. The angle of attack is defined here as the angle between the spacecraft longitudinal axis, x and the velocity vector ∇ . This condition gives the maximum disturbance torque since the drag area is maximum and also the moment arm is maximum.

The projected drag area A is obtained by

$$A = \int dA = DL \quad (A-17)$$

where:

D - diagonal of the spacecraft cross-section. This is 105 inches for HEAO-C

L - length of spacecraft; 370 inches for HEAO-C.

Putting the values in Equation A-17 gives

$$A = 270 \text{ ft}^2.$$

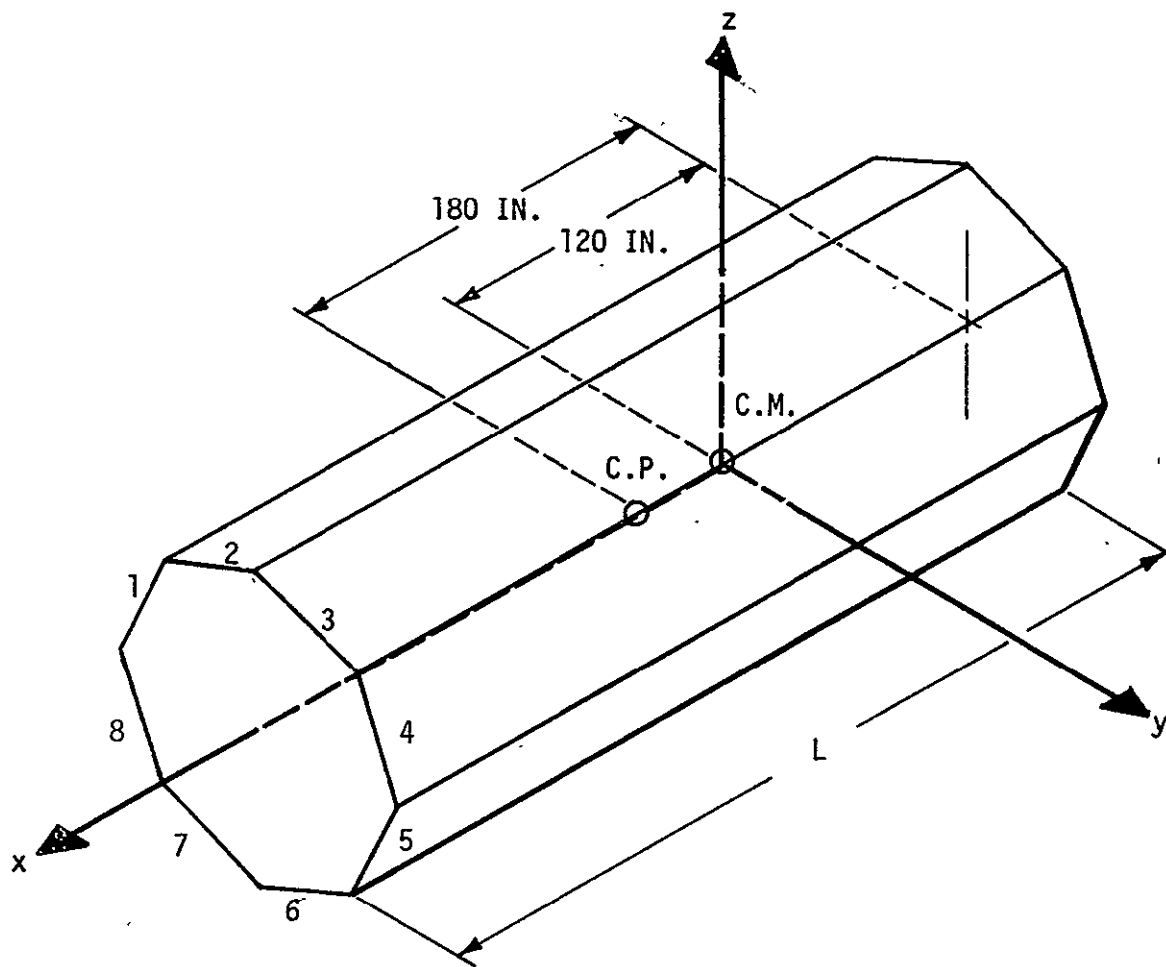
For an angle of attack of 90 degrees, Equation A-15 can be simplified to

$$d\bar{F} = -\rho v^2 (2 - f_n) \bar{n} dA. \quad (A-18)$$

Substituting Equation A-18 in Equation A-16 gives

$$\begin{aligned} \bar{T}_a &= \left[\int -\rho v^2 (2 - f_n) \bar{n} dA \right] \ell \\ &= -\rho v^2 (2 - f_n) A \ell \bar{n}. \end{aligned}$$

Substituting the values of different quantities in the above equation gives the magnitude of the maximum torque as



NOTES:

C.P. - CENTER OF PRESSURE

C.M. - CENTER OF MASS

1 THROUGH 8 - REPRESENTS THE SIDE SURFACES OF THE SPACECRAFT

1, 2, AND 3 - ARE THE SOLAR PANEL SURFACES

FIGURE A-76. LOCATION OF CENTER OF PRESSURE FOR ANGLE OF ATTACK OF 90 DEGREES

$$T_a = -4.80 \times 10^{-16} \times (24,874)^2 (2 - 0.8) \times 270 \times \frac{60}{12}$$

$$= 0.000482 \text{ ft-lbf .}$$

Thus the maximum aerodynamic torque is about two orders of magnitude smaller than the maximum gravity torque in the y or z axes.

Magnetic Torque

The magnetic disturbance torque is caused by the interaction of the magnetic moment of the spacecraft with the Earth's magnetic field. For a magnetically clean spacecraft this torque should be very small in comparison to the gravity torque. However, on the HEAO-C spacecraft, it is proposed to use magnetic torquers for the desaturation of the CMGs. These magnetic torquers will induce magnetic moments in any ferromagnetic objects on the spacecraft and especially in the optical bench, which is made of Invar material.

The optical bench structure is a truss about 30 feet long and 8 feet in diameter. Whenever magnetic torquers are energized for desaturation of the CMGs, the optical bench will be magnetized and the induced magnetic moment in the optical bench will then produce a disturbance torque. Because of the complex structure of the optical bench, a detailed analysis is required to determine the magnetic moment induced. This analysis is beyond the scope of the present study. However, the induced magnetic moment may be significant and may produce a significant disturbance torques on the spacecraft.

Solar Radiation Torque

The solar radiation force $\overline{dF_s}$ on a differential area dA can be expressed as

$$\begin{aligned} \overline{dF}_S = & -\nu \{ (1 + \nu) (\overline{x}_S \cdot \overline{n})^2 \overline{n} + (1 - \nu) (\overline{x}_S \cdot \overline{n}) \\ & \times [\overline{n} \times (\overline{x}_S \times \overline{n})] \} dA \end{aligned} \quad (A-19)$$

where

ν - solar pressure constant. In the vicinity of the Earth this is equal to 0.94×10^{-7} lbf/ft²

ν - surface reflectivity

\overline{x}_S - unit vector to the Sun

\overline{n} - outward unit vector normal to the surface.

The surface reflectivity value is 0.3 for solar panels and 0.7 for other surfaces.

The maximum radiation pressure acts on a surface when the normal to the surface is along the solar vector. For this condition Equation A-19 reduces to

$$\overline{dF}_S = -\nu (1 + \nu) \overline{n} dA . \quad (A-20)$$

Integration of Equation 20 gives the total force on a surface area A as

$$\overline{F}_S = -\nu (1 + \nu) A \overline{n} . \quad (A-21)$$

Equation A-21 shows that the maximum solar force acts when $(1 + \nu)$ is maximum. This will be the case when none of the solar panels are exposed to the Sun, since solar panels have a lower reflectivity than other surfaces. To meet this requirement the offset angle from the Sun line has to be at least 135 degrees. This is not going to be the case in actual flight, as the offset angle is limited to 30 degrees. Therefore to simulate the actual flight conditions the reflectivity value ν is taken as 0.5; this is the average of 0.3 (solar panel surfaces) and 0.7 (nonsolar panel) surfaces.

Equation A-21 now reduces to

$$\bar{F}_S = -1.5 v A \bar{n}. \quad (\text{A-22})$$

The value of A, 270 ft², is obtained from Equation A-17. The torque T_S is given by

$$T_S = F_S \cdot l \quad (\text{A-23})$$

where *l* is the moment arm; i. e., the distance between center of pressure and center of mass of the spacecraft. The value of *l* is 60 inches as, shown in Figure A-76.

Substituting the above values into Equation A-23 gives

$$\begin{aligned} T_S &= -1.5 \times 0.94 \times 10^{-7} \times 270 \times \frac{60}{12} \\ &= 0.00019 \quad \text{ft-lbf.} \end{aligned}$$

Thus it is seen that the maximum solar radiation torque is of the same order of magnitude as the aerodynamic torque, but smaller by about three orders of magnitude than the maximum gravity torque in the y or z axes

Internal Disturbance Torques

Internal disturbance torques on an unmanned spacecraft can result from internal moving parts (rotating machinery) and venting of fuel or gases. The HEAO-C spacecraft uses about 12 electric motors for the movement of experiment components. The movement of experiment components is deliberately made slowly and is performed during the time when experimental observations are not being made. The reason for doing so is to eliminate the effect of the internal moving components on the pointing accuracy of the spacecraft.

The movement of experiments from one place to another is accomplished in about 5 minutes. During this time, torque is applied by the electric motors to accelerate the experiment mass and then torque is reversed to decelerate the experiment mass. Momentum builds up during the acceleration process but this same momentum is taken out gradually during the deceleration process, thus leaving no net angular momentum after the movement of the experiment has stopped.

A sample calculation was made to find out the disturbance torque produced by the movement of the high resolution spectrometer detector assembly. The weight of this assembly is 310 lbm and the dimensions are about 75 by 40 by 30 inches. The assembly is required to move (rotate) on the longitudinal axis by 90 degrees in 5 minutes. The torque required for this rotation is 0.0014 ft-lbf. The angular momentum imparted by this torque is about 0.25 ft-lbf-sec. If it is assumed that three of the 12 electric motors are operating simultaneously for 5 minutes and are producing torque in the same direction, then the total disturbance torque will be 0.0042 ft-lbf and the total angular momentum will be 0.75 ft-lbf-sec. This total disturbance torque is about 6 percent of the maximum gravity torque in the y or z axes and the angular momentum imparted to the spacecraft is very small because of short duration of application of torque. From the above analysis it appears that the pointing accuracy of the spacecraft, while pointing on a target can be maintained even if the components are moved internally.

Conclusions

Thus, from the analysis of external disturbance torques it is seen that the predominant torque is due to gravity gradient. Torques due to other external sources are very small in comparison to gravity torque. Also from the analysis of internal disturbance torques it is seen that the duration of application these torques is small (less than

5 minutes) and that there is no net angular momentum accumulated after the application of these torques. Table A-1 summarizes the disturbance torque acting and the momentum accumulated in one orbit time.

TABLE A-1. MAXIMUM DISTURBANCE TORQUE AND MOMENTUM ACCUMULATION IN ONE ORBIT

Source	Torque (ft-lbf)			Momentum Accumulated in One Orbit (ft-lbf-sec)		
	x axis	y axis	z axis	x axis	y axis	z axis
Gravity gradient secular torque	0.001	0.077	0.076	3	220	220
Aerodynamic torque	0.000	0.000	0.000	-	-	-
Solar radiation torque	0.000	0.000	0.000	-	-	-
Magnetic torque	TO BE DETERMINED →					
Internal components motion	0.000	0.000	0.000	-	-	-
TOTAL	0.001	0.077	0.076	3	220	220

OTHER CMG CONFIGURATIONS CONSIDERED

A configuration of three scissored pairs of GMGs was selected for the baseline HEAO-C layout, weight, and power allocations. Other configurations that were considered are discussed here and consist of

- Three single-degree-of-freedom gyros
- Three two-degree-of-freedom gyros
- Four single-gimbal gyros.

Three Single-Degree-of-Freedom Gyros

Figure A-77 shows the arrangement of these gyros considered. The momentum in the individual axis for three equal size gyros can be written as

$$\begin{aligned}H_x &= h [\cos \alpha_y - \sin \alpha_z] \\H_y &= h [\cos \alpha_z - \sin \alpha_x] \\H_z &= h [\cos \alpha_x - \sin \alpha_y]\end{aligned}\tag{A-24}$$

where

- H_x, H_y, H_z - angular momentum in x, y, and z axes, respectively
- h - gyro angular momentum
- α_x - gimbal angle for the gyro placed on the x axis
- α_y - gimbal angle for the gyro placed on the y axis
- α_z - gimbal angle for the gyro placed on the z axis.

The reaction torque acting on the vehicle due to a changing net angular momentum of the GMG system is the negative time derivative

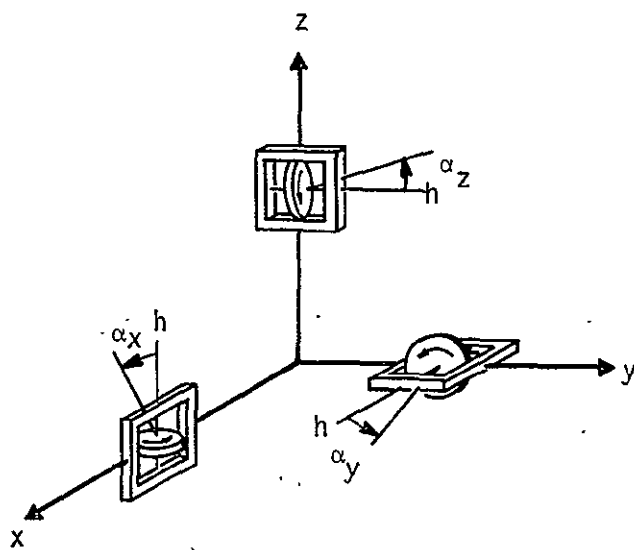


FIGURE A-77. THREE SINGLE-DEGREE-OF-FREEDOM (SINGLE GIMBALLED) GYROS .

of Equation A-24 with respect to inertial space. This may be expressed as

$$T = - \frac{d H_j}{dt} . \quad (A-25)$$

Equation A-25 may be expressed in matrix form as

$$\begin{vmatrix} T_x \\ T_y \\ T_z \end{vmatrix} = -h \begin{vmatrix} 0 & -\sin \alpha_y & -\cos \alpha_z \\ -\cos \alpha_x & 0 & -\sin \alpha_z \\ -\sin \alpha_x & -\cos \alpha_y & 0 \end{vmatrix} \begin{vmatrix} \dot{\alpha}_x \\ \dot{\alpha}_y \\ \dot{\alpha}_z \end{vmatrix} \quad (A-26)$$

where $\dot{\alpha} = \frac{d\alpha}{dt}$.

It is evident from Equation A-26 that there is cross-coupling among the axes. For small gimbal angles the cross-coupling is very small but for large gimbal angles the cross coupling is significant. This is one of the disadvantages of this system.

From Equation A-24, it is noted that the maximum storage capability in each individual axis is $2h$. For combined axes storage the capability per axis decreases. The worst condition occurs when two axes need equal storage and the third axis needs no storage; i. e., $H_x = 0$ and $H_y = H_z = H$. For this condition

$$H = \sqrt{2} h .$$

For 100 ft-lbf-sec momentum storage capability required in each axis, we get

$$h = \frac{100}{\sqrt{2}} = 70 \text{ ft-lbf-sec.}$$



The weight of a single gimbled CMG having 70 ft-lbf-sec momentum is 40 lbm. The power required is 12 watts average and 60 watts peak (Refs. A-2 and A-3). For a system of three CMGs the total weight is 120 lbm, and the power requirement is 36 watts average and 150 watts peak.

Three Two-Degree-of-Freedom Gyros

Figure A-78 shows the arrangement of these gyros. Each gyro has two gimbals, an inner gimbal and an outer gimbal. The advantage of using two gimbals on a gyro is that it allows the momentum vector to be oriented in any direction. The maximum momentum possible in the system is obtained when all CMG momentum vectors are parallel. This maximum momentum is equal to three times the momentum of one gyro for three equal size gyros; and this maximum momentum vector can be directed along any axis. Thus this arrangement of gyros has a spherical momentum envelope and 100 percent momentum utilization. The other advantage of this system is redundancy because of the extra degree of freedom.

The disadvantages of this arrangement are:

- The output torque is limited to the capability of the gimbal torquer
- Without a special control law this arrangement can have inner gimbal lock at low momentum level
- For certain momenta orientations this arrangement can result in a hang up. In other words torque cannot be delivered in the desired direction without excessive cross coupling. This occurs when the momenta of the CMGs lie parallel or antiparallel to the direction of the commanded momenta.

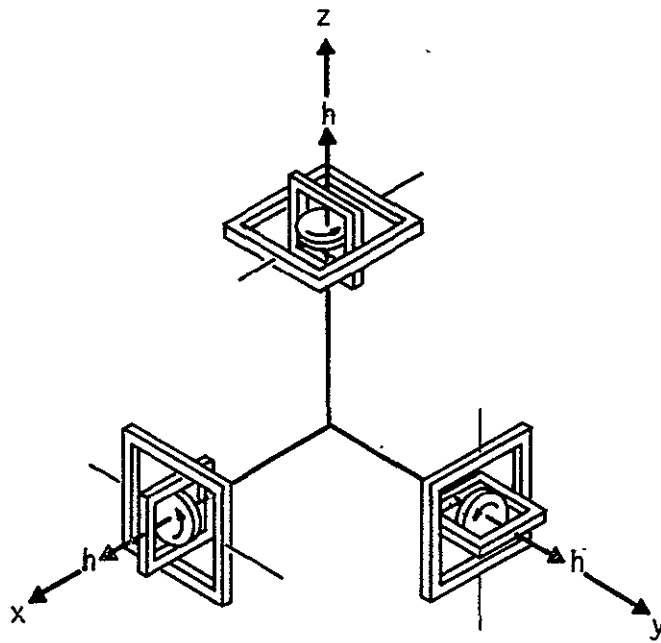


FIGURE A-78. THREE TWO-DEGREE-OF-FREEDOM (DOUBLE GIMBALLED) GYROS

The momentum of each gyro required for three equal size gyros is $100/3 = 34$ ft-lbf-sec or about 40 ft-lbf-sec. The weight and power required for one gyro are

- Weight = 40 lbm
- Power = 10 watts (average)
50 watts (peak).

The total system weight is therefore 120 lbm and the total power requirement is 30 watts (average) and 150 watts (peak) (Refs. A-2, A-3).

Four Single-Gimbal-Gyros

The arrangement of these gyros is shown in Figure A-79. The gimbal axes of four gyros lie in the x-z plane. The angular momentum vectors of CMG No. 1 and CMG No. 3 (as marked in Figure A-79) point in the y direction when gimbal angles α_1 and α_3 are zero. These gimbal angles are measured from the y axis. The positive directions of α_1 and α_3 are as indicated in Figure A-79. The angular momentum vectors of CMG No. 2 and CMG No. 4 point in the -y direction when gimbal angles α_2 and α_4 are zero. The gimbal angles α_2 and α_4 are measured from the -y axis. The positive directions of α_2 and α_4 are as indicated in Figure A-79.

Figure A-80 shows the path of motion for the angular momentum vectors of the four CMGs. The angular momentum components in the x, y, and z axes can be written from inspection of Figure A-80:

$$H_x = h [-\sin \alpha_2 + \sin \alpha_4]$$

$$H_y = h [\cos \alpha_1 - \cos \alpha_2 + \cos \alpha_3 - \cos \alpha_4]$$

$$H_z = [\sin \alpha_1 - \sin \alpha_3] .$$

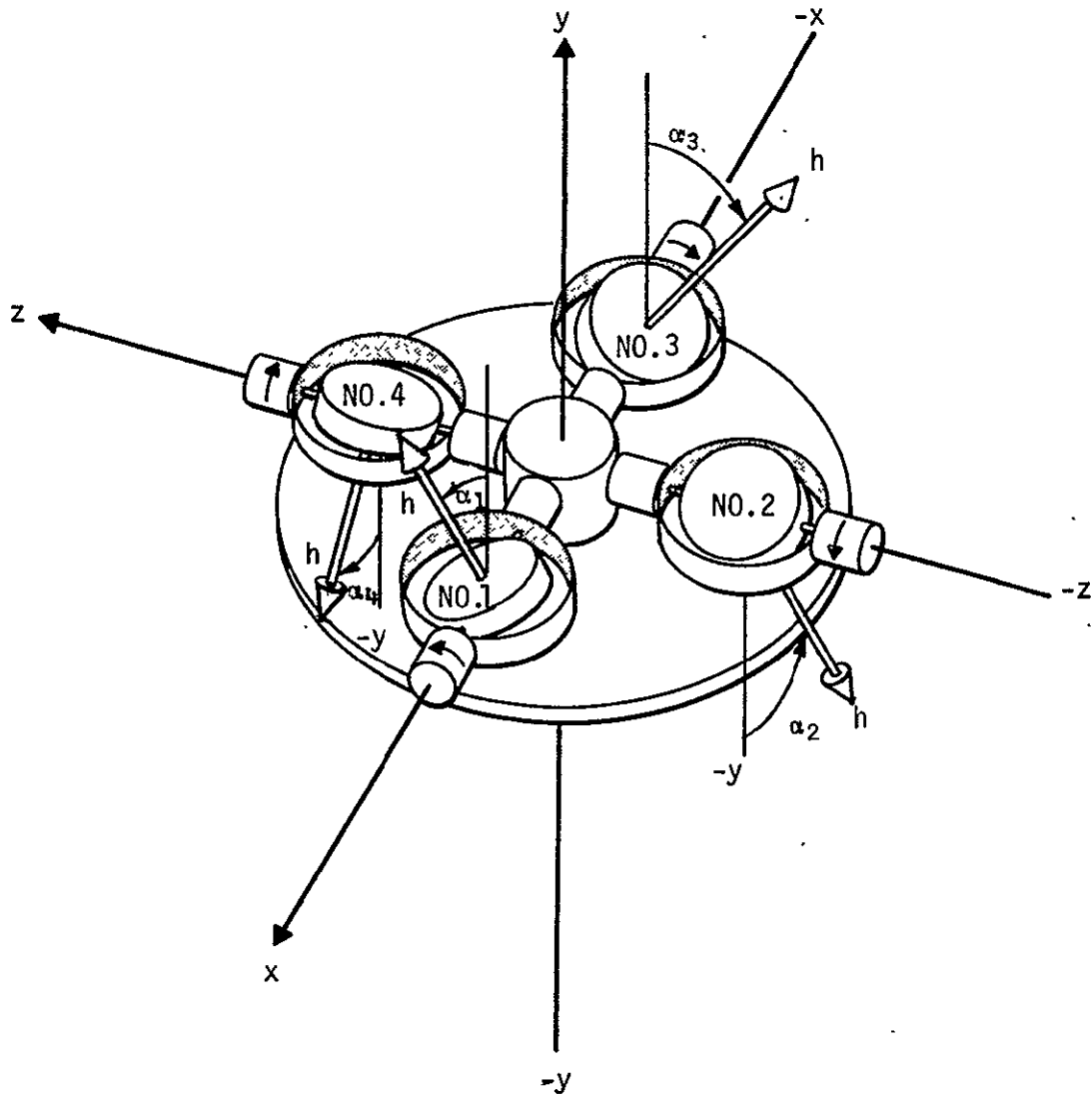


FIGURE A-79. ARRANGEMENT OF FOUR SINGLE-DEGREE-OF-FREEDOM GYROS

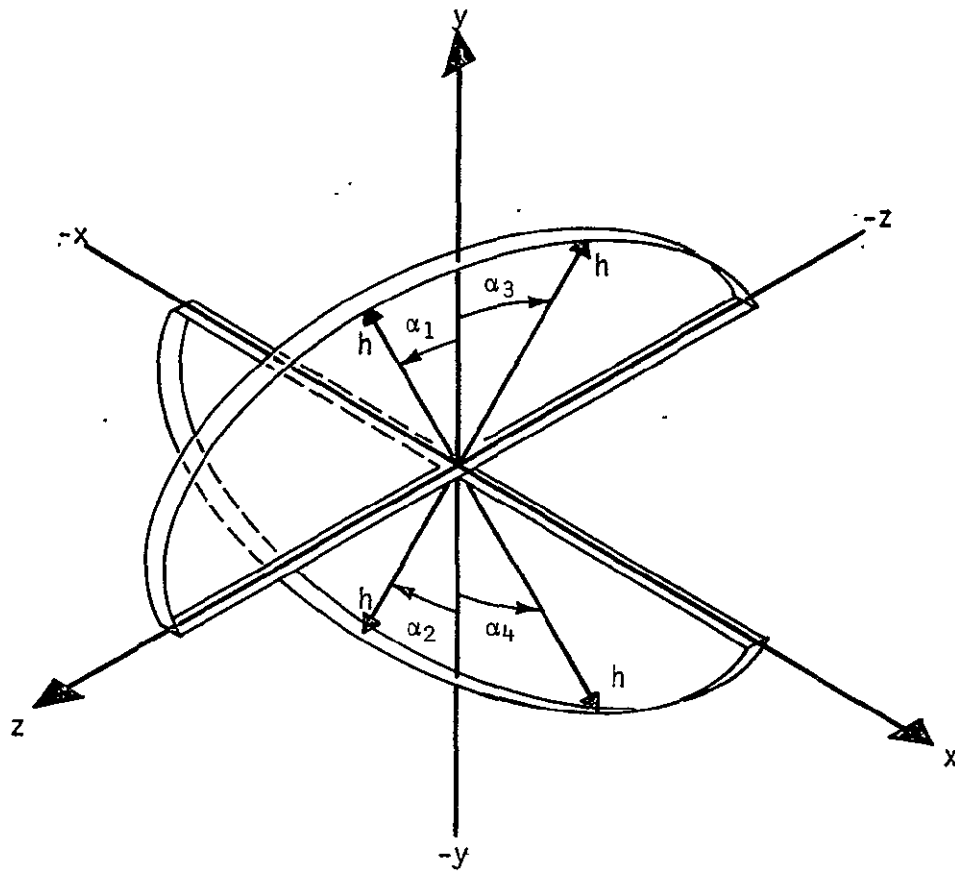


FIGURE A-80. THE PATH OF MOTION OF THE ANGULAR MOMENTUM VECTORS FOR FOUR CMGs

The reaction torque acting on the vehicle due to exchange of momentum is

$$\begin{aligned}
 T_x &= -\frac{dH_x}{dt} = -h [-\dot{\alpha}_2 \cos \alpha_2 + \dot{\alpha}_4 \cos \alpha_4] \\
 T_y &= -\frac{dH_y}{dt} = -h [-\dot{\alpha}_1 \sin \alpha_1 + \dot{\alpha}_2 \sin \alpha_2 - \dot{\alpha}_3 \sin \alpha_3 + \dot{\alpha}_4 \sin \alpha_4] \\
 T_z &= -\frac{dH_z}{dt} = -h [\dot{\alpha}_1 \cos \alpha_1 - \dot{\alpha}_3 \cos \alpha_3] .
 \end{aligned} \tag{A-27}$$

Equation A-27 can be expressed in matrix form

$$\begin{vmatrix} T_x \\ T_y \\ T_z \end{vmatrix} = -h \begin{vmatrix} 0 & -\cos \alpha_2 & 0 & \cos \alpha_4 \\ -\sin \alpha_1 & \sin \alpha_2 & -\sin \alpha_3 & \sin \alpha_4 \\ \cos \alpha_1 & 0 & -\cos \alpha_3 & 0 \end{vmatrix} \begin{vmatrix} \dot{\alpha}_1 \\ \dot{\alpha}_2 \\ \dot{\alpha}_3 \\ \dot{\alpha}_4 \end{vmatrix} \tag{A-28}$$

For this configuration a very simple constant gain steering law can be used. One form of this steering law for gimbal rate commanded control is

$$\begin{vmatrix} \dot{\alpha}_1 \\ \dot{\alpha}_2 \\ \dot{\alpha}_3 \\ \dot{\alpha}_4 \end{vmatrix} = \begin{vmatrix} 0 & -\frac{1}{2\sqrt{2}} & \frac{1}{\sqrt{2}} \\ -\frac{1}{\sqrt{2}} & \frac{1}{2\sqrt{2}} & 0 \\ 0 & -\frac{1}{2\sqrt{2}} & -\frac{1}{\sqrt{2}} \\ \frac{1}{\sqrt{2}} & \frac{1}{2\sqrt{2}} & 0 \end{vmatrix} \begin{vmatrix} T_{xc} \\ T_{yc} \\ T_{zc} \end{vmatrix} \tag{A-29}$$

where T_{xc} , T_{yc} , and T_{zc} are the torques commanded. These are some function of rate and attitude error of the vehicle. From Equations A-28

and A-29 the reaction torques applied to the vehicle can be expressed as

$$\begin{vmatrix} T_x \\ T_y \\ T_z \end{vmatrix} = \begin{vmatrix} \frac{1}{\sqrt{2}} [\cos \alpha_2 + \cos \alpha_4] & \frac{1}{2\sqrt{2}} [-\cos \alpha_2 + \cos \alpha_4] & 0 \\ \frac{1}{\sqrt{2}} [-\sin \alpha_2 + \sin \alpha_4] & \frac{1}{2\sqrt{2}} [\sin \alpha_1 + \sin \alpha_2 + \sin \alpha_3 + \sin \alpha_4] & \frac{1}{\sqrt{2}} [-\sin \alpha_1 + \sin \alpha_3] \\ 0 & \frac{1}{2\sqrt{2}} [-\cos \alpha_1 + \cos \alpha_3] & \frac{1}{\sqrt{2}} [\cos \alpha_1 + \cos \alpha_3] \end{vmatrix} \begin{vmatrix} T_{xc} \\ T_{yc} \\ T_{zc} \end{vmatrix} \quad (A-30)$$

For $\alpha_1 = \alpha_2 = \alpha_3 = \alpha_4 = 45$ degrees, the matrix of Equation A-30 reduces to an identity matrix and therefore there is no cross coupling for this condition. As disturbance torque acts, the gimbal angles will change and then the above matrix will be cross-coupled. For gimbal angles in the vicinity of 45 degrees the amount of cross coupling is very small. Therefore all the gimbal angles should be set initially at 45 degrees to reduce the matrix of Equation A-26 to an identity matrix; this will eliminate cross coupling for the initial (and reference) gimbal positions.

The maximum storage capability, for a gimbal angle range of ± 60 degrees, occurs along each individual axis as $|H_x| = |H_z| = 1.73 h$ and $|H_y| = h$. For combined axis storage, the capability per axis for a gimbal angle range of ± 80 degrees, is 1.97 h in either the x or z axes and approximately h in the other two axes. Thus the minimum storage capability in any axis is greater than or equal to h; i. e.,

$$H_x = H_y = H_z \geq h.$$

Therefore the value of h required is 100 ft-lbf-sec.

The weight of one CMG of 100 ft-lbf-sec momentum capability is 45 lbm. The power required by one CMG is 13 watts (average and 52 watts (peak) (Refs. A-2, A-3). For a system of four CMGs the total weight is then 180 lbm and the power required is 52 watts (average) and 208 watts (peak).

REFERENCES - APPENDIX A

- A-1. Weidner, Don K., ed., "Natural Environment Criteria for the NASA Space Station Program", NASA Technical Memorandum, NASA TMX-53865, October 32, 1969
- A-2. Nichol, K. C., "Research and Investigation on Satellite Attitude Control - Part I" and "Investigation of Space Vehicle Attitude Control Techniques - Part II", Technical Report AFFDL-TR-64-168, Air Force Flight Dynamics Laboratory, Wright Patterson Air Force Base, Ohio, March 1965
- A-3. Steputis, Fred J., "Advanced Astronomy Mission Concepts - Volume III", Subsystem Design, Martin Marietta Corporation Denver, Colorado, April 1969